A Multimodal Approach to Identify Asbestos and Characterise Clinically Relevant Mesothelioma Biomarkers

Oana Maria Voloacă

A thesis submitted in partial fulfilment of the requirements of Sheffield Hallam University for the degree of Doctor of Philosophy

May 2022

Candidate Declaration

I hereby declare that:

- I have not been enrolled for another award of the University, or other academic or professional organisation, whilst undertaking my research degree.
- None of the material contained in the thesis has been used in any other submission for an academic award.
- I am aware of and understand the University's policy on plagiarism and certify that this thesis is my own work. The use of all published or other sources of material consulted have been properly and fully acknowledged.
- The work undertaken towards the thesis has been conducted in accordance with the SHU Principles of Integrity in Research and the SHU Research Ethics Policy. The LA-ICP-TOFMS data presented in Chapter 4 and 5 were obtained through acquisition carried out by Mr Calum Greenhalgh at NU Instrument Laboratories, Wrexham, UK. The LA-ICP-TOFMS analysis of tissue sections presented in Chapter 6 was performed by Dr Sarah Theiner, Department of Analytical Chemistry, University of Vienna, Vienna, Austria. I played a major role in the preparation and execution of the experiment, sample preparation, and data analysis. Interpretation of the results represents my own work.

The word count of the thesis is 50,814.

Name	Oana Maria Voloacă
Award	PhD
Date of Submission	6th of May 2022
Faculty	Health and Wellbeing
Director(s) of Studies	Dr Sarah Haywood-Small

Acknowledgements

I would like to extend my gratitude to everyone that has been by my side and influenced my PhD journey throughout the past years. It's been an amazing opportunity, with highs and lows, laughter and tears. I have made lifelong friendships, gathered some of the best memories of my life and, despite the challenges, I wholeheartedly enjoyed it.

I would particularly like to thank my Director of Studies, Dr Sarah Haywood-Small, for believing in me and giving me the opportunity to pursue this project. Thank you for your encouragement, support, care for my well-being, and all the memories created together. Additionally, I would like to thank the rest of my team, Prof Malcolm Clench and Dr Laura Cole, for sharing your knowledge with me over the years, and for being there whenever I needed support and reassurance.

A special thanks to Dr Mel Lacey and Dr Nikki Jordan-Mahy for instilling my passion for research and encouraging me to apply for this project. With that, I would also like to extend my thanks to Dr Catherine Duckett, who has been an amazing "Friendly PGRT" that saved the day on multiple occasions. Thank you for always listening to my needs and trying your best to help, even beyond your role as a PGRT. I would also like to thank Dr Sue Campbell, who has been a great support in the last few months. The folks in the BMRC are lucky to have you as their PGRT.

I would like to offer a special mention to the charity that has funded this project, The June Hancock Mesothelioma Research Fund, and to all the people involved with the charity, some that I had the pleasure of meeting over the years. I would like to give a special mention to Kate and Kimberley. Your work is truly remarkable. Deep inside I like to believe that together we're making June proud.

I would also like to thank my collaborators. This has truly been a collaborative effort and for that I am grateful. I would like to mention here Dr Amy Managh, Calum Greenhalgh, Dr Gunda Koellensperger, and last but not least Dr Sarah Theiner. I am so grateful I got to work with each and every one of you and I am

so happy I got to meet you personally, Sarah. Calum, thank you for sharing your ICP, badminton, music, and Thai food knowledge with me. I thoroughly enjoyed my time in Loughborough.

Thank you to everyone in the BMRC, staff members, PhD students, and technical team. You are all a great bunch of people, always willing to help. I would like to give a special mention to Paul, for always checking in on me and making sure my head is in the right place. You're one of the kindest people I have met, and I am lucky to have met you. With that, I would like to thank Joe and Josh, my MS troopers, Filipe, Katie, and Alex, for sharing your knowledge with me whenever I needed help. Alex, thanks for spending hours guiding me through those montages. Let's never have to do that again. To the rest of the BMRC crew, thanks for all the Pub Fridays, weird lunch stories, office banter, nights out in Gatsby's (and beyond) and for making life as a PhD student truly special.

To my BMRC Team that started this journey with me, thank you for all these years. We were definitely one of the best groups and I am looking forward to seeing how successful you all become. A special thanks to my girls, Lucy, Paula, Katie, and Sonia. You were always there for me and helped me through some of the hardest times in my life and for that I am grateful. You are all very special to me and I will cherish the memories that we made forever.

A big thank you to all my lovely people from back home, who continuously supported me and made me feel appreciated. Ovidiu, so proud to call you my best friend. I know you'll always have my back, and I am immensely grateful for having you in my life. Andra, I am so glad we reconnected and thank you for being one of my closest friends. Andrada, thank you for being so proud of me and for sticking around all these years. Florin, who would have thought you will become such an important part of my life. Thank you so much for everything, for guiding me to a better self and helping me find a solution to any challenge, for listening to me complain about this PhD one too many times, and for making me smile through everything.

To my family, you are everything to me. Thank you to my older brother, George. I am so lucky to always have someone look out for me no matter what. I am thankful for the time spent together over the last year and for your help during this PhD. Finally, I would like to thank my wonderful parents. Your sacrifices paved the way to my successes, and I will never be able to thank you enough for everything that you have done for us. All I can do is continue to love you endlessly and make you proud.

Abstract

Malignant mesothelioma (MM) is an aggressive cancer of the mesothelium, with long latency and poor overall survival (OS), associated with occupational and environmental exposure to asbestos and other mineral fibres (MF). Considering that early diagnosis has been linked to an improvement in prognosis and treatment response, there is an urgent need for reliable MM biomarkers. Additionally, current asbestos identification techniques lack sensitivity and fail to detect shorter fibres or fibre fragments. Accurately identifying MF within MM samples is not only essential in aiding early diagnosis, but it also plays a key role in linking this diagnosis to asbestos exposure, which has high implications in legal, social, and political matters. The aim of the current project is to (1) develop MM cellular models suitable for laser ablation inductively coupled plasma mass spectrometry (LA-ICP-MS) imaging, (2) identify various MF based on their metal content within MM *in vitro* models as well as patient samples using a combination of LA-ICP-MS and LA-ICP-time of flight (TOF)MS instrumentation, (3) investigate the MM metallome in human tissue samples using LA-ICP-MS elemental mapping, and (4) characterise a panel of emerging MM biomarkers using a multi-modal approach.

For the first time, this study has developed an asbestos detection technique using LA-ICP-MS imaging to identify MF within MM samples. High-resolution and high-speed analysis suggests that LA-ICP-MS imaging has the potential to be ultimately integrated in the clinical workflow to aid the identification of patients at an earlier and more treatable stage to improve survival outcomes. Moreover, the selected panel of biomarkers was characterised in cellular models, whilst novel biomarkers were tentatively identified using matrix assisted laser desorption ionisation (MALDI)-MS imaging of tissue microarrays, setting the basis for vital future investigations, and ultimately supporting MM biomarker discovery, early diagnosis, and improved prognosis.

Contents

List of Figures……..……i

List of Tables ……..…xxvi

Abbreviations……...xxx

Chapter 1 Introduction 1

1.1 Introduction to Cancer 2

1.2 Introduction to Mesothelioma 4

1.2.1 Mesothelioma overview 4

1.2.2 Mesothelioma demographics 4

1.2.3 Mesothelioma classification and staging.....7

1.2.4 Histologic subtyping of mesothelioma.....10

1.2.5 Clinical presentation.....11

1.2.6 Diagnosis workflow and current challenges 12

1.2.7 Disease monitoring and treatment strategies.....13

1.2.8 Considerations for MPM pathogenesis 14

1.2.9 Genomics of mesothelioma 20

1.3 Mineral fibres.....25

1.3.1 History of asbestos 25

1.3.2 Types of mineral fibres.....25

1.3.3 Methods of detecting asbestos and other mineral fibres in biological samples 33

1.4 Introduction to analytical techniques 35

1.4.1 Basics of mass spectrometry 35

1.4.2 LA-ICP-MS Imaging 39

1.4.3 MALDI-MS Imaging 41

1.5 Emerging mesothelioma biomarkers 42

1.6 Aims, Objectives, and Hypothesis of the Study 50

Chapter 2 Materials and Methods 52

2.1 Materials 53

2.1.1 Chemical reagents 53

2.1.2 Cell lines 54

2.1.3 Human tissues 55

2.1.4 Antibodies and isotype controls 56

2.1.5 Mineral fibres 58

2.2 Methods 58

2.2.1 Mammalian cell culture 58

2.2.2 Mineral fibres 60

2.2.3 The effect of mineral fibres on monolayer integrity and confluency 61

2.2.4 Sample preparation and optimisation for LA-ICP-MS analysis 65

2.2.5 LA-ICP-MS analysis of 2D monolayers 67

2.2.6 Development of a 3D model 70

2.2.7 LA-ICP-MS analysis of 3D cell-plugs sections 72

2.2.8 LA-ICP-MS analysis of frozen human tissues 75

2.2.9 Tissue histology 79

2.2.10 Biomarker characterisation 80

2.2.11 MALDI-MS imaging of TMAs 83

Chapter 3 Optimisation of Cell Density, Viability and Mineral Fibres Treatment 86

3.1 Introduction 87

3.1.1 Introduction to the chapter 87

3.1.2 Hypothesis 90

3.1.3 Aims of the chapter 90

3.2 Results and Discussion 90

3.2.1 Asbestos and other mineral fibres 90

3.2.2 The Effect of mineral fibres on immortalised cells 95

3.3 Conclusion 120

Chapter 4 LA-ICP-MS Imaging of Human Mesothelioma Cell Lines 122

4.1 Introduction 123

4.1.1 Introduction to the chapter 123

4.1.2 Hypothesis 127

4.1.3 Aims 127

4.2 Results and Discussion 128

4.2.1 Optimisation of mineral fibre dose for LA-ICP-MS (Instrument 1) ... 128

4.2.2 Optimisation of laser parameters for LA-ICP-MS analysis 129

4.2.3 Single-element detection of asbestos fibres 131

4.2.4 Multi-elemental LA-ICP-MSI of single mineral fibres in 2D mesothelioma models 135

4.2.5 LA-ICP-TOFMS (Instrument 2) imaging of single mineral fibres in 2D malignant pleural mesothelioma models 146

4.3 Conclusion 158

Chapter 5 LA-ICP-MS Imaging of 3D Malignant Pleural Mesothelioma Models 161

5.1 Introduction 162

5.1.1 Introduction to the chapter 162

5.1.2 Hypothesis 166

5.1.3 Aims of the chapter 166

5.2 Results and Discussion 167

5.2.1 Development of a 3D mesothelioma model 167

5.2.2 Histology of MPM cell plugs 171

5.2.3 The Impact of laser fluence 173

5.2.4 LA-ICP-MS serial ablation 174

5.2.5 The link between spot size, signal intensity, and time of acquisition 177

5.2.6 Treatment and dose optimisation....183
5.2.7 Multi-elemental LA-ICP-MS analysis....184
5.2.8 Blind sample classification using LA-ICP-TOFMS imaging....193
5.3 Conclusion....196
Chapter 6 Multimodal LA-ICP-MS Imaging of Human Mesothelioma Tissues 200
6.1 Introduction....201
6.1.1 Introduction to the chapter....201
6.1.2 Hypothesis....208
6.1.3 Aims of the chapter....208
6.2 Results and Discussion....208
6.2.1 Tissue architecture and histology....208
6.2.2 High-resolution, single element LA-ICP-MS analysis (Instrument 1) 215
6.2.3 Analysis of human MPM tissues by LA-ICP single-quad system (Instrument 3) 217
6.2.4 Analysis of human MPM tissues by LA-ICP triple-quad MS system (Instrument 4) 221
6.2.5 Analysis of human MPM tissues by LA-ICP-TOFMS (Instrument 5) 235
6.3 Conclusion....251
Chapter 7 Multimodal Biomarker Characterisation in Malignant Mesothelioma 256
7.1 Introduction....257

7.1.1 Introduction to the chapter 257

7.1.2 Hypothesis 258

7.1.3 Aims of the chapter 259

7.2 Results and Discussion 259

7.2.1 Biomarker characterisation using flow cytometry 259

7.2.2 Biomarker characterisation and localisation 262

7.2.3 Biomarker discovery using MALDI-MS imaging 271

7.3 Conclusion and future perspectives 286

Chapter 8 Conclusion 289

8.1 Overview 290

8.2 Asbestos and MF detection in cellular models using LA-ICP-MS imaging 290

8.3 Asbestos and MF detection in human tissues samples using LA-ICP-MSI 292

8.4 Characterisation of MPM metallome based on LA-ICP-MSI of human mesothelioma tissues 293

8.5 Multi-modal characterisation of emerging biomarkers 293

8.6 Future directions 294

8.7 Concluding remarks 295

References.....297

Appendix.....347

List of Figures

Figure 1.1 Mesothelioma annual deaths for Great Britain, as of 2021. Data made available by HSE.gov.uk (Mesothelioma statistics for Great Britain, 2021). Data for 2019 are provisional. Note that although some deaths that occurred in 2019 were registered later due to the first wave of the SARS-CoV-2 (COVID-19) pandemic in 2020, the number of late registrations by March 2021 (the cut-off for inclusion in these statistics) was similar to the number expected based on patterns of late registrations in previous years. 5

Figure 1.2 Mesothelioma annual deaths (1980-2018) and predicted future deaths to 2040 in Great Britain. Lower and upper prediction intervals included. Data made available by HSE.gov.uk (Mesothelioma statistics for Great Britain, 2021). 6

Figure 1.3 UK deaths from pleural mesothelioma compared with other lung diseases, 2012. Pie chart based on data published by British Lung Foundation (Mesothelioma statistics). Percentages shown for top 3 pathologies with highest mortality (*i.e.,* lung cancer, pneumonia, and chronic obstructive pulmonary disease (COPD)). 7

Figure 1.4 Schematic diagram of MPM staging system (I-IV). Figure adapted from Mesothelioma.com. Stage I – the cancer is contained on a single layer of the pleura; Stage II- the tumour has now reached the lymph node and has expanded to the lung; Stage III- the cancer spread into the organs nearby; Stage IV- tumour has metastasised to the chest, neck, abdomen, and bones (Berzenji *et al.*, 2018). 10

Figure 1.5 Histologic subtyping of mesothelioma. Histology images adapted from (Galateau-Salle *et al.*, 2016). The main mesothelioma subtypes are epithelioid (53-70%), biphasic (12-27%), and sarcomatoid (11-19%). Percentages may vary based on various studies and reports, with epithelioid always being the most common one and sarcomatoid the least common mesothelioma subtype. 11

Figure 1.6 Schematic diagram of main components and events linked to inflammatory pathways in mesothelioma. Diagram adapted from Sayan & Mossman, (2015). After MF exposure, the fibres get internalised into the cells causing ROS, that trigger NALP3 inflammasome and caspase-1 activation. Once caspase-1 is activated, IL-1β and IL-18 get matured and released. NALP3 Inflammasome also induces caspase-1 pyroptosis (apoptotic and necrotic cell death). This in turn leads to release of other mediators such as IL-1α and high-mobility group box 1 protein (HMGB1). All together, these chemokines and cytokines drive chronic inflammation associated with pathogenic events in fibre associated diseases (lung cancer, mesothelioma, pulmonary fibrosis, and other asbestos-related diseases) (Sayan & Mossman, 2015). 16

Figure 1.7 The HMGB1 role in MPM development. Figure adapted from (Carbone & Yang, 2012). MF are embedded within the HMC of the pleura, causing necrotic cell death and the release of HMGB1 into the extracellular space. Subsequently, the NALP3 inflammasome gets activated which induces the caspase-1 cascade to secrete IL-1β, eliciting macrophages thus triggering an inflammatory response and secreting TNF-α. The combination of the two cytokines promotes survival of asbestos-damaged HMCs and allows transformation to mesothelioma (Carbone & Yang, 2012). 18

Figure 1.8 The EMT in the development of MPM. Figure adapted from (Ramundo *et al.*, 2021). RNS- reactive nitrogen species; ZEB- Zinc finger E-box binding homeobox; TGF-β- Transforming growth factor beta; TNF-α- Tumour necrosis factor α. Asbestos fibres induce chronic inflammation, the release of growth factors and cytokines, and oxidative stress. These processes impact the levels of certain transcription factors and miRNAs, leading to EMT and malignant cell transformation. 20

Figure 1.9 Genetic alterations potentially involved in MM pathogenesis. Figure adapted from (McCambridge *et al.*, 2018). *NF2* encodes the Merlin protein, a key regulator of the Hippo pathway. Mutated *NF2* leads to inactivation of the Hippo pathway and cell proliferation and survival through YAP1 activation. Additionally, inactivation of *NF2* results in FAK hyperactivation, which subsequently impacts

on essential cellular events. Defatinib, a FAK inhibitor is a potential MM cytotoxic drug. Phosphatase and tensin homolog gene (*PTEN*) negatively regulate phosphoinositide 3-kinase (PI3K)/AKT pathway. Loss of *PTEN* function leads to overactivation of PI3K/AKT pathway leading to cell growth and proliferation. Mutated *BAP1* results in activation of the enhancer of zeste 2 polycomb repressive complex 2 subunit (EZH2), which in turn leads to trimethylation of histone 3 lysine 27 (H3K27) and consequently to malignant transformation. *CDKN2A* encodes p16INK4A and p14ARF. p16INK4A is fundamental in hyperphosphorylation and subsequent inhibition of the retinoblastoma pathway, essential in cell cycle progression. When p14ARF is inactivated, MDM2 levels increase. Increased production of MDM2 negatively regulates p53 production and results in increased cell survival. Similarly, loss of p53 can be caused by a mutation in TP53 gene, which encodes for this tumour suppressor protein (McCambridge *et al.*, 2018). 24

Figure 1.10 Schematic of a magnetic sector field mass analysers. The SF uses magnetic field to separate ions of different *m/z* values. Firstly, a high voltage is applied to the ions to accelerate them into the magnetic sector. A continuous ion source is generated and supplied from the ionisation unit to the magnetic sector. The ions are exposed to the magnetic field and subsequently deflected according to Fleming's left-hand rule (*i.e.,* deflections differ based on the *m/z* where lighter ions (of the same charge) will experience more deflection). As the direction of the ion changes, a centrifugal force (f2) acts on the ion. For the ions to pass through the magnetic field region and reach the detector, it must travel along a curved path of a given radius (r) where f1 and f2 are balanced. By keeping the ion acceleration voltage V constant and varying the magnetic flux B (or keeping B constant and varying V), a detector placed on the corresponding path radius r could detect any mass m. Figure adapted from Technologynetworks. 37

Figure 1.11 Schematic of a quadrupole mass analyser. The quadrupole contains four parallel cylindrical metal rods (electrodes with a hyperboloidal interior surface) inside a vacuum chamber, positioned equidistant from the centre axis. Both a direct current (D.C.) and high frequency alternating current (AC) are

applied to the quadrupole, so that only the ions with the target *m/z* successfully pass and get to the detector. The quantity of ions that reach the detector is measured as signal intensity. The ions pass through a tiny orifice and enter the quadrupole where a voltage of the same polarity is applied to diagonally opposite poles and opposite voltage polarity is applied to adjacent poles. When a combination of the DC voltage and high-frequency AC voltage is applied to each pole, an electric field with a rapidly varying phase is generated within the quadrupole. Figure adapted Creative-proteomics. 37

Figure 1.12 Schematic of a TOF mass analyser. The TOF MS is a simple construction, consisting of an accelerator, a field-free region, a reflectron and detector inside a high vacuum chamber called a flight tube. In brief, it separates and detects ions of different *m/z* by measuring the time taken for the ions to travel through a field-free region. Ions generated in an ionisation unit are accumulated and introduced in pulses to a flight tube, and then accelerated by applying a high acceleration voltage between the electrodes. Given a constant acceleration voltage as well as kinetic energy, each ion flies at its unique velocity inside the flight tube to reach the ion detector, which is higher for ions with smaller masses and lower for ions with larger masses. Figure adapted from Shimadzu. 38

Figure 1.13 Schematic diagram of a typical LA-ICP-MS set-up. The components include (1) laser source (2) aerosol transport, (3) atomisation, vaporisation, and ionisation of the aerosols in the ICP torch, (4) mass analyser and (5) detection and data output. Figure adapted from Barbosa & Sussulini (2020).....41

Figure 1.14 Schematic diagram of a typical MALDI-MS set-up. The main components are (1) ionisation source, where molecules within the sample are ionised, (2) mass analyser, where ions are separated by their mass to charge ratio, figure includes the SYNAPT G2 HDMS arrangement (3) detector, for the measurement of ion relative abundance, resulting then in (4) a mass spectrum. There is also a data system connected to the instrument, which includes computer and software, for the acquisition and processing of data derived from MS (not shown in the diagram). 42

Figure 2.1 Layout of a 96-well plate used for the RealTime-Glo™ Annexin V Apoptosis and Necrosis Assay. Different cell lines were typically seeded in rows B-D to row E-G.....64

Figure 3.1 MF stock solutions. (A-E) MF decanted at the bottom of the glassware. (F-J) MF mixed in the PBS solution. (A, F) Actinolite; (B, G) Amosite- brown asbestos; (C, H) Chrysotile-white asbestos; (D, I) Crocidolite- blue asbestos; (E, J) Wollastonite- non-asbestiform control. Note the differences in density between different types of MF. 92

Figure 3.2 Brightfield images of the MF in PBS solution. The physical properties of each individual fibre type can be noted in the close-up images. Scale bars: top row 1000 µm, bottom row 500 µm. 93

Figure 3.3 Different range of concentration for each individual fibre type. The physical properties of the mineral fibres can be noted in the brightfield images. Representative of at least 3 fields of view. Scale bar- 1000 µm.....94

Figure 3.4 NCI-H28 cells treated with actinolite fibres (0-25 µg /mL) after 24h, 48h, and 72h of exposure. The cell monolayers show no changes to low concentrations of actinolite after 24h and 48h. Non-viable cells are more visible at higher concentrations after 72h. Representative images of at least 3 fields of view. Positive control- staurosporine (10 µM); Vehicle control- PBS; Scale bar- 1000 µm. 96

Figure 3.5 MSTO-211H cells treated with actinolite fibres (0-25 µg /mL) after 24h, 48h, and 72h of exposure. Cell death is apparent after 24h, even at lower concentrations. At high concentrations the cells appear to be completely non-viable, clumping around the actinolite fibres. Representative images of at least 3 fields of view. Positive control- staurosporine (10 µM); Vehicle control- PBS; Scale bar 1000 µm. 97

Figure 3.6 MSTO-211H, NCI-H28, and NCI-H1975 cells metabolic activity following exposure to actinolite fibres represented by fluorescent intensity counts. Data were normalised against vehicle control, and it was considered significantly

different compared with the vehicle control by two-way ANOVA analysis (n=9), followed by a Dunnett test for multiple comparisons to a control. The link between fibre type, dose, and exposure time and cellular viability. *p between 0.01 and 0.04; **p< 0.01; ****p<0.0001; ns- not significant. 101

Figure 3.7 NCI-H28, MSTO-211H, and NCI-H1975 cells metabolic activity following exposure to MF represented by fluorescent intensity counts. Data recorded after 24, 48, and 72 hours of MF exposure. Data were normalised against vehicle control, and it was considered significantly different compared with the vehicle control by one-way ANOVA analysis (n=9), followed by a Geisser-Greenhouse correction to adjust for the lack of sphericity of data, followed by a Dunnett test for multiple comparisons to a control. Error bars n=9 from 3 independent experiments. *p between 0.01 and 0.04; **p< 0.01; ****p<0.0001; ns- not significant. 104

Figure 3.8 NCI-H28 cells treated with different MF (3-12 µg /mL) for 24h. Limited cell death was induced by the fibres, with the exception of high doses of amosite and chrysotile. Representative images of at least 3 fields of view. Positive control- staurosporine (10 µM); Negative control- RPMI media; Vehicle control- PBS; Scale bar- 1000 µm. 106

Figure 3.9 NCI-H28 cells treated with different MF (3-12 µg /mL) for 7 days. Confluent monolayers can be noted for most of the treatments, with the exception of the cells treated with chrysotile (high dose). Some cellular clumping can also be noted for the monolayers exposed to amosite fibres (high dose). Representative images of at least 3 fields of view. Positive control- staurosporine (10 µM); Negative control- RPMI media; Vehicle control- PBS; Scale bar- 1000 µm. 107

Figure 3.10 MSTO-211H cells treated with different MF (3-12 µg /mL) for 24h. Amosite and chrysotile fibres induced the highest levels of cell death, especially for higher doses. Representative images of at least 3 fields of view. Positive control- staurosporine (10 µM); Negative control- RPMI media; Vehicle control- PBS; Scale bar- 1000 µm. 109

Figure 3.11 MSTO-211H cells treated with different MF (3-12 µg /mL) for 7 days. High confluency with limited cell death was noted for the non-asbestiform control, wollastonite. High levels of cell death can be noted after treatment with actinolite, amosite, and chrysotile (medium/ high doses). Representative images of at least 3 fields of view. Positive control- staurosporine (10 µM); Negative control- RPMI media; Vehicle control- PBS; Scale bar- 1000 µm. 110

Figure 3.12 Met-5A cells treated with different MF (3-12 µg /mL) for 24h. Fibres appeared to have a limited effect on the cells. Representative images of at least 3 fields of view. Positive control- staurosporine (10 µM); Negative control- RPMI media; Vehicle control- PBS; Scale bar- 1000 µm. 112

Figure 3.13 Met-5A cells treated with different MF (3-12 µg /mL) for 7 days. Amosite and chrysotile fibres induced high levels of cell death, proportional with fibre concentration. Representative images of at least 3 fields of view. Positive control- staurosporine (10 µM); Negative control- RPMI media; Vehicle control- PBS; Scale bar- 1000 µm. 113

Figure 3.14 MSTO-211H real-time apoptosis (luminescence) and necrosis (fluroscence) levels over 72h. The data were recorded every 2 hours. Statistical analysis two-way ANOVA, followed by a Dunett comparison test for multiple variables. Significance $p<0.05$ between vehicle control and MF treated experimental groups. 115

Figure 3.15 NCI-H28 real-time apoptosis (luminescence) and necrosis (fluroscence) levels over 72h. The data were recorded every 2 hours. Statistical analysis two-way ANOVA, followed by a Dunett comparison test for multiple variables. Significance $p<0.05$ between vehicle control and MF treated experimental groups. 117

Figure 3.16 Met-5A real-time apoptosis (luminescence) and necrosis (fluroscence) levels over 72h. The data were recorded every 2 hours. Statistical analysis two-way ANOVA, followed by a Dunett comparison test for multiple variables. Significance $p<0.05$ 119

Figure 4.1 Actinolite dose titration in 2D cell cultures. (A) 12 µg/ mL, (B) 6 µg/ mL. (C) 3 µg/ mL. Data is presented as ^{24}Mg signal/ counts. Areas with actinolite fibres visible using basic optical microscopy were selected for proof-of-concept. The laser parameters were: spot diameter of 2 µm, 20 Hz repetition frequency, 40 µm s^{-1} scan speed.....129

Figure 4.2 Spot size optimisation. (A) Detection of actinolite fibres within NCI-H28 cells based on the high Mg content using a spot size of 2 µm. The total time of acquisition was ~30 min for a 200 x 200 µm sample area. (B) Detection of actinolite fibres within NCI-H28 cells based on the high Mg content in the fibres using a spot size of 1 µm. The time of acquisition nearly doubled. 131

Figure 4.3 Detection of malignant mesothelioma based on magnesium content. **(**A) Light microscopy image of the NCI-H28 cells. (B) LA-ICP-MS image corresponding to the same area based on the Mg content in the cells. 131

Figure 4.4 Detection of crocidolite based on magnesium content. (A) Light microscopy image showing a long crocidolite fibre within a mesothelioma cell. (B) LA-ICP-MS image of the same area based on the Mg content in the sample. Note the crocidolite fibres fragments engulfed by the cells that were not visible with light microscopy. (C) LA-ICP-MS image of the same area normalised against the cellular background by increasing the intensity bar.....132

Figure 4.5 Detection of chrysotile based on magnesium content. (A) Light microscopy image showing the long, curly specific appearance of chrysotile fibres prior to ablation. (B) LA-ICP-MS image formed based on the high Mg content in the sample. Note how the chrysotile fibres maintain their shape and the extra fibre fragments within the mesothelioma cells that were not noticeable in the optical image. (C) LA-ICP-MS image of the same area normalised against the cellular background by increasing the intensity bar showing only the signal gave by the chrysotile fibres and fibre fragments. 133

Figure 4.6 Detection of amosite based on magnesium content. **(**A) Light microscopy image showing the coarse, needle-like amosite fibres prior to

ablation. (B) LA-ICP-MS image formed based on the high Mg content in the sample. Small amosite fragments can be easily identified using this technique. (C) LA-ICP-MS image of the same area normalised against the cellular background by increasing the intensity bar showing only the signal gave by the amosite fibres and fibre fragments. 134

Figure 4.7 Detection of actinolite based on magnesium content. (A) Light microscopy image showing the elongated, flattened actinolite fibres prior to ablation. (B) LA-ICP-MS image formed based on the high Mg content in the sample. Numerous actinolite fragments are present withing the cells. (C) LA-ICP-MS image of the same area normalised against the cellular background by increasing the intensity bar showing only the signal gave by the actinolite fibres and fibre fragments. 135

Figure 4.8 NCI-H28 cells cultured in a fibre free environment. A, D & G- Microscope perspective of the areas prior to ablation. B, E & H- Elemental distribution as analysed by LA-ICP-MSI. Intensity bar was adjusted in the right hand-side column to normalise against the cellular background (C, F & I). B & C- show the low ^{57}Fe distribution within the mesothelioma cells. High ^{24}Mg intensity counts are presented in E & F, whereas H & I show the significantly low overall ^{29}Si content in NCI-H28 cells. 137

Figure 4.9 NCI-H28 monolayer cultured with chrysotile. A, D & G- Microscope perspective of the areas prior to ablation. Areas with fibres visible using optical microscopy were selected for proof of concept. Note the physical aspect of the fibres typical to chrysotile. B, E & H- Elemental distribution as analysed by LA-ICP-MSI. Intensity bar was adjusted in the right hand-side column to normalise against the cellular background (C, F & I). B & C show the low ^{57}Fe distribution within the sample. Chrysotile is known for its limited iron content, and this is reflected in the metal counts. E & F present the relatively high ^{24}Mg intensity signal in the fibres visible in microscope images, as well as smaller fragments within the cell layer that could not be seen initially. H & I present the ^{29}Si distribution within the matrix and chrysotile fibres. LA-ICP-MS preserves the curly shapes of the chrysotile fibrils. 139

Figure 4.10 NCI-H28 cells cultured with amosite fibres. A, D & G- Microscope perspective of the areas prior to ablation. Areas with fibres visible using optical microscopy were selected for proof of concept. B, E & H- Elemental distribution as analysed by LA-ICP-MSI. Intensity bar was adjusted in the right hand-side column to normalise against the cellular background (C, F & I). As expected, higher ^{57}Fe distribution is presented in B & C compared to serpentine fibres. Note the shorter fibres and fibre amosite fibre fragments spread all over the sample as shown using LA-ICP-MSI. ^{24}Mg counts within the sample are shown in E & F. Note the engulfed amosite fibres not visible in the microscopic image. H& I show ^{29}Si distribution within the matrix and amosite fibres. 141

Figure 4.11 NCI-H28 cells cultured with crocidolite fibres. A, D & G- Microscope perspective of the areas prior to ablation. Areas with fibres visible using optical microscopy were selected for proof of concept. B, E & H- Elemental distribution as analysed by LA-ICP-MSI. Intensity bar was adjusted in the right hand-side column to normalise against the cellular background (C, F & I). The highest ^{57}Fe concentration is presented in B & C which coincides with the nominal composition of crocidolite. ^{24}Mg counts can be seen in E & F. Hardly any fibres can be seen in the corresponding microscopic images. The LA-ICP-MS images offer information beneath the cellular layer, exposing the crocidolite fibres based on ^{29}Si content (H& I). 142

Figure 4.12 NCI-H28 cells cultured with actinolite fibres. A, D & G- Microscope perspective of the areas prior to ablation. Areas with fibres visible using optical microscopy were selected for proof of concept. B, E & H- Elemental distribution as analysed by LA-ICP-MSI. Intensity bar was adjusted in the right hand-side column to normalise against the cellular background (C, F & I). The high concentration of ^{57}Fe within the actinolite structure allows for detection of multiple elongated fibres and fibre fragments within the sample (B & C). E & F show the ^{24}Mg counts within the sample. Note the actinolite fibres not visible in the microscopic image. H & I present ^{29}Si distribution within the matrix and the fibres. Overall, the normalised images on the right-hand side column confirm that the

number of fibres within the samples is significantly higher than presented in the optical images. 144

Figure 4.13 NCI-H28 cells cultured with a non-asbestiform control, wollastonite. A, D & G- Microscope perspective of the areas prior to ablation. Areas with fibres visible using optical microscopy were selected for proof of concept. B, E & H- Elemental distribution as analysed by LA-ICP-MSI. Intensity bar was adjusted in the right hand-side column to normalise against the cellular background (C, F & I). No significant ^{57}Fe and ^{24}Mg signals were given by the wollastonite fibres (B, C, E & F). On the other hand, wollastonite is a silicate and was therefore expected to be identified based on the ^{29}Si content. This is shown in H & I where the ^{29}Si distribution corresponds to the wollastonite fibres visible in the optical image on the left. 145

Figure 4.14 Elemental mapping of actinolite. A 400 × 200 µm sample area of MSTO-211H cells spiked with actinolite was ablated. (A) Fibres are visible as dark needle shaped objects in the microscopic image. (B-F) LA-ICP-MS images of the ^{24}Mg, ^{23}Na, ^{28}Si, ^{40}Ca, and ^{56}Fe distribution within the actinolite fibres and cell matrix are shown in panels. As expected, actinolite fibres yielded values for all the elements, but sodium. 148

Figure 4.15 Elemental mapping of actinolite. A 400 × 200 µm sample area of MSTO-211H cells spiked with actinolite was ablated. (A) Fibres are visible as dark needle shaped objects in the microscopic image. (B-F) LA-ICP-MS images of the ^{39}K, ^{31}P, ^{27}Al, ^{55}Mn, and ^{48}Ti distribution within the actinolite fibres and cell matrix are shown in panels. No significant signal was given by the actinolite fibres for this panel of elements. 149

Figure 4.16 Elemental mapping of amosite. A 400 × 200 µm sample area of MSTO-211H cells spiked with amosite fibres was ablated. (A) Amosite fibres are visible as dark, long foreign bodies or as shorter fibre fragments in the microscopic image. (B-F) LA-ICP-MS images of the ^{24}Mg, ^{23}Na, ^{28}Si, ^{40}Ca, and ^{56}Fe distribution within the actinolite fibres and cell matrix are shown in panels. (E) Analysis of ^{40}Ca expression fails to detect amosite fibres against the cellular

background. (C) Similarly, no amosite fibres can be identified based on the ^{23}Na content. 150

Figure 4.17 Elemental mapping of amosite fibres. A 400 × 200 µm sample area of MSTO-211H cells spiked with amosite was ablated. (A) Amosite fibres are visible as dark, long foreign bodies or as shorter fibre fragments in the microscopic image. (B-F) LA-ICP-MS images of ^{39}K, ^{31}P, ^{27}Al, ^{55}Mn, and ^{48}Ti distribution within the actinolite fibres and cell matrix are shown in panels. Interestingly, the amosite fibres can be identified based on the ^{55}Mn that substitutes into the nominal composition of this amphibole (E). 151

Figure 4.18 Elemental mapping of crocidolite. A 400 × 200 µm sample area of MSTO-211H cells spiked with crocidolite fibres was ablated. (A) Crocidolite fibres can be seen as long, dark fibres with shorter fragments also present. (B-F) LA-ICP-MS images of the ^{24}Mg, ^{23}Na, ^{28}Si, ^{40}Ca, and ^{56}Fe distribution within the actinolite fibres and cell matrix are shown in panels. Multiple shorter fibres and fibre fragments can be identified based on the main components of crocidolite: magnesium, silicon, and iron (B, D, F). Crocidolite also yields signals for ^{23}Na, however the high sodium content in the biological matrix hinders clear detection of individual fibres (C). 153

Figure 4.19 Elemental mapping of crocidolite fibres. A 400 × 200 µm sample area of MSTO-211H cells spiked with crocidolite was ablated. (A) Crocidolite fibres are presented in the microscopic image as long, dark fibres with shorter fragments also present. (B-F) LA-ICP-MS images of the ^{39}K, ^{31}P, ^{27}Al, ^{55}Mn, and ^{48}Ti distribution within the actinolite fibres and cell matrix are shown in panels. No crocidolite fibres can be clearly identified based on these elements. 154

Figure 4.20 Elemental mapping of wollastonite. A 400 × 200 µm sample area of MSTO-211H cells spiked with crocidolite fibres was ablated. Two foreign bodies can be observed in the microscopic image (A). (B-F) LA-ICP-MS images of the ^{24}Mg, ^{23}Na, ^{28}Si, ^{40}Ca, and ^{56}Fe distribution within the actinolite fibres and cell matrix are shown in panels. No Si or Ca content suggests that only the longer

fibre is wollastonite (D, E). The unknown sample impurity yielded high signals of ^{56}Fe (F). 156

Figure 4.21 Elemental mapping of wollastonite. A 400 × 200 µm sample area of MSTO-211H cells spiked with crocidolite fibres was ablated. Two foreign bodies can be observed in the microscopic image (A). (B-F) LA-ICP-MS images of the ^{39}K, ^{31}P, ^{27}Al, ^{55}Mn, and ^{48}Ti distribution within the actinolite fibres and cell matrix are shown in panels. 157

Figure 5.1 Human malignant mesothelioma 3D multicellular spheroids (MCS). Top (A-D) Brightfield microscopy 40X. Down (E-H) Hoechst 33342 and Propidium Iodide staining of the MCS. (A) Brightfield image of an untreated MSTO-211H MCS with a diameter of 873.7 µm. (B) Brightfield image of a MSTO-211H MCS co-cultured with 3 µg/mL actinolite fibres solution with a total diameter of 905.9 µm. (C) Brightfield image of an untreated NCI-H28 MCS with a diameter of 648.0 µm. Human epithelioid mesothelioma cells tend to form smaller, more compact MCS compared to the ones formed by the MSTO-211H biphasic cells. (D) Brightfield image of NCI-H28 cells co-cultured with 3 µg/ mL actinolite fibres solution. The cells and fibres aggregate but fail to form a spherical MCS like the one presented in panel C. Median diameter of the aggregate reaches 675.4 µm. (E-H) present the corresponding fluorescent images after staining with Hoechst 33342 and Propidium Iodide (Texas red- hypoxic core, DAPI blue- viable outer layer). 168

Figure 5.2 Mesothelioma organ-dots. (A) Brightfield images of the 3D organ-dots. (B) Fluorescent imaging following staining with Hoechst 33342 and Propidium Iodide (Texas red- hypoxic core, DAPI blue- viable outer layer). 169

Figure 5.3 Development of a 3D cell-plug. (A-D) Plastic mould used to embed snap frozen cell plugs in HMPC/PVP media. (E-G) Plastic mould used to snap freeze cell pellets spiked with MF into cell plugs. MSTO-211H (H) and NCI-H28 (I) cell plugs embedded in HMPC/PVP media, ready for cryosectioning. The lipid bilayer that forms the cellular membrane confers the slight yellow appearance of the cell plugs within the white opaque embedding media. 171

Figure 5.4 Histological staining of an actinolite treated cell-plug section. A- H&E staining x 40 magnification; B- H&E staining x 200 magnification; C- H&E staining x 400 magnification; D- H&E staining x 400 magnification with actinolite fibres. Actinolite fibres are shown by the dotted circles. 172

Figure 5.5 Optimisation of laser fluence. LA-ICP-MS data acquired with (A) ≈18 J/cm^{-2}, (B) ≈20 J/cm^{-2}, and (C) ≈22 J/cm^{-2}. The scale bar values were adjusted in D-F to emphasise the magnesium signal yielded by the actinolite fibres. Laser energy 45, 50 and 55% respectively. Spot size 2µm. 174

Figure 5.6 Post-ablation brightfield microscopy images of a MSTO-211H cell-plug section. (A) 200 x 200 µm area after LA-ICP-MS analysis of a 20 µm thick section. Note the biological material left post-ablation. (B) 200x 200 µm area after LA-ICP-MS analysis of a 12 µm thick section. The sample was fully ablated in one cycle of analysis. Both samples were ablated using the same laser pulse energy. 175

Figure 5.7 Serial ablation of a MSTO-211H cell-plug section. (A) First ablation of a 200 x 200 µm area. The red square focuses on a smaller area (80 x 80 µm) with no actinolite fibres identified after the first analysis. The images below offer a closer look of the same selected area for each layer. (B) Second ablation of the same section. Note the actinolite fibres present in the same selected smaller area. (C) Third ablation of the cell-plug section. Signal from the actinolite fibres was still registered within the same area, but the signal intensity differs based on the fibre orientation (shown by the red arrows). (D) Final ablation of the section. Some signal yielded by the actinolite fibres was acquired. There was minimum to no signal yielded by the biological matrix at this stage. Laser fluence ≈18 J/cm^{-2}, spot size 2 µm, 20 Hz repetition rate.....176

Figure 5.8 Serial ablation of a NCi-H28 cell-plug section. (A) First ablation of a 200 x 200 µm area. The red square focuses on a smaller area (80 x 80 µm) with identifiable actinolite fibres. The images below offer a closer look of the same selected area for each layer. (B) Second ablation of the same section. Note the ^{24}Mg signal recorded around the same zone, possibly from the same, long fibre.

(C) Third ablation of the cell-plug section. Signal from the actinolite fibre was still registered within the same area, but the signal intensity differs based on the fibre orientation (shown by the red arrows). (D) Final ablation of the section. Minimum to no signal was registered after this cycle of analysis. Laser fluence ≈18 J/cm^{-2}, spot size 2 µm, 20 Hz repetition rate.....177

Figure 5.9 LA-ICP-MS analysis of a 500 x 500 µm area of an actinolite-treated MSTO-211H cell-plug using a 1 µm spot size. (A) Cellular matrix and actinolite ^{24}Mg signal distribution. (B) LA-ICP-MS data normalised against the cellular background to emphasise the signal yielded by the actinolite fibres. The red squares present ROIs containing actinolite fibres. A zoomed in version is presented underneath. Some small actinolite fibres were identified within the compact cell-plug. 179

Figure 5.10 LA-ICP-MS images of a 500 x 500 µm area of an actinolite-treated MSTO-211H cell-plug using a 2 µm spot size. (A) Cellular matrix and actinolite ^{24}Mg signal distribution. (B) LA-ICP-MS data normalised against the cellular background to emphasise the signal yielded by the actinolite fibres. The red squares present ROIs containing actinolite fibres. A zoomed in version is presented underneath. Note the increased signal intensity range indicated by the scale bar (> 10000 ^{24}Mg signal/ counts). 180

Figure 5.11 LA-ICP-MS analysis of a 200 x 200 µm area of an actinolite-treated MSTO-211H cell-plug using a 1 µm spot size. (A) Cellular matrix and actinolite ^{24}Mg signal distribution. (B) LA-ICP-MS data normalised against the cellular background to emphasise the signal yielded by the actinolite fibres. The red squares present ROIs containing actinolite fibres. A zoomed in version is presented underneath. Small actinolite fibres were identified as ^{24}Mg “hot-spots”. 182

Figure 5.12 LA-ICP-MS images of a 200 x 200 µm area of an actinolite-treated MSTO-211H cell-plug using a 2 µm spot size. (A) Cellular matrix and actinolite ^{24}Mg signal distribution. (B) LA-ICP-MS data normalised against the cellular background to emphasise the signal yielded by the actinolite fibres. The red

squares present ROIs containing actinolite fibres. A zoomed in version is presented underneath. Note the increased signal intensity range compared to the figure above indicated by the scale bar (> 15000 ^{24}Mg signal/ counts). 183

Figure 5.13 Mineral fibre dose optimisation based on the LA-ICP-MS analysis. (A) LA-ICP-MS image of a low-dose cell-plug section (30 µL) (B) LA-ICP-MS image of a medium-dose cell-plug section (60 µL). Some ^{24}Mg "hot spots" are present within the cellular background which can indicate the presence of actinolite fragments. (C) LA-ICP-MS image of a high-dose cell-plug section (100 µL). Actinolite fibres can be identified based on the high ^{24}Mg signal. 184

Figure 5.14 LA-ICP-MSI of a MSTO-211H cell-plug section. (A) Brightfield image of the 400 x 400 µm ablated area. An artefact can be observed in the brightfield image. No iron signal was recorded from this artefact after analysis (B-C). D-Brightfield image of the 400 x 400 µm ablated area. E- Magnesium distribution following LA-ICP-MS analysis. The scale bar was adjusted in panel C and F for consistency with the rest of the LA-ICP-MS data. 186

Figure 5.15 LA-ICP-MSI of a MSTO-211H cell-plug treated with amosite fibres. (A, D) Brightfield images of the 400 x 400 µm areas prior to ablation. No identifiable amosite fibres present in the optical images. (B) Amosite fibres detected based on the high iron content. (E) Magnesium distribution following LA-ICP-MS analysis. No clear, identifiable amosite fibres are present. (C, F) Signal intensity bar was adjusted to focus on the signal yielded from the fibres. 187

Figure 5.16 LA-ICP-MSI of a MSTO-211H cell-plug treated with crocidolite fibres. (A, D, G) Brightfield images of the 400 x 400 µm areas prior to ablation. No identifiable crocidolite fibres present in the optical images. (B) Crocidolite fibres detected based on the high iron content. (E) Magnesium distribution following LA-ICP-MS analysis. Crocidolite fibres can be seen in the lower part of the image, as well as in the top region, as hot magnesium signal spots. (H) Detection of crocidolite fibres across the ablated area based on high silicon content. (C, F, I) Signal intensity bar was adjusted to focus on the signal yielded from the fibres

and consistency between data. Notably, iron signal appears to be lower than the one yielded by the rest of the asbestiform fibres.....189

Figure 5.17 LA-ICP-MSI of a MSTO-211H cell-plug treated with actinolite fibres. (A, D, G) Brightfield images of the 400 x 400 µm areas prior to ablation. Areas with some identifiable bodies were selected for analysis as ROIs. (B) Actinolite fibres detected based on the iron content. (E) Magnesium distribution following LA-ICP-MS analysis. Actinolite fibres can be identified based on the high content of magnesium. Note the actinolite fibres unidentifiable in the optical image, particularly the central fibre and the cluster from top right corner. (H) Detection of actinolite fibres across the ablated area based on high silicon content. (C, F, I) Signal intensity bar was adjusted to focus on the signal yielded from the fibres and consistency between data.....191

Figure 5.18 LA-ICP-MSI of a MSTO-211H cell-plug treated with wollastonite fibres. (A, D, G) Brightfield images of the 400 x 400 µm areas prior to ablation. Areas with some identifiable bodies were selected for analysis as ROIs. As expected, no signal was recorded for iron detection (C). (E) Magnesium distribution of the biological matrix following LA-ICP-MS analysis. (H) Detection of wollastonite fibres based on the silicon content. No significant signal was recorded. (C, F, I) Signal intensity bar was adjusted for consistency between data across different MF. 193

Figure 5.19 Blind sample classification using LA-ICP-TOFMS imaging. Analysis of the full range of characteristic elements was carried out for the same area (0.75 x 1.50 mm) of a MSTO-211H cell-plug treated with an unknown type of MF. (A) Mg distribution following LA-ICP-TOFMS analysis. One large fibre of approximately 120 µm in length and some smaller fragments of below 50 µm in length can be identified based on the high magnesium content. (B) Si distribution of the sample following analysis. (C) Ca signals across the ablated area. Some signal was given by the cellular matrix. No signal was yielded by the MF. (D) Fe distribution following LA-ICP-TOFMS analysis. Based on the overall elemental signal, the MF were correctly classified as amosite. 195

Figure 6.1 Brightfield images of unstained human MPM tissue sections. (A) Patient 1, pleura; Talc deposits can be observed as black, crystal-like impurities deposited in a linear manner. Red arrow points at a long, thin impurity. (B) Patient 2, chest wall; No significant artefacts are present in this section. (C) Patient 3, lung; Red arrow indicates a possible asbestos body or cluster, based on typical appearance and size.....212

Figure 6.2 Tissue histology following H&E staining (A-E) and Perls' Prussian Blue staining (F-J). Patient 1&5- pleura; Patient 2- chest wall; Patient 3&4- lung. (A-E) Nuclei are stained purple by the haematoxylin, whilst eosin stains cytoplasm and extracellular matrix pink. (F-J) Nuclei are stained pink with Nuclear Fast Red. The blue staining in panel (A&F) is caused by edge effect. 213

Figure 6.3 H&E staining (A-E) and Perls' Prussian Blue staining (F-J). A- Talc deposits are less visible following H&E staining. (B) Area of fibrosis is highlighted by the intense purple coloration. Traces of oedema can be noted, mainly in the stroma. (C) Mixed mesothelioma, with spindle cells more preeminent at the top region. (E) Desmoplastic growth present in the lower left corner, with areas of aggressive, spindle like cells in the rest of the area. (F) Red arrow points at the talc deposits that did not stain for ferric iron. (H) Possible uncoated asbestos fibres are indicated by the arrow. (I) Coated ferruginous bodies are shown in blue. The size and distribution correspond to asbestos bodies deposition. (J) Possible impurities, smaller fibres might be present.....214

Figure 6.4 (A) Brightfield image of a healthy human lung tissue section layers of the pleura (bottom to top) lung parenchyma, basement membrane, connective tissue, elastic plate, medium subcutaneous, mesothelial cells. (B) Mg distribution within a healthy human lung tissue section determined by LA-ICP-MS analysis. with a 2 µm spot size 1000 x 1000 area 0 µm spacing between lines. 216

Figure 6.5 (A) Brightfield image of a MPM tissue section layer of the pleura. No tissue architecture characteristic to advanced biphasic or sarcomatoid MPM. (B) Mg distribution within a healthy human lung tissue section determined by LA-ICP-

MS analysis with a 2 μm spot size 1000 x 1000 area 0 μm spacing between lines. 217

Figure 6.6 LA-ICP-MSI of two distinct areas of MPM tissue from Patient 1 (P1). (B-E) Elemental distribution of ^{23}Na, ^{24}Mg, ^{57}Fe, and ^{29}Si in the first selected area (A1). Spot size 6 μm, laser energy 55%, 5 sweeps. (G-J) Elemental distribution of ^{23}Na, ^{24}Mg, ^{57}Fe, and ^{29}Si in the second selected area (A2). Spot size 6 μm, laser energy 50%, 5 sweeps. Note the high ^{24}Mg counts yielded by the black particulates present in A and F. ^{57}Fe signal was recorded in the vicinity of the impurities. ^{29}Si signal yielded by the particulates was slightly increased in E (higher laser energy) and corresponded with the black impurities. 219

Figure 6.7 LA-ICP-MSI of a region of MPM tissue. Spot size 6 μm, laser energy 50%, 8 sweeps. No visible impurities in the brightfield image (A). ^{13}C and ^{24}Mg distribution was uniform, corresponding to the cellular arrangement (B & C). (D) ^{57}Fe signal may highlight areas of increased inflammation. 220

Figure 6.8 LA-ICP-MSI of two distinct areas of MPM tissue from Patient 3. (B-D) Elemental distribution of ^{13}C, ^{24}Mg, and ^{29}Si in the first selected area. Spot size 6 μm, laser energy 50%, 8 sweeps. (F-I) Elemental distribution of ^{13}C, ^{24}Mg, ^{29}Si, and ^{57}Fe in the second selected area. Spot size 6 μm, laser energy 50%, 8 sweeps. Some impurities can be noted in the brightfield images of the ROIs (A and E). 220

Figure 6.9 Overlay of brightfield and LA-ICP-MS images for Patient 1, Area 1. (A) Brightfield image of the whole tissue section showing the ablated ROI. (B) Mosaic overlay of brightfield image and ^{56}Fe distribution. (C) Perls' Prussian Blue staining of the ablated area. (D) H&E staining of the ablated area. (E) A closer view of the ablated area presenting the black impurities. (F) LA-ICP-MS image of the ROI. High ^{56}Fe counts were recorded from the impurities. High ^{56}Fe can be noted above the impurities and toward the top of the ROI, towards the top layer of the tissue section. 223

Figure 6.10 Overlay of brightfield and LA-ICP-MS images for Patient 1, Area 2. (A) Brightfield image of the whole tissue section showing the ablated ROI. (B) Mosaic overlay of brightfield image and ^{56}Fe distribution determined by LA-ICP-MSI. (C) Perls' Prussian Blue staining of the ablated area. (D) H&E staining of the ablated area. (E) Zoomed in version of the ROI. (F) LA-ICP-MS image of the ROI. The heterogeneous ^{56}Fe distribution can be noted.....224

Figure 6.11 Overlay of brightfield and LA-ICP-MS images for Patient 1, Area 3. (A) Brightfield image of the whole tissue section showing the ablated ROI. (B) Mosaic overlay of brightfield image and ^{23}Na distribution determined by LA-ICP-MSI. (C) Perls' Prussian Blue staining of the ablated area. (D) H&E staining of the ablated area. (E) Zoomed in version of the ROI, showing a complete lack of tissue architecture, characteristic to neoplastic development. (F) LA-ICP-MS image of the ablated area based on ^{23}Na counts.....225

Figure 6.12 Overlay of brightfield and LA-ICP-MS images for Patient 1, Area 4. (A) Brightfield image of the whole tissue section showing the ablated ROI. (B) Mosaic overlay of brightfield image and ^{23}Na distribution determined by LA-ICP-MSI. (C) Perls' Prussian Blue staining of the ablated area. (D) H&E staining of the ablated area. (E) Zoomed in version of the ROI. (F) LA-ICP-MS image of the ablated area, presenting a more homogenous distibution of ^{23}Na. 226

Figure 6.13 Overlay of brightfield and LA-ICP-MS images for Patient 1, Area 5. (A) Brightfield image of the whole tissue section. (B) Mosaic overlay of brightfield image and ^{44}Ca distribution determined by LA-ICP-MSI. (C) Perls' Prussian Blue staining of the ablated area. (D) H&E staining of the ablated area. Note the lack of coloration around the impurities. (E) Zoomed in version of the ROI. (F) LA-ICP-MS image, no significant counts recorded for ^{44}Ca.....227

Figure 6.14 Overlay of brightfield and LA-ICP-MS images for Patient 1, Area 6. (A) Brightfield image of the whole tissue section showing the ablated ROI. (B) Mosaic overlay of brightfield image and ^{44}Ca distribution determined by LA-ICP-MSI. (C) Perls' Prussian Blue staining of the ablated area. (D) H&E staining of the ablated area. (E) Zoomed in version of the ROI, showing black crystal-like

impurities and a longer, thinner impurity. (F) LA-ICP-MS image of the ablated area with no significant counts recorded for ^{44}Ca. 228

Figure 6.15 Elemental map of selected ROIs based on either ^{27}Al, ^{39}K, or ^{56}Fe signal. (A&E) Brightfield images pre-ablation. 5 µm spot size, 1.4 J cm^{-2} laser fluence. Intensity bars were set to the same values for comparison purposes and represent total counts per second. 230

Figure 6.16 Elemental map of selected ROIs based on either ^{23}Na, ^{26}Mg, or ^{29}Si signal. (A&E) Brightfield images pre-ablation. 5 µm spot size, 1.4 J cm^{-2} laser fluence. Intensity bars were set to the same values for comparison purposes and represent total counts per second. Note the background interferences present in panel (B-D). 230

Figure 6.17 Elemental map of selected ROIs based on either ^{31}P, ^{44}Ca, or ^{55}Mn signal. (A&E) Brightfield images pre-ablation. 5 µm spot size, 1.4 J cm^{-2} laser fluence. Intensity bars were set to the same values for comparison purposes and represent total counts per second. 231

Figure 6.18 Elemental map of selected ROIs based on either ^{27}Al, ^{29}Si, or ^{44}Ca signal. (A&E) Brightfield images pre-ablation. 5 µm spot size, 0.75 J cm^{-2} laser fluence. Intensity bars were set to the same values for comparison purposes and represent total counts per second. ROIs were specifically selected to include black, crystal-like particulates. 232

Figure 6.19 Elemental map of selected ROIs based on either ^{27}Al, ^{39}K, or ^{56}Fe signal. (A&E) Brightfield images pre-ablation. 5 µm spot size, 1.4 J cm^{-2} laser fluence. Intensity bars were set to the same values for comparison purposes and represent total counts per second. 233

Figure 6.20 Elemental map of selected ROIs based on either ^{23}Na, ^{26}Mg, or ^{29}Si signal. (A&E) Brightfield images pre-ablation. 5 µm spot size, 1.4 J cm^{-2} laser fluence. Intensity bars were set to the same values for comparison purposes and represent total counts per second. 234

Figure 6.21 Elemental map of selected ROIs based on either ^{31}P, ^{44}Ca, or ^{55}Mn signal. (A&E) Brightfield images pre-ablation. 5 µm spot size, 1.4 J cm^{-2} laser fluence. Intensity bars were set to the same values for comparison purposes and represent total counts per second. 234

Figure 6.22 LA-ICP-TOFMS analysis of 3D MPM models treated with crocidolite. (A) Brightfield image of the ablated area. (B-E) Crocidolite fibres yielded high counts of ^{23}Na, ^{24}Mg, ^{29}Si, and ^{56}Fe and can be noted against the ^{31}P signal generated by the biological matrix. The following laser ablation parameters were used: round laser spot size of 4 µm, fixed dosage mode of 2, repetition rate of 250 Hz, and the parallel lines overlapped one another by 2 µm. 237

Figure 6.23 LA-ICP-TOFMS analysis of 3D MPM models treated with amosite. (A) Brightfield image of the ablated area. (B-C) Amosite fibres yielded high counts of ^{29}Si and ^{56}Fe and can be noted against the ^{31}P signal generated by the biological matrix. The following laser ablation parameters were used: round laser spot size of 4 µm, fixed dosage mode of 2, repetition rate of 250 Hz, and the parallel lines overlapped one another by 2 µm. 237

Figure 6.24 LA-ICP-TOFMS analysis of 3D MPM models treated with chrysotile. (A) Brightfield image of the ablated area. (B-D) Chrysotile fibres yielded high counts of ^{24}Mg, ^{29}Si, and ^{56}Fe and can be noted against the ^{31}P signal generated by the biological matrix. The following laser ablation parameters were used: round laser spot size of 4 µm, fixed dosage mode of 2, repetition rate of 250 Hz, and the parallel lines overlapped one another by 2 µm. 238

Figure 6.25 LA-ICP-TOFMS analysis Patient 1. (A) Brightfield image of the ablated area showing the black, crystal-like particulates. Signal intensity maps of (B) $^{24}Mg^+$, (C) $^{27}Al^+$, (D) $^{28}Si^+$, (E) $^{31}P^+$, (F) $^{56}Fe^+$, (G) $^{63}Cu^+$, and (H) $^{66}Zn^+$ obtained by LA-ICP-TOFMS imaging. The impurities are indicated by white arrows. The following laser ablation parameters were used: round laser spot size of 2 µm, fixed dosage mode of 2, repetition rate of 250 Hz, and the parallel lines overlapped one another by 2 µm. 240

Figure 6.26 LA-ICP-TOFMS analysis of Patient 2. (A) Brightfield image of the ablated area showing the fibrotic region. Signal intensity maps of (B) $^{24}Mg^{+}$, (C) $^{31}P^{+}$, (D) $^{56}Fe^{+}$, (E) $^{32}S^{+}$, (F) $^{66}Zn^{+}$ obtained by LA-ICP-TOFMS imaging. The following laser ablation parameters were used: round laser spot size of 2 µm, fixed dosage mode of 2, repetition rate of 250 Hz, and the parallel lines overlapped one another by 2 µm. 242

Figure 6.27 LA-ICP-TOFMS analysis of Patient 3. (A) Brightfield image of a region of interest of a lung tissue sample. Possible impurities are indicated by black arrows. Signal intensity maps of (B) 23Na+, (C) 24Mg+, (D) 28Si+, (E) 31P+, (F) 44Ca+, (G) 56Fe+, (H) 66Zn+ and (I) 88Sr+ obtained by LA-ICP-TOFMS imaging. The fibre type structure and other impurities are indicated by white arrows. The following laser ablation parameters were used: round laser spot size of 2 µm, fixed dosage mode of 2, repetition rate of 250 Hz, and the parallel lines overlapped one another by 2 µm. 245

Figure 6.28 Serial ablation of the same area. Signal intensity maps of (A) $^{44}Ca^{+}$ following the first set of analysis, with white arrows indicating the localisation of the impurities. (B, G) $^{56}Fe^{+}$, (C, H) $^{88}Sr^{+}$, (D, F) $^{44}Ca^{+}$, (E) $^{24}Mg^{+}$ of visible impurities in the lung tissue sample. The following laser ablation parameters were used: a repetition rate of 250 Hz, a pixel size of 2 µm and a fluence of 3 J cm-2. 246

Figure 6.29 LA-ICP-TOFMS analysis of Patient 3. (A) Bright-field image of a region of interest of a lung tissue sample showing no visible impurities. Signal intensity maps of (B) $^{24}Mg^{+}$, (C) $^{31}P^{+}$, (D) $^{56}Fe^{+}$, (E) $^{28}Si^{+}$, and (F) $^{64}Zn^{+}$, obtained by LA-ICP-TOFMS imaging. The following laser ablation parameters were used: round laser spot size of 4 µm, fixed dosage mode of 2, repetition rate of 250 Hz, and the parallel lines overlapped one another by 2 µm.....247

Figure 6.30 LA-ICP-TOFMS analysis of Patient 4. (A) Bright-field image of a region of interest of a lung tissue sample with visible impurities indicated by the white arrows. Signal intensity maps of (B) $^{24}Mg^{+}$, (C) $^{31}P^{+}$, (D) $^{56}Fe^{+}$, (E) $^{63}Cu^{+}$, and (F) $^{64}Zn+$, obtained by LA-ICP-TOFMS imaging. (G-H) Overlay of biological

$^{31}P^+$ with $^{88}Sr^+$ and $^{28}Si^+$ signal, respectively. The following laser ablation parameters were used: round laser spot size of 4 µm, fixed dosage mode of 2, repetition rate of 250 Hz, and the parallel lines overlapped one another by 2 µm. 249

Figure 7.1 Expression of mesothelin, HMGB1, and VISTA in a panel of immortalised cells. Data acquired from three independent experiments. HeLa cells were used as positive control for mesothelin and HMGB1. U937 were used as a positive control for VISTA expression. Expression of the corresponding isotype controls are shown in blocked grey. 261

Figure 7.2 Relative expression of mesothelin, HMGB1, and VISTA in a panel of immortalised cells. HeLa and U937 were used as positive control cells for mesothelin and HMGB1, and VISTA, respectively. Data is presented as mean fluorescent index (MFI) ±SD (n=3) and was normalised against the corresponding isotype controls. 262

Figure 7.3 Mesothelin and HMGB1 expression in a positive control cell line (representative images from three independent experiments). Mesothelin was detected in the membrane of methanol fixed HeLa monolayers grown on glass coverslips using mesothelin rabbit polyclonal antibody, followed a Goat Anti-Rabbit IgG (H+L) secondary antibody, Alexa Fluor Plus 488 (green). HMGB1 expression was detected in the nucleus of HeLa cells using HMGB1 recombinant rabbit monoclonal antibody, followed by a Goat Anti-Rabbit IgG (H+L) secondary antibody, Alexa Fluor Plus 488 (green). The nuclei were counterstained with DAPI (blue). An overlay is presented in the right-hand side column. 263

Figure 7.4 Mesothelin, HMGB1, and VISTA expression in a mesothelial cell line (representative images from three independent experiments). Mesothelin was detected in the membrane of fixed Met-5A monolayers using mesothelin rabbit antibody, followed a Goat Anti-Rabbit IgG (H+L) secondary antibody, Alexa Fluor Plus 488 (green). HMGB1 expression was detected in the nucleus of Met-5A cells using HMGB1 recombinant rabbit monoclonal antibody, followed by a Goat Anti-Rabbit IgG (H+L) secondary antibody, Alexa Fluor Plus 488 (green). Low VISTA

expression can be noted following fixation and staining with VISTA recombinant rabbit monoclonal antibody, followed by a Goat Anti-Rabbit IgG (H+L) secondary antibody, Alexa Fluor Plus 488 (green). The nuclei were counterstained with DAPI (blue). An overlay is presented in the right-hand side column. 264

Figure 7.5 Mesothelin, HMGB1, and VISTA expression in biphasic mesothelioma cells (representative images from three independent experiments). Mesothelin was detected in the membrane of methanol fixed MSTO-211H monolayers grown on glass coverslips using mesothelin rabbit polyclonal antibody, followed a Goat Anti-Rabbit IgG (H+L) secondary antibody, Alexa Fluor Plus 488 (green). HMGB1 expression was detected in the cytoplasm and around the nucleus of MSTO-211H cells using HMGB1 recombinant rabbit monoclonal antibody, followed by a Goat Anti-Rabbit IgG (H+L) secondary antibody, Alexa Fluor Plus 488 (green). Membrane-bound VISTA can be seen following fixation and staining with VISTA recombinant rabbit monoclonal antibody, followed by a Goat Anti-Rabbit IgG (H+L) secondary antibody, Alexa Fluor Plus 488 (green). The nuclei were counterstained with DAPI (blue). An overlay is presented in the right-hand side column. 266

Figure 7.6 H28 Mesothelin, HMGB1, and VISTA expression in epithelioid mesothelioma cells (representative images from three independent experiments). Mesothelin was detected in the membrane of methanol fixed NCI-H28 monolayers grown on glass coverslips using mesothelin rabbit polyclonal antibody, followed a Goat Anti-Rabbit IgG (H+L) secondary antibody, Alexa Fluor Plus 488 (green). HMGB1 expression was detected in the nucleus and cytoplasm of NCI-H28 cells using HMGB1 recombinant rabbit monoclonal antibody, followed by a Goat Anti-Rabbit IgG (H+L) secondary antibody, Alexa Fluor Plus 488 (green). Membrane-bound VISTA can be seen following fixation and staining with VISTA recombinant rabbit monoclonal antibody, followed by a Goat Anti-Rabbit IgG (H+L) secondary antibody, Alexa Fluor Plus 488 (green). The nuclei were counterstained with DAPI (blue). An overlay is presented in the right-hand side column. 268

Figure 7.7 Mesothelin, HMGB1, and VISTA expression in a NSCLC control cell line (representative images from three independent experiments). Mesothelin was detected in the membrane of methanol fixed NCI-H1975 monolayers grown on glass coverslips using mesothelin rabbit polyclonal antibody, followed a Goat Anti-Rabbit IgG (H+L) secondary antibody, Alexa Fluor Plus 488 (green). Low HMGB1 expression was detected in the nucleus of NCI-H1975 cells using HMGB1 recombinant rabbit monoclonal antibody, followed by a Goat Anti-Rabbit IgG (H+L) secondary antibody, Alexa Fluor Plus 488 (green). No expression recorded for VISTA. The nuclei were counterstained with DAPI (blue). An overlay is presented in the right-hand side column. 270

Figure 7.8 Schematic diagram of the TMA layout. Legend: Adr- adrenal gland, Abd- Abdominal cavity, Blo- Blood vessel, Lun- Lung, Mes- Mesentery, Ome- Omentum, Per-Pericardium,Ple- Pleura, Ret- Retroperitoneum; Green- Normal tissue, Blue- Malignant tumour, Purple (lightest to darkest)- (stage I, II, III, and IV malignant pleural mesothelioma), Light blue/ peach- Benign tumour. Information provided by the supplier (Amsbio).....273

Figure 7.9 Histological presentation of the TMA following H&E staining. Each core has a diameter of 1.5 mm. Normal lung and pericardium tissues shown in Row A and Row B. The rest of the cores are malignant mesothelioma tumours of various types and stages or benign tissue (G10, G11, H10 & H11). Figure adapted from (Biomax.us.).....274

Figure 7.10 Representative MALDI-MS image of the whole TMA section. Overview of the TMAs based on signals for *m/z* 796.414 (blue- upper part predominantly) and *m/z* 857.492 (red- lower section). Signal intensity bars were adjusted to ensure visualisation of all 80 cores.....275

Figure 7.11 MALDI-MS matrix profile. Mass spectra acquired in positive mode; spectra display peaks within the mass range m/z 700-1500. Mass spectrum annotated with common matrix peaks. Peak picking was carried out in MMass and the settings were set at a S/N threshold of 5, and the picking height was

100%. Both the absolute intensity threshold and the relative intensity threshold was set to 0 with baseline correction and smoothing applied. 277

Figure 7.12 Representative MALDI-MS images of the most intense α-CHCA signal peaks. 278

Figure 7.13 Flipped MALDI-MS spectra of duplicate cores B2 (red) and B3 (blue). Mass spectra acquired in positive mode; spectra display peaks within the mass range m/z 870-1035. Histological staining of the two cores are presented in the right-hand corner, with typical healthy lung tissue arhitechture present. Peak picking was carried out in MMass and the settings were set at a S/N threshold of 5, and the picking height was 100%. Both the absolute intensity threshold and the relative intensity threshold was set to 0 with baseline correction and smoothing applied. 279

Figure 7.14 Flipped MALDI-MS spectra of core D8 (red) and D11 (blue). Mass spectra acquired in positive mode; spectra display peaks within the mass range m/z 870-1035. Peak picking was carried out in MMass and the settings were set at a S/N threshold of 5, and the picking height was 100%. Both the absolute intensity threshold and the relative intensity threshold was set to 0 with baseline correction and smoothing applied. 281

Figure 7.15 Differences in A) m/z 985.597 signal intensity, B) histological presentation, and C) ion distribution between tissue cores with same pathological diagnosis, TNM, and stage. 282

Figure 7.16 Top- Histological profile of selected cores (A9 Lung- Normal tissue, D8 Pleura- Malignant tumour stage I, E7 Lung- malignant tumour and H9 Pleura- Malignant tumour stage IV). Colours of the borders match the colour of each spectrum. Bottom- Offset spectra of the selected individual cores within the mass range m/z 870-1035. Peak picking was carried out in MMass and the settings were set at a S/N threshold of 5, and the picking height was 100%. Both the absolute intensity threshold and the relative intensity threshold was set to 0 with baseline correction and smoothing applied. Selected region presented in the

dotted box includes peaks of interest and the corresponding putatively assigned peptide sequence. Individual spectrum presented in order of peak intensity. .283

Figure 7.17 Representative MALDI-MS images A) *m/z* 944.530 B) *m/z* 957.593 C) *m/z* 971.565 D) *m/z* 985.597. The presence of selected peaks is associated with malignant events, with limited signal in the non-cancerous core (A9). Low intensities of the selected peaks are associated with more aggressive types of malignancy. 286

List of Tables

Table 1.1 The 8th TNM classification for MPM according to the IASLC, 2016. Table designed and adapted from Berzenji *et al.* (2018). T1- Tumour involving the ipsilateral parietal pleura; T2- Tumour involving each of the ipsilateral pleural surfaces (parietal, mediastinal, diaphragmatic, and visceral pleura) with at least one of the following features (a) confluent visceral pleural tumour (including the fissures) (b) involvement of diaphragmatic muscle or (c) invasion of the lung parenchyma; T3- Tumour involving each of the ipsilateral pleural surfaces with at least one of the following features (a) invasion of the endothoracic fascia, (b) extension into the mediastinal fat, (c) solitary, completely resectable focus invading soft tissues of the chest wall and (d) non-transmural involvement of the pericardium; T4- Tumour involving each of the ipsilateral pleural surfaces with at least one of the following features (a) diffuse or multifocal invasion of soft tissues of the chest wall, (b) any rib involvement, (c) invasion of the peritoneum through the diaphragm, (d) invasion of any mediastinal organ, (e) direct extension to the contralateral pleura, (f) invasion of the spine or brachial plexus and (g) transmural invasion of the pericardium (with or without pericardial effusion) or myocardium invasion; N0- No regional lymph node metastases; N1- Metastases in the ipsilateral bronchopulmonary, hilar, or mediastinal lymph nodes; N2- Metastases in the contralateral bronchopulmonary, hilar, or mediastinal lymph nodes or ipsilateral or contralateral supraclavicular lymph nodes; M0- No evidence of distant metastases; M1- Evidence of distant metastases; 9

Table 1.2 Symptoms at initial presentation in MPM cases. The percentage is based on n=90. *Other symptoms include aphonia and dysphagia, distension, sensation of pressure in the right upper quadrant, nausea, bad taste in mouth, perceived tachycardia, and headache. Table adapted from (Woolhouse *et al.*, 2018).....12

Table 1.3 Adapted from the International Agency for Research on Cancer (IARC Monographs, 2012). Asbestos (Chrysolite, Amosite, Crocidolite, Tremolite, Actinolite, and Anthophyllite).....32

Table 1.4 Chemical composition of the MF used in this study. Table adapted from Korchevskiy *et al.,* 2019.....33

Table 1.5 Advantages and limitations of the main mass analysers employed in this study.....39

Table 1.6 Established, emerging, and novel biomarkers in malignant mesothelioma (individual or panel). 49

Table 2.1 Manufacturers and suppliers.....54

Table 2.2 Mammalian immortalised cell lines used throughout the study.....55

Table 2.3 Human tissues used in the project. 56

Table 2.4 Conjugated antibodies employed for flow cytometry analysis. All antibodies employed in this section were monoclonal antibodies. The antibody concentrations and volumes presented in the table were selected based on the manufacturer recommendation. 56

Table 2.5 Isotype controls employed for flow cytometry analysis. Concentrations were selected based on manufacturer recommendation. 57

Table 2.6 Primary and secondary antibodies used for immunofluorescence experiments. 57

Table 2.7 Mineral fibres employed in the study. The stock concentration was 1 mg/ mL in PBS. 58

Table 2.8 Selected LA-ICP-MS parameters following optimisation. These parameters were employed for single and multi-element LA-ICP-MS analysis. 68

Table 2.9 Selected Instrument 1 LA-ICP-MS parameters following optimisation. 74

Table 2.10 Experimental parameters and data acquisition parameters used for LA-ICP-MSI. 77

Table 2.11 HTX sprayer settings for trypsin and CHCA matrix deposition. 85

Table 3.1 Asbestos validation by PLM. The table presents the observed morphology and pleochroism of the four asbestos types. 91

Table 6.1 Patient information and sample details as provided by the supplier (Amsbio). *Not included in the SDS; MF visible by brightfield microscopy. 211

Table 7.1 Calculated mass error and signal to noise (S/N) values for duplicate cores. Mass error >20 are shown in red.....280

Table 7.2 Observed peptides after *in situ* digestion and MALDI-MS analysis. Observed m/z values in positive ion mode, the mass error (ppm), peptide sequence, and the protein function are included.....284

Abbreviations

μ-PIXE	Micro particle induced X-ray emission
ADP	Adenosine diphosphate
ATP	Adenosine triphosphate
ARD	Asbestos related diseases
ARK-1	Aurora-related kinase 1
ASS1	Argininosuccinate synthase 1
ATP	Adenosine triphosphate
BAP1	BRCA1-associated protein 1
BSA	Bovine serum albumin
CDKN2A	Cyclin-dependent kinase inhibitor 2A gene
CEA	Carcinoembryonic antigen
COPD	Chronic obstructive pulmonary disease
CT	Computerised tomography
DAMP	Damage-associated molecular pattern
ddPCR	Droplet digital polymerase chain reaction
EDX	Energy dispersive X-ray spectroscopy
ELISA	Enzyme-linked immunosorbent assay
EM	Electron microscopy
EP	Ethyl pyruvate
EPA	Environmental Protection Agency
EZH2	Enhancer of zeste 2 polycomb repressive complex 2 subunit
FAK	Focal adhesion kinase
FISH	Fluorescent *in situ* hybridisation
FM	Fluorescence microscopy

GC-MS	Gas chromatography mass spectrometry
H2A	Histone 2A
H3K27	Histone 3 lysine 27
H&E	Haematoxylin and eosin
HA	Hyaluronic acid
Hoechst/ PI	Hoechst 33342 and propidium iodide
HMC	Human mesothelial cells
HMGB1	High mobility group box 1
HPMC/PVP	Hydroxypropyl methylcellulose/polyvinylpyrrolidone
IASLC	International Association for the Study of Lung Cancer
LA-ICP-MS	Laser ablation inductively coupled plasma mass spectrometry
LA-ICP-MSI	Laser ablation inductively coupled plasma mass spectrometry imaging
LC-ESI-MS/MS	Liquid chromatography electrospray ionisation tandem mass spectrometry
LC-MS	Liquid chromatography mass spectrometry
LOD	Limit of detection
MALDI MS	Matrix-assisted laser desorption ionisation mass spectrometry
MCS	Multicellular spheroids
MDM2	Murine double minute 2
MF	Mineral fibres
MM	Malignant mesothelioma
MPM	Malignant pleural mesothelioma
MRI	Magnetic resonance imaging
MTAP	Methylthioadenosine phosphorylase

NALP3	NACHT, LRR, and PYD domains-containing protein 3
NF2	Neurofibromatosis type 2 gene
NSCLC	Non-small cell lung cancer
OCT	Optical cutting temperature
OS	Overall survival
PARP	Poly (ADP-ribose) polymerase
PBS	Phosphate buffer solution
PBST	0.1% Triton X-100 prepared in PBS
PCM	Phase contrast microscopy
PD-L1	Programmed death-ligand 1
PFA	Paraformaldehyde
PLM	Polarised light microscopy
PS	Phosphatidylserine
PTE	Potential toxic element
PTEN	Phosphatase and tensin homolog gene
ROI	Region of interest
ROS	Reactive oxygen species
RT-qPCR	Real time quantitative polymerase chain reaction
SEM	Scanning electron microscopy
SEM	Standard error of the mean
SIADH	Syndrome of inappropriate antidiuretic hormone secretion
SIMS	Secondary ion mass spectrometry
SMRP	Soluble mesothelin-related protein
S/N	Signal to noise
SV40	Simian virus 40
T	Tetrahedral

TB	Tuberculosis
TEM	Transmission electron microscopy
TFA	Trifluoroacetic acid
TGF-β	Transforming growth factor beta
TOF	Time of flight
TNF-α	Tumour necrosis factor alfa
TNM	Tumour, node, and metastasis
TMA	Tissue microarray
UICC	Union for international cancer control
VISTA	V-domain immunoglobulin suppressor of T cell activation
XFM	X-ray fluorescence microscopy
XPCμT	X-ray phase-contrast micro-tomography
XRF	X-ray fluorescence
YAP1	Yes associated protein-1
ZEB	Zinc finger E-box binding homeobox

Chapter 1 Introduction

1.1 Introduction to Cancer

Cancer is reportedly the leading cause of mortality worldwide, with highest incidence rates prevalent in high-income countries. Intensive research carried out in the last decades has led to decreased mortality rates of the most common types of cancers in these countries. Decreased mortality rates are thought to be due to a better understanding of the risk factors, new screening programmes, early detection strategies, as well as tailored and improved treatment options (Torre *et al.*, 2016). Despite all these advancements, more than 14.1 million people are still diagnosed each year, with over 8.2 million cancer deaths being reported yearly worldwide. Moreover, IARC predicts nearly 30 million cases worldwide by 2040. In the UK only, more than half of new cases of cancer reported between 2015-2017 are breast, prostate, lung, or bowel cancer. The cancer incidence in the UK is ranked higher than 90% of the rest of the world, which roughly equivalents to a person being diagnosed of cancer every two minutes (Ferlay *et al.*, 2012).

Cancer is defined as the uncontrollable division of abnormal, genetically altered cells (Torre *et al.*, 2016). Tumours are formed of clonally derived cells, the cells in the tumour are thought to be derived from a single, abnormal cell that lost normal control mechanisms and therefore carry the mutations of the first cancer cell (Graham & Sottoriva, 2017). There are over 200 types of cancer; lung, colorectal, breast, and prostate cancer are some of the most prevalent ones in high-income countries, whereas stomach, liver, oesophageal, and cervical cancer account for the most neoplasms in the majority of developing countries (Torre *et al.*, 2016). Malignancies can be caused by either external or preventable risk factors, internal factors, or a combination of the two. The external factors can be roughly classified as lifestyle-related risk factors such as tobacco, diet and alcohol, infectious agents (*e.g.,* Epstein-Barr virus, hepatitis B virus, human papilloma virus, human T-cell lymphotropic virus, hepatitis C virus, Kaposi's sarcoma herpes virus, and Merkel cell polyomavirus), reproductive factors and exogenous hormones (*e.g.* hormonal contraceptives), and environmental factors (*e.g.,* UV radiation, asbestos exposure, chemical exposure) (Arem & Loftfield,

2018; Schottenfeld *et al.*, 2013). Potential internal and intrinsical related risk factors include spontaneous errors in DNA replication (unavoidable) and partially-modifiable endogenous risk factors including inherited susceptibility, immunity and inflammation, and hormones (Wu *et al.*, 2018). In recent years, the question of interdependence between risk factors has been the main subject of intensive scientific debate. For example, one study reported that unavoidable intrinsic DNA replication errors, known as the 'bad luck' hypothesis, account for over 60% of tissue cancer burden (Tomasetti, Li, & Vogelstein, 2017). On the other hand, other studies have concluded that cancer aetiology is strongly correlated to extrinsic factors and that the rates of DNA replication errors by intrinsic processes do not fully account for the current cancer risks (Wu *et al.*, 2016). Both intrinsic and extrinsic factors contribute to the complex nature of each individual cancer.

Despite the intricate processes that are involved in the development of neoplastic diseases, the research carried out in the last three decades has revolutionised our understanding of cancer. Arguably, one of the most significant pieces of work in the last three decades was Hanahan and Weinberg's seminal paper reporting the six biological capabilities acquired throughout tumorigenic development. These are notoriously known as the hallmarks of cancer (Hanahan & Weinberg, 2000). The hallmarks are 1) sustaining proliferative signalling, 2) evading growth suppressors, 3) resisting cell death, 4) enabling replicative immortality, 5) inducing angiogenesis, and 6) activating invasion and metastasis. Given the continuous scientific work throughout the decade, Hanahan and Weinberg published an updated version of their earlier work which includes four more underlying hallmarks and tumour enabling characteristics that include 7) genome instability and mutation, 8) tumour-promoting inflammation, 9) deregulating cellular energetics, and 10) avoiding immune destruction (Hanahan & Weinberg, 2011).

Finally, the most recent review incorporated four new parameters including 1) unlocking phenotypic plasticity, 2) non-mutational epigenetic reprogramming, 3) polymorphic microbiomes, and 4) senescent cells (Hanahan, 2022). These core

attributes define conceptual parameters of cancer biology, genetics, and pathogenesis.

1.2 Introduction to Mesothelioma

1.2.1 Mesothelioma overview

Malignant mesothelioma (MM) is a fatal and aggressive cancer of the mesothelial cells on the serosa surface, a layer of epithelial mesothelial cells that lines all the cavities. MM development is strongly linked to occupational and environmental exposure to asbestos and other emerging mineral fibres (MF) (Carbone & Yang, 2012). Additionally, carbon nanotubes have emerged in recent years as potential MM inducers (Chernova *et al.*, 2017; Xie *et al.*, 2021). The prognosis of mesothelioma is poor due to the lack of specific biomarkers, difficulty of making diagnosis in the early stage, rapid progression, high invasiveness, and lack of effective treatment (Ai & Stevenson, 2014).

Mortality in MM cases is associated with cumulative exposure to asbestos (dose/ exposure time)(Luberto *et al.*, 2019). However, inherited mutations play a significant role in MM predisposition in a subset of patients. It has been proposed that a combination of inherited mutations and asbestos fibres may induce MM with shorter latencies, following short-term exposure or exposure to relatively low doses of asbestos (Klebe *et al.*, 2021).

1.2.2 Mesothelioma demographics

Mesothelioma is a relatively rare disease that accounted for 30,443 new cancer cases (0.2%) and 25,576 cancer deaths (0.3%) worldwide in 2018 (Sung *et al.*, 2021). However, the statistics and graphs presented in this section include data regarding mesothelioma demographics focused on Great Britain and the United Kingdom. Around 80% of mesothelioma cases occur in men, mainly due to the higher likelihood of men involved in the asbestos industry or the armed forces (Zanconati *et al.*, 2017). The death rate in males has started to slowly decline in the recent years (down 9%), whilst female deaths have remained the same (Mesothelioma statistics for great britain, 2021.) (Figure 1.1). The total number of

annual deaths caused by mesothelioma has significantly increased over the last 50 years due to the widespread industrial use of asbestos during 1950-1980s and the long latency period from the inhalation of the asbestos fibres to symptom onset (Figure 1.2).

Mesothelioma is primarily diagnosed in older people (> 70 years). Nevertheless, over 20% of diagnoses are in people aged 51–60. The disease is rare in people under the age of 50 (Røe & Stella, 2015). According to a statistics project on mesothelioma led by British Lung Foundation, 2,172 men and 398 women were registered as new cases of mesothelioma in the UK (2018). These correspond to incidence rates of 5.2 per 100,000 for males and 0.8 per 100,000 for females.

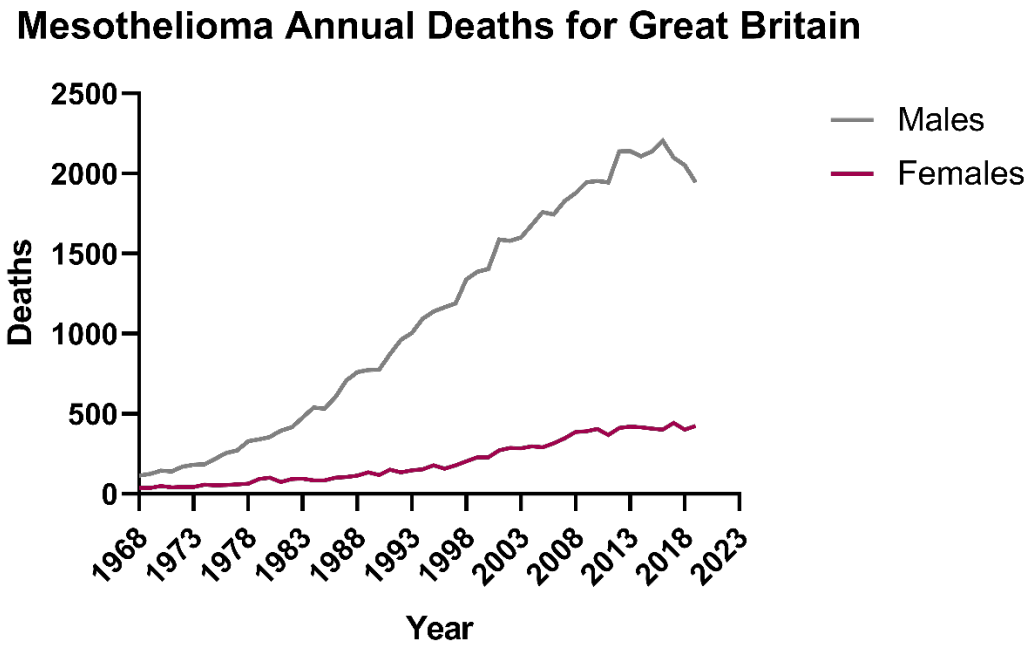

Figure 1.1 Mesothelioma annual deaths for Great Britain, as of 2021. Data made available by HSE.gov.uk (Mesothelioma statistics for Great Britain, 2021). Data for 2019 are provisional. Note that although some deaths that occurred in 2019 were registered later due to the first wave of the SARS-CoV-2 (COVID-19) pandemic in 2020, the number of late registrations by March 2021 (the cut-off for inclusion in these statistics) was similar to the number expected based on patterns of late registrations in previous years.

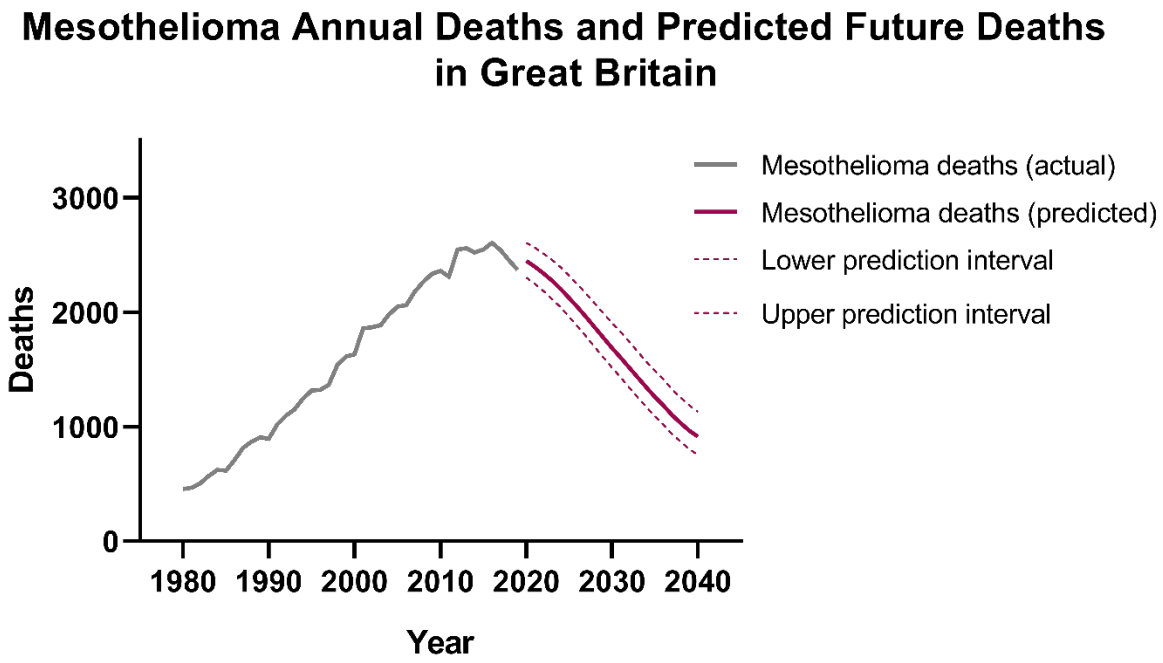

Figure 1.2 Mesothelioma annual deaths (1980-2018) and predicted future deaths to 2040 in Great Britain. Lower and upper prediction intervals included. Data made available by HSE.gov.uk (Mesothelioma statistics for Great Britain, 2021).

Pleural mesothelioma, the most common type of MM, represented 2.1% deaths out of the total UK deaths caused by lung diseases (Figure 1.3). Despite the low mortality incidence, Public Health England reported mesothelioma as the cancer with the lowest five-year survival estimates (7.2% between 2014-2018), compared to pancreatic cancer (7.3%) and brain cancer (12.8%). The overall survival (OS) rate is more than twice as high than lung cancer OS, the most common cause of death amongst lung diseases (Wong, 2021) (Figure 1.3). Moreover, a diagnosis of cancer can cause significant psychological distress. According to a large cohort study, patients with mesothelioma had the highest risk of suicide 6 months post diagnosis (8.61-fold risk compared with the general population) (Henson *et al.*, 2019).

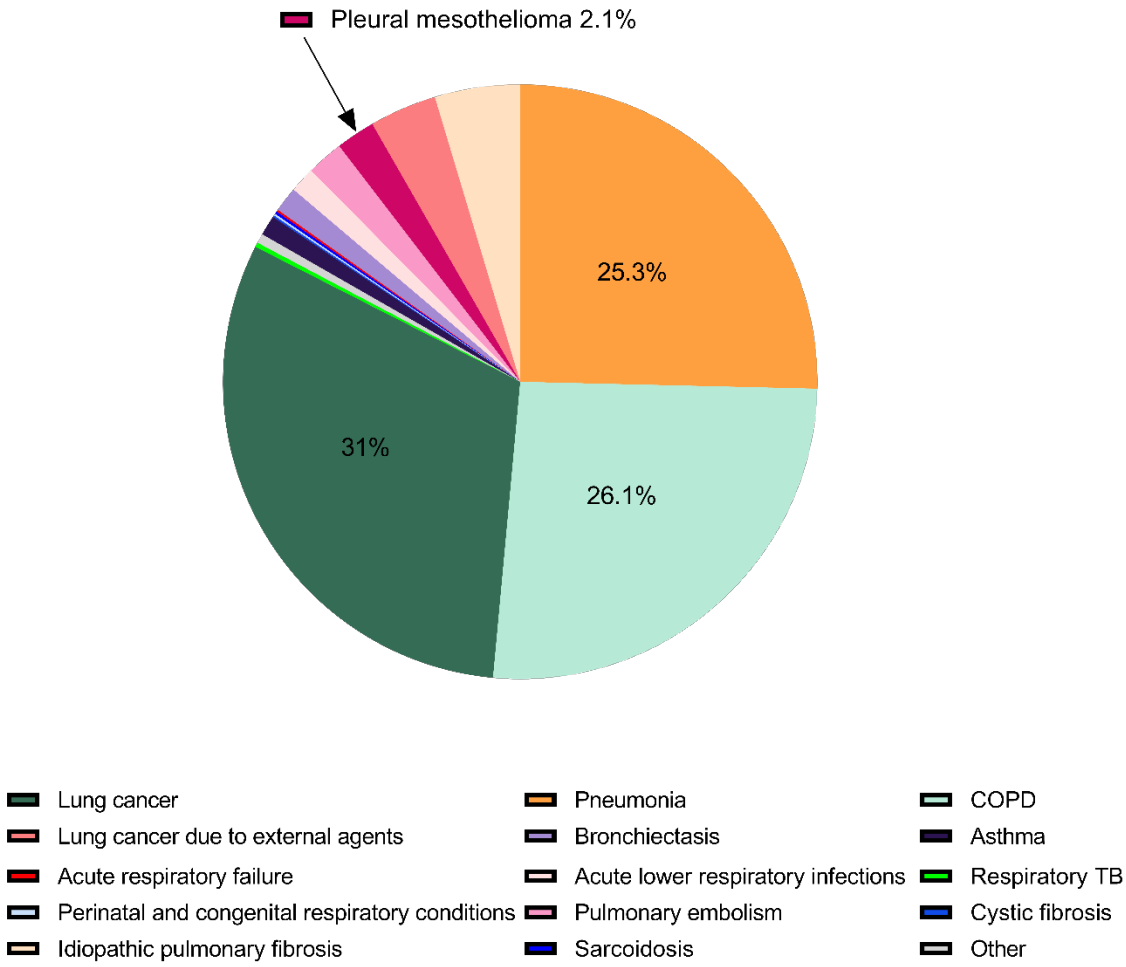

Figure 1.3 UK deaths from pleural mesothelioma compared with other lung diseases, 2012. Pie chart based on data published by British Lung Foundation (Mesothelioma statistics). Percentages shown for top 3 pathologies with highest mortality (*i.e.,* lung cancer, pneumonia, and chronic obstructive pulmonary disease (COPD)).

1.2.3 Mesothelioma classification and staging

MM has a long latency period averaged at around 30-40 years post-exposure (Bononi *et al.*, 2015). Given that MF usually get inhaled and reach the pleura via the lymphatic system, most MM cases occur in the pleura of the lungs (80%), classed as malignant pleural mesothelioma (MPM). Tumours are mostly contained around the stomata and the lymphoid patches called Kampmeier's foci

in the basal side of the parietal pleura (Røe & Stella, 2015). Around 20% of MM cases occur on the lining of the peritoneum, known as peritoneal mesothelioma. Some cases of mesothelioma affecting the pericardium, testis, and tunica vaginalis have also been reported (Mezei *et al.*, 2017). MPM is the only type of mesothelioma currently having an official staging system, ranging from I-IV (Figure 1.4). Additionally, a more detailed tumour, node, and metastasis (TNM) staging system is also employed during the diagnosis process to inform prognosis, OS, and treatment strategies. The latest International Association for the Study of Lung Cancer (IASLC) TNM staging for MPM is presented in Table 1.1 adapted from (Berzenji, Van Schil, & Carp, 2018). The T component of the TNM staging system normally describes the size and extent of the tumour (Feng & Yang, 2019). However, MPM has a nonconventional growth pattern presenting multiple nodules which detach and spread along the pleural surfaces often accompanied with pleural effusions (Berzenji *et al.*, 2018). Based on this characteristic, tumour size is not one of the main descriptors of MPM disease extent, although it might play a role in disease prognosis (Rusch *et al.*, 2016).

Stage	Mesothelioma stage grouping		
	T	N	M
I			
IA	T1	N0	M0
IB	T2,3	N0	M0
II	T1,2	N1	M0
III			
IIIA	T3	N1	M0
IIIB	T1–3	N2	M0
IV	T4	N0–2	M0
	Any T	Any N	M1

Table 1.1 The 8th TNM classification for MPM according to the IASLC, 2016. Table designed and adapted from Berzenji *et al.* (2018). T1- Tumour involving the ipsilateral parietal pleura; T2- Tumour involving each of the ipsilateral pleural surfaces (parietal, mediastinal, diaphragmatic, and visceral pleura) with at least one of the following features (a) confluent visceral pleural tumour (including the fissures) (b) involvement of diaphragmatic muscle or (c) invasion of the lung parenchyma; T3- Tumour involving each of the ipsilateral pleural surfaces with at least one of the following features (a) invasion of the endothoracic fascia, (b) extension into the mediastinal fat, (c) solitary, completely resectable focus invading soft tissues of the chest wall and (d) non-transmural involvement of the pericardium; T4- Tumour involving each of the ipsilateral pleural surfaces with at least one of the following features (a) diffuse or multifocal invasion of soft tissues of the chest wall, (b) any rib involvement, (c) invasion of the peritoneum through the diaphragm, (d) invasion of any mediastinal organ, (e) direct extension to the contralateral pleura, (f) invasion of the spine or brachial plexus and (g) transmural invasion of the pericardium (with or without pericardial effusion) or myocardium invasion; N0- No regional lymph node metastases; N1- Metastases in the ipsilateral bronchopulmonary, hilar, or mediastinal lymph nodes; N2- Metastases in the contralateral bronchopulmonary, hilar, or mediastinal lymph nodes or ipsilateral or contralateral supraclavicular lymph nodes; M0- No evidence of distant metastases; M1- Evidence of distant metastases;

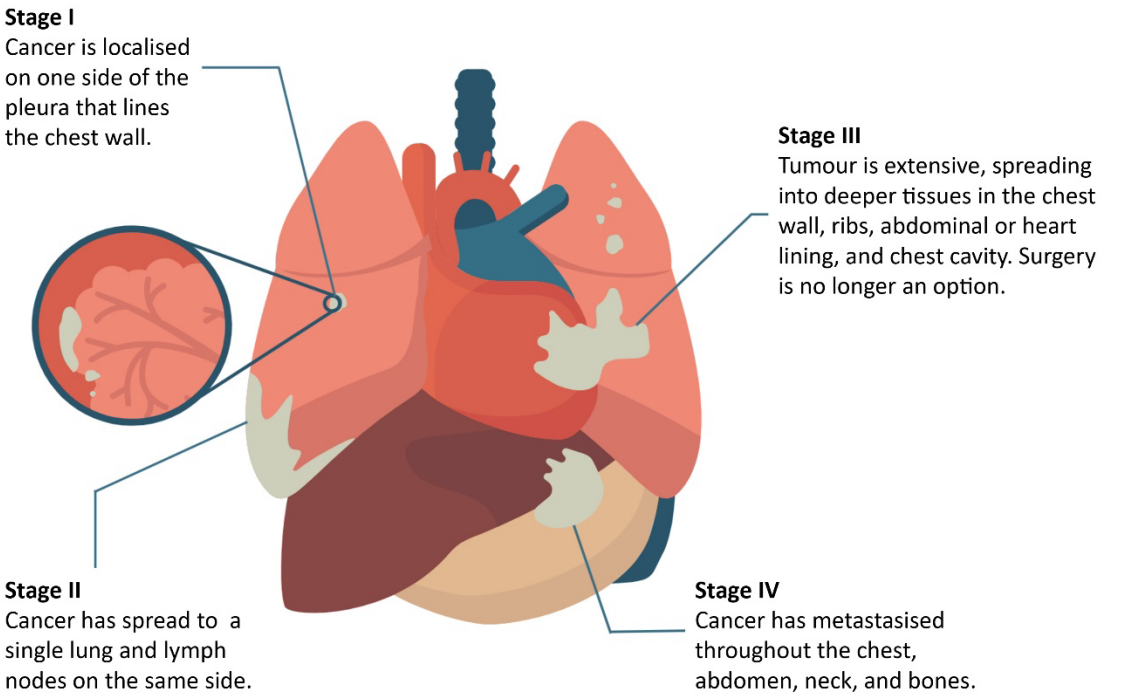

Figure 1.4 Schematic diagram of MPM staging system (I-IV). Figure adapted from Mesothelioma.com. Stage I – the cancer is contained on a single layer of the pleura; Stage II- the tumour has now reached the lymph node and has expanded to the lung; Stage III- the cancer spread into the organs nearby; Stage IV- tumour has metastasised to the chest, neck, abdomen, and bones (Berzenji *et al.*, 2018).

1.2.4 Histologic subtyping of mesothelioma

MM is a rare tumour arising from the mesothelial cells on the serosa surface, a layer of epithelial mesothelial cells that lines all the cavities (Galateau-Salle *et al.*, 2016). Histologically, MM can be classified into three types: epithelioid (≈53-70%), sarcomatoid (≈11-19%), and biphasic (≈12-27%), although according to the new WHO classification there are more than 16 subtypes. Patients with sarcomatoid and biphasic tumours have significantly less chances of survival compared to patients with epithelioid MM (Galateau-Salle *et al.*, 2016). Although the histological classification only partially captures the tumour heterogeneity observed at both the molecular and clinical level, it has a crucial prognostic value and may be of interest for guiding therapeutic strategies. Figure 1.5 presents the three main types of MM, alongside their histological presentation following haematoxylin and eosin (H&E) staining.

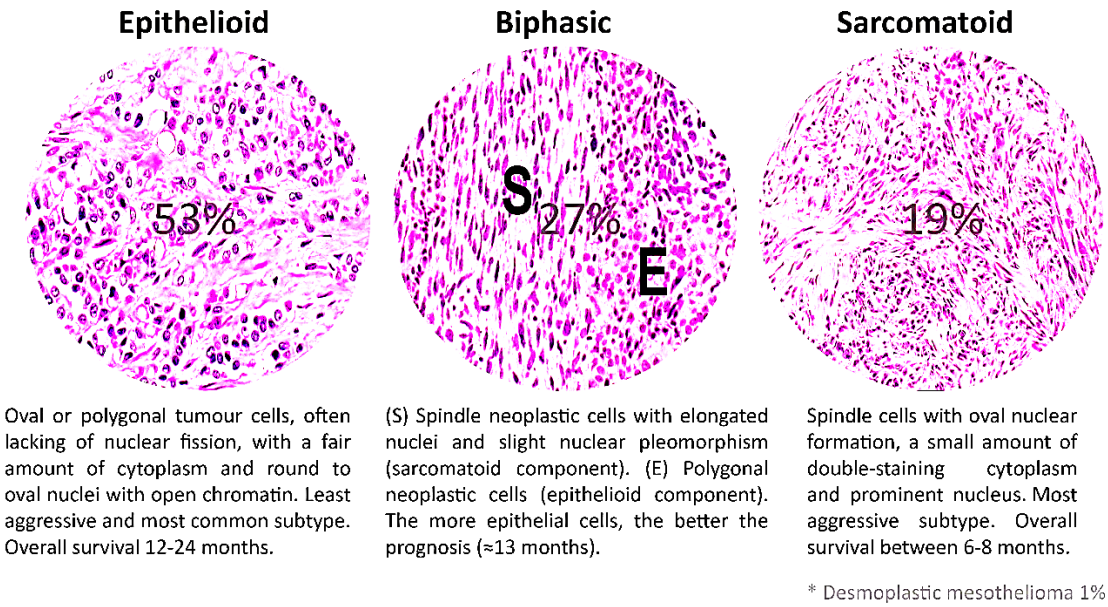

Figure 1.5 Histologic subtyping of mesothelioma. Histology images adapted from (Galateau-Salle *et al.*, 2016). The main mesothelioma subtypes are epithelioid (53-70%), biphasic (12-27%), and sarcomatoid (11-19%). Percentages may vary based on various studies and reports, with epithelioid always being the most common one and sarcomatoid the least common mesothelioma subtype.

1.2.5 Clinical presentation

MPM is characterised by aggressive disease progression followed later by systemic manifestations of disease (Bibby *et al.*, 2016). Consequently, the cancer is already at a locally advanced stage when patients start presenting symptoms, the primary morbidity for these patients arising from local disease burden (British Thoracic Society Standards Of Care Committee, 2007). The majority of patients with MPM present with dyspnoea, chest pain or both. Initially, dyspnoea is linked to the presence of pleural effusions (≈70% of patients) and is later on caused by restricted respiratory movement and encasement of the lung by the actively extending tumour (Bibby *et al.*, 2016). Chest pain is common and usually worsens as the disease progresses, particularly if the tumour has invaded the chest wall. Other symptoms of MPM include fatigue, anorexia, weight loss, sweats, and malaise (British Thoracic Society Standards Of Care Committee, 2007). Typical MPM symptoms are presented in Table 1.2. Asymptomatic presentation has also

been reported and has been linked to better prognosis due to early diagnosis (Bibby *et al.*, 2016).

Symptom	% Affected
Pain (pleuritic and non-pleuritic)	69
Shortness of breath	59
Fever, chills, or sweats	33
Weakness, fatigue, or malaise	33
Cough	27
Weight loss	24
Anorexia	11
Sensation of heaviness or fullness in chest	7
Hoarseness	3
Early satiety	2
Myalgias	2
Others*	1

Table 1.2 Symptoms at initial presentation in MPM cases. The percentage is based on n=90. *Other symptoms include aphonia and dysphagia, distension, sensation of pressure in the right upper quadrant, nausea, bad taste in mouth, perceived tachycardia, and headache. Table adapted from (Woolhouse *et al.*, 2018).

1.2.6 Diagnosis workflow and current challenges

According to the latest guidelines published by the British Thoracic Society, the current investigation workflow involves an urgent chest X-ray of symptomatic patients, followed by a pleural evaluation computerised tomography (CT) scan (Woolhouse *et al.*, 2018). Further referral for a magnetic resonance imaging (MRI) is recommended to help differentiate between malignant and benign cases (Revelli *et al.*, 2016). A thorough investigation into possible asbestos exposure throughout life should be carried out, also considering the prospect of para exposure by exploring details of relative and/or partner occupations (Woolhouse *et al.*, 2018). Additional procedures include medical thoracoscopy, fine-needle

aspiration biopsy, pleural effusion cytology with the cell-block method, and pleural biopsy through video-assisted thoracic surgery (VATS pleural biopsy). Immunohistochemistry is then carried out on the biopsy. A combination of at least two positive mesothelial markers (calretinin, cytokeratin 5/6, Wilms tumour 1, D-240) and at least two negative adenocarcinoma immunohistochemical markers (TTF1, CEA, Ber-EP4) is advised for differential diagnosis of MPM (van Zandwijk *et al.*, 2013). Despite the current methodology, difficulties still remain in relation to early diagnosis, notably due to the lack of biomarkers of exposure and pre-symptoms biomarkers.

1.2.7 Disease monitoring and treatment strategies

MPM is fatal in most cases, with oncological treatment and procedures only modestly impacting the prognosis and OS. The combination of platinum agents with pemetrexed has been the standard-of-care treatment for unresectable MPM, although outcomes remain poor. Where licensed (not applicable to the UK), bevacizumab can be added to this regime (Woolhouse *et al.*, 2018).

Accurate staging of MPM is critical when surgery is considered to be part of multimodality treatment approaches. Pleurodesis is often carried out to prevent recurrent pleural effusions. It is performed by instillation of a sclerosant such as talc into the pleural space, which causes subsequent inflammation leading to adhesions between the visceral and parietal pleura (van Zandwijk *et al.*, 2013).

Amongst novel therapy combinations, nivolumab plus ipilimumab has shown clinical benefits for MPM patients OS, in a phase 3 trial (Baas *et al.*, 2021). Another novel approach was the use of adjuvants that block the exogenous supply of the amino acid arginine, particularly in argininosuccinate synthetase 1 (ASS1) deficit tumours. Cisplatin and pemetrexed were used in combination with the arginine degrading pegargiminase in ASS1 deficient patients, and appeared to improve OS, particularly for biphasic and sarcomatoid patients (Szlosarek *et al.*, 2020).

1.2.8 Considerations for MPM pathogenesis

The complete MPM pathogenesis is still not completely understood, despite decades of dedicated research. One of the most established proposed pathways suggests that asbestos fibres get inhaled through the airways, reaching the lungs, where they get lodged between the pleural layers and the wall of the chest cavity. This prolonged exposure to asbestos induces a continuous production of reactive oxidative stress and subsequent chronic inflammation, thus promoting a potential disease/carcinogenesis process (Røe & Stella, 2015). MPM tumours are heterogeneous, presenting an intricate pattern of molecular changes, including genetic, chromosomic, and epigenetic alterations (Blanquart, Jaurand, & Jean, 2020).

Asbestos fibres are cytotoxic, clastogenic and mutagenic, meaning that in contact with human cells, the fibres can induce specific structural and numerical chromosomal aberrations, as well as oncogene and tumour suppressor gene mutations, such as K-RAS and p53, respectively (Huang *et al.*, 2011). The section below addresses some of the processes and changes triggered by the presence of asbestos fibres in the human body, as reported in recent literature.

1.2.8.1 The inflammatory pathway

Bielefeldt-Ohmann and colleagues (1994) were the first to report that the initial physiological response to asbestos deposition is inflammation (Bielefeldt-Ohmann *et al.*, 1994). However, after nearly three decades, the cascade of events taking place between recruitment of activated macrophages and onset of MPM is still not completely understood.

It has been reported that macrophages produce IL-1β in response to MF specifically through NACHT, LRR, and PYD domains-containing protein 3 (NALP3) inflammasome (Dostert *et al.*, 2008). Kadariya and colleagues have reported that IL-1β induced inflammation is strongly associated with MM onset (Kadariya *et al.*, 2016). Using an inflammasome-deficient Asc knockout model and a clinically relevant IL-1R antagonist, Anakinra, they showed a significant

correlation between IL-1β-dependent inflammation process and development of asbestos induced MM in murine models (Kadariya *et al.*, 2016).

Similarly, Thompson and colleagues used a combination of *in vitro* and *in vivo* models to investigate the role of NALP3 inflammasome in the release of the proinflammatory cytokines IL-1β and IL-18. They reported that subsequent to NALP3-dependent IL-1β release, human mesothelial cells transition to fibroblastic cells with a gain of mesenchymal markers (vimentin and N-cadherin)(Thompson *et al.*, 2017). A schematic diagram describing the components, assembly, and biologic events linked to activation of the NALP3 inflammasome is presented in Figure 1.6.

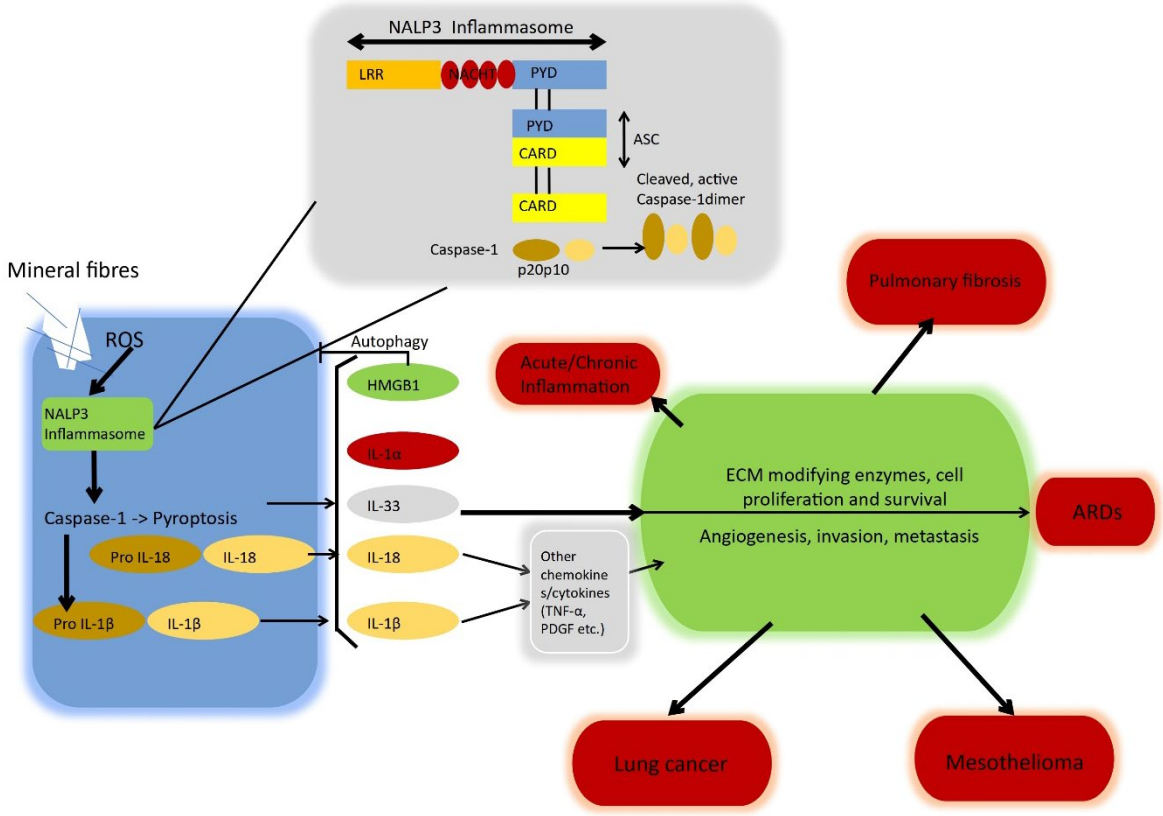

Figure 1.6 Schematic diagram of main components and events linked to inflammatory pathways in mesothelioma. Diagram adapted from Sayan & Mossman, (2015). After MF exposure, the fibres get internalised into the cells causing ROS, that trigger NALP3 inflammasome and caspase-1 activation. Once caspase-1 is activated, IL-1β and IL-18 get matured and released. NALP3 Inflammasome also induces caspase-1 pyroptosis (apoptotic and necrotic cell death). This in turn leads to release of other mediators such as IL-1α and high-mobility group box 1 protein (HMGB1). All together, these chemokines and cytokines drive chronic inflammation associated with pathogenic events in fibre associated diseases (lung cancer, mesothelioma, pulmonary fibrosis, and other asbestos-related diseases) (Sayan & Mossman, 2015).

1.2.8.2 The role of HMGB1 in MPM development

Another reported key element in MPM pathogenesis is the regulated form of necrosis of human mesothelial cells (HMC), which triggers an inflammatory cascade thought to be involved in MPM development. Yang and colleagues (2010) were the first to report that MF cause HMC necrosis followed by activation of poly(ADP-ribose) polymerase, H_2O_2 secretion, ATP depletion, but most importantly translocation of high-mobility group box 1 protein (HMGB1) from the nucleus to the cytoplasm, and into the extracellular space. HMGB1, a damage-

associated molecular pattern (DAMP) protein, is a key initial step in the pathogenesis of MPM and provides a link between asbestos-induced necrotic cell death, chronic inflammation, and ultimately DNA mutation (Carbone & Yang, 2012). Extracellular HMGB1 has been previously reported as a key pro-inflammatory cytokine in other conditions such as severe acute pancreatitis (Yasuda *et al.*, 2006), lupus nephritis and systemic lupus erythematosus (Schaper, Westra, & Bijl, 2014; Zickert *et al.*, 2012), and arthritis (Hamada *et al.*, 2008).

The role of HMGB1 in MPM pathogenesis as proposed by (Carbone & Yang, 2012) is shown in more detail in Figure 1.7. (Jube *et al.*, 2012) concluded that transformed HMC upregulate HMGB1 production, which is critical in cell migration and proliferation, invasiveness, and cell motility. The research group was the first one to report that antibody-mediated blockade of HMGB1 has high therapeutic potential. (Yang *et al.*, 2015) reported acetylsalicylic acid as a possible HMGB1 inhibitor with high antitumourigenic activity in xenograft mice. Another possible inhibitor agent for HMGB1, ethyl pyruvate (EP), was described in systemic inflammation nearly a decade before the proposed MM-HMGB1 link by (Ulloa *et al.*, 2002). (Pellegrini *et al.*, 2017) investigated whether EP can suppress MM in cell cultures and murine models and concluded that EP impaired cell proliferation, motility, and anchorage-dependent growth *in vitro* and reduced HMGB1 serum levels *in vivo* (Pellegrini *et al.*, 2017).

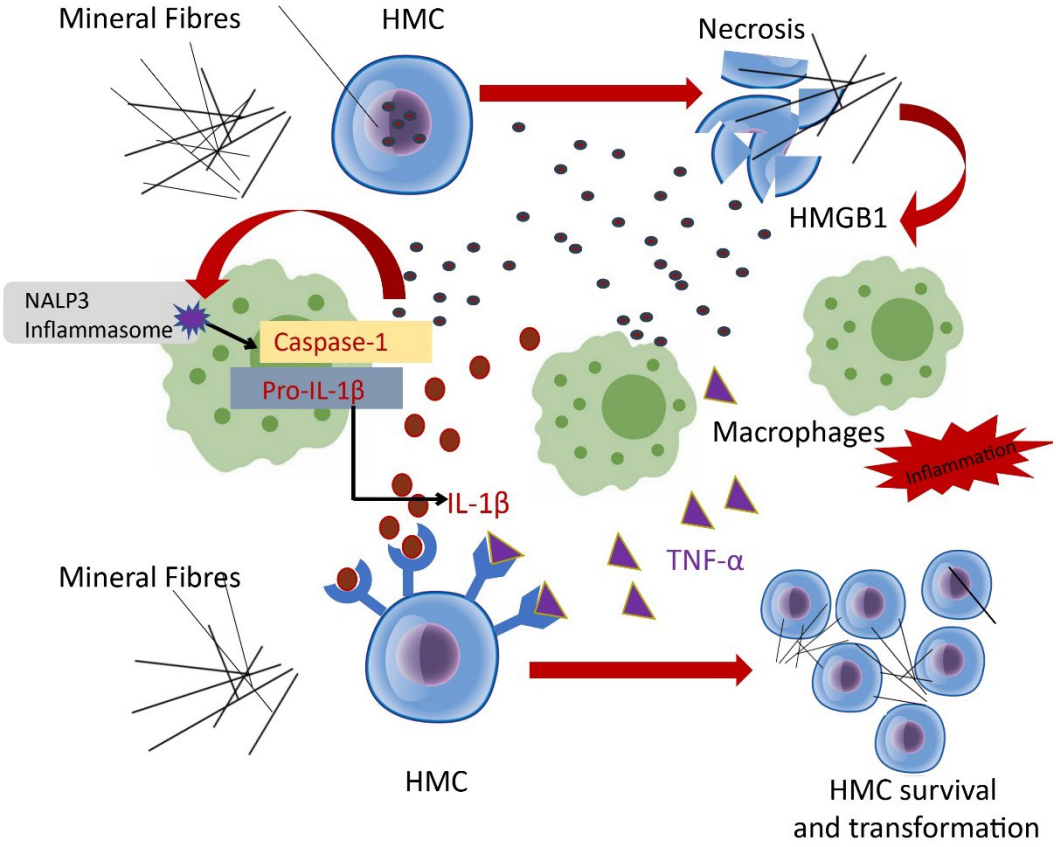

Figure 1.7 The HMGB1 role in MPM development. Figure adapted from (Carbone & Yang, 2012). MF are embedded within the HMC of the pleura, causing necrotic cell death and the release of HMGB1 into the extracellular space. Subsequently, the NALP3 inflammasome gets activated which induces the caspase-1 cascade to secrete IL-1β, eliciting macrophages thus triggering an inflammatory response and secreting TNF-α. The combination of the two cytokines promotes survival of asbestos-damaged HMCs and allows transformation to mesothelioma (Carbone & Yang, 2012).

1.2.8.3 The role of reactive oxidative species in mesothelioma pathogenesis

Macrophages are thought to be responsible for MF internalisation into the cells (Ishida *et al.*, 2019). This type of phagocytosis, known as frustrated phagocytosis, has been reported to induce chronic production of reactive oxidative species (ROS) (Nuvoli *et al.*, 2018). Once the MF are internalised, the chemical environment is changed and they are exposed to higher concentrations of adenosine diphosphate (ADP), citrate and other organic acids that can act as chelators, while ascorbate or cysteine can be involved in redox cycling. Iron chelators (*e.g.,* transferrin) can mobilise Fe away from MF. Given the

bioavailability of Fe, the reductants can produce deleterious ROS (Aust, Cook, & Dodson, 2011). Upregulated production of ROS causes DNA structure and function damage, deterioration of proteins, carbohydrates and lipids, increased mutational events, oncogenic transformation, and ultimately malignancies (Nuvoli *et al.*, 2018). Interestingly, researchers have channelled the cellular potential to cause cell death via ROS production to target malignant cells for apoptosis using ROS-generating drugs such as Cisplatin (Stewart *et al.*, 2007) and Exemestane (Nuvoli *et al.*, 2018).

1.2.8.4 Epithelial-to-mesenchymal transition role in MPM onset

Epithelial-to-mesenchymal transition (EMT) is associated with cancer onset and progression and is caused by different types of inducers, such as transforming growth factor β (TGF-β), the main inducer of EMT, and oxidative stress. EMT is a biologic process by which epithelial cells lose their junctions and apical–basal polarity, acquire the expression of mesenchymal markers, and manifest a migratory phenotype (Ramundo *et al.*, 2021). During EMT, epithelial cells acquire a mesenchymal phenotype by modulating certain proteins (Ramundo *et al.*, 2021). The role of EMT in tumour development and progression has been reported in several cancers including prostate, lung, liver, pancreatic, and breast cancers (Ribatti, Tamma, & Annese, 2020). In MPM, chrysotile asbestos induced EMT of Met-5A human mesothelial cells by downregulating epithelial markers E-cadherin, β-catenin, and occludin, and simultaneously, by upregulating mesenchymal markers fibronectin, α-SMA, and vimentin (Turini *et al.*, 2019). Additionally, overexpression of emerging EMT genes such as *COL5A2, ITGAV, SPARC,* and *ACTA2* has been positively correlated with immunosuppressive infiltration, and an unfavourable factor to OS of MPM patients (Wu *et al.*, 2022). Literature has reported that MPM aggressiveness might be link to the acquisition of a migratory mesenchymal phenotype in the context of EMT (Casarsa *et al.*, 2011). Figure 1.8 offers an overview of the EMT role in mesothelial transformation, including the transcription factors involved. Among the upregulated transcription factors, Snail acts as an inducer, while Twist and Zinc Finger E-Box Binding Homeobox (ZEB) are primarily responsible for the invasive

mesenchymal phenotype (Ribatti *et al.*, 2020). Tumour-associated macrophages also play a crucial role in activation of EMT in tumour cells, in part by TGF-β secretion (Bonde *et al.*, 2012). MicroRNA (miRNA) expression is also associated with EMT, with expression of specific EMT-related miRNAs varying in MPM histotypes (Ramundo *et al.*, 2021). One such example is miR-205, whose downregulation in biphasic and sarcomatoid MPM has been linked to invasiveness and aggressive behaviour, in the EMT context (Farrell *et al.*, 2016).

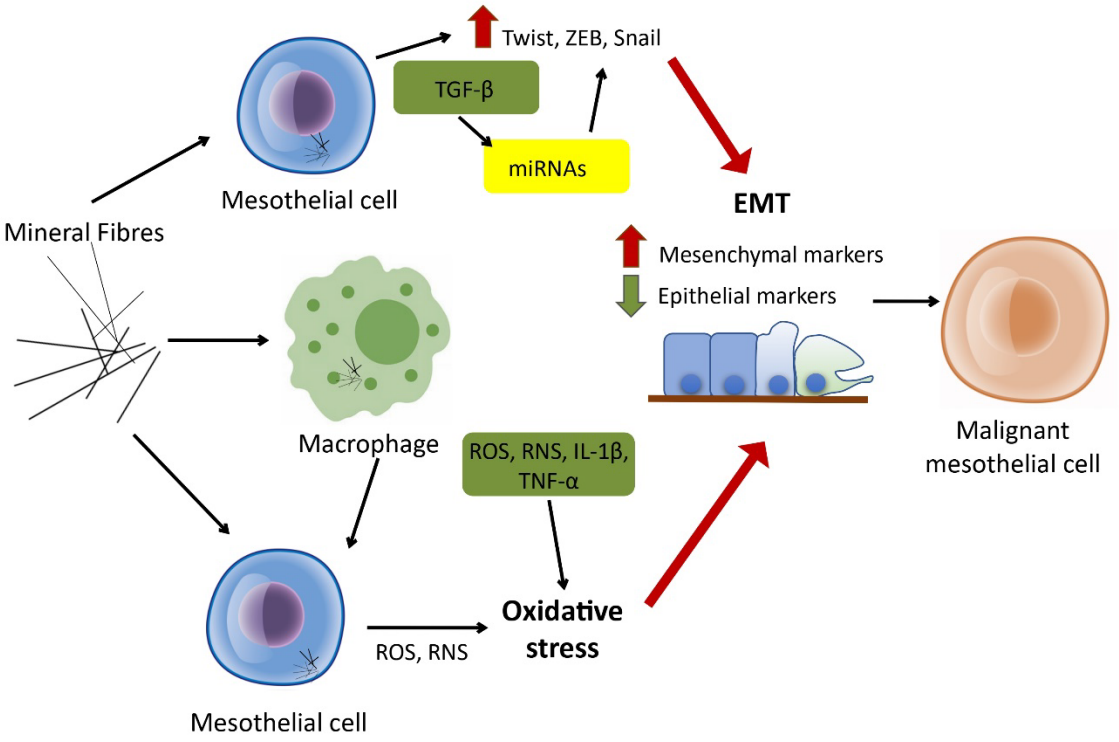

Figure 1.8 The EMT in the development of MPM. Figure adapted from (Ramundo *et al.*, 2021). RNS- reactive nitrogen species; ZEB- Zinc finger E-box binding homeobox; TGF-β- Transforming growth factor beta; TNF-α- Tumour necrosis factor α. Asbestos fibres induce chronic inflammation, the release of growth factors and cytokines, and oxidative stress. These processes impact the levels of certain transcription factors and miRNAs, leading to EMT and malignant cell transformation.

1.2.9 Genomics of mesothelioma

Studies have suggested that understanding the genomic changes involved in MPM progress is essential for successful development of novel diagnostic tools and personalised therapies (Huang *et al.*, 2011). Most common genomic

alterations that drive MPM were identified to be the loss of various tumour suppressor genes such as cyclin-dependent kinase inhibitor 2A gene (*CDKN2A*) (Illei *et al.*, 2003), neurofibromatosis type 2 gene (*NF2*) (Meerang *et al.*, 2016), BRCA1 associated protein 1 gene (*BAP1*) (Xu *et al.*, 2014), and occasionally tumour protein p53 gene (*TP53*) (Hopkins-Donaldson *et al.*, 2006) (Figure 1.9).

1.2.9.1 Loss of *CDKN2A* in MPM development

Homozygous deletion of *P16/CDKN2A* is one of the most encountered genetic mutations in mesothelioma, with around- 75% of reported MPM cases presenting with loss-of-function mutations in *CDKN2A* (Ladanyi, 2005). *CDKN2A* encodes $p16^{INK4A}$ and $p14^{ARF}$, two critical cell cycle regulators. One study used fluorescent *in situ* hybridisation assay (FISH) to investigate the deletions at chromosome region 9p21 targeting the *CDKN2A* and methylthioadenosine phosphorylase (*MTAP)* gene on interphase nuclei in 95 cases of MPM (Illei *et al.*, 2003). They concluded that deletions of *CDKN2A* occurred in 74% of the cases, and MTAP deletions were dependent on *CDKN2A* deletions (Illei *et al.*, 2003). Additionally, homozygous loss of *CDKN2A* has been linked to more aggressive cases of MPM (Ivanov *et al.*, 2009). Based on this knowledge, a recent study suggested the integration of p16 FISH testing as a routine clinical practice in MPM workflow to enhance diagnosis and prognosis accuracy (Marshall *et al.*, 2020).

1.2.9.2 The role of *NF2* inactivation in MPM development

Another established tumour suppressor gene, inactivated in more than 80% of MM cases, is *NF2* that encodes Merlin, a tumour suppressor protein. Biallelic inactivation of *NF2*, located on 22q12, was first documented by (Sekido *et al.*, 1995). Changes in *NF2* gene expression lead to Merlin deficiency, alterations to the Hippo pathway and failure to inactivate the oncogenic Yes Associated Protein-1 (YAP1) by phosphorylation (Meerang *et al.*, 2016). Additionally, inactivation of YAP1 results in focal adhesion kinase (FAK) hyperactivation, which subsequently impacts on essential cellular events such as transcription, translation, ubiquitination, and miRNA biosynthesis (Sato & Sekido, 2018). Genetic alterations in other components of the Hippo pathway such as

amplification of YAP1 have also been recently reported (Mizuno *et al.*, 2012; Rehrauer *et al.*, 2018; Zhang, Wen-Qian *et al.*, 2017). Investigation of Merlin functions in MM can have high implications in the management and treatment of MM cases. For instance, one study by Meerang and colleagues (Meerang *et al.*, 2016) showed a correlation between low cytoplasmic Merlin expression and shorter OS. Using tissue microarray samples from two different patient cohorts (pre- and post- chemotherapy), the group used immunohistochemistry to link expression of Merlin, YAP1 and its target genes, and Survivin (apoptosis inhibitor) to poor prognosis in MM patients.

1.2.9.3 The role of *TP53* in MPM progression

TP53 gene, a tumour suppressor gene located at 17p13.1 encodes for p53 and plays a critical role in control of cell cycle and apoptosis. *TP53* abnormalities have been found in less than 20% of MM cases, a low percentage compared to other human malignancies (≈50%) (Sekido, 2010). However, it has been reported that most MM tumours present wild type p53 with deletion of $p14^{ARF}$ and $p16^{INK4A}$, which are essential in downregulating Murine Double Minute 2 (MDM2). When MDM2 is upregulated, p53 gets ubiquitylated and loses its essential function in cell cycle arrest and apoptosis (Bahnassy *et al.*, 2012). Loss-of-function mutation in *TP53* has been associated with cases of mesothelioma in extremely young patients (Hassan *et al.*, 2019).

1.2.9.4 The link between *BAP1* mutation and predisposition to MPM

First and second-hand exposure to asbestos are the main risk factors of MPM. However, studies have shown that only 5% of asbestos workers will develop mesothelioma in their lifetime (Below *et al.*, 2011). Further reading suggests a link between inactivating germline mutations of *BAP1* gene and a predisposition to MPM upon exposure to a reduced level of MF (Ohar *et al.*, 2016). *BAP1* is a deubiquitinating enzyme with key roles in DNA repair and gene expression regulation (McCambridge *et al.*, 2018). *BAP1* is a tumour suppressor gene located on 3p21 first reported to be involved in MM by Delsite and colleagues *BAP1* inactivation through somatic mutations has been found in 23% of MPM

samples; however other studies reported higher rates (42% and 61%) (Delsite *et al.*, 2011; Yoshikawa *et al.*, 2012).

BAP1 gene alteration is not enough to lead to spontaneous MPM cases, but individuals presenting *BAP1* mutation tend to develop MM earlier in life (Pulford *et al.*, 2017). Chou *et al.*, (2018) reported an increase in tumour invasiveness MM in *BAP1* +/- knock-out mice models. Contrariwise, McGregor and colleagues (McGregor *et al.*, 2015) suggested that *BAP1* loss is associated with epithelioid MPM and thus *BAP1* mutated cases have higher survival rates (McGregor *et al.*, 2015). In a similar fashion, (Baumann *et al.*, 2015) reported a 7-fold increase in survival among patients with germline *BAP1* mutation (n=10,556). More studies support these findings (Chou *et al.*, 2018). Targeting *BAP1* role in MPM development might have implications in close monitoring and early intervention, however genetic screening strategies are currently not taken into consideration (McGregor *et al.*, 2015).

It is essential to note that loss of *BAP1* is mostly associated with epithelioid subtypes (Yoshikawa *et al.*, 2012). On the other hand, loss of *NF2* function is associated with a more aggressive behaviour and is mainly found in sarcomatoid subtypes (Blum *et al.*, 2019).

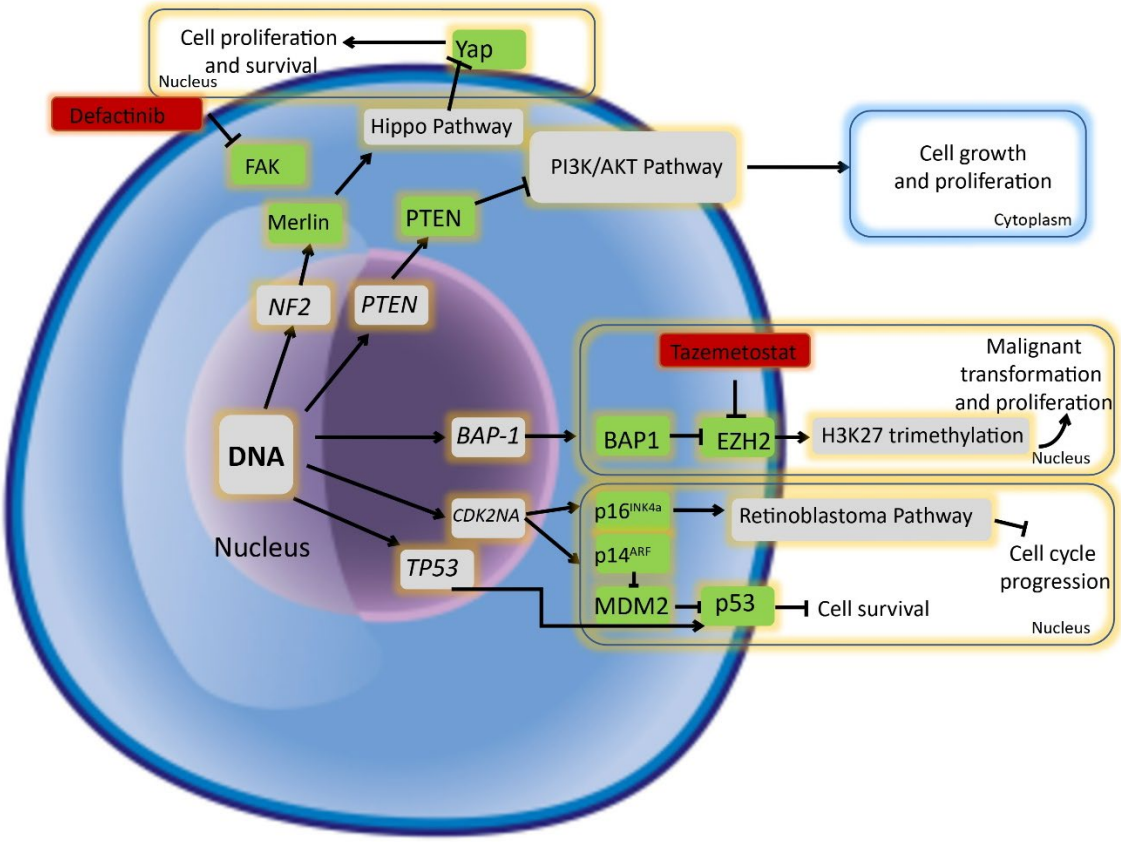

Figure 1.9 Genetic alterations potentially involved in MM pathogenesis. Figure adapted from (McCambridge *et al.*, 2018). *NF2* encodes the Merlin protein, a key regulator of the Hippo pathway. Mutated *NF2* leads to inactivation of the Hippo pathway and cell proliferation and survival through YAP1 activation. Additionally, inactivation of *NF2* results in FAK hyperactivation, which subsequently impacts on essential cellular events. Defatinib, a FAK inhibitor is a potential MM cytotoxic drug. Phosphatase and tensin homolog gene (*PTEN*) negatively regulate phosphoinositide 3-kinase (PI3K)/AKT pathway. Loss of *PTEN* function leads to overactivation of PI3K/AKT pathway leading to cell growth and proliferation. Mutated *BAP1* results in activation of the enhancer of zeste 2 polycomb repressive complex 2 subunit (EZH2), which in turn leads to trimethylation of histone 3 lysine 27 (H3K27) and consequently to malignant transformation. *CDKN2A* encodes p16INK4A and p14ARF. p16INK4A is fundamental in hyperphosphorylation and subsequent inhibition of the retinoblastoma pathway, essential in cell cycle progression. When p14ARF is inactivated, MDM2 levels increase. Increased production of MDM2 negatively regulates p53 production and results in increased cell survival. Similarly, loss of p53 can be caused by a mutation in TP53 gene, which encodes for this tumour suppressor protein (McCambridge *et al.*, 2018).

1.3 Mineral fibres

1.3.1 History of asbestos

Asbestos has been known to humanity for thousands of years with reports about a fire-retardant material dating back to Ancient Egypt (Virta, 2006). Interestingly, the harmful effects of the MF have also been documented thousands of years ago by Greek and Roman philosophers (Virta, 2006). The exploitation of asbestos mines had begun just after the Industrial Revolution, but the intensive growth of the industry did not happen until the beginning of the 20th century (Virta, 2006). With the onset of World War II, asbestos production skyrocketed through 1942 to meet increased war demands, peaking in the '70s (Bononi *et al.*, 2015). Asbestos was officially declared a human carcinogen by the US Environmental Protection Agency (EPA), the International Agency for Research on Cancer (IARC) of the World Health Organization, and the National Toxicology Program more than 20 years ago (Ramazzini, 2011). Despite being banned in most developed countries, the population is still exposed to asbestos fibres during incorrectly performed removal procedures, or in buildings with altered asbestos containing material (Boulanger *et al.*, 2014).

1.3.2 Types of mineral fibres

The term "asbestos" is a general term and refers to silicate minerals that are naturally composed of polyfilamentous bundles of extremely long, flexible fibres with a small diameter that can be easily inhaled when broken into fibrils (IARC Monographs, 2012). These naturally occurring silicate MF were used intensively in the ‘70s due to their physical properties (sound absorption, average tensile strength, affordability, and resistance to fire, heat, and electricity). The MF are classified into two subgroups: (i) the amphiboles, a group of rod-like fibres including amosite (brown asbestos), crocidolite (blue asbestos), anthophyllite, actinolite, and tremolite; and (ii) the serpentine group, consisting of chrysotile (white asbestos) (Bononi *et al.*, 2015). More details on these MF are presented in Table 1.3 and Table 1.4.

There are some conflicting arguments within the literature on the precise identification and relative MF levels needed to cause MM. The potency of inducing asbestos-related diseases such as pleural plaques, asbestosis, and MM reportedly differs from one fibre to another due to difference in chemical structure, and therefore in solubility of fibres in the lung (IARC Monographs, 2012). This resistance property of MF also known as biopersistence was first reported by Stanton and Wrench (Stanton & Wrench, 1972) as the “Stanton fibre hypothesis”.

1.3.2.1 Serpentine asbestos- Chrysotile

Chrysotile or ‘white asbestos’ is the most versatile type of asbestos, accounting for about 90% of the total asbestos industry (Qi *et al.*, 2013). It is the only established asbestiform serpentine fibre and it is found in serpentine rocks formed under hydrothermal conditions. Most of the chrysotile deposits contain 2-10% chrysotile which is separated from the rock by a series of intensive processes. Principal mines are based in Canada, Southern Rhodesia, and Swaziland. Chrysotile is very long compared to the other fibres with extremely fine fibrils (250 Å in diameter). The extracted long fibres were generally used in textiles, whilst shorter fibres were mainly used in construction. Despite the thin fibrils, it has a relatively high tensile strength (106 lb/ in^2) (Eichhorn *et al.*, 2009). However, compared to the amphiboles, serpentines have a very low resistance to acid (IARC Monographs, 2012). Chrysotile is a phyllosilicate, hydrated crystal containing 13% water. The characteristic concentric hollow core is given by the spatial imbalances between Mg and silica ions within the tetrahedral and octahedral sheets (Tannapfel, 2011). Magnesium is an essential component of chrysotile. The oncogenic potential is reduced when the surface charge changes from positive to negative caused by a reduction or loss of Mg. Mg also affects the breakdown of MF within the human body making chrysotile less biopersistent (*i.e.,* more susceptible to being eliminated by the human cells through phagocytosis) (Pierce *et al.*, 2008).

1.3.2.2 Crocidolite

Crocidolite, also known as the ‘blue asbestos’ is made up of brittle fibres, generally harder and more flexible than other amphibole fibres. The straight, needle-like fibres are easily inhaled and have reportedly longer biopersistence in the lungs (Nagai & Toyokuni, 2012). It is mined mainly in South Africa from banded ironstones. It has a similar strength as chrysotile, but its resistance to acid is significantly higher (IARC Monographs, 2012).

Several studies have tried to quantify the potency of different fibres, including crocidolite. One such systematic attempt to quantify the differences has used the percentage of mesothelioma deaths of all deaths expected per unit of cumulative exposure (Rm) as the variable for their meta-analysis. They concluded that the potency ratio between chrysotile, amosite, and crocidolite was 1:100:500 for mesothelioma and 1:10:50 for inducing lung cancer (Hodgson & Darnton, 2000). Despite these findings, the reasons why crocidolite is such a potent carcinogen have not been completely elucidated. It has been previously documented that iron ions play a key role in MF toxicity because of the chemical properties allowing them to catalyse generation of ROS (Ghio *et al.,* 2004; Kamp, 2009). However, the question remains why some iron-poor amphiboles can still induce severe cases of asbestos related diseases (ARDs). One possible explanation was recently given by Andreozzi and colleagues (Andreozzi *et al.*, 2017). Using high resolution transmission electron microscopy energy-dispersive X-ray spectroscopy and spin trapping electron paramagnetic resonance spectroscopy, they showed that the high potency of crocidolite compared to other amphiboles is given by the specific Fe^{2+}, Fe^{3+} surface sites, rather than the total number of Fe ions in the chemical formula (Andreozzi *et al.*, 2017).

Physical properties can also play a role in MF potency. The fibre-cell contact is the first step in initiation of MM pathogenesis (Carbone & Yang, 2012). There is still a gap in knowledge on how these fibres exactly interact with the cells, whether the MF are engulfed by cells via an active process, or they penetrate the cells via a passive process. For example, one study suggested that crocidolite fibres enter the mesothelial cells via an active cellular process, known as frustrated

endocytosis (Nagai & Toyokuni, 2012). The researchers showed crocidolite fibres were engulfed within mesothelial cells, covered by typical vesicular membrane structures (Nagai & Toyokuni, 2012). It has been long established that the surface charge of the MF plays an important role in fibre-cell interaction. For example, one study showed that crocidolite and amosite are negatively charged and bind different surface proteins than the chrysotile, which is positively charged (Scheule & Holian, 1990). Despite these findings being reported more than 30 years ago, the actual binding mechanism is still not completely understood. One possible explanation was first described by Boylan et al. (Boylan *et al.*, 1995) and supported by Pande and colleagues (2006), which proposed that crocidolite fibres internalisation is mediated by αvβ5 integrin (Pande, Mosleh, & Aust, 2006).

1.3.2.3 Amosite

Amosite is the second most common amphibole after crocidolite. It is a chain silicate with brittle and less flexible fibres that contains less water than the serpentine fibres. It has a much greater clearance halftime (*i.e.,* decades) being more resistant to biofragmentation than the chrysotile (Tannapfel, 2011). Amosite occurs in similar geological formations as other amphiboles in South Africa, in some places even found in association with crocidolite. Amosite frequently occurs as very long fibres of up to about 10 inches in length. Amosite is weaker than crocidolite and is not usually sufficiently flexible to be spun and woven (IARC Monographs, 2012). Interestingly, when researching ARDs, scientists face different challenges depending on the fibre type. For example, amosite fibres have a simple structure, but their chemical relationships are complex, whereas chrysotile is chemically simple but structurally complex (Tannapfel, 2011).

1.3.2.4 Actinolite and tremolite

Actinolite and tremolite are naturally occurring MF. These fibrous minerals may occur in both asbestiform or non-asbestiform varieties and are natural components of rocks and soils (Baumann *et al.*, 2015). Actinolite and tremolite are amphiboles with similar properties to amosite and crocidolite (length/diameter ratio >3:1, a high surface area, width <0.25 μm). Mesothelioma cases caused by

these MF are known as environmental cases and normally occur in younger populations, with a 1:1 male: female ratio. Actinolite and tremolite are typically weak MF, and have some specialised applications, particularly in electrical insulation (Baumann *et al.*, 2015). The MF are widely distributed in the metamorphosed mafic, ultramafic, and carbonate rocks of South Africa, Italy, and Finland as well as in other countries but in smaller proportions (IARC Monographs, 2012). Like the rest of the MF reviewed above, actinolite and tremolite are monoclinic crystals, meaning they normally form a rectangular prism with a parallelogram as its base (Gopal, Narasimhulu, & Rao, 2004). There is a gap in literature specifically on the effects of actinolite on *in vitro* or *in vivo* models mainly because it is not easily accessible for research purposes.

1.3.2.5 Non-asbestiform minerals and other emerging carcinogenic fibres

The intricate chemical and physical properties of MF have led to inconsistencies in the scientific literature (Below *et al.*, 2011). There are ~400 additional MF in nature, and although these fibres are not termed “asbestos” they still have potential to induce MM in a similar fashion as the established MF previously described. Moreover, the exact chemical formulations of each type of fibre vary with the location from which it was mined, adding to the complexity of this material (Hoch *et al.*, 2007).

One such naturally occurring MF is erionite, which literature reported to have a higher potency in inducing MM than some asbestos fibres (Gualtieri *et al.*, 2017). A different example recounted in literature is antigorite. Antigorite is classed as a polymorphous serpentine mineral, meaning it has the same chemical formula as chrysotile, but the atoms are arranged into different structures (Wagner, 2015). Due to these chemical differences, antigorite has not been yet classed as a carcinogen, even though it was linked to a MM epidemic in New Caledonia, after being used as road gravel (Wagner, 2015). Other studies have also revealed potential cellular toxicity of antigorite by upregulating production of hydroxyl and nitric oxide radicals in the lungs from macrophages, as well as triggering inflammation, a key player in MM pathogenesis (Pugnaloni *et al.*, 2010; Venera Cardile *et al.*, 2007).

Another emerging non-regulated asbestiform mineral is palygorskite, also known as attapulgite. There are conflicting arguments in the current literature on palygorskite's ability to induce MM. These contradictory results reported more than 30 years ago might be due to the differences in palygorskite samples (fibre length, purity etc.) (Larson *et al.*, 2016). A more recent study employed primary HMC, as well as murine models, to investigate whether palygorskite alone can induce MM and concluded that this MF does not elicit inflammatory responses *in vivo* and no mice exposed to it had developed MM (Larson *et al.*, 2016).

Another mineral, wollastonite (pyroxenoid, with a nominal composition $CaSiO_3$) a naturally occurring calcium silicate that is produced in both powder and fibrous forms and presents a structural geometry similar to that of crocidolite (Aust *et al.*, 2011). Additionally, natural occurring wollastonite has a needle-like shape and may contain trace amounts of Al, Fe, Mg, Mn, K, and Na, all of which led the researchers to investigate its carcinogenic properties (Aust *et al.*, 2011). In short, there is currently little evidence that wollastonite alone is enough to induce MM in human cohorts or animal studies. The low tumorigenic properties are attributed to the high solubility of wollastonite in the human body (McConnell, Hall, & Adkins, 1991). However, naturally occurring wollastonite may be contaminated with asbestos fibres so health and safety (H&S) procedures should still be followed (Maxim & McConnell, 2005).

Technical name	Common name	Non-asbestos mineral analogue	Idealised chemical formula	Colour	Decomposition temperature (°C)	Chemical Properties	Physical Properties	Literature	Geographic Distribution
Serpentine									
Chrysotile	White asbestos	Lizardite; Antigorite	$[Mg_3[Si_2O_5](OH)_4]_n$	White, grey, yellowish	600-850	Two-layered silicate with a hollow central core. Positive surface charge. Degradable in dilute acids.	Curled. Length: several mm to more than 10 cm. Flexible fibres	Qi *et al.,* 2013	Canada (Quebec), USA (Vermont, California), Russia, China
Amphiboles									
Actinolite	Unspecified	Actinolite	$[Ca_2Mg_4Fe^{2+}[Si_8O_{22}](OH)_2]_n$	Green	450-900	Double chain silicate, negative surface charge in water.	Brittle fibres, asbestiform and non-asbestiform states.	Baumann *et al.,* 2015	South Africa (Cape Province), Italy
Amosite	Brown asbestos	Grunerite	$[Mg_{1.5}Fe^{2+}_{5.5}[Si_8O_{22}](OH)_2]_n$	Brown, greyish	600-900	Double chain silicate, can be resistant to acids, negative surface charge in water.	Long, straight, coarse fibres. Can be flexible.	Levin *et al.,* 2016	South Africa
Crocidolite	Blue asbestos	Riebeckite	$[Na_2Fe^{2+}_3Fe^{3+}_2[Si_8O_{22}](OH)_2]_n$	Lavender, blue green	400-900	Double chain silicate, resistant to acids, negative	Shorter, thinner, flexible	Andreozzi *et al.,* 2017; Nagai&	South Africa, Western Australia

						surface charge in water.	fibres. Less heat resistant.	Toyokuni 2012	
Tremolite	Unspecified	Tremolite	$[Ca_2\ Mg_2\ [Si_8O_{22}](OH)_2]_n$	White to pale green	950-1040	Double chain silicate, resistant to acids, negative surface charge in water.	Brittle fibres, asbestiform and non-asbestiform states. Common contaminant in talc and chrysotile.	Andreozzi *et al.,* 2017; Yamashita *et al*., 2013	Turkey, Cyprus Greece

Table 1.3 Adapted from the International Agency for Research on Cancer (IARC Monographs, 2012). Asbestos (Chrysolite, Amosite, Crocidolite, Tremolite, Actinolite, and Anthophyllite)

Percent composition (%)	H	O	Na	Mg	Al	Si	Ca	Ti	Mn	Fe
Wollastonite		24.18				41.32				
Actinolite	0.24	45.01	0.59	9.71	1.39	25.64	8.6	0.11	0.13	8.58
Chrysotile	1.45	51.96		26.31		20.27				
Amosite (Grunerite)	0.2	38.34				22.43				39.03
Amosite (Cummingtonite)	0.26	49.18		21.79		28.78				
Crocidolite (Riebecktite)	0.22	41.03	4.91			24.01				29.84

Table 1.4 Chemical composition of the MF used in this study. Table adapted from Korchevskiy *et al.,* 2019.

1.3.3 Methods of detecting asbestos and other mineral fibres in biological samples

1.3.3.1 Brightfield and polarised light microscopy

Accurately identifying MF within biological samples is not only essential in aiding early diagnosis of MPM, but it also plays a key role in linking this diagnosis to asbestos exposure, which has high implications in legal, social, and political matters (Capella, Bellis, & Belluso, 2016). The asbestos geological classification (aspect ratio ≥3:1, length ≥5μm, and width <0.25μm) was developed to facilitate the counting of the MF using polarised light microscopy (PLM) and standard microscopy techniques, which was the gold standard method of asbestos identification in 1970s-1980s (Gylseth *et al.*, 1985) and was not based on the potency of the fibre segments or shorter fibres to induce ARDs (Egilman *et al.*, 2019). The lack of sensitivity of these methods has been highlighted in publications back in early 1990s. Additionally, standard microscopy cannot distinguish between MF and other natural-occurring or artificial fibres making some MF considerably hard to detect and quantify (Dement *et al.*, 2015). These

limitations have shifted the attention of the research community to more sensitive techniques such as scanning electron microscopy (SEM) and energy dispersive X-ray analysis (EDAX) (Monsó *et al.*, 1991).

1.3.3.2 Electron microscopy

More established and sensitive methods of asbestos identification and quantification, such as SEM and transmission electron microscopy (TEM), generally employ chemical digestion of the tissues in order to eliminate the organic matrix, thus losing all the spatial information (Dement *et al.*, 2015). However, SEM with energy dispersive spectroscopy (EDS) can also offer insight into the presence of asbestos fibres in formalin fixed samples, as well as information regarding the dimensional characteristics of these MF (Visonà *et al.*, 2021). However, these imaging methods cannot differentiate between asbestiform and non-asbestiform fibres, failing to univocally identify certain minerals and to detect low concentrations of MF that are less than 0.20 µm in diameter (Capella *et al.*, 2016; Visonà *et al.*, 2021). Additionally, manual examination under microscopy is time-consuming and can be reader-dependent (Bardelli *et al.*, 2021). The advantage of using TEM is that it can reveal asbestos crystallographic structure and level of crystallinity by performing selected area electron diffraction (Germine & Puffer, 2020). Nevertheless, these instruments are less accessible, and require complex and invasive sample preparation, to achieve good quality images (Bardelli *et al.*, 2021).

1.3.3.3 X-ray microscopy

Methods of differentiating MF based on surface charge, such as SEM and TEM are limited in clinical applicability since non-asbestiform amphiboles are virtually identical to asbestiform amphibole fibres in morphology, crystal structure, refractive index, and chemical composition (Schiller, Payne, & Khalafalla, 1980). Given the similarities in chemical structures between the MF (*i.e.,* silicates), and also the proportional discrepancies of main elements such as Fe, Ca, and Mg between each fibre type, elemental analysis has gained popularity in recent years compared to the other methods presented above, such as SEM and TEM. One

example employed an in-air micro-particle induced X-ray emission (in-air micro-PIXE) system to identify the location of asbestos bodies in lung tissue sections (Shimizu *et al.*, 2008) However, this has only been achieved with limited spatial resolution. Sub-micrometer lateral resolution has been reported in a study by Pascolo *et al*., (2011) who employed soft X-ray imaging and X-ray fluorescence (XRF)microscopy to investigate elemental lateral distribution of asbestos bodies in lung tissue samples (Pascolo *et al.*, 2011). Given the complexity of the techniques used in the study, there are limitations in its applicability in a clinical setting, and it is therefore presented more as a research tool for the study of the chemical interactions between fibres and cells. Another recent approach to counting asbestos bodies in lung tissue samples employed X-ray phase-contrast micro-tomography (XPCμT), a tridimensional imaging technique coupled to an automated counting routine for unbiased total fibre count. However, this proof-of-concept method is time-consuming and has only been shown in a very limited number of samples (Bardelli *et al.*, 2021).

1.4 Introduction to analytical techniques

1.4.1 Basics of mass spectrometry

Mass spectrometry (MS) is an established analytical technique capable of molecular analysis by ionisation of chemical species and subsequent sorting of the ions by their mass to charge ratio (*m/z*). The principal elements of a mass spectrometer instrument include the (a) ionisation source, where molecules within the sample are ionised (*i.e.,* the addition or removal of an electron to create an ion), (b) mass analyser, where ions are separated by their *m/z*, (c) detector, for the measurement of ion relative abundance, resulting then in a mass spectrum (*i.e.*, *m/z* ratios of the ions present in a sample plotted against their intensities), and a (d) data system, which includes computer and software, for the acquisition and processing of data derived from MS. Most commercially available MS offer different configurations of ionisation sources, mass analysers and detectors.

Over the last decade, technical advancements in instrumentation have allowed vast improvements in MS speed, spatial resolution, and sensitivity. In addition,

MS modalities employing a wide range of ionisation sources have been developed including: matrix-assisted laser desorption ionisation (MALDI), a soft ionisation technique which employs laser energy and an absorbing matrix; secondary ionisation mass spectrometry (SIMS), using a focused primary beam of ions resulting in the analysis of secondary ions ejected from the sample surface; desorption electrospray ionisation (DESI), an ambient ionisation methodology via a solvent spray; laser ablation inductively coupled plasma (LA-ICP) involves a nanosecond-pulsed laser to the sample surface (Russo *et al.*, 2020).

MS separates ions based on the *m/z* by applying electrostatic fields. Electrostatic manipulation of ion flow in analogy with light manipulation by optical lenses is called ion optics. There are a variety of mass analysers and they can be classified by how the ions are being introduced such as continuous or pulsed modes. MS analysers can be categorised as tandem MS/MS systems or single mass analysers, which include the magnetic sector field (SF) (Figure 1.10), quadrupole (Figure 1.11), and time-of-flight (TOF) analysers (Figure 1.12).

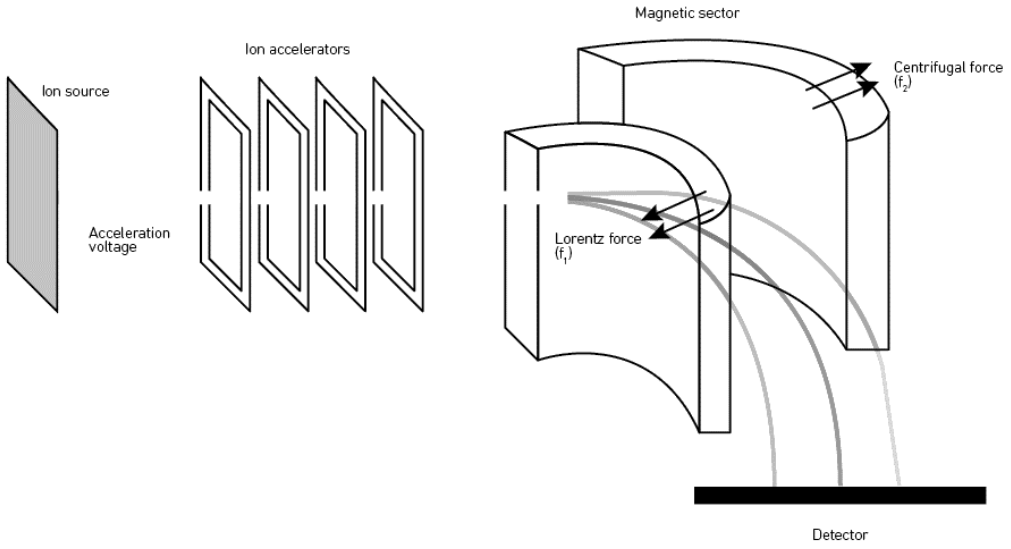

Figure 1.10 Schematic of a magnetic sector field mass analysers. The SF uses magnetic field to separate ions of different *m/z* values. A high voltage is applied to the ions to accelerate them into the magnetic sector. A continuous ion source is generated and supplied from the ionisation unit to the magnetic sector. The ions are exposed to the magnetic field and subsequently deflected (*i.e.,* deflections differ based on the *m/z* where lighter ions (of the same charge) will experience more deflection). As the direction of the ion changes, a centrifugal force (f2) acts on the ion. For the ions to pass through the magnetic field region and reach the detector, it must travel along a curved path of a given radius (r) where f1 and f2 are balanced. By keeping the ion acceleration voltage constant and varying the magnetic flux B, a detector placed on the corresponding path could detect any mass (Shimadzu). Figure adapted from Technologynetworks.

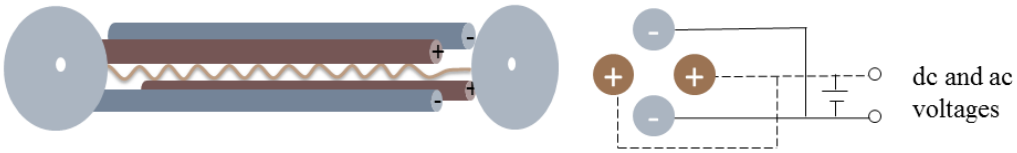

Figure 1.11 Schematic of a quadrupole mass analyser. The quadrupole contains four parallel cylindrical metal rods (electrodes with a hyperboloidal interior surface) inside a vacuum chamber, positioned equidistant from the centre axis. Both a direct current (D.C.) and high frequency alternating current (AC) are applied to the quadrupole, so that only the ions with the target *m/z* successfully pass and get to the detector. The quantity of ions that reach the detector is measured as signal intensity. The ions pass through a tiny orifice and enter the quadrupole where a voltage of the same polarity is applied to diagonally opposite poles and opposite voltage polarity is applied to adjacent poles. When a combination of the DC voltage and high-frequency AC voltage is applied to each pole, an electric field with a rapidly varying phase is generated within the quadrupole (Shimadzu). Figure adapted Creative-proteomics.

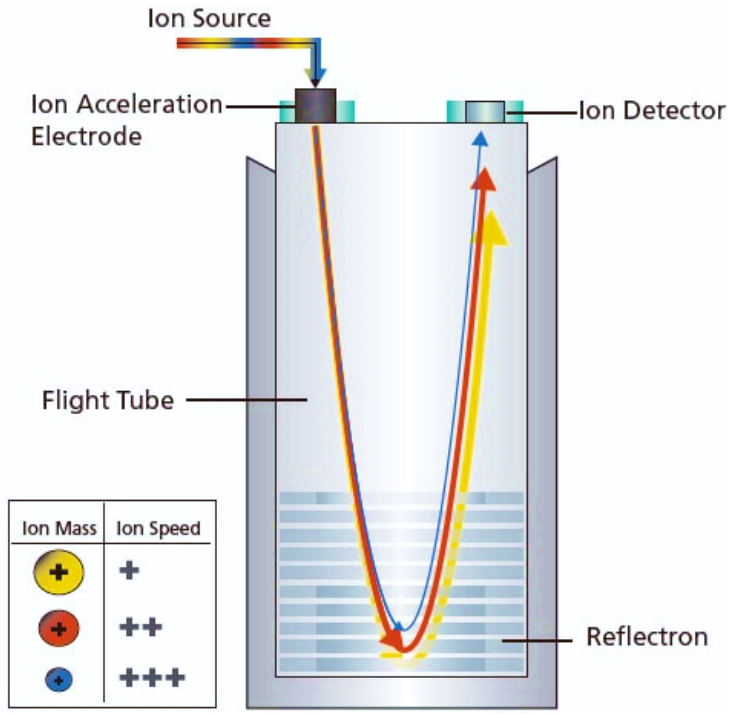

Figure 1.12 Schematic of a TOF mass analyser. The TOF MS is a simple construction, consisting of an accelerator, a field-free region, a reflectron and detector inside a high vacuum chamber called a flight tube. In brief, it separates and detects ions of different *m/z* by measuring the time taken for the ions to travel through a field-free region. Ions generated in an ionisation unit are accumulated and introduced in pulses to a flight tube, and then accelerated by applying a high acceleration voltage between the electrodes. Given a constant acceleration voltage as well as kinetic energy, each ion flies at its unique velocity inside the flight tube to reach the ion detector, which is higher for ions with smaller masses and lower for ions with larger masses. Figure adapted from Shimadzu.

The advantages and limitations of the aforementioned mass analysers are presented in Table 1.5.

Mass Analyser	Description	Advantages	Limitations
Magnetic Sector	Scanning Continuous	High resolution High dynamic range High reproducibility High sensitivity	Expensive and bulky Slow scan speed High vacuum required Difficult to couple with pulsed ionisation techniques and LC

Quadrupole	Scanning Mass Filter Continuous	Compact and simple Relatively cheap Good selectivity Moderate vacuum required well suited for coupling to LC	Limited mass range Low resolution Little qualitative information
Time-of-Flight	Non-scanning Pulsed	High sensitivity and ion transmission High resolution Excellent mass range Fast scan speed	Requires pulsed introduction to MS Requires fast data acquisition

Table 1.5 Advantages and limitations of the main mass analysers employed in this study.

1.4.2 LA-ICP-MS Imaging

Laser ablation inductively coupled plasma mass spectrometry (LA-ICP-MS) was introduced as a viable analytical method by Gray in 1985 (Gray, 1985), and has rapidly become the gold standard for multi-elemental and isotopic analysis of a wide variety of solid samples including metals and alloys (Steenstra *et al.*, 2019), geological samples (Liao *et al.*, 2019), and biological samples such as plants (Pedrosa *et al.*, 2019), cells and tissues (Voloaca *et al.*, 2020; Voloaca *et al.*, 2022). The samples are normally placed in the sampling chambers, at atmospheric pressure. A typical LA-ICP set-up is composed of three main parts: (1) laser ablation for generation of sample aerosols, (2) aerosol transport, and (3) atomisation, vaporisation, and ionisation of the aerosols in the ICP torch. In brief, LA-ICP-MS involves vaporising small parts of a sample using a focused pulse of laser energy. Sample preparation is virtually non-existent, avoiding sample-digestion-related problems such as incomplete digestion of certain minerals (Lin *et al.,* 2016). The aerosol mist passes through a spray chamber, where the larger droplets are removed. The fine droplets are carried by the Ar gas flow to the ICP plasma torch. The sample aerosol obtained by solution nebulisation or laser ablation is introduced into the high-temperature ICP (around 9000 K), where the aerosol is evaporated, dissociated, atomised, and ionised to generate ions. Most elements that pass through the Ar plasma are converted efficiently to singly

charged positive ions. The positively charged ions are extracted from the Ar plasma into the high vacuum of the MS via the interface of sampler and skimmer cones (small cone apertures, of around 0.5 to 1.0 mm are preferred as they provide optimum vacuum conditions) (Douglas *et al.*, 2015). Subsequently, the ions pass through the interface cones, where they are steered and focused into a narrow beam using an ion “lens” with different voltages. In terms of isotopes selected for elemental analysis by LA-ICP-MS, the relative abundance of the analysed isotopes and isobars should be considered firstly. Commonly, the selected analysed isotope should be interference-free or the least interfered and high abundant isotope (Lin *et al.,* 2016). A simple external calibration method is sufficient for qualitative imaging of various elements across biological samples. The calibration is generally based on the sensitivity obtained by analysis of a reference material containing over 20 analysed elements of known concentrations, in which the fractionation factors of all the elements in the reference materials are considered to be the same as those in samples.

By continuously analysing across sample and recording information for each individual spot, a map of the elemental composition can be formed. This is also known as LA-ICP-MS imaging (LA-ICP-MSI) (Figure 1.13). Despite being predominantly used previously to visualise the distribution of metallic elements in pathologies associated with metal-dependent processes (Becker *et al.*, 2010), LA-ICP-MSI has been gaining momentum in other applications such as drug monitoring and receptor expression (Douglas *et al.*, 2015), and forensic science (Orellana *et al.*, 2013).

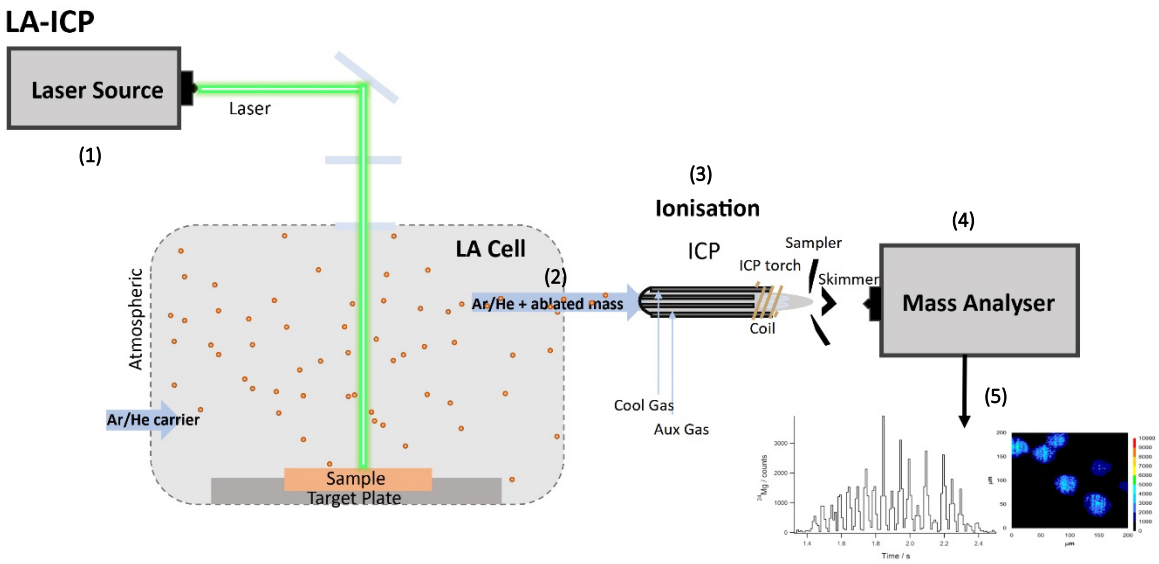

Figure 1.13 Schematic diagram of a typical LA-ICP-MS set-up. The components include (1) laser source (2) aerosol transport, (3) atomisation, vaporisation, and ionisation of the aerosols in the ICP torch, (4) mass analyser and (5) detection and data output. Figure adapted from Barbosa & Sussulini (2020).

1.4.3 MALDI-MS Imaging

Matrix assisted laser desorption ionisation (MALDI) has become established in the mass spectrometry imaging community as the gold-standard ionisation technique for biological and clinical applications. In brief MALDI mass spectrometry (MS) imaging employs a laser in order to desorb and ionise the analytes of interest mixed with a matrix such as alpha-Cyano-4-hydroxycinnamic acid (CHCA) matrix, which aid in the desorption/ ionisation process into the gas phase. Direct analysis is then performed by a raster of the sample by the laser beam (Norris & Caprioli, 2013). The main components are (1) ionisation source, where molecules within the sample are ionised by being protonated or deprotonated with the nearby matrix molecules, (2) mass analyser, where ions are separated by their mass to charge ratio, (3) detector, for the measurement of ion relative abundance, resulting then in (4) a mass spectrum. There is also a data system connected to the instrument, which includes computer and software, for the acquisition and processing of data derived from MS. The most common MALDI ionisation format is for analyte molecules to carry a single positive charge. A typical MALDI MS set-up is presented in Figure 1.14. MALDI MS can be

employed in small molecules studies (> 500 *m/z*) (Russo *et al.*, 2018; Shariatgorji *et al.*, 2014), lipidomics studies (Hart *et al.*, 2011; Lukowski, Weaver, & Hummon, 2017), and proteomics research (typical peptide range 800-2000 *m/z*) (Bradshaw *et al.*, 2013; Flint *et al.*, 2020; Mascini *et al.*, 2018).

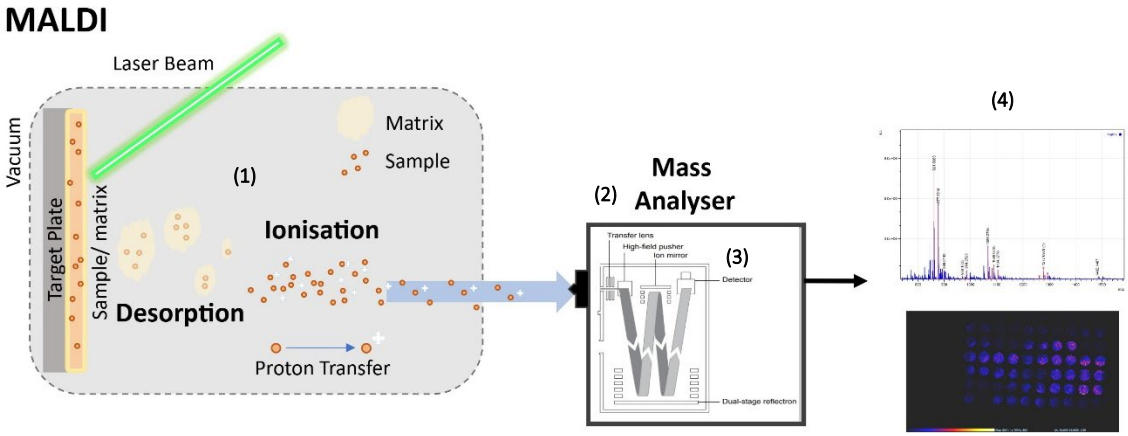

Figure 1.14 Schematic diagram of a typical MALDI-MS set-up. The main components are (1) ionisation source, where molecules within the sample are ionised, (2) mass analyser, where ions are separated by their mass to charge ratio, figure includes the SYNAPT G2 HDMS arrangement (3) detector, for the measurement of ion relative abundance, resulting then in (4) a mass spectrum. There is also a data system connected to the instrument, which includes computer and software, for the acquisition and processing of data derived from MS (not shown in the diagram).

1.5 Emerging mesothelioma biomarkers

An ideal MPM biomarker should be inexpensive, reproducible, easy to obtain, and easily sampled with a minimally invasive technique (Weinstein & Ludwig, 2005). Biomarkers offer an indication of the biological state of the person being investigated and can be categorised in five main groups; (a) diagnostic biomarkers, that help differentiate between different pathologies or between a pathology and a normal state, (b) monitoring biomarkers, which help assess the evidence of exposure to a medical product or environmental agent, (c) pharmacodynamic/response biomarkers, which measure the changes in response to exposure to a medical product or environmental factor, (d) prognostic biomarkers, that can identify the likelihood of a clinical event, disease recurrence, or disease progression in patients with a certain medical condition, and (e)

predictive biomarkers, meaning that the presence or change in levels of the biomarker can help predict the chances of an individual to be impacted by exposure to a medical product or environmental agent (Califf, 2018). To date, soluble mesothelin-related peptides (SMRPs) constitute the only Food and Drug Administration (FDA)- approved biomarker for MM. However, SMRP lacks specificity and there is an urgent need to validate a robust MPM biomarker panel that meets the criteria. Some of the candidate biomarkers that have stood out in recent literature are presented in Table 1.6.

	Type of Biomarker	Methods	Controls	Results	Limitations	Conclusion	Literature
Established biomarkers							
SMRP	Diagnostic/ Monitoring	Serum; Enzyme-linked immunosorbent assay (ELISA)	Healthy, non-malignant, asbestos-exposed, and other malignancies	SMRP was increased in 52% and 5% of MPM patients and asbestos-exposed individuals, respectively. Concentrations in non-malignant and malignant conditions were similar to those in healthy controls	Genetic variability could impact the levels of SMRP and potentially limit the clinical usefulness (Goricar *et al.,* 2020)	SMRP remains the only FDA-approved MPM biomarker; Limited clinical applicability due to inadequate specificity	Beyer *et al.,* 2007
Osteopontin	Differential	Serum; ELISA	Subjects with asbestos-related non-malignant pulmonary disease and subjects without exposure to asbestos	Serum osteopontin levels were significantly higher in the group with pleural mesothelioma than in the group with exposure to asbestos	Unable to be validated as a biomarker in several studies (Grigoriu *et al.,* 2007; Paleari *et al*., 2009)	Serum osteopontin can help differentiate between exposed subjects and MPM cases	Pass *et al.,* 2005
Fibulin-3	Prognostic/ Differential	Human tissue microarray (TMA)	Normal mesothelial tissue	Fibulin-3 was highly expressed in tumour tissues rather than adjacent tissues. High expression of fibulin-3 in tumour tissue linked to poor	Small tissue samples in the TMA not representative of the whole sample of tissue	Fibulin-3 in tumour tissue was a novel biomarker of poor survival of mesothelioma	Zhaoqiang *et al.,* 2020

				survival in patients with mesothelioma			
Calretinin	Diagnostic/ Differential	Serum; ELISA	Subjects with asbestosis, pleural plaques, and occupationally asbestos-exposed subjects without asbestos-related diseases	MM patients had a significantly higher calretinin concentration than subjects without disease, subjects with pleural plaques or subjects with asbestosis (all $p < 0.001$). The histological type was significantly associated with serum calretinin: patients with sarcomatoid MM had lower calretinin than patients with the epithelioid type ($p = 0.001$)	Combination with SMRP is recommended for highest predictive value	Calretinin could serve as a diagnostic marker differentiating between MM and other asbestos-related diseases or asbestos-exposed controls without asbestos-related diseases	Zupanc *et al.*, 2021
Mesothelin	Diagnostic/ Prognostic	Plasma, pleural fluid; ELISA	Benign, Malignant (non-MM)	Mesothelin levels were elevated in 3% of the samples reported as non-malignant, 30% of the atypical or suspicious samples, 14% of the samples reported as non-MM malignancy and 79% of MM samples	Low specificity for MM, high expression in other malignancies	A mesothelin-positive pleural effusion indicates the likely presence of malignancy (79% for MM and 94% for malignancy)	Creaney *et al.*, 2014
Emerging biomarkers							

High mobility group box 1 (HMGB1)	Differential	Human mesothelioma cells, patient serum; ESI-LC-MS, LC-MS/MS, ELISA	Human mesothelial cells, asbestos exposed subjects, patients with benign pleural effusions or malignant pleural effusions not due to MM, and healthy controls	Hyper-acetylated HMGB1 levels were significantly increased in MM patients compared to asbestos-exposed individuals and healthy controls	Small-size study, a larger cohort is needed for validation	Hyper-acetylated HMGB1 is an accurate differential biomarker between MM patients and subjects with occupational exposure to asbestos and unexposed controls/ healthy controls	Napolitano *et al.*, 201
Argininosuccinate synthetase 1 (ASS1)	Diagnostic/ Therapeutic	3D spheroids, TMAs; qRT-PCR, Immunohistochemistry	Publicly available datasets of gene expression of MPM and normal tissues; Healthy TMAs	ASS1 was expressed in 50% of the MPM tumours. ASS1 levels were significantly higher in MPM compared to healthy tissues. Reduction of ASS1 expression by siRNA significantly sensitised mesothelioma spheroids to the pro-apoptotic effects of bortezomib and of cisplatin plus pemetrexed	Conflicting arguments about ASS1 levels in MPM, ASS1 has been found to be deficient in MPM by other studies (Dillon *et al.,* 2004)	Expression of ASS1 protein might play an important role in chemotherapy resistance. ASS1 overexpressed in tumour regions compared to normal tissue.	Barbone *et al.,* 2016
Aurora-related kinase 1 (ARK1)	Diagnostic/ Prognostic	TMA; Immunohistochemistry	Normal peritoneal mesothelium	Immunohistochemical data showed that ARK1 was highly expressed in MM tissue in	Normal peritoneal mesothelium used as	ARK1 could be an optimal diagnostic biomarker and a	Guo *et al.,* 2021

				comparison with normal mesothelial tissue and has been correlated with poor prognosis	a control; low sample pool	potential prognostic marker for MM	
BRCA1-associated protein 1 (BAP1)	Predictive	Human tissues; Immunohistochemistry	MM patients that received “best supportive care” compared to patients treated with pemetrexed	Higher OS was observed in the pemetrexed group for BAP1- versus BAP1+ (OS=20 vs 10 months, $p<0.01$)	Small cohort, limited controls	Loss of BAP1 expression in MM prior to pemetrexed is a significant positive predictive biomarker for OS, regardless of histological subtype	Panou *et al.*, 2020
V-domain Ig suppressor of T cell activation (VISTA)	Prognostic	TMA; Immunohistochemistry	N/A	High staining for VISTA was associated with prolonged median survival	Small sample size, no healthy/ exposed controls	VISTA is a novel prognostic biomarker and potential therapeutic target	Rooney *et al.*, 2019
Programmed death-ligand 1 (PD-L1)	Predictive/ Prognostic	Mesothelioma tissues; Immunohistochemistry	N/A	The median survival time for PD-L1 negative group was nearly 3x as high than the positive group; All patients with sarcomatoid subtype were positive for PD-L1 suggesting a correlation	Limited sample size, data included a higher proportion of patients with no chemotherapy	Patients with positive PD-L1 might have a better response to immunotherapy compared to PD-L1 negative patients, Positive PD-L1 expression correlated to a lower median survival	Nguyen *et al.*, 2018

Novel biomarkers/ panel of biomarkers							
miRNA 197-3p	Asbestos exposure	Serum; RT-qPCR and ddPCR	Healthy subjects of similar age	miR-197-3p was found to be 2.6X down-regulated in exposed vs healthy subjects. Inverse correlation was detected between miR-197-3p expression level and cumulative asbestos exposure.	No MM included	Circulating miR-197-3p is down regulated in sera from exposed workers and might be a new potential biomarker of asbestos exposure	Frontini et al., *2021*
miR-625-3p	Prognostic	EV-enriched serum before and after treatment; qPCR	MM patients with poor treatment outcome and MM patients with good treatment outcome based on OS (n=20)	Post treatment, miR-625-3p and miR-126-3p levels were significantly increased in MM patients with poor treatment outcome	Small sample size, no information on *BAP1* mutation status or other germline mutations	Serum EV-enriched miR-625-3p was associated with treatment outcome and survival of MM	Goricar *et al.*, 2021
2-ethyl-1-hexanol Ethyl propionate Cyclohexanol	Diagnostic/ Differential	Headspace volatile organic compounds (VOCs); GC-MS	Mesothelial cell line (Met-5A)	2-ethyl-1-hexanol was significantly increased in both MSTO-211H and NCI-H28 cells compared to control	Immortalised cell lines, early-stage technique, lacks specificity to MM	VOCs show potential for a diagnostic mesothelioma breath test	Little *et al.,* 2020

Isoleucine 5-dihydrocortisol	Diagnostic	Plasma of cell line-derived xenograft model; GC-MS	BALB/c nude mice with no injected treatment (n=10)	23 metabolites were obtained, including 6 up-regulated and 17 down-regulated. Out of these, Isoleucine 5-dyhydrocortisol were downregulated in the mesothelioma model compared to control	Limited controls, proof-of-concept study	Isoleucine and 5-dyhydrocortisol show potential as diagnostic markers	Gao et al., 2022
Hyaluronic acid (HA) Pleural carcinoembryonic antigen (CEA)	Differential	MPM and lung cancer patient serum	Lung cancer patients	Statistical analysis revealed that a combination of pleural CEA <6.0 ng/mL and HA >30,000 ng/mL can confirm MM with high specificity (98.3%)	Retrospective study, small number of MM compared to lung cancer, cytologically positive (class IV or V) pleural effusion for all patients	Positive results of pleural CEA and HA, can be used to diagnose MM	Takeshi et al., 2022

Table 1.6 Established, emerging, and novel biomarkers in malignant mesothelioma (individual or panel).

1.6 Aims, Objectives, and Hypothesis of the Study

The main aims of this project were (i) to investigate the capabilities of LA-ICP-MSI as a novel asbestos and other MF detection tool and (ii) to characterise emerging mesothelioma biomarkers using a multi-modal approach. In order to achieve these aims the following objectives were investigated:

Chapter 3

- Optimisation of MF and the effect of the fibres on human malignant mesothelioma cells and non-cancerous human mesothelium cells.

Chapter 4

- Development and optimisation of a proof-of-concept method to detect some of the most common types of MF within cellular cytospins based solely on the chemical composition of these fibres.
- Optimisation of the sample preparation steps and LA-ICP-MS analysis parameters for maximum elemental intensity signals.

Chapter 5

- Development of a complex 3D MPM model suitable for LA-ICP-MS sample preparation and analysis.
- Optimisation of the sample preparation steps and LA-ICP-MS analysis parameters for maximum elemental intensity signals.
- Identification of MF within a blind 3D sample using LA-ICP-TOFMS detection of the elements between mass 23 (Na) and mass 238 (U).

Chapter 6

- Detection of asbestos and other MF in human MPM tissue samples of different pathologies using multi modal LA-ICP-MSI.
- Characterisation of MPM metallome using multi-elemental LA-ICP-MSI and high resolution, ultra-fast LA-ICP-TOFMS analysis of human mesothelioma tissues.

Chapter 7

- Biomarker characterisation and preliminary detection of possible biomarkers using a multimodal approach which included techniques such as flow cytometry, fluorescent microscopy, and MALDI-MSI.

Given the nature of the study, the ultimate aim is to integrate the techniques presented herein into the clinical workflow in order to improve the diagnosis and OS of MPM patients.

The hypothesis of the study was that LA-ICP-MS analysis allows for detection of asbestos and other MF in different models of MM, including 3D models and human tissue samples. Secondly, we hypothesised that MPM immortalised cells and TMA human tissue samples express certain emerging biomarkers at different rates, when compared to non-cancerous and NSCLC control cells, and healthy or lung cancer tissue, respectively.

Chapter 2 Materials and Methods

2.1 Materials

2.1.1 Chemical reagents

All chemical reagents were purchased from Sigma-Aldrich or Thermo Fisher Scientific unless otherwise stated. All manufacturers and suppliers are shown in Table 2.1.

Supplier	Location
Abcam	Cambridgeshire, UK
Agar Scientific	Essex, UK
Amsbio	Oxfordshire, UK
ATCC/ LGC Standards	Middlesex, UK
Beckman Coulter	Indianapolis, IN, USA
Biolegend	London, UK
Bio-Techne	Oxon, UK
BioTek	Vermont, USA
CellPath	Newtown, UK
Corning	NY, USA
Elemental Scientific Lasers	Bozeman, Montana, USA
FAST ComTec GmbH	Oberhaching, Germany
Health & Safety Laboratory	Buxton, UK
HTX Technologies	Bedfordshire, UK
Fisher Scientific	Leicestershire, UK
LC Laboratories	Massachusetts, USA
Leica Biosystems	Wetzlar, Germany
Lonza	Basel, CH
National Institute for Standards and Technology	Gaithersburg, MD, USA
New Wave Research	CA, USA

Nu Instruments	Wrexham, UK
Olympus Life Sciences	Tokyo, Japan
PerkinElmer	MA, USA
Promega	Southampton, UK
RND Systems	Abingdon, UK
Sakura	California, USA
Scientific Laboratory Supplies	Hessle, UK
Sigma-Aldrich	Poole, UK
Teledyne Photon Machines	Bozeman, MT, USA
Thermo Fisher Scientific	Paisley, UK
TOFWERK AG	Thun, Switzerland
VWR International	Leicestershire, UK
Waters Corporation	Milford, MA, USA
ZEISS	Oberkochen, Germany

Table 2.1 Manufacturers and suppliers.

2.1.2 Cell lines

All cells used in this study were human immortalised commercial cell lines free of mycoplasma and were handled in sterile laminar hoods at all times. All cell lines were commercially supplied by ATCC/LGC. The full list of cells employed in the study is presented in Table 2.2.

Cell Line	**Morphology**	**Relevant Characteristics**
MSTO-211H (CRL-2081™)	Fibroblast	Biphasic mesothelioma of the lung, no prior radiation or chemotherapy
NCI-H28 [H28] (CRL-5820™)	Fibroblast	Stage 4, epithelioid malignant pleural mesothelioma; lung, derived from metastatic site: pleural effusion
NCI-H1975 [H-1975, H1975] (CRL-5908™)	Epithelial	Adenocarcinoma; non-small cell lung cancer

Met-5A (CRL-9444™)	Epithelial	Derived from pleural fluids obtained from non-cancerous individuals and transfected with the pRSV-T plasmid
U-937 (CRL-1593.2™)	Monocyte	Malignant cells obtained from the pleural effusion of a patient with histiocytic lymphoma; suspension cell culture
HeLa (CCL-2™)	Epithelial	Adenocarcinoma, cervix

Table 2.2 Mammalian immortalised cell lines used throughout the study.

2.1.3 Human tissues

Human tissue sections were purchased from Amsbio and details are presented in Table 2.3.

Patient no	Sample ID	Supplier code	Description	Application
N/A	CX0000000185	CS814500	Pleura; Mesothelioma of pleura, metastatic donor; Frozen	LA-ICP-MSI
N/A	N/A	500029027	Human lung, including bronchioles; Normal; Frozen	LA-ICP-MSI
1	FR00035469	CS536817	Pleura; Mesothelioma of pleura; Frozen; 5 slides x 2 sections, 5 µm thickness	Histology, LA-ICP-MSI
2	FR00002E6B	CS604708	Chest wall; Mesothelioma of pleura, epithelial; Frozen; 5 slides x 2 sections, 5 µm thickness	Histology, LA-ICP-MSI
3	FR00004AF8	CS500965	Lung; Mesothelioma of pleura; Frozen; 5 slides x 2 sections, 5 µm thickness	Histology, LA-ICP-MSI
4	FR0002002E	CS516290	Lung; Mesothelioma of pleura; Frozen; 5 slides x 2 sections, 5 µm thickness	Histology, LA-ICP-MSI
5	FR00005E39	CS502022	Pleura; Mesothelioma of pleura; Frozen; 5 slides x 2 sections, 5 µm thickness	Histology, LA-ICP-MSI
N/A	N/A	MS801b	Mesothelioma microarray with mesothelium tissue, containing 38 cases of mesothelioma and	MALDI-MS imaging

	other cases, 10 cases of mesothelium tissue, duplicate core per case; FFPE; 1x slide; 5 µm thickness	

Table 2.3 Human tissues used in the project.

2.1.4 Antibodies and isotype controls

2.1.4.1 Flow cytometry

Details of the antibodies and isotype controls used for flow cytometry are provided in Table 2.4 and Table 2.5 below.

Name	**Host Species**	**Reactivity**	**Working concentration**	**Supplier & catalogue number**
PE Anti-Mesothelin	Rabbit	Human	2.5 µg/ mL	Abcam #ab252136
Alexa Fluor® 488 anti-HMGB1	Mouse	Human, Mouse, Rat	2.5 µg/ mL	Biolegend #651410
Alexa Fluor® 647 anti-human IL-1β	Mouse	Human, Cross-Reactivity: Baboon	5 µL/ 10^6 cells	Biolegend #508208
VISTA Mouse anti-Human, APC, Clone: B7H5DS8	Mouse	Human	5 µL/ 10^6 cells	Invitrogen eBioscience™ #17-1088-42
Human Mesothelin PE-conjugated	Rat	Human	10 µL/ 10^6 cells	RND Systems #FAB32652P
Human VISTA/B7-H5/PD-1H Alexa Fluor® 647-conjugated	Mouse	Human	10 µL/ 10^6 cells	RND Systems #FAB71261R

Table 2.4 Conjugated antibodies employed for flow cytometry analysis. All antibodies employed in this section were monoclonal antibodies. The antibody concentrations and volumes presented in the table were selected based on the manufacturer recommendation.

Specificity/ Type	**Label**	**Source**	**Supplier & catalogue number**

Mouse IgG2B	Alexa Fluor® 647	Mouse	RND Systems #IC0041R
Mouse IgG1	Alexa Fluor® 647	Mouse	Biolegend #400136
Mouse IgG2B	Alexa Fluor® 488	Mouse	Biolegend #400329
Rat IgG2A	PE	Rat	RND Systems #IC006P
Rat IgG2A	APC	Rat	RND Systems #IC006A

Table 2.5 Isotype controls employed for flow cytometry analysis. Concentrations were selected based on manufacturer recommendation.

2.1.4.2 Immunofluorescence

Details of the primary and secondary antibodies used for immunofluorescence are presented in Table 2.6 below. All the antibodies were supplied by Thermo Fisher Scientific. Dilution was carried out according to manufacturer recommendation. Incubation of the sample with antibody dilution buffer without the primary antibody was performed to assess non-specific binding of secondary antibody in the cell sample. ProLong™ Diamond Antifade Mountant with DAPI (Thermo Fisher Scientific) was used to secure the coverslips onto the glass slides and stain the nuclei with DAPI.

Name/ Clone	**Host Species**	**Reactivity**	**Antibody type**	**Dilution**	**Catalogue number**
VISTA Antibody /BLR035F	Rabbit	Human	Primary Monoclonal	1:100-1:200	#A700-035
HMGB1/ SA39-03	Rabbit	Human	Primary Monoclonal	1:50-1:100	#MA5-31967
Mesothelin	Rabbit	Human	Primary Polyclonal	1:50-1:100	#PA5-96525
Highly Cross-Adsorbed Antibody Alexa Fluor 488	Goat	Rabbit	Secondary Polyclonal	1:250-1:500	#A32731

Table 2.6 Primary and secondary antibodies used for immunofluorescence experiments.

2.1.5 Mineral fibres

All MF were kindly donated by Santia Asbestos Management Ltd. and were all Asbestos Quality Control Samples (Health & Safety Laboratory) commercialised for research purposes (Table 2.7). UICC amosite, UICC chrysotile, UICC crocidolite, actinolite, and wollastonite were ordered from Health & Safety Laboratory (UK). Stocks were stored in Santia Asbestos Management Ltd laboratory.

Fibre type	Supplier Product Code	Common Name
UICC Amosite	HSL 043	Brown Asbestos
UICC Chrysotile	HSL 043	White Asbestos
UICC Crocidolite	HSL 043	Blue Asbestos
Wollastonite	HSL 044	N/A
Actinolite	HSL 036	N/A

Table 2.7 Mineral fibres employed in the study. The stock concentration was 1 mg/ mL in PBS.

2.2 Methods

2.2.1 Mammalian cell culture

2.2.1.1 Cell growth and complete media preparation

Human malignant mesothelioma cell lines MSTO-211H and NCI-H28 and human mesothelial cells Met-5A were commercially acquired from ATCC®. Human non-small-cell lung carcinoma (NSCLC) cell line NCI-H1975 was kindly donated by Dr Neil Cross (Biomolecular Sciences Research Centre, Sheffield Hallam University, Sheffield, UK). U937 and HeLa cells were provided by Jonathan Kilby (Faculty of Medicine, Dentistry & Health, University of Sheffield, Sheffield, UK). The MSTO-211H, NCI-H28, NCI-H1975, and U937 cells were routinely cultured in RPMI-1640 medium containing L-glutamine supplemented with foetal bovine serum (FBS) to a final concentration of 10% (v/v) and penicillin/ streptomycin to a final concentration of 1% (v/v). The Met-5A were cultured according to the supplier's

culture method in Medium 199 containing 1.5 g/ L sodium bicarbonate (Scientific Laboratory Supplies) supplemented with 10% (v/v) foetal bovine serum, 3.3 nM epidermal growth factor (EGF), 400 nM hydrocortisone, 870 nM zinc-free bovine insulin, 20 mM HEPES and 1% (v/v) penicillin/ streptomycin (final concentrations). HeLa cells were routinely cultured in DMEM medium supplemented with 10% (v/v) FBS and penicillin/ streptomycin to a final concentration of 1% (v/v). All cells were cultured in Nunc EasYFlasks (Thermo Fisher Scientific) T75 cell culture flasks at 37°C with 5% CO_2 in air in a humidified incubator.

2.2.1.2 Cell passaging

The cells were grown until the monolayer reached about 80-90% confluency, before passaging (every 3-5 days for MSTO-211H, NCI-H28, HeLa and NCI-H1975 cells, and 7 days for Met-5A cells). Cultures were maintained by removing half of the conditioned media and replacing it with fresh media every 3 days or when needed. For passaging, the cell media was discarded, and the cell monolayer was washed with 5 mL of phosphate-buffered saline (PBS). In order to detach the cells off the plastic vessel, 3 mL of Trypsin-EDTA were added to each flask which was then incubated for 5 min at 37°C, 5% CO_2. The Trypsin-EDTA was neutralised by adding 5 mL of fresh media and the cell suspensions were then transferred to a fresh tube for centrifugation (200x g, 5 min, room temperature (RT)). The supernatant was discarded, and the cell pellet was resuspended in fresh complete media at a density of $1x10^5$ cells/ mL. The cells were cultured up to passage 35. A fresh vial of cells was thawed and used after reaching a high passage number to ensure that the cells have not undergone genetic mutations. U937 were sub-cultured every 3 to 4 days by removing 1/10 of the whole volume of cell suspension and mixing it with fresh RPMI media ($1x10^5$ viable cells/ mL).

2.2.1.3 Cryopreservation of cells

Cells were cryopreserved for long term storage in liquid nitrogen. Cells at high confluency (<90%) were harvested as described above, pelleted, and

resuspended in 1 mL freezing media (complete media supplemented with 5% (v/v) dimethyl sulfoxide (DMSO)). Cell suspensions were transferred into cryopreservation tubes, placed into a Thermo Fisher Scientific Mr Frosty™ at -80°C. After 24 hours, the tubes were stored in a liquid nitrogen dewar for long term storage. When early passage cells were needed, the cell suspensions were quickly thawed in a water bath at 37°C and transferred into fresh complete media. The cells were allowed to adhere for 24 hours before replacing the media to remove the DMSO. All the floating cells in the media were retained by gentle centrifugation (125 x g for 5 min) and added back to the original culture.

2.2.1.4 Cell counting

Prior to experiments, cells were counted using the Countess II FL Automated Cell Counter (Thermo Fisher Scientific). Cell suspension was mixed with an equal volume of trypan blue (10 µL) and pipetted into a Countess Chamber slide (Thermo Fisher Scientific). Total cell counts, viable and non-viable cell numbers were automatically generated. Cells were calculated as the number of cells per mL of suspension. Only viable cells were considered in the calculations.

2.2.1.5 Mycoplasma testing

All cells were confirmed to be negative for mycoplasma every three months using the MycoAlert™ Mycoplasma Detection Kit (Lonza). Cells were stored in a mycoplasma free liquid nitrogen dewar for long term storage.

2.2.2 Mineral fibres

2.2.2.1 Preparation of mineral fibres

The MF were handled in specially designed laminar flow hoods (Santia Asbestos Management Ltd. Laboratories) and 1 mg/ mL stock solutions were prepared in PBS. The solutions were autoclaved at 121°C in order to be sterilised and stored at RT. The fibres solutions were passed 5 times through a 22-gauge needle prior to treatment for better separation of the fibrils.

2.2.2.2 Fibre dose optimisation

MF solutions (actinolite, amosite, chrysotile, crocidolite, and wollastonite) were titrated in 24 well-plates, at concentrations starting at 25 µg/ mL decreasing to 12 µg/ mL, 6 µg/ mL, 3 µg/ mL, and down to 1.5 µg/ mL. The solutions were prepared in triplicates. The wells were imaged using the Cytation™5 Cell Imaging Multi-Mode Reader (BioTek) at 40x magnification.

2.2.3 The effect of mineral fibres on monolayer integrity and confluency

2.2.3.1 Brightfield imaging following actinolite exposure

Experiments were performed on early passage NCI-H28 and MSTO-211H cell lines at about 80% confluency. Cells were harvested, counted, and prepared as aforementioned. For the cell viability experiments, $2.5x10^4$ cells were seeded in each well of a 24-well plate and allowed to adhere to the bottom of the well for 24 hours. After incubation at 37 ºC, 5% CO_2, the monolayers were treated for 24 hours with actinolite solutions prepared in cell culture media at concentrations ranging from 0 to 25 µg/ mL. PBS was used for the vehicle control (PBS volume corresponding to the PBS volume added for the highest actinolite concentration). Staurosporine stock (apoptotic inducer) was prepared in DMSO (10 mM stock concentration) sterile filtered, aliquoted, and stored at -20°C until use. Final concentration (10 µM working concentration) was achieved by diluting drug aliquots in standard growth media. All solutions were prepared freshly prior to use. Cell monolayers were imaged using the Cytation™5 Cell Imaging Multi-Mode Reader after 24, 48, and 72 hours, respectively.

2.2.3.2 AlamarBlue® viability assay following actinolite exposure

For the alamarBlue® viability assay, human MPM cells (MSTO-211H and NCI-H28) and the NSCLC control, NCI-H1975 were seeded in 24 well plates at a density of $2.5x10^4$ cells/ well and incubated for 24 hours at 37ºC, 5% CO_2. The cultures were treated with different doses of actinolite fibres (concentration ranging from 0 to 25 µg/ mL). Staurosporine (10 µM) was used as an apoptotic inducer and PBS was used as a vehicle control (volume of PBS corresponding to

PBS volume for the highest actinolite dose). A 1% (w/v) alamarBlue® stock solution was freshly prepared by dissolving Resazurin powder in complete cell media. The stock solution was sterile filtered and added to the wells to a final concentration of 0.02% (v/v). After 4 hours of incubation at 37ºC, 5% CO_2, the fluorescence intensity was measured with the Cytation™5 Cell Imaging Multi-Mode Reader (excitation/emission: 530-560/590 nm). The viability was measured after 24, 48, and 72 hours post-treatment. The analysis was carried out in triplicates and in 3 independent experiments. In order to obtain the net fluorescence units, blank wells (no-cell background control) containing only media and reagent were also analysed. The recorded values (intrinsic reagent fluorescence units) were subtracted from every sample well to obtain the final data. The data were analysed, and graphs were generated using GraphPad Prism 6.0 (GraphPad Software, La Jolla, CA, USA). Data expressed as the standard error of the mean (SEM). A two-way ANOVA analysis followed by a Dunnett test for multiple comparisons to a control were applied for statistical analysis. Data were considered significant compared to the vehicle control as long as $p<0.05$.

2.2.3.3 AlamarBlue® viability assay following mineral fibre treatment

For the alamarBlue® viability assay, human MPM cells (MSTO-211H and NCI-H28) and normal mesothelial control, Met-5A were seeded in 24 well plates at a density of $2.5x10^4$ cells/ well and incubated for 24 hours at 37ºC, 5% CO_2. The cultures were treated with 3 µg/ mL MF solutions (actinolite, amosite, chrysotile, crocidolite, and wollastonite). Staurosporine (10 µM) was used as an apoptotic inducer (positive control) and PBS was used as a vehicle control (volume of PBS corresponding to PBS volume for the MF treatment). The cellular viability was measured after 24, 48, and 72 hours post treatment using alamarBlue® viability assay. A 1% (w/v) alamarBlue® stock solution was freshly prepared by dissolving Resazurin powder in complete cell media. The stock solution was sterile filtered and added to the wells to a final concentration of 0.02% (v/v). After 4 hours incubation at 37ºC, 5% CO_2, the fluorescence intensity was measured with the Cytation™5 Cell Imaging Multi-Mode Reader (excitation/emission: 530-560/590

nm). The analysis was performed in triplicates and on three independent occasions. To obtain the net fluorescence units, blank wells (no-cell background control) containing only media and reagent were also analysed. The recorded values (intrinsic reagent fluorescence units) were subtracted from every sample well to obtain the final data. The data were analysed, and graphs were generated using GraphPad Prism 6.0. Data expressed as SEM. A one-way ANOVA analysis (n=9) was applied with a Geisser-Greenhouse correction to adjust for the lack of sphericity of data, followed by a Dunnett test for multiple comparisons to a control were applied for statistical analysis. Data were considered significant compared to the vehicle control as long as $p<0.05$.

2.2.3.4 Brightfield imaging of the cell monolayers following exposure to different MF

Cells were harvested, counted, and prepared as aforementioned in Section 2.2.1.2 and 2.2.1.4. For the viability experiments, $2.5x10^4$ cells were seeded in each well of a 24-well plate and allowed to adhere to the bottom of the well for 24 hours. After incubation at 37ºC, 5% CO_2, the monolayers were treated with MF solutions (actinolite, amosite, chrysotile, crocidolite, and wollastonite) at 3, 6, or 12 µg/ mL. PBS was used for the vehicle control (PBS volume corresponding to the PBS volume added for the highest MF concentration). Staurosporine (10 µM working concentration) was used as a positive control. No treatment was added to the negative control wells. All solutions were prepared freshly prior to use. The monolayers were imaged using the Cytation™5 Cell Imaging Multi-Mode Reader after short-term exposure (24 hours) and long-term exposure (7 days).

2.2.3.5 RealTime-Glo™ Annexin V Apoptosis and Necrosis Assay

Human MPM cells, MSTO-211H and NCI-H28, and human mesothelium cells, Met-5A were harvested, counted, and seeded in Costar® 3917 solid white bottom 96-well plates ($6x10^3$ cells/ well). PBS was added to the outer wells of the plates to maintain humidity throughout the long-term real-time experiment (200 µL per well). The plates were then placed in a humidified tissue culture incubator for 24 hours to allow the cells to reattach and recover before dosing.

After 24 hours, the media was removed and the cells were treated with either low dose (3 µg/ mL) or high dose (12 µg/ mL) of actinolite, crocidolite, or wollastonite, prepared in prewarmed complete culture medium. PBS was added to the media in the negative control wells as a matched vehicle excipient (total volume corresponding to the total PBS volume from the high dose treatment). Staurosporine was initially used as an apoptotic inducer (positive control) at a concentration of 10 µM. The concentration was reduced to 1 µM to avoid overflowing issues based on initial data. Instrument gain settings were also adjusted accordingly. In order to obtain the net fluorescence units, blank wells (no-cell background control) containing only media and 2X Detection Reagent were analysed. The recorded values were subtracted from every sample well to obtain the final data. The 96-well plate layout is presented in Figure 2.1.

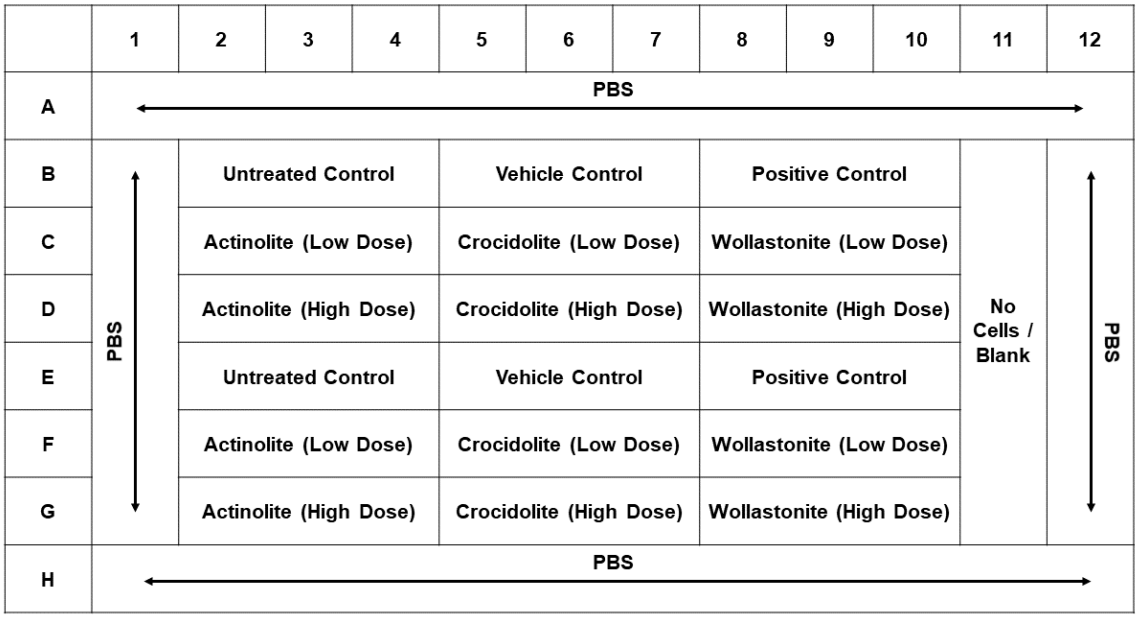

Figure 2.1 Layout of a 96-well plate used for the RealTime-Glo™ Annexin V Apoptosis and Necrosis Assay. Different cell lines were typically seeded in rows B-D to row E-G.

The RealTime-Glo™ Annexin V Apoptosis and Necrosis Assay (Promega) contained the following reagents: Annexin V NanoBiT™ Substrate (1000x), CaCl2 (1000x), Necrosis Detection Reagent (1000x), Annexin V-SmBiT (1000x), and Annexin V-LgBiT (1000x). The 2X Detection Reagent was freshly prepared for immediate use. In order to prepare the 2X Detection Reagent, 12 µL of 1000x

Annexin NanoBiT® Substrate were added to 6000 µL specific prewarmed complete medium and vortexed immediately. Next, 12 µL of 1000x $CaCl_2$ were pipetted into the falcon tube containing Annexin V NanoBiT® Substrate at a 500-fold dilution, followed by a 10-second vortex. Subsequently, 12 µL of 1000x Necrosis Detection Reagent were pipetted at a 500-fold dilution. The falcon tube was vortexed again for 10-15 seconds to ensure homogeneity. Finally, 12 µL of each 1000x Annexin V-SmBiT and 1000x Annexin V-LgBiT were added to the medium. The whole solution was mixed carefully by inversion, to avoid bubble formation and kept on ice. 100 µL of the 2x Detection Reagent prepared in complete medium (specific to each cell line) were added to all wells in the 96-well assay plate, except the outer wells containing only PBS. All wells contained a final volume of 200 µL. The plate was placed in the prewarmed, humidified instrument which was set to automatically shake the plate for 30 seconds at 500 rpm to mix the components.

The luminescence and fluorescence were read at 485/525-530nm (excitation/emission). The data were recorded in real-time over a period of 72 hours (at 2-hour intervals) using Cytation™5 Cell Imaging Multi-Mode Reader in kinetic mode, equipped with a temperature and atmospheric control, set to 37°C and 5% CO_2. Edge effects were prevented by pipetting PBS in the outer wells. The analysis was carried out once for the MPM cells to optimise instrumentation parameters and controls, followed by 3 independent experiments for each cell line to acquire the final data.

The data were analysed, and graphs were generated using GraphPad Prism 6.0 (GraphPad Software, La Jolla, CA, USA). Data expressed as SEM. A two-way ANOVA analysis followed by a Dunnett test for multiple comparisons to a control were applied for statistical analysis. Data were considered significant compared to the vehicle control as long as $p<0.05$.

2.2.4 Sample preparation and optimisation for LA-ICP-MS analysis

This work was performed in collaboration with Dr Amy J Managh and Mr Calum Greenhalgh in the Chemistry Department, Loughborough University. All samples

were prepared at Sheffield Hallam University. The instrument set-up employed for this work comprised of a soft NWR Image 266 nm laser ablation system coupled to an Element XR sector-field ICP mass spectrometer (*i.e.,* Instrument 1). Method development for Mg detection was based on earlier work carried out as part of a Sheffield Hallam University MSci project led by Dr Sarah Haywood-Small. Data acquisition and was performed equally in the Chemistry Department at Loughborough University by Miss Oana M Voloaca and Mr Calum Greenhalgh. ROIs selection, data analysis, and data interpretation were carried out by the author, Oana M Voloaca.

2.2.4.1 Fibre dose

For the LA-ICP-MSI analysis, MSTO-211H ($10x10^4$ cells/ well) were seeded in 6-well plates and incubated at 37ºC, 5% CO_2 for 24 hours ahead of exposure to actinolite fibres. For dose optimisation experiments, the monolayers were treated with actinolite solutions (3, 6, and 12 µg/ mL) for 24 hours. After 24 hours, the cells and fibres were harvested and prepared into cell suspensions ($5x10^4$ cells/ mL). A volume of 200 µL of cell and fibres suspension was cytospun at 400 g for 3 minutes onto glass slides.

2.2.4.2 Sample preparation for LA-ICP-MS analysis of cell monolayers

For the LA-ICP-MSI analysis, NCI-H28 or MSTO-211H ($10 x10^4$ cells/ well) were seeded in 6-well plates and incubated at 37ºC, 5% CO_2 for 24 hours ahead of exposure to MF solutions. For the single-element detection of MF as well as multi-elemental LA-ICP-MSI, the cells were exposed to 3 µg/ mL solutions of either actinolite, crocidolite, amosite, chrysotile, or wollastonite. After 24 hours, the cells and fibres were harvested and prepared into cell suspensions ($5x10^4$ cells/ mL). A volume of 200 µL of cell and fibres suspension was cytospun at 400 g for 3 minutes onto glass slides or plastic slides (multi-elemental LA-ICP-MSI).

2.2.4.3 Laser energy

Laser energy was optimised between 45% e and 65% e, using 20 Hz repetition frequency, 40 μm s^{-1} scan speed and 2 μm spot size. Final laser energy was selected to be 45% e, given a fluence value of ≈18 J cm^{-2}.

2.2.4.4 Spot size

Samples were prepared as presented in Section 2.2.4.2. LA-ICP-MS analysis was carried out with a spot size of 1 or 2 μm and the time of acquisition was recorded.

2.2.5 LA-ICP-MS analysis of 2D monolayers

2.2.5.1 Single-element detection of mineral fibres

The instrument set-up employed for this work comprised of a soft NWR Image 266 nm laser ablation system coupled to an Element XR sector-field ICP mass spectrometer (Thermo Fisher Scientific) (Instrument 1). The final selected laser parameters for the rest of the analysis are presented in Table 2.8. ^{24}Mg was selected as the target isotope for single-element detection. The ablated area for each run of analysis was set to 200 x 200 μm. Daily tuning was carried out using pre-established tuning parameters.

Parameter	ICP-MS
Radio frequency power	1070 W
Ar Cool gas flow rate	15.5 L min^{-1}
Ar Auxiliary gas flow rate	0.9 L min^{-1}
Ar sample gas flow rate	0.475 L min^{-1}
He gas flow rate	1.45 L min^{-1}
Mass resolution	Low
Detection mode	Counting
	Laser
Laser spot diameter	2 µm
Laser fluence	18 J cm^{-2}
Repetition frequency	20 Hz
Scan speed	40 µm s^{-1}

Table 2.8 Selected LA-ICP-MS parameters following optimisation. These parameters were employed for single and multi-element LA-ICP-MS analysis.

2.2.5.2 Multi-elemental LA-ICP-MS analysis of single mineral fibres in 2D mesothelioma models

The NWR Image 266 nm laser ablation system coupled to an Element XR sector-field ICP mass spectrometer (Thermo Fisher Scientific) was employed for multi-elemental LA-ICP-MS analysis. The selected elements were ^{57}Fe, ^{24}Mg, and ^{29}Si. LA-ICP-MS parameters were optimised for maximum ^{24}Mg, ^{29}Si, ^{57}Fe ion sensitivity (Table 2.8). Each element was measured in triplicate, for every sample containing individual MF. The ablated area for each run of analysis was set to 200 x 200 µm. Ablated lines were parallel to each other with no gaps between the lines to ensure full ablation of the area. A 2-s laser warmup period and 2-s washout time were allowed before and after each line. These elements were imaged separately, due to the slow scanning speed of the ICP-MS instrument compared with the fast response of the laser ablation system. A P7882 photon counter board (FAST ComTec GmbH) was connected to the ion detection board

of the mass spectrometer to collect the data and the signal was monitored using MCDWIN software (FAST ComTec GmbH). This allowed for blind time free collection of the data using a 10-ms dwell time.

2.2.5.3 Data analysis for LA-ICP-MS imaging

The resulting element counts per second data were exported in CSV format for image visualisation and further processing. Data processing was carried out using an in-house software, LA-ICP-MS ImageTool (Reid-IT Limited, Loughborough, UK) with the final graphic production performed using Dplot Software (HydeSoft Computing, Vicksburg, MS, USA).

2.2.5.4 LA-ICP-TOFMS imaging of single mineral fibres in 2D monolayers

This part of the work was conducted by Calum Greenhalgh at the NU Instruments laboratories in collaboration with Dr Amy J Managh, Phil Shaw and Ariane Donard using a novel LA-ICP-TOFMS prototype instrumentation. Sample preparation was conducted at Sheffield Hallam University by Oana M Voloaca. All the data interpretation was carried out by the author, Oana M Voloaca. A NWR193 laser ablation system (Elemental Scientific Lasers) was coupled to a Vitesse Time-of Flight ICPMS (Nu Instruments) (*i.e.,* Instrument 2). The LA system incorporated a prototype TwoVol3 chamber configured with the imaging cup and was fitted with a Dual Concentric Injector (DCI) for fast washout. Helium gas flows of 1.2 L min^{-1} and 0.55 L min^{-1} were used through the cup and the outer chamber respectively, with an argon gas flow of 0.7 L min^{-1} introduced through the DCI. The laser ablation parameters were as follows: 3 mm spot diameter, 50 Hz repetition frequency, 150 mm s^{-1} scan speed, ≈4 J cm^{-2} fluence. Data was collected for the full mass range, but subsequent data analysis focused on the following isotopes ^{23}Na, ^{24}Mg, ^{27}Al, ^{28}Si, ^{31}P, ^{39}K, ^{40}Ca, ^{48}Ti, ^{55}Mn, and ^{56}Fe.

2.2.6 Development of a 3D model

2.2.6.1 Organ dot

To prepare the organ dots, Millicell polycarbonate cell culture inserts (0.4 µm pore size) were placed in a 6-well plate. 1 mL of cell culture media was carefully added on the sides of the inserts without covering the top of the membrane. MSTO-211H and NCI-H28 cells were harvested, counted, and prepared in suspension as stated in Section 2.2.1.1. To create the dot, 5 µL of cell suspension ($2x10^4$ cells/ dot) were carefully pipetted on top of the membrane, ensuring that the drop maintained the convex shape, before the media evaporated to allow the cells within the suspension to aggregate and form the organ-dot. The plate was incubated for 48 hours at 37°C in a humidified 5% CO_2 incubator.

2.2.6.2 Multicellular spheroids

Multicellular spheroids (MCS) were prepared by seeding MSTO-211H, NCI-H28, and NCI-H1975 cells ($6x10^3$ cells/ well) in a Corning® Costar® Ultra-Low Attachment (Corning) 96-well plate with clear round bottom wells which allowed the cells to aggregate and form MCS after incubation at 37°C, 5% CO_2. For the co-culture MCS model, actinolite fibres were added to the cell suspension prior to seeding the cells, to a final concentration of 3 µg/ mL. The MCS were then allowed to grow for 7 days 37°C before carrying out any experiments. MCS started forming after 48 hours. For both models, the media was carefully changed every 3 days, without disturbing the 3D MCS.

2.2.6.3 Hoechst 33342 and propidium iodide staining

Hoechst 33342 and propidium iodide (Hoechst/ PI) (Sigma) dye stock solutions were prepared by dissolving the contents of each vial (100 mg) in 10 mL of deionised water (dH_2O) to create a 10 mg/ mL (16.23 mM) solution. The stock was diluted with a factor of x2000 before staining the MCS on Day 7. The well plate was incubated for 10 minutes, protected from the light, and imaged using the Olympus IX81 Fluorescent Microscope.

2.2.6.4 Preparation of cell plugs

MSTO-211H and NCI-H28 cells were grown in T175 cell culture flasks for 48 hours (or until ≈80% confluent). Once the cells reached the desired confluency, the cell monolayers were detached from the flasks and centrifuged for 5 minutes at 400 g. The cell pellets from 5 flasks ($5x10^6$ cells per flask) were then combined in a 1 mL Eppendorf tube. 100 µL of MF stock solutions (1 mg/ mL) were added to the tube and centrifuged together for 5 minutes at 500 g. Following centrifugation, the supernatant was poured off into a waste pot. The remaining medium was carefully discarded using a 100 µL automatic pipette. The cell pellet was kept on ice until further preparation. Three different embedding media were tested as a method optimisation step. Firstly, 10% (w/v) gelatin embedding media was prepared by dissolving gelatin powder in heated dH_2O (45°C). The gelatin media maintained a fluid state at a temperature of 37°C or above. Optimal cutting temperature (OCT) compound was also tested as an option with no preparation required. Hydroxypropyl methylcellulose (HPMC) and polyvinylpyrrolidone (PVP) (HPMC/PVP media) was prepared by dissolving 7.5 g HPMC with 2.5 g PVP in 90mL dH_2O. In order to get rid of the bubbles, the embedding media was placed at -4°C for at least 24 hours or until ready to use. The media was placed on ice whilst preparing the plugs to maintain a constant temperature. The cell plugs were prepared by transferring the dense cell pellet to a 50x20 mm plastic mould, followed by flash freezing in liquid nitrogen. Secondly, the frozen cell pellet was carefully removed from the mould, sandwiched between 2 layers of embedding media in a second 130 x 200 mm plastic mould, and flash frozen in liquid nitrogen. Cell plugs were stored at -80°C until cryotomy.

2.2.6.5 Sample preparation and storage

The cell plugs were cryosectioned using a Leica CM1520 cryostat set at -18°C at different thicknesses. The section thicknesses varied between 12 µm to 50 µm depending on the subsequent analysis step. The sections were stored at -80°C until analysis.

2.2.6.6 Haematoxylin and eosin staining of 3D cell-plugs

The sections were stained with Mayer's haematoxylin and eosin (H&E) staining solutions. Firstly, the slides were fixed in 4% (v/v) paraformaldehyde (PFA) for 10 minutes. The nuclei were then stained for 5 minutes with haematoxylin, excess haematoxylin was then removed by immersion in running tap water for 5 minutes. This was also used as an alkaline environment required to turn the nuclear staining from red to a blue colour. The cytoplasm was stained for 1 minute by submersion in eosin stain, followed by the first 100% (v/v) ethanol wash (5 minutes). The slides were passed through a couple extra alcohol wash steps to dehydrate the tissues and remove all traces of water. The alcohol washes were followed by several Sub-X Clearing medium (Leica Biosystems) changes (3 washes, 5 minutes) to aid with tissues clearing prior to mounting in Pertex® (CellPath) and covering with glass coverslips. The slides were stored indefinitely in a dark slide box. The sections were imaged using an Olympus IX81 Microscope (Olympus Life Sciences).

2.2.7 LA-ICP-MS analysis of 3D cell-plugs sections

2.2.7.1 Optimisation of laser power

Laser power was optimised for the analysis of cell-plug sections by adjusting the laser energy from 45% e to 50% e and up to 55% e, with resulting laser fluence values of ≈18 J cm^{-2}, ≈20 J cm^{-2}, and ≈22 J cm^{-2}, using a spot size of 2 µm. The final selected power was 45% e (≈18 J cm^{-2}).

2.2.7.2 Optimisation of section thickness

MSTO-211H and NCI-H28 cell-plugs treated with actinolite fibres were cryosectioned at 12, 20, and 50 µm thicknesses. Each 200 x 200 µm selected area was ablated in 4 different rounds of analysis (serial ablation of the same area). ^{24}Mg signal counts were recorded for each round of analysis and analysed as separate files.

2.2.7.3 Optimisation of spot size and ablated area

MSTO-211H cell-plug sections treated with actinolite were analysed using most of the parameters in Table 2.9, apart from spot size and repetition frequency. In order to select the optimal laser spot diameter and the optimal ablation area, LA-ICP-MS analysis of ^{24}Mg was performed using a spot size of either 1 or 2 µm for areas of 200 x 200 µm or 500 x 500 µm. The time of acquisition was recorded for each of the 4 different experiments. The final selected parameters were a laser spot diameter of 2 µm and an area of 400 x 400 µm (acquisition time just over an hour).

2.2.7.4 Dose optimisation

Cell-plugs were prepared by adding different volumes of MF actinolite solutions and sectioned as described in Section 2.2.6.4. 200 x 200 µm areas were ablated and analysed based on ^{24}Mg signal counts using LA-ICP-MS with the parameters shown in Table 2.9. The cell-plugs contained either a low-dose of actinolite (30 µL), medium-dose (60 µL), or high-dose (100 µL).

2.2.7.5 LA-ICP-MS multi-elemental analysis of 3D cell-plugs

Analysis was performed using the same set-up used for the analysis of 2D monolayers and by employing the same methodology as described above (Instrument 1). The ablated areas were 400 x 400 µm in size. Analysis was carried out in triplicates for each isotope (n=3), and for each type of MF and an untreated control. A total number of 45 rounds of analysis were carried out.

Parameter	ICP-MS
Radio frequency power (W)	1070
Ar Cool gas flow rate (L min^{-1})	15.5
Ar Auxiliary gas flow rate (L min^{-1})	0.9 L min^{-1}
Ar sample gas flow rate (L min^{-1})	0.5 L min^{-1}
He gas flow rate (L min^{-1})	1.65 L min^{-1}
Mass resolution	Low
Detection mode	Counting
	Laser
Laser spot diameter (μm)	2
Laser fluence (J cm^{-2})	18
Repetition frequency (Hz)	20
Scan speed (μm s^{-1})	40

Table 2.9 Selected Instrument 1 LA-ICP-MS parameters following optimisation.

2.2.7.6 Blind sample classification using LA-ICP-TOFMS imaging (Instrument 2)

This part of the work was conducted by Calum Greenhalgh at the NU Instruments laboratories in collaboration with Dr Amy J Managh, Phil Shaw and Ariane Donard using a novel LA-ICP-TOFMS prototype instrumentation. Sample preparation was conducted at Sheffield Hallam University by Oana M Voloaca. The blind sample was prepared by Oana M Voloaca, with the analysis carried out by Calum Greenhalgh. All the data interpretation was carried out by the author, Oana M Voloaca. Helium gas flows of 1.2 L min^{-1} and 0.55 L min^{-1} were used through the cup and the outer chamber respectively, with an argon gas flow of 0.7 L min^{-1} introduced through the DCI. The laser ablation parameters were as follows: 3 μm spot diameter, 50 Hz repetition frequency, 150 mm s^{-1} scan speed, ≈4 J cm^{-2} fluence. Data was collected for the full mass range, but subsequent data analysis focused on the following isotopes ^{23}Na, ^{24}Mg, ^{27}Al, ^{28}Si, ^{31}P, ^{39}K, ^{40}Ca, ^{48}Ti, ^{55}Mn, and ^{56}Fe. Ablation area of the MSTO-211H cell-plug section was 0.75 x 1.50 mm. The cell-

plug contained MF (unknown to the analyser). The MF was identified based on ^{24}Mg, ^{28}Si, ^{40}Ca, and ^{56}Fe recorded counts.

2.2.7.7 Data analysis

The resulting element counts per second data were exported in CSV format for image visualisation and further processing. Data processing was carried out using an in-house software, LA-ICP-MS ImageTool (Reid-IT Limited, Loughborough, UK) with the final graphic production performed using Dplot Software (HydeSoft Computing, Vicksburg, MS, USA).

2.2.8 LA-ICP-MS analysis of frozen human tissues

2.2.8.1 Tissue analysis using sector-field ICP set-up (Instrument 1)

The analysis was conducted using the NWR Image 266 nm laser ablation system coupled to an Element XR sector-field ICP mass spectrometer (Instrument 1). The ICP parameters are shown in Table 2.9. Tuning of the instrument settings was performed using a NIST SRM 612 glass certified reference material (National Institute for Standards and Technology). The laser parameters were selected as following: laser spot diameter 2 µm, laser fluence ≈20 J cm^{-2}, 40 Hz, scan speed 80 µm s^{-1}. The samples analysed were commercially supplied frozen human tissue sections of healthy human lung (AMSBIO, code 500029027) or pleura section, mesothelioma of pleura (AMSBIO, code CS814500) (Table 2.3). ^{24}Mg was selected as target isotope. Analysis was carried out for 1000 x 1000 µm areas of the first 2 tissue sections presented in Table 2.3. Data was analysed and images were produced as described in Section 2.2.5.3.

2.2.8.2 Analysis of human MPM tissues by LA-ICP single-quad MS system (Instrument 3)

Experiments were conducted using a NexION 350X ICPMS (PerkinElmer) coupled to an UP-213 LA system (New Wave Research) with a frequency quintupled 213 nm Nd: YAG laser (*i.e.,* Instrument 3). Laser parameters were optimised to a 6 µm spot size with laser power 46%, 25 µm/s scan speed, 0.07 J

cm^{-2} laser fluence, and 20 Hz repetition rate. The sample was ablated line by line with 6 µm raster spacing at 1.31 min acquisition time. For the ICP-MS instrument there was a direct flow with a rate of 1.4 L/min. The following settings were used in standard mode with an 18 L/min plasma gas flow, 1.2 L/ min auxiliary gas flow at 1600 W RF power. Isotopes monitored included ^{29}Si, ^{24}Mg, ^{13}C, ^{23}Na, ^{57}Fe, and the instrument was controlled using Syngistix software. Data analysis was achieved using Iolite Software on Igor Pro (WaveMetrics, USA).

2.2.8.3 Analysis of human MPM tissues by LA-ICP triple-quad MS system (Instrument 4)

Sample analysis was conducted externally at the London Metallomics Facility, King's College London by Dr Maral Amrahli. An Analyte Excite 193 nm ArF*excimer-based LA system (Teledyne Photon Machines) was used, equipped with the HelEx II two-volume ablation cell (*i.e.,* Instrument 4). The LA system was coupled to an iCAP TQ ICP-mass spectrometer (Thermo Fisher Scientific) via the Aerosol Rapid Introduction System (ARIS). Tuning of the instrument settings was performed using a NIST SRM 612 glass certified reference material (National Institute for Standards and Technology), optimising for low laser-induced elemental fractionation through monitoring of $^{238}U^{+}/^{232}Th^{+}$ ratios, low oxide formation (<1%) monitoring $^{232}Th^{16}O^{+}/^{232}Th^{+}$ ratios, and high sensitivity for $^{59}Co^{+}$, $^{115}In^{+}$ and $^{238}U^{+}$. LA-ICP-MS images were acquired in a fixed dosage mode, with a vertical and horizontal spatial resolution of 5 µm. Target elements were initially analysed in groups of 3 (^{27}Al, ^{39}K, and ^{56}Fe, ^{23}Na, ^{26}Mg, and ^{29}Si, ^{26}Mg, ^{29}Si, and ^{44}Ca, and ^{31}P, ^{44}Ca, and ^{55}Mn). All parameters are shown in Table 2.10. Samples were mounted inside a bespoke three slide sample holder of the HelEx II two-volume ablation cell (Teledyne Photon Machines). To correct for instrumental drift, a series of NIST 612 standard ablation scans were performed before and after each group of worms. ICP-MS and positional data were reconstructed using the HDF-based Image Processing software (HDIP, Teledyne Photon Machines Inc., Bozeman, MT, USA). A bespoke pipeline, written in Python (version 3.8), was used to generate elemental images from reconstructed data and statistics. Negative values, attributed to instrumental noise, were replaced with zeros. All

LA-ICP-MS images are displayed using the same threshold for the intensity bars to enable a direct visual comparison between conditions.

Laser	**Area**	**NIST 612 Scans**
Energy density (J cm^{-2})	1.4	2.0
Repetition rate (Hz)	382	382
Scan speed (µm s^{-1})	159.167	1273.33
Beam waist diameter (µm)	5 (Circle)	40 (Circle)
Scanning Mode	Fixed Dosage	Fixed Dosage
Scanning Direction	Uni-directional	Uni-directional
Effective Dosage (shots per position)	12	12
He Carrier gas flow rate (L min^{-1})	0.6	0.6
iCAP TQ ICP-MS		
RF power (W)	1550	1550
Ar plasma gas flow rate (L min^{-1})	14	14
Ar auxiliary gas flow rate (L min^{-1})	0.8	0.8
Nebuliser gas flow rate (L min^{-1})	1.03	1.03
He Carrier gas flow rate (L min^{-1})	3.25	3.25
Acquired m/z ratios (amu)	^{31}P, ^{44}Ca, ^{55}Mn,	^{31}P, ^{44}Ca, ^{55}Mn,
	^{27}Al, ^{39}K, ^{56}Fe	^{27}Al, ^{39}K, ^{56}Fe
	^{23}Na, ^{26}Mg, ^{29}Si	^{23}Na, ^{26}Mg, ^{29}Si
	^{29}Si, ^{26}Mg, ^{44}Ca	^{29}Si, ^{26}Mg, ^{44}Ca
	^{27}Al, ^{39}K, ^{56}Fe	^{27}Al, ^{39}K, ^{56}Fe

Table 2.10 Experimental parameters and data acquisition parameters used for LA-ICP-MSI.

2.2.8.4 Analysis of human MPM tissues by LA-ICP-TOFMS (Instrument 5)

The work was conducted in collaboration with Dr Sarah Theiner from University of Vienna. Analysis was carried out at the Institute of Analytical Chemistry, Faculty of Chemistry, University of Vienna (Vienna, Austria). An Iridia 193 nm

laser ablation system (Teledyne Photon Machines) was coupled to an icpTOF 2R ICP-TOFMS instrument (TOFWERK AG) (*i.e.,* Instrument 5). The LA system was equipped with a low-dispersion ablation cell in a Cobalt ablation chamber and coupled with the aerosol rapid introduction system (ARIS) to the ICP-TOFMS. An optimised He carrier gas flow of 0.60 L min^{-1} was used and an Ar make-up gas flow of ~0.90 L min^{-1} was introduced through the low-dispersion mixing bulb of the ARIS. Daily tuning of the instrument settings was performed using NIST SRM612 glass certified reference material (National Institute for Standards and Technology) and was aimed at high sensitivity across the elemental mass range. Optimisation was based on high intensities for $^{24}Mg^{+}$, $^{59}Co^{+}$, $^{115}In^{+}$ and $^{238}U^{+}$, low oxide formation based on the $^{238}U^{16}O^{+}/^{238}U^{+}$ ratio (<2%) and low elemental fractionation based on the $^{238}U^{+}/^{232}Th^{+}$ ratio (~1). Daily optimisation aimed for low aerosol dispersion characterised by the pulse response duration for $^{238}U^{+}$ based on the FW0.01 M criterion, *i.e.,* the full peak width of the 238U+ signal response obtained upon a single laser shot, at 1% of the height of the maximum signal intensity.

Laser ablation sampling was performed at a repetition rate of 250 Hz, using a 4 µm spot size (circular) with an interspacing of 2 µm between the lines and the individual pixels (fixed dosage mode 2) resulting in a pixel size of 2 µm x 2 µm. Selective ablation of the biological samples was achieved by selecting an energy density below the ablation threshold of glass and above the ablation threshold of the samples. Tissue samples and gelatin micro-droplets were removed quantitatively using a fluence of 1 J cm^{-2} and 0.40 J cm^{-2}, respectively.

The icpTOF 2R ICP-TOFMS instrument has a specified mass resolution (R = m/Δm) of 6000 (full width half-maximum definition) and allows the analysis of ions from m/z = 14-256. The integration and read-out rate match the LA repetition rate. The instrument was equipped with a torch injector of 2.5 mm inner diameter and nickel sample and skimmer cones with a skimmer cone insert of 2.8 mm in diameter. A radio frequency power of 1450 W, an auxiliary Ar gas flow rate of ~ 0.80 L min-1 and a plasma Ar gas flow rate of 15 L min^{-1} was used.

LA-ICP-TOFMS data were recorded using TofPilot 1.3.4.0 (TOFWERK AG, Thun, Switzerland) and saved in the open-source hierarchical data format (HDF5, www.hdfgroup.org). Post-acquisition data processing was performed with Tofware v3.2.0, which is a TOFWERK data analysis package and used as an add-on on IgorPro (Wavemetric Inc., Oregon, USA). The data processing included (1) drift correction of the mass peak position in the spectra over time via time-dependent mass calibration (2) determining the peak shape and (3) fitting and subtracting the mass spectral base line. LA-ICP-TOFMS data were further processed with HDIP (HDF-based Image Processing, Teledyne Photon Machines, Bozeman, MT, USA) software version 1.5. to generate 2D elemental images (Voloaca *et al.*, 2022).

2.2.9 Tissue histology

The human MPM tissue sections were fixed in 10 % (v/v) formalin for 75 minutes and then washed in PBS, prior to staining with either routine H&E stain or Perls' Prussian Blue staining solutions (Advanced Testing Iron Stain, Thermo Scientific).

2.2.9.1 Haematoxylin and eosin staining of frozen human tissue sections

For H&E staining, the slides were placed in haematoxylin for 5 minutes and rinsed under tap water for 5 more minutes. The cytoplasm was stained for 1 minute by submersion in eosin stain, followed by the first 100% (v/v) ethanol wash (5 minutes). The slides were passed through a couple extra alcohol wash steps to dehydrate the tissues and remove all traces of water (3 changes of absolute anhydrous alcohol for 5 minutes each). The alcohol washes were followed by several Sub-X Clearing medium (Leica Biosystems) changes (3 washes, 5 minutes) to aid with tissue clearing prior to mounting in Pertex® (CellPath) and covering with glass coverslips. The slides were stored indefinitely in a dark slide box. The sections were imaged with an Olympus BX60 light microscope in manual stitching mode, at 100x magnification. The images were processed and visualised using CellSens software (Olympus Life Science).

2.2.9.2 Perls' Prussian Blue staining frozen human tissue sections

Human frozen tissue sections were stained for ferric iron presence according to Perls' Prussian Blue reaction (Perls' Prussian Blue Staining Kit, Thermo Fisher Scientific). Working iron stain solution was freshly prepared by mixing equal volumes of potassium ferrocyanide solution and hydrochloric acid solution. Firstly, the sections were submerged in deionised water for 1 minute, and then stained in working iron stain solution for 30 minutes at room temperature. The sections were once again washed in deionised water for 1 minute before counterstaining the nuclei with nuclear red thiazin stain solution for 30 seconds to achieve desired contrast, followed by an extra deionised water wash for 30 seconds. Finally, the sections were dehydrated in 2 changes of absolute anhydrous alcohol for 1 minute each and then cleared in 3 changes of xylene substitute for 1 minute each. Glass coverslips were mounted on top of all the sections using Pertex® mountant (CellPath). The sections were imaged with an Olympus BX60 light microscope in manual stitching mode, at 100x magnification. The images were processed, and visualised using CellSens software (Olympus Life Science).

2.2.10 Biomarker characterisation

2.2.10.1 Sample preparation for flow cytometry analysis- Intracellular staining

The samples were prepared using eBioscience™ Intracellular Fixation & Permeabilization Buffer Set (Thermo Fisher Scientific). The permeabilisation buffer was prepared by mixing 1-part 10x concentrate with 9 parts distilled water. A total of 8.5 mL of 1x permeabilization buffer was prepared for each sample. Human mesothelioma cells, NCI-H28 and MSTO-211H, human mesothelium cells Met-5A, NSCLC cells NCI-H1975, and positive control cells U937 and HeLa cells were cultured in T125 flasks until the cultures reached 80% confluency. The cells were subsequently harvested and prepared in suspension. The cell suspensions were passed through Fisherbrand™ Sterile Cell Strainer (100 µm porosity) to eliminate any unwanted debris. The cells were transferred to 75 mm round bottom flow cytometry test tubes ($10x10^5$ cells/ tube). The cell pellet was

washed with eBioscience™ Flow Cytometry Staining Buffer (Thermo Fisher Scientific), and then centrifuged at 400 g 5 minutes. After the last wash, the supernatant was discarded, and the sample was pulse vortexed in the residual volume (≈100 µL) to dissociate the pellet. The cells were fixed in 100 µL IC Fixation Buffer and pulse vortexed to mix. The samples were incubated for 60 minutes at RT, protected from light. Following the incubation, the samples were washed twice with 2 mL of 1x permeabilisation buffer and centrifuged after each wash at 500 g for 5 minutes at RT. The pellets were then resuspended in 100 µL 1x permeabilisation buffer and stained with anti-HMGB1 (5 µL/ tube) or AF488 isotype control (5 µL/ tube). Unstained tubes were used for controls. The samples were incubated for 60 minutes at RT protected from the light. After the staining, the samples were washed twice with 2 mL of 1x permeabilisation buffer and centrifuged after each wash at 500 g for 5 minutes at RT. The pellets were washed with flow cytometry staining buffer and analysed using a CytoFLEX Flow cytometer (Beckman Coulter). CytExpert software was used for acquisition and analysis across the entire platform.

2.2.10.2 Sample preparation for flow cytometry analysis- Intranuclear staining

Intranuclear proteins were stained following sample preparation using eBioscience™ Foxp3 / Transcription Factor Staining Buffer Set (Invitrogen). The Foxp3 Fixation/ Permeabilization working buffer was freshly prepared by mixing 1x Foxp3 Fixation/ Permeabilization Concentrate with 3x Foxp3 Fixation/ Permeabilization diluent. 1 mL was needed per test tube. The 1x working solution of Permeabilization buffer was prepared by mixing 1 part of Permeabilization buffer with 9 parts of distilled water. A total volume of 8.5 mL was required per test tube. Human mesothelioma cells, NCI-H28 and MSTO-211H, human mesothelium cells Met-5A, NSCLC cells NCI-H1975, and positive control cells U937 and HeLa cells were cultured in T125 flasks until the cultures reached 80% confluency. The cells were subsequently harvested and prepared in suspension. The cell suspensions were passed through Fisherbrand™ Sterile Cell Strainer (100 µm porosity) to eliminate any unwanted debris. The cells were transferred to 75 mm round bottom flow cytometry test tubes ($10x10^5$ cells/ tube). The cell

pellet was washed with eBioscience™ Flow Cytometry Staining Buffer (Invitrogen), and then centrifuged at 400 g for 5 minutes. After the last wash, the supernatant was discarded, and the sample was pulse vortexed in the residual volume (≈100 µL) to dissociate the pellet. 1 mL of Foxp3 Fixation/Permeabilization working solution was added to each tube and pulse vortexed. The tubes were incubated for 30-60 minutes at 2-8°C, protected from light. After incubation, 2 mL of 1X Permeabilization Buffer were added to each tube. The tubes were centrifuged at 400-600 x g for 5 minutes at RT. The step was repeated. Directly conjugated antibodies/ isotype controls were added to each tube and incubated for 60 min at RT, protected from light. Tubes containing unstained cells were also used as controls. Following antibody incubation, the pellets were washed twice with 2 mL of 1X Permeabilization Buffer. After centrifugation at 400-600 x g for 5 minutes at RT, the supernatant was discarded, and the pellets were washed with flow cytometry buffer before analysis with a CytoFLEX Flow cytometer.

2.2.10.3 Data analysis

Data was recorded and saved as .fcs files. FlowJo Software (BD Biosciences, NJ, USA) was used for data analysis and to produce the flow histograms. Mean fluorescence index (MFI) was calculated based on median intensity. Data were plotted using GraphPad Prism 6.0 (GraphPad Software, La Jolla, CA, USA).

2.2.10.4 Sample preparation for immunofluorescence analysis

Round glass coverslips (12 mm diameter) were carefully placed in a 24 well-plate and sterilised with 100% (v/v) ethanol for at least 10 minutes. The ethanol was removed, and the coverslips were washed twice with PBS. Following the last wash, the coverslips were left to completely dry in a cell culture laminar flow hood. Once the coverslips were ready, mesothelioma cells (NCI-H28, MSTO-211H), human mesothelium cells (Met-5A), NSCLC cells (NCI-H1975), and control cell line HeLa were prepared in suspension and seeded onto the coverslips (5x 10^4 cells per well). The plates were incubated for 48 hours at 37°C, 5% CO_2. After 48 hours of incubation, the cells were fixed in 4% (v/v) cold PFA for 10 minutes and

were permeabilised with 0.1% (v/v) Triton X-100 prepared in PBS (PBST) for 15 minutes at RT. The layers were then blocked for 45 minutes at RT with 2% bovine serum albumin (BSA) prepared in PBS. The cells were then labelled overnight with primary antibodies diluted in 0.1% BSA (anti-HMGB1 1:50, anti-mesothelin 1:50, anti-VISTA 1:100). Following the incubation, the cells were washed 3 times with 0.1% PBST for 3 minutes before labelling with the secondary antibody diluted in PBST (AF488 1:250) for 1 hour at RT. The coverslips were then mounted onto glass slides using ProLong™ Diamond Antifade Mountant with DAPI (Thermo Fisher Scientific). The slides were left to dry in the dark at 4°C for 24 hours and then stored in a dark slide box until analysis.

2.2.10.5 Confocal analysis

The LSM 800 confocal microscope (ZEISS) was used with Zen Blue software (ZEISS). All samples were imaged using a 40 X plan-apochromat oil objective. To image DAPI staining, a 405 nm diode laser at 0.3% laser transmission with a maximum output of 5 mW was used. For imaging of fluorophores excited at 488 nm, a 488 nm diode laser at 0.2 % laser transmission with a maximum output of 10 mW was used. Pixel time was set to 1, averaging to 4. Gain was set between 800-880 V.

2.2.11 MALDI-MS imaging of TMAs

2.2.11.1 Sample preparation- Antigen retrieval

Tissue microarrays were supplied as formalin-fixed paraffin-embedded (FFPE) tissue sections. Firstly, the paraffin was removed from the section. The TMA slide was washed twice in 100% (v/v) xylene substitute for 5 min, followed by a 100% (v/v) isopropanol wash (5 min). The section was then washed in graded pure ethanol solutions (100%, 95%, 70%, and 50% (v/v), 5 min for each concentration). Following the ethanol washes, the slide was immersed in liquid chromatography mass spectrometry (LC-MS) grade water for 5 seconds. Antigen retrieval was subsequently carried out in order to unmask antigenic epitopes on the tissue surface by placing the slide containing the TMA in a 50 mL falcon tube

completely filled with 50 mM Tris Buffer solution (9.5 pH). The sealed falcon tube was then placed in a 95°C water bath for 20 min.

2.2.11.2 Sample preparation- Tissue fixation and lipid removal

The TMA was fixed in 70% and 90% (v/v) ethanol solutions for 1 min each, followed by immersion in $CHCl_3$ for 30s in order to remove lipids and small molecules. The section was placed in a tube containing a solution of ethanol, glacial acetic acid, and water (90:9:1) for 1 min in order to trigger protonation for positive mode analysis.

2.2.11.3 Trypsin and matrix deposition

Sequence grade modified trypsin (Promega) was supplied lyophilised in 20 µg vials and prepared in 25 mM $NH_4(HCO_3)$. Both trypsin and matrix solutions (5 mg/mL α-CHCA in 50% ACN:0.1% trifluoroacetic acid (TFA)) were deposited onto the tissues using the spray-coat method with a M3+ HTX TM-Sprayer™ automated sprayer (HTX Technologies). The settings used to spray the trypsin and matrix are presented in Table 2.12.

Matrix	Trypsin	CHCA
Solvent	Ambic	50%ACN:0.1% TFA
Temperature (°C)	37	40
# Passes	8	6
Concentration (mg /mL)	0.2	5
Flow rate (mL/ min)	0.015	0.03
Velocity (mm/ min)	1200	750
Track spacing (mm)	3	2
Pattern	HH	CC
Pressure (psi)	10	10
Gas flow (l/ min)	3	3
Drying time (s)	5	0

Nozzle height (mm)	40	40

Table 2.11 HTX sprayer settings for trypsin and CHCA matrix deposition.

2.2.11.4 Analysis

Mass spectra was manually acquired on a Waters MALDI Synapt G2 HDMS mass spectrometer (Waters Corporation, U.K.) equipped with a Nd:YAG laser operated at 1 kHz. Instrument calibration was performed using phosphorus red. Spectra was acquired in positive mode, with Ion mobility function on, full scan sensitivity mode within a *m/z* range 700-1800, laser spot size 100 µm, laser wavelength 355 nm and a laser energy at 250 arbitrary units.

2.2.11.5 Data processing

Data was acquired and converted to .txt file format using MassLynx™ software (Waters Corporation) and analysed using mMass 3 open-source software (Strohalm *et al.*, 2010). Peak picking settings were set at a signal to noise (S/N) threshold of 5, and the picking height was 100%. Both the absolute intensity threshold and the relative intensity threshold was set to 0 with baseline correction and smoothing applied. Identification of values were based on putative assignments using Uniprot Online Tool (Uniprot.) and published literature. ROIs of individual cores were selected and MALDI MS images were generated using HDI v1.6 software (Waters Corporation). Normalisation against the highest intensity peak was attempted but was not presented due to limited signal yielded by the sample compared to matrix.

Chapter 3 Optimisation of Cell Density, Viability and Mineral Fibres Treatment

3.1 Introduction

3.1.1 Introduction to the chapter

One important aspect of this research was to ultimately apply LA-ICP-MSI to spatially resolve asbestos fibres at cellular resolution. Given that asbestos and other MF can induce cell death (Yu *et al.*, 2019), this chapter outlines the initial experiments performed to ensure cell viability and structural integrity was maintained within the MPM cell lines following exposure.

Initial parameters such as cell number, MF fibre concentration, and exposure time were optimised in each case. Furthermore, this was extended to determine the role that fibre type plays in cellular viability, and whether cell death is dose and time-dependent. MSTO-211H, NCI-H28, and a mesothelial cell line, Met-5A, were exposed to different MF fibres at low concentrations over 72 hours. The work was performed in accordance with previous studies but adapted to this niche project. The low dose (3 µg /mL) was selected for LA-ICP-MS sample preparation but also as a baseline for future cell viability investigations.

Previously, cytotoxic effects of asbestos fibres have been investigated both in *in vitro* cellular models (Casalone *et al.*, 2018), as well as in animal models (Altomare *et al.*, 2005; Trevisan *et al.*, 2016), with reports present from as early as 1970s (Davis, Bolton, & Garrett, 1974). Most studies have investigated the relationship between asbestos exposure, cytotoxicity, and asbestos-induced cellular and molecular alterations on human or animal derived mesothelial cells (Casalone *et al.*, 2018; Kopnin *et al.*, 2004), lung fibroblasts (Yu *et al.*, 2019), or macrophages (Nadeau & Lane, 1988). However, data on the impact of asbestos on transformed MPM cells is limited. Moreover, most reports focus on the cytotoxic effect of the most prevalent fibres, such as crocidolite and chrysotile (Qi *et al.*, 2013), and less on naturally occurring tremolite and actinolite (Ricchiuti *et al.*, 2021) or non-asbestiform fibres, such as wollastonite (Maxim & McConnell, 2005).

The panel of MF included some of the most common types of asbestos, but also a non-asbestiform control, not yet classed as carcinogenic, known as wollastonite (Maxim & McConnell, 2005). In terms of cell viability, a calcium inosilicate control can determine if the decrease in cell viability is triggered by a physical trauma to the cells by a foreign body or a chemical reaction between MF and cell membrane. Wollastonite does not contain any Fe atoms in its chemical formula which was previously reported to be involved in MM pathogenesis cascade presumably via catalytic action by the Fenton reaction (Toyokuni, 2002). Additionally, the free radicals generated by the Fe molecules trigger asbestos-induced oxidative stress at molecular level and are largely held as one of the causes of asbestos malignant effect (Pietrofesa *et al.*, 2016). Secondly, wollastonite was used as a control for LA-ICP-MS analysis to investigate the specificity of this technique in terms of distinguishing between asbestos and non-asbestiform impurities.

MF cytotoxicity was determined by monitoring cellular viability over time based on the metabolic activity. AlamarBlue® was employed as a simple high throughput assay to assess viability over time. Compared to other viability assays, alamarBlue® reagent is non-toxic and allows for multiple time points measurements (Walzl *et al.*, 2014). The assay uses resazurin, a cell permeable, non-fluorescent compound that is blue in colour. Based on the metabolic activity of the viable cells, resazurin is reduced to resorufin, a compound that is red in colour and highly fluorescent. Viable cells continuously convert resazurin to resorufin, increasing the overall fluorescence and colour of the media surrounding cells (Larsson *et al.*, 2020; Walzl *et al.*, 2014).

Asbestos fibres have been reported to induce cell death *in vitro*, although the exact mechanisms are yet to be fully elucidated. One hypothesis is that asbestos induces cell death through reactive oxygen species (ROS) production and subsequent DNA damage (Broaddus *et al.*, 1996; Jimenez *et al.*, 1997). However, these reports predate recent investigations that suggest that asbestos-induced cell death is a regulated form of necrosis linked to overall carcinogenesis (Yang *et al.,* 2010). Current technology can help distinguish between the two main types

of cell death (*i.e.,* apoptosis and necrosis) and help build the knowledge around MPM pathogenesis. Apoptosis is described as an energy-dependant, programmed process of autonomous cellular dismantling, with no subsequent inflammation. The hallmarks of apoptosis include internucleosomal DNA fragmentation and caspase activation (Fink & Cookson, 2005). Necrosis has initially been characterised as a passive, accidental cell death resulting from environmental factors, with uncontrolled initiation of an inflammatory cascade (Fink & Cookson, 2005). However, more recent studies have established a strong link between necrosis and subsequent activation of poly (ADP-ribose) polymerase (PARP), depletion of intracellular ATP, and release of high-mobility group box 1 protein (HMGB1), a key player of MPM pathogenesis that triggers the inflammatory cascade (Yang *et al.,* 2010).

Despite being an inexpensive, fast, and high-throughput assay, alamarBlue® cannot distinguish between different cell death types and only provides information on the cell viability based on the metabolic activity of the cultures. For a detailed understanding of the cell death processes, a novel RealTime-Glo™ Annexin V Apoptosis and Necrosis Assay was used in the final steps of the study. The non-lytic, kinetic assay measures the exposure of phosphatidylserine (PS) on the outer leaflet of the cell membrane during the apoptotic process. Once the cell membrane is compromised due to necrosis, the DNA-specific pro-fluorescent dye is released and measured as fluorescence intensity (Kupcho *et al.*, 2018). The assay can simultaneously measure early apoptosis and subsequent necrosis levels in real time, over an extended period of 72 hours, with measurements taken every 2 hours. It is possible to gain information on the apoptotic/ necrotic event and timing of cell death induced by MF.

Therefore, the initial studies explored the cytotoxicity of various MF in relation to immortalised human MPM cells, as a critical optimisation step for future investigations. Additionally, this optimisation step may inform future studies beyond the scope of this project. Lastly, the data on apoptosis and necrosis levels induced by different MF over a period of time can lead to a better understanding of the biology and pathogenesis of MPM, which in turn may enable identification

of effective treatment targets and facilitate the development of a personalised treatment approach.

3.1.2 Hypothesis

The cytotoxicity of asbestos and other MF can be monitored *in vitro* by employing human malignant mesothelioma cells and non-cancerous human mesothelium cells. Various MF can affect the cellular viability at different rates, depending on cell and fibre type, concentration, and exposure time.

3.1.3 Aims of the chapter

The main aim of this chapter was to optimise the MF preparation, dosage, and concentration for future LA-ICP-MSI analysis and other investigations. Additionally, the optimisation steps offered insight into the impact various MF (actinolite, amosite, chrysotile, crocidolite, and wollastonite) have on human malignant mesothelioma cells and non-cancerous human mesothelium cells.

3.2 Results and Discussion

3.2.1 Asbestos and other mineral fibres

3.2.1.1 Fibre preparation and validation

The asbestos fibres were research-grade, UICC-accredited. All the MF were prepared in specially designed laminar flow hoods to avoid inhalation of the fibrils. Each fibre type was validated based on the morphology, colour, and pleochroism (*i.e.,* colour in relation to the spatial orientation of the polarised light) by employing Polarised Light Microscopy (PLM). The observed properties were compared to asbestos laboratory standards, as well as natural, synthetic, and artificial MF. Fibre validation was conducted in collaboration with a team of asbestos disposal experts from Santia Ltd. All asbestos fibres appeared to have a standard fibrous morphology. Actinolite and crocidolite fibres proved to exhibit the highest degree of pleochroism, whilst the rest of the fibres showed little colour contrast under polarised light. Crocidolite appeared blue (parallel) and grey (perpendicular).

Actinolite changed from green parallel to the polariser to pale green, grey or yellow when perpendicular to the polariser (Table 3.1).

Asbestos type	Actinolite	Amosite	Chrysotile	Crocidolite
Morphology	Fibrous	Fibrous	Fibrous	Fibrous
Pleochroism (parallel)	Green	None	None	Blue
Pleochroism (perpendicular)	Pale green/grey	Light brown	None	Grey

Table 3.1 Asbestos validation by PLM. The table presents the observed morphology and pleochroism of the four asbestos types.

3.2.1.2 Mineral fibre storage and physical properties

The MF were stored in glass bottles in sterile PBS solution to prevent fibres being inhaled. Figure 3.1 presents the MF stock solutions. The differences in density across the asbestos and wollastonite fibres can be seen in Figure 3.1 A-E, where the fibres decanted at the bottom of the glassware. Same mass of fibres was initially weighted in each bottle. MF with lower density (*e.g.,* actinolite and chrysotile) tended to occupy more space in the non-mixed solutions, whilst the more compact fibres deposited at the bottom (*e.g.,* amosite, crocidolite, and wollastonite). Due to the high number of fibres, the typical colours can also be noted, particularly in the mixed solutions presented in Figure 3.1 F-J (*i.e.,* actinolite- greenish tint, amosite- brown/ greyish shade, chrysotile and wollastonite- white, crocidolite- blue).

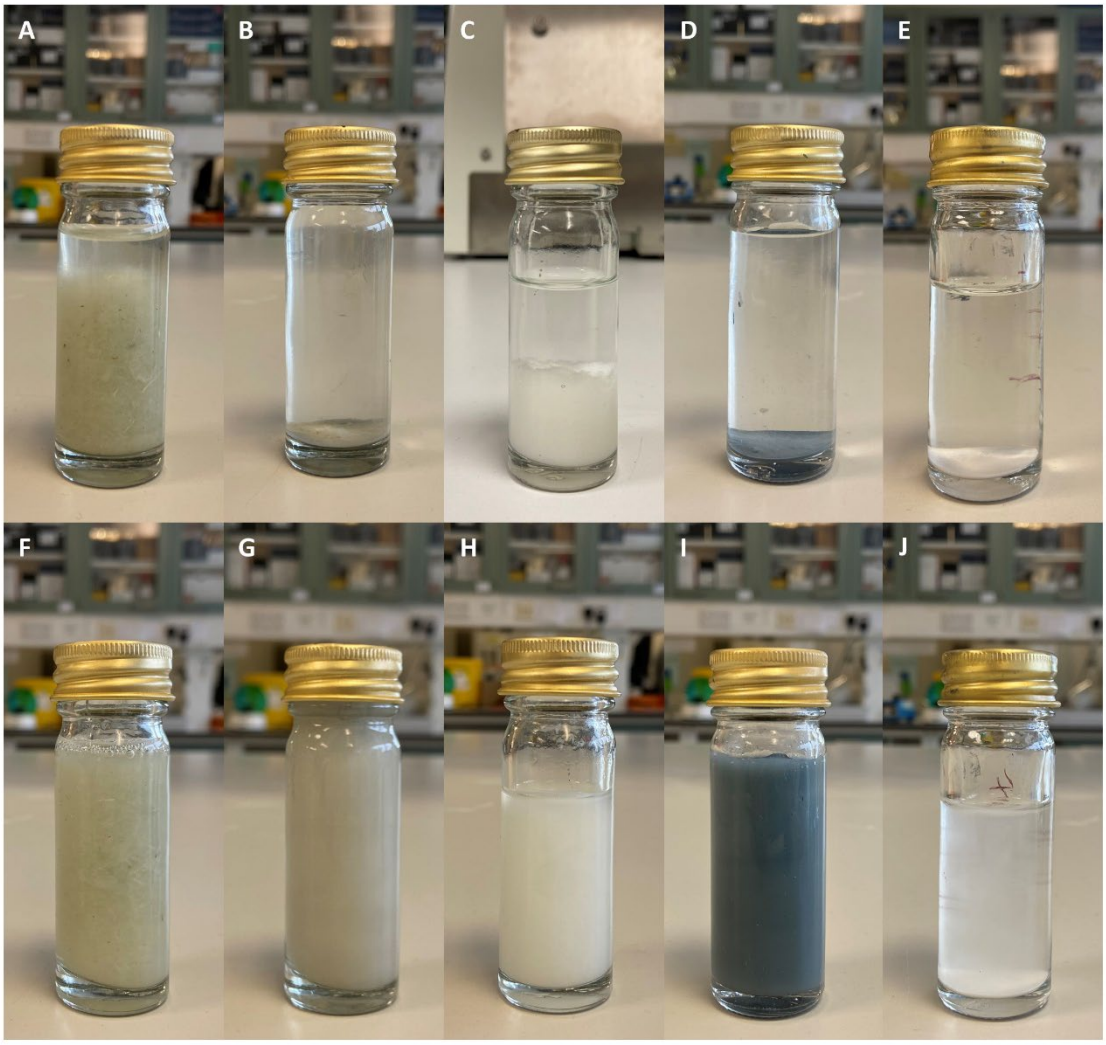

Figure 3.1 MF stock solutions. (A-E) MF decanted at the bottom of the glassware. (F-J) MF mixed in the PBS solution. (A, F) Actinolite; (B, G) Amosite- brown asbestos; (C, H) Chrysotile-white asbestos; (D, I) Crocidolite- blue asbestos; (E, J) Wollastonite- non-asbestiform control. Note the differences in density between different types of MF.

Following the preparation on the stock solutions, the MF were imaged using brightfield microscopy (Figure 3.2). Actinolite fibres appeared to be longer and thinner, with some shorter fragments also present. The asbestos fibres known to have higher potency to induce MPM, such as amosite and crocidolite, appeared to be shorter, needle-like with several shorter fibres and fibre fragments visible throughout the image. Some really long amosite fibres can be noted (over 500 µm). Chrysotile's unique physical appearance can be noted, with long curled fibres bundled up in clusters. Finally, the crystal-like shape of wollastonite can

also be observed. The wollastonite fibres appeared to be longer and thicker, which is one of the physical properties that makes this fibre a poor carcinogen (Rosenthal *et al.*, 1994).

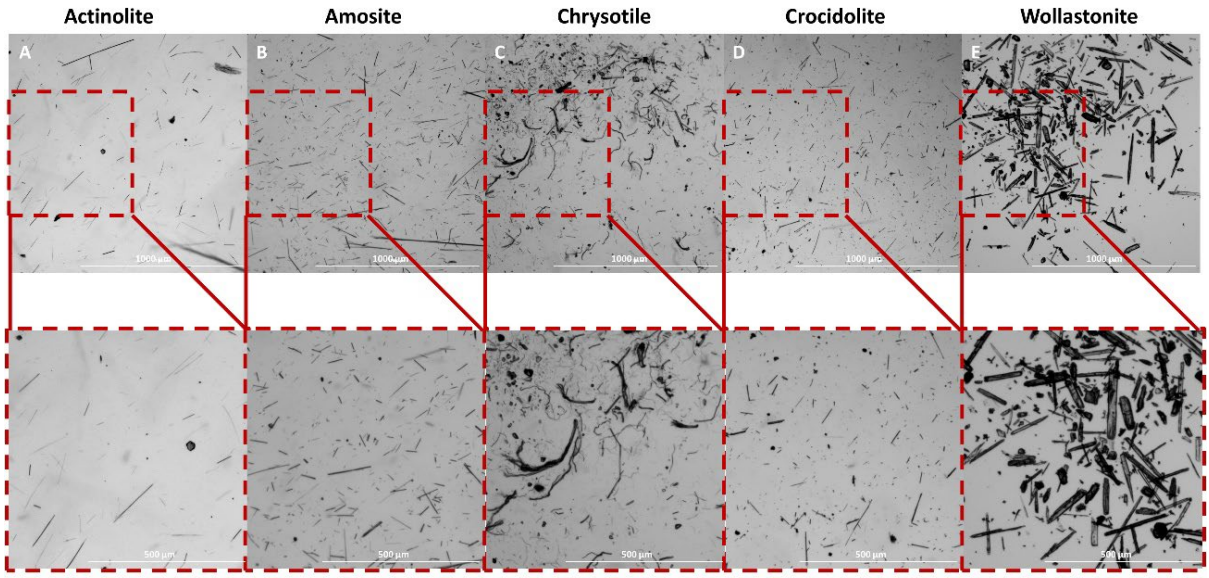

Figure 3.2 Brightfield images of the MF in PBS solution. The physical properties of each individual fibre type can be noted in the close-up images. Scale bars: top row 1000 µm, bottom row 500 µm.

3.2.1.3 Mineral fibres treatment optimisation

The initial work focused on developing a 2D cellular model co-cultured with asbestos and other MF, suitable for LA-ICP-MS analysis. Given the limited access to asbestos safe laminar flow hoods, the fibres were kept in solution at all times and the fibre treatment was expressed as µg/ mL. Several previous studies have taken this approach of expressing dry weight of asbestos per volume of liquid (Pollastri *et al.*, 2016; Yu *et al.*, 2019; Yu *et al.*, 2019), rather than dry weight of asbestos per treated area (Casalone *et al.*, 2018; Kopnin *et al.*, 2004).

The ideal fibre concentration was desired to be high enough to test the hypothesis that LA-ICP-MS can identify MF in small regions of interest (ROIs), without overabundance of signal. Furthermore, the right dose would recapitulate the standardised content of >2 asbestos bodies per 1 cm^2 lung section area and would be comparable to *in vivo* occurrences of smaller fibres and fibre fragments

not visible with brightfield microscopy previously associated with MPM onset (Bononi *et al.*, 2015). Figure 3.3 shows the fibre count in relation to the concentration of solution. Physical properties of each fibre type, such as length, thickness, and shape can also be noted. Due to difference in density, fibre counts vary between each fibre type, for the same concentration of fibres. The same concentration was used in the follow up experiments for consistency.

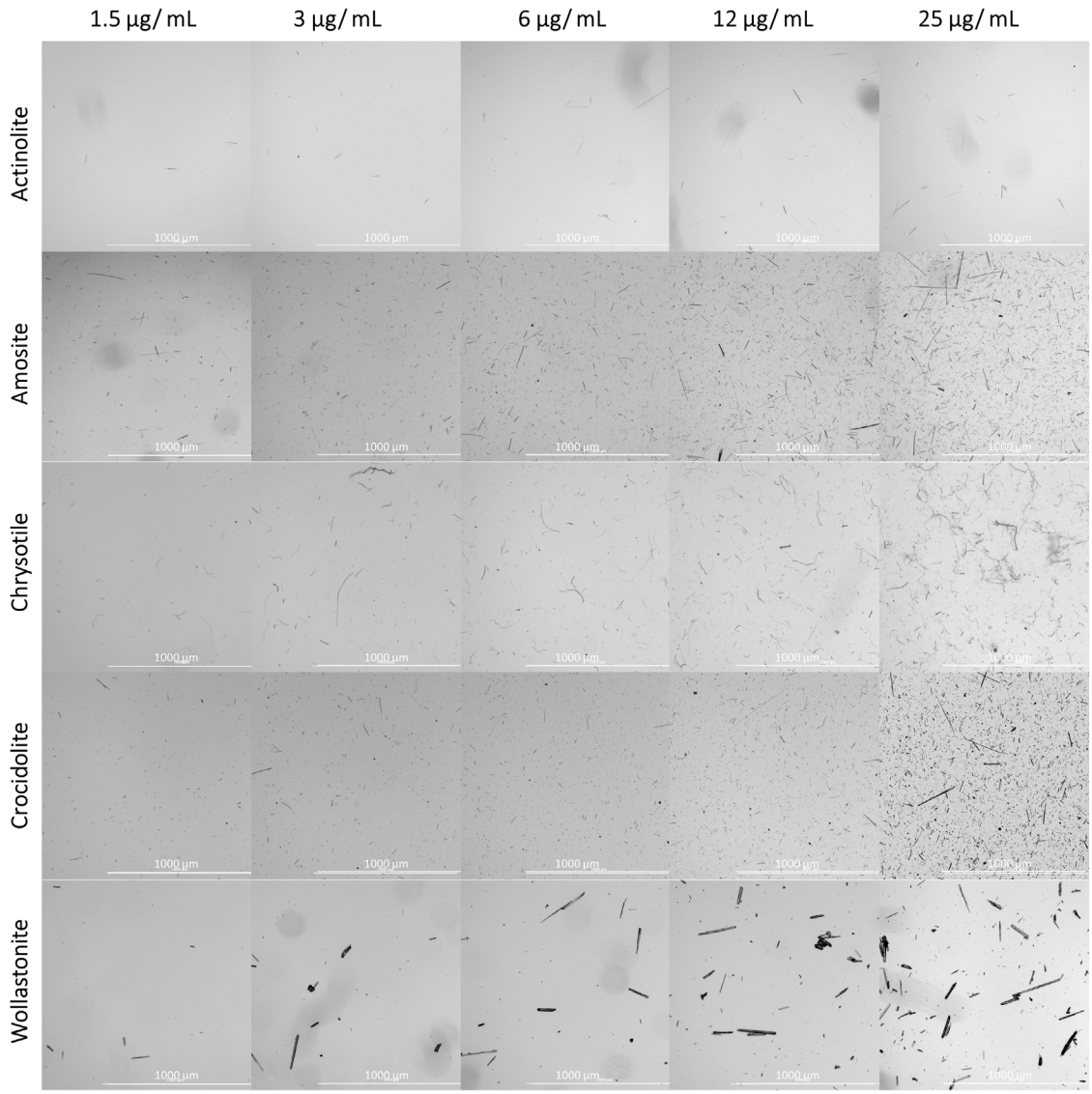

Figure 3.3 Different range of concentration for each individual fibre type. The physical properties of the mineral fibres can be noted in the brightfield images. Representative of at least 3 fields of view. Scale bar- 1000 µm.

3.2.2 The Effect of mineral fibres on immortalised cells

3.2.2.1 Cellular viability after actinolite treatment

The initial work focused on assessing the impact of various concentrations of actinolite fibres on immortalised human mesothelioma cells at three different time points by brightfield microscopy. The work was carried out to optimise cell number, cell viability, MF concentration, and exposure time prior to 2D LA-ICP-MSI. Actinolite fibres detection was used to optimise LA-ICP-MS parameters so this was the first step in model development. The interaction between actinolite fibres at different concentrations and mesothelioma cells (MSTO-211H and NCI-H28) was monitored using brightfield microscopy at 3 different time points. Staurosporine (1mM), a known apoptosis inducer (Zhang *et al.,* 2004), was used as a positive control. PBS was used as a vehicle control to match the volume of PBS added with the highest concentration of actinolite fibres. The time points were selected based on the existing knowledge and literature, to allow the fibres to lodge within the MPM cells, with no more than five visible fibres per cm^2. Additionally, the percentage of viable cells was selected to be between 80 and 90% to be able to cytospin the cell-fibres mixture prior to LA-ICP-MS analysis. Figure 3.4 and Figure 3.5 are composed of a series of brightfield images taken of NCI-H28 and MSTO-211H cells treated with various concentrations of actinolite fibres, as well as a positive and a vehicle control, taken after 24, 48, and 72 hours, respectively. Cells decreased in size during the apoptotic process caused by staurosporine treatment. Similar shrinkage can be noted around the actinolite fibres, particularly above 6 µg/ mL. Dead cells appeared to clump around the larger actinolite fibres, suggesting cell damage. This process was more noteworthy for MSTO-211H cells, where the actinolite fibres significantly decreased overall cellular viability. The MSTO-211H cells were established from a patient with no prior radiation or chemotherapy. It has also been reported by the supplier that this cell line reaches a saturation density of 4×10^5 cells per cm^2 and will afterwards slough off of the surface still in a viable state, mirroring the metastatic origin of this cell line (ATCC.).

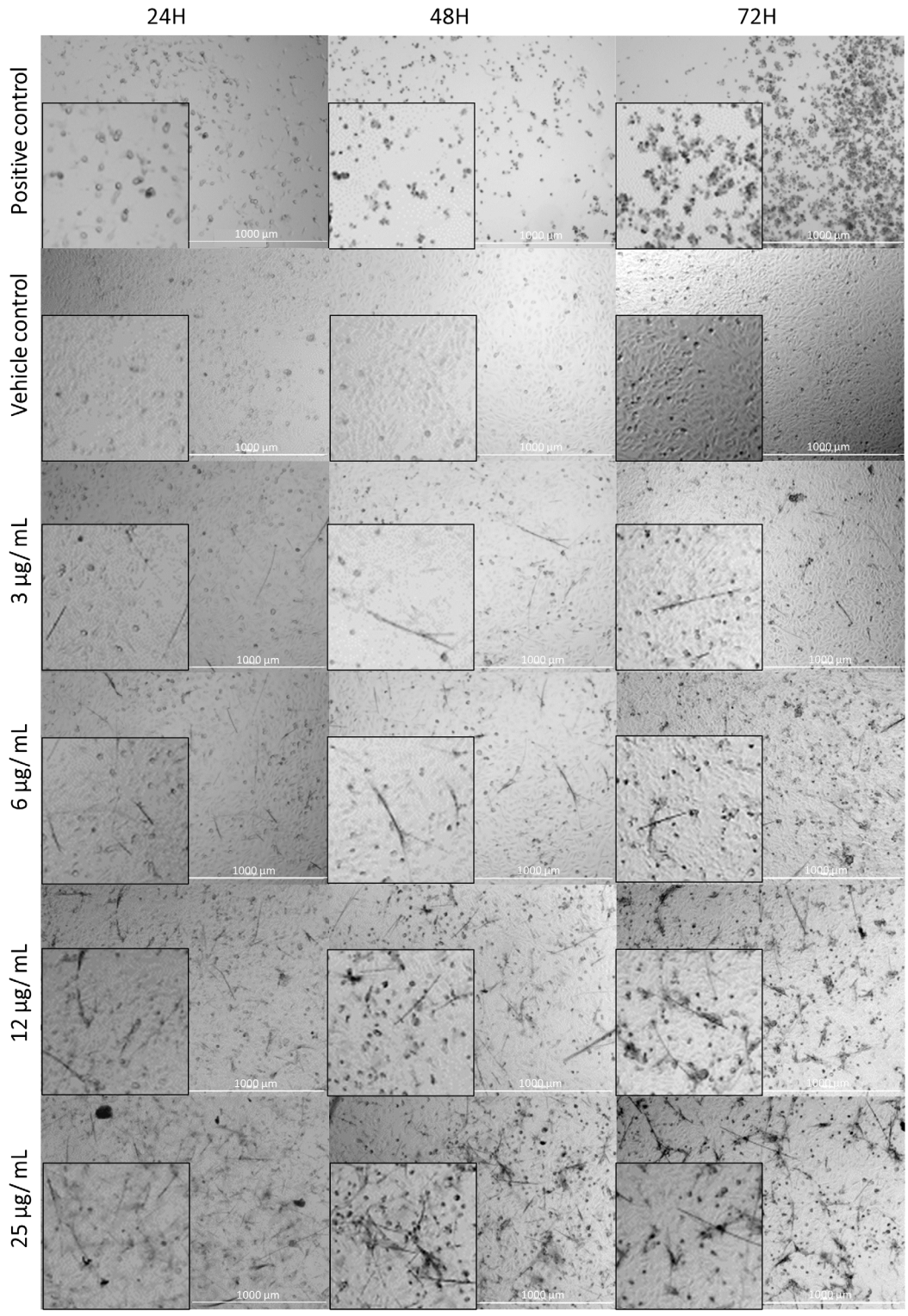

Figure 3.4 NCI-H28 cells treated with actinolite fibres (0-25 µg /mL) after 24h, 48h, and 72h of exposure. The cell monolayers show no changes to low concentrations of actinolite after 24h and 48h. Non-viable cells are more visible at higher concentrations after 72h. Representative images of at least 3 fields of view. Positive control- staurosporine (10 µM); Vehicle control- PBS; Scale bar- 1000 µm.

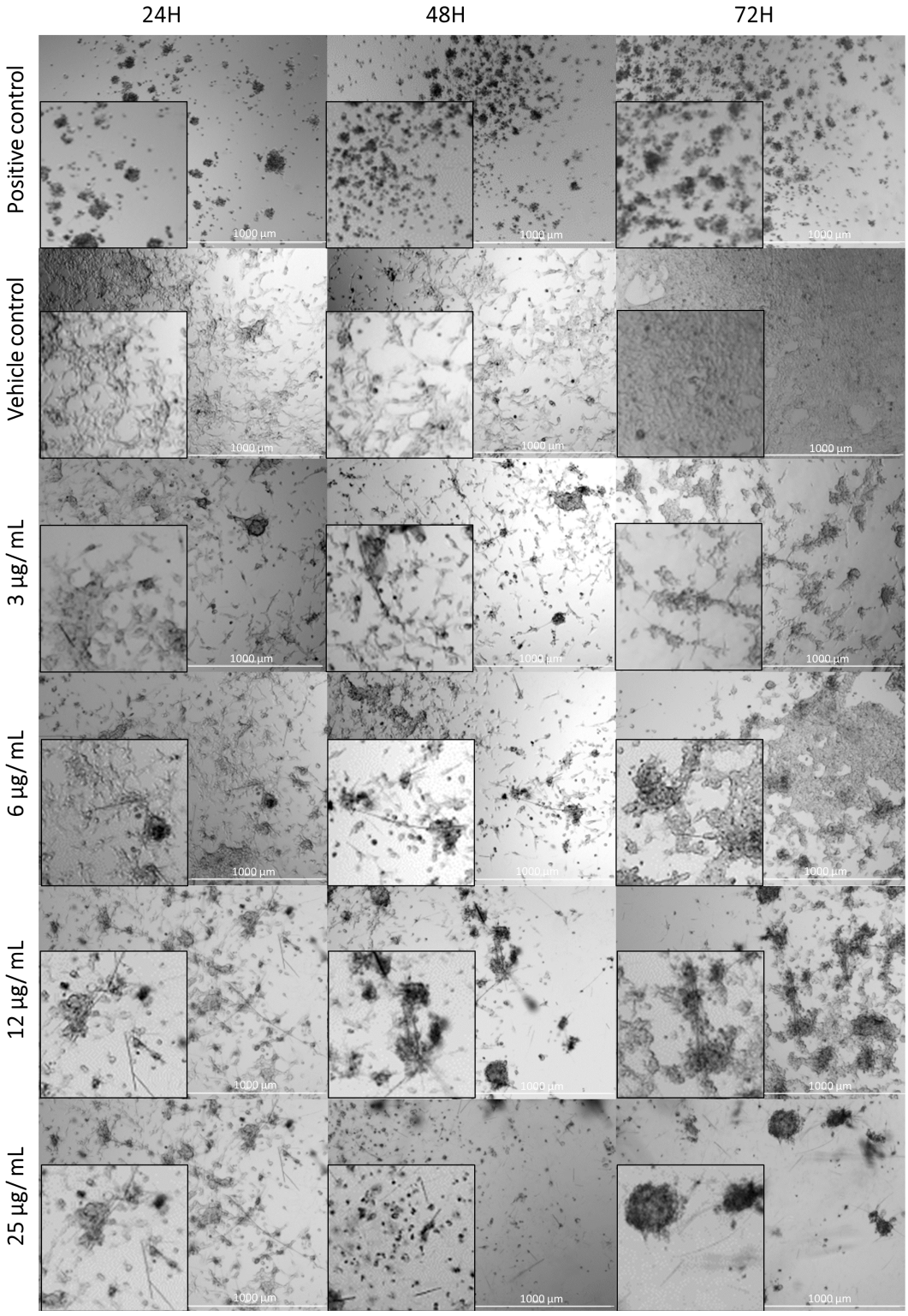

Figure 3.5 MSTO-211H cells treated with actinolite fibres (0-25 µg /mL) after 24h, 48h, and 72h of exposure. Cell death is apparent after 24h, even at lower concentrations. At high concentrations the cells appear to be completely non-viable, clumping around the actinolite fibres. Representative images of at least 3 fields of view. Positive control- staurosporine (10 µM); Vehicle control- PBS; Scale bar 1000 µm.

Another method to assess the effect of actinolite fibres on the monolayers was to measure cellular viability. Cell death has been previously reported as the hallmark of MPM pathogenesis. Although other MF have been reported in literature (Casalone *et al.*, 2018), there is currently very limited data on the effect of the actinolite on *in vitro* cell cultures. Comparing cell viability of actinolite exposed cell layers to unexposed cells can offer insight into the degree of cell death caused by actinolite fibres.

The viability of two MPM cell lines and a control NSCLC cell line, NCI-H1975, after 24h, 48 h, and 72h of being exposed to different concentrations of actinolite is presented in the graphs below (Figure 3.6). Staurosporine was used as a positive drug control. Data represent the mean average of 3 replicates and are presented as percentage of viable cells, normalised against vehicle control.

The viability of MSTO-211H cells was significantly impacted by the number of actinolite fibres which played an extremely significant role (88.27% of the total variance). This clear dose dependent decrease in viability was also observed in the microscopy images from Figure 3.5. One hypothesis was that MSTO-211H cells of metastatic origins were less likely to have been exposed to asbestos fibres *in vivo*, which can explain the extremely significant impact of actinolite on the viability. The cell line was established from a biphasic MPM patient with no previous treatment history, suggesting a decrease in acquired defects in the apoptosis machinery induced by chemotherapy.

Chemotherapy drugs are antimetabolic agents that take effect through activation of caspases and calcium-dependent nucleases to induce apoptosis of malignant cells (Chen, Zeng, & Zhou, 2018). This knowledge suggests that MSTO-211H has no drug-induced mutations in the apoptotic machinery, resulting in increased susceptibility to chemical and physical apoptosis inducers. Interestingly, statistical analysis showed that treatment has a similar effect at all times, meaning that in this case the dose-time interaction was not considered significant ($p > 0.05$). Compared to vehicle control, the cells exposed to actinolite fibres, regardless of dose, showed an extremely significant decrease in viability after 24h, maintaining this trend at all time points (Figure 3.6).

In terms of the effect of actinolite fibres on epithelioid MPM cells, NCI-H28, only exposure to higher concentration of actinolite (>12 μg/ mL) caused a significant decrease in viable cells after 24h, when compared to the vehicle control treated cells. The limited decrease in cell viability of this cell line for lower concentrations can be explained by the tissue origin of the cells (*i.e.,* lung tissue), which is known to be constantly interacting with asbestos fibres in MPM patients with known exposure. Indeed, other studies have reported apoptotic resistance in cells exposed to low doses of asbestos, for longer periods of time (Matsuzaki *et al.*, 2018). Additionally, NCI-H28 has been reported to contain a homozygous deletion of the β-catenin gene (Shigemitsu *et al.*, 2001), suggesting that Wnt-1 mediated apoptotic resistance, a well-established blockage mechanism, is acquired in this case through non-canonical pathways, as previously demonstrated (Liang *et al.*, 2004). This notable difference in apoptosis resistance between MSTO-211H and NCI-H28 cells has been suggested before, with the latter needing over 3 times the drug concentration to induce a significant decrease in cellular viability (Moriyama *et al.*, 2018).

Results suggest an association between dose and exposure time, the data being extremely significant for all treatment options after 72h (dose-time interaction accounting for 13.05% of the total variance). Similar to MSTO-211H data, the number of fibres also played a key role in increased cell death (dose effect 51.65% of total variance). This dose/time dependent increase in cell death was also noted in the pictorial representation above (Figure 3.4).

Lastly, NCI-H1975, a NSCLC cell line, was employed as a control cell line, to investigate whether cancer type plays a role in viability response. Statistical analysis revealed that dose-time interaction played a less significant role than the concentration of actinolite fibres, which accounted for a striking 83.08% of the total variance. Exposure to low dose of actinolite resulted in no significant decrease in cell viability when compared to vehicle control, across all time points (Figure 3.6). Interestingly, the level of cell death was more statistically significant after 48h compared to longer exposure. After 72h cells appear to develop

apoptotic resistance, with no statistically significant difference in viability between vehicle control treated cells and cells treated with actinolite fibres at low doses.

These noteworthy differences in viability under different treatment regimens, over different periods of time, across the cell lines panel indicate that cell death may be influenced more by the chemical structure of actinolite, rather than the physical properties.

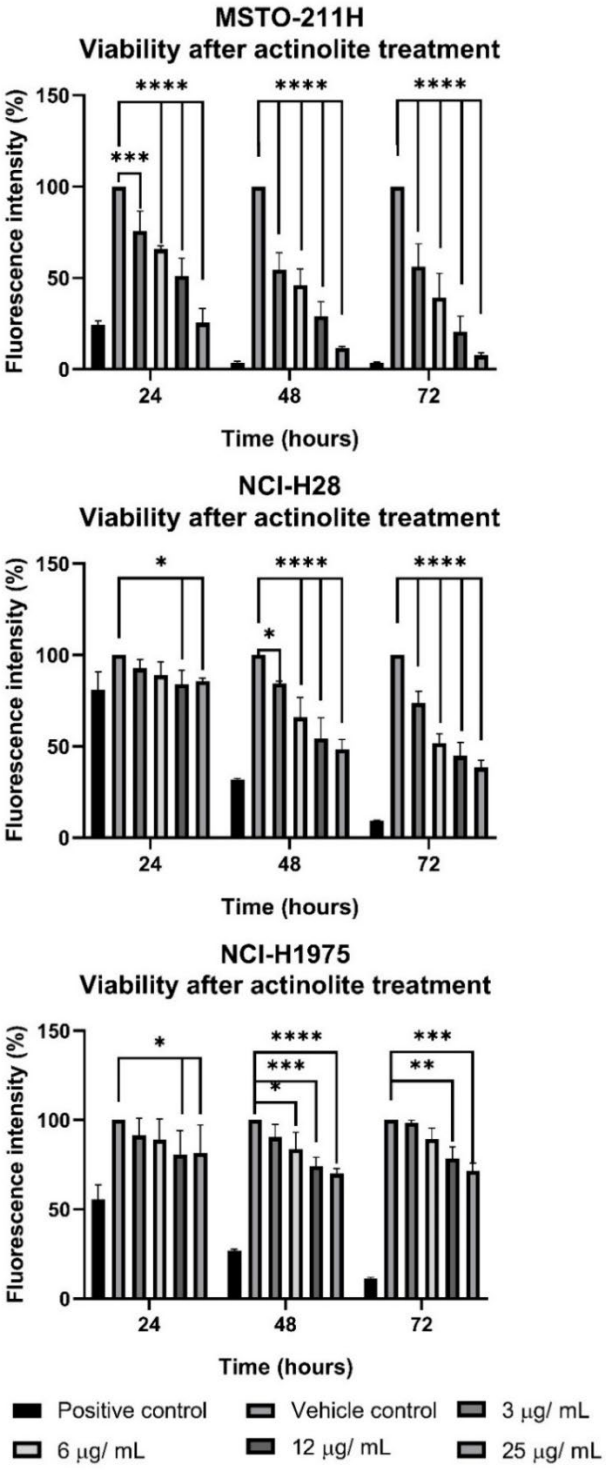

Figure 3.6 MSTO-211H, NCI-H28, and NCI-H1975 cells metabolic activity following exposure to actinolite fibres represented by fluorescent intensity counts. Data were normalised against vehicle control, and it was considered significantly different compared with the vehicle control by two-way ANOVA analysis (n=9), followed by a Dunnett test for multiple comparisons to a control. The link between fibre type, dose, and exposure time and cellular viability. *p between 0.01 and 0.04; **p< 0.01; ****p<0.0001; ns- not significant.

3.2.2.2 The link between fibre type, dose, and exposure time and cellular viability

Investigating the viability rates of various cell types after exposure to different MF at a low dose, over certain periods of time, can offer insight into mechanisms of action of asbestos and highlights the need for an updated IARC classification and stricter regulations.

Cellular viability was measured based on the metabolic activity as fluorescence intensity over 72 hours of exposure. Data were normalised against the vehicle control. All cell lines were treated with low doses of MF (3 µg/ mL). Staurosporine was used as a cell death inducer control (positive control). For the epithelioid cell line, there was no significant decrease in cellular viability after 24h for most of the treatment regimens, with the exception of crocidolite which induced a statistically significant decrease in cellular viability, indicating a cell death pathway caused by chemical factors. Interestingly, the difference in viability stopped being significant after 72 hours, indicating that NCI-H28 cells may acquire cell death resistance when exposed to small concentrations of crocidolite fibres, over longer periods of time. On the other hand, chrysotile and wollastonite fibres induced cell death in a time-dependent manner, suggesting cellular and DNA damage through physical trauma. This cellular response may also be explained by the origins of NCI-H28, morphology, and previous asbestos exposure (Figure 3.7).

MSTO-211H cells presented a different viability trend, with most of the extremely significant events happening after only 24h, similar to the actinolite data presented above in Figure 3.6, suggesting limited mutations in the acquired apoptosis resistance pathways. However, in the case of low dose treatment with other fibre types, the cell death levels plateaued over time. After 72h, the data for amosite, crocidolite, and wollastonite treated cells were no longer statistically significant (Figure 3.7). The MSTO-211H cells appeared to develop cell death resistance to low doses of MF after longer exposure. Indeed, literature has reported increased mutations arising from loss of heterozygosity after exposure to asbestos fibres after only 24h up to 72h (Both, Turner, & Henderson, 1995; Xu, A. *et al.*, 2007).

No significant decrease in viability was recorded for the Met-5A cells exposed to different MF treatment, with the exception of chrysotile. Previous studies have reported on the short-term high cytotoxicity of chrysotile (Levresse *et al.*, 1997; Van Oss *et al.*, 1999). One possible mechanism is the early amorphisation of chrysotile fibres once in contact with Met-5a cell membranes, forming a silica-rich skeleton documented to induce production of HO· and ROS in synergy with surface iron species (Pollastri *et al.*, 2016). Interestingly, the fibres reported as most cytotoxic (*i.e.,* amosite and crocidolite) did not induce any significant decrease in viability over time, suggesting a long-term cytotoxic effect, with increased biopersistence. Similar to chrysotile, actinolite induced significant cell death after short-term exposure, suggesting a common mechanism specific to softer fibre types, more prone to dissolution (Figure 3.7).

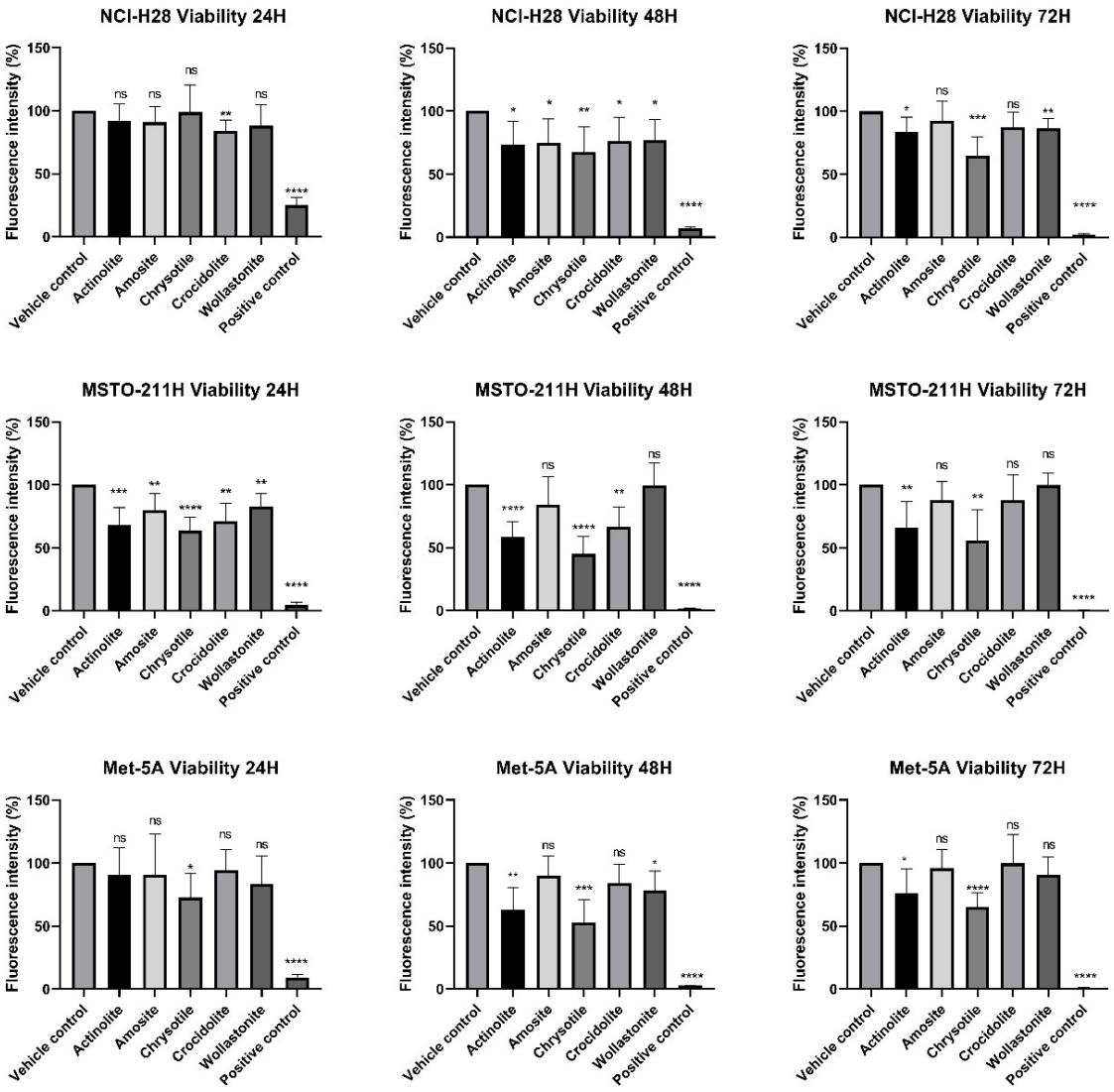

Figure 3.7 NCI-H28, MSTO-211H, and NCI-H1975 cells metabolic activity following exposure to MF represented by fluorescent intensity counts. Data recorded after 24, 48, and 72 hours of MF exposure. Data were normalised against vehicle control, and it was considered significantly different compared with the vehicle control by one-way ANOVA analysis (n=9), followed by a Geisser-Greenhouse correction to adjust for the lack of sphericity of data, followed by a Dunnett test for multiple comparisons to a control. Error bars n=9 from 3 independent experiments. *p between 0.01 and 0.04; **p< 0.01; ****p<0.0001; ns- not significant.

Fibre-cell interaction over different periods of time was also monitored using brightfield microscopy. The cultures were imaged after short-term exposure (24 hours) and long-term exposure (7 days). The figures below reveal the physical properties of the fibres, such as size and shape, in regard to the cells, the impact

the fibres have on the viability of these cells, as well as the tendency of the asbestos bodies to chemically attract cell fragments and form cell-fibres clumps. Asbestos fibres have been documented to attract proteins rich in β-sheet structures that coat the fibres and might play a role in MPM pathogenesis (Pascolo *et al.*, 2015). The cell clumps formed particularly after treatment with high dose of chrysotile and amosite, after long-term exposure. The cell line more susceptible to clumping appeared to be MSTO-211H, which previously showed the highest level of early cell death.

Top panel presents the cellular morphology after treatment with staurosporine, PBS, or untreated, respectively (Figure 3.8, Figure 3.9). The MF treatment was expressed as weight of dry fibres per ml of PBS solution. The treatment protocol was adapted according to resources and limited access to specialised laminar flow hoods, and to ensure the experiments follow the right H&S guidelines. A closer view of selected 1 mm^2 areas offer a visual interpretation of fibre concentration (*i.e.,* fibre number per mm^2). The number of fibres per mm^2 is proportional to fibre concentration.

Figure 3.8 and Figure 3.9 present NCI-H28 monolayers after exposure to various MF at three different doses after short-term (*i.e.,* 24 hours) and long-term exposure (*i.e.,* 7 days), respectively. After 24 hours, only the high doses of amosite and chrysotile disrupted the NCI-H28 monolayers. After 7 days in co-culture, the cell confluency appeared to be high, reaching 90-100%, similar to vehicle control treated cells. In contrast, the confluency appeared to be low for the cells treated with chrysotile which showed significant degradation, especially around the long, curly chrysotile fibres. Some cellular clumping can also be noted for the monolayers exposed to high concentrations of amosite fibres. The reduced susceptibility of NCI-H28 to cellular damage by MF might be explained by acquired apoptosis resistance due to previous treatment strategies, but also due to the different reactive molecules present in the membrane structure of NCI-H28 cells that alter chemical interactions between cells and fibres (Fazzini *et al.*, 2014). Wollastonite fibres appeared to have limited influence over the degree of cellular confluency after at both time points.

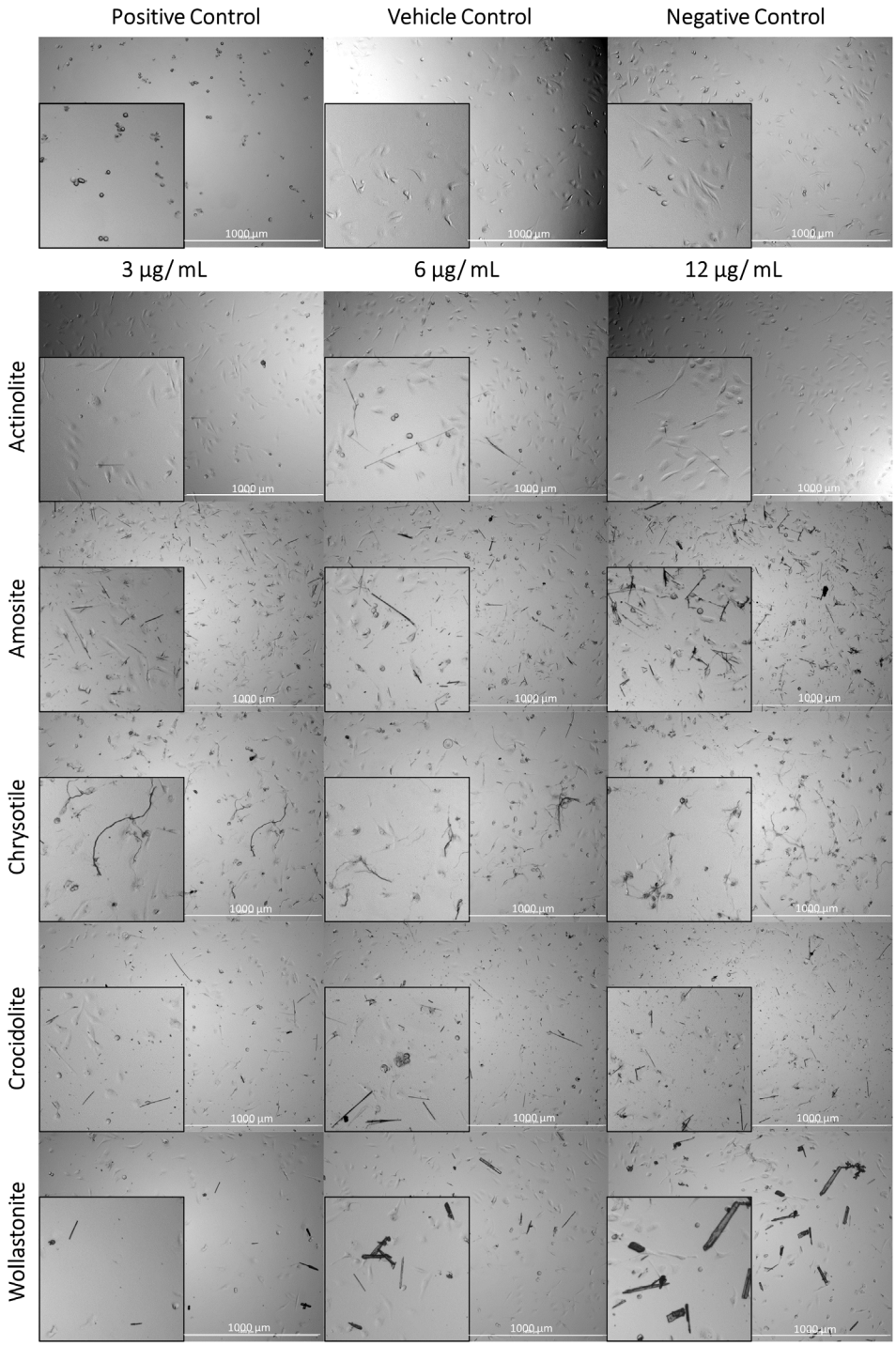

Figure 3.8 NCI-H28 cells treated with different MF (3-12 µg /mL) for 24h. Limited cell death was induced by the fibres, with the exception of high doses of amosite and chrysotile. Representative images of at least 3 fields of view. Positive control- staurosporine (10 µM); Negative control- RPMI media; Vehicle control- PBS; Scale bar- 1000 µm.

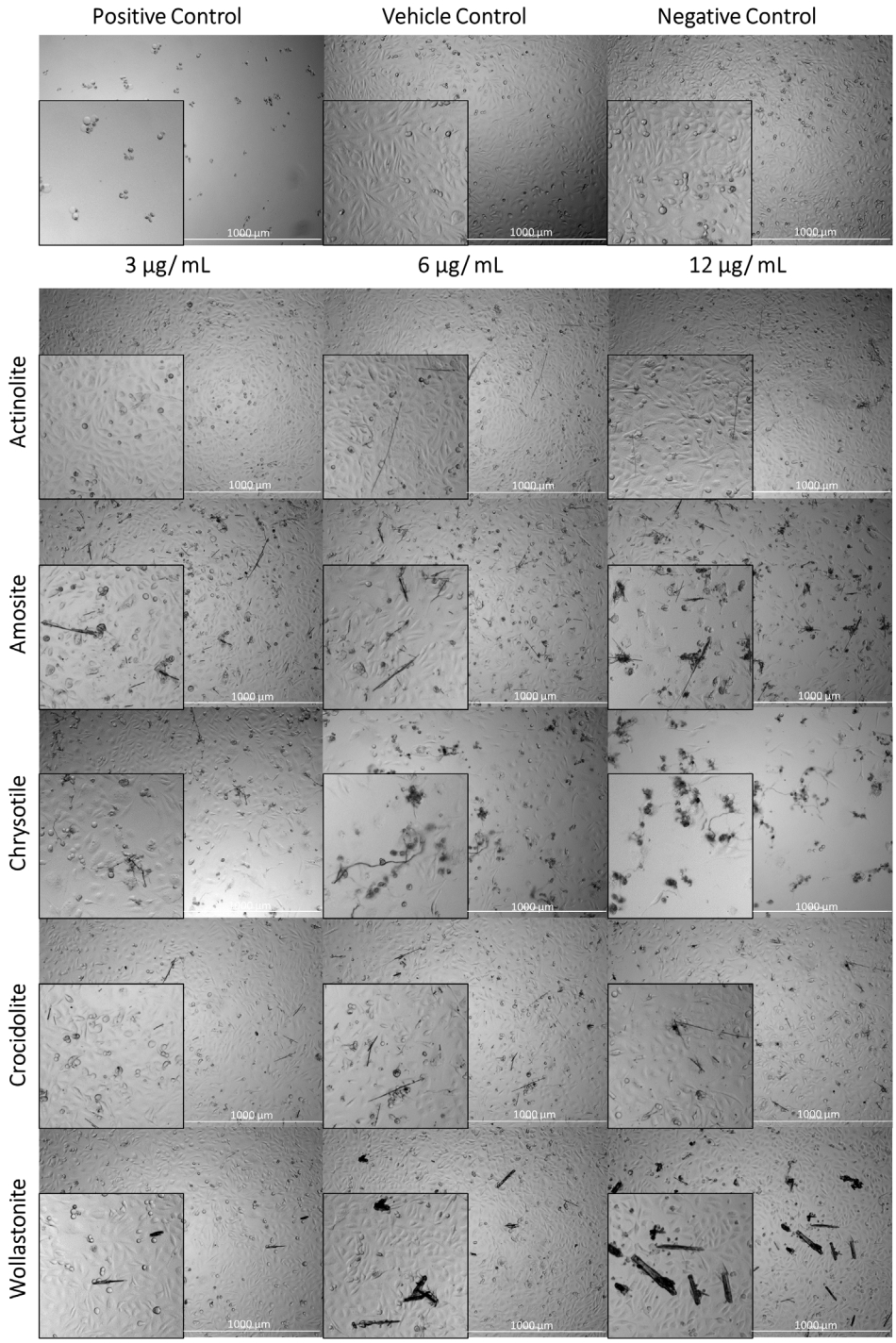

Figure 3.9 NCI-H28 cells treated with different MF (3-12 µg /mL) for 7 days. Confluent monolayers can be noted for most of the treatments, with the exception of the cells treated with chrysotile (high dose). Some cellular clumping can also be noted for the monolayers exposed to amosite fibres (high dose). Representative images of at least 3 fields of view. Positive control- staurosporine (10 µM); Negative control- RPMI media; Vehicle control- PBS; Scale bar- 1000 µm.

Similar to the viability data presented above, MSTO-211H cells showed significant levels of cellular damage, even after short-term exposure (Figure 3.10). On the other hand, after long-term exposure, cells started to develop resistance to MF damage. Moreover, the MF appeared coated with cell debris. This mechanism limited translocation of fibres, as well as physical and chemical interaction with the rest of cells, allowing viable cells to divide. Cellular confluency increased for most treatments, with the exception of chrysotile. High confluency was noted for the non-asbestiform control, wollastonite. Interestingly, chrysotile fibres appeared to be the most cytotoxic, in line with the viability data presented above, however this high cytotoxicity might be limited to relatively short-term exposure (compared to *in vivo* scenario). Additionally, actinolite fibres appeared to have a similar effect on the cellular monolayer, particularly after 7 days (Figure 3.11).

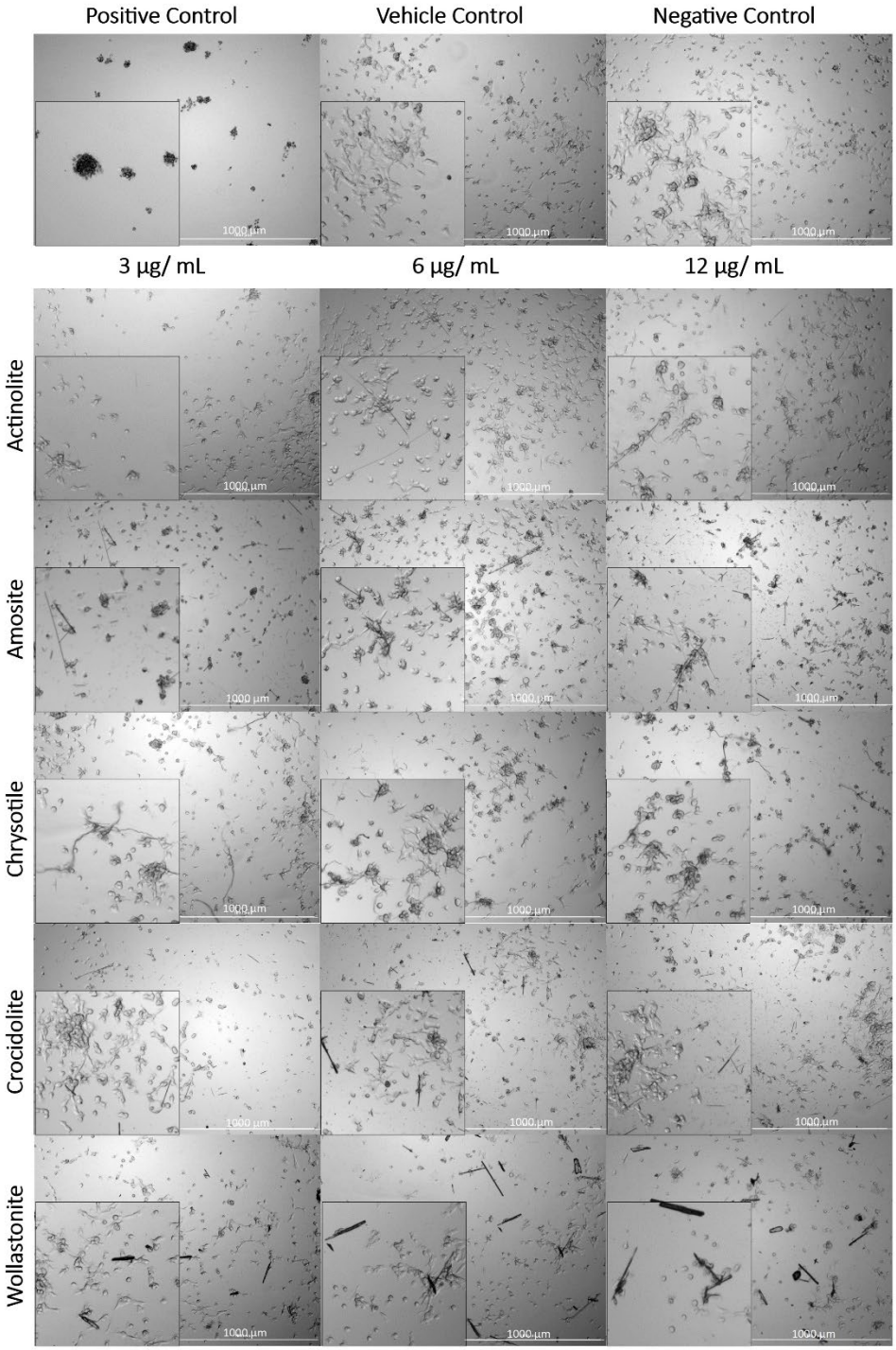

Figure 3.10 MSTO-211H cells treated with different MF (3-12 µg /mL) for 24h. Amosite and chrysotile fibres induced the highest levels of cell death, especially for higher doses. Representative images of at least 3 fields of view. Positive control- staurosporine (10 µM); Negative control- RPMI media; Vehicle control- PBS; Scale bar- 1000 µm.

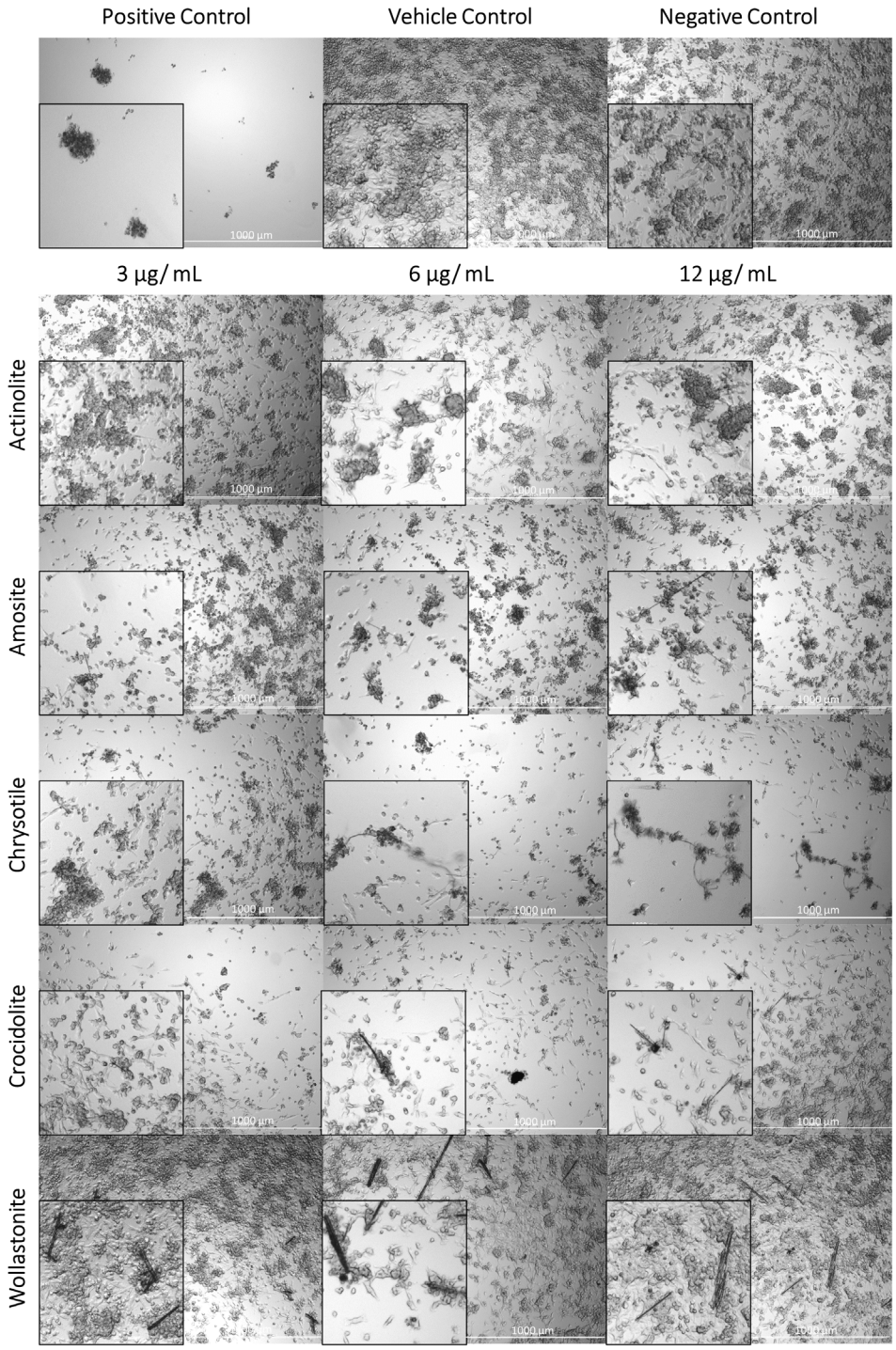

Figure 3.11 MSTO-211H cells treated with different MF (3-12 µg /mL) for 7 days. High confluency with limited cell death was noted for the non-asbestiform control, wollastonite. High levels of cell death can be noted after treatment with actinolite, amosite, and chrysotile (medium/ high doses). Representative images of at least 3 fields of view. Positive control- staurosporine (10 µM); Negative control- RPMI media; Vehicle control- PBS; Scale bar- 1000 µm.

Met-5A cells were transformed using a pRSV-T plasmid, derived from SV-40 virus. SV-40 is known to suppress the cell death machinery of transformed cells, which can have a knock-down effect on cytotoxicity experiments (Sheard & Vojtesek, 2002). Met-5A cells were noted to have a longer doubling time, when cultured in 2D. This resulted in a low confluency after 24h, even for the vehicle and negative controls (Figure 3.12). However, after 7 days the impact of MF at different concentrations is notable, particularly for amosite and chrysotile treated cells. Interestingly, exposure to low doses of crocidolite had little effect on overall cellular confluency. Similar results were observed for wollastonite treated cells (Figure 3.13).

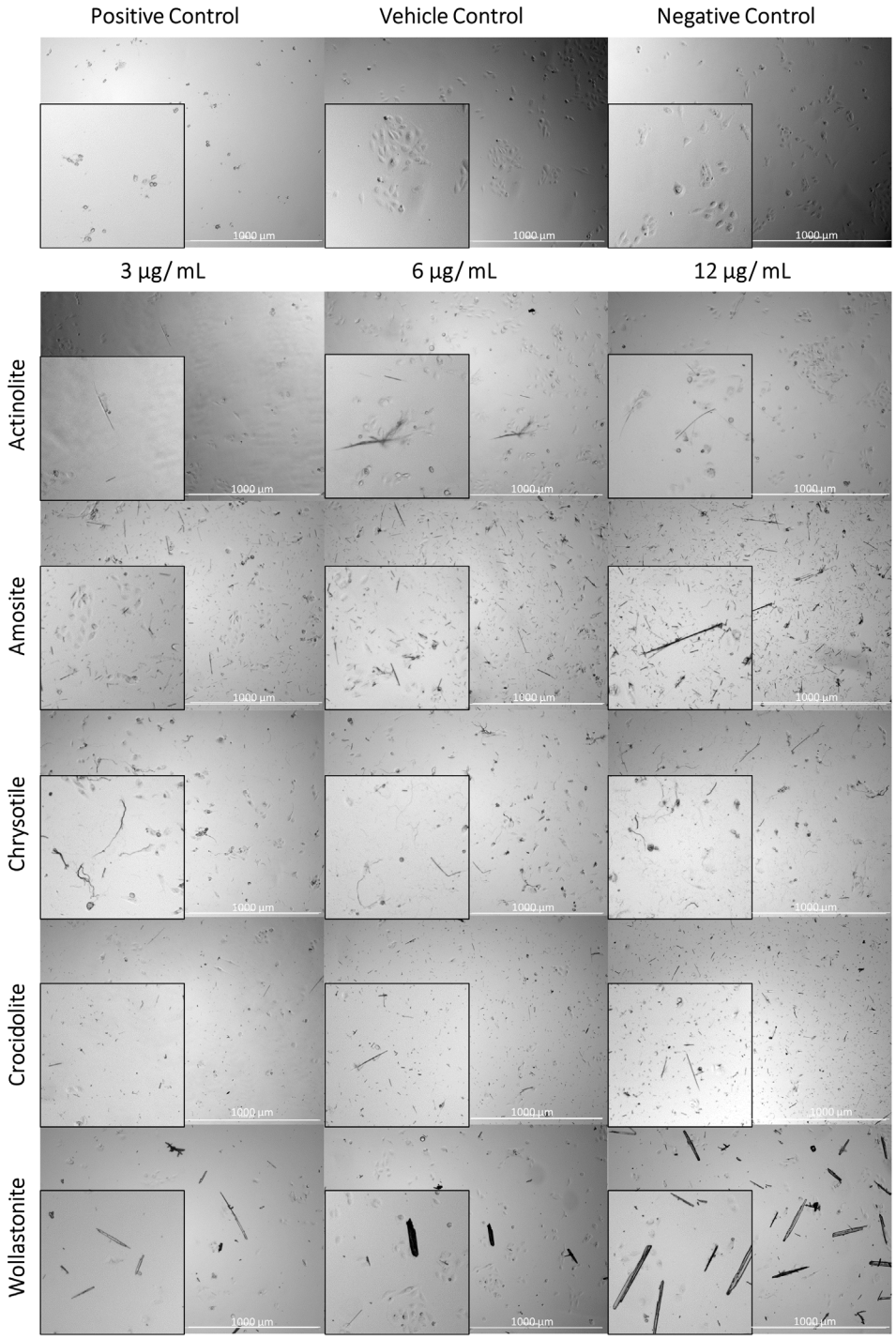

Figure 3.12 Met-5A cells treated with different MF (3-12 µg /mL) for 24h. Fibres appeared to have a limited effect on the cells. Representative images of at least 3 fields of view. Positive control- staurosporine (10 µM); Negative control- RPMI media; Vehicle control- PBS; Scale bar- 1000 µm.

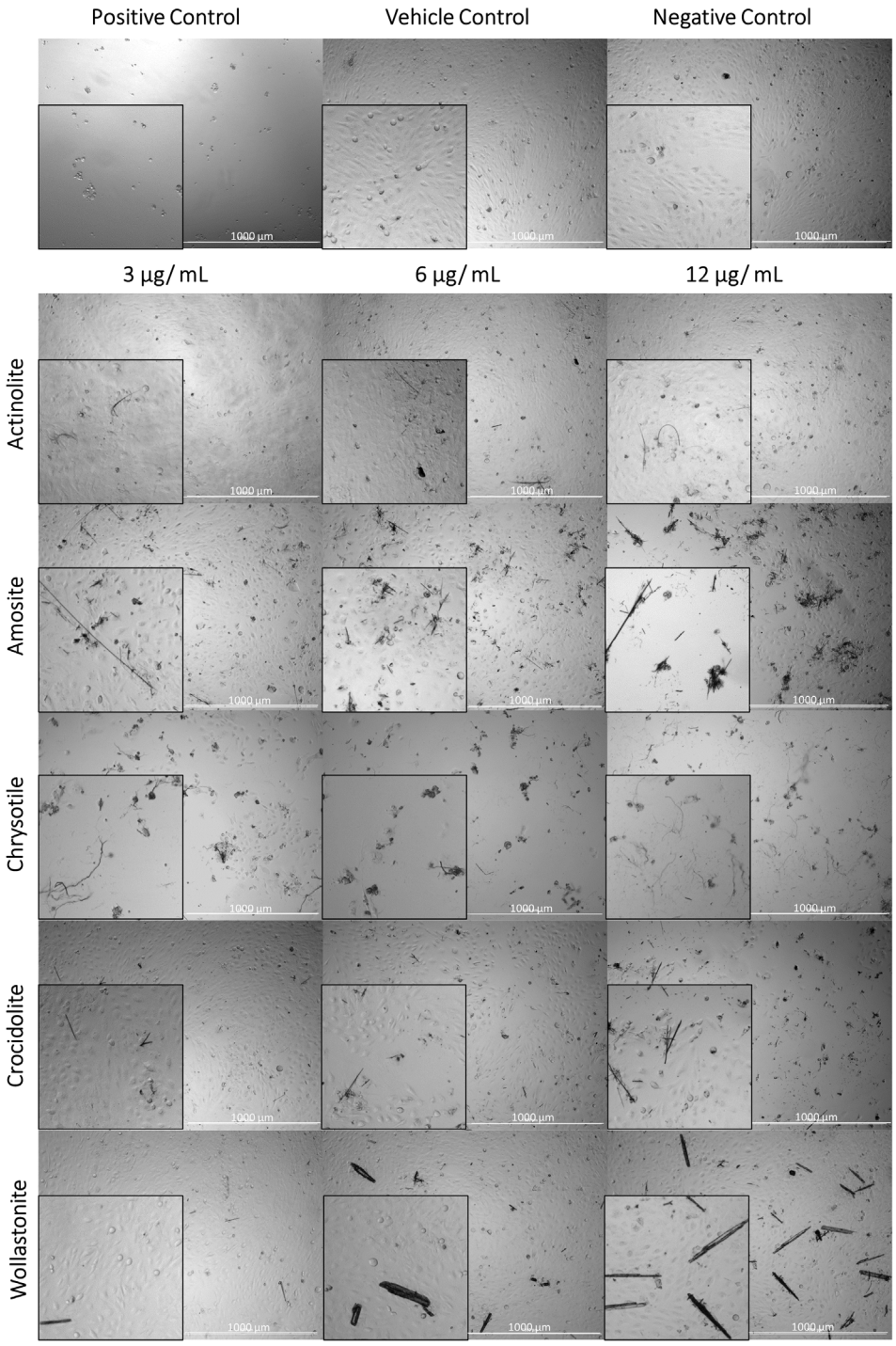

Figure 3.13 Met-5A cells treated with different MF (3-12 µg /mL) for 7 days. Amosite and chrysotile fibres induced high levels of cell death, proportional with fibre concentration. Representative images of at least 3 fields of view. Positive control- staurosporine (10 µM); Negative control- RPMI media; Vehicle control- PBS; Scale bar- 1000 µm.

3.2.2.3 The real-time apoptotic and necrotic effect of mineral fibres

Once it has been established that cellular viability was significantly impacted by fibre type, exposure time, and concentration of MF, the cell death mechanisms were investigated, with a focus on apoptosis and necrosis. Human MPM cell lines and human mesothelial Met-5A were exposed to actinolite, crocidolite, and the non-asbestiform, wollastonite, at a low vs high dose, for a period of 72 hours. The levels of early apoptosis were recorded in real time, every 2 hours, based on the luminescence signal. In a similar fashion, necrosis levels were monitored based on the fluorescence intensity signal. Statistical analysis investigated the correlation between exposure time and treatment, for each individual cell line.

Figure 3.14 presents the apoptosis and necrosis data for MSTO-211H cell line following exposure to three different types of MF. The data were compared to the data recorded for the PBS vehicle control treated cells. Interestingly, earlier viability studies that measured the metabolic activity of this cell line over a similar period of time and exposure to MF, showed a significant difference in cellular viability between MF treated cells and vehicle control, particularly after short-term exposure (24h). The decrease in metabolically active cells was attributed to early cell death mechanisms, such as apoptosis. However, real-time data showed no significant increase in apoptosis and necrosis levels following exposure to crocidolite, actinolite, and wollastonite, when compared to vehicle control treated cells. There are around 34 cell death modes that can be roughly classified in two groups: physiological (senescent death and apoptosis) and pathological (necrosis and stress-induced cell death) (Liu *et al.*, 2018). This broad classification of different cell death types serves as an explanation for the low levels of early apoptosis, suggesting MF might also induce several different types of cell death and reduce the number of metabolically-active cells via different mechanisms.

On the other hand, MSTO-211H necrosis levels over time showed an ascending trend, with actinolite and crocidolite at high doses inducing the highest levels of necrotic events, which continue past the 72-hour experiment endpoint.

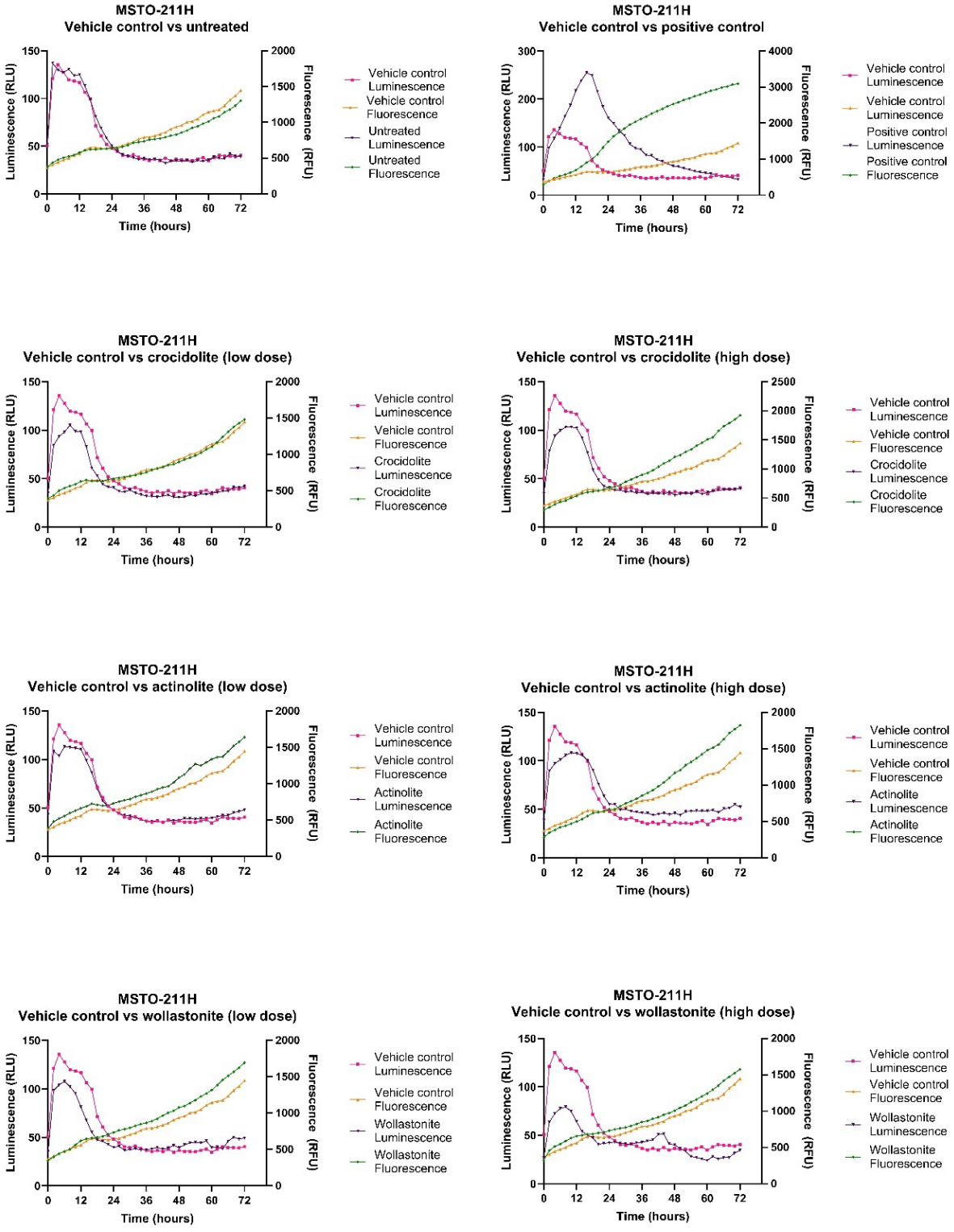

Figure 3.14 MSTO-211H real-time apoptosis (luminescence) and necrosis (fluroscence) levels over 72h. The data were recorded every 2 hours. Statistical analysis two-way ANOVA, followed by a Dunett comparison test for multiple variables. Significance $p<0.05$ between vehicle control and MF treated experimental groups.

The epithelioid cell line NCI-H28 behaved in a different manner, especially when exposed to crocidolite fibres. Specifically, high doses of crocidolite fibres induced early apoptosis after only 4h of culture. Interestingly, high dose of wollastonite also induced extremely significant levels of apoptosis after 8h, suggesting that this mechanism is linked to physical trauma, rather than a chemical reaction between fibres and cell membrane. The peak apoptosis levels for high crocidolite treated cells was reached after 14h, and stopped being significant after 38 hours, whilst the recorded apoptosis data for high wollastonite treated cells were significant for less than 24h (around 16h). Early apoptosis was followed by necrosis.

Necrosis levels were statistically significant after 20h for the cells exposed to high concentration of crocidolite and after 24h for high wollastonite treated cells. Interestingly, after 34h, all but the low actinolite treated cells, expressed significant levels of necrosis. All treatment regimens induced statistically extremely significant necrosis after 64h, which was maintained until the last reading point (72h) (Figure 3.15). This *in vitro* data highlights the key role necrosis plays in MPM onset and on some level appears to reflect the long latency typical to this pathology. Moreover, despite not being the major pathway in asbestos-induced cell death, results suggest that early apoptosis might play a more important role than previously considered (Yang *et al.,* 2010) and might have a synergistic effect with delayed necrosis levels that are generated over longer periods of time.

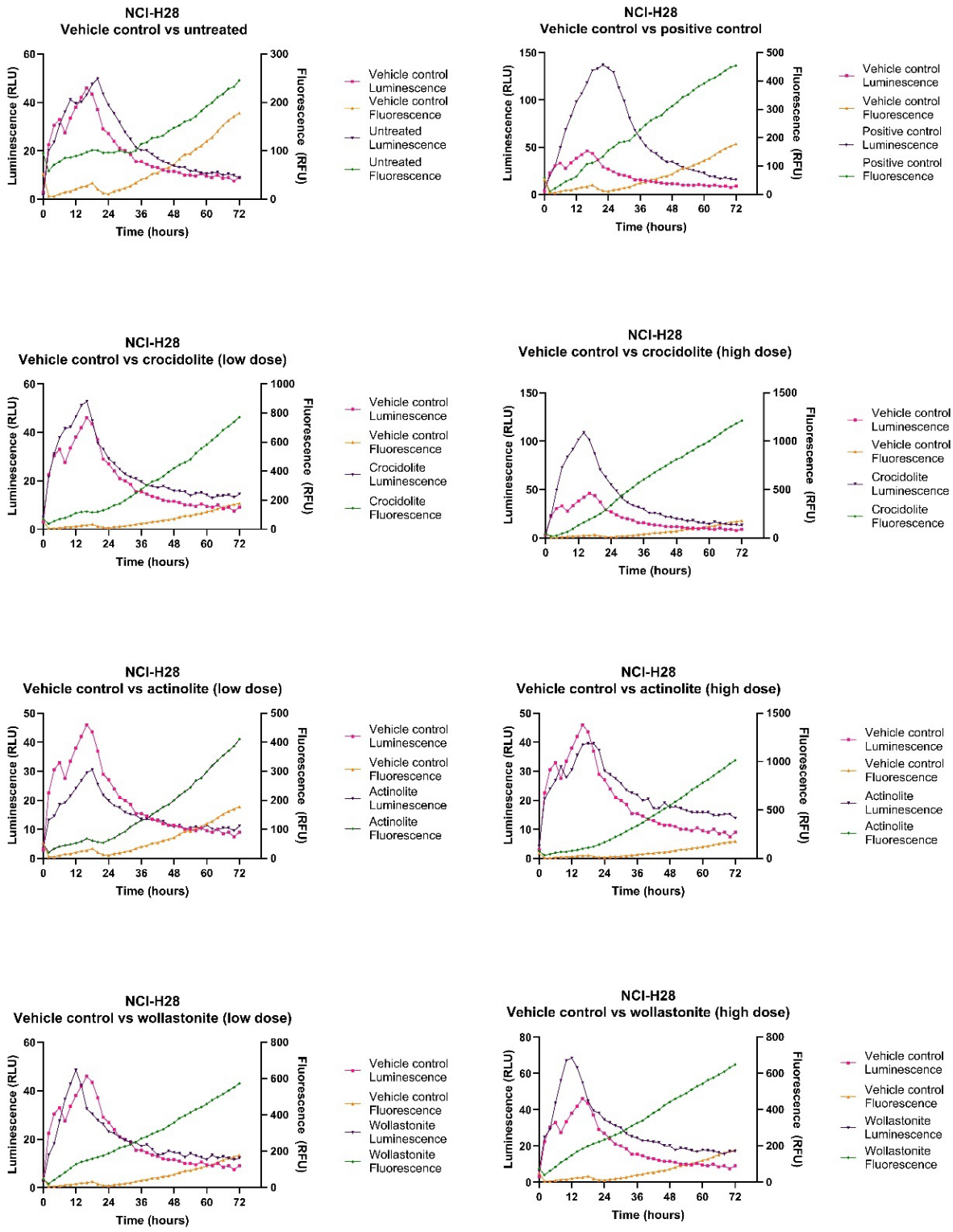

Figure 3.15 NCI-H28 real-time apoptosis (luminescence) and necrosis (fluroscence) levels over 72h. The data were recorded every 2 hours. Statistical analysis two-way ANOVA, followed by a Dunett comparison test for multiple variables. Significance $p<0.05$ between vehicle control and MF treated experimental groups.

Met-5A cells presented a different cell death kinetic signature when exposed to different MF, at various concentrations. In this case, PS translocation caused by apoptotic events was provoked after about 12h of exposure to high concentration of crocidolite, reaching significance for all high doses after 24h. Moreover, significant levels of apoptosis were noted for all treatment strategies after 48h. Dead cell fluorescence due to secondary necrosis began after 30h for the high crocidolite treatment. The necrosis detection reagent indicated negligible cell death up until 48h for the rest of high doses. The secondary levels of necrosis showed a growing trend past the endpoint of the assay, which is in line with proposed MPM pathogenesis (Yang *et al.,* 2010).

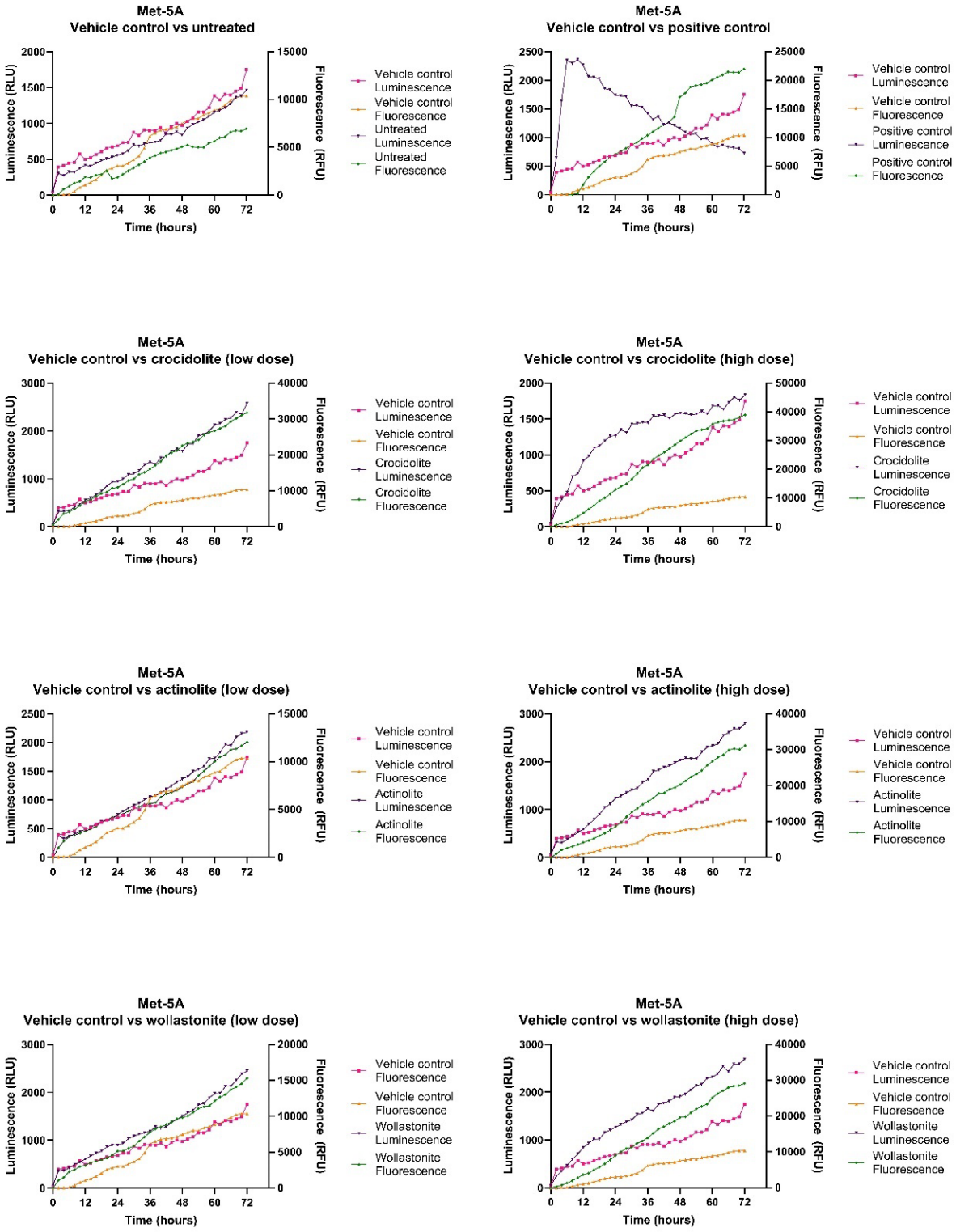

Figure 3.16 Met-5A real-time apoptosis (luminescence) and necrosis (fluroscence) levels over 72h. The data were recorded every 2 hours. Statistical analysis two-way ANOVA, followed by a Dunett comparison test for multiple variables. Significance $p<0.05$

3.3 Conclusion

Optimisation steps represent the baseline for all the future experiments covered in this project. It was essential to optimise each variable, from cell number, MF type and concentration, to MF exposure time and time points. Investigating the effect asbestos and other MF have on different cellular models not only optimised sample preparation protocols for future LA-ICP-MS analysis, but it also added to the knowledge surrounding MPM onset and pathogenesis.

Initially, MF preparation, storage, and treatment optimisation were established. The health risks of these fibres were considered at all times, and all the protocols were adapted to follow strict guidelines. The fibre concentration was firstly optimised for LA-ICP-MS analysis to ensure the work recapitulates *in vivo* events, with enough fibres to be detected within the cell models, but little enough to maintain the cell viability relatively high and not produce an overabundance in elemental signal. First optimisation steps focused on the interaction of actinolite fibres with different cell lines, followed by a similar investigation into the impact various asbestos types and a non-asbestiform control have over different periods of time on MPM and normal mesothelial cells. Finally, the work was taken further, looking into the difference in apoptosis and necrosis levels induced by different MF over a period of time. The data were collected in real time by employing a novel kinetics assay, with measurements taken every 2h over a 72-hour period. These results offer some insight into different mechanisms of action of these MF and highlighted once again the heterogeneity of this pathology.

The optimisation steps helped note some key findings. Firstly, chrysotile induced significant levels of early cell death in all cell lines, suggesting that chrysotile is more cytotoxic than previously reported. This finding further adds to the growing evidence that an updated MF classification is required (Yu *et al.*, 2019). Conflicting evidence with respect to the cytotoxic effects of chrysotile further explain why it is the only asbestos type still sold in certain parts of the world (95% of asbestos traded over the last century) (Baur & Frank, 2021).

Secondly, real-time kinetic data showed that early apoptosis might play a synergistic role in MPM development, with the major cell death pathway being necrosis. Moreover, the results highlight the heterogeneity of these MF and the different mechanisms of action. However, a plethora of studies suggest that studying apoptosis *in vitro* has several limitations and can only provide an idea of the *in vivo* scenario (Liu *et al.*, 2013; Liu *et al.*, 2018).

Despite the limitations of this study around the cell death pathways involved in MPM, mainly due to the use of secondary cell cultures, the scope of this work was to optimise the cell-MF interaction for future LA-ICP-MS experiments. Therefore, the cell model, the fibre type, concentration, and exposure time, were all selected considering the final aim of the project- detection of MF based on the elemental content.

Chapter 4 LA-ICP-MS Imaging of Human Mesothelioma Cell Lines

The work presented in this chapter was carried out in collaboration with Loughborough University

4.1 Introduction

4.1.1 Introduction to the chapter

The causal relationship between MPM and asbestos fibres has been established for over seven decades (Carbone & Yang, 2017). Therefore, the identification of MF within human lung tissue samples is not only essential in aiding early diagnosis of MPM, but it also plays a key role in linking this malignancy to asbestos exposure, which has high implications in legal, social, and political matters (Capella *et al.*, 2016). As part of the current diagnosis workflow, it is essential to detect MF in the lung tissues to complete pathological diagnosis of MPM and other ARD in correlation to asbestos exposure.

Routine quantification method uses phase contrast microscopy (PCM) to count only the fibres that adhere to the definition mentioned in the Chapter 1, Section 1.3.3.1., failing to detect certain types of MF such as cleavage fragments, short or thin fibres or naturally occurring MF (*e.g.*, erionite), despite all of these being previously reported to cause ARD (Jasani & Gibbs, 2012; Korchevskiy, Rasmuson, & Rasmuson, 2019; Schiller *et al.*, 1980).

More established methods of asbestos identification and quantification, such as Scanning Electron Microscopy (SEM) and Transmission Electron Microscopy (TEM) generally employ chemical digestion of the tissues in order to eliminate the organic matrix, thus losing all the spatial information offered by imaging techniques (Dement *et al.*, 2015). A possible alternative to PCM with similar sensitivity as SEM and TEM was presented by Ishida *et al.,* (2010) who employed fluorescence microscopy (FM) to spatially resolve airborne asbestos tagged with an amphibole sensitive protein, GatZ. The method presented identifies the common types of amphibole fibres based on their surface characteristics (*i.e.,* surface charge, shape, hydrophobicity, and surface chemistry) (Ishida *et al.*, 2010).

However, methods of differentiating MF based on surface charge are not reliable since non-asbestiform amphiboles are virtually identical to asbestiform amphibole

fibres in morphology, crystal structure, refractive index, and chemical composition (Schiller *et al.*, 1980). Moreover, amphiboles have nearly identical crystal structure and differ only in the proportion (or presence/absence) of Mg, Fe, Na, and Ca ions exposed at the cleavage plane (Ishida *et al.*, 2010). Differentiation between the types of amphibole asbestos is therefore beyond the reach of the FM capabilities.

Given the similarities in chemical structures between the MF (*i.e.,* silicates) but also the proportional discrepancies of main elements such as Fe, Ca, and Mg between each fibre type, elemental analysis has gained popularity in recent years compared to optical methods (Benton, 2013; Kido *et al.*, 2017). One of the first reports used an in-air micro particle induced X-ray emission (μ-PIXE) system to identify the location of asbestos bodies in lung tissue sections (Shimizu *et al.*, 2008). However, this has only been achieved with limited spatial resolution. Sub-micrometre lateral resolution has been reported in a study by Pascolo *et al*. who employed soft X-ray imaging and X-Ray Fluorescence (XRF) microscopy to investigate elemental lateral distribution of asbestos bodies in lung tissue (Pascolo *et al.*, 2011). Given the complexity of the techniques used in the study, the limitations revolve around the applicability in a clinical setting, as it is presented more as a research tool on chemical interactions between fibres and cells. The introduction of novel techniques in a clinical setting requires high accuracy, high sensitivity, and high throughput. Additionally, the strict requirements for extensive validation and reproducibility pose a significant challenge to introduction of new techniques into clinical settings. Indeed, LA-ICP-MS bioimaging has been mainly used as a research tool as previously described in Chapter 1, Section 1.4.1. However, recent technological advancements have made LA-ICP-MS bioimaging gain more and more interest as a clinical tool (Becker *et al.*, 2010; Pornwilard *et al.*, 2013; Shariatgorji *et al.*, 2016).

In order to achieve the high accuracy, sensitivity, and throughput desired in clinical settings, a dual-volume ablation cell with an integrated ICP torch was employed as a novel detection tool. Experiments were performed in rastering ablation mode. LA-ICP-MSI methods were optimised to spatially resolve the most

common MF (amosite, actinolite, chrysotile, and crocidolite), as well as a non-asbestiform control, wollastonite, in models of mesothelioma based on the high magnesium, iron, and silicon content. The recorded ICP-MS signal was correlated with total particle counts generated during laser ablation as well as particle size distribution.

Although low dispersion, single conduit, laser ablation set-ups allow for high-resolution imaging at cellular or subcellular level (Van Acker *et al.*, 2019; Voloaca *et al.*, 2020) with a relatively high speed, the settling time of the sector-field mass analysers employed in this study limited the ability to monitor multiple nuclides during signal pulses delivered by these type of set-ups (Theiner *et al.*, 2020). The drive towards use of higher speed LA systems has contributed to a rise in the popularity of time-of-fight (TOF) ICP-MS systems for imaging applications (Burger *et al.*, 2015; Theiner *et al.*, 2020). TOF mass analysers enable pseudo-simultaneous detection of the full mass range, which is advantageous for analysis of the fast-transient signals from modern LA units. These recent technological developments have therefore expanded the capability of LA-ICP-MS to the point where it now warrants investigation as a tool to rapidly detect and identify fibres in tissue.

Data between mass range 23 (Na) and mass 238 (U) was collected, but many elements in this large mass range are not known to be present in either the MF or the MSTO-211H cells and gave rise to only background signal. Subsequent data analysis therefore focussed on 10 elements that are either part of the biological samples, matrix constituents of the MF or have been known to substitute into one of the fibre types studied (^{23}Na, ^{24}Mg, ^{27}Al, ^{28}Si, ^{31}P, ^{39}K, ^{40}Ca, ^{48}Ti, ^{55}Mn, and ^{56}Fe). The main functions of these elements are explained below.

Sodium is indispensable for normal body functions, acting as a key electrolyte in regulating blood pressure, muscle processes, and immune functions (Grillo *et al.*, 2019; Wilck *et al.*, 2019). It has been reported that intranuclear sodium levels increase more than three-fold in cancerous cells (Nagy *et al.*, 1981). Sodium is also one of the main components of the most potent amphibole, crocidolite (Chapter 1, Section 1.3.2 Table 1.2).

Magnesium is the second most abundant intracellular cation and plays a key role as a cofactor in over 300 enzymatic reactions, many of which are adenosine triphosphate (ATP)-generating reactions (Jahnen-Dechent & Ketteler, 2012). Although the link between Mg and cancer cells is an ongoing research question, proliferating cells have been reported to contain more Mg than quiescent cells (Wolf, Cittadini, & Maier, 2009). Magnesium is also a main nominal element of actinolite, amosite, chrysotile, widely known to substitute into crocidolite (Kusiorowski *et al.*, 2015). Aluminium, titanium, and manganese were also selected because they have been known to substitute into some amphiboles (Mutch *et al.*, 2016; Surour, 2015). Aluminium has been reported to partially substitute for silicon in the tetrahedral (T) site of amphiboles (Papike & Cameron, 1976).

The silicate tetrahedron (SiO_4) is the basic chemical unit of all MF, asbestiform and non-asbestiform. Mapping silicon signal plays an essential part in identification of MF within MPM samples.

Phosphorus is a key element with a role in many biological processes, for instance for DNA synthesis, ATP synthesis, and protein phosphorylation. In tumour cells, the concentration of phosphorus typically increases primarily because malignant cells upregulate ribosome biogenesis (Nagy, 2007), which has been reported to be an essential part of cell cycle progression and malignant cell proliferation. Potassium is a key cation in the intracellular fluid and plays a vital role in the maintenance of normal cell functions (Elmarimi *et al.*, 2004). Moreover, higher levels of potassium have been reported in the serum of mesothelioma patients, most likely linked to typical thrombocytosis (Li *et al.*, 2017).

During analysis, a collision–reaction cell was used to reduce nitrogen and argon related interferences, enabling ^{40}Ca to be measured without interference from ^{40}Ar, and ^{56}Fe to be measured without polyatomic interference from $^{40}Ar^{16}O$. This proved to be advantageous because comparison of iron and calcium signals can be crucial in enabling differentiation between certain fibre types.

Iron is a key part of the tumour microenvironment, facilitating the production of oxygen radicals. This in turn has been linked to malignant transformation of cells by directly damaging DNA, leading to mutagenicity, or protein and lipid modifications within malignant cells, resulting in more aggressive tumour behaviour (Pfeifhofer-Obermair *et al.*, 2018). Asbestos biopersistence is attributed to its specific physio-chemical characteristics, including the iron content (up to 30% (w/w) of Fe) and the ability to absorb iron from the surrounding environment (Pascolo *et al.*, 2013) Hence, the inclusion of iron is essential not only for detection of Fe intrinsic to asbestos fibres, but also endogenous iron deposited on asbestos bodies after long-term exposure in MPM patients.

In the present work, a soft NWR Image 266 nm laser ablation system coupled to an Element XR sector-field ICP-MS (Instrument 1) was used for elemental detection of single mesothelioma cells treated with MF. A highspeed LA platform and a prototype ICP-TOFMS were also employed together for the first time to evaluate the potential for rapid multi-elemental detection of fibres. The work was carried out using a NWR193 laser ablation system coupled to a Vitesse time-of-fight ICPMS (Instrument 2) in the NU Instruments Laboratories (Wrexham, UK) under the aid and supervision of Phil Shaw and Ariane Donard (NU Instruments employees).

4.1.2 Hypothesis

The hypothesis of this chapter was that different types of MF (actinolite, amosite, crocidolite, chrysotile, and wollastonite) can be spatially identified in 2D samples based on their elemental profile using either a single-element approach (*i.e.,* magnesium detection), multi-element analysis (*i.e.,* magnesium, iron, and silicon) or pseudo-spontaneous detection of the elements between mass 23 (Na) and mass 238 (U) by employing a novel imaging technique, LA-ICP-MS.

4.1.3 Aims

The main aim of the chapter was the development and optimisation of a proof-of-concept method to detect some of the most common types of MF within cellular

cytospins based solely on the Mg content of these fibres. The subsequent aims were to expand the analysis to more elements including Si, Mg, and Fe, in order to detect MF more accurately within 2D cytospins on plastic slides and to demonstrate the use of novel prototype instrumentation for pseudo-spontaneous detection of the elements between mass 23 (Na) and mass 238 (U) in 2D models spiked with various MF.

4.2 Results and Discussion

4.2.1 Optimisation of mineral fibre dose for LA-ICP-MS (Instrument 1)

According to the “Guidelines on autopsy practice- Industrial/occupational-related lung disease deaths including asbestos” (Osborn *et al.*, 2017) adapted from the Helsinki Criteria (Henderson *et al.*, 1997), the causal attribution of asbestos includes >2 asbestos bodies per 1 cm^2 lung section area. Being the first work of this kind, fibre dosage was essential in order to replicate the biological environment as closely as possible. The aim was to include areas of clear visible fibres using standard optical microscopy, alongside the ones only visible by LA-ICP-MSI. The concentration of MF was therefore selected not only based on the viability data presented in the earlier chapter (Chapter 3, Section 3.2.2.1), but also on the LA-ICP-MS images shown below (Figure 4.1).

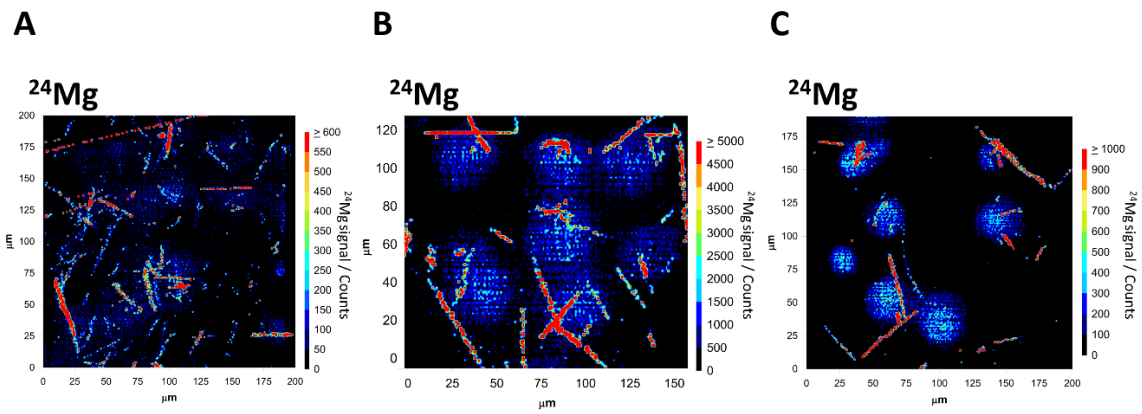

Figure 4.1 Actinolite dose titration in 2D cell cultures. (A) 12 µg/ mL, (B) 6 µg/ mL. (C) 3 µg/ mL. Data is presented as ^{24}Mg signal/ counts. Areas with actinolite fibres visible using basic optical microscopy were selected for proof-of-concept. The laser parameters were: spot diameter of 2 µm, 20 Hz repetition frequency, 40 µm s^{-1} scan speed.

4.2.2 Optimisation of laser parameters for LA-ICP-MS analysis

4.2.2.1 Laser pulse energy

LA-ICP-MS parameters were initially optimised for maximum ^{24}Mg ion sensitivity, whilst ensuring individual pulse responses could be resolved at the stated repetition frequency. A 20 Hz repetition frequency, 40 µm s^{-1} scan speed and ≈18 J cm^{-2} fluence were used during ablation. One of the most important characteristics of this patented instrumentation is the fast washout time. A 2-seconds laser warm up with a 2-seconds washout time were used during data acquisition meaning that a 200 x 200 µm area can be ablated in less than 30 minutes. Data were recorded as ^{24}Mg intensity per counts and was captured at 10 ms intervals by the P7882 photon counter external data acquisition board connected to the ion detection board of the ICP-MS. The signal was monitored and captured using MCDWIN software as described previously (Managh *et al.*, 2016).

The samples consisted of a mix of biological material (*i.e.,* cancerous cells) and MF with extreme physical properties. Laser fluence had to be optimised for this particular type of samples (Greenhalgh *et al.*, 2020). The fluence is defined as

the energy of a laser pulse divided by the area it is ablating. Fluence value varies based on the laser energy used for ablation. A laser pulse will ablate a sample if the laser has an energy density (fluence) that is above a certain threshold. Because this ablation threshold is sample-specific the laser fluence requires optimisation for each sample material. During the optimisation steps, the laser pulse energy varied between 45% e- 65% e. Total sample ablation was achieved at 50% e, which was employed throughout the rest of the experiments.

4.2.2.2 Spot size

Detection of actinolite fibres based on the high Mg content was selected for the LA-ICP-MS method development. The range for the laser parameters was chosen based on previous work carried out on biological samples with the same instrumentation (Douglas *et al.*, 2015). The laser parameters influence the speed, lateral resolution, limit of detection and time of acquisition of the data and are crucial in achieving the overall aim. Spot size can make the difference between failing to detect small fragments and increased fragmentation of fibres. Older LA-ICP-MS designs allowed for typical resolutions of 5-100 µm (Van Malderen, Van Acker, & Vanhaecke, 2020). Greater spot sizes (>10 µm) do not allow for cellular analysis since the typical human cell size varies between 10-100 µm (Oikonomou & Jensen, 2017). Moreover, in terms of this research, a smaller spot size is required to spatially resolve small asbestos fibres or fibre fragments (<5 µm) that standard microscopy methods cannot detect (Egilman *et al.*, 2019). Given the holistic design of the instrument, improved spatial resolution, with lateral resolutions of a few µm are easily attainable. Spot sizes as low as 1 µm were used in the optimisation of this method. However, reducing the spot size drastically increases the time of acquisition and therefore the clinical applicability of this imaging tool. Moreover, optimisation analysis showed that a spot size of 2 µm offers the right balance between great cellular resolution and time of acquisition (Figure 4.2 A). Additionally, the image acquired with 1 µm spot size is more fragmented, leading to discontinuation of the MF (Figure 4.2 B). Based on the results presented in Figure 4.2, a laser spot diameter of 2 µm was used for future experiments.

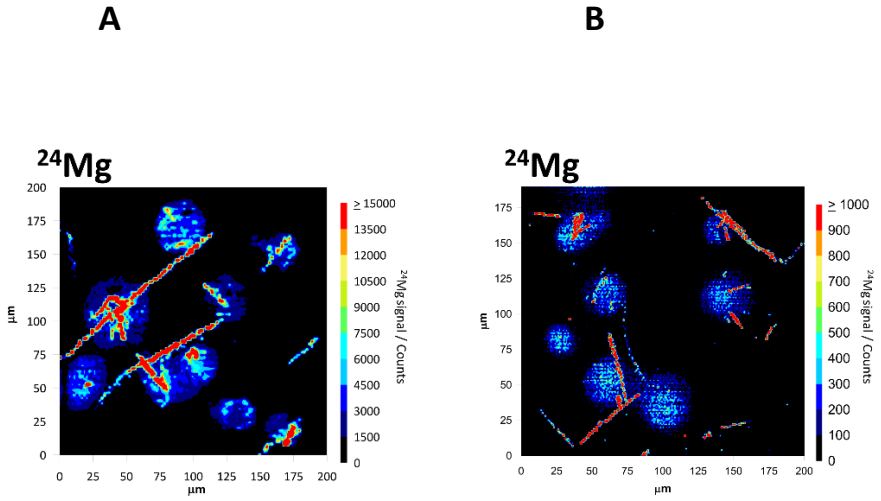

Figure 4.2 Spot size optimisation. (A) Detection of actinolite fibres within NCI-H28 cells based on the high Mg content using a spot size of 2 µm. The total time of acquisition was ~30 min for a 200 x 200 µm sample area. (B) Detection of actinolite fibres within NCI-H28 cells based on the high Mg content in the fibres using a spot size of 1 µm. The time of acquisition nearly doubled.

4.2.3 Single-element detection of asbestos fibres

Malignant mesothelioma cells that have not been exposed to any MF *in vitro* were imaged based on the magnesium content using LA-ICP-MS, forming an ideal biological matrix for the visualisation of MF using this technique (Figure 4.3). The data offered a baseline for Mg content within biological samples.

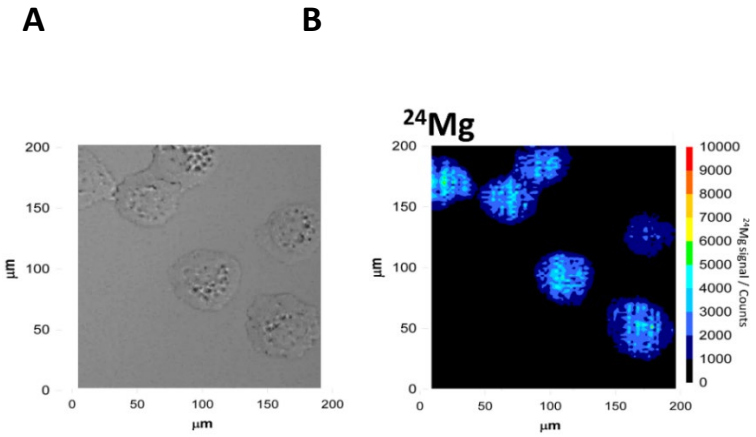

Figure 4.3 Detection of malignant mesothelioma based on magnesium content. **(**A) Light microscopy image of the NCI-H28 cells. (B) LA-ICP-MS image corresponding to the same area based on the Mg content in the cells.

Magnesium is part of the chemical composition of most asbestiform minerals. Although it is not part of the idealised chemical formulation of crocidolite, the composition varies in natural samples where magnesium is often found as a trace element (IARC Monographs, 2012). In order to support the hypothesis that asbestos fibres can be spatially resolved based on the various Mg content, initial LA-ICP-MS analysis has been carried out on 2D cell samples treated with various MF. The results for some of the most prevalent asbestos fibres including crocidolite, actinolite, chrysotile and amosite, as well as a negative control of untreated cells are presented in the following figures. The crocidolite fibres yielded high ^{24}Mg intensity counts, confirming that crocidolite fibres can indeed be detected based on their Mg content which is vital given the high biopersistence and carcinogenicity of fibre (Figure 4.4) (Hodgson & Darnton, 2000).

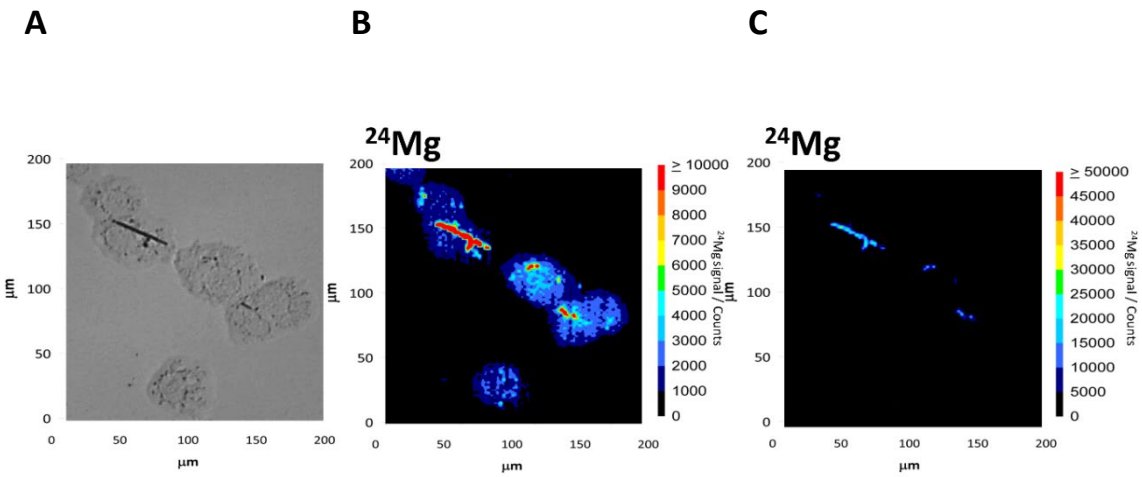

Figure 4.4 Detection of crocidolite based on magnesium content. (A) Light microscopy image showing a long crocidolite fibre within a mesothelioma cell. (B) LA-ICP-MS image of the same area based on the Mg content in the sample. Note the crocidolite fibres fragments engulfed by the cells that were not visible with light microscopy. (C) LA-ICP-MS image of the same area normalised against the cellular background by increasing the intensity bar.

As one of the main elements that make up chrysotile, magnesium can be easily detected in samples treated with this very common type of fibre. High ^{24}Mg signals can easily differentiate chrysotile fibres from a cellular background, where fibres maintain the curled, long physical properties characteristic of white

asbestos. This is a benefit of using a smaller spot size and a soft ablation laser set at a relatively low laser energy (50% e). Figure 4.5 shows the presence of chrysotile fibres within a 2D mesothelioma sample using optical microscopy and LA-ICP-MS analysis.

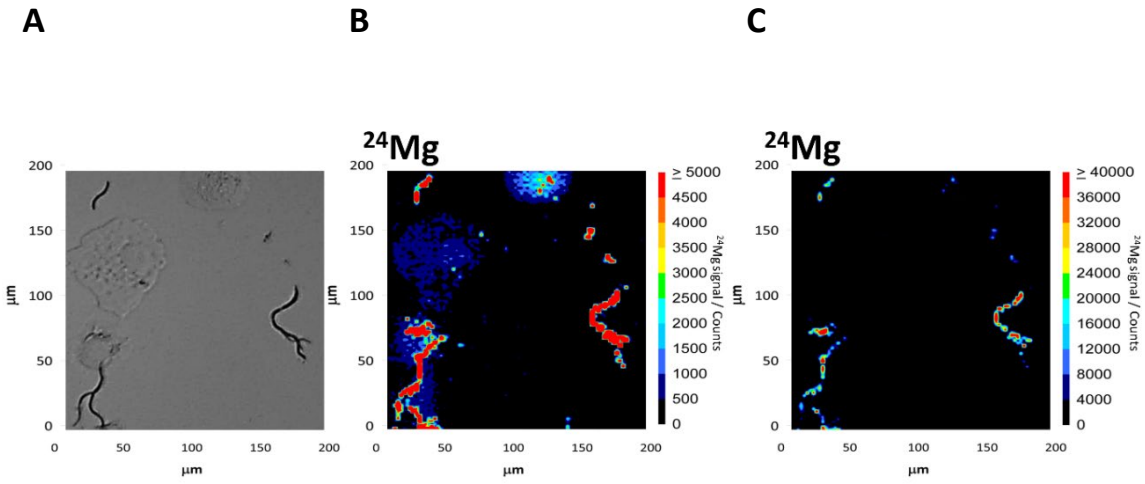

Figure 4.5 Detection of chrysotile based on magnesium content. (A) Light microscopy image showing the long, curly specific appearance of chrysotile fibres prior to ablation. (B) LA-ICP-MS image formed based on the high Mg content in the sample. Note how the chrysotile fibres maintain their shape and the extra fibre fragments within the mesothelioma cells that were not noticeable in the optical image. (C) LA-ICP-MS image of the same area normalised against the cellular background by increasing the intensity bar showing only the signal gave by the chrysotile fibres and fibre fragments.

Amosite asbestos is the second most carcinogenic asbestos type, and it is thus essential to be able to detect it in the samples. Amosite is still widespread in the UK despite being banned in the early 1980s. Amosite can be found as a variety of grunerite or cummingtonite, the later one containing magnesium in its chemical composition (Deer, Howie, & Zussman, 2013). In the current analysis, the amosite fibres yielded high magnesium signals, suggesting these were an asbestiform variety of cummingtonite asbestos, the most prevalent in the UK (Pollastri *et al.*, 2017). The coarse acicular amosite fibres can be seen in the light microscopy image, however smaller fibre fragments within the cells can only be identified using LA-ICP-MSI (Figure 4.6 A-C).

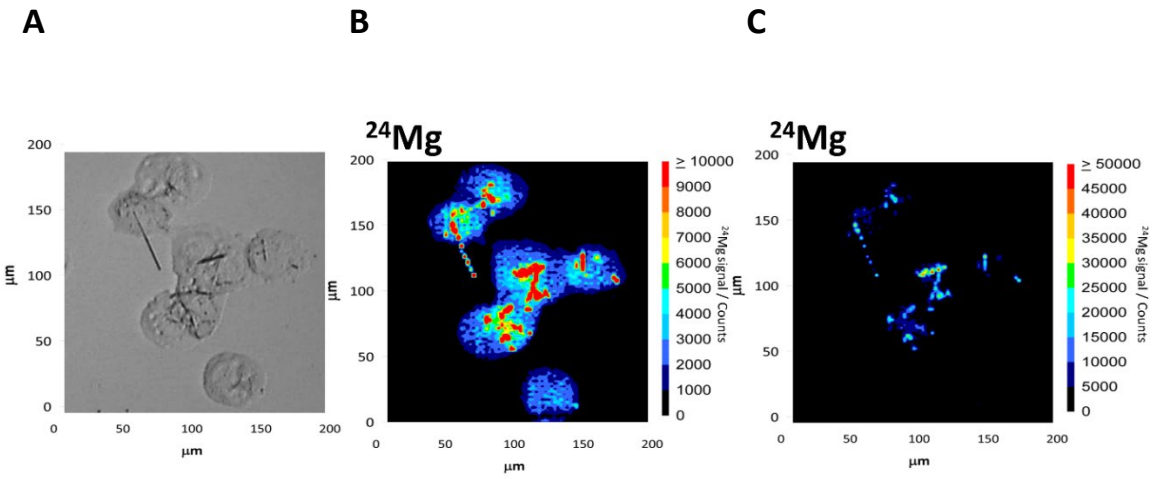

Figure 4.6 Detection of amosite based on magnesium content. **(**A) Light microscopy image showing the coarse, needle-like amosite fibres prior to ablation. (B) LA-ICP-MS image formed based on the high Mg content in the sample. Small amosite fragments can be easily identified using this technique. (C) LA-ICP-MS image of the same area normalised against the cellular background by increasing the intensity bar showing only the signal gave by the amosite fibres and fibre fragments.

There is a lot of debate around the carcinogenicity of actinolite fibres, despite the clear link between actinolite exposure and tumour development (Pott *et al.*, 1989). Actinolite is classed as carcinogenic by IARC as one of the five amphiboles, despite being found in both asbestiform and non-asbestiform forms. It is also one of the most common talc impurities (IARC Monographs, 2012). Acting as an intermediate mineral in the formation of magnesium-rich tremolite, actinolite contains a high percentage of Mg in its chemical formula. This allows for detection of actinolite using LA-ICP-MSI, including the smaller fragments within mesothelioma cells. Actinolite detection based on the Mg content is presented in Figure 4.7.

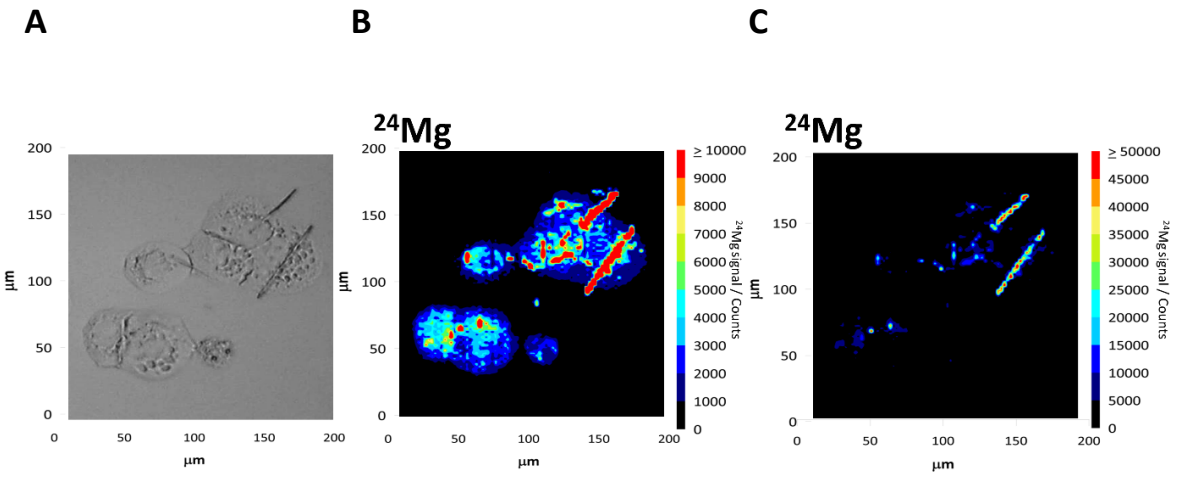

Figure 4.7 Detection of actinolite based on magnesium content. (A) Light microscopy image showing the elongated, flattened actinolite fibres prior to ablation. (B) LA-ICP-MS image formed based on the high Mg content in the sample. Numerous actinolite fragments are present withing the cells. (C) LA-ICP-MS image of the same area normalised against the cellular background by increasing the intensity bar showing only the signal gave by the actinolite fibres and fibre fragments.

4.2.4 Multi-elemental LA-ICP-MSI of single mineral fibres in 2D mesothelioma models

Detection of the most prevalent types of asbestos fibres based on the Mg content was proven in the initial studies. However, it is essential to include other elements in the detection panel. Si, Ca, and Fe are amongst the most common elements shared between these MF. With five MF types and an untreated control, and three different elemental targets, each measured in three replicates, a total of 54 (200 x 200 µm) images were acquired in this investigative study. There were no significant inconsistencies found between the replicates. The data were selected based on intensity signal, proof-of-concept, and presence of fibre fragments not visible in the brightfield images.

The MF were identified by LA-ICP-MS based on the Fe, Mg, and Si content. Method optimisation included the selection of the right isotopes for each element. Firstly, mapping the iron distribution within biological samples has proven difficult due to common interferences of ^{56}Fe with the plasma gas (May & Wiedmeyer,

1998). For this work, ^{57}Fe proved to be a valuable alternative, offering above-background signals for all the asbestos fibres used. Secondly, ^{24}Mg, the most abundant stable isotope of magnesium was selected after method optimisation, generating high signal for all sample types. Finally, regardless of whether they are classified as carcinogenic asbestiform fibres, all MF are silicates and therefore detection of silicon was a key step. To avoid the interferences caused by the high silicon content in glass slides, all samples were prepared on plastic slides. Analysis was optimised for the best signal intensity of MF. Despite being the second most abundant isotope, ^{29}Si generated signals above the background noise, allowing clear identification of all MF. Of the other major matrix components, ^{16}O is undetectable via ICP-MS, whilst ^{40}Ca and ^{44}Ca analysis was attempted but was unsuccessful due to high interferences from the plasma gas (data not shown). The signal intensity scale in the LA-ICP-MS images can be adjusted to display the full signal range of the fibres. In these data the intensity scale was kept consistent between samples and the background signal from the cells was removed from the images in order to facilitate easier identification of fibres.

4.2.4.1 Untreated

NCI-H28 cells are a well-established model for epithelioid MPM, the most prevalent type of mesothelioma (75-80% cases) (Bononi *et al.,* 2015) and provide a biologically relevant matrix for the MF. Analysis was therefore carried out initially on 2D cell models in order to ensure the elemental signals provided by the MF were above the cellular background before moving on to more biologically complex samples. To assess whether different types of MPM would give different signal background, a biphasic cell line, MSTO-211H, was also used as a matrix (data not presented). There was no significant difference in either ^{24}Mg, ^{57}Fe, or ^{29}Si intensity signals generated by the two cellular models. The elemental intensity generated by the NCI-H28 cells is presented in Figure 4.8 (A-C). Note the signal intensity generated by the ^{24}Mg (Figure 4.8 B), present at detectable and relatively homogeneous levels within the biological matrix, making it a suitable choice to aid correlation of the LA-ICP-MS and microscopic images.

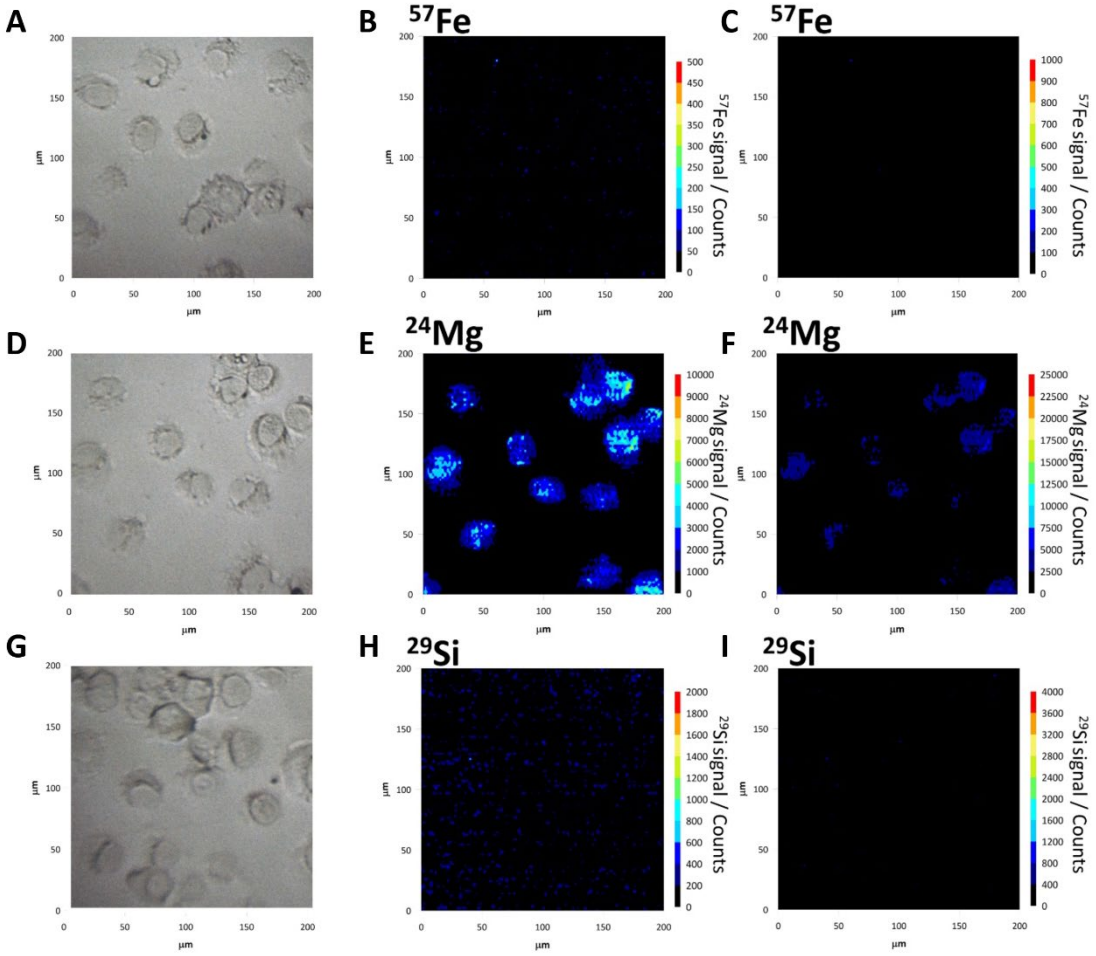

Figure 4.8 NCI-H28 cells cultured in a fibre free environment. A, D & G- Microscope perspective of the areas prior to ablation. B, E & H- Elemental distribution as analysed by LA-ICP-MSI. Intensity bar was adjusted in the right hand-side column to normalise against the cellular background (C, F & I). B & C- show the low ^{57}Fe distribution within the mesothelioma cells. High ^{24}Mg intensity counts are presented in E & F, whereas H & I show the significantly low overall ^{29}Si content in NCI-H28 cells.

4.2.4.2 Chrysotile

Chrysotile is known for its long, curled appearance and short biopersistence in the lungs (Bononi *et al.*, 2015). The slightly decreased carcinogenicity of chrysotile, when compared to other asbestos fibres, is mainly attributed to the low iron concentration. Although the hazardous nature of serpentine fibres is not questioned, chrysotile fibres are very flexible and are not resistant to acids. This might explain why, despite being used extensively in industry throughout the decades, the number of chrysotile fibres detected in human tissue is significantly

lower than the number of amphiboles (Feder *et al.*, 2017). Another explanation would be the current clinical sample preparation for MF detection which involves the use of acids to disintegrate the biological matrix (Dement *et al.*, 2015), which in turn can deteriorate chrysotile fibres. This is one more reason why LA-ICP-MS might prove to be a more superior clinical tool than the current methodology.

Chrysotile contains trace amounts of iron as an impurity (1-6%) where iron molecules replace magnesium in the outer Mg-hydroxide octahedral or silicon in the inner silica tetrahedral (Mohanty *et al.*, 2018). These trace amounts of Fe allow for visualisation of chrysotile fibres and fibre fragments in Figure 4.9 A. As a matrix component of chrysotile, representing 26.31% of its nominal composition, magnesium can be easily detected within the chrysotile long fibres, as well as in shorter fragments (Figure 4.9 B). Another clear example of the long physical appearance of chrysotile, can also be noted in Figure 4.9 C. Apart from identification of the single, long fibre, LA-ICP-MS images allow for visualisation of smaller fragments.

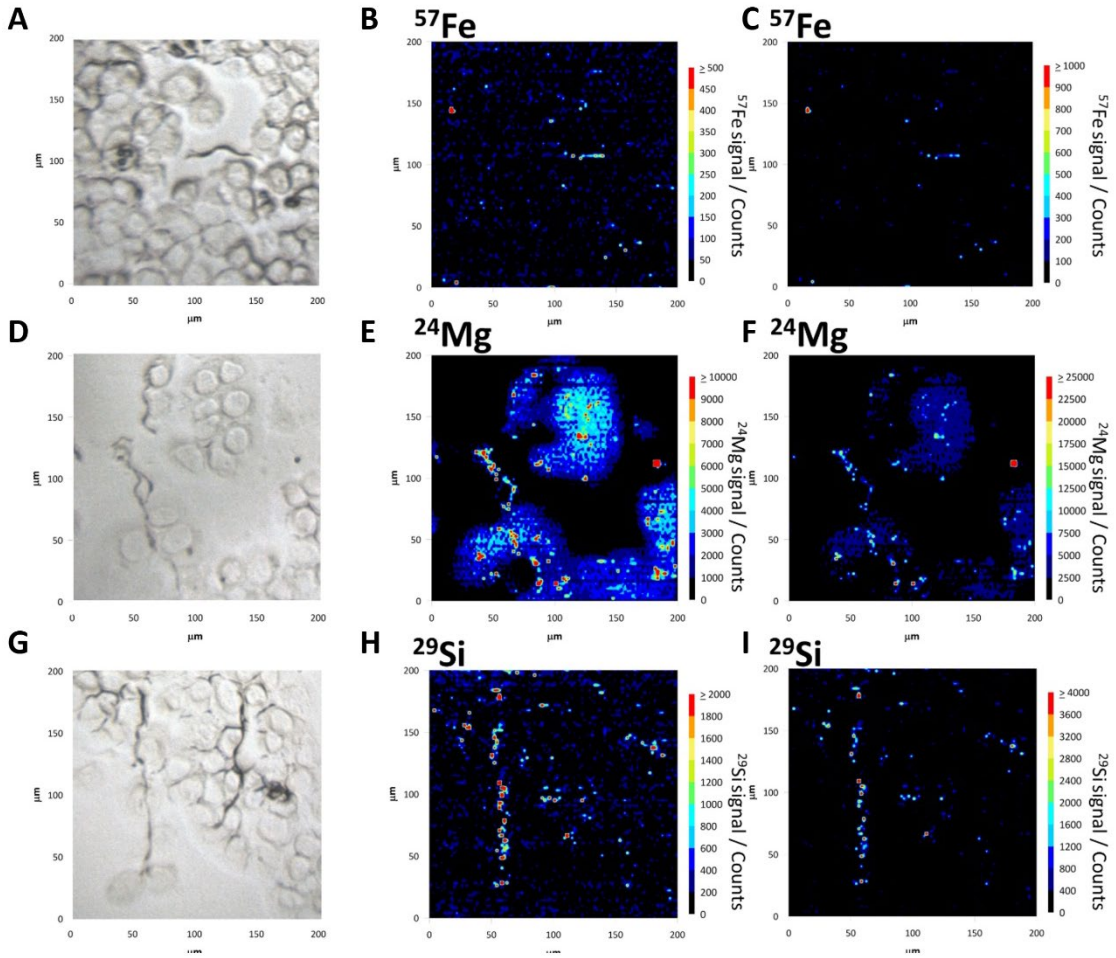

Figure 4.9 NCI-H28 monolayer cultured with chrysotile. A, D & G- Microscope perspective of the areas prior to ablation. Areas with fibres visible using optical microscopy were selected for proof of concept. Note the physical aspect of the fibres typical to chrysotile. B, E & H- Elemental distribution as analysed by LA-ICP-MSI. Intensity bar was adjusted in the right hand-side column to normalise against the cellular background (C, F & I). B & C show the low ^{57}Fe distribution within the sample. Chrysotile is known for its limited iron content, and this is reflected in the metal counts. E & F present the relatively high ^{24}Mg intensity signal in the fibres visible in microscope images, as well as smaller fragments within the cell layer that could not be seen initially. H & I present the ^{29}Si distribution within the matrix and chrysotile fibres. LA-ICP-MS preserves the curly shapes of the chrysotile fibrils.

4.2.4.3 Amosite

Amosite asbestos is, chemically speaking, one of the most ideal MF to be identified by LA-ICP-MS based on its Fe, Mg and Si content. Fe represents more than 39% of the nominal composition of amosite, which is reflected in the high

signal intensity presented in Figure 4.10 A. Similarly, magnesium is also present, albeit in a smaller percentage, in amosite fibres (Figure 4.10 B). Being a proof-of-concept study, regions containing visible fibres, as determined by optical microscopy, were selected for analysis. The pre-ablation, corresponding optical images were included in the left columns of the figures for comparison with the LA-ICP-MS images. It was noted that in cases where fibres disappear within or underneath a cell in the microscopic images, they were still noticeable in the LA-ICP-MS images based upon their metal signal (Figure 4.10, panels B-C). This is an advantage of LA-ICP-MS compared to microscopic methods. It has been reported that MF shorter than 5 μm normally get engulfed by cells through frustrated phagocytosis, whereas longer fibres can get lodged in the internuclear bridge of the cells (Ishida *et al.*, 2019). Localisation does vary between cell types. In clinical samples and experimental animal models, fibres are usually contained in both fibroblasts and macrophages (Pinkerton *et al.*, 1984). However, the internalisation of asbestos fibres into various non-phagocytic mesothelial cells has also been reported by many researchers (Nagai & Toyokuni, 2012). Given the sample preparation, the localisation of the fibres varies between the samples, supporting the hypothesis that LA-ICP-MS can ablate and detect MF regardless of the positioning. One such example is presented in Figure 4.10 B.

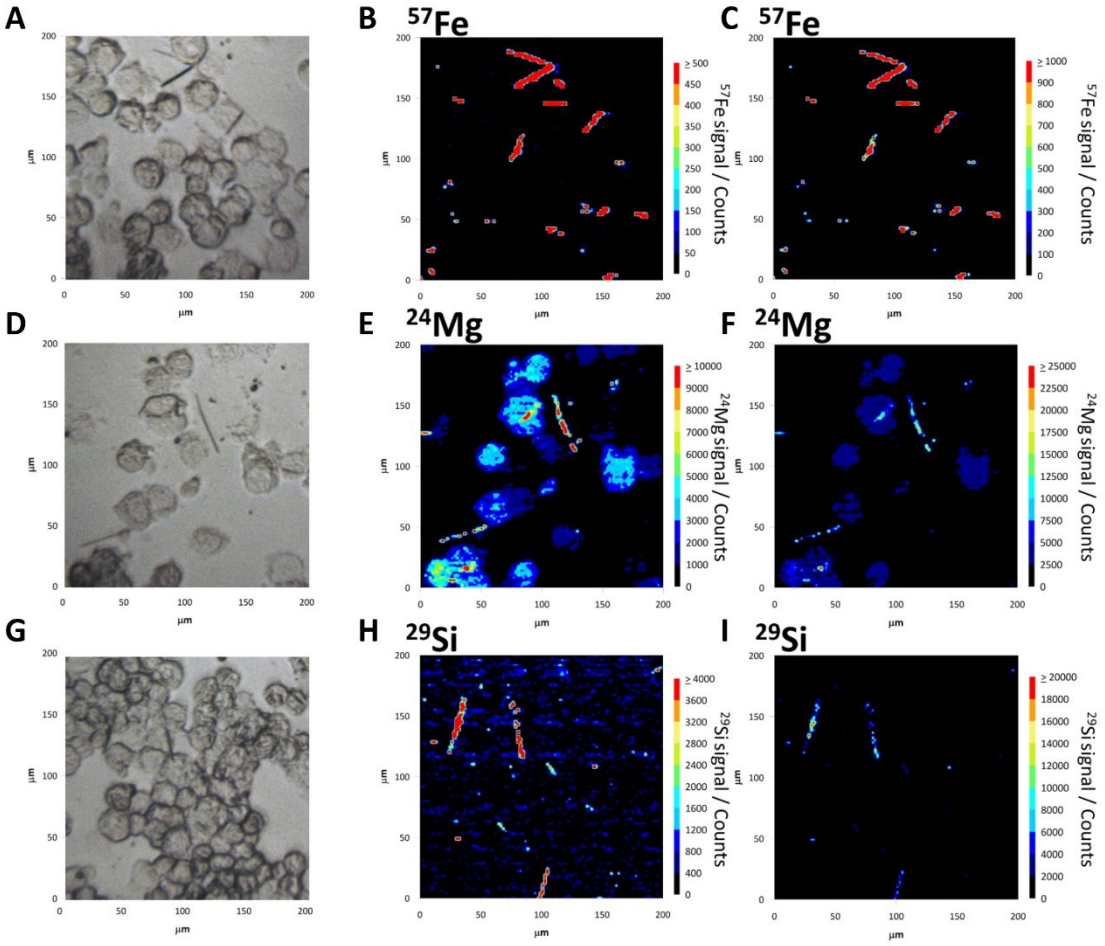

Figure 4.10 NCI-H28 cells cultured with amosite fibres. A, D & G- Microscope perspective of the areas prior to ablation. Areas with fibres visible using optical microscopy were selected for proof of concept. B, E & H- Elemental distribution as analysed by LA-ICP-MSI. Intensity bar was adjusted in the right hand-side column to normalise against the cellular background (C, F & I). As expected, higher ^{57}Fe distribution is presented in B & C compared to serpentine fibres. Note the shorter fibres and fibre amosite fibre fragments spread all over the sample as shown using LA-ICP-MSI. ^{24}Mg counts within the sample are shown in E & F. Note the engulfed amosite fibres not visible in the microscopic image. H& I show ^{29}Si distribution within the matrix and amosite fibres.

4.2.4.4 Crocidolite

Importantly, the difference in nominal composition between the elements that make up the MF selected in the panel is mirrored in the intensity generated by analysis. For instance, the Fe content in chrysotile presented earlier in Figure 4.9 A compared to crocidolite (Figure 4.11 A), which brings the work a step closer to differentiating between the fibres in blind analysis based solely on elemental

composition. As a very common impurity in crocidolite, magnesium signal can easily provide spatial information of the position of the crocidolite fibres (Figure 4.11 B). Likewise, a high ^{29}Si signal is shown in Figure 4.11 C, both in longer crocidolite fibres as well as in the shorter fragments.

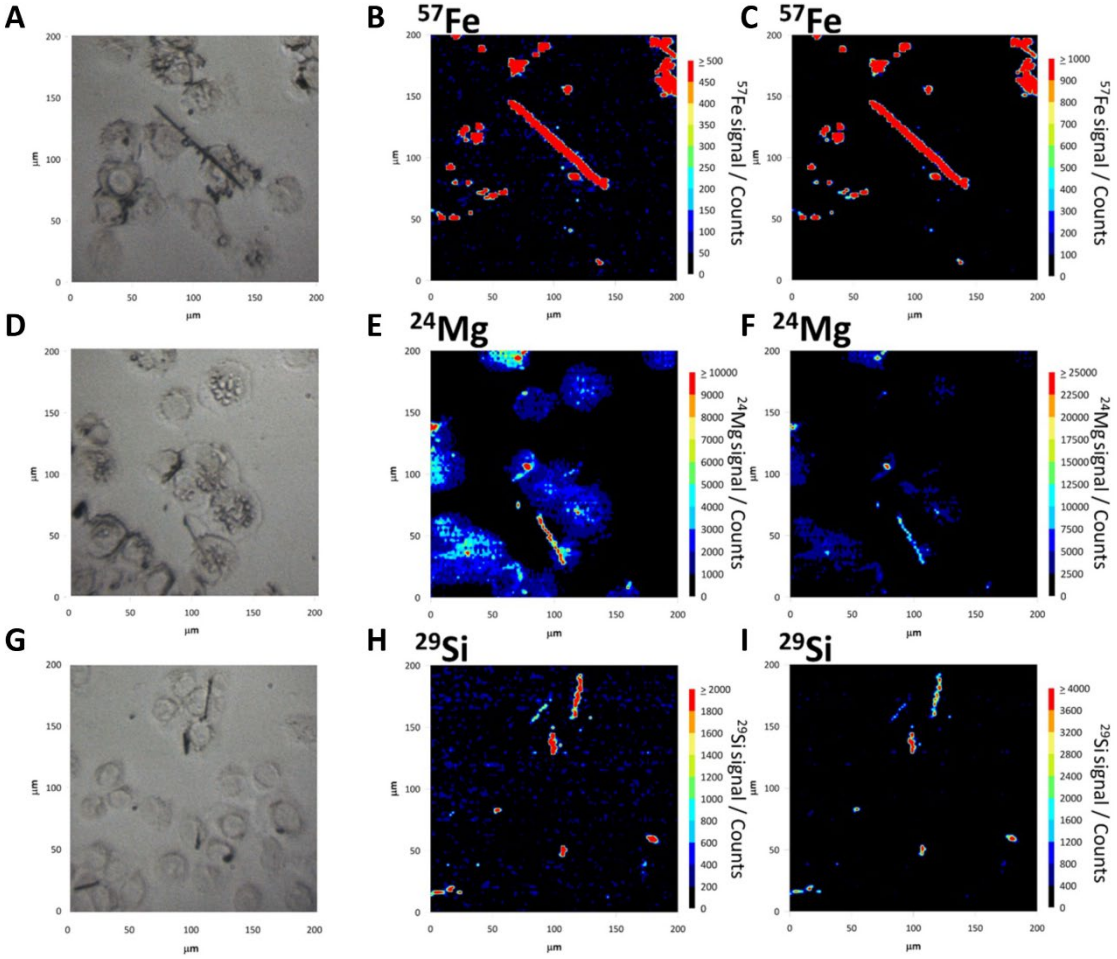

Figure 4.11 NCI-H28 cells cultured with crocidolite fibres. A, D & G- Microscope perspective of the areas prior to ablation. Areas with fibres visible using optical microscopy were selected for proof of concept. B, E & H- Elemental distribution as analysed by LA-ICP-MSI. Intensity bar was adjusted in the right hand-side column to normalise against the cellular background (C, F & I). The highest ^{57}Fe concentration is presented in B & C which coincides with the nominal composition of crocidolite. ^{24}Mg counts can be seen in E & F. Hardly any fibres can be seen in the corresponding microscopic images. The LA-ICP-MS images offer information beneath the cellular layer, exposing the crocidolite fibres based on ^{29}Si content (H& I).

4.2.4.5 Actinolite

Actinolite has a rather limited commercial use, but it has been reported as a common contaminant for chrysotile, tremolite, and talc (Fujiwara *et al.*, 2005). As a notable physical characteristic, actinolite fibres are translucent to transparent, which can complicate the identification of actinolite using standard optical methods (Parvizi-Majidi & Begum, 2015). Apart from the physical characteristics, which are similar to those of more potent amphiboles (*i.e.,* crocidolite and amosite), the high content of iron within the actinolite fibres plays an essential role in the aforementioned carcinogenicity and correlation between naturally occurring fibres and MPM. This allows for identification of actinolite fibres and fibre fragments within cellular aggregates as presented in Figure 4.12 A. Despite being an intermediate member between magnesium-rich tremolite and iron-rich ferro-actinolite, actinolite fibres are rich in magnesium, yielding high ^{24}Mg signal in actinolite treated samples (Figure 4.12 B). Actinolite fibres can be detected based on the silicon content as presented in Figure 4.12 C. Moreover, the debris caused by sample processing that appears as strange bodies in the brightfield microscopy image on the left-hand side were confirmed to be sample preparation and storage artefacts since there was no ^{29}Si signal detected in the corresponding LA-ICP-MS images.

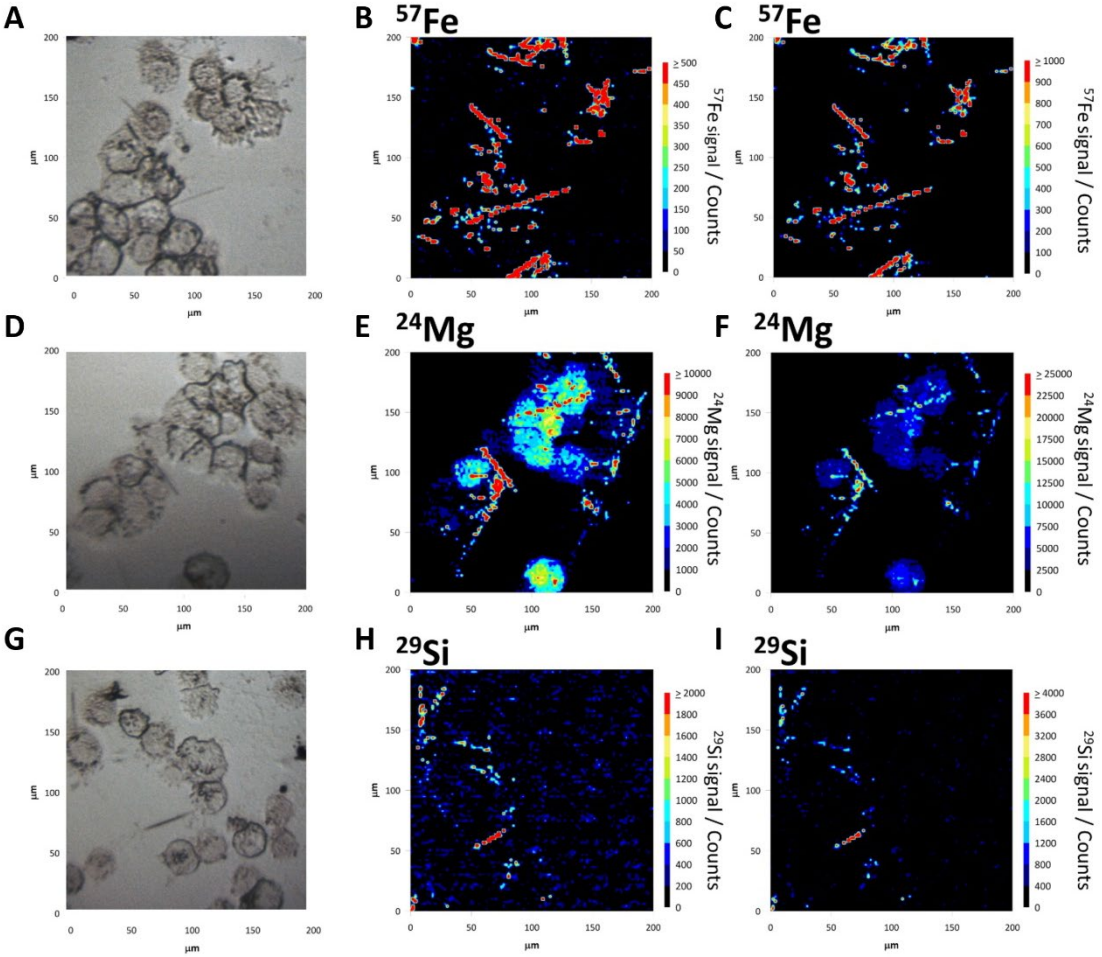

Figure 4.12 NCI-H28 cells cultured with actinolite fibres. A, D & G- Microscope perspective of the areas prior to ablation. Areas with fibres visible using optical microscopy were selected for proof of concept. B, E & H- Elemental distribution as analysed by LA-ICP-MSI. Intensity bar was adjusted in the right hand-side column to normalise against the cellular background (C, F & I). The high concentration of ^{57}Fe within the actinolite structure allows for detection of multiple elongated fibres and fibre fragments within the sample (B & C). E & F show the ^{24}Mg counts within the sample. Note the actinolite fibres not visible in the microscopic image. H & I present ^{29}Si distribution within the matrix and the fibres. Overall, the normalised images on the right-hand side column confirm that the number of fibres within the samples is significantly higher than presented in the optical images.

4.2.4.6 Wollastonite

Wollastonite was selected as a negative control MF due to its similar chemical and physical properties to established asbestos fibres. It is a calcium inosilicate mineral with no established association to MPM (Maxim & McConnell, 2005).

Mined in a similar fashion to other MF, wollastonite can contain other metal impurities including Fe (Gilbert, 2017), which might explain the slight ^{57}Fe signal present in Figure 4.13 A. On the other hand, no magnesium was present in the wollastonite samples, as shown by the LA-ICP-MS images (Figure 4.13 B). As expected, high ^{29}Si was generated in the case of this MF (Figure 4.13 C). Notably, some impurities present in the optical image were proven not to be wollastonite, confirming the high selectivity of this technique.

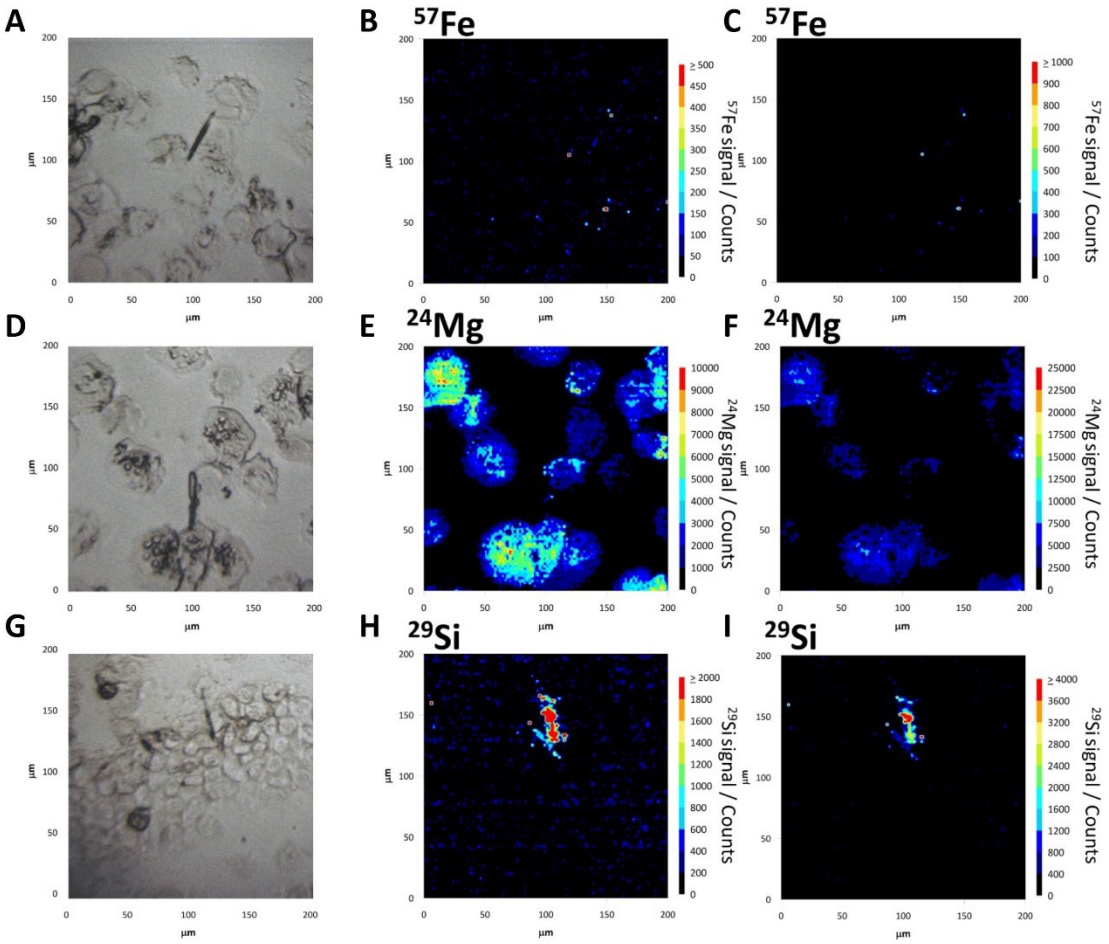

Figure 4.13 NCI-H28 cells cultured with a non-asbestiform control, wollastonite. A, D & G- Microscope perspective of the areas prior to ablation. Areas with fibres visible using optical microscopy were selected for proof of concept. B, E & H- Elemental distribution as analysed by LA-ICP-MSI. Intensity bar was adjusted in the right hand-side column to normalise against the cellular background (C, F & I). No significant ^{57}Fe and ^{24}Mg signals were given by the wollastonite fibres (B, C, E & F). On the other hand, wollastonite is a silicate and was therefore expected to be identified based on the ^{29}Si content. This is shown in H & I where the ^{29}Si distribution corresponds to the wollastonite fibres visible in the optical image on the left.

4.2.5 LA-ICP-TOFMS (Instrument 2) imaging of single mineral fibres in 2D malignant pleural mesothelioma models

Identification of fibres within biological samples is a complex challenge, since these matrices often contain background levels of the metals of interest. Moreover, some of the most abundant elements that make up asbestos fibres (*e.g.,* Fe, Ca) are common ICP-MS polyatomic interferences caused by the plasma gases. It has been previously shown in this chapter that the most common types of asbestos yield signals higher than the signals generated by the biological matrix (*i.e.,* mesothelioma cells). However, this data was limited to less abundant stable isotopes of magnesium, iron, and silicon detection.

A prototype LA-ICP-TOFMS was employed for pseudo-spontaneous detection of the elements between mass 23 (Na) and mass 238 (U). Data was collected for the full mass range, but subsequent data analysis focused on 10 elements relevant to this work (^{23}Na, ^{24}Mg, ^{27}Al, ^{28}Si, ^{31}P, ^{39}K, ^{40}Ca, ^{48}Ti, ^{55}Mn, and ^{56}Fe).

To overcome some of the limitations mentioned above, the mass spectrometer employed an always-on collision–reaction cell, which used a hydrogen flow of 5 sccm and a He flow of 5 sccm to remove nitrogen, argon, and their related polyatomic interferences. This allowed the major isotopes of ^{28}Si, ^{39}K, ^{40}Ca, and ^{56}Fe to be used, improving the signal to background levels seen in the images.

LA-ICP-TOFMS data is presented for MSTO-211H cells previously cultured with four different types of MF, added to the cell monolayers after 24 hours, once the cells reached a confluency of around 70%. Figure 4.14-21 show the resulting LA-ICP-TOFMS data for several characteristic elements in actinolite, amosite, crocidolite, and wollastonite fibres. Figure 4.14-4.21 A represent the light microscopy images corresponding to the ablated area (400 x 200 µm). The light microscopy images taken prior to ablation were included to ease direct comparison between MF identified in optical images and LA-ICP-TOFMS images. The figures are presented as the elemental maps of each fibre type.

4.2.5.1 Actinolite

Actinolite fibres can be spatially resolved based on high ^{24}Mg, ^{28}Si, ^{40}Ca, and ^{56}Fe signal counts (Figure 4.14 B, D-F). Calcium is present to a much lesser extent in actinolite (≈9% of its nominal composition), but it is not a matrix component of the other two fibre types studied. Therefore, calcium detection, alongside the other nominal components of amphiboles, indicates the presence of actinolite.

Interestingly, little to no signal was given by the biological matrix compared to the previously presented data based on ^{24}Mg isotope counts. The intensity bar was adjusted to emphasise the fibre signal. Given that ^{24}Mg is the most abundant stable magnesium isotope and that asbestos fibres have a high Mg content, the signal yielded by the cellular matrix was below the 1400 ^{24}Mg /CPS threshold. MSTO-211H cells can however be distinguished based on the high ^{23}Na, ^{39}K, and ^{31}P content characteristic of transformed malignant cells (Figure 4.14 C, Figure 4.15 B, C) (Nagy *et al.*, 1981).

Particularly, higher intranuclear sodium levels can be seen in the actinolite treated MSTO-211H human mesothelioma cells (Figure 4.14 C). This reinforces the clinical and research versatility of this technique. Iron is part of the nominal formula of actinolite, albeit in smaller proportions (≈8.58%) which is reflected in the mid-range ^{56}Fe signal intensity presented in Figure 4.14 F. This is significant for future prospects of using this technique for correct classification of asbestos and other MF.

No significant signal was detected for ^{27}Al, ^{55}Mn, and ^{48}Ti following LA-ICP-TOFMS analysis (Figure 4.15 D-F). Some background noise is visible, particularly for ^{48}Ti.

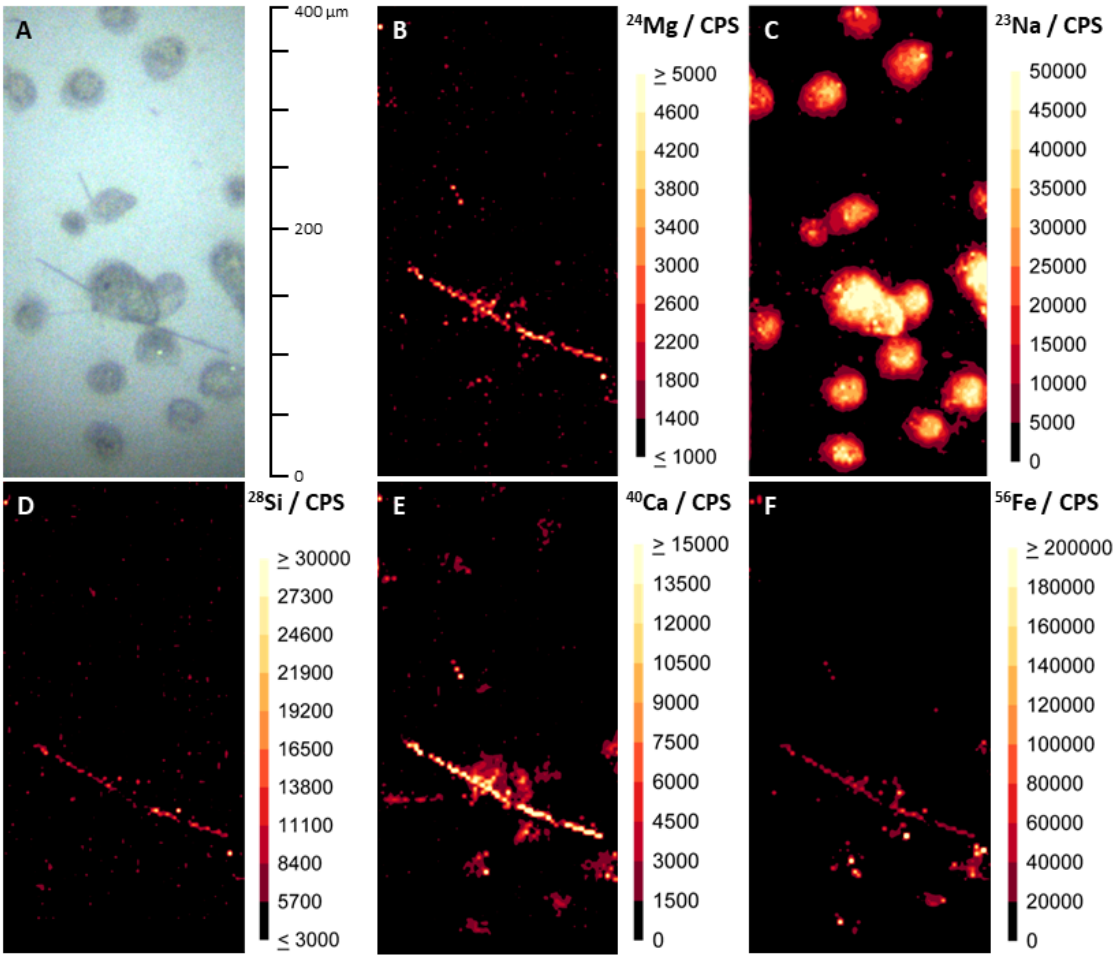

Figure 4.14 Elemental mapping of actinolite. A 400 × 200 µm sample area of MSTO-211H cells spiked with actinolite was ablated. (A) Fibres are visible as dark needle shaped objects in the microscopic image. (B-F) LA-ICP-MS images of the ^{24}Mg, ^{23}Na, ^{28}Si, ^{40}Ca, and ^{56}Fe distribution within the actinolite fibres and cell matrix are shown in panels. As expected, actinolite fibres yielded values for all the elements, but sodium.

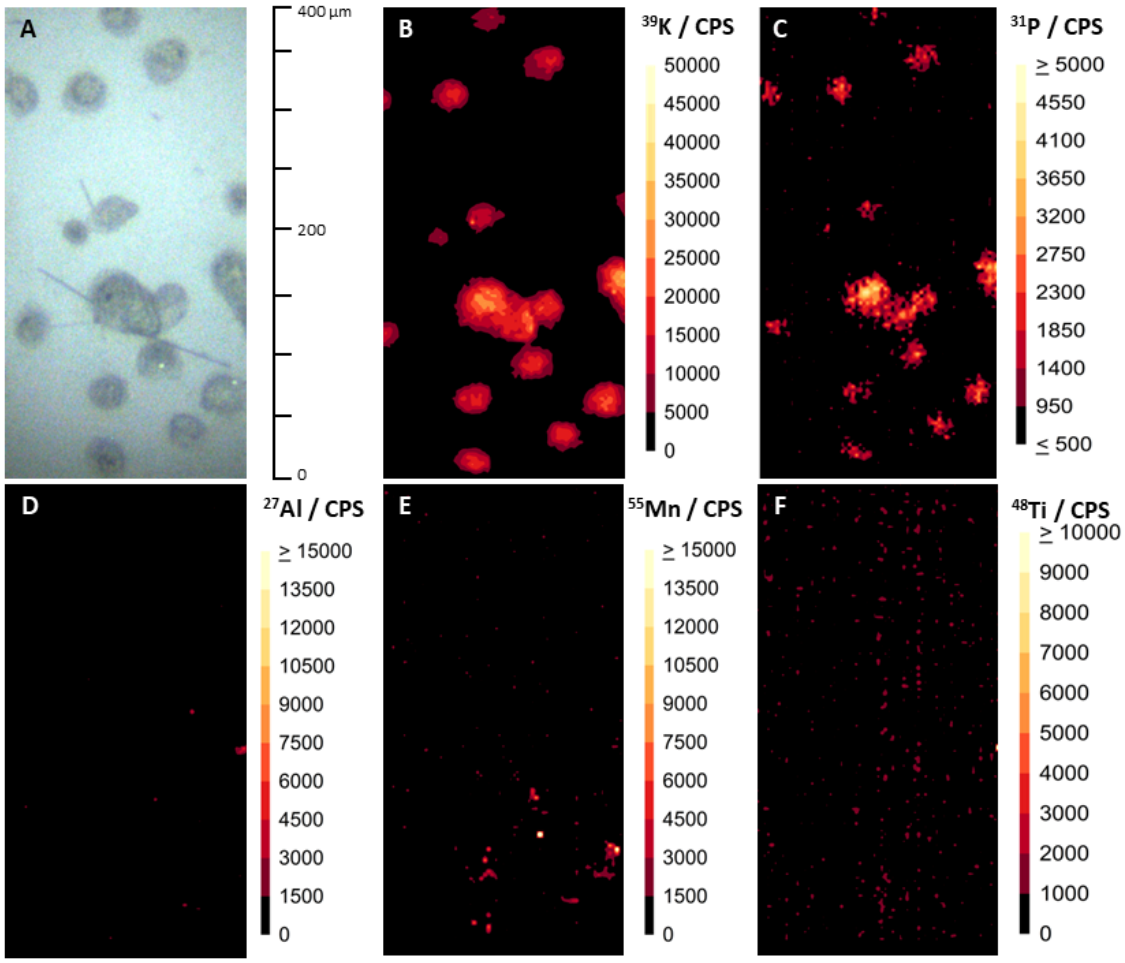

Figure 4.15 Elemental mapping of actinolite. A 400 × 200 µm sample area of MSTO-211H cells spiked with actinolite was ablated. (A) Fibres are visible as dark needle shaped objects in the microscopic image. (B-F) LA-ICP-MS images of the ^{39}K, ^{31}P, ^{27}Al, ^{55}Mn, and ^{48}Ti distribution within the actinolite fibres and cell matrix are shown in panels. No significant signal was given by the actinolite fibres for this panel of elements.

4.2.5.2 Amosite

The ^{24}Mg signals were strongest for amosite, where Mg accounts for >20% of the nominal composition of its cummingtonite form. Amosite fibres and some fibre fragments can be identified in Figure 4.16 A. Sodium is a matrix component of crocidolite but not amosite, so analysis of sodium was also evaluated as a way to visually distinguish these two fibre types (Figure 4.16 B- C). However, the very high level of sodium in biological matrices (*e.g.,* the dense cluster of cells in Figure 4.16 B), along with the common use of PBS to prepare cell samples, may interfere with the

interpretation of fibres. This serves to confirm that analysis of a single element would be insufficient to distinguish between these two fibre types and a full elemental map is required for a clear fibre identification.

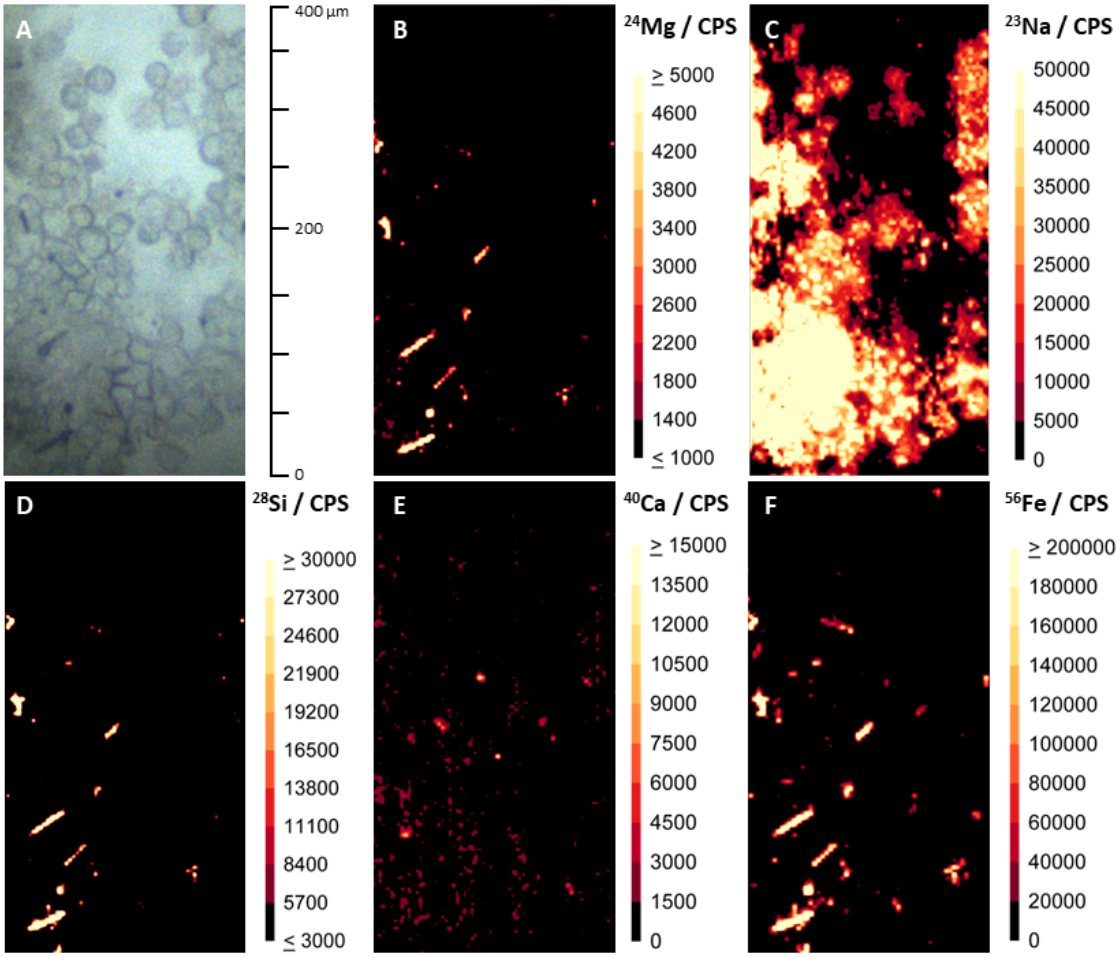

Figure 4.16 Elemental mapping of amosite. A 400 × 200 µm sample area of MSTO-211H cells spiked with amosite fibres was ablated. (A) Amosite fibres are visible as dark, long foreign bodies or as shorter fibre fragments in the microscopic image. (B-F) LA-ICP-MS images of the ^{24}Mg, ^{23}Na, ^{28}Si, ^{40}Ca, and ^{56}Fe distribution within the actinolite fibres and cell matrix are shown in panels. (E) Analysis of ^{40}Ca expression fails to detect amosite fibres against the cellular background. (C) Similarly, no amosite fibres can be identified based on the ^{23}Na content.

Similarly, the high ^{39}K signal in Figure 4.17 B is also given by the biological matrix and the PBS used for sample preparation, where high potassium intensity corresponds to clusters of malignant MSTO-211H cells.

Manganese is a known impurity in some amphiboles, including actinolite and amosite (Surour, 2015). Amosite fibres can be visualised in Figure 4.17 E based on the ^{55}Mn counts. No significant signal was detected in the other MF. Aluminium and titanium were also selected because they have been known to substitute into some amphiboles, but that was not observed here (Figure 4.17 D, F).

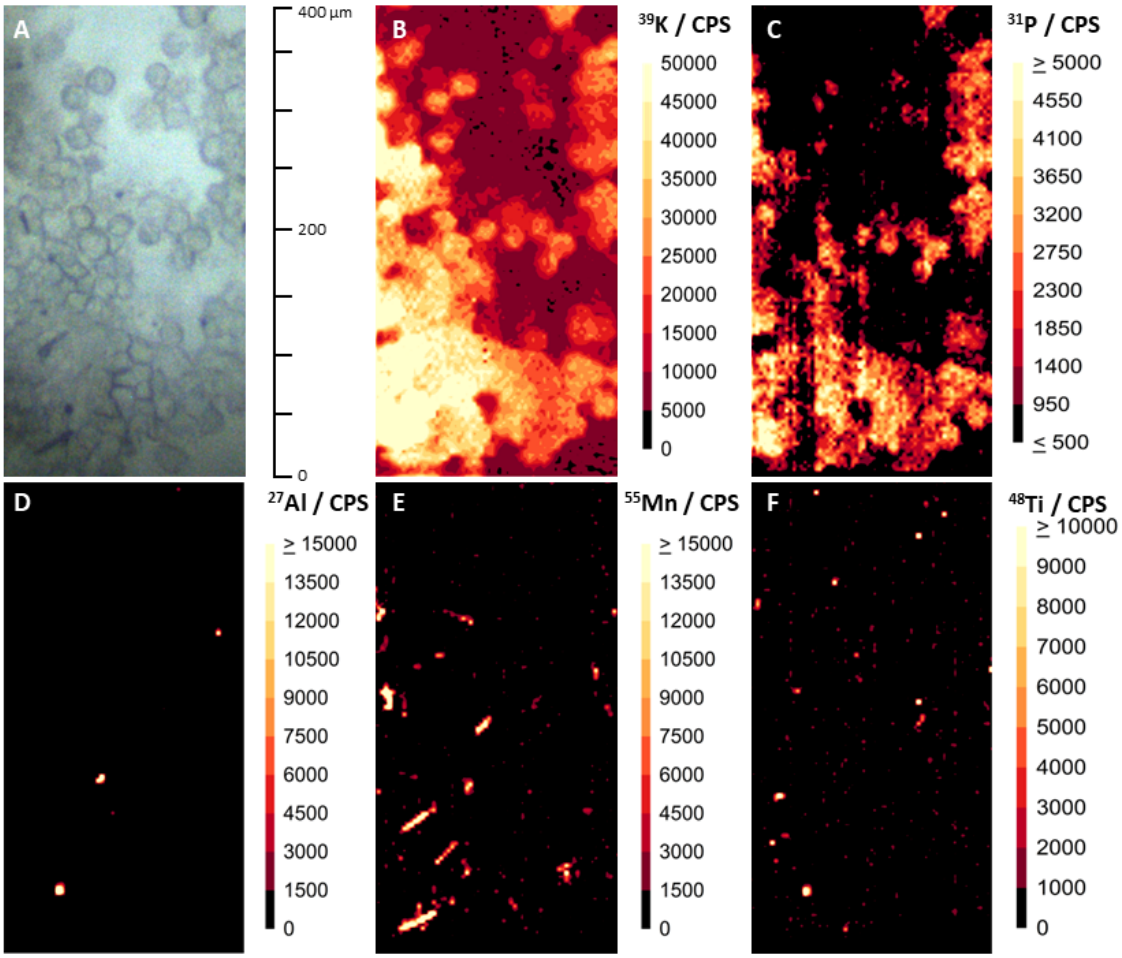

Figure 4.17 Elemental mapping of amosite fibres. A 400 × 200 µm sample area of MSTO-211H cells spiked with amosite was ablated. (A) Amosite fibres are visible as dark, long foreign bodies or as shorter fibre fragments in the microscopic image. (B-F) LA-ICP-MS images of ^{39}K, ^{31}P, ^{27}Al, ^{55}Mn, and ^{48}Ti distribution within the actinolite fibres and cell matrix are shown in panels. Interestingly, the amosite fibres can be identified based on the ^{55}Mn that substitutes into the nominal composition of this amphibole (E).

4.2.5.3 Crocidolite

Some crocidolite derivatives have been reported to contain Mg substitutes in the Z^{2+} position or Mg as impurities, which can explain the high ^{24}Mg signals yielded by crocidolite fibres in Figure 4.18 B. The signal intensity for ^{40}Ca yielded by crocidolite fibres was not above the cellular matrix (Figure 4.18 E) suggesting that like amosite, crocidolite can also be distinguished from actinolite and wollastonite, which are MF rich in calcium, through visual comparison of the calcium images.

Crocidolite contains more than 28% Fe in its nominal structure which has been reported to be directly proportional to the high carcinogenicity of the blue asbestos (Hodgson & Darnton, 2000). The intensity scale bars were consistent in values for all the data presented. Amphiboles such as crocidolite were expected to yield higher signals for ^{56}Fe, as presented below in Figure 4.18 F.

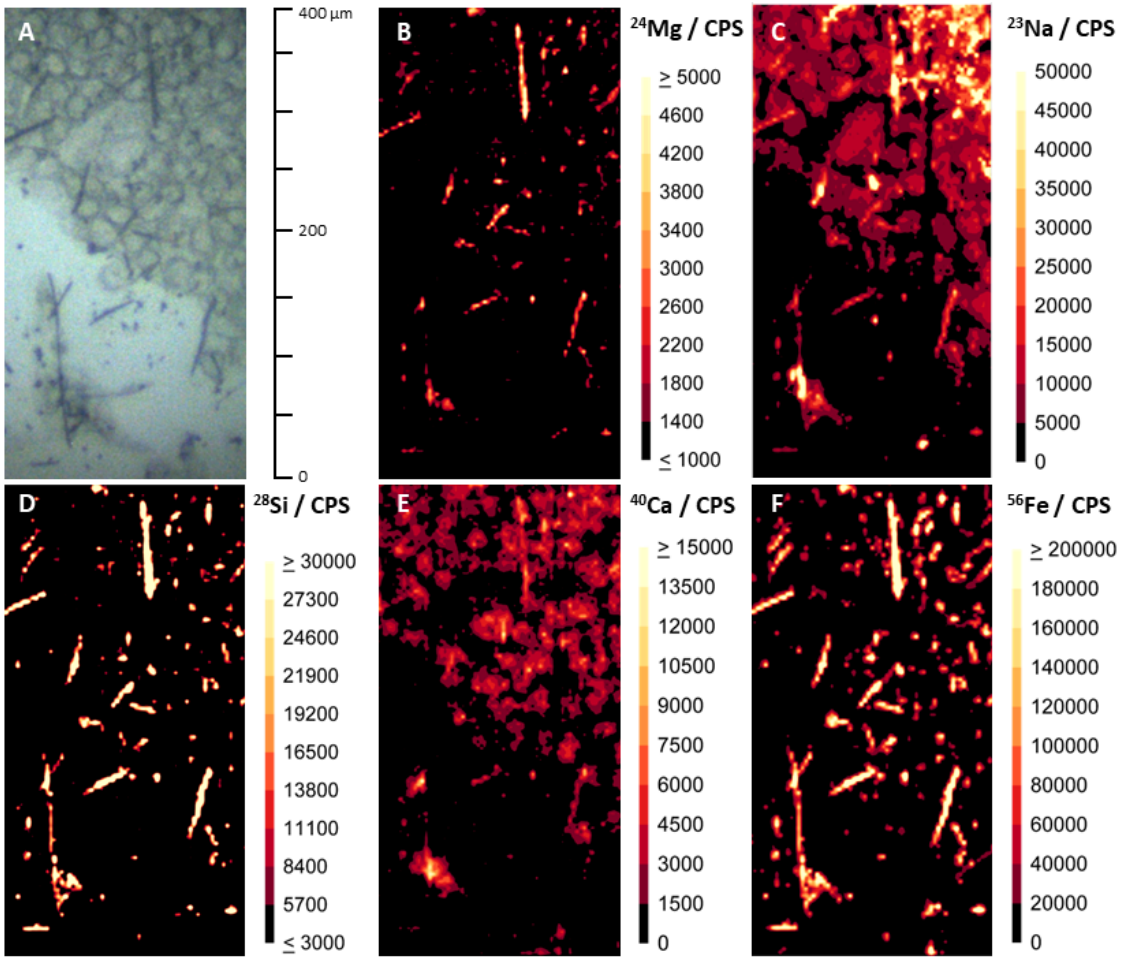

Figure 4.18 Elemental mapping of crocidolite. A 400 × 200 µm sample area of MSTO-211H cells spiked with crocidolite fibres was ablated. (A) Crocidolite fibres can be seen as long, dark fibres with shorter fragments also present. (B-F) LA-ICP-MS images of the ^{24}Mg, ^{23}Na, ^{28}Si, ^{40}Ca, and ^{56}Fe distribution within the actinolite fibres and cell matrix are shown in panels. Multiple shorter fibres and fibre fragments can be identified based on the main components of crocidolite: magnesium, silicon, and iron (B, D, F). Crocidolite also yields signals for ^{23}Na, however the high sodium content in the biological matrix hinders clear detection of individual fibres (C).

High levels of K are present in the MSTO-211H cells that act as a biological matrix for the MF (Figure 4.19 B). However, the PBS solution used in the sample preparation steps contains high levels of K. Likewise, the MF were stored in PBS at all times due to H&S measures, which might explain the overall signal distribution of ^{39}K in Figure 4.19 B.

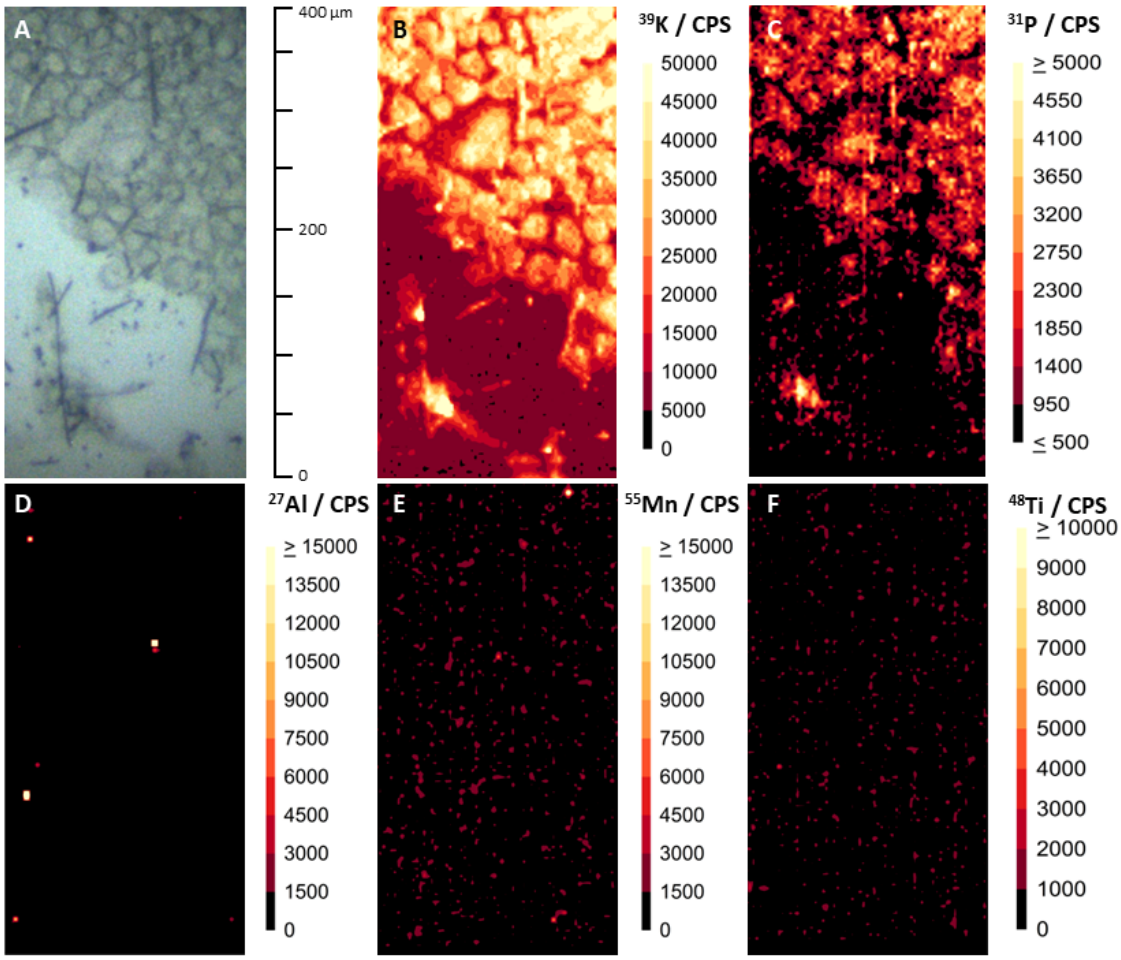

Figure 4.19 Elemental mapping of crocidolite fibres. A 400 × 200 µm sample area of MSTO-211H cells spiked with crocidolite was ablated. (A) Crocidolite fibres are presented in the microscopic image as long, dark fibres with shorter fragments also present. (B-F) LA-ICP-MS images of the ^{39}K, ^{31}P, ^{27}Al, ^{55}Mn, and ^{48}Ti distribution within the actinolite fibres and cell matrix are shown in panels. No crocidolite fibres can be clearly identified based on these elements.

4.2.5.4 Wollastonite

Wollastonite was used as a non-asbestiform control with potential carcinogenicity (Maxim & McConnell, 2005). Mg was found to varying extents in all three of the asbestos fibres studied herein, but only traces were observed in the wollastonite control (Figure 4.20 panel B). Identifying such impurities of MF classed as non-asbestiform silicates can give insight into the possible link between these types of fibres and idiopathic MPM or other pulmonary complications (Baumann, Ambrosi, & Carbone, 2013; Huuskonen *et al.*, 1983).

Detection based on Si signal is essential in classifying strange bodies as MF. It is established that all fibres are silicates (Chapter 1, Section 1.3.2, Table 1.3) and contain Si as a matrix element. Thus, strong ^{28}Si signals were observed for all four fibre types (Panel D, Figure 4.14, Figure 4.16, Figure 4.18 and Figure 4.20), enabling rapid differentiation of the MF from the cellular background as well as any non-fibrous artefacts or impurities present on the sample. One clear example is presented in Figure 4.20 where one of the foreign bodies shown in the optical image (Figure 4.20 A) yielded above the background signal for ^{23}Na, ^{40}Ca, and ^{56}Fe (Figure 4.20 C, E, F), but no signal for ^{28}Si (Figure 4.20 D). It can therefore be concluded that only one of the strange bodies is a wollastonite fibre (*i.e.,* the longer fibre).

Fe is present at varying percentage levels in the three asbestos fibre types, but it is not a matrix component of the wollastonite control. The distribution pattern of ^{56}Fe (Figure 4.20 F) therefore enabled rapid discrimination between the three asbestos fibres and the control sample. Furthermore, calcium is a major matrix component of wollastonite, representing ≈35% of its nominal composition which is reflected in the high intensity of ^{40}Ca in Figure 4.20 E.

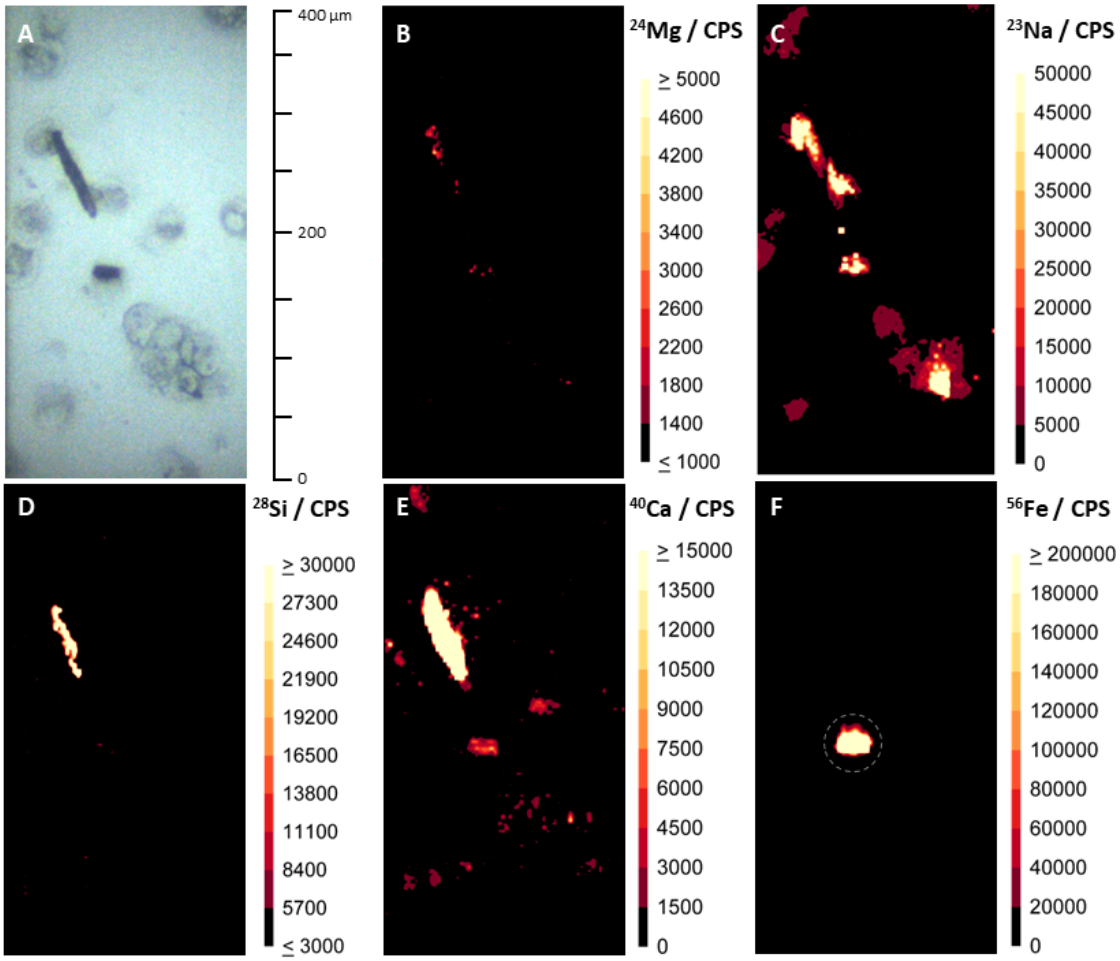

Figure 4.20 Elemental mapping of wollastonite. A 400 × 200 µm sample area of MSTO-211H cells spiked with crocidolite fibres was ablated. Two foreign bodies can be observed in the microscopic image (A). (B-F) LA-ICP-MS images of the ^{24}Mg, ^{23}Na, ^{28}Si, ^{40}Ca, and ^{56}Fe distribution within the actinolite fibres and cell matrix are shown in panels. No Si or Ca content suggests that only the longer fibre is wollastonite (D, E). The unknown sample impurity yielded high signals of ^{56}Fe (F).

High levels of P are seen within the cell clusters presented in the figures above (Figure 4.15, Figure 4.17 and Figure 4.19, panel C), with P accumulation being more noticeable intracellularly. There are no significant levels of P in any of the asbestiform fibres, however wollastonite fibres can be detected based on ^{31}P counts. Wollastonite has been reported as a substrate for removing soluble phosphorus from secondary wastewater (Brooks *et al.*, 2000). It is therefore established that the high concentration of calcium within the wollastonite leads to chemical precipitation of calcium phosphates and P adsorption. Adsorption is

also possible through either ion or ligand exchange at soil surfaces (Brooks *et al.*, 2000). This chemical property explains why this calcium metasilicate yielded a high intensity signal of ^{31}P (Figure 4.21 C). Some trace contents of K and Ti were also observed, but not to a significant level (Figure 4.21 B, F), whilst no signal was detected in Figure 4.21 panels D-E.

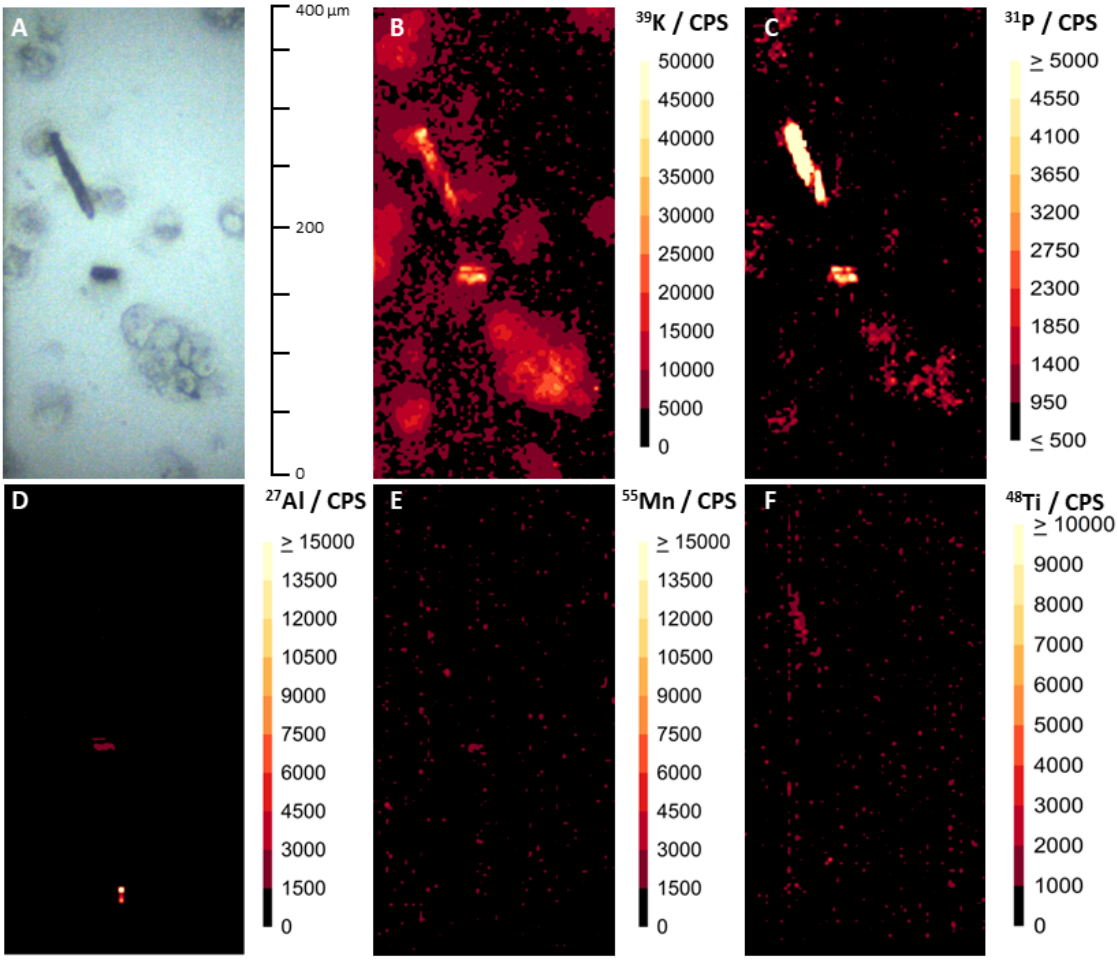

Figure 4.21 Elemental mapping of wollastonite. A 400 × 200 µm sample area of MSTO-211H cells spiked with crocidolite fibres was ablated. Two foreign bodies can be observed in the microscopic image (A). (B-F) LA-ICP-MS images of the ^{39}K, ^{31}P, ^{27}Al, ^{55}Mn, and ^{48}Ti distribution within the actinolite fibres and cell matrix are shown in panels.

4.3 Conclusion

The poor treatment response and short-term survival of MPM patients are largely attributed to late diagnosis and lack of a standardised screening method. Moreover, current detection of asbestos fibres by microscopy exhibits poor sensitivity, with numerous fibres being undetectable, even in patients with heavy asbestos exposure (Capella *et al.*, 2016).

This is the first study to employ LA-ICP-MSI to spatially resolve multiple MF within a cellular background based on the nominal composition of the fibres (Voloaca *et al.*, 2020). Initial studies focused on detection of Mg, due to the low level of polyatomic interference. Mg is also present in most of the MF, either as part of the molecular structure or as a common substitute. Therefore, Mg was selected as the target element for method optimisation, including sample preparation, analysis parameters and data processing. Amongst the most essential parameter is laser energy which was optimised to give total ablation of the samples, whilst providing optimal signal for both cells and MF. Additionally, the spot size can also play an important role in fragmentation effects and to a lesser extent in signal intensity (for constant laser pulse energy) (Diwakar *et al.*, 2013).

Once the methods were optimised, analysis of Fe, Si, and Ca was attempted on MPM cells exposed to various MF. In this work, chrysotile, actinolite, amosite, crocidolite, and wollastonite were selected to be part of the panel of MF to be detected based on the metal content. The panel was carefully selected to include both the most common type of asbestos (*i.e.,* chrysotile) (Bononi *et al.*, 2015), as well as the MF with the highest carcinogenicity and bioresistance (*i.e.,* crocidolite) (Andreozzi *et al.*, 2017).

Detection of ^{40}Ca was not possible due to polyatomic interferences from the ^{40}Ar present in the plasma gas. Detection based on ^{44}Ca was attempted but failed to produce a significant signal. Secondary isotopes were selected for iron and silicon to avoid any interferences and allow clear identification of fibres within the 2D samples. Plastic slides were employed to help reduce the background signal for ^{29}Si, typically generated by the use of glass slides.

In order to investigate the capability of LA-ICP-MS to identify different MF based on the elemental composition, regions of interest (ROIs) were carefully selected to include fibres visible using brightfield microscopy. Using this technique, the visible fibres were successfully identified. Moreover, shorter fibres, fibre fragments, fibres engulfed by the cells, as well as sample impurities, were all additionally detected in the LA-ICP-MS images. This supports the hypothesis that LA-ICP-MSI is a superior MF detection technique, with strong clinical potential.

The set-up used for the early experiments allowed for high-resolution, high-speed analysis at a cellular level. However, the capability of the Element XR sector-field ICP mass spectrometer to monitor multiple signals was limited by the settling time of sector-field instruments. Consequently, a prototype laser ablation inductively coupled plasma time-of-flight mass spectrometry (LA-ICP-TOFMS) set-up was employed for pseudo-simultaneous detection of a full range of key elements. It was apparent from the initial experiments that TOF technology offers an advantage over sector-field technology for this application, particularly when used with high-speed laser ablation platforms. Monitoring multiple nuclides simultaneously allows not only for visualisation of individual MF, but also for differentiation between different types of MF in human tissue patient samples with unknown exposure.

The use of a collision–reaction cell during analysis meant that polyatomic interferences related to nitrogen and argon were reduced. Analysis of ^{40}Ca was possible without interferences from ^{40}Ar, whilst ^{56}Fe was detected without polyatomic interference from $^{40}Ar^{16}O$. Calcium and iron are amongst the most essential elements to be detected as part of this study since they are crucial in classification of certain fibre types, with iron also playing a key role in MPM pathogenesis and fibre biopersistence.

A panel of 10 elements was selected for data analysis including the main nominal components of the fibres used in the study (Si, Mg, Ca, and Fe), elements that are known to substitute into amphiboles (Mn, Al, and Ti), and elements that are part of the biological matrix and play key roles in maintaining homeostasis and tumour microenvironment (Na, K, and P).

The proof-of-concept data present an alternative to existing approaches for fibre characterisation and may offer the possibility of conducting complementary LA-ICP-MS measurements within the same specimen. For example, identification of asbestos fibres in lung tissue may complement existing LA-ICP-MS measurements of candidate metallodrugs in lung tumours (Greenhalgh, Karekla *et al.*, 2020; Karekla *et al.*, 2017). It is estimated that only six of approximately 400 fibre types present in nature are regulated under the generic name of asbestos (Carbone *et al.*, 2019). Many more potentially carcinogenic fibres are unregulated and continue to cause human exposure and mesothelioma. Future multi-elemental LA-ICP-MS analysis of previously unstudied, candidate fibres would help to elucidate their role in the development of mesothelioma and other asbestos-related lung diseases.

The data presented herein reflect the hypothesis that LA-ICP-MS has the potential to screen for the presence of asbestiform and non-asbestiform fibres in more mesothelioma samples. The work sets the basis for future multi-element analysis carried out on more complex samples, such as 3D mesothelioma models and human tissue samples.

Chapter 5 LA-ICP-MS Imaging of 3D Malignant Pleural Mesothelioma Models

The work presented in this chapter was carried out in collaboration with Loughborough University

5.1 Introduction

5.1.1 Introduction to the chapter

The use of three-dimensional (3D) models has gained popularity in the last decade and it is now one of the fastest growing experimental approaches in life sciences (Ravi *et al.*, 2015). MPM is characterised by locally aggressive disease during tumour development, which is then followed by specific symptoms of disease (Cramer *et al.*, 2019). The tumour has been reported to form a 3D mass that reportedly generates aggregates in the pleural fluid (Broaddus, Follo, & Barbone, 2017). The 3D morphology, that develops from a 2D pleural monolayer, may be the underlying issue in terms of chemoresistance associated with MPM (Barbone *et al.*, 2016). This disease manifestation confirms that a biologically relevant 3D model of MPM is of particular significance.

Employing 3D models within the research workflow offers another avenue of study in various research areas. These models have several benefits compared to 2D monolayers, especially in the study of mechanisms of cell death (Follo *et al.*, 2016), drug development and combination therapies (Barbone *et al.*, 2016), gene expression (Barbone *et al.*, 2016), biomarker identification (Kanellakis *et al.*, 2020), tumour microenvironment (Cramer *et al.*, 2019), and precision medicine (Mazzocchi *et al.*, 2018). Some of the most established benefits of 3D cell cultures include a more accurate representation of the *in vivo* cytoarchitecture, cell-to-cell and cell-to-extracellular matrix interaction, efficient reproduction of tumour-like microenvironment (Webber, Yeung, & Clayton, 2015) (*i.e.,* hypoxic core, apoptosis-resistance, presence of resident cells) and the possibility of maintaining organotypic explant cultures (Ravi *et al.*, 2015).

Many different methods of modelling mesothelioma in 3D are now established, both *in vitro* and *ex vivo.* These are ideally suited for studying MPM and have been employed by different research groups throughout the years. The use of spheroids (*e.g.,* hanging drop, liquid overlay method etc.), organoids (*e.g., ex vivo* tumour spheroids), and gel-based models (*e.g.,* Matrigel, collagen, agarose etc.)

are amongst the most extensive choices, each presenting advantages and disadvantages depending on the application.

For example, a study by Cramer *et al*., (2019) has explored four different types of 3D MPM models to study the link between the epidermal growth factor receptor (EGFR) and photodynamic therapy efficacy in MPM, including agarose models, agarose/collagen I combination, hanging drop method, and a Matrigel based model. The group has reported that the mesothelioma cells tend to poorly proliferate when employing the first two methods, whilst the spheroids formed using the hanging drop method are generally too inconsistent for future analysis. The Matrigel-based model was reported to be the most efficient in recapitulating the *in vivo* environment relevant for this study (Cramer *et al.*, 2019). Nevertheless, the MCS approach remains the most widely employed model in the drug evaluation field (Lazzari, Couvreur, & Mura, 2017).

Alternatively, precision medicine and targeted therapy studies tend to use 3D tumour organoids or tumours fragments directly from fresh tumour biopsies to provide patient-specific models. These models act as essential tools in treatment optimisation prior to initiation of therapy in mesothelioma patients (Mazzocchi *et al.*, 2018; Nagle *et al.*, 2018).

There is a limited number of MPM models that involve the presence of asbestos or other types of MF. These models are mostly represented by 2D monolayers of mesothelial cells, such as Met-5A cells, exposed to various types of MF, which investigate cytotoxicity of the fibres and post-exposure cellular response MF (Casalone *et al.*, 2018). Pleural and peritoneal mesotheliomas have also been induced in rodents following exposure to erionite or asbestos fibres (Robinson *et al.*, 2011). However, animal models are costly and ethically challenging (Van Norman, 2019).

To our knowledge there is no current *in vitro* 3D model of mesothelioma containing asbestos fibres. Although the patient-derived *ex vivo* cultures might have fibres present, in this instance these are not considered purely *in vitro* models. There are a few possible explanations for the lack of 3D co-cultures of

mesothelioma cells with MF. Firstly, research-grade MF can be hard to obtain and pose high H&S risks. Secondly, the addition of MF requires adjustments to the current protocols and the model development can be expensive and time-consuming. Lastly, most *in vitro* studies use tumour models grown from mesothelioma cells, in which case the cell-asbestos fibre interaction might not be required.

Given the lack of available options, the first step was to develop a 3D MPM model consisting of mesothelioma cell lines co-cultured with different types of MF, that resemble the *in vivo* cell and asbestos fibres environment. It is essential to use MPM cells as a biological matrix which have been shown previously to yield elemental background signals comparable to patient-derived samples. Additionally, the identification of MF by LA-ICP-MSI in 3D models offers critical information on how the MF respond to the sample preparation steps (*i.e.,* embedding, sectioning), as well as the importance of the spatial orientation of these MF in regard to the sectioning plan. Based on the previous knowledge presented earlier, as well as several optimisation steps, a suitable 3D model was developed for LA-ICP-MS analysis.

The limited size of the established 3D models can be an impediment when analysing by LA-ICP-MSI. Despite this, the technological developments in the recent years and the expansion of 3D models, have allowed LA-ICP-MSI to be employed in the study of trace element distribution within 3D cellular cultures. For example, one group has monitored platinum distribution across a clump of multiple 3D tumour spheroids using a 10 µm spot size (Theiner *et al.*, 2016). Flint *et al.,* (2020) have also employed LA-ICP-MSI to investigate Mg, Zn, and Cu distribution across an aggregated 3D cell culture adenocarcinoma model (Flint *et al.*, 2020). The models presented by both groups were reported to be larger than 500 µm in diameter.

Sample preparation for LA-ICP-MS analysis is of major importance and the optimal sample preparation strategy is still yet to be defined. Additionally, to increase the clinical applicability, sample preparation must be consistent or similar to current protocols employed in clinical settings. There are a few sample

preparation combinations, fit for different purposes, but there is one that has emerged as the current gold standard: formalin fixation and paraffin embedding (FFPE). There are several advantages to using this method, but in terms of metallomics studies, the substantial number of sample preparation steps has been reported to heavily influence the signal and distribution of alkaline metals (Bonta *et al.*, 2016). Conversely, unfixed, snap-frozen samples have been shown to provide the most accurate means of analysis of metals in tissue samples and therefore represent the actual *in vivo* conditions in the best way (Bonta *et al.*, 2016). The main disadvantage of using snap frozen samples is that, due to the low temperatures, the samples can be harder to section into thinner sections (2-5 µm) and as serial sections. In terms of LA-ICP-MS analysis on snap-frozen samples, there have been reports of analysis on sections ranging from 20 µm (Theiner *et al.*, 2016) to 10 µm (Bonta *et al.*, 2017; Flint *et al.*, 2020).

In the current work, the 3D MPM model was treated as a tumour tissue and the sample preparation steps were optimised for prime signal distribution across the sample. The spot size, laser pulse energy, and repetition rate play an important role and were all optimised accordingly. At this stage, the focus has been to investigate the correlation between spot size, signal intensity, and time of acquisition. It is essential to optimise and understand the processes and parameters during the laser ablation stage, and how these could influence the ICP-MS signal, and thereby affect the accuracy of MF detection.

Similar to the work presented in Chapter 4.2.1-2, optimisation was based on the ^{24}Mg signal yielded by the 3D samples. Subsequent multi-elemental analysis was carried out on samples co-cultured with four different MF using the same high-speed, dual-chamber instrumentation presented in the previous chapter. The analysis was carried out in triplicates for each target element and fibre type. All the images selected to be included in the results section were representative of the overall data.

In order to efficiently analyse multiple elements in a single cycle, the short sample pulse transmitted by a fast-washout ablation cell to the ICP-MS must be detected by a fast mass analyser. In this work, detection of the full mass range of a blind

sample was possible by using the highspeed LA platform coupled to the prototype ICP-TOFMS presented in the previous chapter (Instrument 2). Data analysis focused on the main isotopes present within MF and biological matrix in order to investigate whether different MF could be correctly identified from one another solely based on the LA-ICP-TOFMS signals. The fibres were successfully categorised as amosite based on the signal intensity yielded by the main nominal components of amosite. LA-ICP-MS Data acquisition and was performed equally in the Chemistry Department at Loughborough University by Miss Oana M Voloaca and Mr Calum Greenhalgh. ROIs selection, data analysis, and data interpretation were carried out by the author, Oana M Voloaca.

The LA-ICP-TOFMS analysis was carried out by Calum Greenhalgh at the NU Instruments laboratories in collaboration with Dr Amy J Managh, Phil Shaw and Ariane Donard using a novel LA-ICP-TOFMS prototype instrumentation. Sample preparation and data interpretation were conducted by the Oana M Voloaca.

5.1.2 Hypothesis

The first hypothesis of this chapter was that employing 3D MPM models closely recapitulates the preparation and analysis steps of human clinical samples. Secondly, it was hypothesised that different MF can be detected and correctly identified within 3D MPM models based on the nominal composition using LA-ICP-MSI and LA-ICP-TOFMS imaging, respectively.

5.1.3 Aims of the chapter

The initial aim of this chapter was to develop a more complex 3D MPM model that would be suitable for LA-ICP-MS analysis and will recapitulate the human tumour samples collected from MPM patients. Secondly, the aim was to optimise the sample preparation and LA-ICP-MS analysis for maximum elemental intensity signals. Finally, the aim was to employ LA-ICP-TOFMS analysis to correctly identify the MF within a blind sample based on pseudo- simultaneous detection of the elements between mass 23 (Na) and mass 238 (U).

5.2 Results and Discussion

5.2.1 Development of a 3D mesothelioma model

5.2.1.1 Multicellular spheroid model

Multicellular tumour spheroids (MCS) are scaffold-free, spherically self-assembled aggregates of malignant cells displaying an intermediate complexity between 2D monolayers and animal models. MCS present a number of advantages over other 3D models. Firstly, the presence of a hypoxic core resembles the avascular region characteristic to the tumour microenvironment (Figure 5.1 E-H). *In vivo,* malignant structures that develop in between capillaries receive nutrients and oxygen through diffusion, from the exterior towards the core (Saggar *et al.*, 2013). In this work, MCS were developed in 96 well plates coated with a hydrophilic, neutrally charged hydrogel coating which inhibited specific and nonspecific cellular binding. This in turn forced mesothelioma cells into a suspended state which enabled 3D MCS to start forming over time (≈6 days). MSTO-211H and NCI-H28 MCS developed after 7 days in culture are presented in Figure 5.1. The biphasic cell line formed larger MCS (≈ 900 µm) which held a spherical shape in both untreated (Figure 5.1 A) and treated cultures (Figure 5.1 B). Contrariwise, NCI-H28, cells of epithelioid origin, successfully formed MCS in the untreated cultures (Figure 5.1 C), but the addition of actinolite fibres impeded the formation of MCS (Figure 5.1 D). Despite being more biologically relevant and presenting a characteristic tumour microenvironment, the 3D MCS co-cultured with MF tended to be mechanically unstable and inconsistent for further manipulation including fixation, embedding, and sectioning.

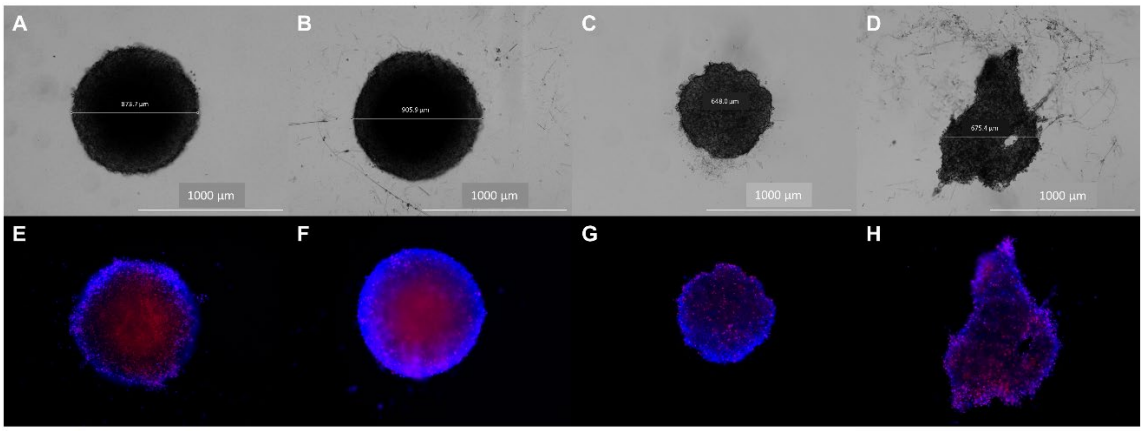

Figure 5.1 Human malignant mesothelioma 3D multicellular spheroids (MCS). Top (A-D) Brightfield microscopy 40X. Down (E-H) Hoechst 33342 and Propidium Iodide staining of the MCS. (A) Brightfield image of an untreated MSTO-211H MCS with a diameter of 873.7 µm. (B) Brightfield image of a MSTO-211H MCS co-cultured with 3 µg/mL actinolite fibres solution with a total diameter of 905.9 µm. (C) Brightfield image of an untreated NCI-H28 MCS with a diameter of 648.0 µm. Human epithelioid mesothelioma cells tend to form smaller, more compact MCS compared to the ones formed by the MSTO-211H biphasic cells. (D) Brightfield image of NCI-H28 cells co-cultured with 3 µg/ mL actinolite fibres solution. The cells and fibres aggregate but fail to form a spherical MCS like the one presented in panel C. Median diameter of the aggregate reaches 675.4 µm. (E-H) present the corresponding fluorescent images after staining with Hoechst 33342 and Propidium Iodide (Texas red- hypoxic core, DAPI blue- viable outer layer).

5.2.1.2 Organ-dot

The organ-dot model was developed in house as a novel air-liquid interface model. The model is in principle a reverse hanging drop model, grown on sterile, specifically designed, cellular inserts. By carefully pipetting a low volume of cell or cell-fibres suspension, the malignant cells were allowed to aggregate and form 3D structures within the drop. Apart from the 3D structure, the model displayed the typical regions associated with cancerous structures (i) a necrotic core (red), which has a high rate of apoptosis due to low oxygen and nutrients levels; (ii) a non-proliferative region, where the cells display a state of dormancy as a result of hypoxia; and (iii) a proliferative edge (blue) (Flint *et al.*, 2020) (Figure 5.2). The advantages of this model were that it allowed for fibre-mesothelioma cells co-culture and required limited sample preparation steps. However, the challenges

revolved around consistency of sample thickness and background interference from the membrane material.

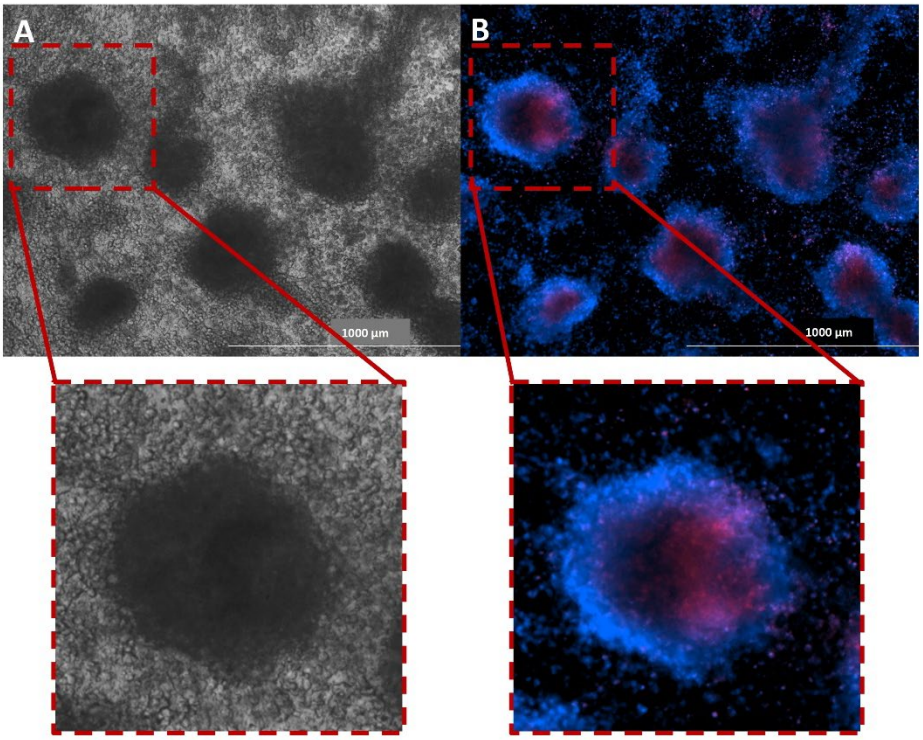

Figure 5.2 Mesothelioma organ-dots. (A) Brightfield images of the 3D organ-dots. (B) Fluorescent imaging following staining with Hoechst 33342 and Propidium Iodide (Texas red- hypoxic core, DAPI blue- viable outer layer).

5.2.1.3 Cell-plug

Investigating whether LA-ICP-MSI could be applied for 3D samples was an essential proof-of-concept step, before advanced tissue analysis. A 3D model does not only mimic the cellular environment of a MPM tumour, but it also replicates the spatial orientation of the MF that become lodged within the serosal surface of the lungs prior to tumour formation. However, developing a novel 3D model for such a niche application can be expensive and time-consuming. The use of cell pellets or 'cell-plugs' containing different types of MF is an easy, affordable alternative to more complex gel, scaffolds, or organoid 3D models. Moreover, most 3D models are no larger than 1 mm. Human mesothelioma tumours vary in size but average around 60 mm (He *et al.*, 2020). The model developed for this study was around 50 x 20 mm and contained over 25 million

mesothelioma cells mixed with various concentrations of MF. Cell number, MF dose concentration as well as embedding media and sample preparation steps were optimised.

The model was developed using plastic moulds of different shapes and sizes (Figure 5.3 A-G). A detailed explanation of the model is given in Chapter 2, Section 2.2.6.4 but briefly the cells were transferred to a smaller mould and snap frozen in liquid nitrogen (Figure 5.3 A-C). The frozen pellet was then embedded in hydroxypropyl methylcellulose/polyvinylpyrrolidone (HMPC/PVP) media, and subsequently snap frozen in liquid nitrogen. HMPC/PVP media was the media of choice as it can be used at low temperatures (4°C) helping preserve the snap-frozen cell pellet, exhibited adequate structural integrity during cryosectioning at -18°C, and adhered well to both glass and plastic slides whilst retaining the cell-plug morphology. During the optimisation steps, gelatin and optimal cutting temperature (OCT) media were also considered as possible embedding media. Gelatin had to be prepared at 45°C and remained in liquid form down to 37°C. This high temperature of the gelatin affected the structure of the freshly snap-frozen cell pellet, and this option was therefore discarded. OCT is generally the preferred choice for sectioning at low temperatures using a cryostat as it is cheap and widely available. However, using OCT as embedding media resulted into increased fragmentation of the section during cryosectioning and low adherence between the section and slides, particularly the plastic ones. Consequently, HMPC/PVP media was the ideal option.

Cell-plug sections within the HMPC/PVP media are presented in Figure 5.3 H (MSTO-211H) and Figure 5.3 I (NCI-H28). The cell layer can be visually identified by the slight yellow appearance of the cell plugs within the white opaque embedding media, conferred by the lipid bilayer that forms the cellular membrane (Qiu *et al.*, 2018). Following the sample preparation, the cell plugs were serial-sectioned at -18°C and stored at -80°C until LA-ICP-MSI analysis.

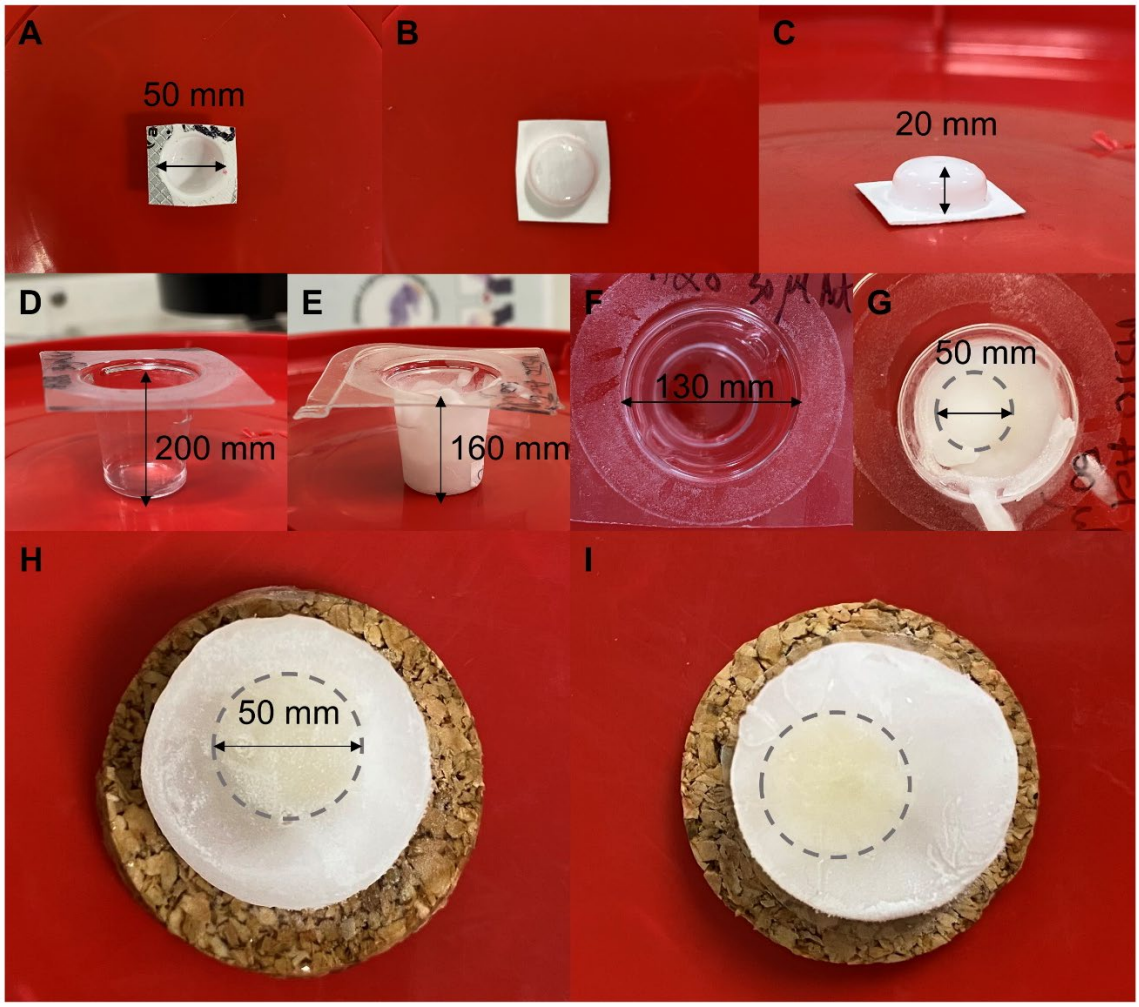

Figure 5.3 Development of a 3D cell-plug. (A-D) Plastic mould used to embed snap frozen cell plugs in HMPC/PVP media. (E-G) Plastic mould used to snap freeze cell pellets spiked with MF into cell plugs. MSTO-211H (H) and NCI-H28 (I) cell plugs embedded in HMPC/PVP media, ready for cryosectioning. The lipid bilayer that forms the cellular membrane confers the slight yellow appearance of the cell plugs within the white opaque embedding media.

5.2.2 Histology of MPM cell plugs

Haematoxylin and eosin (H&E) tissue staining is one of the most widely employed histological techniques and it allows the study of cells and tissues characteristics and structure. Haematoxylin is deep blue/purple, positively charged, cationic dye which reacts to negatively charged, basophilic cell components, such as nucleic acids. In a typical tissue, this aluminium-based dye stains the nuclei blue. Eosin is pink and stains proteins non-specifically, staining the cytoplasm and extracellular matrix with different degrees of pink intensities (Fischer *et al.*, 2008).

The histology of an actinolite treated cell-plug section is presented in Figure 5.4. The section was stained with H&E. The overall size and shape of MPM cells appear to be often abnormal. Moreover, some MPM cells are characterised by a large nucleus, having an irregular size and shape, with prominent nucleoli, and a scarce and intensely coloured cytoplasm (Figure 5.4 B-C). Multinucleation can also be observed in the MPM cells. Identification of MF, in this case actinolite fibres, is difficult in H&E images due to size, orientation, and the compact cellular layer. Actinolite fibres were identified in Figure 5.4 D, as pointed out by the dotted circles.

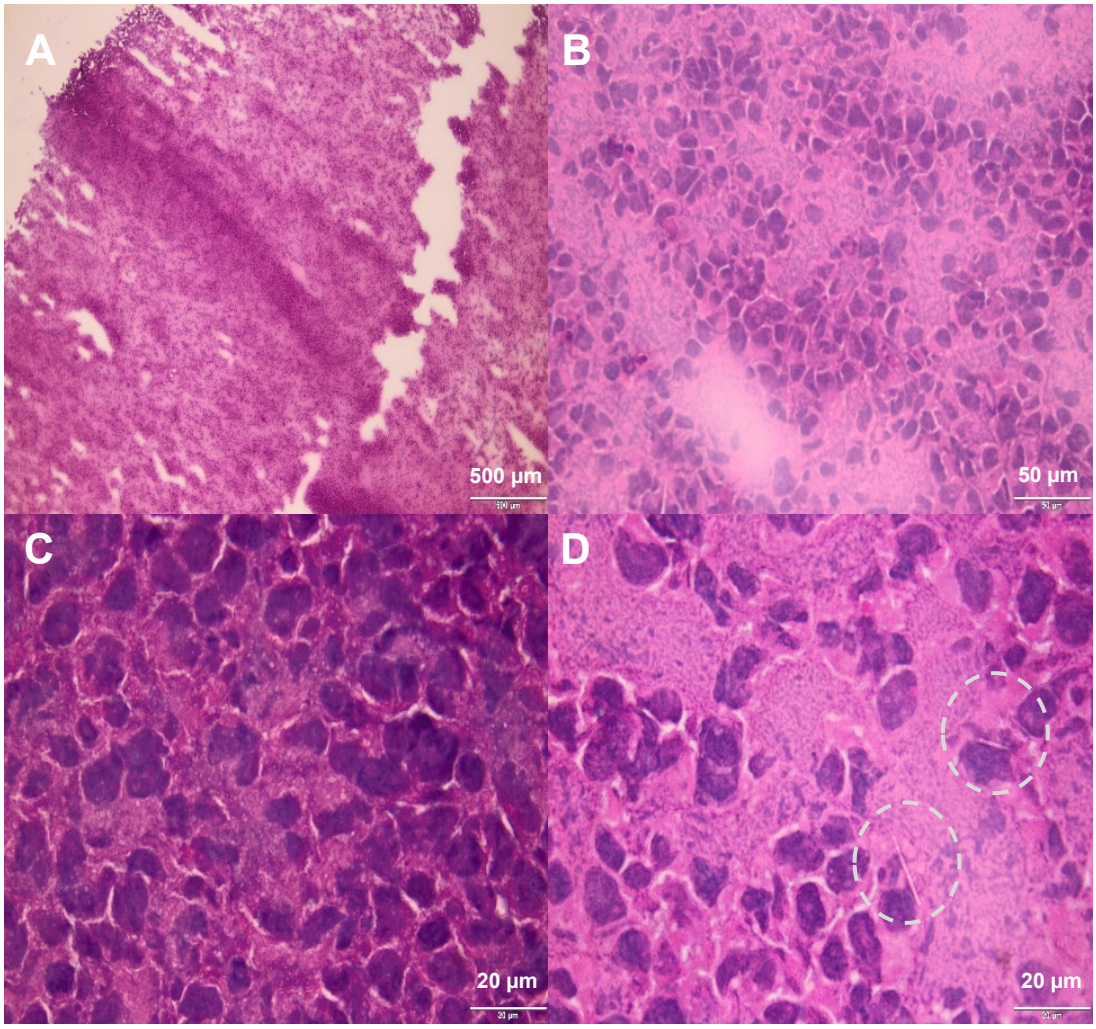

Figure 5.4 Histological staining of an actinolite treated cell-plug section. A- H&E staining x 40 magnification; B- H&E staining x 200 magnification; C- H&E staining x 400 magnification; D- H&E staining x 400 magnification with actinolite fibres. Actinolite fibres are shown by the dotted circles.

5.2.3 The Impact of laser fluence

The fluence is sample-specific, meaning that the laser pulse energy needs to be optimised for each sample material. Despite the 3D samples being similar to the 2D samples analysed previously, there are a few characteristics of the 3D sections that required attention in terms of laser pulse energy optimisation. Firstly, the cell-plug is composed of compact MPM cells, allowing for a more uniform distribution of cellular matrix across the slide, with a constant thickness across the sample. Secondly, the 2D samples contain more integral MF that can require higher laser energy to be spatially resolved. In contrast, given the sample preparation steps, the 3D sections were expected to contain more fibre fragments.

High laser energy values (45-55% e) were chosen to ensure complete ablation of the sample, including the acid-resistant asbestos fibres. Total ablation was confirmed through microscopic observation of the resulting laser craters. A spot size of 2 µm was used in these experiments. The laser fluence values ranged between 18 J/cm^{-2} (Figure 5.5 A, D), 20 J/ cm^{-2} (Figure 5.5 B, E), and 22 J/ cm^{-2} (Figure 5.5 C, F). Full ablation after a single cycle of analysis was achieved for all three values. A laser fluence value over 10 J/cm^{-2} is classed as high (Van Acker *et al.*, 2019). It is important to reach a balance between total sample ablation, optimal signal intensity, and laser overheating.

It has been reported that increasing the laser fluence leads to an increase in explosive boiling and plasma shielding effects, which in turn can affect the overall ablation efficiency (Markopoulos *et al.*, 2016). Moreover, high energy can lead to overheating and possible ablation of the plastic slide surface and consequent interferences. Examples of LA-ICP-MSI data collected after ablation with different laser fluence are presented in Figure 5.5 A-F. Actinolite fibres were spatially resolved in all three examples and there were no significant signal intensity differences between the settings (4-fold or more). Less ridges were present in the LA-ICP-MSI image when employing a softer laser fluence (Figure 5.5 A, D) suggesting that high laser energies can lead to overlap onto the neighbouring spots. Intensity scale bar was adjusted in Figure 5.5 D-F for emphasis of actinolite

fibres ^{24}Mg signal. Following this optimisation step, all analysis was carried out using a fluence of ≈18 J/cm^{-2}, which ensures total sample ablation, whilst avoiding overheating and plasma shielding effects.

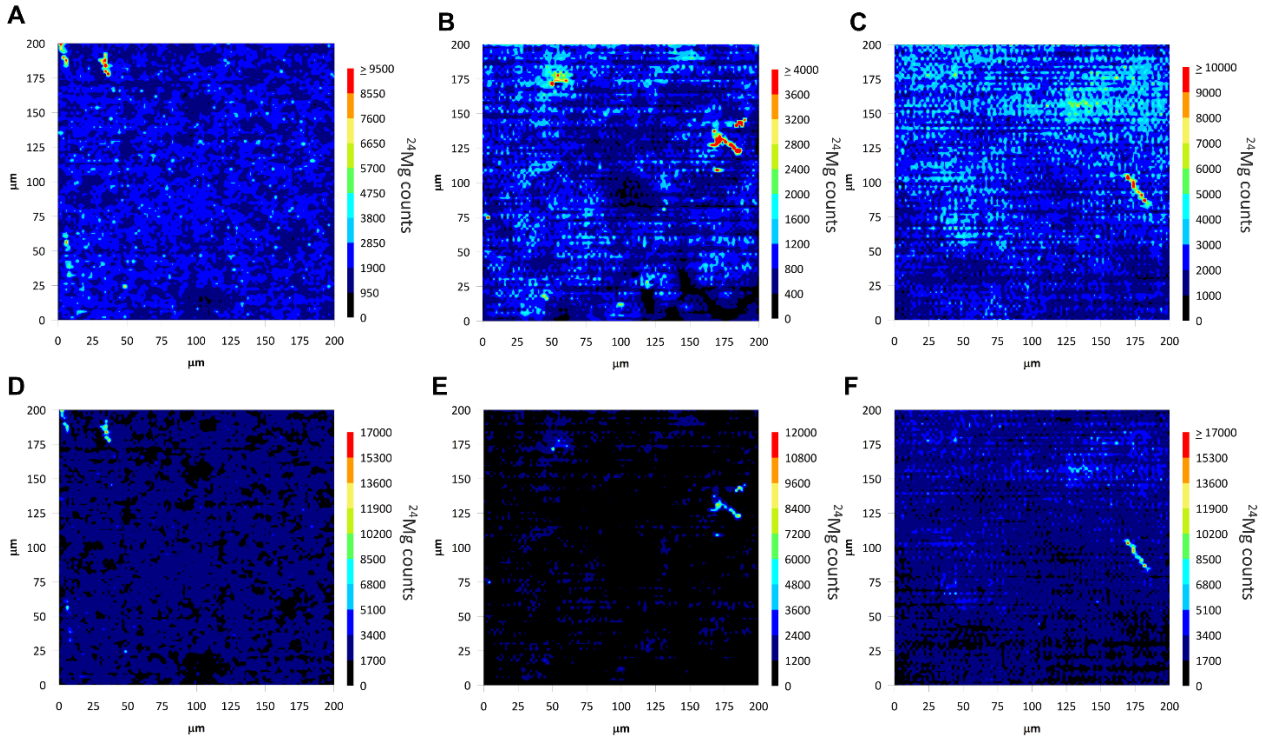

Figure 5.5 Optimisation of laser fluence. LA-ICP-MS data acquired with (A) ≈18 J/cm^{-2}, (B) ≈20 J/cm^{-2}, and (C) ≈22 J/cm^{-2}. The scale bar values were adjusted in D-F to emphasise the magnesium signal yielded by the actinolite fibres. Laser energy 45, 50 and 55% respectively. Spot size 2µm.

5.2.4 LA-ICP-MS serial ablation

The biological samples used for LA-ICP-MSI are normally sectioned between 5-20 µm (Neumann *et al.*, 2020a; Theiner *et al.*, 2016). Thin sections like this are generally fully ablated within a few laser shots (*i.e.,* during one cycle of analysis) (Limbeck *et al.*, 2015). However, this is determined by the sample type, instrumentation, and laser energy.

On one hand, serial ablation allows for optimisation of the sample thickness. Full ablation of the selected area is generally desired for LA-ICP-MSI data. Initially, a 20 µm thick sample section was ablated to optimise the sample thickness. It was

observed that biological material was left post ablation (Figure 5.6 A) which raised the interest in serial ablation of thicker sections to gain insight into fibre orientation.

Based on these findings and previous issues encountered with cryosectioning of thin sections (5-10 µm), the sample thickness was optimised to be 12 µm. This thickness resulted in ease of manoeuvring of the sections and increased adherence of the sections to the plastic slides. The samples were also fully ablated during one cycle of analysis, with no material left post-ablation using the same laser fluence (≈18J cm^{-2}) (Figure 5.6 B).

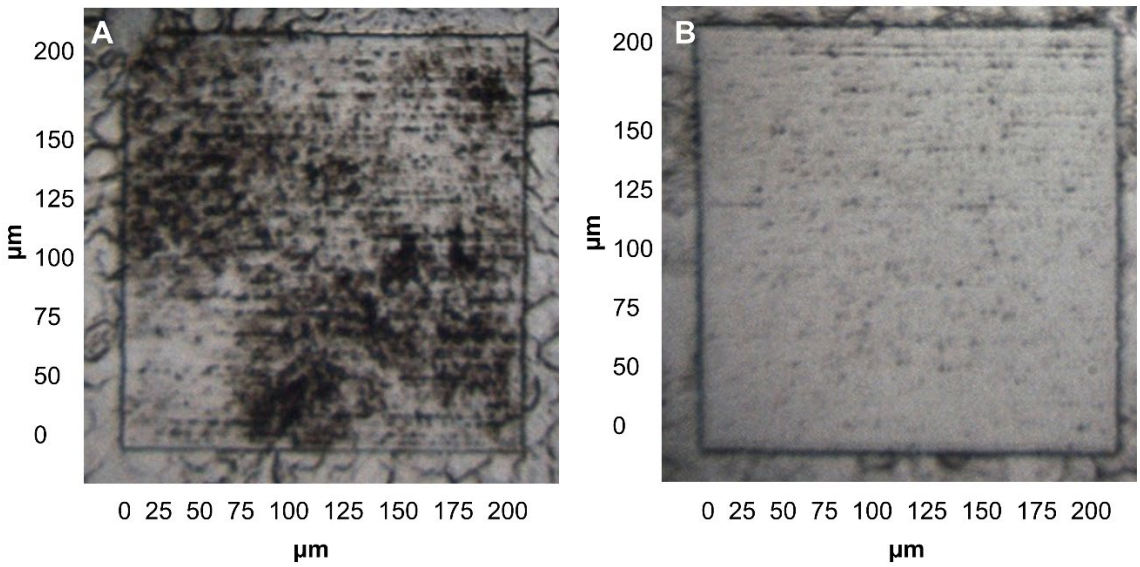

Figure 5.6 Post-ablation brightfield microscopy images of a MSTO-211H cell-plug section. (A) 200 x 200 µm area after LA-ICP-MS analysis of a 20 µm thick section. Note the biological material left post-ablation. (B) 200x 200 µm area after LA-ICP-MS analysis of a 12 µm thick section. The sample was fully ablated in one cycle of analysis. Both samples were ablated using the same laser pulse energy.

On the other hand, serial analysis of the same area proved to offer insight into the spatial orientation of the MF within the 3D cell-plugs. Sectioning the cell-plugs at low thicknesses (5-10 µm) resulted in fragmentation of transversely positioned MF. In thick sections (>50 µm), MF are able to maintain the spatial orientation as shown in the figures below. Figure 5.7 presents a series of four serial ablations of the same 200 x 200 µm area of a 50 µm-thick MSTO-211H cell-plug section.

Similarly, Figure 5.7 presents LA-ICP-MSI data of multiple ablations of a 50 µm-thick NCI-H28 cell-plug section. The same smaller area of each layer (80 x 80 µm) with identifiable actinolite fibres was zoomed in for comparison. These are presented underneath the full LA-ICP-MS image.

For instance, no actinolite fibres were detected within the small red square after the first ablation (Figure 5.7 A). High ^{24}Mg signal was given by a number of actinolite fibres following the second ablation of the same area (Figure 5.7 B). Different sections of the same fibres can be identified in Figure 5.7 C, suggesting a slanting orientation of the fibres within the section. Some signal yielded by the actinolite fibres was recorded following the last ablation (Figure 5.7 D). There was minimum to no signal yielded by the biological matrix at this stage.

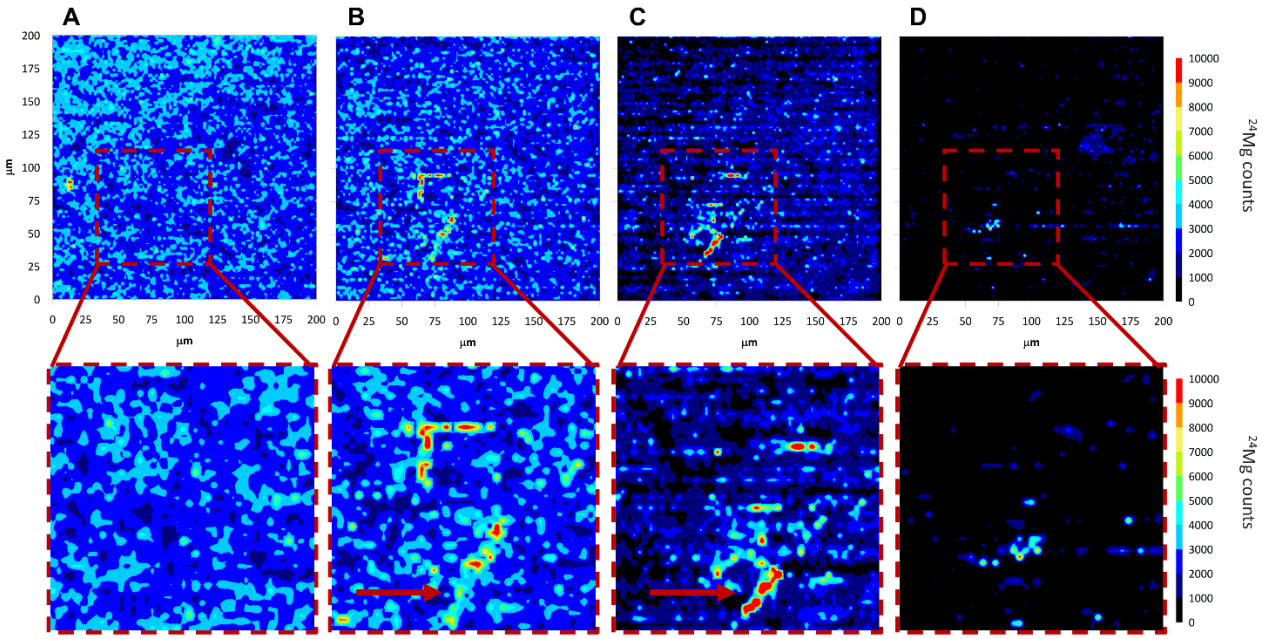

Figure 5.7 Serial ablation of a MSTO-211H cell-plug section. (A) First ablation of a 200 x 200 µm area. The red square focuses on a smaller area (80 x 80 µm) with no actinolite fibres identified after the first analysis. The images below offer a closer look of the same selected area for each layer. (B) Second ablation of the same section. Note the actinolite fibres present in the same selected smaller area. (C) Third ablation of the cell-plug section. Signal from the actinolite fibres was still registered within the same area, but the signal intensity differs based on the fibre orientation (shown by the red arrows). (D) Final ablation of the section. Some signal yielded by the actinolite fibres was acquired. There was minimum to no signal yielded by the biological matrix at this stage. Laser fluence ≈18 J/cm^{-2}, spot size 2 µm, 20 Hz repetition rate.

A second example is presented in Figure 5.8 A-D. In this instance, actinolite fibres were identified after the first cycle of analysis (Figure 5.8 A). Signal from the same fibres was also recorded after the second ablation (Figure 5.8 B). The location and signal intensity presented in Figure 5.8 A-C suggest the presence of a long actinolite fibre, located transversely, as indicated by the red arrows. No significant signal was acquired following the last round of analysis (Figure 5.8 D).

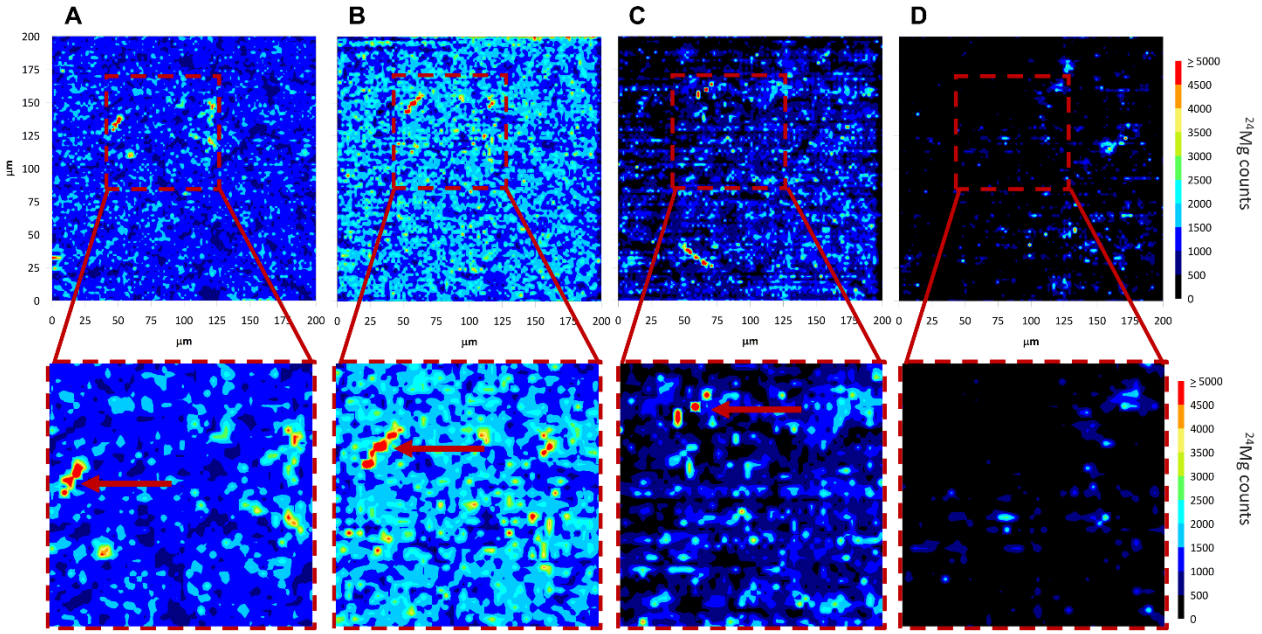

Figure 5.8 Serial ablation of a NCi-H28 cell-plug section. (A) First ablation of a 200 x 200 µm area. The red square focuses on a smaller area (80 x 80 µm) with identifiable actinolite fibres. The images below offer a closer look of the same selected area for each layer. (B) Second ablation of the same section. Note the ^{24}Mg signal recorded around the same zone, possibly from the same, long fibre. (C) Third ablation of the cell-plug section. Signal from the actinolite fibre was still registered within the same area, but the signal intensity differs based on the fibre orientation (shown by the red arrows). (D) Final ablation of the section. Minimum to no signal was registered after this cycle of analysis. Laser fluence ≈18 J/cm^{-2}, spot size 2 µm, 20 Hz repetition rate.

5.2.5 The link between spot size, signal intensity, and time of acquisition

There is a drive towards faster and higher resolution LA-ICP-MSI, employing spot sizes as small as 1-5 µm or even sub-micrometre sizes (Van Malderen *et al.,* 2020). In LA-ICP-MSI analysis, spatial resolution is determined by several factors, including the laser spot size (the lower the spot size, the higher the lateral

resolution and direction in which the laser travels across the sample (Seaman, 2017). Despite the benefits of high-resolution LA-ICP-MS, there is still some compromise regarding sample size, signal intensity, and time of acquisition.

For this part of the work, the ICP-MS signal intensity for ^{24}Mg, image resolution, and time of acquisition were monitored for two different spot sizes (1 or 2 μm diameter) applied to different sample surface areas (200 x 200 μm or 500 x 500 μm). The spot size, time of acquisition, crater dimensions, and laser fluence were all interlinked. Smaller spot sizes appeared to minimise the damage of the ablated surface, offering detailed, high-resolution LA-ICP-MS images, whilst maintaining sample architecture. Nevertheless, LA-ICP-MS sensitivity was inversely proportional to the size of the laser spot. The difference in ^{24}Mg signal intensity can be noted in Figure 5.9 vs Figure 5.10, and in Figure 5.11 vs Figure 5.12. The signal intensity, as shown on the scale bar on the right hand-side of the figure, was up to 7x higher for a 500 x 500 μm area ablated using a 2 μm spot size (Figure 5.10) compared to the signal acquired after ablating the same size are with a 1 μm spot size (Figure 5.9). Moreover, for smaller areas (200 x 200 μm) the signal intensity increased 10-fold when using a 2 μm spot size (Figure 5.12). A gradient effect was noted in Figure 5.9 most likely due to a shift in stage calibration caused by the long period of time required for data acquisition. This loss of calibration can have an effect on the Z position in opposite corners of the sample, leading to the gradient effect noticed in the figure.

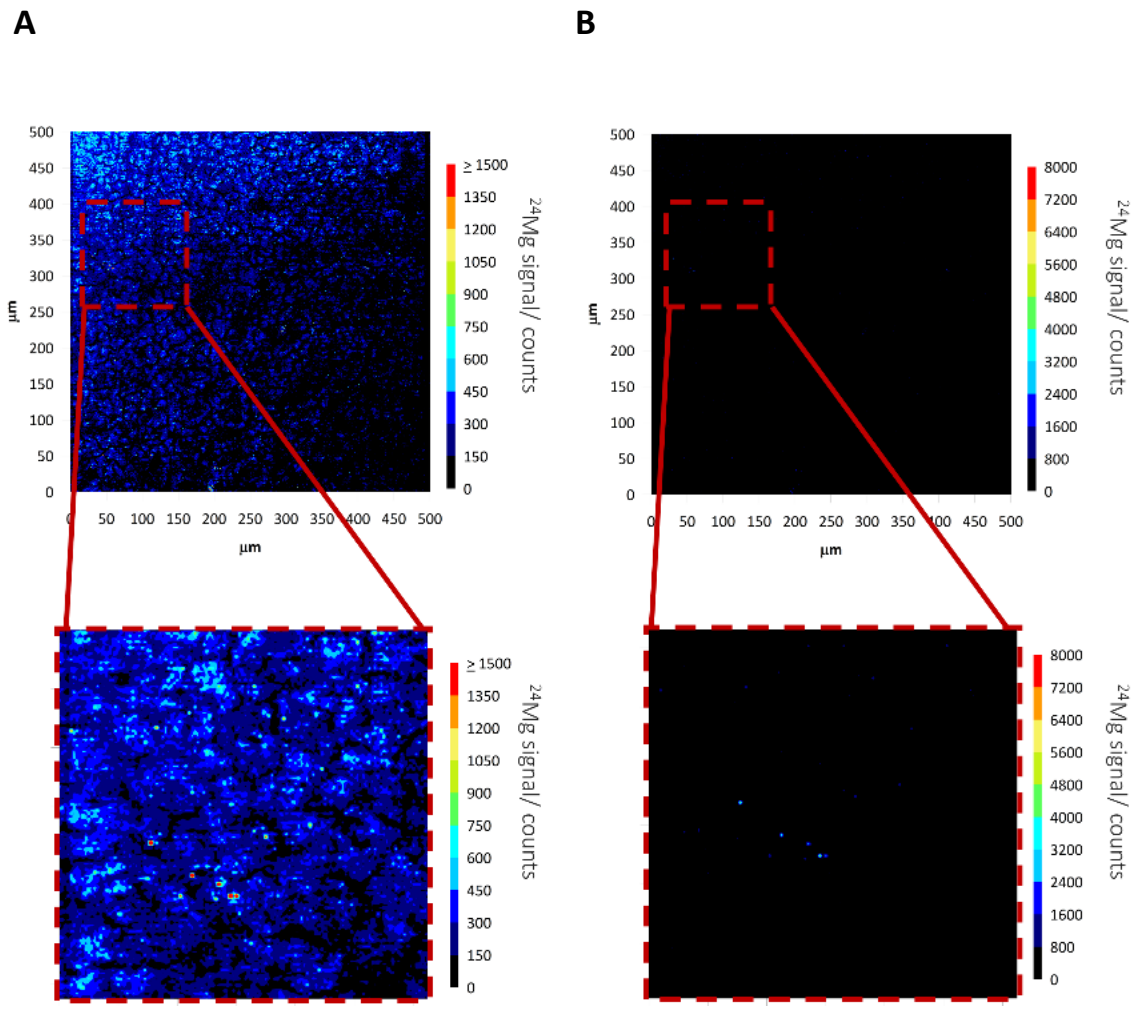

Figure 5.9 LA-ICP-MS analysis of a 500 x 500 µm area of an actinolite-treated MSTO-211H cell-plug using a 1 µm spot size. (A) Cellular matrix and actinolite ^{24}Mg signal distribution. (B) LA-ICP-MS data normalised against the cellular background to emphasise the signal yielded by the actinolite fibres. The red squares present ROIs containing actinolite fibres. A zoomed in version is presented underneath. Some small actinolite fibres were identified within the compact cell-plug.

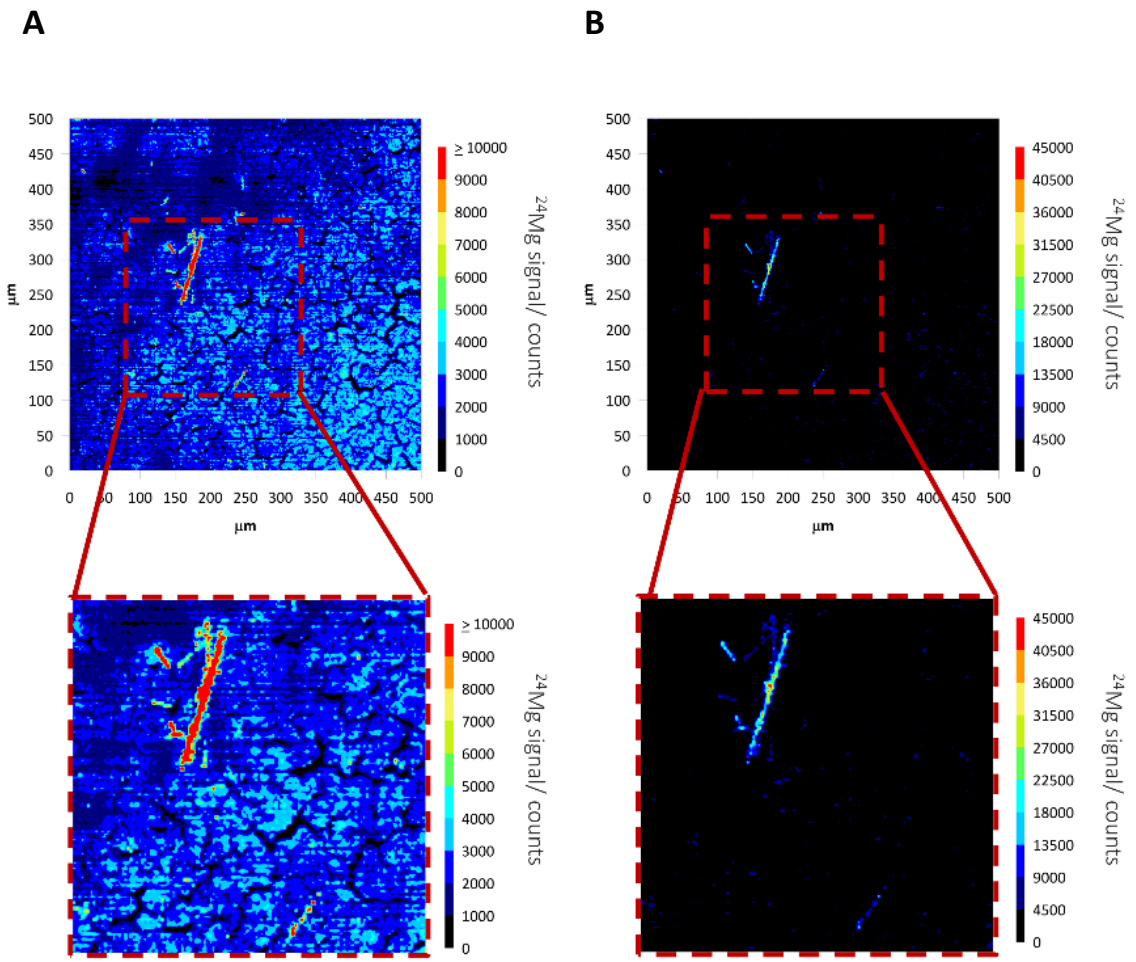

Figure 5.10 LA-ICP-MS images of a 500 x 500 µm area of an actinolite-treated MSTO-211H cell-plug using a 2 µm spot size. (A) Cellular matrix and actinolite ^{24}Mg signal distribution. (B) LA-ICP-MS data normalised against the cellular background to emphasise the signal yielded by the actinolite fibres. The red squares present ROIs containing actinolite fibres. A zoomed in version is presented underneath. Note the increased signal intensity range indicated by the scale bar (> 10000 ^{24}Mg signal/ counts).

The ability of current instrumentation to acquire data at cellular resolution was demonstrated in the previous chapter (Chapter 4, Section 4.2.2) and the time of acquisition was also mentioned. Indeed, using a smaller spot size can increase the level of detail presented in a LA-ICP-MS image and can be used to detect sub-micrometre fibre fragments, which can be otherwise overlooked (Figure 5.9). However, the total time of acquisition doubled as the spot size was reduced from 2 to 1 µm.

The total area that is selected for analysis is critical for this type of work. Compared to 2D samples, it has proven challenging to select ROIs containing MF as seen through the brightfield microscopy within the 3D cell-plugs. For these types of samples, a larger area can offer more information and help support the hypothesis. Nonetheless, ablating large surface areas is expensive and time-consuming. There is a fine line between attaining high resolution images, fast analysis, and relatively large sample surfaces.

For clinical samples, full sample analysis is recommended. However, for 3D sections a compromise can be made regarding spot size, time of acquisition, and surface area. A full cycle of analysis of a 500 x 500 µm surface area carried out with a 2 µm spot size took over 4 times the amount of time required to ablate a 200 x 200 µm area. The time of acquisition doubled again in order to acquire the data presented in Figure 5.9. In order to apply this technique in clinical settings, the time of acquisition has to be maintained within a feasible range (<4 hours).

Analysis was carried out with the same laser pulse energy. Based on the optimisation data presented below (Figure 5.11 and Figure 5.12), a 2 µm spot size was selected for future analysis. In terms of surface area, 400 x 400 µm areas were analysed in the following multi-elemental experiments.

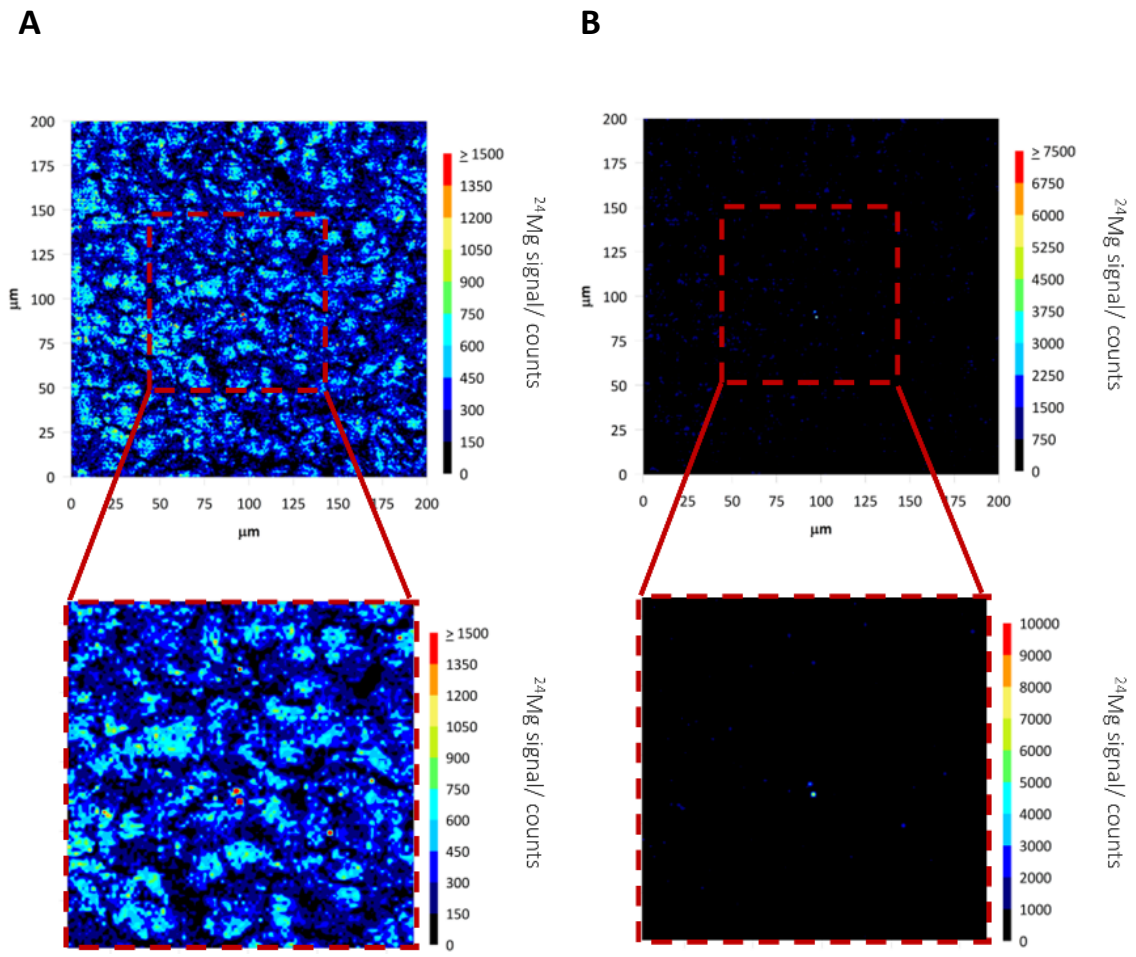

Figure 5.11 LA-ICP-MS analysis of a 200 x 200 µm area of an actinolite-treated MSTO-211H cell-plug using a 1 µm spot size. (A) Cellular matrix and actinolite ^{24}Mg signal distribution. (B) LA-ICP-MS data normalised against the cellular background to emphasise the signal yielded by the actinolite fibres. The red squares present ROIs containing actinolite fibres. A zoomed in version is presented underneath. Small actinolite fibres were identified as ^{24}Mg "hot-spots".

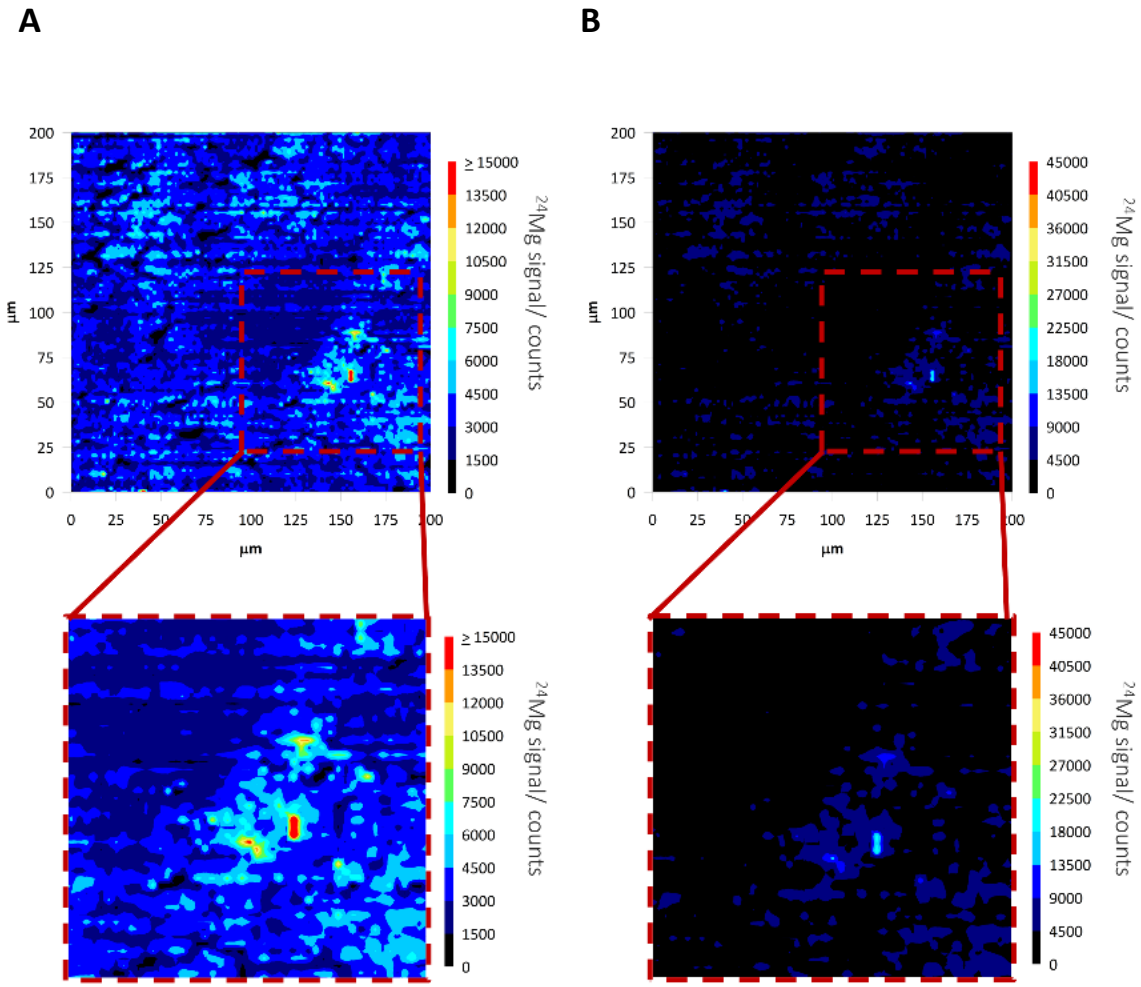

Figure 5.12 LA-ICP-MS images of a 200 x 200 µm area of an actinolite-treated MSTO-211H cell-plug using a 2 µm spot size. (A) Cellular matrix and actinolite ^{24}Mg signal distribution. (B) LA-ICP-MS data normalised against the cellular background to emphasise the signal yielded by the actinolite fibres. The red squares present ROIs containing actinolite fibres. A zoomed in version is presented underneath. Note the increased signal intensity range compared to the figure above indicated by the scale bar (> 15000 ^{24}Mg signal/ counts).

5.2.6 Treatment and dose optimisation

As a key intermediate step between 2D cellular analysis and complex human tissue analysis, the analysis of 3D models required the presence of at least one MF per selected section in order to prove the hypothesis. Being the first study to investigate the possibility of detecting MF in a novel MPM model, fibre dosage had to be optimised based on LA-ICP-MS signal. The MF dose range was selected based on the total volume of cells. In order to recapitulate the clinical

scenario, fibre density had to include at least 2 asbestos bodies per 200 x 200 µm ablated section. Figure 5.13 presents the LA-ICP-MSI data collected after analysis of different MSTO-211H cell-plugs treated with different concentrations of actinolite solution. The cell-plugs contained either a low-dose of actinolite (30 µL of 1 mg/mL stock), medium-dose (60 µL of 1 mg/mL stock), or high-dose (100 µL of 1 mg/mL stock\). Limited signal above the cellular matrix was detected in the low-dose model (Figure 5.13 A). Areas with high ^{24}Mg signal intensity or ^{24}Mg "hot-spots" are shown in Figure 5.13 B, which can indicate the presence of actinolite fragments as a result of the cell-plug cryosectioning. A cluster of actinolite fibres was identified in Figure 5.13 C, the high dose model. The presence of MF in small sections is essential in supporting this study's hypothesis, before progressing to the analysis of larger areas of human tissue samples. Hence, a high-dose model was selected for the following multi-elemental LA-ICP-MS analysis of the 3D models.

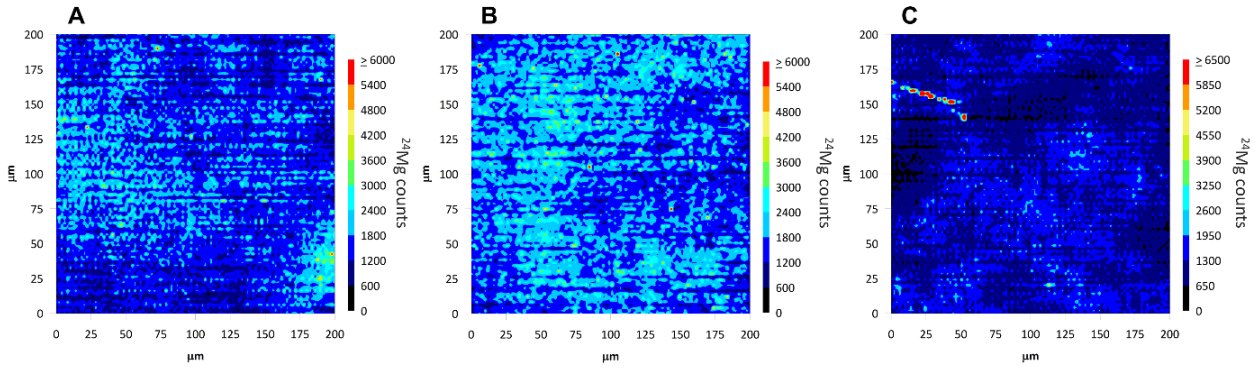

Figure 5.13 Mineral fibre dose optimisation based on the LA-ICP-MS analysis. (A) LA-ICP-MS image of a low-dose cell-plug section (30 µL) (B) LA-ICP-MS image of a medium-dose cell-plug section (60 µL). Some ^{24}Mg "hot spots" are present within the cellular background which can indicate the presence of actinolite fragments. (C) LA-ICP-MS image of a high-dose cell-plug section (100 µL). Actinolite fibres can be identified based on the high ^{24}Mg signal.

5.2.7 Multi-elemental LA-ICP-MS analysis

Once the laser ablation parameters were optimised for optimal generation of sample aerosols, the attention focused on identifying different MF and MF fragments within 3D cell-plugs sections based on Mg, Si, and Fe content. In a similar way to the multi-elemental work presented in Chapter 4.2.4, samples were

prepared on plastic slides for minimisation of background signals originating from the support material and high sensitivity trace element measurements with optimal accuracy. Analysis was performed in triplicates for each isotope (n=3). A total of 45 sections were ablated in order to acquire the desired data. The chosen LA-ICP-MS images are representative for all the repeats. LA-ICP-MS measurements provided signals above background level for all selected elements on most of the samples analysed, except for silicon detection in the control sample and the amosite-treated cell-plug.

5.2.7.1 Untreated

An untreated MSTO-211H cell-plug (*i.e.,* no added MF) was used as a negative control to prove the specificity of LA-ICP-MSI to various MF. In order to investigate this hypothesis, a 400 x 400 µm surface area containing a visible impurity was selected for analysis based on iron signal (Figure 5.14 A). No ^{57}Fe signal was registered following the ablation process (Figure 5.14 B-C).

Similar to the results on 2D samples presented in Chapter 4.2.4, the MPM cells used as a biological matrix yielded ^{24}Mg signal above the background, with the cell clusters seen in Figure 5.14 D corresponding to higher magnesium intensities presented in Figure 5.14 E. The scale bar was adjusted in Figure 5.14 panel C and F for consistency with the rest of the LA-ICP-MS data. Silicon analysis was carried out but failed to produce above-the threshold signal intensity (data not presented).

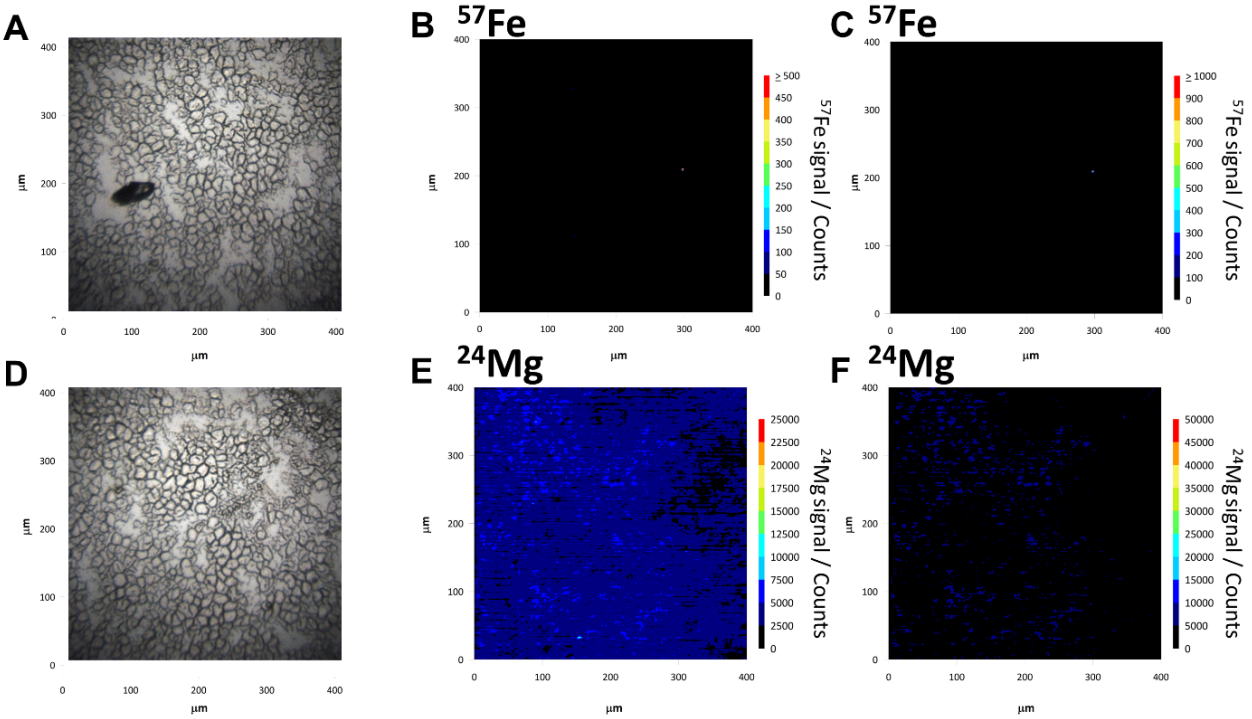

Figure 5.14 LA-ICP-MSI of a MSTO-211H cell-plug section. (A) Brightfield image of the 400 x 400 µm ablated area. An artefact can be observed in the brightfield image. No iron signal was recorded from this artefact after analysis (B-C). D- Brightfield image of the 400 x 400 µm ablated area. E- Magnesium distribution following LA-ICP-MS analysis. The scale bar was adjusted in panel C and F for consistency with the rest of the LA-ICP-MS data.

5.2.7.2 Amosite

The nature of the MSTO-211H cell-plug and the resolution of the optical microscope employed impeded the identification of amosite fibres in the brightfield images (Figure 5.15 A, D). However, following LA-ICP-MSI elemental mapping based on ^{57}Fe signal, amosite fibres and smaller fibre fragments were detected, with some amosite clusters identified on the left portion of the ablated surface (Figure 5.15 B, C). Iron analysis is an excellent target for detection and identification of amosite fibres.

Although amosite can contain magnesium as an impurity, there were no amosite fibres detected based on ^{24}Mg signal yielded by the amosite-treated MSTO-211H cell-plug section (Figure 5.15 E, F). Interestingly, the same UICC amosite fibres were previously used for 2D analysis, and it was established that these fibres do

contain some magnesium in their structure. Notably, given the compact nature of the cell-plug, the signal yielded by the biological matrix is relatively high and distributed across the sample. This supports the argument that 3D MPM models closely resemble human tissue architecture and cellular distribution. Moreover, small fragments, created following the sample preparation steps, might be present but fail to yield signals above the matrix. Finally, it proved to be challenging to select ROIs containing visible amosite fibres. There were no amosite fibres identified based on magnesium signal in the LA-ICP-MS data presented in Figure 5.15 E, F. Silicon analysis was attempted but failed to produce above-the threshold signal intensity (data not presented).

LA-ICP-MS data for fibres and biological matrix is presented in Figure 5.15 B, E. The scale bar for signal intensity was adjusted in Figure 5.15, panel C & F to focus solely on the signal yielded by the amosite fibres.

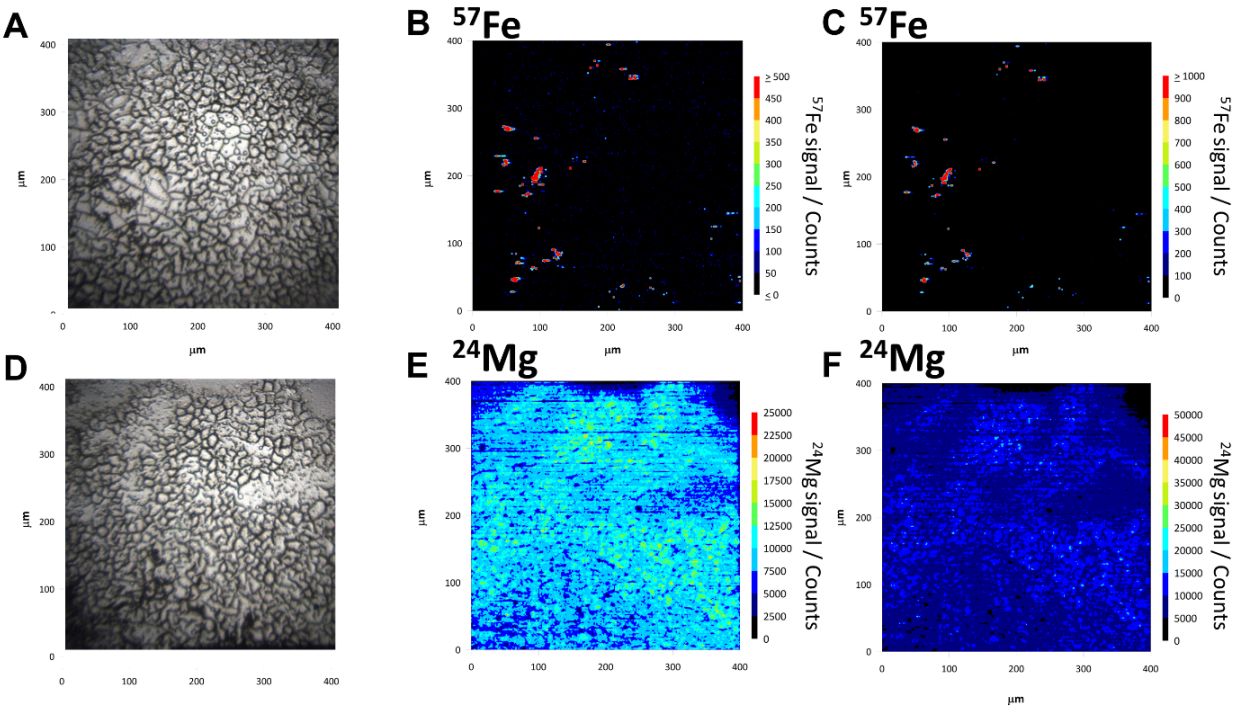

Figure 5.15 LA-ICP-MSI of a MSTO-211H cell-plug treated with amosite fibres. (A, D) Brightfield images of the 400 x 400 µm areas prior to ablation. No identifiable amosite fibres present in the optical images. (B) Amosite fibres detected based on the high iron content. (E) Magnesium distribution following LA-ICP-MS analysis. No clear, identifiable amosite fibres are present. (C, F) Signal intensity bar was adjusted to focus on the signal yielded from the fibres.

5.2.7.3 Crocidolite

Fibres embedded within the cells or lodged in the cellular matrix were undetectable by low depth penetration techniques, such as microscopy (Figure 5.16 A, D & G). Crocidolite fibres were identified based on Fe, Mg, and Si signals.

The crocidolite specific Fe^{2+} and Fe^{3+} surface sites that confer blue asbestos its high carcinogenic properties, also helped identify crocidolite fibres following LA-ICP-MS mapping of ^{57}Fe signal counts. Iron distribution in a crocidolite-treated cell-plug section is presented in Figure 5.16, panel B and C. Interestingly, the ^{57}Fe signal was lower for crocidolite compared to the data presented for above for amosite fibres. This is particularly noticeable in panel C of Figure 5.16 and Figure 5.15, respectively, where the signal intensity bar was increased to >1000.

Magnesium can substitute into crocidolite nominal structure, allowing the fibres to be detected following LA-ICP-MSI mapping of ^{24}Mg. Despite the strong signal yielded by the MPM cells, a cluster of crocidolite fibres was identified in the lower part of Figure 5.16 E. The fibres were also detected in Figure 5.16 F, where the signal intensity bar was adjusted for consistency. Some crocidolite fragments were also detected as high magnesium signal spots.

Crocidolite fibres were successfully spatially resolved based on the silicon content characteristic to these ferruginous silicates. Clusters of crocidolite fibres and smaller, fibre fragments were detected across the ablated area (Figure 5.16 H). The high signal intensity was maintained in Figure 5.16 following the increase of the scale bar value (>4000).

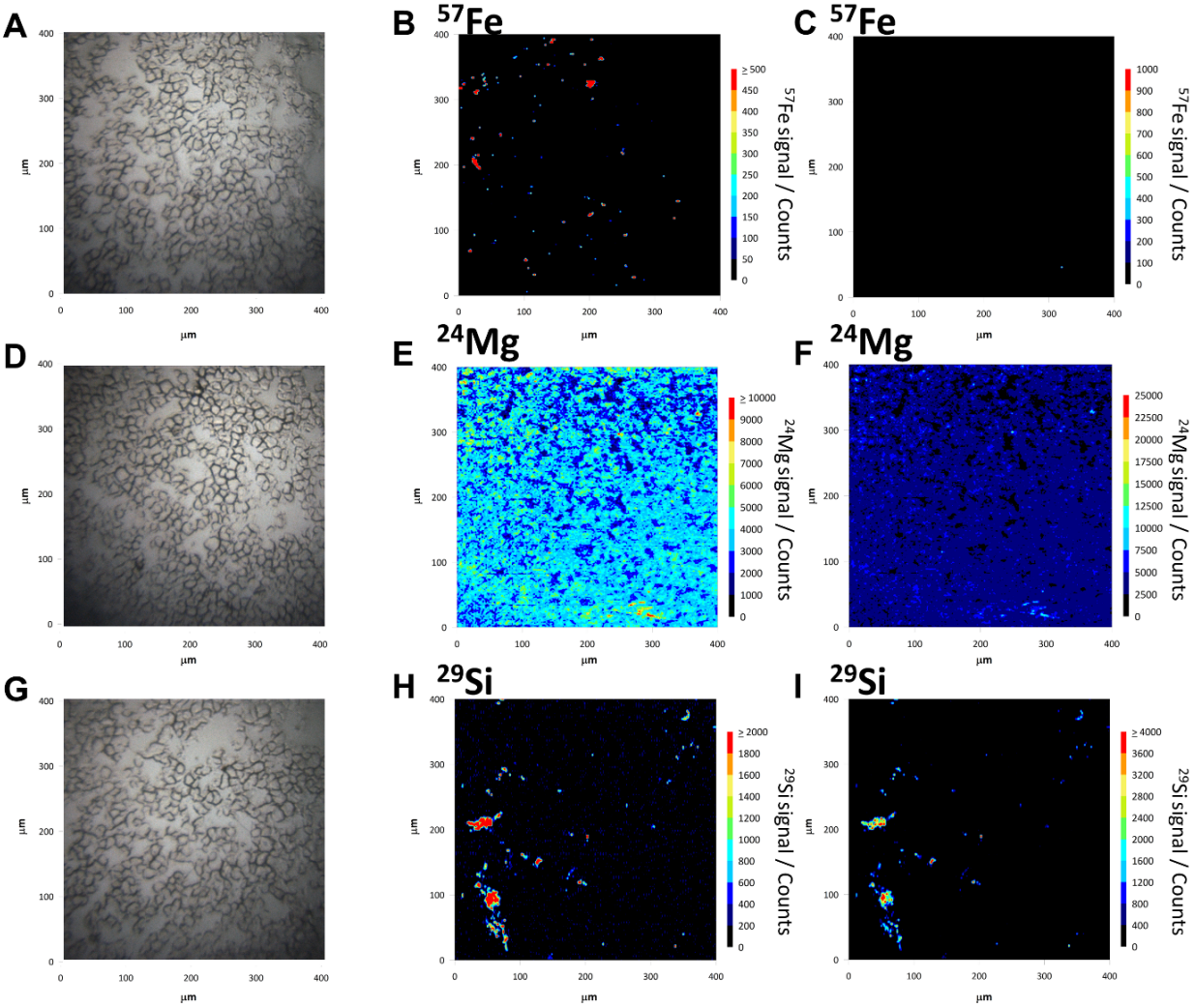

Figure 5.16 LA-ICP-MSI of a MSTO-211H cell-plug treated with crocidolite fibres. (A, D, G) Brightfield images of the 400 x 400 µm areas prior to ablation. No identifiable crocidolite fibres present in the optical images. (B) Crocidolite fibres detected based on the high iron content. (E) Magnesium distribution following LA-ICP-MS analysis. Crocidolite fibres can be seen in the lower part of the image, as well as in the top region, as hot magnesium signal spots. (H) Detection of crocidolite fibres across the ablated area based on high silicon content. (C, F, I) Signal intensity bar was adjusted to focus on the signal yielded from the fibres and consistency between data. Notably, iron signal appears to be lower than the one yielded by the rest of the asbestiform fibres.

5.2.7.4 Actinolite

ROIs with possible actinolite fibres were selected for LA-ICP-MS analysis. Some foreign bodies identified in the optical images (Figure 5.17, panels A, D, G) proved to be artefacts, supporting the ability of LA-ICP-MSI to differentiate between target MF and other sample impurities. Some of these can be observed by visual comparison with the LA-ICP-MS images and are particularly noticeable in the images presenting the magnesium distribution of the 3D MPM model (Figure 5.17 E, F).

Actinolite fibres were spatially resolved based on all three elements of interest. High ^{57}Fe signals were distributed across the sampled area, mapping the location of the actinolite fibres and fibre fragments within the section (Figure 5.17 B, C).

The actinolite fibres yielded the highest magnesium signal intensity compared to the other MF. Integral fibres can also be identified, with long actinolite fibres present in Figure 5.17 E. Some actinolite fibres were identified based on silicon signal. Apart from the fibres seen in the optical images, additional unidentifiable actinolite fibres were identified in the LA-ICP-MS data (Figure 5.17 H, I). The signal intensity bar was adjusted in Figure 5.17 panels C, F, and I for data consistency.

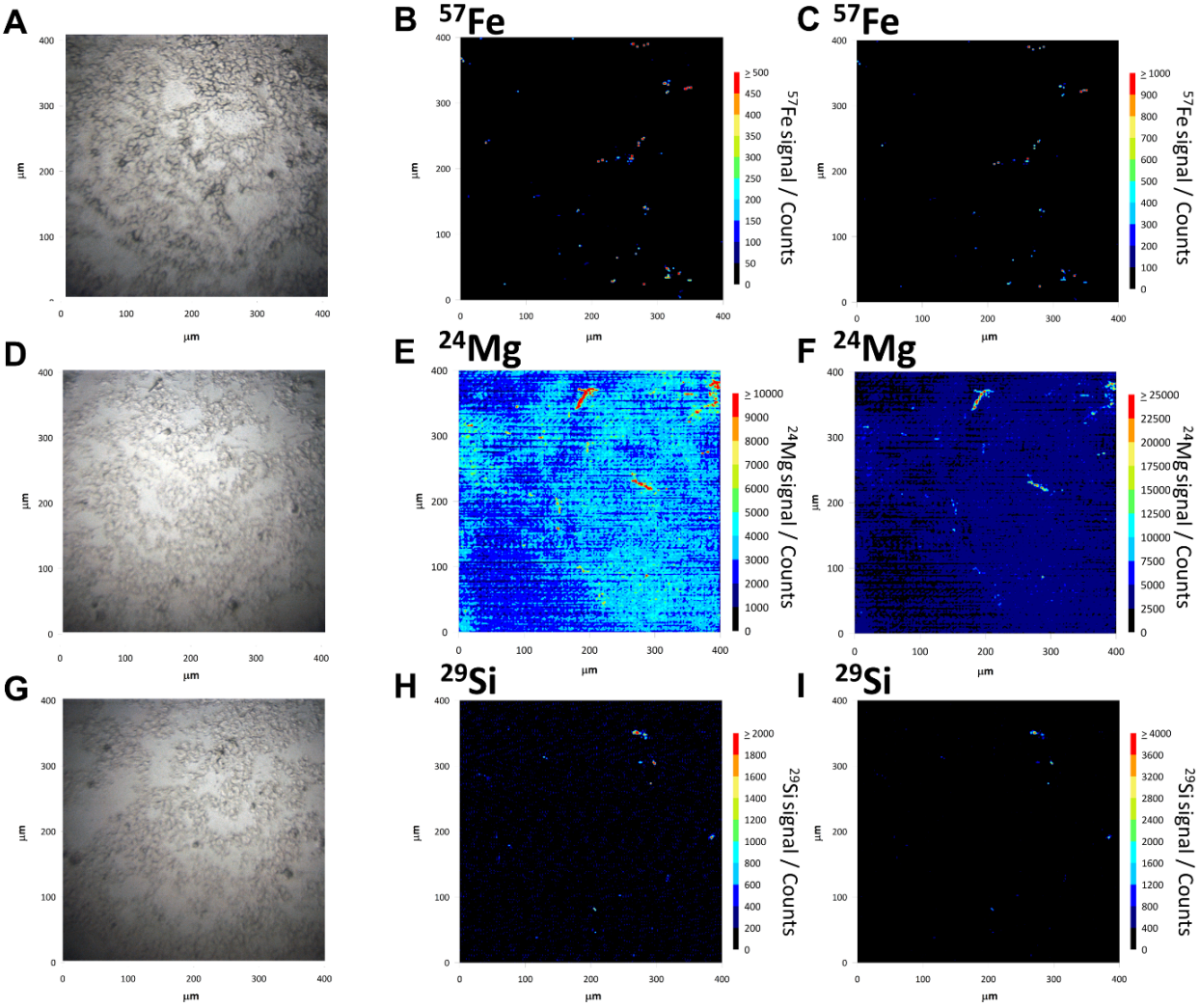

Figure 5.17 LA-ICP-MSI of a MSTO-211H cell-plug treated with actinolite fibres. (A, D, G) Brightfield images of the 400 x 400 µm areas prior to ablation. Areas with some identifiable bodies were selected for analysis as ROIs. (B) Actinolite fibres detected based on the iron content. (E) Magnesium distribution following LA-ICP-MS analysis. Actinolite fibres can be identified based on the high content of magnesium. Note the actinolite fibres unidentifiable in the optical image, particularly the central fibre and the cluster from top right corner. (H) Detection of actinolite fibres across the ablated area based on high silicon content. (C, F, I) Signal intensity bar was adjusted to focus on the signal yielded from the fibres and consistency between data.

5.2.7.5 Wollastonite

A MSTO-211H cell-plug containing the non-asbestiform wollastonite was prepared and analysed by LA-ICP-MS. Regions with identifiable wollastonite fibres or fragments were selected for ablation (Figure 5.18 A, D, and G). There was no significant ^{57}Fe and ^{24}Mg signal detected following the analysis (Figure 5.18 B and E). The signal intensity bar was adjusted in Figure 5.18 panels C, F, and I for data consistency across the samples.

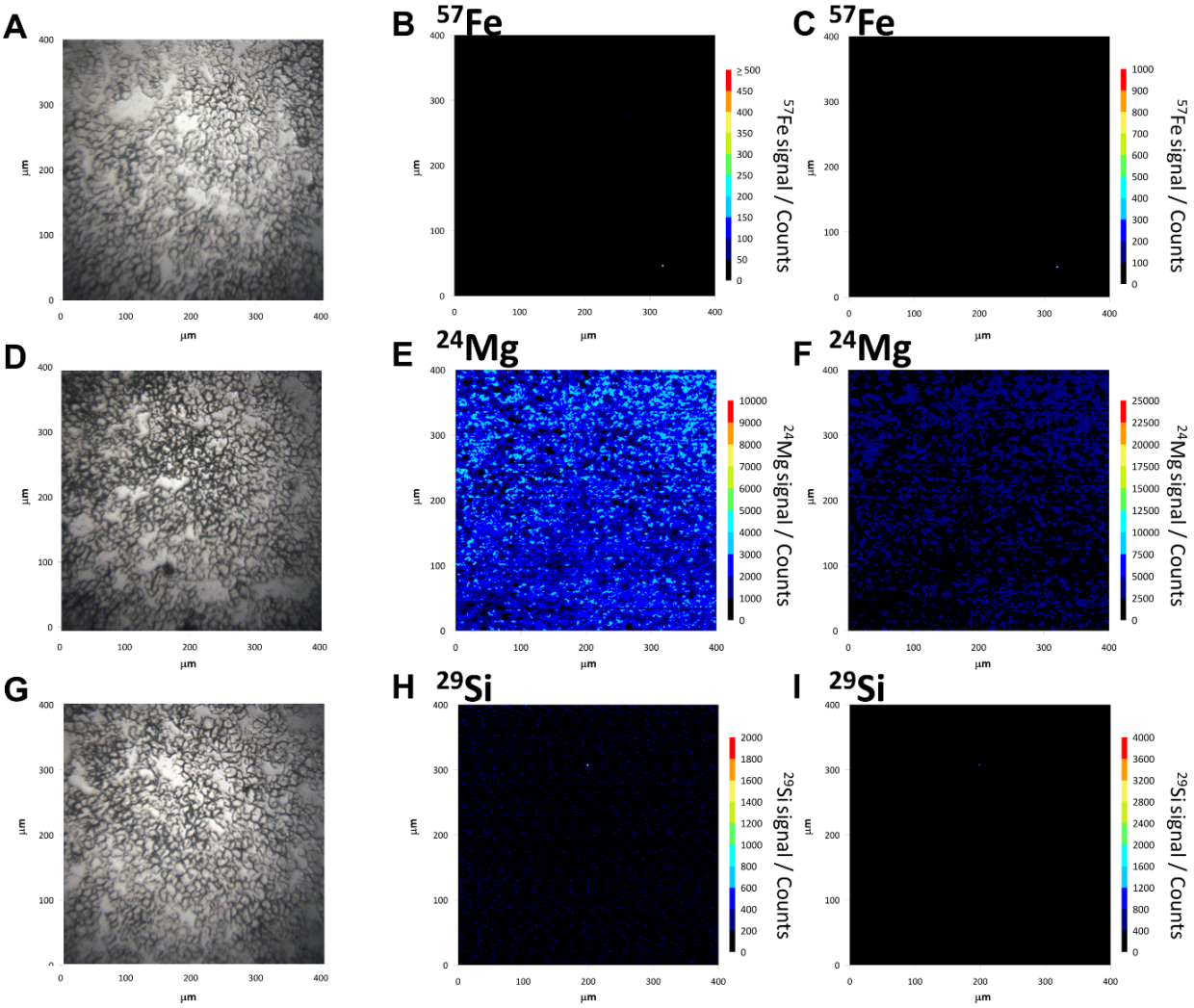

Figure 5.18 LA-ICP-MSI of a MSTO-211H cell-plug treated with wollastonite fibres. (A, D, G) Brightfield images of the 400 x 400 µm areas prior to ablation. Areas with some identifiable bodies were selected for analysis as ROIs. As expected, no signal was recorded for iron detection (C). (E) Magnesium distribution of the biological matrix following LA-ICP-MS analysis. (H) Detection of wollastonite fibres based on the silicon content. No significant signal was recorded. (C, F, I) Signal intensity bar was adjusted for consistency between data across different MF.

5.2.8 Blind sample classification using LA-ICP-TOFMS imaging

Unlike sector field mass analysers, TOF mass analysers such as the Vitesse ICP-TOFMS, are capable of pseudo-spontaneous detection of the elements between mass 23 (Na) and mass 238 (U) within one cycle of analysis.

After demonstrating that MF can be detected in both 2D monolayers, as well as 3D MPM cell-plug sections based on either magnesium, iron, or silicon content,

the next step was to test the ability of LA-ICP-TOFMS analysis to correctly classify the fibres within a blind sample. The cell-plug containing an “unknown” fibre type was prepared, sectioned, and analysed as a ‘blind’ sample. A record was kept of the MF identity in order to validate the LA-ICP-TOFMS result.

The full mass range was detected but the analysis focused on the main nominal components of the MF used in this study (*i.e.,* magnesium, iron, calcium, and silicon). The densely packed nature of the 3D cultures better mimics the conditions under which patient tissue are analysed. Fibres embedded within the cells are invisible to low penetration depth techniques, such as microscopy. However, the 193 nm laser successfully penetrated through the tissue, revealing one large fibre of approximately 120 µm in length and some smaller fragments of below 50 µm in length (Figure 5.19). Magnesium, iron, and silicon were observed in high amounts in these images (panels A, B and D) with an absence of calcium signal (panel C). Analysis of the full range of characteristic elements enabled the correct identification of the fibres as amosite, demonstrating the potential of the technique for identification of fibres in complex tissue matrices.

The knowledge acquired following LA-ICP-TOFMS analysis of 2D samples was applied in the correct classification of the fibres shown in Figure 5.19. Overall data suggested that the MF can be classed as asbestiform silicates, with high magnesium content, and iron as an integral part of the nominal structure. No signal was detected for ^{40}Ca. Actinolite and wollastonite were therefore eliminated as feasible options. Finally, when comparing the ^{56}Fe signal intensity with the one yielded by the MF in the 2D samples (Chapter 4.2.5), data suggested that the fibres detected in the blind samples were amosite fibres and this was subsequently confirmed as correct identification.

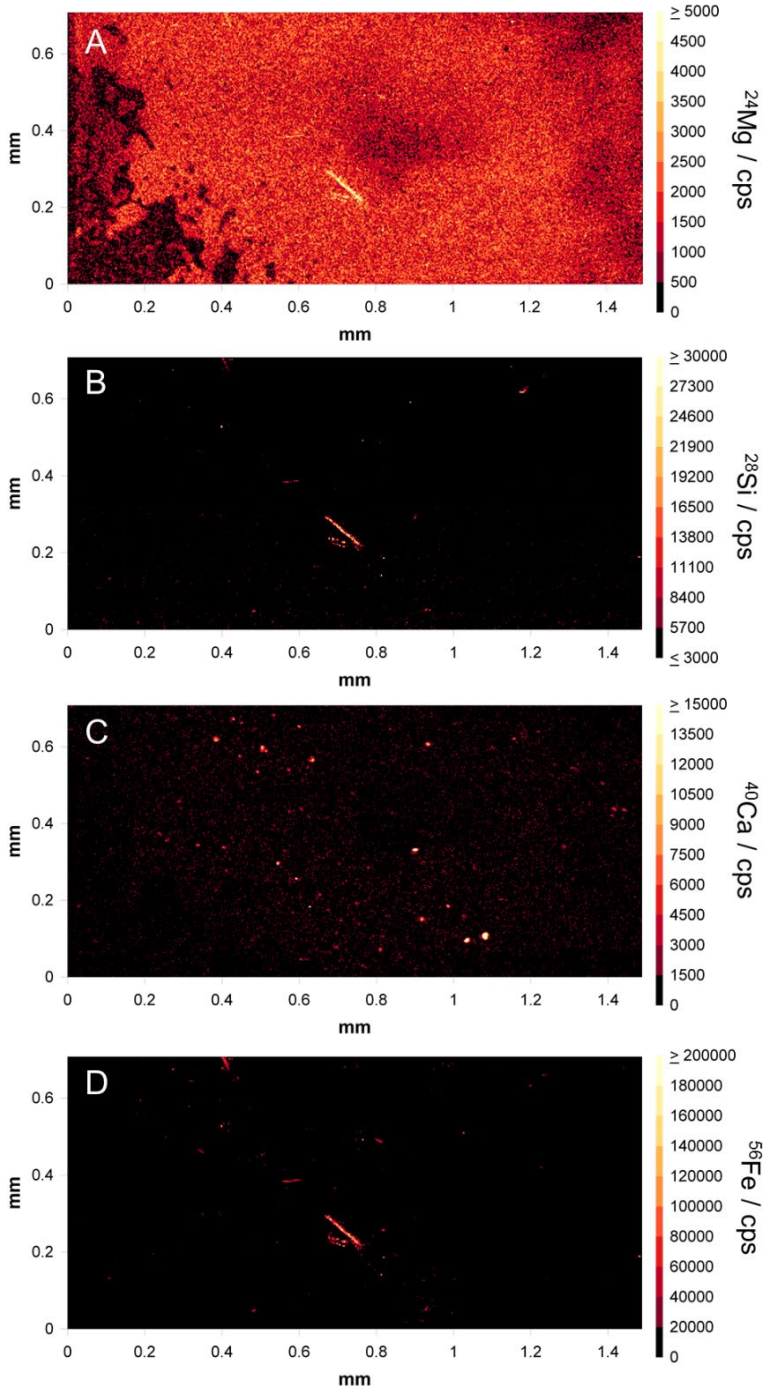

Figure 5.19 Blind sample classification using LA-ICP-TOFMS imaging. Analysis of the full range of characteristic elements was carried out for the same area (0.75 x 1.50 mm) of a MSTO-211H cell-plug treated with an unknown type of MF. (A) Mg distribution following LA-ICP-TOFMS analysis. One large fibre of approximately 120 µm in length and some smaller fragments of below 50 µm in length can be identified based on the high magnesium content. (B) Si distribution of the sample following analysis. (C) Ca signals across the ablated area. Some signal was given by the cellular matrix. No signal was yielded by the MF. (D) Fe distribution following LA-ICP-TOFMS analysis. Based on the overall elemental signal, the MF were correctly classified as amosite.

5.3 Conclusion

Mapping the elemental distribution of characteristic MF components within 3D MPM models using LA-ICP-MSI was an intermediate step between the preliminary 2D cell analysis presented in Chapter 4 and the more complex analysis of clinical tissue samples. This is the first study to employ LA-ICP-MS and LA-ICP-TOFMS imaging to spatially resolve multiple MF within a novel 3D MPM model based on the elemental characteristics.

The first step of this study was to develop a suitable 3D MPM model containing MF. A MCS approach was tested in the first instance. MCS co-cultured with different MF successfully developed in special hydrophilic 96 well plates. However, this model proved to be mechanically unstable and inconsistent for further sample preparation steps. The second 3D approach involved a novel model that required limited sample preparation (*i.e.,* no embedding and sectioning). However, monitoring the sample thickness was complicated, and there were concerns regarding background interferences from the membrane material. Finally, the 3D MPM cell-plug was developed as an alternative to 3D MCS at a larger scale. By employing different-sized plastic moulds, the sample preparation was cheap and easy, and allowed for consistency between samples.

For the 3D analysis, the optimisation steps are crucial to help understand the processes and parameters during the laser ablation stage which could influence the ICP-MS signal. Relatively high laser fluence values were selected for optimisation to ensure complete ablation of cellular matrix and MF. Following the optimisation steps, a softer laser fluence was chosen, to avoid plasma shielding effects, whilst achieving total ablation of the sample surface.

Initial optimisation studies were carried out on 20 µm sample sections, a size within the typical range of LA-ICP-MSI sample thicknesses (Theiner *et al.*, 2016). Interestingly, following the ablation of 20 µm thick samples some residual material was observed. This finding led to the hypothesis multiple serial analysis of the same area can provide insight into fibre orientation and the prospect of 3D sample reconstruction.

LA-ICP-MS data, acquired following serial ablation of the same thicker area or analysis of thinner serial sections, have the potential to be reconstructed in 3D using specialist software. Not enough data was collected following four cycles of analysis of 50 µm thick samples for 3D reconstruction. However, invaluable information regarding MF behaviour within 3D models was presented. Another option for 3D reconstruction would be imaging 5-10 µm thick cell-plug serial sections, at least over 10 sections. Ablating the same area of a cell-plug would be difficult in serial sections given the large area of the cell plug and small area that is generally ablated. One solution would be fully ablating the whole surface area of the samples. However, given the large size of the section, ablating the whole area at low lateral resolution (1-2 µm laser spot size) would be highly expensive and time consuming.

Regardless, this finding offers future prospects of 3D reconstruction of human tissue samples, preserving the exact location and orientation the asbestos fibres. This has high implications in further understanding MPM pathology and the correlation between fibre location and disease development. For the purpose of this study, a thinner section size was chosen for the rest of the experiments (12 µm), which ensures complete ablation of the surface area selected.

Another pivotal optimisation step involved the selection of the spot size, surface area, and time of acquisition to ensure optimal signal intensity. There is an interdependent link between these factors which was presented herein, and finding the right balance was crucial. Optimal signal intensity can play an essential role in failing to detect small fibre fragments, influence the accuracy of quantitative analysis, and therefore the future prospect of classifying fibre types based on the elemental profile. Indeed, the correlation between spot size and signal intensity has been investigated before (Diwakar *et al.*, 2013). However, the data presented in this chapter showed a difference in signal intensity up to 10 times higher between different spot sizes, reinforcing the importance of optimisation steps.

In a clinical setting, it is of utmost importance to gather as much information as possible, with a limited time of acquisition. Therefore, analysis was carried out with a 2 µm spot size, which provided cellular information with the highest signal intensity. For elemental mapping, the surface areas selected were 400 x 400 µm. Higher dose cell-plugs were also selected in this preliminary study to ensure the presence of MF within the analysed sections.

Once the laser parameters were optimised for magnesium signal in actinolite-treated cell-plugs, the analysis was expanded to include detection of three asbestiform fibres and one non-asbestiform control in 3D MPM models, based on iron, silicon, and magnesium content. Silicon distribution was unsuccessful for the untreated control and amosite-treated cell-plug. The failure might be attributed to a fault in the instrumentation. However, ^{29}Si mapping of crocidolite, actinolite, and wollastonite was achieved. Similarly, all samples were spatially resolved based on the ^{24}Mg and ^{57}Fe signal intensity. Notably, LA-ICP-MSI was capable of detecting small fibres fragmented due to the sample preparation steps, as high intensity “hot spots” across the ablated surface.

Finally, a novel prototype LA-ICP-TOFMS was employed to obtain the full mass range of a surface area within a cell-plug prepared with an unknown MF. Characteristic elements were selected for future data analysis. Unknown MF were spatially resolved within a 0.75 x 1.50 mm area. Signal was detected for all selected isotopes, but ^{40}Ca. Based on this finding, and the signal intensity generated for ^{56}Fe, the fibres were correctly classed as amosite fibres. This is the first time a MF was correctly categorised using LA-ICP-MSI (Greenhalgh, Voloaca *et al.*, 2020). Nevertheless, more quantitative analysis is needed in this field to fully support the capability of LA-ICP-TOFMS imaging to accurately classify unknown samples.

Overall, the data presented in this chapter reinforces the sample mapping and depth profiling capabilities of LA-ICP-MSI, even in 3D MPM models. Moreover, the data supports the hypothesis that by employing more advanced techniques such as LA-ICP-TOFMS imaging, MF can be identified and correctly categorised, based solely on the elemental information acquired after a single cycle of

analysis. The work brings the prospect of introducing LA-ICP-MSI within a clinical setting one step closer, bridging the gap between 2D analysis and complex human tissue analysis.

Chapter 6 Multimodal LA-ICP-MS Imaging of Human Mesothelioma Tissues

The work presented in this chapter was carried out in collaboration with University of Vienna and Loughborough University

6.1 Introduction

6.1.1 Introduction to the chapter

In recent years, there has been a growing interest in determining the spatial inhomogeneous elemental distribution of biological tissues (Stewart, 2019). Regulation of uptake, assimilation, intracellular compartmentation, and intercellular translocation of trace metals is vital in maintaining the homeostasis of living organisms (Serra *et al.*, 2020). Mapping the cellular and the subcellular metallome offers insight into the fundamental biological processes and helps understand the chemical make-up during disease states (Stewart, 2019).

Several analytical techniques have been employed for trace metal detection in biological tissue. These techniques have been previously categorised in two main groups: (1) techniques that record the mass of the atom using mass spectrometry, such as LA-ICP-MS and secondary ion mass spectrometry (SIMS), and (2) techniques which detect the electronic structure of the atoms, for example X-ray Fluorescence Microscopy (XFM), Micro Particle-Induced X-ray Emission (μ-PIXE) and other electron microscopy (EM) methods such as energy dispersive X-ray spectroscopy (EDX) (Ackerman, Lee, & Chang, 2017).

LA-ICP-MS has been established as the workhorse for metallomics analysis of biological tissues and presents several attractive features when compared to the rest of the above-mentioned techniques. Firstly, LA-ICP-MS is capable of analysing tissues as thin as 5 μm, but thicker sections (>20 μm) can also be analysed and can provide insight into changes of elemental concentration in the z-dimension (Bonta *et al.*, 2017). Secondly, there is no sample preparation required, as long as the sample fits inside the sampling chamber of the instrument. Non-conducting biological sample surfaces can also be ablated easily compared to SIMS or nano-SIMS. Additionally, LA-ICP-MSI provides single-isotopic information (*e.g.,* ^{56}Fe vs ^{57}Fe) which is of particular interest in isotope uptake studies (Bondanese *et al.*, 2016). Although LA-ICP-MS typically uses the most abundant isotope for elemental mapping to ensure maximum counts per

second, secondary isotopes have been monitored in some instances in this work in order to avoid common polyatomic interferences.

Another advantage is that LA-ICP-MSI has been reported to have one of the lowest limits of detection (LOD) (Lobinski, Moulin, & Ortega, 2006), although this can be influenced by several factors. For instance, in a quadrupole set-up, the LOD is determined by the number of monitored masses, the dwell time, and the sweep and settling time of the quadrupole (Doble *et al.*, 2021). Moreover, recent advancements in instrumentation, laser ablation cell design, have resulted in improvement in the absolute sensitivity (Douglas *et al.*, 2015).

LA-ICP-MSI has been employed to analyse a wide variety of biological tissue, including plant tissue (Callahan *et al.*, 2016), animal tissue (Neumann *et al.*, 2020b), and human tissue samples. In terms of human tissue, some of the most studied samples include brain tissues (Cruz-Alonso *et al.*, 2019), liver tissue samples (Kim *et al.*, 2018), but also MPM tissues (Bonta *et al.*, 2014) or teeth sections (Miliszkiewicz *et al.*, 2017).

Despite technical advancements, the standardised asbestos detection process has remained unchanged in over three decades (Roggli & Pratt, 1983). Most asbestos identification techniques employ tissue digestion, meaning that the spatial information cannot be preserved. The main detection techniques are light microscopy, SEM, and TEM. Fibre type classification can be achieved by energy-dispersive X-ray (EDX) analysis. We have previously demonstrated the capabilities of LA-ICP-MS as a tool for imaging asbestos and other MF *in situ* (Greenhalgh *et al.*, 2020; Voloaca *et al.*, 2020), providing detailed spatial information about the fibre size, thickness, and orientation within MPM models. This chapter takes the applicability of this technique one step further, investigating whether LA-ICP-MSI can detect MF in human MPM tissue samples with unknown asbestos exposure based on proof-of-concept data presented in the Chapter 4 and Chapter 5.

In this study, commercially obtained human MPM were analysed as a means of standardisation between multiple LA-ICP-MS experiments. The advantages of

using commercial tissues include limited sample preparation, consistency between samples, quick and easy access, and limited ethical requirements. Additionally, due to the collaborative nature of this work, commercial tissues can be analysed in multiple laboratories without high ethical implications. The main disadvantages of using commercial tissues revolve around the increased cost of these samples and limited sample variety. In addition, there are some ethical and legal concerns around the commercialisation of tissues and distributors that are profiting off biological material that had been initially donated for medical applications or for scientific research (Pirnay *et al.*, 2015).

Human MPM tissue samples were selected to include MPM tissues of different pathology, staging, and tumour origin/ finding for two main reasons resonating with the aims of this study- detecting MF and mapping the MPM metallome. It has been long established that asbestos fibres can be detected at different levels in all organs in subjects with known asbestos exposure (Auerbach *et al.*, 1980; Huang *et al.*, 1988). Asbestos fibres have been mostly reported to be found in tissue originating from the lungs, human lungs having limited defence mechanisms to eliminate the invasive fibres from the alveoli of the lung (Feder *et al.*, 2017). High fibre deposition in the lung interstitium is likely to be due to dual translocation routes, as fibres reach the lung from both the alveoli and from the blood (Miserocchi *et al.*, 2008).

The MF previously detected in pleura of MPM patients tend to be ultrafine fibres (length <5 μm; diameter <0.25 μm) (Carbone *et al.*, 2012), because these fibres tend to travel larger distances due to low steric hindrance (Miserocchi *et al.*, 2008). MPM samples resected from the pleura were thus included in the study. Several environmental and occupational inhalants (*i.e.,* cigarette smoke, environmental pollution) also accumulate in the lungs and pleura. Such asymptomatic deposits can be found in various quantities among most urban residents and tobacco smokers (Pascolo *et al.*, 2015). These particulates are thought to accumulate over time in MPM patients, which in combination with asbestos fibres can have a synergistic carcinogenic effect. Lastly, due to increased pleural retention, asbestos fibres rarely tend to pass the parietal pleura

and reach the chest wall (Donaldson *et al.*, 2010). Analysis of MPM tissue resected from the chest wall region was therefore included in the study, as a negative control.

Apart from asbestos and MF detection, LA-ICP-MSI can also provide insight into the metal homeostasis dysregulation in MPM, particularly with the use of a LA-ICP-TOFMS instrument. Changes in metal homeostasis, such as manganese, copper, or zinc have been investigated in cell lines (Hasegawa *et al.*, 2008), and despite the reported implication of zinc dependant proteases in MPM chemoresistance (Bellefroid, 2018), limited investigations have been made into Zn distribution in human MPM tissue samples. Zinc plays an essential role in cell growth and proliferation, thus being enriched in high metabolic tumour regions, with lower levels present in stroma and the rest of the tissue (MacDonald, 2000; Riesop *et al.*, 2015). Zinc has been proposed as a tumour grading biomarker, with Zn mapping being achieved in human breast cancer tissues by using LA-ICP-MSI (Rusch *et al.*, 2021).

Data on MPM metallomics mainly focuses on the analysis of iron assimilation and ferruginous bodies formation (Pascolo *et al.*, 2013), failing to cover how trace metals impart key functions in neoplastic development. The detrimental effects of metal deficiencies are testimony to their contribution in overall homeostasis, but dysregulation or overload of metals is just as significant. Metals like iron and copper are strongly linked to ROS generation via the catalytic Fenton and Haber–Weiss reaction (Kehrer, 2000). ROS production is one of the hallmarks of MPM pathogenesis (Okazaki *et al.*, 2020). Iron availability is also a key driver of inflammation, by triggering pro-tumorigenic responses in macrophages and other immune cells (Serra *et al.*, 2020). Overabundance of iron levels indicates cellular sequestration, linked to anaemia in cancer patients (Brown *et al.*, 2020), and poor prognosis in MPM patients (Berardi *et al.*, 2016).

Depending on their role in the homeostatic mechanisms, metals distribution is inhomogeneous within organs and organelles (Serra *et al.*, 2020). Metal ions are found in high concentrations within organs with high metabolic activity (Hasegawa *et al.*, 2008). One such example is magnesium, an essential

intracellular and extracellular cation and enzymatic cofactor. In the respiratory system, magnesium is thought to function as an antagonist to calcium ion influx to the smooth muscles, regulating bronchial activity (Landon & Young, 1993). Additionally, magnesium can act as an anti-inflammatory agent involved in the release of histamine from mast cells (Kılıc *et al.*, 2018).

Potassium, calcium, and sodium imbalance contributes to several cancer hallmarks presented in Chapter 1, Section 1.1, including altered growth signalling, proliferation, angiogenesis, invasion, and metastasis (Leslie *et al.*, 2019). LA-ICP-MSI can be employed as a tool for monitoring the intratumoral ionic distribution within human MPM tissues.

Areas of necrosis present in tumours are associated with aggressive neoplastic characteristics and are known to release intracellular potassium ions into the tumour microenvironment (Eil *et al.*, 2016). Moreover, this overabundance of potassium has been linked to a drop in T-cell efficiency, by triggering these immune cells to regain stem-cell-like properties and significantly reduce their tumour-killing abilities (Vodnala *et al.*, 2019). Another key electrolyte enriched in solid tumours is sodium (Leslie *et al.*, 2019). With essential roles in the osmolarity of the tumour microenvironment, overabundance of sodium can impact cell volume, metabolism, and immune processes (Leslie *et al.*, 2019). Monitoring metallome disturbances may open avenues to therapeutic targets, tumour biomarkers discovery, as well as understanding the intricate process of MPM onset and progression.

In this work, the human MPM tissues were analysed using four different LA-ICP-MS set-ups based on several factors including instrument availability, instrument capability and performance, preliminary data, and time restraints. Initially, the tissue samples were mapped for asbestos and other MF detection, based on the nominal structure of these fibres. Secondly, by employing multi-elemental LA-ICP-MS and high-resolution LA-ICP-TOFMS imaging, trace metal mapping of human MPM tissue samples was achieved, with the focus on Zn, Mg, Fe, Na, and K dyshomeostasis.

The first set-up was the ultra-low volume, high-speed LA-ICP-MS set-up, also employed for analysis of 2D and 3D MPM models (data presented in Chapter 4 and Chapter 5). The work was carried out in collaboration with Loughborough University by Oana Voloaca and Calum Greenhalgh. ROIs, data analysis, and data interpretation was carried out by the author, Oana M Voloaca. The holistic design of the instrument, formed by a two-volume laser ablation cell and an integrated ICP torch, was designed to minimise aerosol dispersion for fast, efficient sample transport. The set-up included a soft NWR Image 266 nm laser ablation system coupled to an Element XR sector-field ICP mass spectrometer. This resulted in discrete sample analysis with reported improvement in absolute mass sensitivity (Douglas *et al.*, 2015). Despite the high resolution, with cellular definition capabilities, the analysis was limited to one nuclide per ablated area. In this work, Mg was selected as target metal based on early data presented in Chapter 4 and Chapter 5.

The second set of analysis was conducted using a NexION 350X ICPMS coupled to a NWR UP-213 LA system with a frequency quintupled 213 nm Nd: YAG laser. The single quadrupole instrument consists of a unique triple cone interface that prevents dispersion of ions and sample deposition on internal surfaces, which is extremely valuable when analysing samples possibly containing asbestos fibres. Due to the nature of samples, the laser and ICP settings had to be optimised to ensure ablation of possible MF without ablating the glass slide surface.

Due to the limited capabilities of the previously employed instruments, the human MPM tissue samples were shipped externally to be analysed with a more advanced instrument set-up. The instrumentation, based at King's College London Metallomics Facility, boasted a high energy Analyte Excite 193 nm laser with a HelEx II Active 2-Volume Ablation Cell, coupled to a triple-quad Thermo iCapTQ, for greater control over isobaric interferences and sub-ppt sensitivity. The system delivered high spatial resolution elemental mapping at cellular level. The laser ablation system presented the fire-on-the-fly lasing technology synchronised to the stage motion, which combined with fast washout ablation cells, make precision depth profiling of spots, lines, and areas possible.

With increased low-dispersion LA set-ups capabilities, sequential quadrupole mass analysers are reaching their limitations, permitting the detection of only a few nuclides at a time (Theiner *et al.*, 2020). The fast transient signals delivered by these set-ups require mass analysers capable of fast data acquisition, high read-out speed, and limited dead time in the duty cycle. Furthermore, the ability to detect multiple isotopes (quasi)simultaneously is also desired, particularly in clinical settings. Due to these exceptional features, the LA-ICP-TOFMS can be employed to detect and categorise asbestos and other MF, based solely on the slight differences in their nominal structure. The system can also identify unknown asbestos trace metal impurities, which potentially play a more important role in carcinogenesis than initially considered (Bloise *et al.*, 2020) In addition to this, the elemental map can simultaneously provide invaluable insight into metallome distribution across malignant tissues.

The set-up consisted of a high energy Iridia 193 nm laser ablation system coupled to an icpTOF 2R ICP-TOFMS instrument. The LA system was equipped with a low-dispersion ablation cell in a Cobalt ablation chamber and coupled with the aerosol rapid introduction system (ARIS) to the ICP-TOFMS (Van Malderen *et al.*, 2020). The Cobalt chamber stands out from the other dual volume sample chambers, with its low gas usage (He usage is around 4 to 5 times lower than previous systems). The icpTOF 2R ICP-TOFMS instrument boasted a specified mass resolution ($R = m/\Delta m$) of 6000 (full width half-maximum definition) which allows the analysis of ions from m/z = 14-256. The instrument was capable of detecting the entire mass range, but the data was processed for the elements of interest as well as other isotopes with the high counts per second. This work was carried out in collaboration with Dr Sarah Theiner and Prof Gunda Koellensperger of University of Vienna. Analysis and data processing were carried out by Dr Sarah Theiner. ROIs selection and data interpretation were carried out by Oana M Voloaca.

6.1.2 Hypothesis

The main hypothesis of this chapter was that asbestos and other MF can be spatially resolved within human MPM tissue samples by using different LA-ICP-MSI set-ups. Secondly, we hypothesised that asbestos and other MF might be present only in certain tissues that originate from different anatomical sites. Finally, the hypothesis was that LA-ICP-TOFMS imaging can also be employed to provide insight into MPM metallome and elemental disturbance associated with neoplastic transformation.

6.1.3 Aims of the chapter

The main aim of this chapter was to detect asbestos and other MF in human MPM tissue samples of different pathologies and finding sites using multi modal LA-ICP-MSI. Additionally, the aim was to evaluate and compare the capabilities of various LA-ICP-MS systems to spatially resolve these samples based on the elemental composition. The final aim of the work was to determine the metal complement of MPM human tissues using multi-elemental LA-ICP-MSI and high resolution, ultra-fast LA-ICP-TOFMS analysis.

6.2 Results and Discussion

6.2.1 Tissue architecture and histology

The human MPM tissue samples were prepared as serial sections (5 µm thickness), 10 sections per patient, for a total of 5 patients. All the information provided by the supplier, including patient details such as age and gender, as well as tumour origin and finding, pathology, and tumour staging are presented in Table 6.1. Although limited, patient information supported the data interpretation and offered insight into the heterogeneity of this pathology.

Whole unstained tissue sections were imaged using standard brightfield microscopy to give an idea of the tissue size and architecture. Images acquired for three different patients were selected, showing the similarities and differences between pleura (Panel A), chest wall tissue (Panel B) and lung tissue (Panel C).

Possible artefacts can also be observed (Figure 6.1). A similar microscopic view was used in selecting ROIs for LA-ICP-MS analysis using an integrated brightfield microscope.

Routine H&E staining was performed to obtain a comprehensive picture of the microanatomy of each MPM tissue. Nuclear components retain haematoxylin and are shown in a purple/blue shade, whilst the rest of the cytoplasmic components and extracellular matrix are presented in a pinkish colour in Figure 6.2 A-E. Perls' Prussian Blue staining was carried out to detect the ferric iron within asbestiform ferruginous bodies (Figure 6.2 F-J). The staining is based around the potassium ferrocyanide which reacts with the ferric iron to form the ferric ferrocyanide or Prussian Blue.

The black impurities present in Figure 6.1 A might be the result of several factors. Firstly, there is the possibility of carbon and dust accumulation, causing anthracosis of the lungs. Carbon or coal dust pigment, as well as mineral particulates, are virtually ubiquitous air pollutants. In anthracosis carbon particles are found as an accumulation of black pigment in the lung tissue especially around bronchovascular bundles, interlobular septa, and beneath the pleura (Pascolo *et al.*, 2015). However, these mineral particulates retain colour after H&E staining (Mirsadraee, 2014), which was not the case in our study.

The second explanation was that the patient had undergone a common palliative procedure called chemical pleurodesis, most likely using talc as the sclerosant agent. Talc deposition tends to follow a linear pattern across the pleura (Attanoos & Gibbs, 2004). Indeed, brightfield images revealed a linear crystal distribution of the black impurities (Figure 6.1 A). Moreover, the particulates were not always distinguishable following H&E staining of the sections (Figure 6.2 A). Talc crystals have been previously shown to poorly retain H&E stains (Vannucci *et al.*, 2018). Moreover, the particulates did not stain for ferric iron following Perls' Prussian blue staining (Figure 6.2 F) which corresponds to the nominal structure of talc.

H&E staining revealed structural differences across the sample pool that matched the information presented in Table 6.1. The cases presenting a high percentage

tumour showed nuclear irregularity and chromatin clumping by retaining more haematoxylin (Figure 6.2 B), whereas the low percentage tumour with extended stroma retained more eosin (Figure 6.2 A). Other noteworthy features presented in Figure 6.2 are the fibrosis regions for Patient 2 and Patient 4, characterised by increased purple staining, the circular desmoplastic growth around the middle section of Patient 5, and the mixed cellular appearance for Patient 3. Traces left by the alveolar transudate that caused oedema can also be noted in the lower part of Patient 2 tissue section. Although nuclei retained less pigmentation following staining with nuclear fast red than they did from haematoxylin, it was the appropriate nuclear counterstain in order to prevent the substrate colours to be obscured by haematoxylin Figure 6.2 G-J.

A closer view of selected ROIs is presented in Figure 6.3. Tumour heterogeneity can be noted following H&E staining (Figure 6.3 A-E). Perls' Prussian Blue staining provided some insightful information for each patient. Firstly, there was no reaction with the crystal-like structures, indicating the lack of ferric iron on the surface of the particulates. No distinctive staining was present for Patient 2. Asbestos fibres that stained blue can be seen closer in Figure 6.3 I. However, some asbestos bodies have been reported to remain uncoated by endogenous iron (Pascolo *et al.*, 2013). One such example can be seen in Figure 6.3 H, as pointed by the red arrow. Spindle cells characteristic to advanced aggressive biphasic mesothelioma can be observed in Figure 6.3 J, with some possible artefacts indicated by the arrow.

Patient number	Age	Gender	Tissue of Origin/Finding	Sample pathology	TNM	Min stage grouping	% Normal	% Lesion	% Tumour	% Tumour Hypercellular Stroma	% Tumour Hypo/ Acellular Stroma	Pathology Notes	Visible mineral fibres* Yes/No
1	65	Male	Pleura / Pleura	Mesothelioma of pleura, epithelial	pT2pN2pMX	III	0	0	25	75	0	Tumour: epithelial variant; Tumour Stroma Fibroblastic cells, Inflammatory cells	Yes
2	81	Male	Pleura/Chest wall	Mesothelioma of pleura, epithelial.	Not reported	Not reported	0	0	85	15	0	Tumour Stroma Fibrosis, oedema	No
3	62	Male	Pleura / Lung	Tumour Mesothelioma of pleura, mixed	pT3pN1pMX	III	0	0	90	5	5	Pleural mesothelioma with extension along interlobular septa and nodular parenchymal deposits	Yes
4	53	Male	Pleura / Lung	Mesothelioma of pleura	pT3pN1pM1	IV	0	0	65	0	35	Tumour Stroma Fibrosis; Pleural mesothelioma with extension along interlobular septa	Yes
5	57	Male	Pleura / Pleura	Mesothelioma of pleura, biphasic	pTXpNXpMX	Not Reported	0	0	70	15	15	Tumour Stroma Desmoplastic reaction; Tumour Stroma -Fibrosis	Yes

Table 6.1 Patient information and sample details as provided by the supplier (Amsbio). *Not included in the SDS; MF visible by brightfield microscopy.

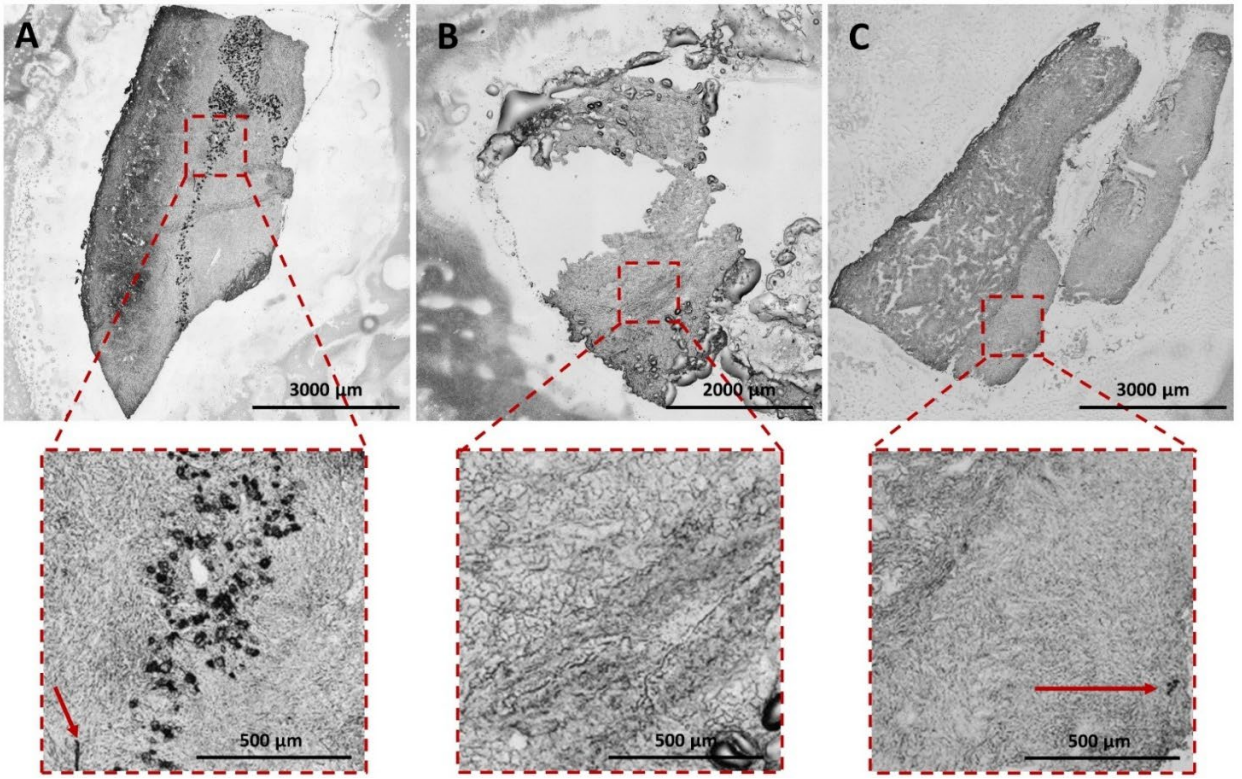

Figure 6.1 Brightfield images of unstained human MPM tissue sections. (A) Patient 1, pleura; Talc deposits can be observed as black, crystal-like impurities deposited in a linear manner. Red arrow points at a long, thin impurity. (B) Patient 2, chest wall; No significant artefacts are present in this section. (C) Patient 3, lung; Red arrow indicates a possible asbestos body or cluster, based on typical appearance and size.

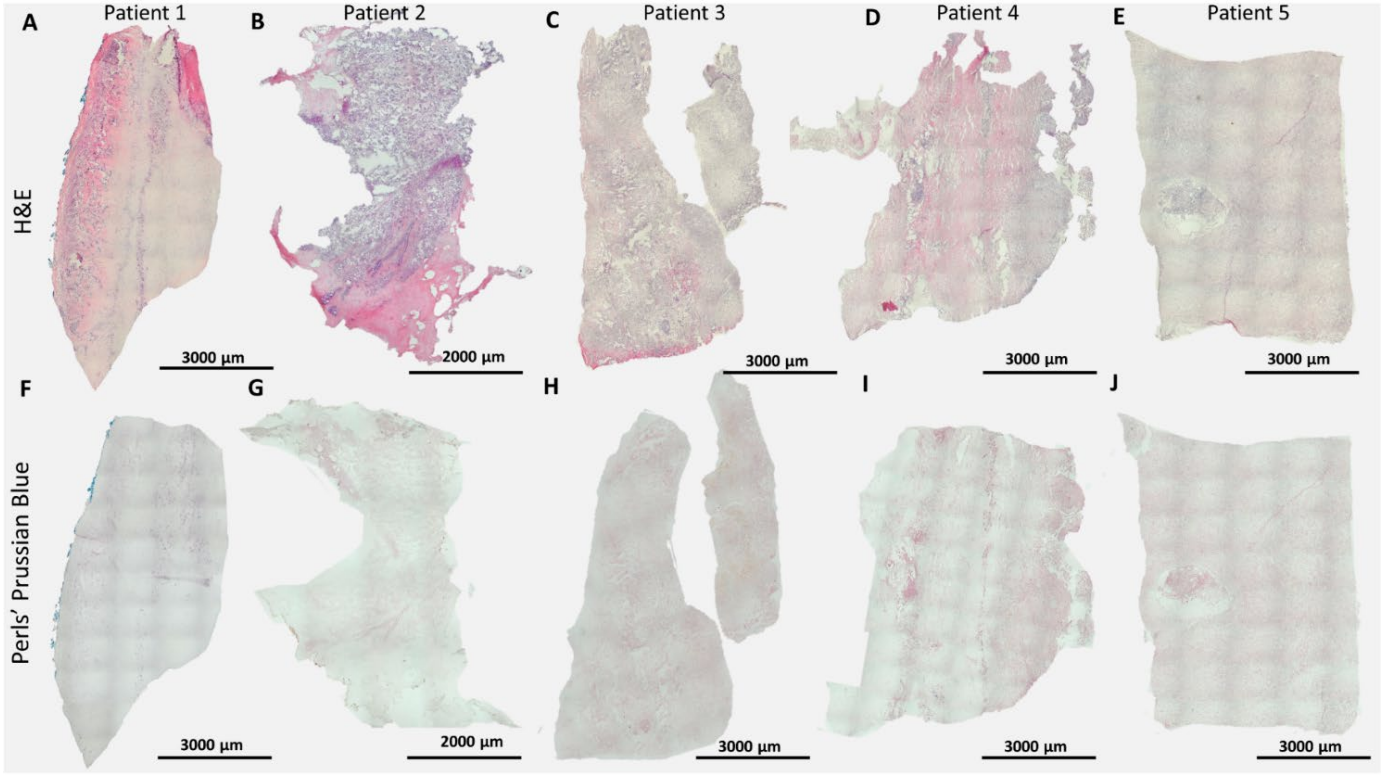

Figure 6.2 Tissue histology following H&E staining (A-E) and Perls' Prussian Blue staining (F-J). Patient 1&5- pleura; Patient 2- chest wall; Patient 3&4- lung. (A-E) Nuclei are stained purple by the haematoxylin, whilst eosin stains cytoplasm and extracellular matrix pink. (F-J) Nuclei are stained pink with Nuclear Fast Red. The blue staining in panel (A&F) is caused by edge effect.

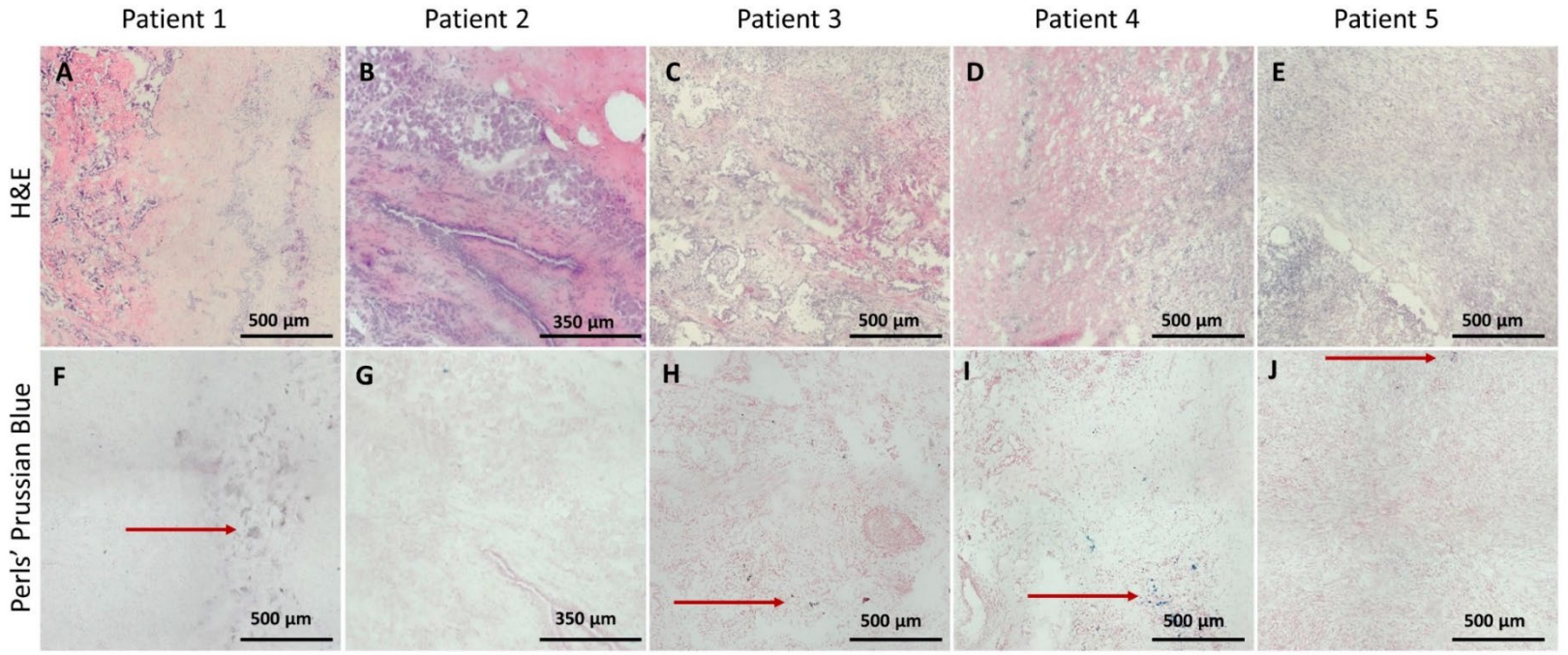

Figure 6.3 H&E staining (A-E) and Perls' Prussian Blue staining (F-J). A- Talc deposits are less visible following H&E staining. (B) Area of fibrosis is highlighted by the intense purple coloration. Traces of oedema can be noted, mainly in the stroma. (C) Mixed mesothelioma, with spindle cells more preeminent at the top region. (E) Desmoplastic growth present in the lower left corner, with areas of aggressive, spindle like cells in the rest of the area. (F) Red arrow points at the talc deposits that did not stain for ferric iron. (H) Possible uncoated asbestos fibres are indicated by the arrow. (I) Coated ferruginous bodies are shown in blue. The size and distribution correspond to asbestos bodies deposition. (J) Possible impurities, smaller fibres might be present.

6.2.2 High-resolution, single element LA-ICP-MS analysis (Instrument 1)

The distribution of magnesium within a healthy human lung section was mapped using high-resolution LA-ICP-MSI. The selected region includes the main layers of the pleura (*i.e.,* the visceral and parietal layers) (Figure 6.4 A). High Mg concentration can be noted around the medium subcutaneous layer and the connective tissue layer which is expected considering its role in smooth muscle contractility (Berardi, Rossana *et al.*, 2019). Additionally, magnesium clusters can be observed around the bronchiole and alveoli in the lung parenchyma (Figure 6.4 B), indicating an area with increased metabolic activity (Kılıc *et al.*, 2018). Interestingly, the top mesothelial cells layer also yielded high magnesium counts following the analysis. Analysis of a healthy section was used as a negative control for mineral fibre detection.

The LA-ICP-MSI set-up allowed for elemental mapping at cellular level, with remarkable resolution and definition of the tissue architecture. However, the lengthy time of acquisition following the ablation of a 1 mm^2 area limits the number of repeats and the applicability of this technique.

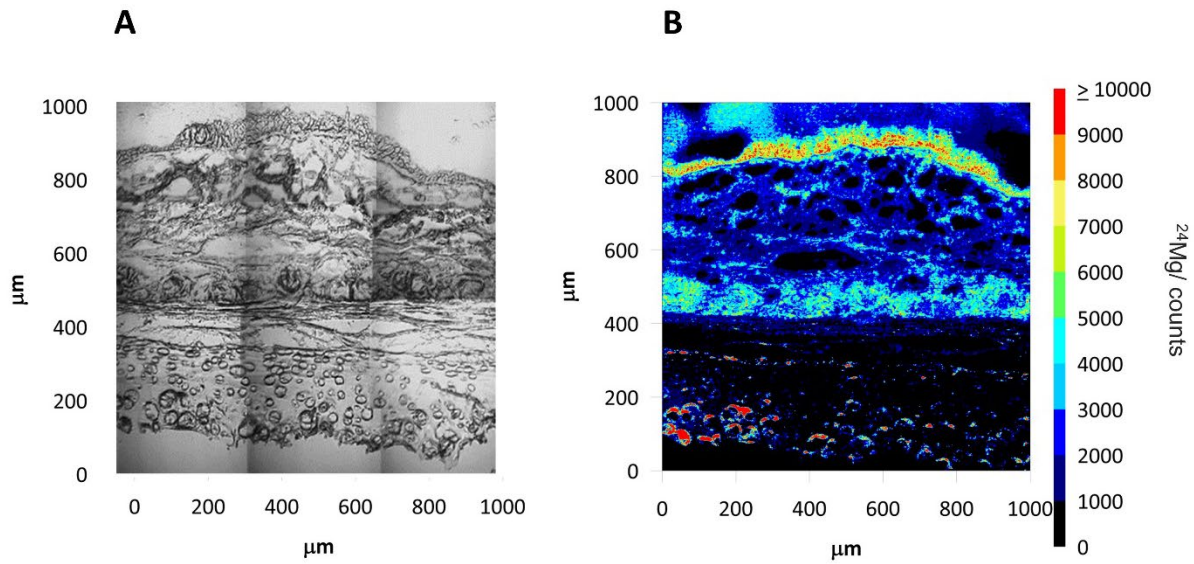

Figure 6.4 (A) Brightfield image of a healthy human lung tissue section layers of the pleura (bottom to top) lung parenchyma, basement membrane, connective tissue, elastic plate, medium subcutaneous, mesothelial cells. (B) Mg distribution within a healthy human lung tissue section determined by LA-ICP-MS analysis. with a 2 µm spot size 1000 x 1000 area 0 µm spacing between lines.

Magnesium has been linked to increased malignant cell proliferation (Cappadone *et al.*, 2021). Human MPM tissue with unknown levels of MF was analysed by LA-ICP-MSI. Magnesium counts were recorded and used to form an elemental map of the Mg distribution. The high Mg counts recorded around the middle of Figure 6.5 B indicate the possible presence of a mineral fibre with high magnesium concentration. Furthermore, the physical properties of the impurities, such as the size and shape, are characteristic to those of asbestos bodies present in MPM patient samples (Pascolo *et al.*, 2015). Although the impurity yielded significantly higher magnesium signal compared to the biological matrix, mapping this element provides details about the typical irregular tissue architecture and distribution of the spindle mesothelioma cells.

Despite the high resolution and the cellular information provided by the LA-ICP-MS image, single-element based detection is not enough to classify the foreign bodies as asbestos fibres. It is, however, a crucial starting point for human MPM tissue analysis with other set-ups. This data shows that the laser and ICP

parameters can be optimised for analysis of soft biological tissue as well as hard, acid resistant MF.

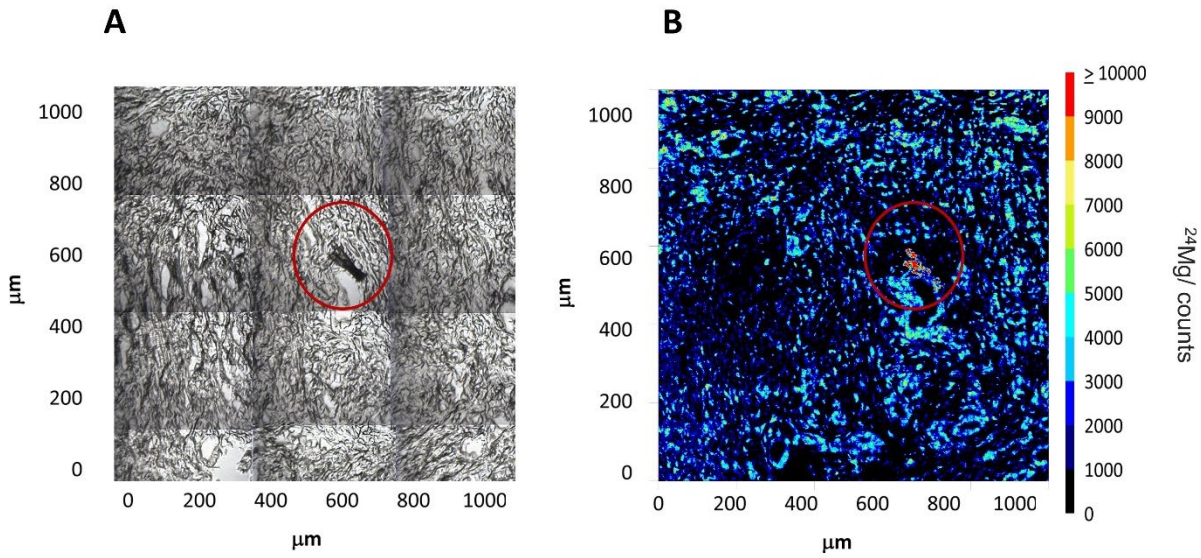

Figure 6.5 (A) Brightfield image of a MPM tissue section layer of the pleura. No tissue architecture characteristic to advanced biphasic or sarcomatoid MPM. (B) Mg distribution within a healthy human lung tissue section determined by LA-ICP-MS analysis with a 2 µm spot size 1000 x 1000 area 0 µm spacing between lines.

6.2.3 Analysis of human MPM tissues by LA-ICP single-quad system (Instrument 3)

The first set of experiments carried out on human MPM tissue samples that targeted multiple elements at once looked for MF in three different MPM patient samples. The malignant tumours were all of pleural origin but were found in different parts including pleura, lung, and chest wall. The ablated areas were selected based on the optical images. This preliminary work was essential for selecting the ROIs and isotopes of interest in the follow up studies.

6.2.3.1 Analysis of pleura tissue- Patient 1

Data acquired for Patient 1 (Figure 6.6) was extremely noteworthy. The two areas selected for ablation presented black, crystal-like impurities that were of high interest for the study. Elemental analysis can help differentiate between coal and dust accumulation and talc deposits resulting from talc pleurodesis. Elemental

analysis by XRF revealed that the main components of the anthracotic structures are Si, K, Al, and Fe (Pascolo *et al.*, 2015).

The black particulates were difficult to ablate, suggesting the presence of MF, possibly talc. Talc is a hydrated magnesium silicate ($Mg_3Si_4O_{10}$ $(OH)_2$) mined in a similar fashion to asbestos fibres. High ^{24}Mg and ^{29}Si counts were therefore expected following laser ablation. A relatively high laser energy (55%) was applied in order to ablate the surface of these crystals (Figure 6.6 A-E). The laser energy was optimised to limit the signal interferences from the glass slide, particularly for ^{29}Si (Figure 6.6 F-J). The high ^{24}Mg signal corresponded to the distribution of the particulates. Interestingly, distribution of ^{57}Fe signal appeared to be mostly around the ^{24}Mg signal and the middle of the area, where there were no talc crystals present. Iron overload has been previously associated with malignant transformation, cancer progression, drug resistance and immune evasion (Brown *et al.*, 2020). Irritants such as talc can trigger an enduring state of inflammation (Vannucci *et al.*, 2018) which in turn may dysregulate iron homeostasis in the lung (Ghio 2008; Pascolo *et al.*, 2015). The ^{29}Si distribution shown in Figure 6.6 E supports the hypothesis that the impurities are indeed hydrated magnesium silicates. Limited signal was recorded for Na, mainly from the biological matrix, presenting a uniform distribution across the tissue (Figure 6.6 B&G).

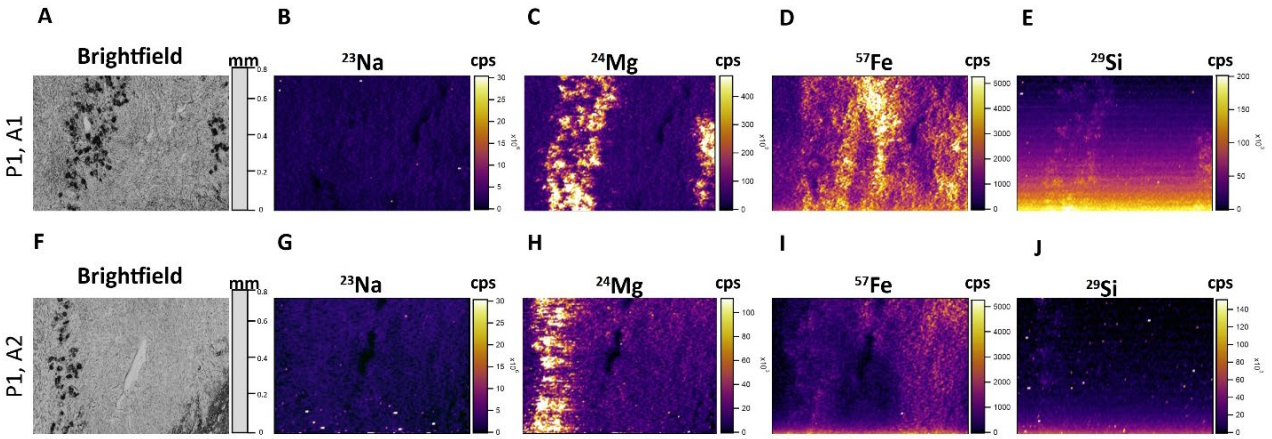

Figure 6.6 LA-ICP-MSI of two distinct areas of MPM tissue from Patient 1 (P1). (B-E) Elemental distribution of ^{23}Na, ^{24}Mg, ^{57}Fe, and ^{29}Si in the first selected area (A1). Spot size 6 µm, laser energy 55%, 5 sweeps. (G-J) Elemental distribution of ^{23}Na, ^{24}Mg, ^{57}Fe, and ^{29}Si in the second selected area (A2). Spot size 6 µm, laser energy 50%, 5 sweeps. Note the high ^{24}Mg counts yielded by the black particulates present in A and F. ^{57}Fe signal was recorded in the vicinity of the impurities. ^{29}Si signal yielded by the particulates was slightly increased in E (higher laser energy) and corresponded with the black impurities.

6.2.3.2 Analysis of chest wall tissue- Patient 2

Due to the limited capabilities of the instrumentation, the parameters had to be adjusted for Patient 2, which yielded very low counts after the first ablation (data not shown). In order to increase the signal, the number of sweeps was increased to 8, whilst the number of targeted elements was reduced from four to three. Despite this adjustment, no significant signal was recorded for Patient 2, particularly due to the lack of MF, but also limited instrument LOD (Figure 6.7). Some ^{13}C and ^{24}Mg signal was homogenously recorded from the biological matrix. Patient 2 was considered a negative control as no asbestos or other MF were expected to be found in this sample considering the finding of the tumour (*i.e.,* chest wall). Notably, ^{57}Fe mapping provides insight into iron sequestration by the malignant cells, linking inflammation to iron overload (Figure 6.7D). However, more detailed analysis is needed to confirm.

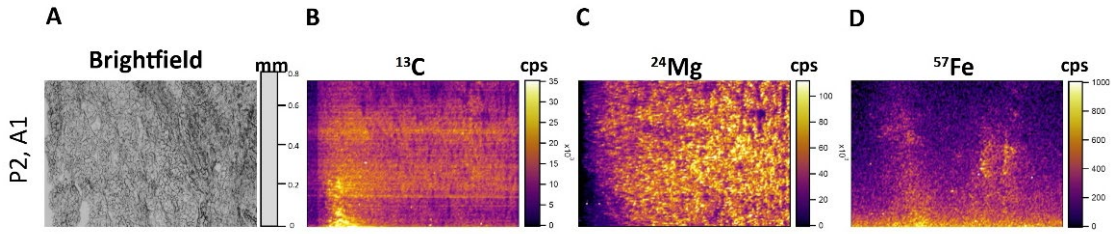

Figure 6.7 LA-ICP-MSI of a region of MPM tissue. Spot size 6 µm, laser energy 50%, 8 sweeps. No visible impurities in the brightfield image (A). ^{13}C and ^{24}Mg distribution was uniform, corresponding to the cellular arrangement (B & C). (D) ^{57}Fe signal may highlight areas of increased inflammation.

6.2.3.3 Analysis of lung tissue- Patient 3

Similar to the data presented above in Figure 6.7, limited counts were recorded following the analysis of Patient 3 (Figure 6.8). ROIs were selected based on noticeable impurities (*i.e.,* possible asbestos fibres), however these failed to yield signals strong enough to be detected by the current instrumentation. Limited ^{13}C and ^{24}Mg signals were yielded by the biological tissue (Figure 6.8 B-C & Figure 6.8 F-G).

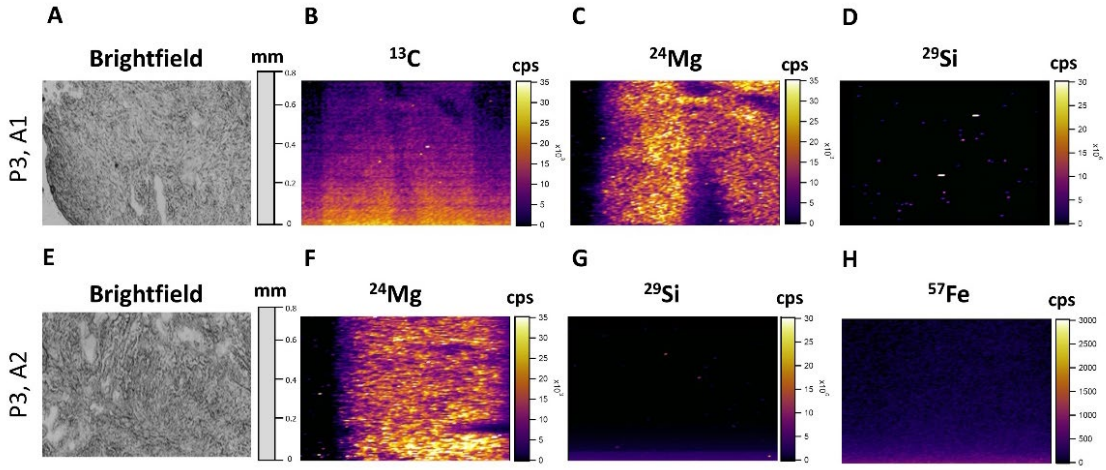

Figure 6.8 LA-ICP-MSI of two distinct areas of MPM tissue from Patient 3. (B-D) Elemental distribution of ^{13}C, ^{24}Mg, and ^{29}Si in the first selected area. Spot size 6 µm, laser energy 50%, 8 sweeps. (F-I) Elemental distribution of ^{13}C, ^{24}Mg, ^{29}Si, and ^{57}Fe in the second selected area. Spot size 6 µm, laser energy 50%, 8 sweeps. Some impurities can be noted in the brightfield images of the ROIs (A and E).

6.2.4 Analysis of human MPM tissues by LA-ICP triple-quad MS system (Instrument 4)

The second set of multi-elemental MPM tissue analysis focused on mapping several different areas of tissue originating from Patient 1 and Patient 2. ROIs from two serial sections were analysed for each patient. ROIs were selected based on the data presented in Section 6.2.3. These included areas of interest containing black impurities known to yield high signals of Mg and Si, but also areas with different cellular morphology and histological presentation. The elements analysed were selected based on asbestos nominal composition, known impurities, as well as target trace metals with a key role in cancer development.

Previous analysis was limited in terms of number of areas ablated, mainly due to the extended time of acquisition. The triple-quadrupole instrument allowed for faster analysis of multiple nuclides at once. The elements were clustered in groups of three to ensure maximum signal with limited interference. Despite a faster time of acquisition compared to previous set-ups, the need for high resolution imaging meant reducing the area of tissue that can be ablated at once. Limited area size may lead to a subjective ROIs selection. Ideally, full tissue analysis is desired, but in this work the areas were selected to include various tissue features.

6.2.4.1 Analysis of pleura tissue- Patient 1

The first set of data (Figure 6.9- Figure 6.14) presents an overlay of the selected ablation areas for two serial sections from Patient 1, with the corresponding LA-ICP-MS image. Brightfield images of the sections before (unstained) and after staining with Perls' Prussian Blue and H&E, as well as a closer view of the LA-ICP-MS image of a selected target element are presented below the overlay. The intensity scale bars were adjusted to the same values for comparison purposes.

The data present the same element of interest for two different areas of the MPM tissue sections to highlight the tumour heterogeneity in terms of architecture and tissue metallome (Figure 6.9-Figure 6.10). There are some noteworthy matters

presented in these figures. Firstly, the crystal-like impurities yielded significant ^{56}Fe counts. Talc is a hydrated magnesium silicate, with small, varying amounts of aluminium, iron, and calcium oxides, depending on the mining site. Limited iron signal coming from the impurities was recorded in the previous analysis. One explanation can be that ^{56}Fe, which was monitored in this instance, is the most common isotope of iron. Additionally, the instrumentation has lower LOD that can monitor trace levels of iron within the structure of talc fibres. Secondly, ^{56}Fe was monitored across both areas by LA-ICP-MSI, as an indicator of tumour specific iron overload. No Perls' Prussian Blue staining was present in the ROIs suggesting that the iron monitored by LA-ICP-MSI is non-heme iron in tissues such as ferritin and hemosiderin.

In terms of Na analysis, the first area selected presented a total lack of tissue architecture, with condensed cellular appearance. ^{23}Na showed an unusual distribution, with higher counts towards the top part of the image (Figure 6.11). The second area presents a more homogenous distribution, with clusters of Na deposits (Figure 6.12).

Hyponatraemia has been previously linked to poor OS in MPM patients (Berardi *et al.*, 2015), but there is limited information regarding Na distribution in the MPM tumour microenvironment. No significant ^{44}Ca signal was recorded in the two ROIs across the tissue section. More importantly, the black impurities, as well as the longer, thinner impurity, did not appear to contain any calcium in their structure (Figure 6.13, Figure 6.14).

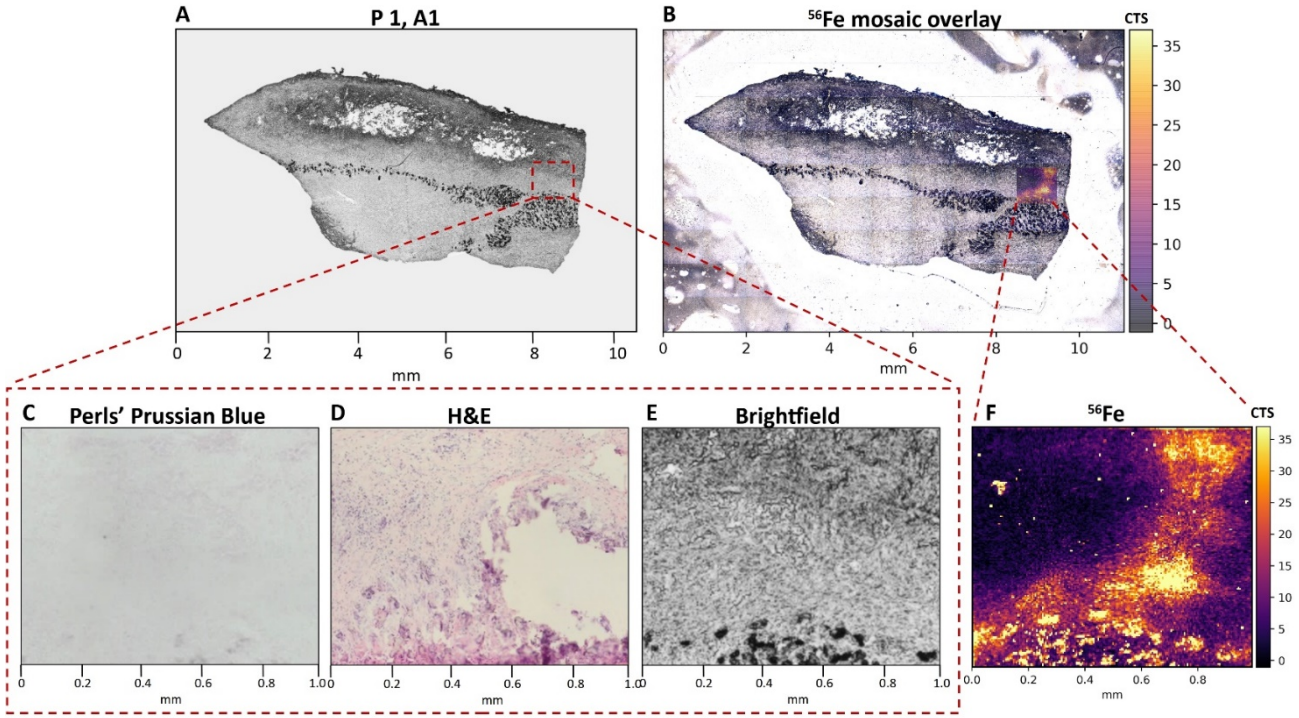

Figure 6.9 Overlay of brightfield and LA-ICP-MS images for Patient 1, Area 1. (A) Brightfield image of the whole tissue section showing the ablated ROI. (B) Mosaic overlay of brightfield image and ^{56}Fe distribution. (C) Perls' Prussian Blue staining of the ablated area. (D) H&E staining of the ablated area. (E) A closer view of the ablated area presenting the black impurities. (F) LA-ICP-MS image of the ROI. High ^{56}Fe counts were recorded from the impurities. High ^{56}Fe can be noted above the impurities and toward the top of the ROI, towards the top layer of the tissue section.

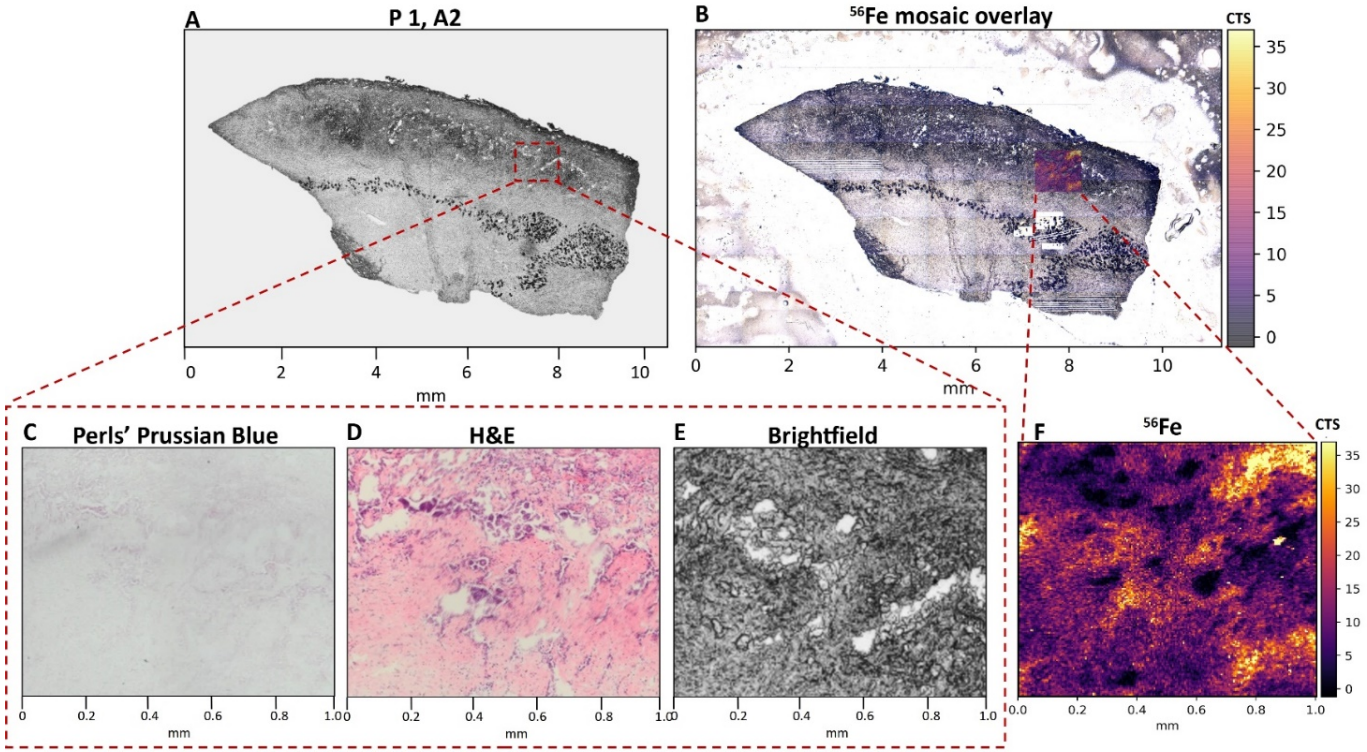

Figure 6.10 Overlay of brightfield and LA-ICP-MS images for Patient 1, Area 2. (A) Brightfield image of the whole tissue section showing the ablated ROI. (B) Mosaic overlay of brightfield image and ^{56}Fe distribution determined by LA-ICP-MSI. (C) Perls' Prussian Blue staining of the ablated area. (D) H&E staining of the ablated area. (E) Zoomed in version of the ROI. (F) LA-ICP-MS image of the ROI. The heterogeneous ^{56}Fe distribution can be noted.

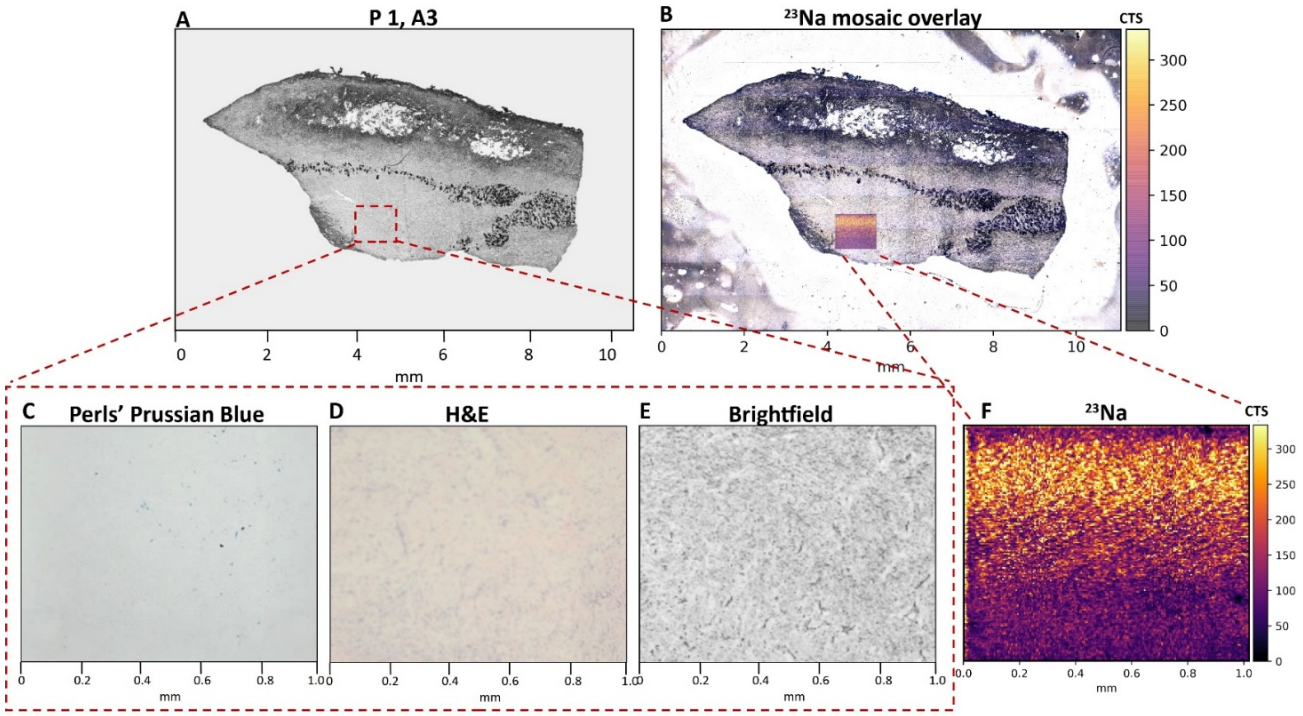

Figure 6.11 Overlay of brightfield and LA-ICP-MS images for Patient 1, Area 3. (A) Brightfield image of the whole tissue section showing the ablated ROI. (B) Mosaic overlay of brightfield image and ^{23}Na distribution determined by LA-ICP-MSI. (C) Perls' Prussian Blue staining of the ablated area. (D) H&E staining of the ablated area. (E) Zoomed in version of the ROI, showing a complete lack of tissue architecture, characteristic to neoplastic development. (F) LA-ICP-MS image of the ablated area based on ^{23}Na counts.

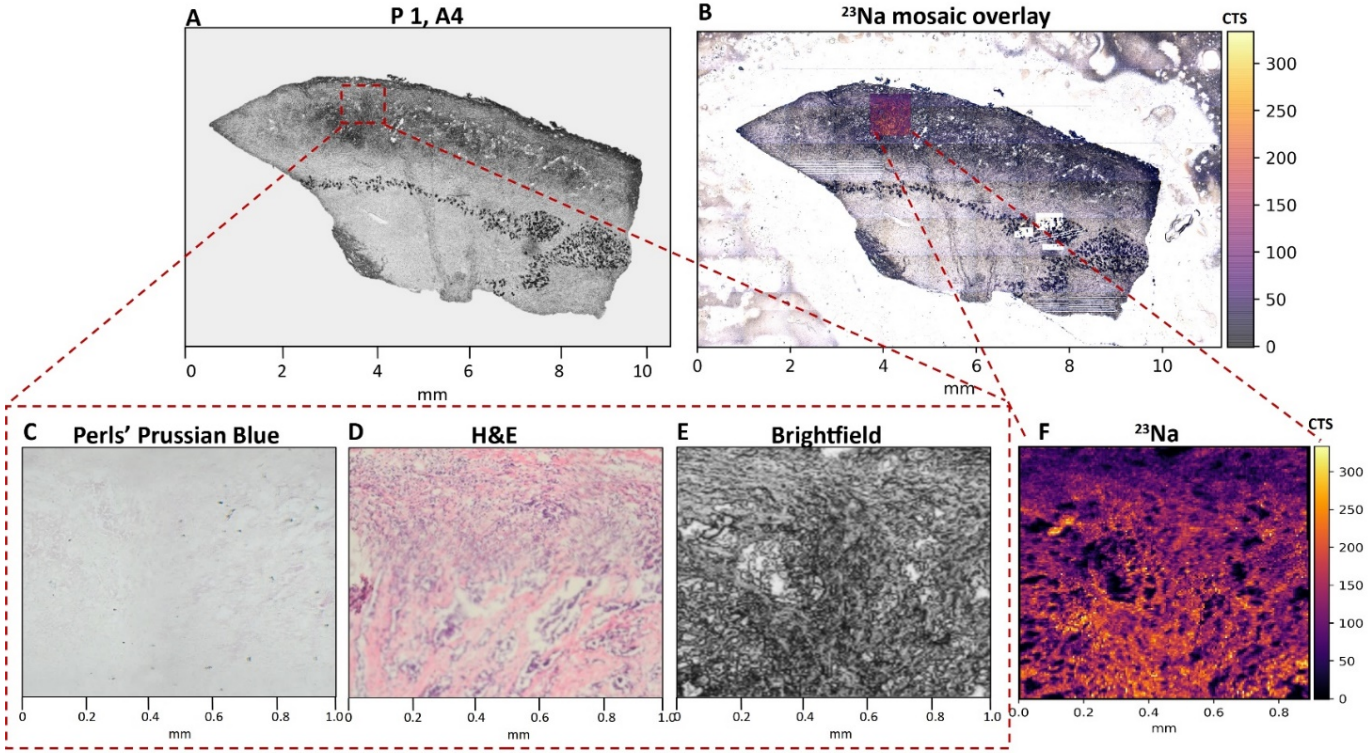

Figure 6.12 Overlay of brightfield and LA-ICP-MS images for Patient 1, Area 4. (A) Brightfield image of the whole tissue section showing the ablated ROI. (B) Mosaic overlay of brightfield image and ^{23}Na distribution determined by LA-ICP-MSI. (C) Perls' Prussian Blue staining of the ablated area. (D) H&E staining of the ablated area. (E) Zoomed in version of the ROI. (F) LA-ICP-MS image of the ablated area, presenting a more homogenous distibution of ^{23}Na.

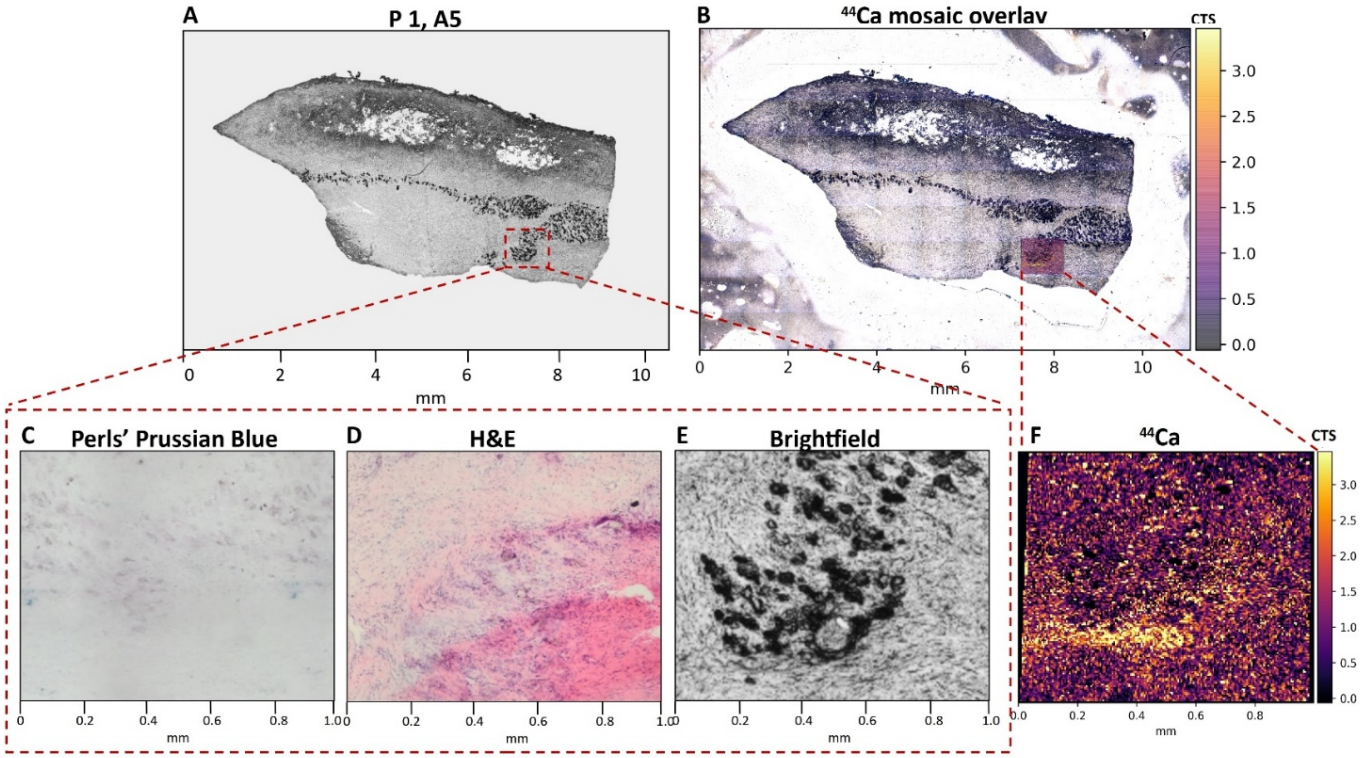

Figure 6.13 Overlay of brightfield and LA-ICP-MS images for Patient 1, Area 5. (A) Brightfield image of the whole tissue section. (B) Mosaic overlay of brightfield image and ^{44}Ca distribution determined by LA-ICP-MSI. (C) Perls' Prussian Blue staining of the ablated area. (D) H&E staining of the ablated area. Note the lack of coloration around the impurities. (E) Zoomed in version of the ROI. (F) LA-ICP-MS image, no significant counts recorded for ^{44}Ca.

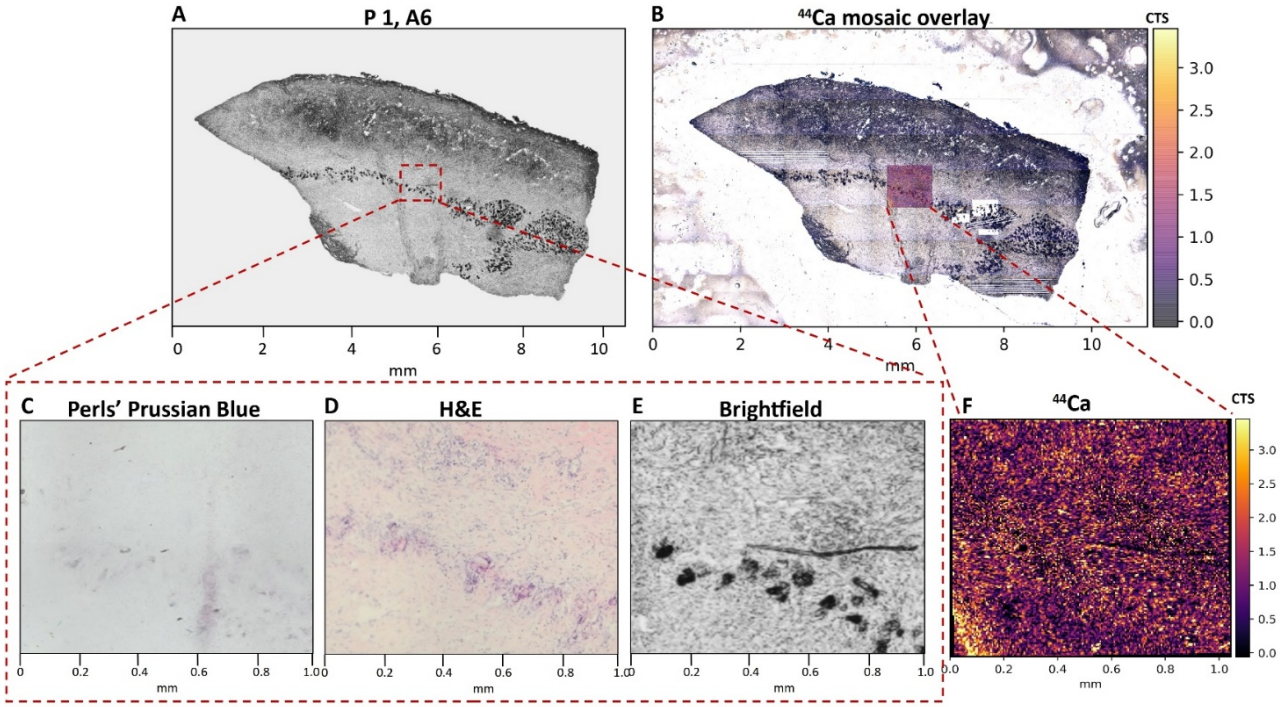

Figure 6.14 Overlay of brightfield and LA-ICP-MS images for Patient 1, Area 6. (A) Brightfield image of the whole tissue section showing the ablated ROI. (B) Mosaic overlay of brightfield image and ^{44}Ca distribution determined by LA-ICP-MSI. (C) Perls' Prussian Blue staining of the ablated area. (D) H&E staining of the ablated area. (E) Zoomed in version of the ROI, showing black crystal-like impurities and a longer, thinner impurity. (F) LA-ICP-MS image of the ablated area with no significant counts recorded for ^{44}Ca.

The targeted nuclides were firstly grouped to reduce interferences in groups of three: ^{27}Al, ^{39}K, and ^{56}Fe, ^{23}Na, ^{24}Mg, and ^{29}Si and finally ^{31}P, ^{44}Ca, and ^{55}Mn. The analysis was carried out in duplicates (2 areas per group) in order to highlight the metallome heterogeneity within the tumour microenvironment.

The black coloured impurities, which were thought to be hydrated magnesium silicates (*i.e.,* talc), required high energy density in order to be ablated (1.4 J cm^{-2}). These yielded high ^{56}Fe signals and proved to contain some trace aluminium (Figure 6.15 B&D). Indeed, a recent study has shown that magnesium silicate hydrate phases tend to incorporate aluminium into both the octahedral and tetrahedral sheets (Bernard *et al.*, 2020). Aluminium was also present in low amounts across the first area. No significant ^{27}Al was recorded for the biological matrix for the second analysis (Figure 6.15 F).

The heterogeneous distribution of K and Na ions between ROIs is specific to malignant tissues (Hare *et al.*, 2015; Leslie *et al.*, 2019) and can provide insight into regions with ion overabundance within MPM microenvironment (Figure 6.15 C&G, Figure 6.16 B&F). Areas with high stroma presence appeared to be more abundant in Na and K, which is an indicator of necrotic regions (Nagy *et al.*, 1981). No significant counts were recorded for ^{24}Mg and ^{29}Si in the first set of analysis (Figure 6.16 C-D&G-H). Similarly, the total count recorded for ^{31}P, ^{44}Ca, and ^{55}Mn was not significantly above the background (Figure 6.17 C-D & G-H). One noteworthy finding was that the talc particles yielded no ^{44}Ca signals, as presented in Figure 6.17 C&G.

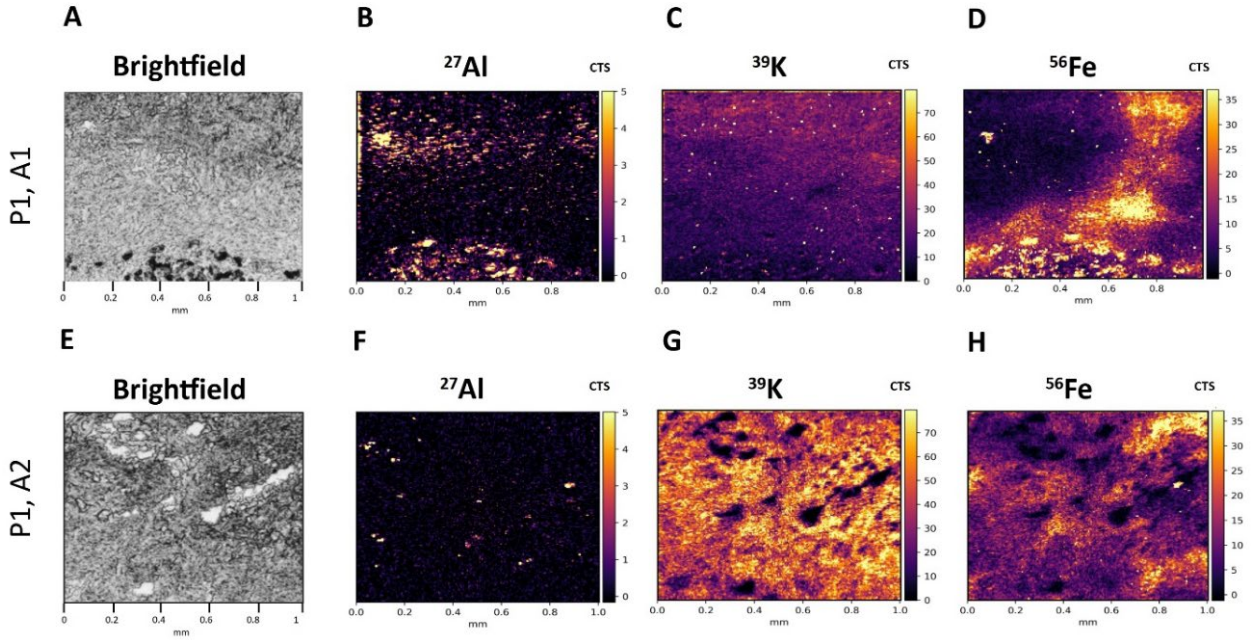

Figure 6.15 Elemental map of selected ROIs based on either ^{27}Al, ^{39}K, or ^{56}Fe signal. (A&E) Brightfield images pre-ablation. 5 µm spot size, 1.4 J cm^{-2} laser fluence. Intensity bars were set to the same values for comparison purposes and represent total counts per second.

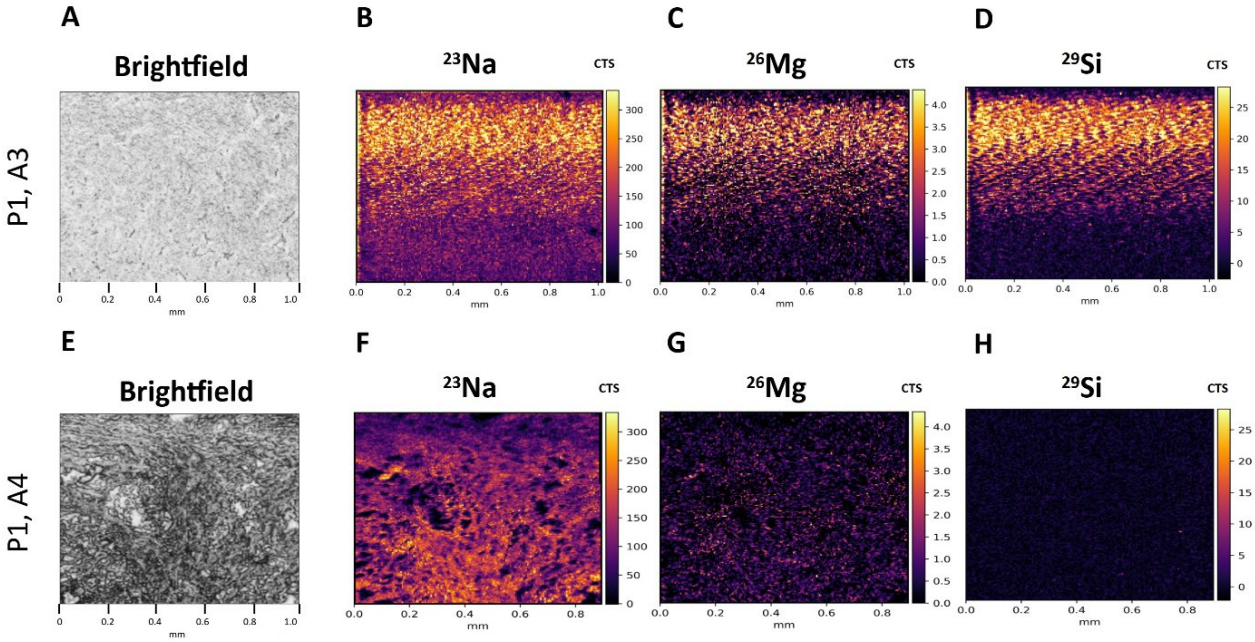

Figure 6.16 Elemental map of selected ROIs based on either ^{23}Na, ^{26}Mg, or ^{29}Si signal. (A&E) Brightfield images pre-ablation. 5 µm spot size, 1.4 J cm^{-2} laser fluence. Intensity bars were set to the same values for comparison purposes and represent total counts per second. Note the background interferences present in panel (B-D).

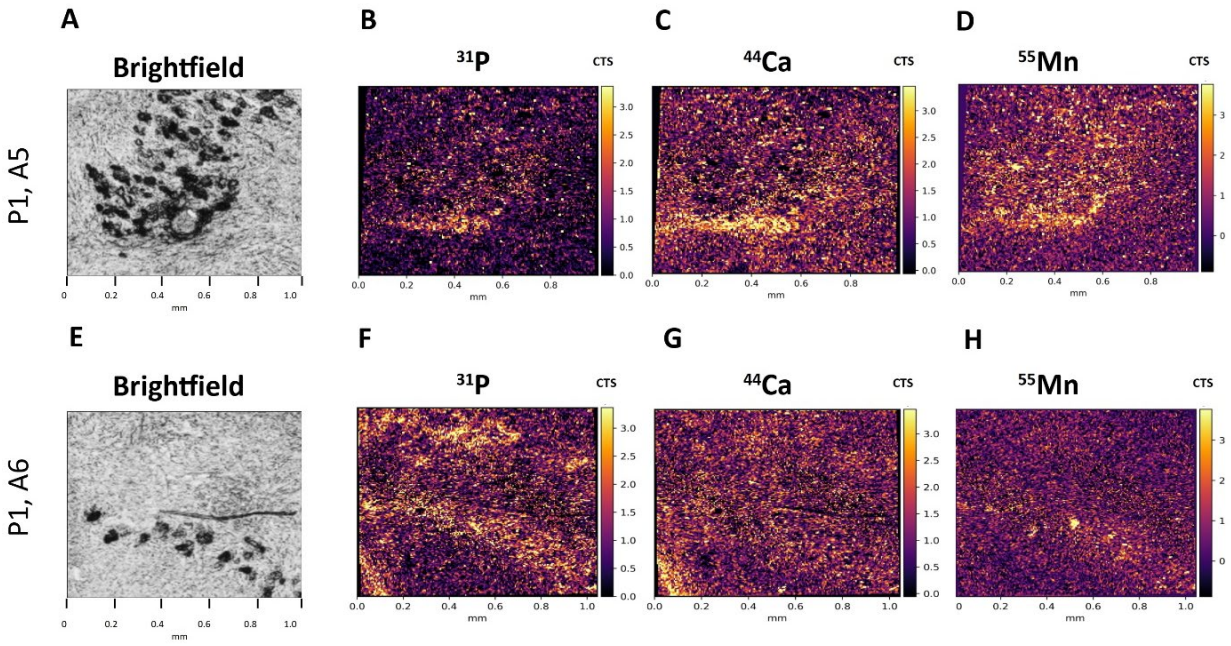

Figure 6.17 Elemental map of selected ROIs based on either ^{31}P, ^{44}Ca, or ^{55}Mn signal. (A&E) Brightfield images pre-ablation. 5 µm spot size, 1.4 J cm^{-2} laser fluence. Intensity bars were set to the same values for comparison purposes and represent total counts per second.

Nuclides groups were randomly assigned to each ROIs. Based on the previous analysis carried out with the single-quad instrument, the attention shifted toward determining the ^{24}Mg and ^{29}Si presence in the black impurities, and the impact on iron homeostasis in their vicinity. Subsequently, more analysis was carried out on two ROIs with significant particulate presence. Aluminium and calcium were also added to the analysis panel as known impurities (Mutch *et al.*, 2016; Surour, 2015). Potassium was selected as a key factor in ionic imbalance (Eil *et al.*, 2016) (Figure 6.18).

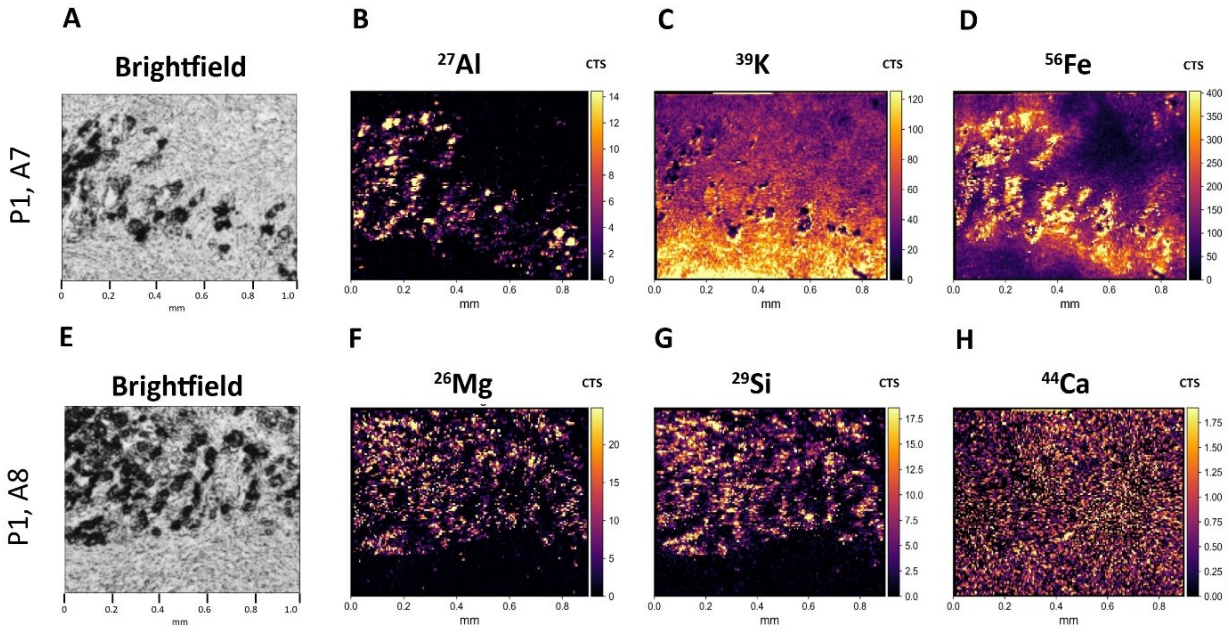

Figure 6.18 Elemental map of selected ROIs based on either ^{27}Al, ^{29}Si, or ^{44}Ca signal. (A&E) Brightfield images pre-ablation. 5 µm spot size, 0.75 J cm^{-2} laser fluence. Intensity bars were set to the same values for comparison purposes and represent total counts per second. ROIs were specifically selected to include black, crystal-like particulates.

6.2.4.2 Analysis of chest wall tissue- Patient 2

The ROIs for Patient 2 were selected to highlight the tissue heterogeneity as seen through optical microscopy. No visible foreign bodies were detected in the brightfield images, which was in line with the guidance provided by the pathology consultant.

Regions with increased ^{39}K and ^{23}Na counts highlighted the tumour specific ion sequestration (Figure 6.19 C&G, Figure 6.20 B&F). However, there was a more noticeable electrolyte homogeneity in between the selected regions, which was expected considering the percentage of tumour region (>90%). Interestingly, iron overload was noted in Figure 6.19 D around the marks left by pulmonary oedema (Table 6.1). There is an established link between increased inflammation, pulmonary oedema, and damage or scarring of the tissue, also known as fibrosis. Pulmonary iron overload has been shown to play a key role in the pathogenesis of pulmonary fibrosis and lung function decline (Puxeddu *et al.*, 2014).

No MF were detected based on the ^{26}Mg, ^{56}Fe or ^{29}Si signal, which are key components of asbestos fibres nominal structures (Figure 6.19, Figure 6.20). Some high intensity spots were recorded for ^{29}Si, possibly from the glass slide. Despite the low total counts, ^{44}Ca showed a uniform distribution. No significant levels were recorded for ^{31}P and ^{55}Mn (Figure 6.21 C-D&G-H).

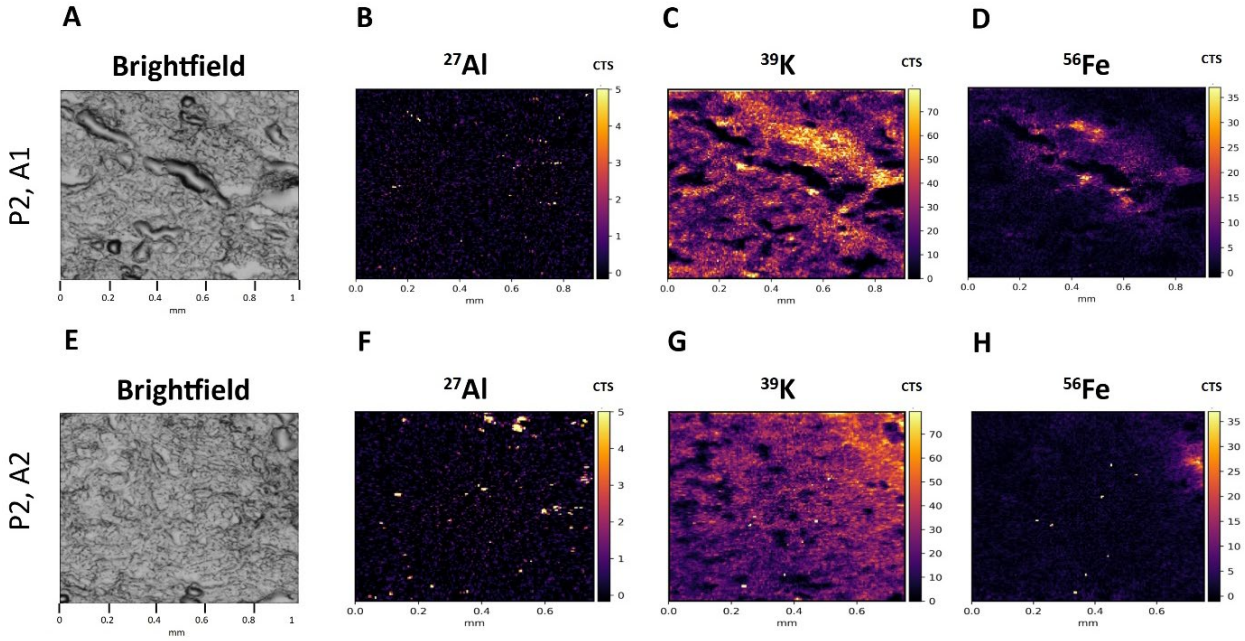

Figure 6.19 Elemental map of selected ROIs based on either ^{27}Al, ^{39}K, or ^{56}Fe signal. (A&E) Brightfield images pre-ablation. 5 µm spot size, 1.4 J cm^{-2} laser fluence. Intensity bars were set to the same values for comparison purposes and represent total counts per second.

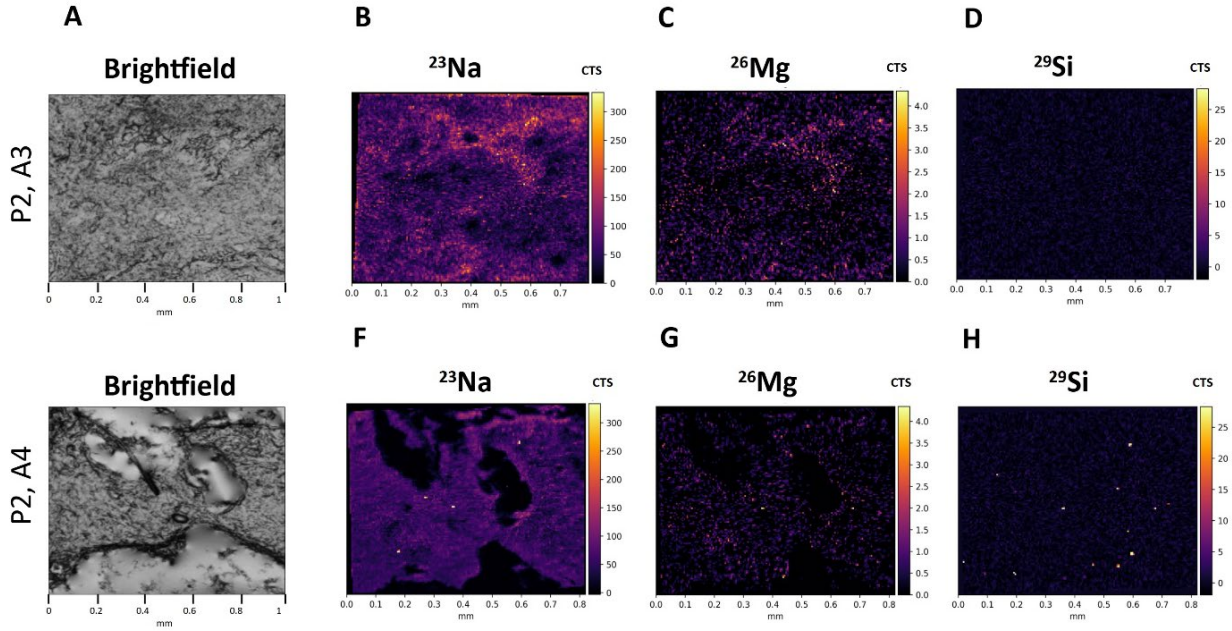

Figure 6.20 Elemental map of selected ROIs based on either ^{23}Na, ^{26}Mg, or ^{29}Si signal. (A&E) Brightfield images pre-ablation. 5 µm spot size, 1.4 J cm^{-2} laser fluence. Intensity bars were set to the same values for comparison purposes and represent total counts per second.

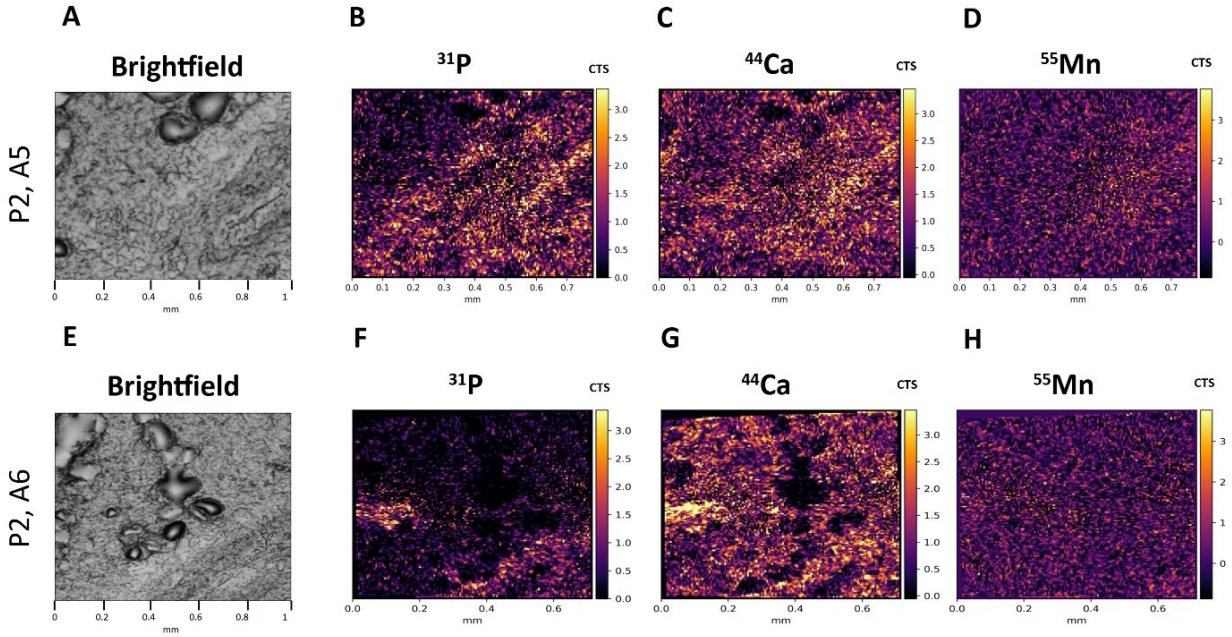

Figure 6.21 Elemental map of selected ROIs based on either ^{31}P, ^{44}Ca, or ^{55}Mn signal. (A&E) Brightfield images pre-ablation. 5 µm spot size, 1.4 J cm^{-2} laser fluence. Intensity bars were set to the same values for comparison purposes and represent total counts per second.

6.2.5 Analysis of human MPM tissues by LA-ICP-TOFMS (Instrument 5)

A state-of-the-art set-up was employed for the final analysis step. Channelling the ultra-fast running abilities of the Iridia laser, coupled with the icpTOF 2R ICP-TOFMS instrument, we were able to pseudo-simultaneously detect all isotopes of selected areas of MPM tissue sections at unprecedented speed, with a resulting pixel size of 2 µm x 2 µm (Voloaca *et al.*, 2022).

The laser and instrument parameters were optimised on 3D MPM models spiked with asbestos fibres, that were prepared to recapitulate the human tissue sections (embedded, flash-frozen, and cryosectioned at 5 µm thickness on glass slides). Laser parameters had to be optimised to ablate both hard asbestos bodies as well as soft biological matrix.

Finally, high-resolution LA-ICP-TOFMS imaging was performed on patient samples of different origins and pathologies (Table 6.1). The selection of MPM tumours localised in different parts of the lung, pleura, or chest wall was essential to show the *in-situ* heterogeneity of MPM metallome, as well as MF translocation and site preference.

6.2.5.1 Optimisation of instrument parameters for LA-ICP-TOFMS analysis

In previous chapters, it was shown that asbestos and other MF subsets can be differentiated within 2D and 3D MPM cell culture models based on their multi-element pattern using LA-ICP-TOFMS imaging. The major constituents of the investigated fibres are the elements Na, Mg, Al, Si, and Fe, which can be also present in biological tissue and/or in the glass substrate. Additionally, the identification of fibres within biological tissue can be challenging as it requires the ablation of soft biological material and hard mineral material in parallel. Therefore, the selection of the laser fluence plays an important role to enable selective and quantitative ablation of biological material from the glass substrate, while the laser fluence has to be high enough to ablate the fibre material. In a first step, an LA-ICP-TOFMS method was evaluated in model systems, using mesothelioma cells spiked with three different types of asbestos fibres. The selection of asbestos

fibres included amosite, crocidolite, and chrysotile, as they present different nominal composition and degrees of carcinogenicity (Hodgson & Darnton, 2000).

In terms of sample preparation, the MPM 3D models were treated as tissue blocks, made to recapitulate the human MPM tissue sections. The same LA parameters as intended for the imaging experiments of the tissue samples were used with a pixel size of 2 µm. Different fluence levels in the range of 0.5 - 3 J cm^{-2} were evaluated resulting in an optimised fluence of 1 J cm^{-2}. At this fluence level, selective ablation of the cells was observed without creating imaging artefacts resulting from co-ablation of the glass substrate. In a next step, it was evaluated whether the fluence is high enough to qualitatively ablate the asbestos fibres present within the cells. For the three different types of asbestos fibres, elemental levels of Na, Mg, Si, and Fe significantly above the biological background were observed. The cells were visualised with the phosphorus signals, which was overlaid with the signals of the elements present in the different fibre types. The recorded signals for each fibre type matched the established nominal structures (Greenhalgh *et al.*, 2020). In detail, crocidolite was characterised by high levels of Na, Mg, Si, and Fe, as shown in Figure 6.22. Both amosite and chrysotile yielded elevated levels of Si and Fe, but Mg was only recorded for chrysotile, known to have Mg in its chemical structure (Figure 6.23, Figure 6.24). Based on these findings, it was shown that the LA-ICP-TOFMS method and the selected fluence and laser parameters in this study are fit-for-purpose for the detection of MF within human MPM tissue samples.

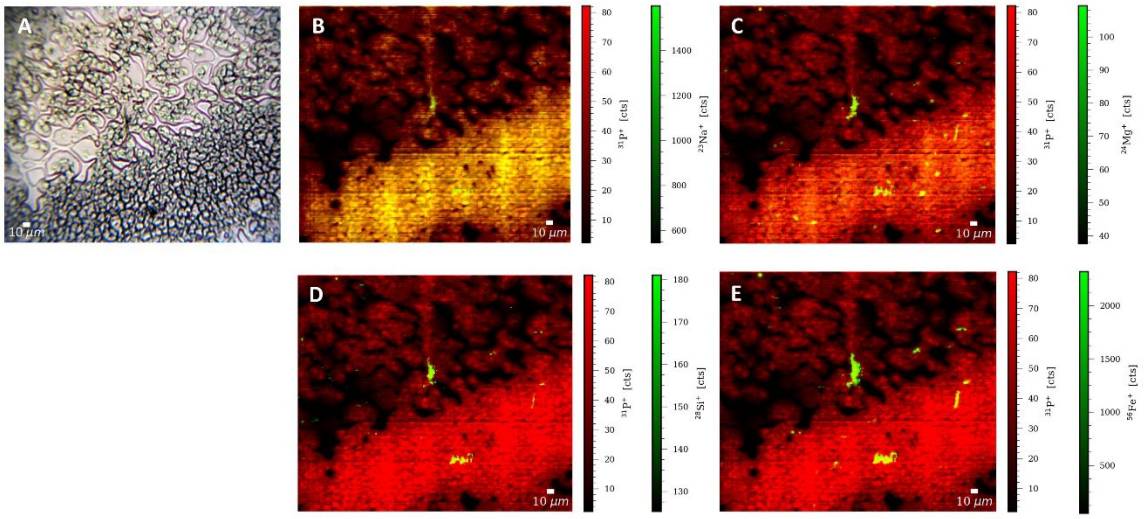

Figure 6.22 LA-ICP-TOFMS analysis of 3D MPM models treated with crocidolite. (A) Brightfield image of the ablated area. (B-E) Crocidolite fibres yielded high counts of ^{23}Na, ^{24}Mg, ^{29}Si, and ^{56}Fe and can be noted against the ^{31}P signal generated by the biological matrix. The following laser ablation parameters were used: round laser spot size of 4 µm, fixed dosage mode of 2, repetition rate of 250 Hz, and the parallel lines overlapped one another by 2 µm.

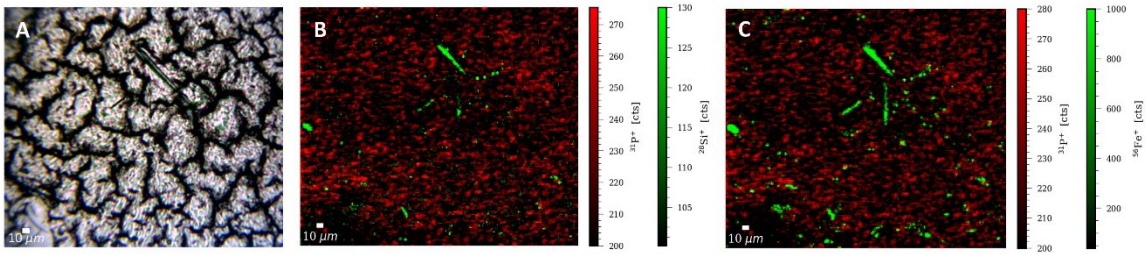

Figure 6.23 LA-ICP-TOFMS analysis of 3D MPM models treated with amosite. (A) Brightfield image of the ablated area. (B-C) Amosite fibres yielded high counts of ^{29}Si and ^{56}Fe and can be noted against the ^{31}P signal generated by the biological matrix. The following laser ablation parameters were used: round laser spot size of 4 µm, fixed dosage mode of 2, repetition rate of 250 Hz, and the parallel lines overlapped one another by 2 µm.

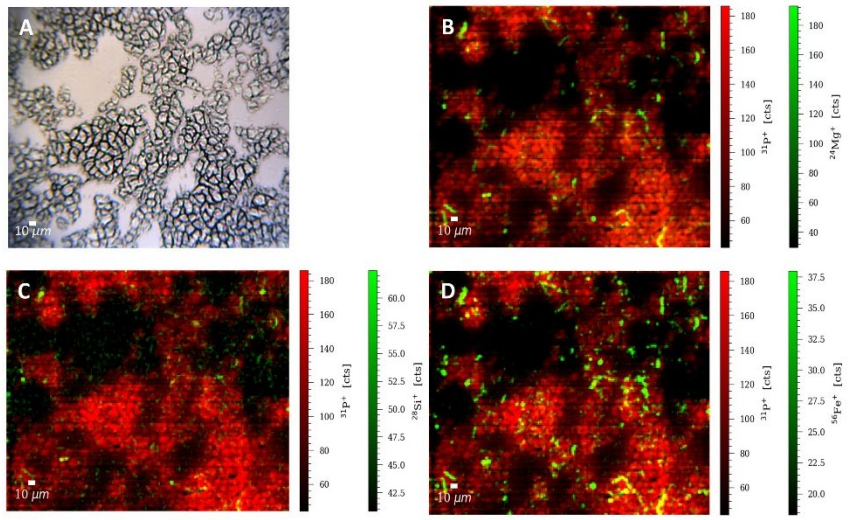

Figure 6.24 LA-ICP-TOFMS analysis of 3D MPM models treated with chrysotile. (A) Brightfield image of the ablated area. (B-D) Chrysotile fibres yielded high counts of ^{24}Mg, ^{29}Si, and ^{56}Fe and can be noted against the ^{31}P signal generated by the biological matrix. The following laser ablation parameters were used: round laser spot size of 4 µm, fixed dosage mode of 2, repetition rate of 250 Hz, and the parallel lines overlapped one another by 2 µm.

6.2.5.2 High-resolution LA-ICP-TOFMS imaging of pleura tissue- Patient 1

Based on the brightfield images of the pleura sample (Figure 6.25 A), ROIs were selected for high-resolution LA-ICP-TOFMS analysis. In this case, several black crystal-like structures (with a diameter of around 20-50 µm) could be observed on the microscopic images of the pleura sample, which were of high interest for the study. Histological analysis revealed that these particulates did not stain for ferric iron (Perls' Prussian blue staining) and did not retain colour following H&E staining, which is a characteristic of talc deposits stains (Vannucci *et al.,* 2018). Additionally, the linear distribution and microscopic presentation of these particulates suggested the presence of talc deposits resulted from talc pleurodesis (Attanoos & Gibbs, 2004). LA-ICP-TOFMS data supported this hypothesis. Talc is a hydrated magnesium silicate mined in a similar fashion to asbestos fibres, with varying amounts of aluminium, iron, and calcium oxides as common impurities, depending on the mining site (Bernard *et al.*, 2020).

Detailed LA-ICP-TOFMS analysis showed that these features were characterised by elevated magnesium and silicon levels, and slightly increased aluminium and

phosphorus levels (compared to the surrounding tissue). A further screening of the LA-ICP-TOFMS elemental distribution maps revealed that these structures also yielded some iron and zinc signals (Figure 6.25). The general structure of talc can be expressed as $Si_4O_{10}M_3(OH)_2$, with Mg occupation at the M sites, and replacement of Mg by ferrous iron (known as minnesotaite) (Ramanaidou *et al.*, 2015). This is likely why the particulates did not stain blue following Perls' Prussian Blue reaction, which interacts with ferric iron.

Tumours are known to be phosphorus-demanding due to increased ribosomal biogenesis in malignant cells which require a high amount of P (Nagy, 2007) Clusters of high P signals can be noted across the section. Additionally, some particulates generated high P counts (Figure 6.25E).

Interestingly, distribution of Fe signal appeared to be significantly increased around the talc deposits, and in between clusters of these magnesium-rich particulates. This was noted previously in Figure 6.6, but the ultra-high resolution of this current set-up allows for a more detailed interpretation of the MPM metallome. Iron overload has been previously associated with malignant transformation, cancer progression, drug resistance, and immune evasion (Brown *et al.,* 2020). Irritants such as talc can trigger an enduring state of inflammation (Vannucci *et al.,* 2018) which in turn may dysregulate iron homeostasis in the lung (Ghio *et al.,* 2008; Pascolo *et al.,* 2015). Iron sequestration by cancerous cells is also a hallmark of neoplastic transformation which can explain the high counts of ^{56}Fe in the vicinity of the talc particulates (Figure 6.25 F) (Serra *et al.*, 2020).

Whilst no significant counts were recorded for Cu (Figure 6.25 G), Zn signals presented a more homogenic distribution across the tissue, with areas of high metabolic activity indicated by Zn overabundance (Figure 6.25 H).

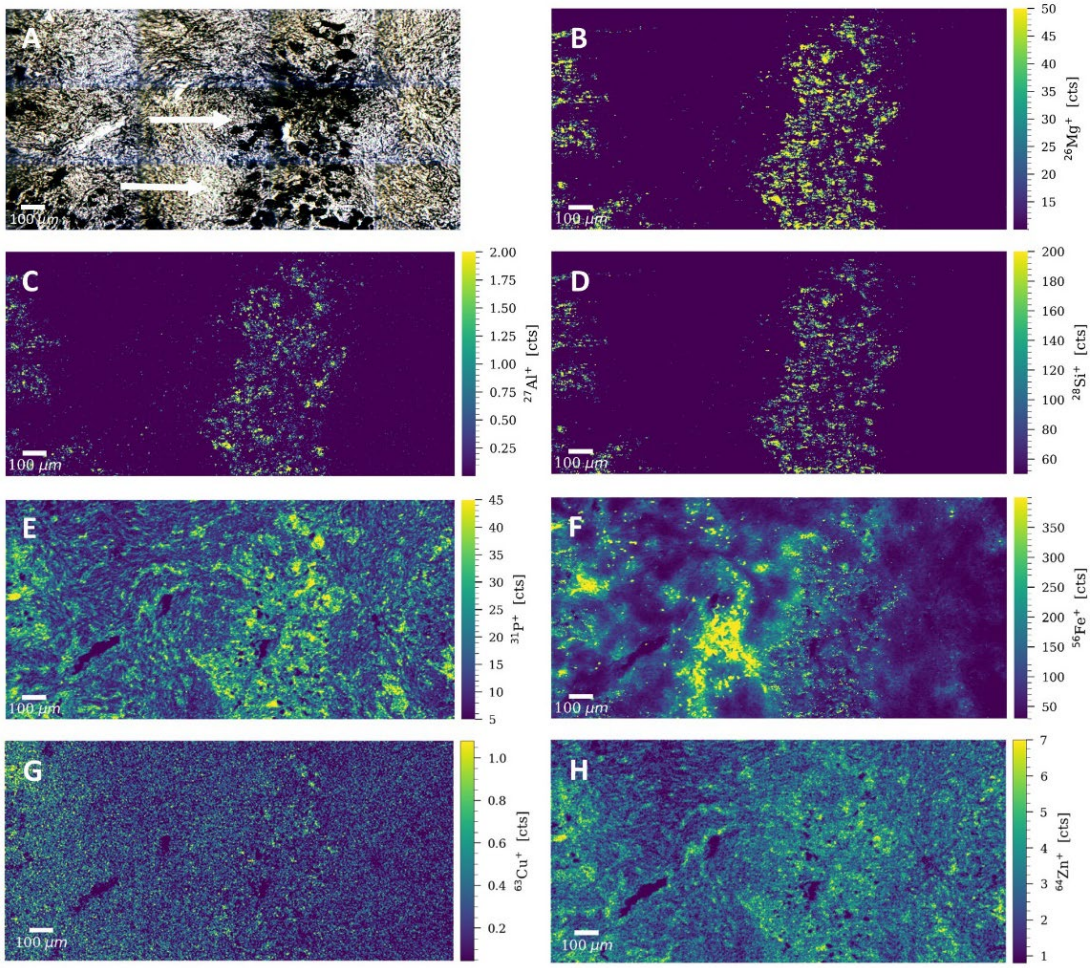

Figure 6.25 LA-ICP-TOFMS analysis Patient 1. (A) Brightfield image of the ablated area showing the black, crystal-like particulates. Signal intensity maps of (B) $^{24}Mg^+$, (C) $^{27}Al^+$, (D) $^{28}Si^+$, (E) $^{31}P^+$, (F) $^{56}Fe^+$, (G) $^{63}Cu^+$, and (H) $^{66}Zn^+$ obtained by LA-ICP-TOFMS imaging. The impurities are indicated by white arrows. The following laser ablation parameters were used: round laser spot size of 2 µm, fixed dosage mode of 2, repetition rate of 250 Hz, and the parallel lines overlapped one another by 2 µm.

6.2.5.3 High-resolution LA-ICP-TOFMS imaging of chest wall tissue -Patient 2

Patient 2 had a known history of oedema and fibrosis. Selected ROI included areas with possible fibrosis caused by prolonged chronic inflammation (Wynn, 2008). Elevated signals of Mg, P, Fe, S, and Zn were recorded around the tissue scar. Magnesium and iron are known drivers of inflammatory responses, by triggering cytokines, macrophages, and other immune cells (Maier *et al.*, 2021; Serra *et al.*, 2020), whilst zinc has been associated with increased cellular

proliferation (MacDonald, 2000). Being an inflammation-driven mechanism characterised by cellular overgrowth, elevated levels of these metals were expected around the fibrotic regions (Figure 6.26 B, D&F).

Fibrosis is characterised by overgrowth, hardening, and/ or scarring of the tissues and is attributed to excess deposition of extracellular matrix (Wynn, 2008). The elevated levels of P around the fibrotic tissue supported the “growth rate hypothesis”, which suggests that C:N:P ratios are influenced by protein synthesis demand (Hessen *et al.*, 2013), and therefore rapidly proliferating cells are rich in P (Nagy, 2007)

Interestingly, sulphur was present across the tissue section, with significant higher levels around the fibrotic tissue (Figure 6.26 E). Glycolytic metabolism is accelerated in cancer cells producing high levels of sulphur-rich compounds via Maillard reaction (Yamagishi *et al.*, 2012), which can explain the high ^{32}S signal surrounding the scar tissue.

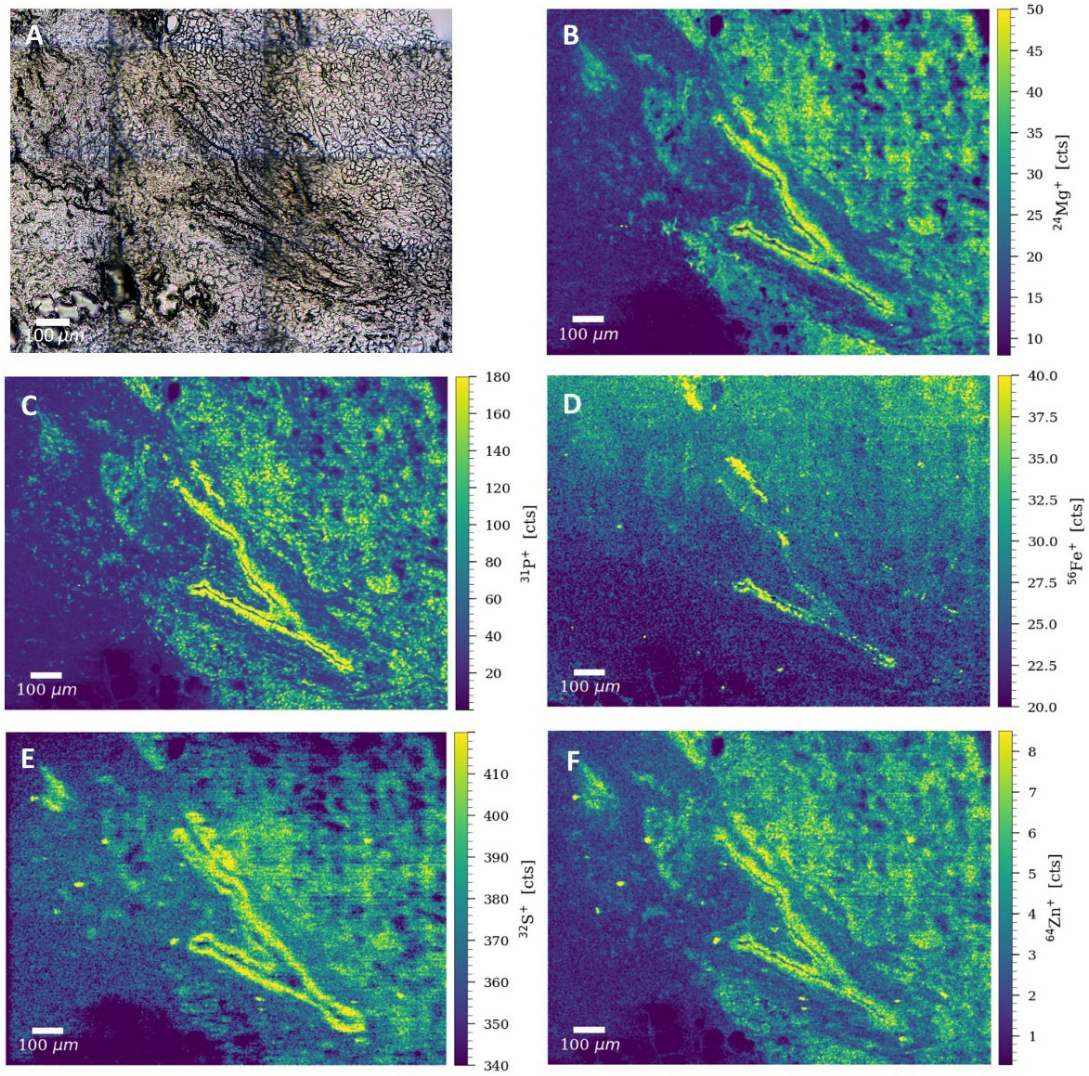

Figure 6.26 LA-ICP-TOFMS analysis of Patient 2. (A) Brightfield image of the ablated area showing the fibrotic region. Signal intensity maps of (B) $^{24}Mg^+$, (C) $^{31}P^+$, (D) $^{56}Fe^+$, (E) $^{32}S^+$, (F) $^{66}Zn^+$ obtained by LA-ICP-TOFMS imaging. The following laser ablation parameters were used: round laser spot size of 2 µm, fixed dosage mode of 2, repetition rate of 250 Hz, and the parallel lines overlapped one another by 2 µm.

6.2.5.4 High-resolution LA-ICP-TOFMS imaging of lung tissue- Patient 3

ROIs were imaged with a pixel size of 2 µm and pixel acquisition rates of 250 Hz (enabled by the signal pulse response of the used LA set-up). Again, the laser fluence was optimised to enable selective and quantitative ablation of biological material from the glass substrate resulting in a fluence of 1.0 J cm^{-2}. Via this approach, it was possible to image biologically essential elements present in

tissue that are also major constituents of the glass substrate, such as Na, Mg, and Ca. This approach, together with the use of an ICP-TOFMS instrument, allowed the analysis of a wide range of elements in the tissue samples including elements with biological key functions from the lower mass range (Serra *et al.*, 2020).

Based on the brightfield images taken prior to laser ablation, different regions of interest with visible black impurities were selected for detailed and high-resolution LA-ICP-TOFMS analysis of human MPM lung tissue samples. The lung tissue sample of Patient 3 showed distinct elemental distributions of magnesium, phosphorus, iron, and zinc, which allowed visualisation of the tissue structure. With the high-resolution adopted in the imaging approach, single cells could be visualised in the tissue structures based on the phosphorus signal. Distinct features of the ROI selected in Figure 6.27 were characterised by elevated levels of Si, Ca, Fe, and Sr significantly above the signals of the biological matrix. One of them resembled a long fibre (with a total length of around 200 µm) comparable to the asbestos fibres in the 2D cell control samples, whereas the other features were round and relatively small (with a size of around 25-30 µm in diameter). The fibre type impurity could be visualised using the $^{44}Ca^{+}$ signal and $^{56}Fe^{+}$ signal, whereas the other features were characterised by elevated Si, Ca, Fe, and Sr signals. The high-resolution (2 µm) allowed for imaging even smaller fibres or fibre fragments (Figure 6.28). Interestingly, one of the long impurities indicated by the white arrows in the brightfield image yielded no significant counts of either of the metals, suggesting the presence of a non-asbestiform foreign body. This finding proves the capabilities of LA-ICP-TOFMS imaging to distinguish asbestiform fibres and other impurities.

A noteworthy finding was the high amount of strontium yielded by 2 out of 3 impurities present in the ROI and indicated by the white arrows (Figure 6.27 E). Sr has been previously reported as a potential toxic element (PTE) present in trace quantities in various types of asbestos, with a key role in MPM pathogenesis (Bloise *et al.,* 2020). Crocidolite fibres have been reported to contain high amounts of Sr, amongst other contaminants, by analysing the metal content of

hair samples of subjects environmentally exposed to this type of asbestos. However, based on this elemental map alone, it is challenging to classify these impurities as crocidolite.

The fibre type structure also displayed lower Mg and P levels than the surrounding tissue. One such example was the Fe signal of the fibre/impurities which proved to be around 20 higher than the surrounding tissue signal. In order to further confirm these results, the remaining fibres which were still visible on the glass slide after ablation with 1 J cm^{-2} were fully ablated using a significantly higher fluence of 3 J cm^{-2} (Figure 6.28). Again, high levels of Si, Ca, Fe, and Sr were detected by LA-ICP-TOFMS, whereas no Si was found in the fibre structure. Moreover, Mg signal generated by one of the impurities was noted following the second ablation and removal of magnesium-enriched biological matrix (Figure 6.28 E). The increase in counts of some elements after ablation with a higher fluence (*i.e.,* Fe and Mg) and total lack of signal displayed for others (*i.e.,* Si) highlighted the difficulty of spatially resolving MF (hard material) within native biochemical environment (soft tissue).

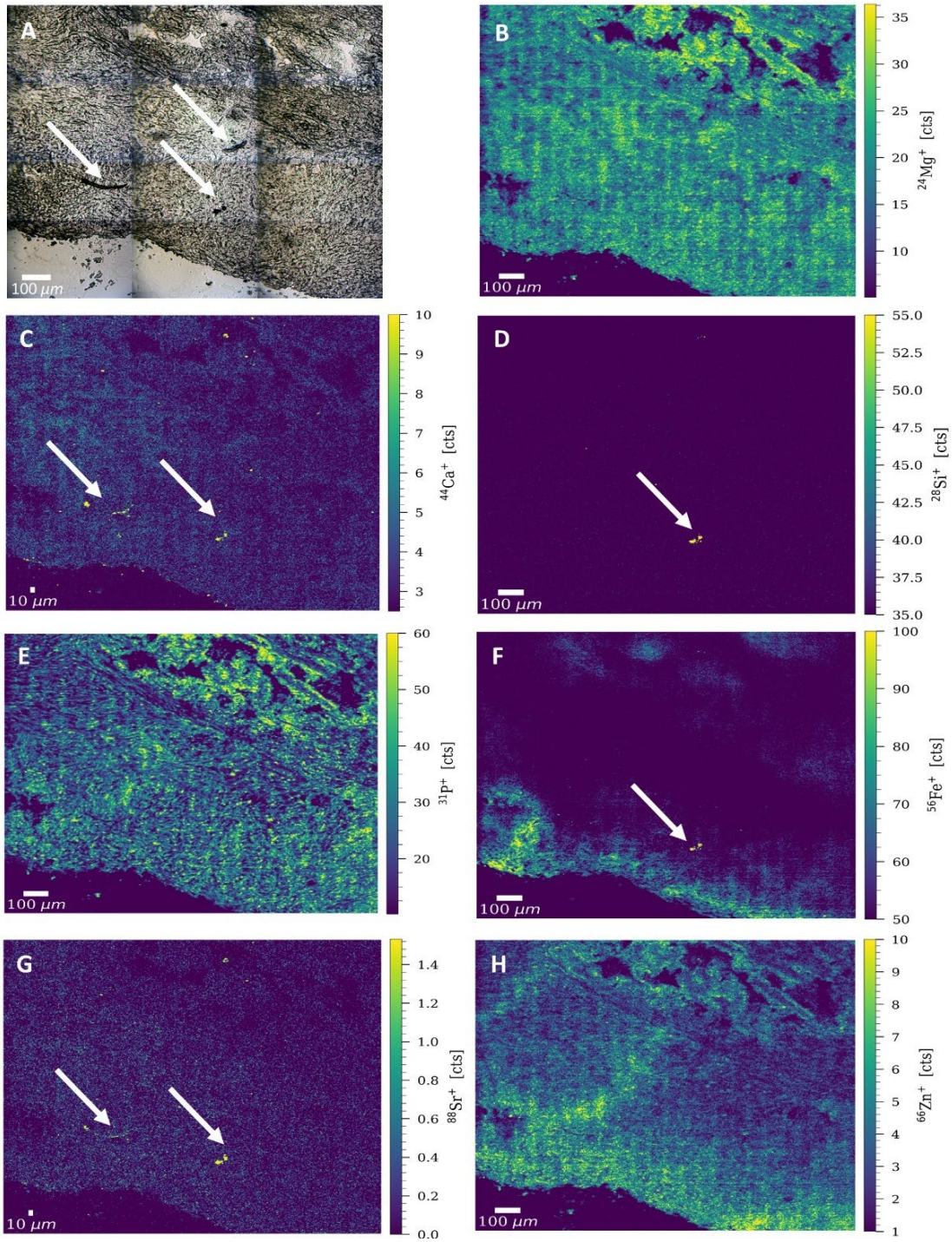

Figure 6.27 LA-ICP-TOFMS analysis of Patient 3. (A) Brightfield image of a region of interest of a lung tissue sample. Possible impurities are indicated by black arrows. Signal intensity maps of (B) 23Na+, (C) 24Mg+, (D) 28Si+, (E) 31P+, (F) 44Ca+, (G) 56Fe+, (H) 66Zn+ and (I) 88Sr+ obtained by LA-ICP-TOFMS imaging. The fibre type structure and other impurities are indicated by white arrows. The following laser ablation parameters were used: round laser spot size of 2 µm, fixed dosage mode of 2, repetition rate of 250 Hz, and the parallel lines overlapped one another by 2 µm.

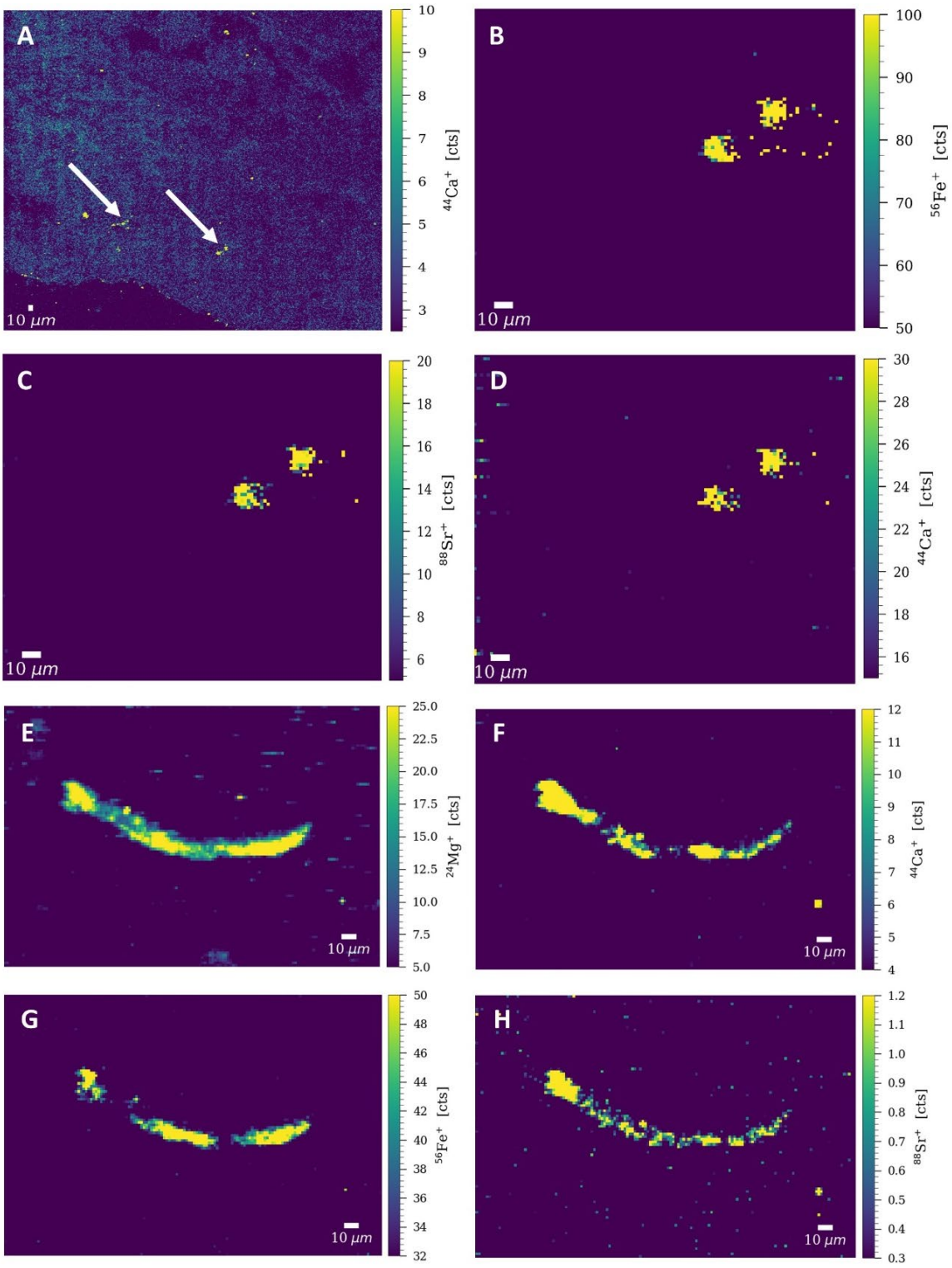

Figure 6.28 Serial ablation of the same area. Signal intensity maps of (A) $^{44}Ca^+$ following the first set of analysis, with white arrows indicating the localisation of the impurities. (B, G) $^{56}Fe^+$, (C, H) $^{88}Sr^+$, (D, F) $^{44}Ca^+$, (E) $^{24}Mg^+$ of visible impurities in the lung tissue sample. The following laser ablation parameters were used: a repetition rate of 250 Hz, a pixel size of 2 µm and a fluence of 3 J cm-2.

In order to investigate the presence of more asbestos fibres and get a more detailed picture of the metallome, a second ROI from Patient 3 was ablated. Similar to previous findings, significant counts of Mg, P, and Zn were noted on the proliferative leaf-like edges, indicating increased metabolic activity (Flint *et al.*, 2020). Regions with enhanced immune cell activity are highlighted by higher Fe counts. No MF were detected in this region, suggesting that fibres tend to accumulate in certain parts of the necrotic formation (Figure 6.29).

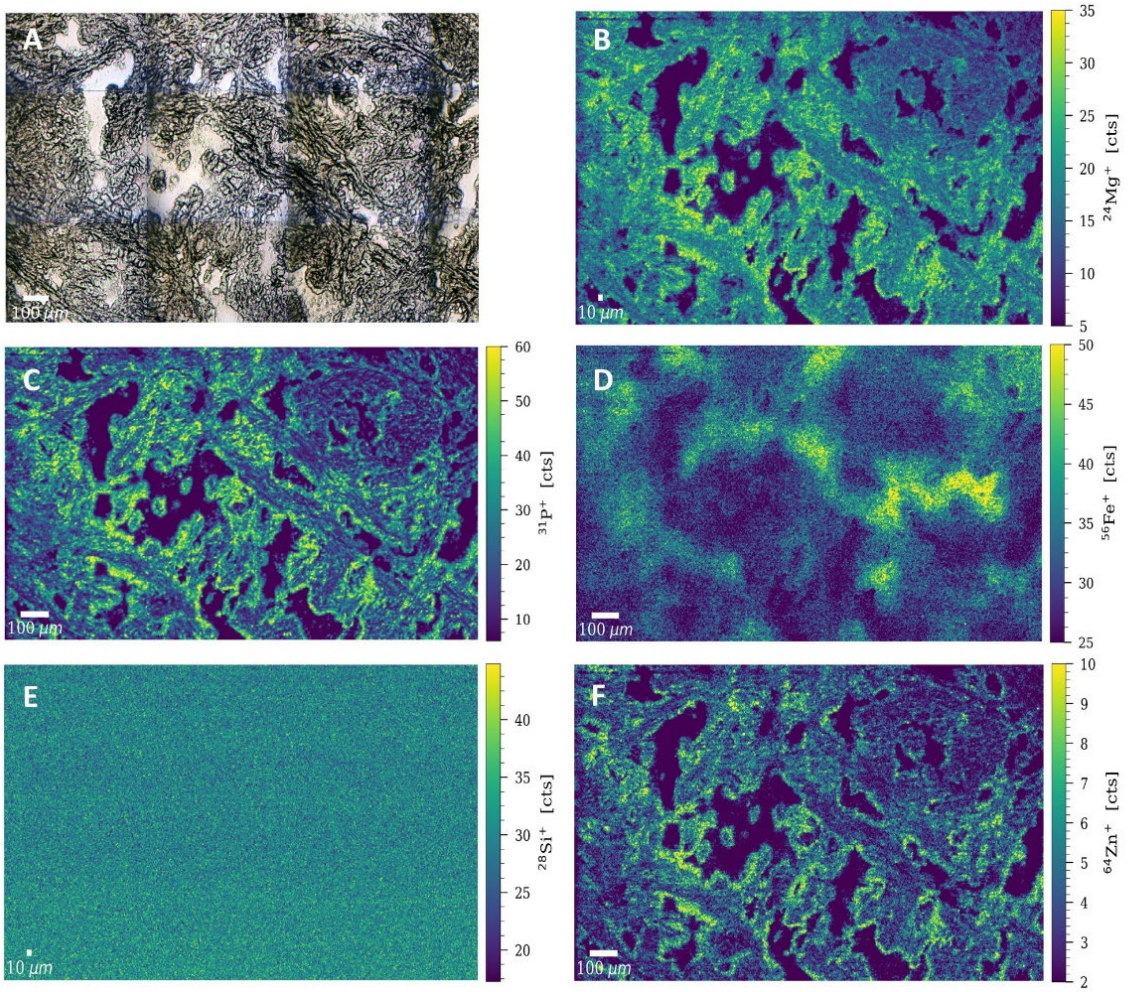

Figure 6.29 LA-ICP-TOFMS analysis of Patient 3. (A) Bright-field image of a region of interest of a lung tissue sample showing no visible impurities. Signal intensity maps of (B) $^{24}Mg^+$, (C) $^{31}P^+$, (D) $^{56}Fe^+$, (E) $^{28}Si^+$, and (F) $^{64}Zn^+$, obtained by LA-ICP-TOFMS imaging. The following laser ablation parameters were used: round laser spot size of 4 µm, fixed dosage mode of 2, repetition rate of 250 Hz, and the parallel lines overlapped one another by 2 µm.

6.2.5.5 High-resolution LA-ICP-TOFMS imaging of lung tissue- Patient 4

In the second lung tissue sample of Patient 4, two clusters of black impurities were identified on the brightfield image as indicated by the white arrows and the ROI was subjected to LA-ICP-TOFMS analysis. The fibres had the typical appearance of ferruginous bodies and stained blue following Perls' Prussian blue reaction, suggesting increased presence of ferric iron coating the asbestos bodies (Figure 6.3 I). Asbestos bodies are not inert structures and are known to trigger endogenous metal mobilisation across the tissue, most noteworthy iron and copper (Pascolo *et al.*, 2013). Iron sequestration by the malignant cells can be noted in Figure 6.30 D. Apart from the endogenous Cu known to coat asbestos fibres, Cu has also been classed as an asbestos contaminant also known as a PTE, due to its abilities to increase the toxic character of asbestos fibres in a synergistic manner (Bloise *et al.*, 2020; Ricchiuti *et al.*, 2021).

Zinc levels also appeared to be elevated, with counts nearly 2x as high compared to the rest of subjects (Figure 6.30 F). Zn is overabundant in cancer tissue containing aggressive malignant cells in contrast to normal stroma (Riesop *et al.*, 2015). The high Si counts supported the hypothesis of the presence of asbestiform silicates. Similar to Patient 3, the foreign bodies yielded no significant Mg signal following the first set of analysis. Moreover, high Sr were also recorded for these impurities which strongly suggests the key roles of this PTE in MPM carcinogenesis.

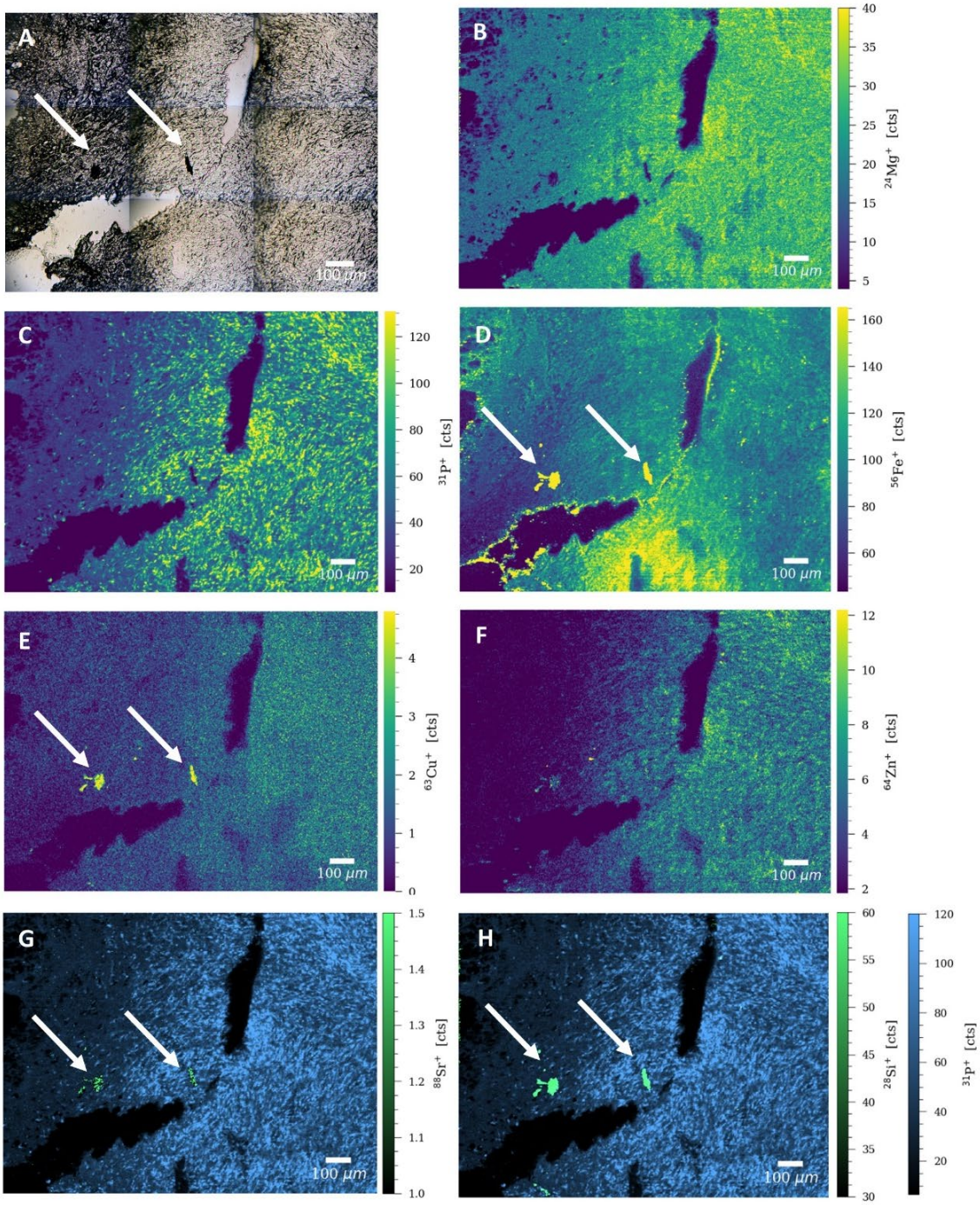

Figure 6.30 LA-ICP-TOFMS analysis of Patient 4. (A) Bright-field image of a region of interest of a lung tissue sample with visible impurities indicated by the white arrows. Signal intensity maps of (B) $^{24}Mg^+$, (C) $^{31}P^+$, (D) $^{56}Fe^+$, (E) $^{63}Cu^+$, and (F) $^{64}Zn+$, obtained by LA-ICP-TOFMS imaging. (G-H) Overlay of biological $^{31}P^+$ with $^{88}Sr^+$ and $^{28}Si^+$ signal, respectively. The following laser ablation parameters were used: round laser spot size of 4 µm, fixed dosage mode of 2, repetition rate of 250 Hz, and the parallel lines overlapped one another by 2 µm.

Despite the small sampling pool (4 subjects), LA-ICP-TOFMS imaging offered some insight into the metallome differences across the subjects. The key metals that drive the MPM pathogenesis were found to be Mg, Zn, P, and Fe. Although there was no significant difference in iron distribution between less aggressive epithelial MPM and mixed MPM (Patient 3), a noteworthy finding was the exceptionally high Fe signals in Patient 1. Pathology notes presented in Table 6.1 showed the presence of inflammatory cells, which can be linked to talc pleurodesis and iron overabundance. The question revolves around the benefits against the damage caused by talc pleurodesis as a palliative procedure and whether it should still remain the gold standard after decades of medical advancements (Vannucci *et al.*, 2018).

Additionally, a slight increase in Zn and P levels correlated with a more advanced MPM stage (IV) in Patient 4 vs the other patients. Overall high Mg counts were observed homogeneously across the subjects with the exception of Patient 1, where the Mg signal was suppressed by the magnesium-rich talc deposits.

6.3 Conclusion

Following a successful identification of asbestos and other MF within MPM cellular models by LA-ICP-MSI, mapping the elemental distribution of human MPM tissue samples was a step further to integrating LA-ICP-MS analysis as a clinical tool. Human MPM tissue samples were commercially obtained and were selected to recapitulate the heterogeneity of this aggressive pathology. The sampling pool included sections of MPM tumours found at different locations (*i.e.,* pleura, chest wall, and lung). Healthy human lung and MPM tissues were initially analysed by high-resolution LA-ICP-MS based on Mg content, as a proof-of-concept step prior to further analysis (samples not included in the sampling pool).

Tissue samples were supplied as serial sections of the same tumour block, which allowed multiple experiments to be run for each patient. Firstly, the unstained sections were imaged using standardised optical microscopy, followed by histological staining with H&E and Perls' Prussian Blue stain. These steps were crucial in understanding the pathophysiology of the tissues and selecting ROIs for LA-ICP-MS analysis. Histological analysis also highlighted the need for a more advanced routine elemental mapping method. For instance, histology techniques were not enough to fully characterise the crystal-like MF present in Patient 1 samples.

All together 4/5 samples were subjected to multi-modal LA-ICP-MS analysis. Based on current literature and advice from a pathologist consultant, asbestos fibres were mainly expected to be detected in the lung tissue samples (Carbone *et al.*, 2012). Ultrafine fibres have been previously reported in the pleura tissue (Carbone *et al.*, 2012), therefore analysis of pleura tissue was carried out. By employing a mixture of LA-ICP-MS systems, asbestos fibres were successfully detected based on elemental content in 2/4 subjects. Additionally, other MF, most likely hydrated magnesium silicates, were successfully identified in 1/4 patients.

First set of imaging experiments employed a two-volume laser ablation cell and an integrated ICP torch coupled to an Element XR sector-field ICP mass spectrometer. The data represented Mg distribution of a healthy human lung and

a MPM tissue section with visible impurities. The resulting images were used as the basis for further multi-elemental tissue analysis. This work was followed by tissue imaging using three different set-ups; LA-ICP coupled to a single-quad MS, LA-ICP coupled to a triple-quad instrument, and a LA-ICP-TOFMS capable to monitor full range of ions with the m/z = 14-256, in a single round of analysis.

Due to the holistic design of the instrumentation, initial analysis was carried out at high spatial resolution (2 μm spot size), allowing for cellular monitoring of Mg levels in healthy human lung tissue. Moreover, MF were successfully mapped based on the high Mg counts. However, despite the high sensitivity and high spatial resolution, the instrument did not allow for monitoring several nuclides at once. Furthermore, due to the long-time of acquisition, the number of samples and replicates was limited, impacting the clinical potential of this technique. On the other hand, the second set-up employed in this study allowed for detection of several ions in a single round of analysis, albeit limited. MF were successfully detected for one of the subjects, along with information regarding ionic distribution within tissues. Nevertheless, the analysis was limited by the low sensitivity and common glass substrate and polyatomic interferences.

However, the data set the basis for faster, more sensitive analysis. The capabilities of the triple-quad MS allowed for detection of multiple targets. Faster acquisition time meant an increase in the number of repeats, critical in underlining the heterogeneity of the MPM metallome, particularly in terms of electrolytes dysregulation. For this experiment, a randomised approach was chosen. No asbestos fibres were detected in the lung tissue, likely because of the lower resolution and limited ablated area. Moreover, to achieve desired sensitivity, the number of elements was limited to 3 per area ablated.

In order to cope with the short transient signals delivered by the LA setup, ICP-TOFMS was coupled to the ultra-fast laser, generating multi-elemental information of the entire mass range. In terms of data, LA-ICP-TOFMS proved to be the ideal set-up, that was able to spatially resolve asbestos and other MF at a high resolution, whilst generating invaluable information regarding the MPM metallome.

Technological advances in micro- and nano-scale imaging are aiming to achieve multi-dimensional and *in situ* measures of metals while maintaining the native biochemical environment. By employing LA-ICP-MS as an imaging tool, ionic imbalance can be monitored in human tissue samples, without the need of sample preparation that can potentially affect the *in vivo* scenario.

Cancer patients are characterised by a variety of metabolic disturbances in homeostasis of key electrolytes such as sodium, potassium, and magnesium, as well as other metal ions such as zinc, iron, phosphorus, and copper both at intratumoral and systemic level (Serra *et al.*, 2020). Monitoring the cellular distribution of these elements *in situ* can provide invaluable insight into disease pathogenesis and the intricate tumour microenvironment (Callejón-Leblic *et al.*, 2019).

Initial work mainly focused on electrolytes disturbances. This type of dysregulation common in cancer patients has been linked to several factors, some related to malignancy, such as syndrome of inappropriate antidiuretic hormone secretion (SIADH) and tumour lysis syndrome; and some related to exogenous factors, such as chemotherapy other associated clinical conditions or palliative treatments (Serra *et al.*, 2020). Our data showed a potential correlation between necrotic regions with aggressive behaviour and increased chemoresistance and enriched K and Na levels. Further analysis focused on monitoring key players in neoplastic progression, including Fe, Mg, Zn, and P. LA-ICP-TOFMS images revealed an overall overabundance of Zn and P around the proliferative regions, whilst high levels of Fe and Mg correlated with areas of high immune cells reactivity.

Despite the limited patient information offered by the supplier, correlation between metal distribution, staging, pathology notes, and histology presentation was attempted. Histological data has shown that ferruginous bodies of asbestos can be identified based on Perls' Prussian blue reaction. However, the staining is not specific for asbestos fibres and fails to detect ultra-fine fibres.

Monitoring the metallome around the talc deposits offered insight into the impact talc pleurodesis has on tissues, and whether the benefits really outweigh the risks. The presence of talc particulates led to a significant increase tissue damage and inflammation, as reflected by the high Fe counts which were up to 10x higher than for the rest of subjects. Another major finding was the presence of strontium within the asbestos fibres, a PTE that might play a key role in MPM onset (Bloise *et al.*, 2020). In terms of metallome distribution, high levels of Mg, Zn, and P were associated with areas of high metabolic activity and increased proliferation.

LA-ICP-MSI has been previously employed to analyse MPM tissues to monitor platinum levels post-treatment (Bonta *et al.*, 2014). However, to our knowledge, this is the first attempt to study the metallome dysregulation in this pathology, covering a broad range of key metal ions. Understanding how these ions interact with the tumour microenvironment can open avenues to novel therapies, diagnosis, and drug-monitoring tools.

As with any study, there are limitations to this work. The main limitation of this study was the low number of patients analysed. Despite the varied pathologies of the samples, more subjects are required for even more conclusive results. Furthermore, healthy lung tissue samples and tissues of different origins should also be investigated to develop an elemental pattern of MPM. This comparison would allow for a clearer picture of the intricate malignant metallome. Additionally, more patient data, such as previous treatment and interventions, symptoms and lifestyle information would benefit in correlating cellular and subcellular ionic distribution and MPM pathology.

Future work will include a higher number of subjects, which will include healthy and benign tissue samples. Based on the data presented herein, LA-ICP-TOFMS will be employed for future imaging as the leading multi-elemental LA-ICP-MS systems. Moreover, trace metal distribution will be monitored quantitatively and qualitatively at high resolution in full tissue sections to better understand the metallome heterogeneity, as well as detailed cellular and subcellular imaging, particularly around the MF. Additionally, LA-ICP-TOFMS metal tagged antibody detection will be employed for novel biomarker discovery.

This study supports the hypothesis that ultimately LA-ICP-TOFMSI has the capability to be employed in clinical settings as a tool for detecting asbestos bodies, monitoring MPM metallome disturbance, and mapping metal-tagged MPM biomarkers, all in a single analysis.

Chapter 7 Multimodal Biomarker Characterisation in Malignant Mesothelioma

7.1 Introduction

7.1.1 Introduction to the chapter

The poor OS linked to MPM stems from the late diagnosis of this pathology due to a lack of reliable biomarkers, particularly ones associated with early onset of disease (Chen, Z. *et al.*, 2017). There is a need to identify and validate MPM biomarkers that cover all the biomarker categories mentioned in Chapter 1, Section 1.5. However, due to the aggressive nature of MPM, but also the long latency to a clear diagnosis, diagnostic and monitoring biomarkers are of utmost importance. Proteomics-based approaches to biomarker discovery and validation have become the gold standard and include techniques such as flow cytometry, ELISA, immunofluorescence imaging, and mass spectrometry.

A multimodal approach was employed in the first part of the work to characterise a panel of emerging protein biomarkers in established cell lines. Flow cytometry enabled quantitative measurements of specific protein levels at cellular level, based on the fluorescence emission by the specific fluorescent probe-labelled cells as they passed through the laser beam. Additionally, immunofluorescent staining of individual cells allowed not only for qualitatively detecting the possible biomarker, but also offered an indication to its localisation within the cell, building on the knowledge around MPM key pathogenic events.

The biomarkers investigated in this chapter have been previously presented in Chapter 1, Section 1.5, Table 1.5, alongside other emerging or established biomarkers of mesothelioma, such as osteopontin and fibulin-3. In short, HMGB1 is a chromosomal protein that acts as a DNA chaperone (Kang *et al.*, 2013). Once translocated outside the cell, HMGB1 becomes a prototypical DAMP (Kang *et al.*, 2013). Translocation of HMGB1 is highly influenced by oxidative stress and plays a key role in inflammation and cell death (Yu & Kang, 2015). The first link between HMGB1 and MPM has been established over a decade ago by the Hang and Carbone group (Hang *et al.,* 2010). HMGB1 has been subsequently investigated by other groups, but mainly in the serum of either MPM patients or asbestos-exposed individuals (Napolitano *et al.*, 2016; Tabata *et al.*, 2013). Mesothelin is

a membrane glycoprotein, overexpressed in certain malignancies, and previously associated with cell adhesion, tumour progression, metastasis, and drug resistance (Shen, Sun, & Zhou, 2020). The clinical applicability of this biomarker has been under debate recently (Blyth & Murphy, 2018; Creaney & Robinson, 2017), and a fresh perspective is needed in terms of characterisation and validation.

VISTA is a type I transmembrane protein linked to T-cell-associated immune response suppression in several human cancers (Huang *et al.*, 2020). VISTA has been studied as a novel immunotherapy target in MPM (Muller *et al.*, 2020) and as a prognostic biomarker, its overexpression being associated with better outcome (Nastase *et al.*, 2021). Extensive validation is needed in order to classify VISTA as a novel clinical biomarker for MPM differentiation.

Secondly, an untargeted MALDI-MSI approach was employed to analyse tissue microarrays (TMAs) containing 80 cores, from 40 patients. MALDI-MSI can help detect emerging biomarkers whilst maintaining spatial information. This is essential in establishing a link between tissue histology and biomarker presence. It is a well-established technique with applications in drug monitoring (Russo *et al.*, 2018), forensic science (Bradshaw *et al.*, 2012; Bradshaw, Denison, & Francese, 2017) and tumour classification (Mascini *et al.*, 2018). In the current work, analysis of TMAs by MALDI-MSI offered key information around (a) method reproducibility, (b) cancer heterogeneity, and (c) detection of novel molecules with biomarker potential.

7.1.2 Hypothesis

The first hypothesis of the study was that the levels of several proteins differ between MPM and control cell lines, having the potential to be characterised as emerging malignant mesothelioma biomarkers. Secondly, we hypothesised that MALDI-MSI of human TMAs can offer insight into the proteomic heterogeneity between healthy and diseased human tissue biopsies and set the basis for detection of novel biomarkers for malignant mesothelioma diagnosis and monitoring.

7.1.3 Aims of the chapter

This chapter focuses on biomarker characterisation and early-stage detection. Initially, this research employed a multimodal strategy to characterise a panel of emerging biomarkers, including mesothelin, HMGB1, and VISTA. Flow cytometry was used to detect and quantify the presence of the markers, whilst fluorescent microscopy offered extra information on the localisation of the markers within mesothelioma or control cells. The second aim was to investigate the difference in healthy and diseased TMAs proteome by using MALDI-MSI. Additionally, we explored the potential of MALDI-MSI as a tool for future biomarker discovery.

7.2 Results and Discussion

7.2.1 Biomarker characterisation using flow cytometry

Flow cytometry was employed to characterise the panel of selected markers: mesothelin, HMGB1, and VISTA (Figure 7.1). The staining protocols were optimised based on known protein expression locus from current literature and protein databases such as UniProt. The data was normalised against isotype control expression and the mean fluorescence intensity was calculated (n=3) and plotted in Figure 7.1. Expression of mesothelin was measured on cell surface, whilst HMGB1 expression was measured intracellularly, and VISTA levels were investigated within the nucleus. The cell suspensions were filtered prior to staining to avoid doublets and false negative staining, but also to remove any debris. The gating strategy was applied to viable cells from the same cell population, ranging from 75-90%. HeLa cells were used as a positive control to validate the mesothelin and HMGB1 antibodies. Mesothelin is an immunogenic glycoprotein that is known to be expressed in HeLa cells (Ye *et al.*, 2019). Notably, HMGB1 is also expressed at high levels in this well-established cell line but is primarily localised in the nucleus (Xia *et al.*, 2017), which explains the low expression following intracellular staining presented in Figure 7.1. U937 cells (human lymphoma cells) were used as a positive control for VISTA expression, having been previously associated with lymphomas (Zhang *et al.*, 2021).

Low levels of mesothelin were detected in Met-5A cells. Interestingly, the cells stained positive for HMGB1 and VISTA. Low positive mesothelin expression was also noted for MSTO-211H and NCI-H28 cells, compared to positive control cells. The high mean fluorescence intensity corresponding to HeLa cells suggested that both the staining protocol and the antibody used in this study were appropriate to help answer the research question, and that although mesothelin was present in the MPM cells, mesothelin lacks cancer specificity (Figure 7.1). HMGB1 was produced in both MPM cell lines, with higher levels present in the biphasic cell line. This finding contradicts a published study, which reported higher HMGB1 expression in NCI-H28 cells, when compared to MSTO-211H and Met-5A cells (Tabata *et al.*, 2013). The group monitored protein expression by ELISA, suggesting that overall HMGB1 levels may be higher in the epithelioid cell line, but cytoplasmic expression is significantly increased in the biphasic cells (Figure 7.1& Figure 7.2). Unexpectedly, low VISTA expression was recorded for NCI-H28, with high expression detected in the MSTO-211H cells. VISTA expression is usually limited in biphasic mesothelioma and more prevalent in epithelioid cases (Muller *et al.*, 2020).

Specificity of the biomarkers was investigated by analysing the expression of mesothelin, HMGB1, and VISTA in a NSCLC control cell line, NCI-H1975. Data suggested that VISTA failed to be MPM specific, with high expression in NCI-H1975 cells. VISTA was previously reported to be overexpressed in NSCLC TMAs, although the marker presented a predominant membranous/cytoplasmic staining pattern (Villarroel-Espindola *et al.*, 2018).

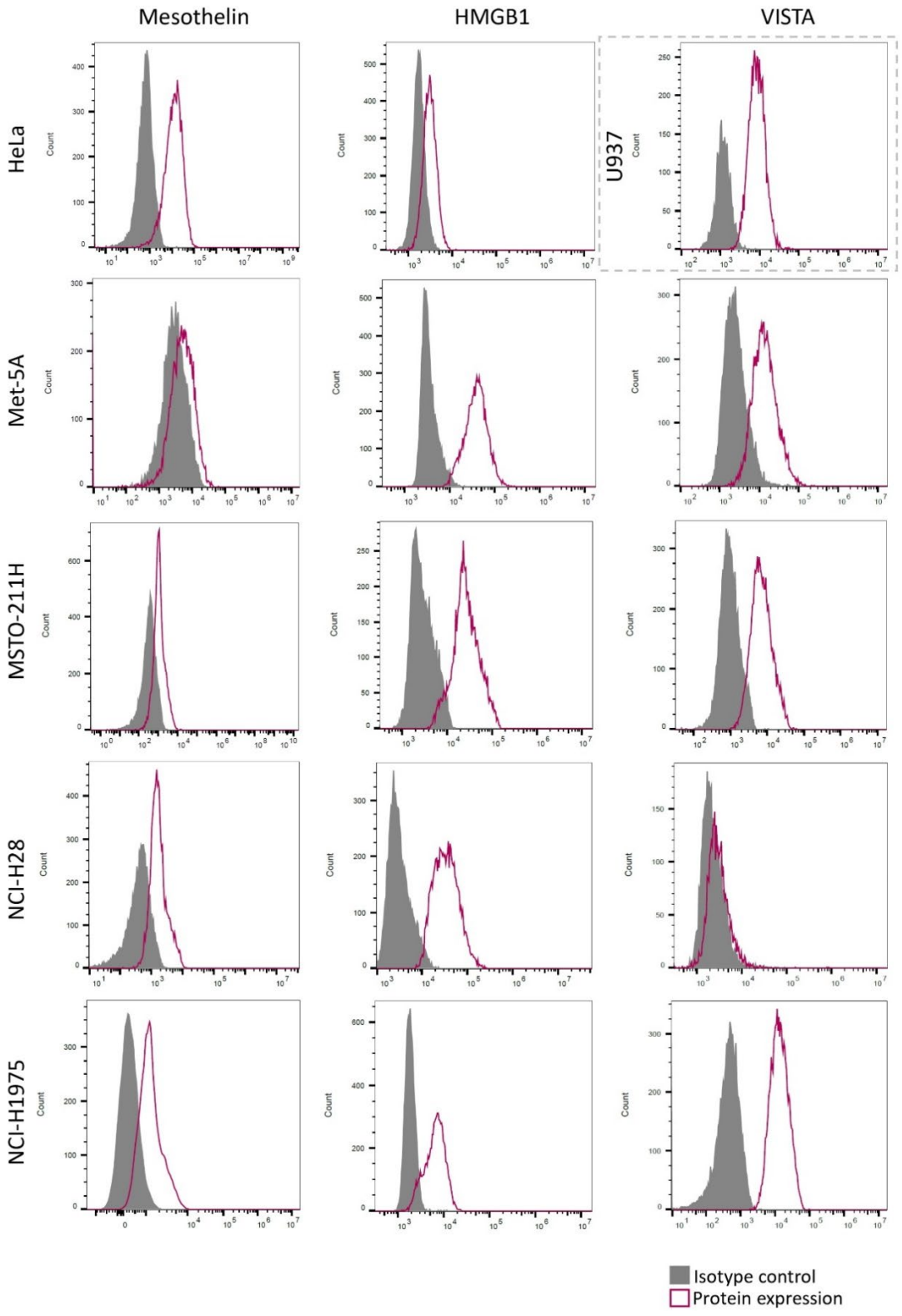

Figure 7.1 Expression of mesothelin, HMGB1, and VISTA in a panel of immortalised cells. Data acquired from three independent experiments. HeLa cells were used as positive control for mesothelin and HMGB1. U937 were used as a positive control for VISTA expression. Expression of the corresponding isotype controls are shown in blocked grey.

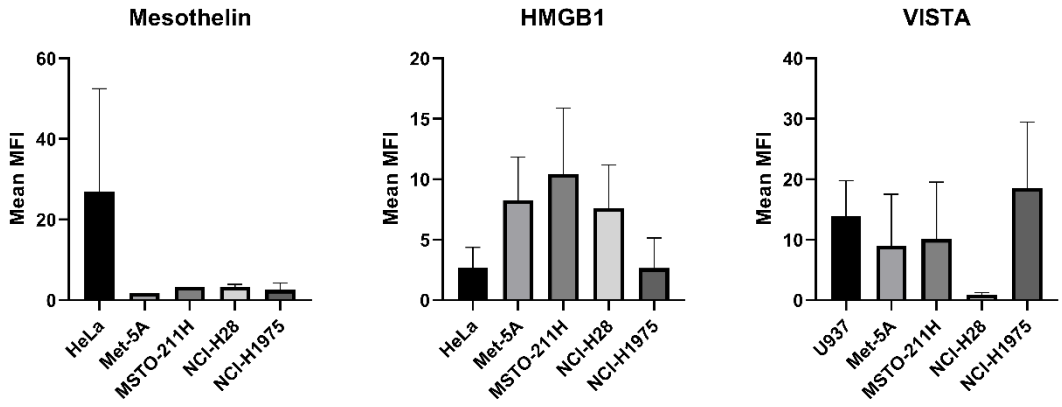

Figure 7.2 Relative expression of mesothelin, HMGB1, and VISTA in a panel of immortalised cells. HeLa and U937 were used as positive control cells for mesothelin and HMGB1, and VISTA, respectively. Data is presented as mean fluorescent index (MFI) ±SD (n=3) and was normalised against the corresponding isotype controls.

7.2.2 Biomarker characterisation and localisation

Immunofluorescent detection of the target proteins helped validate the flow cytometry data. Confocal fluorescent microscopy analysis of the cellular monolayers offered qualitative information regarding the presence/ absence of the target biomarkers. Additionally, it provided an indication on the localisation and possible translocation of the targets.

HeLa cells were used as a positive control to validate the mesothelin and HMGB1 antibodies. Figure 7.3 presents the positive expression of membrane-bound mesothelin and HMGB1 in HeLa cells following immunofluorescent staining. DNA labelling reveals the cell nucleus and is shown in blue (DAPI). Protein expression can be noted in green. An overlay of the two is presented in the right-hand side column.

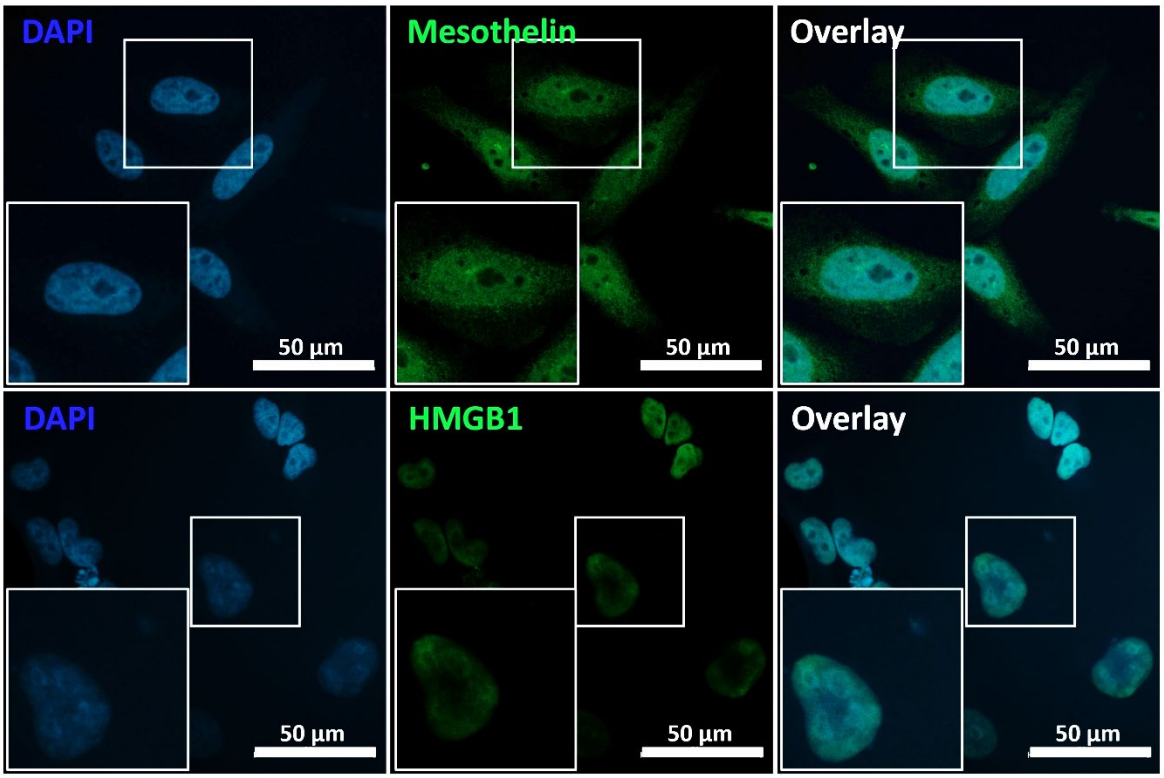

Figure 7.3 Mesothelin and HMGB1 expression in a positive control cell line (representative images from three independent experiments). Mesothelin was detected in the membrane of methanol fixed HeLa monolayers grown on glass coverslips using mesothelin rabbit polyclonal antibody, followed a Goat Anti-Rabbit IgG (H+L) secondary antibody, Alexa Fluor Plus 488 (green). HMGB1 expression was detected in the nucleus of HeLa cells using HMGB1 recombinant rabbit monoclonal antibody, followed by a Goat Anti-Rabbit IgG (H+L) secondary antibody, Alexa Fluor Plus 488 (green). The nuclei were counterstained with DAPI (blue). An overlay is presented in the right-hand side column.

Confocal microscopy revealed positive expression of mesothelin localised heterogeneously on the membrane of Met-5A cells. Expression of mesothelin in normal mesothelial cells, and particularly in Met-5A cells has been reported before (Melaiu *et al.*, 2014). Mesothelin is believed to be involved in cell adhesion in both healthy and malignant cells (Kaeding *et al.*, 2017). Interestingly, HMGB1 expression was solely localised in the nucleus of the mesothelial cells, where it plays a key role in DNA architecture and transcriptional regulation (Xue *et al.*, 2020). VISTA expression has been reported on normal and reactive mesothelium following immunohistochemical staining. Similarly, low expression of VISTA can be noted on the membrane of the Met-5A mesothelial cells (Figure 7.4).

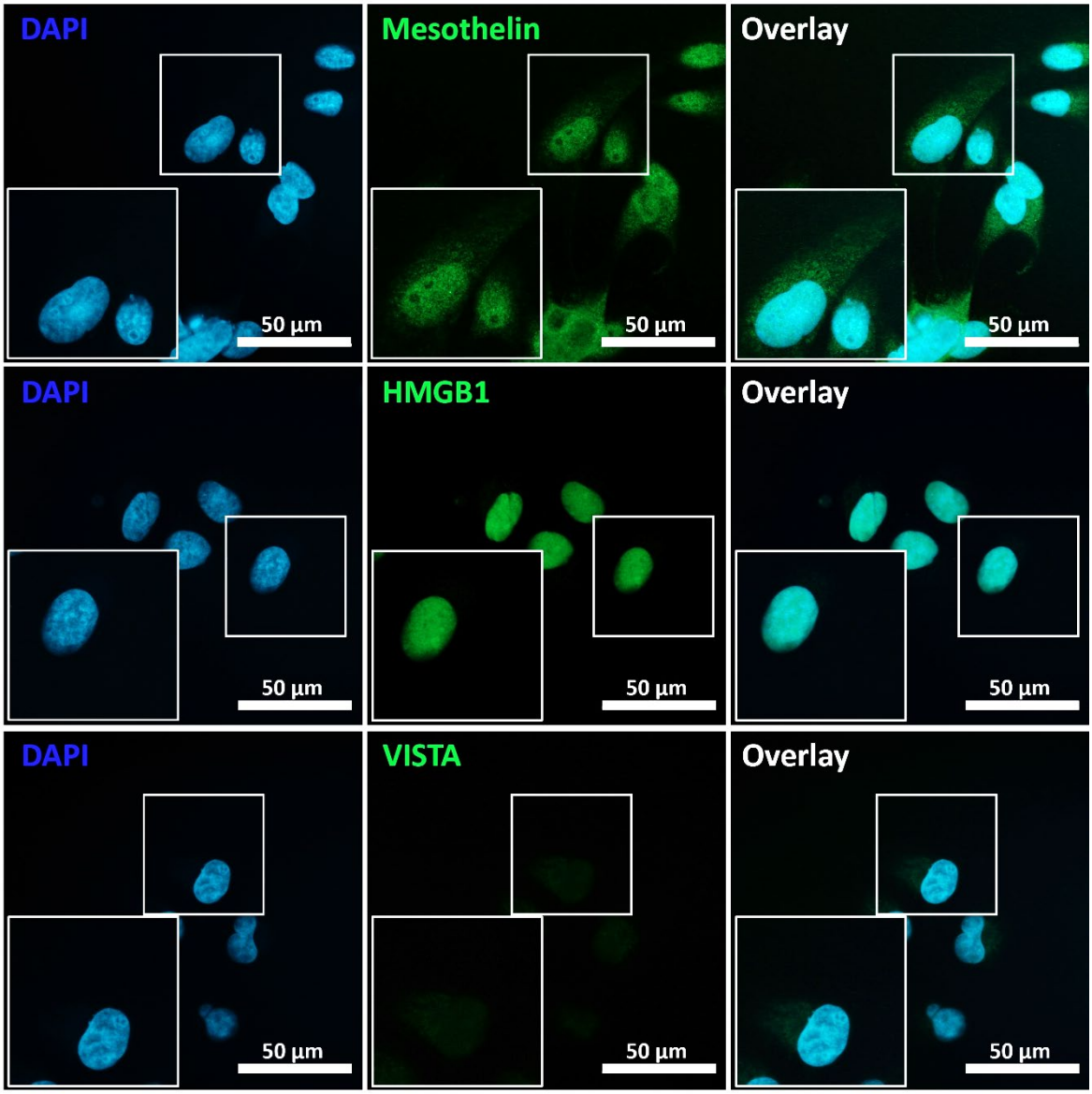

Figure 7.4 Mesothelin, HMGB1, and VISTA expression in a mesothelial cell line (representative images from three independent experiments). Mesothelin was detected in the membrane of fixed Met-5A monolayers using mesothelin rabbit antibody, followed a Goat Anti-Rabbit IgG (H+L) secondary antibody, Alexa Fluor Plus 488 (green). HMGB1 expression was detected in the nucleus of Met-5A cells using HMGB1 recombinant rabbit monoclonal antibody, followed by a Goat Anti-Rabbit IgG (H+L) secondary antibody, Alexa Fluor Plus 488 (green). Low VISTA expression can be noted following fixation and staining with VISTA recombinant rabbit monoclonal antibody, followed by a Goat Anti-Rabbit IgG (H+L) secondary antibody, Alexa Fluor Plus 488 (green). The nuclei were counterstained with DAPI (blue). An overlay is presented in the right-hand side column.

Mesothelin is not specific to MPM, but its expression is enhanced in mesothelioma (Kojima *et al.*, 2020). Moreover, confocal microscopy revealed that mesothelin was expressed diffusely on MSTO-211H cell membrane, but also in clusters of high fluorescent signals localised on the membrane (Figure 7.5). Studying the cellular localisation of HMGB1 may provide a tool to assess the functional impact that HMGB1 translocation has on the MPM pathogenesis. In line with literature, HMGB1 expression was recorded in the nucleus (non-acetylated HMGB1) and cytoplasm of MSTO-211H cells (Tabata *et al.*, 2013). HMGB1 translocation was linked to acetylation of the lysine residues in the two nuclear localisation signals (Napolitano *et al.*, 2016). VISTA expression is associated with better OS, with limited expression in biphasic mesothelioma, and no expression reported in sarcomatoid cases (Muller *et al.*, 2020). Hence, limited VISTA expression was noted on the membrane of MSTO-211H following immunofluorescence staining (Figure 7.5).

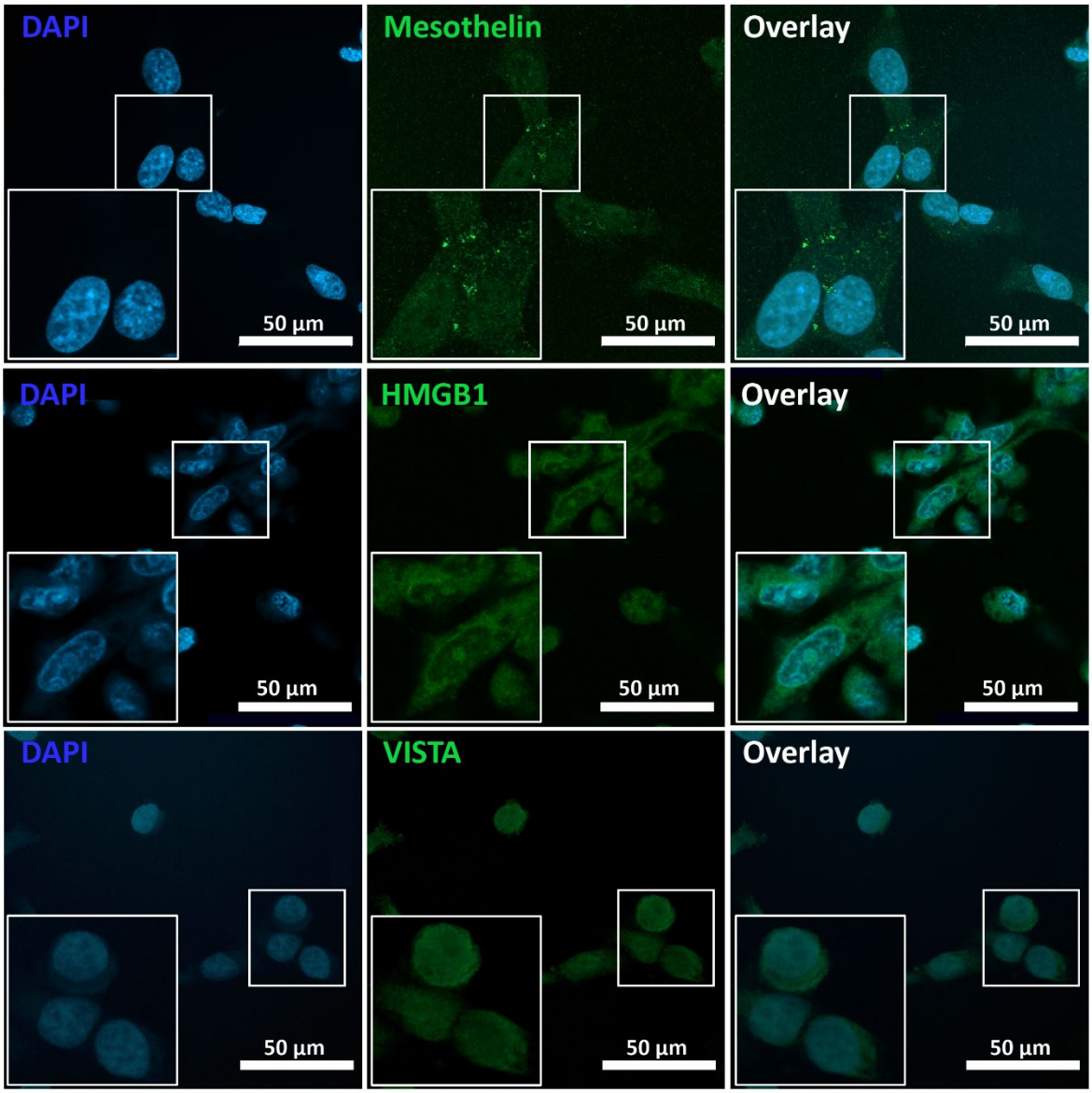

Figure 7.5 Mesothelin, HMGB1, and VISTA expression in biphasic mesothelioma cells (representative images from three independent experiments). Mesothelin was detected in the membrane of methanol fixed MSTO-211H monolayers grown on glass coverslips using mesothelin rabbit polyclonal antibody, followed a Goat Anti-Rabbit IgG (H+L) secondary antibody, Alexa Fluor Plus 488 (green). HMGB1 expression was detected in the cytoplasm and around the nucleus of MSTO-211H cells using HMGB1 recombinant rabbit monoclonal antibody, followed by a Goat Anti-Rabbit IgG (H+L) secondary antibody, Alexa Fluor Plus 488 (green). Membrane-bound VISTA can be seen following fixation and staining with VISTA recombinant rabbit monoclonal antibody, followed by a Goat Anti-Rabbit IgG (H+L) secondary antibody, Alexa Fluor Plus 488 (green). The nuclei were counterstained with DAPI (blue). An overlay is presented in the right-hand side column.

In order to determine whether mesothelin, HMGB1 and VISTA expression were a specific feature of biphasic MSTO-211H cells or a potential feature of malignant mesothelioma cells, analysis was also carried out on NCI-H28 cells, an epithelioid cell line (Figure 7.6). Confocal analysis of NCI-H28 cells revealed that mesothelin was uniformly present on the cell membrane, but also localised in clusters, similarly to the MSTO-211H data presented above in Figure 7.5. These particular mesothelin aggregates suggested that mesothelin presence or level of expression might not be MPM specific, but the pattern of distribution might play a more significant role than previously considered. Preventing aggregation of this glycoprotein could thus become a strategy for anticancer drug development, which has been reported before in different malignancies (Direito *et al.*, 2021; Matafora *et al.*, 2020). Interestingly, HMGB1 appeared to adopt a dispersed cytoplasmic localisation, with some noteworthy nuclear HMGB1 also present, suggesting only a partial translocation of HMGB1 during the malignant development.

VISTA expression was most noteworthy in NCI-H28 cells. Median VISTA score was previously shown to be higher in tumours with epithelioid histology, compared to biphasic and sarcomatoid (Muller *et al.*, 2020). Although some VISTA expression was previously reported in mesothelial cells (Figure 7.4), low levels of this protein are not associated with malignant events. On the other hand, VISTA overexpression in malignant cells suppresses early T-cell activation and proliferation and reduces cytokine production (Mutsaers *et al.*, 2020). Interestingly, VISTA expression has been previously shown to be correlated with mesothelin overexpression (Hmeljak *et al.*, 2018), which can also be noted in Figure 7.6.

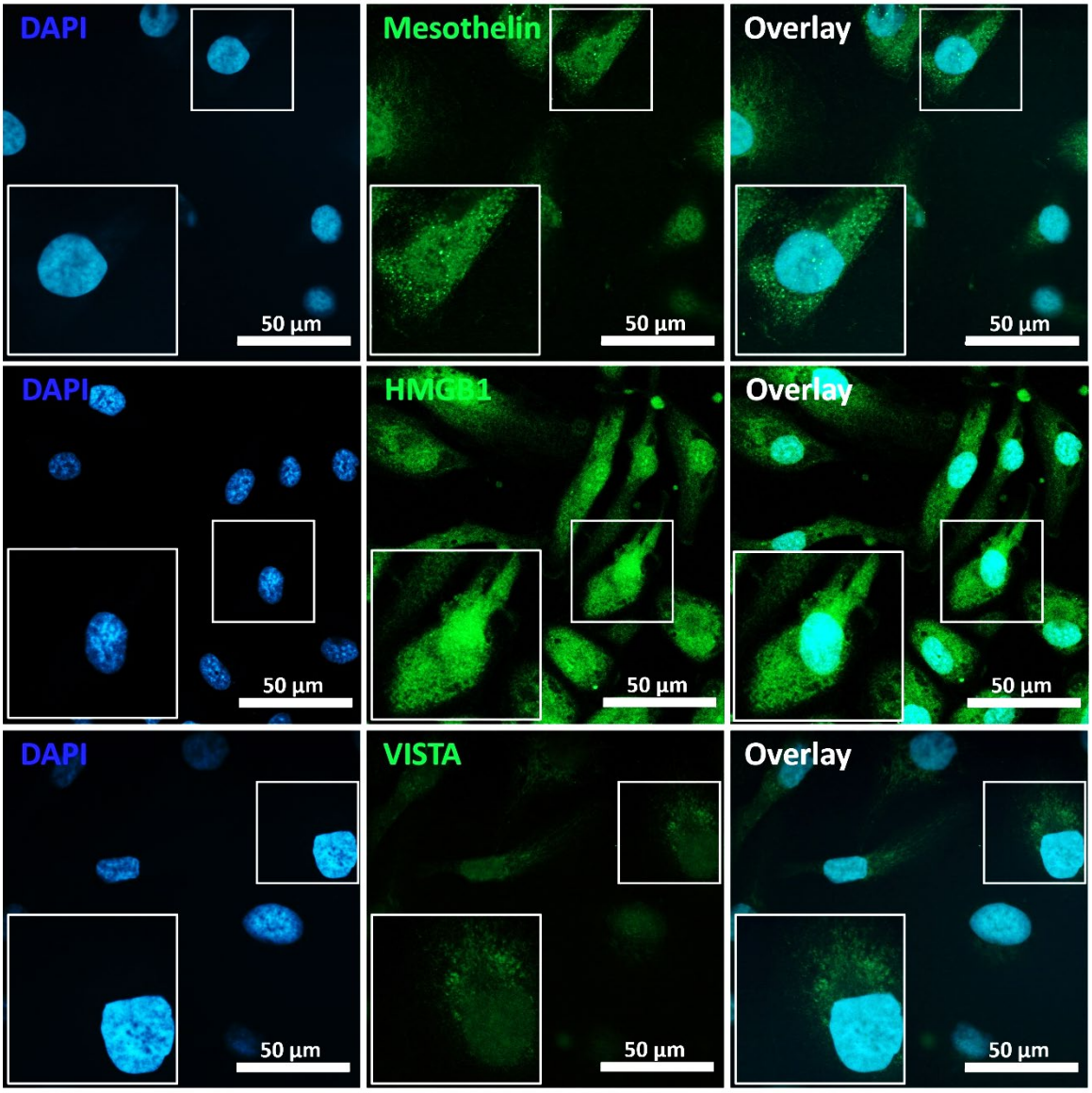

Figure 7.6 H28 Mesothelin, HMGB1, and VISTA expression in epithelioid mesothelioma cells (representative images from three independent experiments). Mesothelin was detected in the membrane of methanol fixed NCI-H28 monolayers grown on glass coverslips using mesothelin rabbit polyclonal antibody, followed a Goat Anti-Rabbit IgG (H+L) secondary antibody, Alexa Fluor Plus 488 (green). HMGB1 expression was detected in the nucleus and cytoplasm of NCI-H28 cells using HMGB1 recombinant rabbit monoclonal antibody, followed by a Goat Anti-Rabbit IgG (H+L) secondary antibody, Alexa Fluor Plus 488 (green). Membrane-bound VISTA can be seen following fixation and staining with VISTA recombinant rabbit monoclonal antibody, followed by a Goat Anti-Rabbit IgG (H+L) secondary antibody, Alexa Fluor Plus 488 (green). The nuclei were counterstained with DAPI (blue). An overlay is presented in the right-hand side column.

Mesothelin expression was noted for the NCI-1975 around the cell membrane, presented in Figure 7.7, which is in line with current literature (Ye *et al.*, 2019). This finding added to the evidence that mesothelin on its own lacks specificity to mesothelioma and cannot be employed as a diagnostic biomarker. However, the mesothelin clusters presented in Figure 7.5 and Figure 7.6 for the two MPM cell lines were not present in the control cells, which might suggest a strong correlation between these protein aggregations and MPM development.

On the other hand, HMGB1 was expressed in NCI-H1975, but was localised around the nucleus. Interestingly, no expression was noted for VISTA, which contradicted the initial flow cytometry data (Figure 7.7). Moreover, literature has reported VISTA protein expression in 99% of NSCLCs (predominantly in the cytoplasm/ membrane) (Villarroel-Espindola *et al.*, 2018). One possible explanation for the lack of VISTA expression could be due to sample deterioration (photobleaching) whilst selecting the ROIs (Jonkman, 2020).

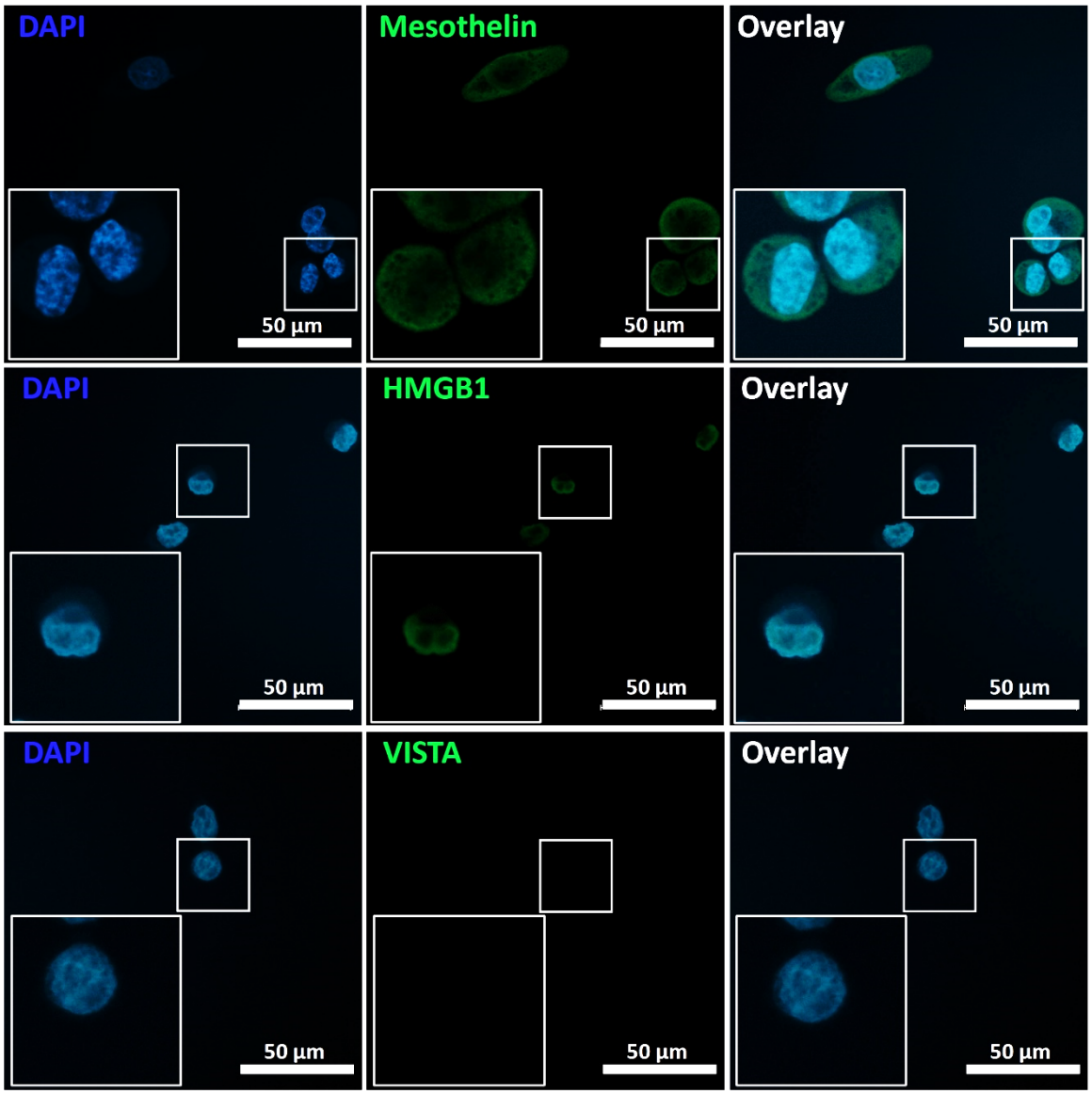

Figure 7.7 Mesothelin, HMGB1, and VISTA expression in a NSCLC control cell line (representative images from three independent experiments). Mesothelin was detected in the membrane of methanol fixed NCI-H1975 monolayers grown on glass coverslips using mesothelin rabbit polyclonal antibody, followed a Goat Anti-Rabbit IgG (H+L) secondary antibody, Alexa Fluor Plus 488 (green). Low HMGB1 expression was detected in the nucleus of NCI-H1975 cells using HMGB1 recombinant rabbit monoclonal antibody, followed by a Goat Anti-Rabbit IgG (H+L) secondary antibody, Alexa Fluor Plus 488 (green). No expression recorded for VISTA. The nuclei were counterstained with DAPI (blue). An overlay is presented in the right-hand side column.

7.2.3 Biomarker discovery using MALDI-MS imaging

7.2.3.1 TMA overview

The selected TMAs contained 80 duplicate cores (1.5 mm core diameter, 5 µm thickness), from 40 different patients. The TMAs covered a range of normal tissues and diseased tissue, from various sites including the most prevalent sites for mesothelioma development (*i.e.,* lung, pleura, abdomen, and pericardium). Adrenal gland malignant tissue (Figure 7.8 A1) was included as a tissue marker control and to indicate the TMAs orientation. A schematic diagram of the tissue types and origins as provided by tissue supplier is presented in Figure 7.8.

Histology staining was conducted to gain a better understanding of the type of tissue samples used to form the TMAs. The top two rows revealed the normal tissue architecture associated with lung tissue, with visible bronchioles, and normal pericardium tissue, which is a simple connective tissue structure lined by a single layer of mesothelial cells (Figure 7.9). H&E staining of the whole slide also underlined the cancer heterogeneity between samples of the same disease, stage, and location. Additionally, the structural difference between some of the cores extracted from the same patient tissue block can also be noted (Figure 7.9). In terms of MPM, the selected tissue cores are heterogeneous at a histological level, showing a complex microenvironment of tumour-stroma components, associated with cancer aggressivity (Ujiie *et al.*, 2015). A total lack of tissue architecture can also be noted, particularly for the lung mesothelioma tumours (Figure 7.9). High resolution H&E images of each individual core were provided by tissue supplier (Biomax.us.).

The TMAs were imaged by MALDI-MS in positive ion mode and spectra were acquired within the range *m/z* 700-1800, laser power at 250 arbitrary units, with ion mobility function enabled. The images were acquired with a pixel size of 100 µm to enable in-depth data processing of each core. The pixel size was selected to be high enough to determine phenotypic regions potentially associated with malignant/ normal tissue, but also to allow data acquisition in one run of analysis (time of acquisition <72 hours).

A representative MALDI-MS image for *m/z* 796.414 (blue- upper part predominantly) and *m/z* 857.492 (red- lower section) is presented in Figure 7.10. An association between *m/z* 796.414 and normal tissue can be noted, whilst *m/z* 857.492 is heavily predominant in the malignant tissue cores.

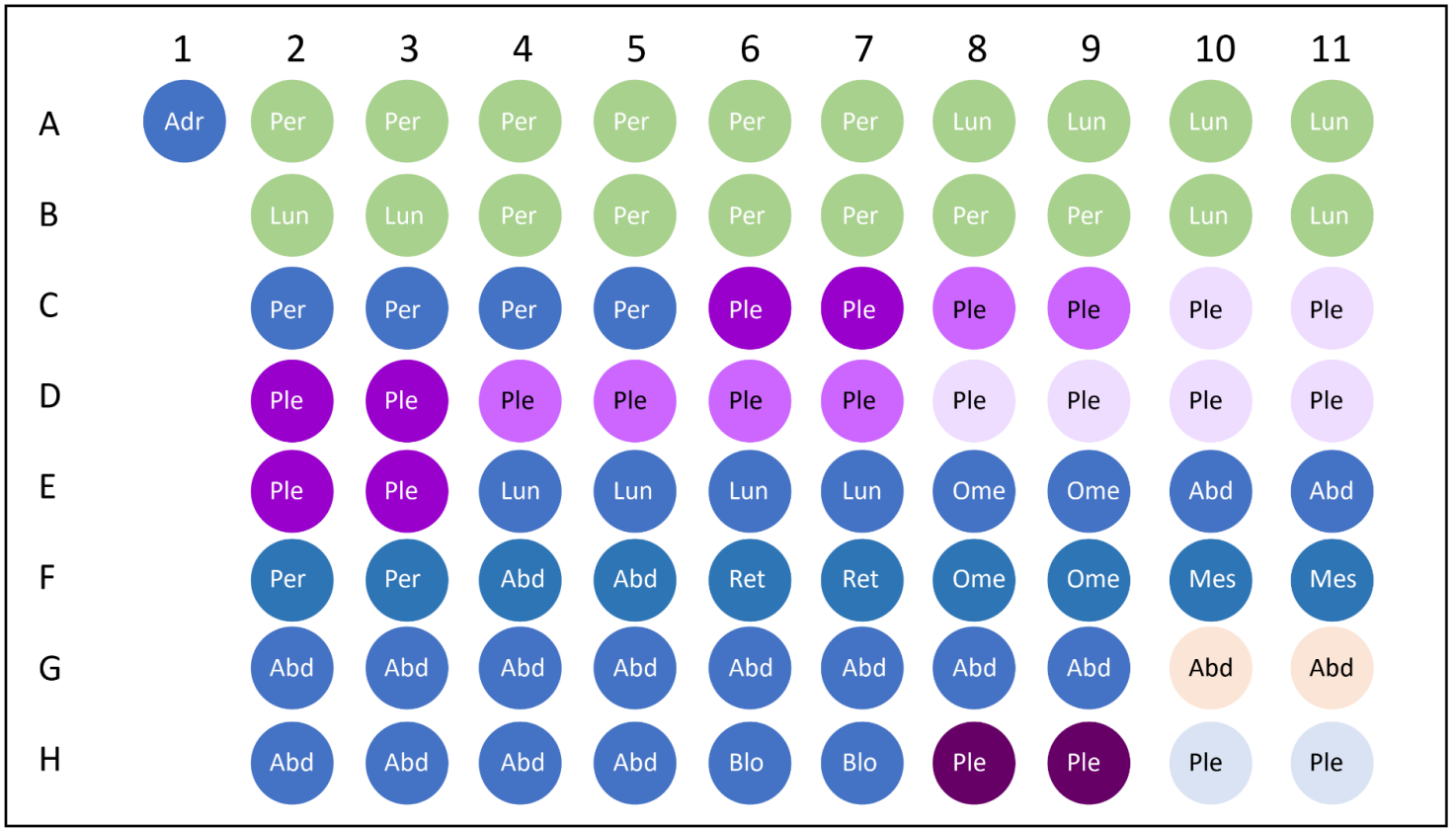

Figure 7.8 Schematic diagram of the TMA layout. Legend: Adr- adrenal gland, Abd- Abdominal cavity, Blo- Blood vessel, Lun- Lung, Mes- Mesentery, Ome- Omentum, Per-Pericardium,Ple- Pleura, Ret- Retroperitoneum; Green- Normal tissue, Blue- Malignant tumour, Purple (lightest to darkest)- (stage I, II, III, and IV malignant pleural mesothelioma), Light blue/ peach- Benign tumour. Information provided by the supplier (Amsbio).

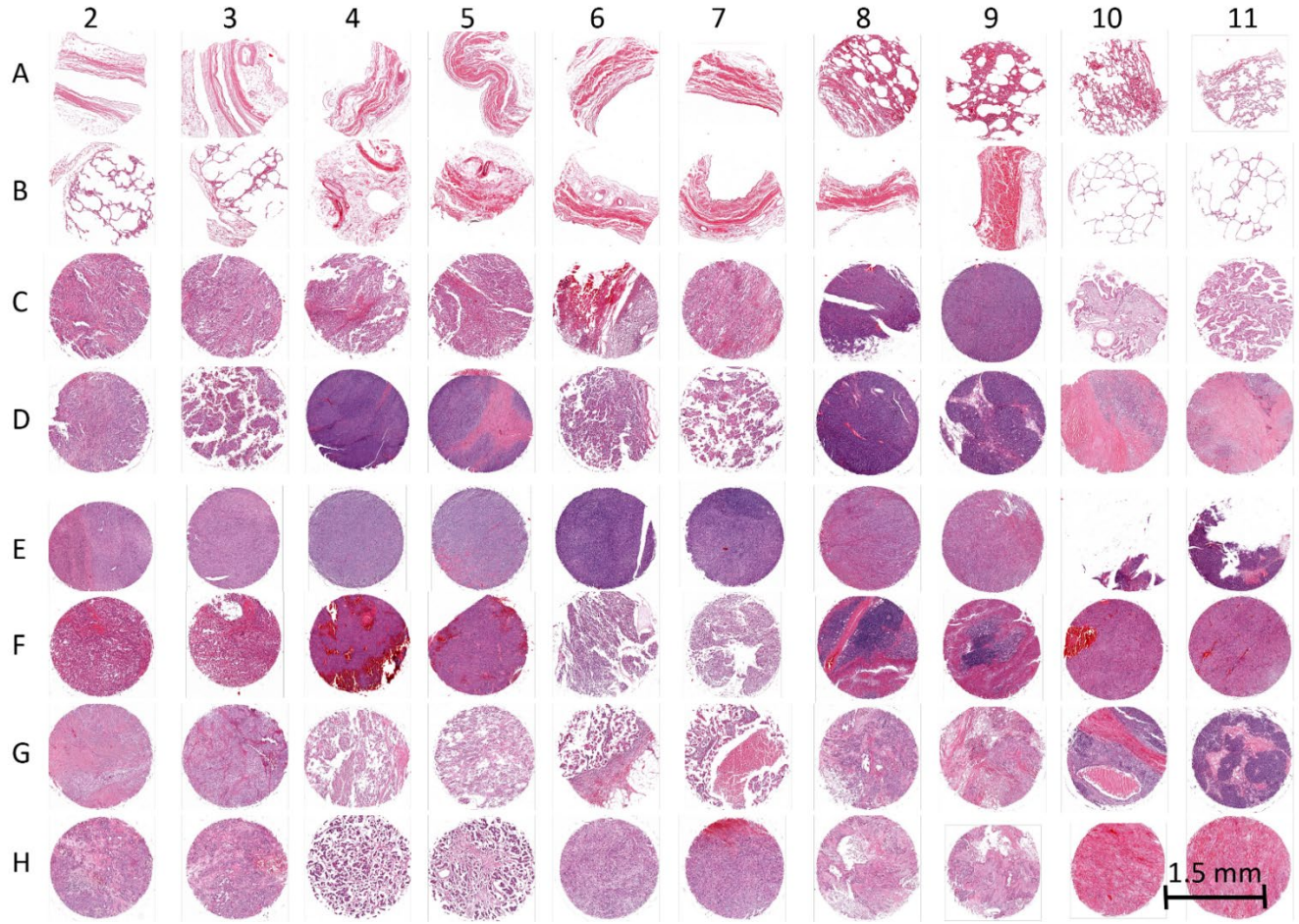

Figure 7.9 Histological presentation of the TMA following H&E staining. Each core has a diameter of 1.5 mm. Normal lung and pericardium tissues shown in Row A and Row B. The rest of the cores are malignant mesothelioma tumours of various types and stages or benign tissue (G10, G11, H10 & H11). Figure adapted from (Biomax.us.)

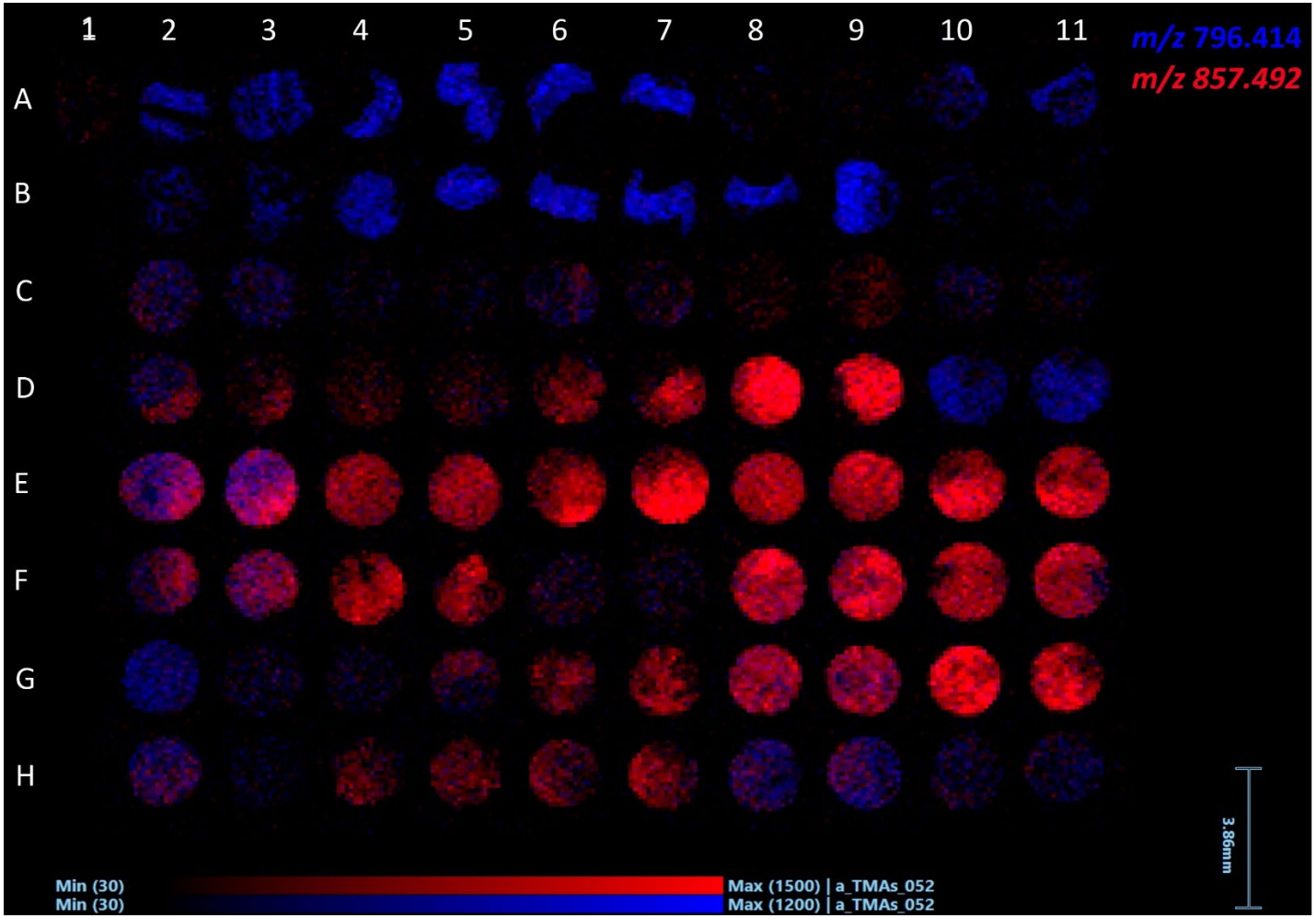

Figure 7.10 Representative MALDI-MS image of the whole TMA section. Overview of the TMAs based on signals for *m/z* 796.414 (blue- upper part predominantly) and *m/z* 857.492 (red- lower section). Signal intensity bars were adjusted to ensure visualisation of all 80 cores.

7.2.3.2 Matrix

In order to obtain the images, α-CHCA was deposited onto the whole TMA slide using the spray-coat method and a HTX TM-Sprayer™ automated sprayer. This is an established, tissue-compatible matrix application method for MALDI-MSI studies employed in a wide range of tissue types and TMAs (Ly *et al.*, 2019; Mascini *et al.*, 2018; Spraggins *et al.*, 2016). Gas flow rate, temperature, and nozzle velocity were selected to control matrix drying time which is essential in preventing analyte delocalisation and the formation of large matrix crystals that can create the so called “hot spots” on MALDI-MS images (parameters presented in Table 2.12). Common α-CHCA peaks are shown in red in the spectrum below (Figure 7.11). Peak picking was carried out in MMass and the settings were set at a signal to noise (S/N) threshold of 5, and the picking height was 100%. Both the absolute intensity threshold and the relative intensity threshold was set to 0 with baseline correction and smoothing applied. Representative MALDI-MS images of the most intense matrix peaks are presented in Figure 7.12 MALDI-MS images of the matrix reveal the TMAs shape and layout. Matrix signals appeared to be mostly uniform, with some areas of higher signal intensity towards the bottom right part of the TMA slide, particularly for *m/z* 861.038.

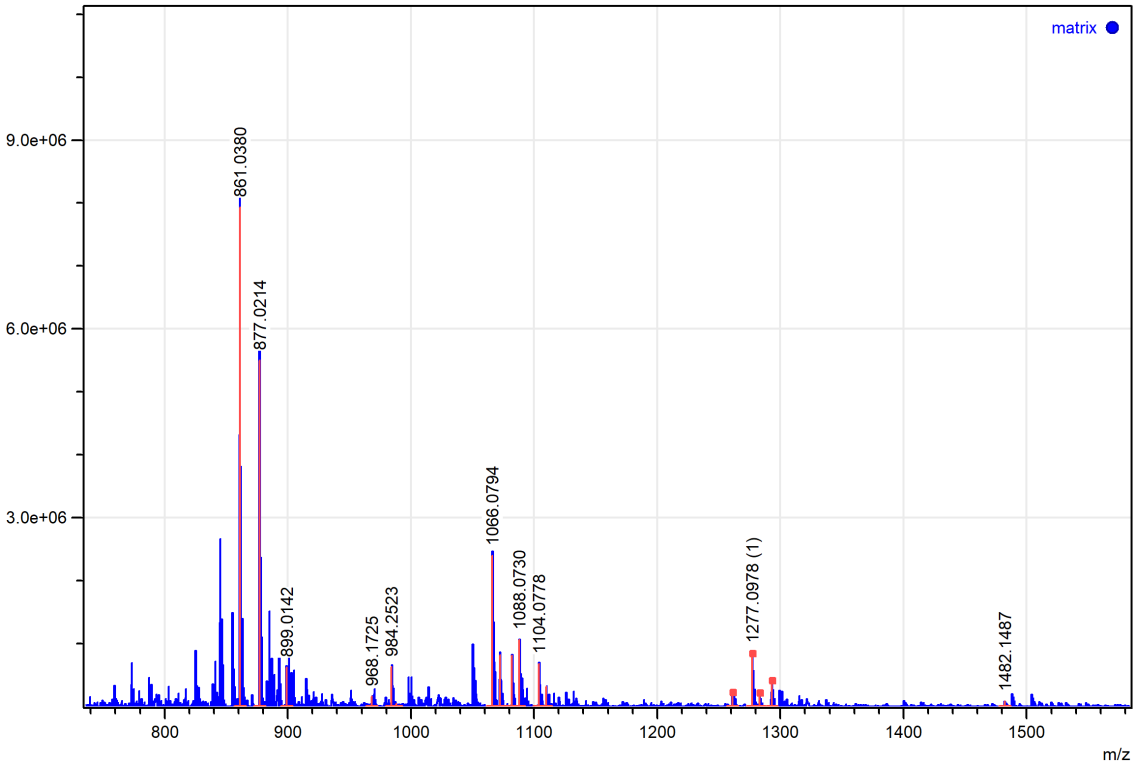

Figure 7.11 MALDI-MS matrix profile. Mass spectra acquired in positive mode; spectra display peaks within the mass range m/z 700-1500. Mass spectrum annotated with common matrix peaks. Peak picking was carried out in MMass and the settings were set at a S/N threshold of 5, and the picking height was 100%. Both the absolute intensity threshold and the relative intensity threshold was set to 0 with baseline correction and smoothing applied.

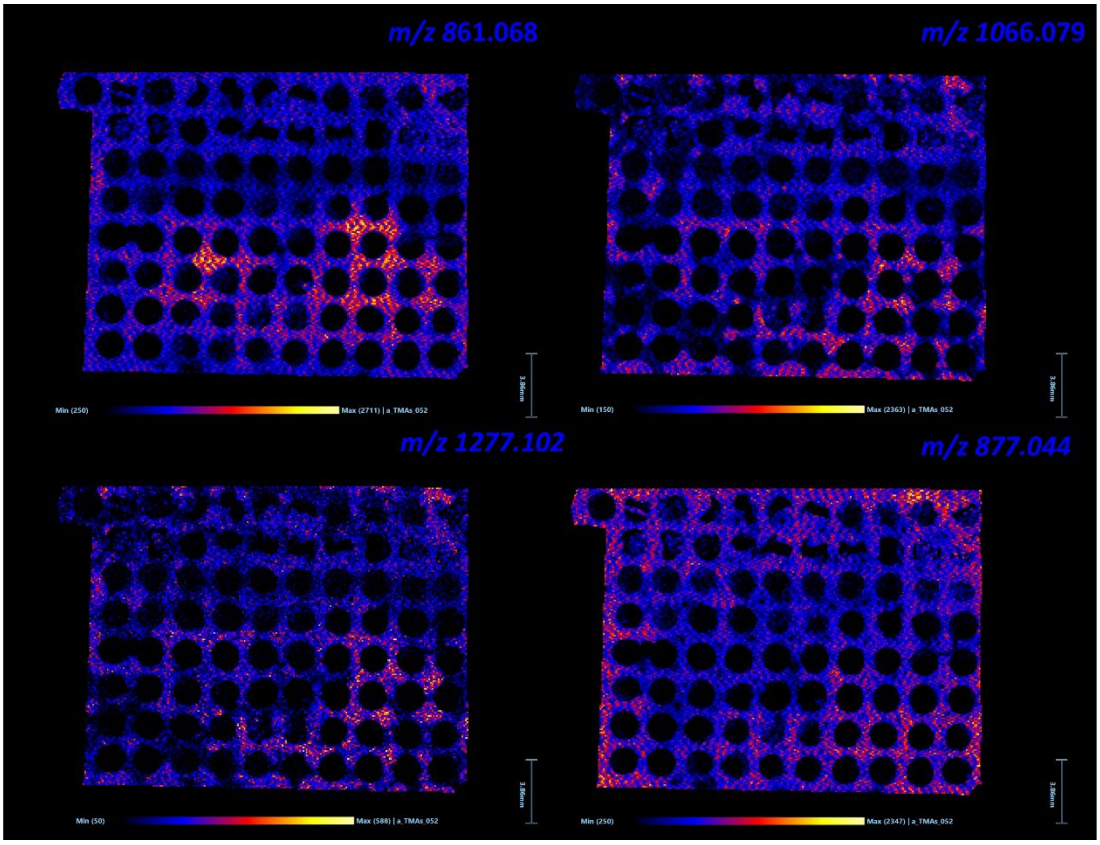

Figure 7.12 Representative MALDI-MS images of the most intense α-CHCA signal peaks.

7.2.3.3 Method reproducibility

Two duplicate cores were selected in order to observe the level of consistency between similar histological regions and analyse the reproducibility of the MALDI-MSI method. The two selected cores represent different needle cores from the same biopsy, and are therefore not identical pieces of tissue, as noted in the H&E images. Mass spectra were obtained from each individual core by selecting ROIs. The mass spectra (shown in Figure 7.13) is presented alongside the representative histological profiles of the cores. The flipped spectra contain peak profiles with a high degree of concordance, demonstrating a consistent and reproducible methodology. Furthermore, the mass error of the observed *m/z* values of the main peaks was calculated. S/N values were also included for each detected peak in both spectra. However, the highest intensity peaks were associated with known matrix peaks. Results are presented in Table 7.1.

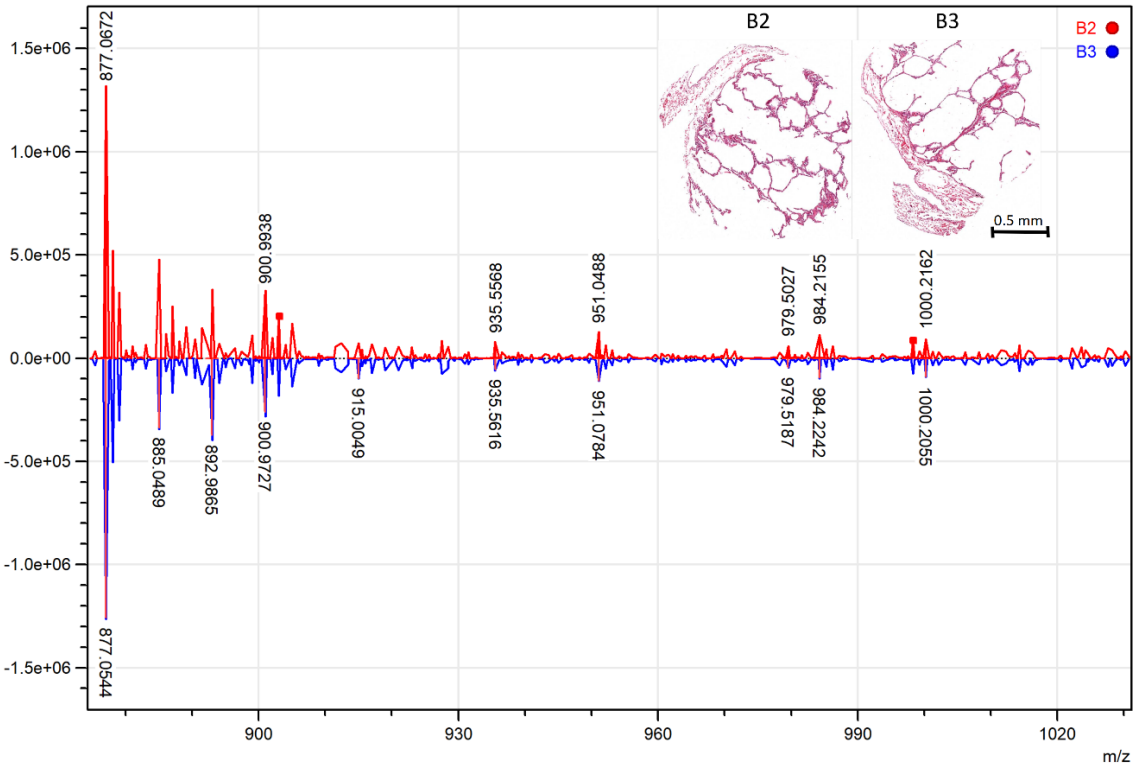

Figure 7.13 Flipped MALDI-MS spectra of duplicate cores B2 (red) and B3 (blue). Mass spectra acquired in positive mode; spectra display peaks within the mass range m/z 870-1035. Histological staining of the two cores are presented in the right-hand corner, with typical healthy lung tissue arhitechture present. Peak picking was carried out in MMass and the settings were set at a S/N threshold of 5, and the picking height was 100%. Both the absolute intensity threshold and the relative intensity threshold was set to 0 with baseline correction and smoothing applied.

Observed *m/z* B2	Observed *m/z* B3	Mass error (ppm)	S/N B2	S/N B3
877.067	877.054	14.5	310.7	242.1
900.993	900.972	23.4	77.1	58.4
903.014	903.015	0.7	50.6	39.4
935.556	935.561	5.1	18.0	11.9
951.048	951.078	31.1	29.7	23.9
979.502	979.518	16.2	13.5	9.9
984.215	984.224	8.8	28.1	21.5
998.239	998.241	1.8	22.0	16.8
1000.216	1000.205	10.6	22.5	20.7

Table 7.1 Calculated mass error and signal to noise (S/N) values for duplicate cores. Mass error >20 are shown in red.

7.2.3.4 Cancer heterogeneity

Analysis of TMAs containing tissue cores from several patients, allowed for investigating the mesothelioma heterogeneity between patients with similar diagnosis (malignant mesothelioma of the pleura, T1N0M0, stage I). Further data analysis resulted in differential spectrum for each individual core, by manually selecting ROIs. Two cores were selected to examine the potential differences in peak signal intensity (Figure 7.14) and ion distribution in MALDI-MS images (Figure 7.15). The patient details regarding age, sex, pathology diagnosis, anatomic site, TNM, grade, stage, and type of tumour were extracted from the product information sheet provided by the supplier. D8 was extracted from a 22-year-old female, whilst D11 was a 58-year-old female. The spectra of the two cores were acquired simultaneously using the same analysis parameters and conditions. Based on the flipped spectra, several differences can be noted in terms of ion presence and signal intensity of selected ions. Peaks of similar intensities can be noted for example *m/z* 927.5 and *m/z* 935.5. On the other hand, higher peak intensities can be observed for peaks such as *m/z* 943.6, *m/z* 979.5, and *m/z* 985.5. The latter was selected to underline not only the differences in

peak intensity in similar tumours, but also the need for a panel of various biomarkers, to account for this typical cancer heterogeneity. Based on putative assignments, *m/z* 985.5 was identified as a key peptide of the BRCA1-associated protein 1 (BAP1). As previously described in Chapter 1, Section 1.2.9.4, BAP1 has been classed as a key player in influencing environmental carcinogenesis, increasing susceptibility to asbestos fibres and early onset of MPM (Cheung & Testa, 2017). A recent study has shown that the median age of MM diagnosis was significantly younger among for BAP1 mutation carriers as compared to non-carriers (Ohar *et al.*, 2016) This was also observed in the spectra and images below Figure 7.14 and Figure 7.15, where *m/z* 985.597 intensity is significantly higher for the younger patient (core D8), suggesting that this patient presented a germline mutation in *BAP1* gene, and could have benefited from further genetic testing.

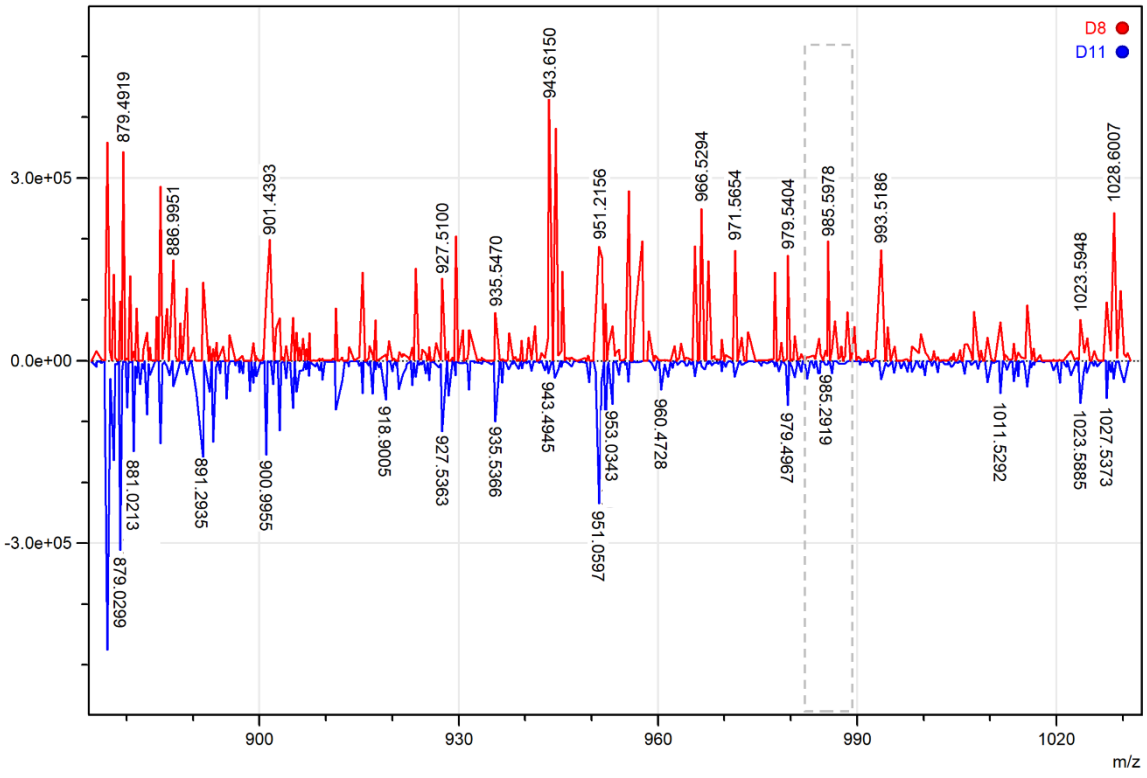

Figure 7.14 Flipped MALDI-MS spectra of core D8 (red) and D11 (blue). Mass spectra acquired in positive mode; spectra display peaks within the mass range m/z 870-1035. Peak picking was carried out in MMass and the settings were set at a S/N threshold of 5, and the picking height was 100%. Both the absolute intensity threshold and the relative intensity threshold was set to 0 with baseline correction and smoothing applied.

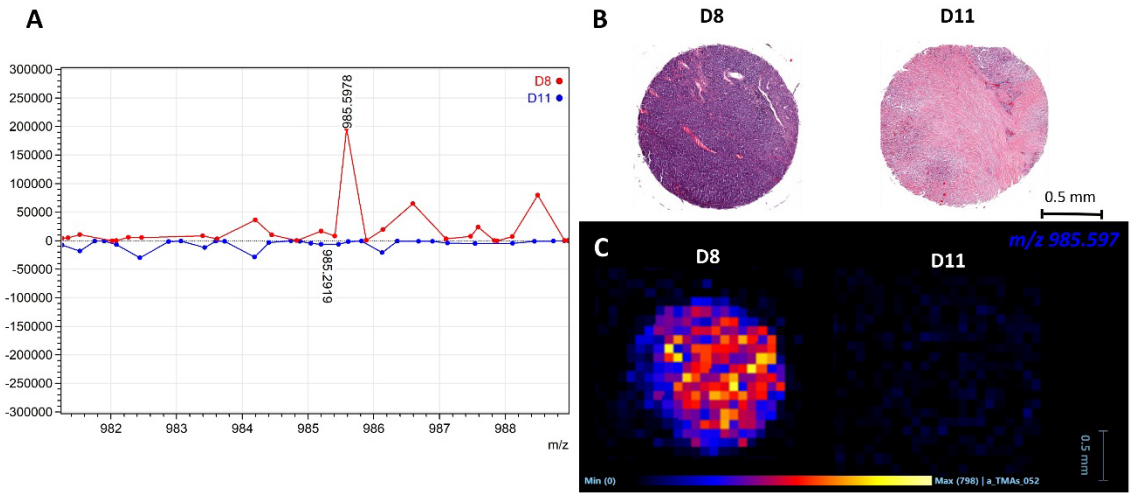

Figure 7.15 Differences in A) m/z 985.597 signal intensity, B) histological presentation, and C) ion distribution between tissue cores with same pathological diagnosis, TNM, and stage.

7.2.3.5 MALDI-MS as a tool for biomarker discovery and validation

Differences between histological tissue and tumour types were highlighted by differences in signal intensity of four selected peaks, *m/z* 944.5, *m/z 957.5 m/z* 971.5, and *m/z* 985.5, that occurred significantly less frequently in normal lung tissue (Figure 7.15, Figure 7.16, and Figure 7.17, A9 (green)) compared to malignant tissue. The intensity of the peptide signals varied across the selected TMAs. The most noteworthy m/z signals were then manually annotated and compared to lists of theoretical masses of emerging MPM markers as presented in current literature (Table 7.2). The corresponding peptide sequences were added to the spectra.

The signal intensity across the panel was not related to molecular features characteristic to certain anatomical sites (*i.e.,* lung vs pleura), and was rather an indicator of cancer progression and aggressiveness (*i.e.,* stage I vs stage IV). These markers might serve to identify patients with better overall prognosis.

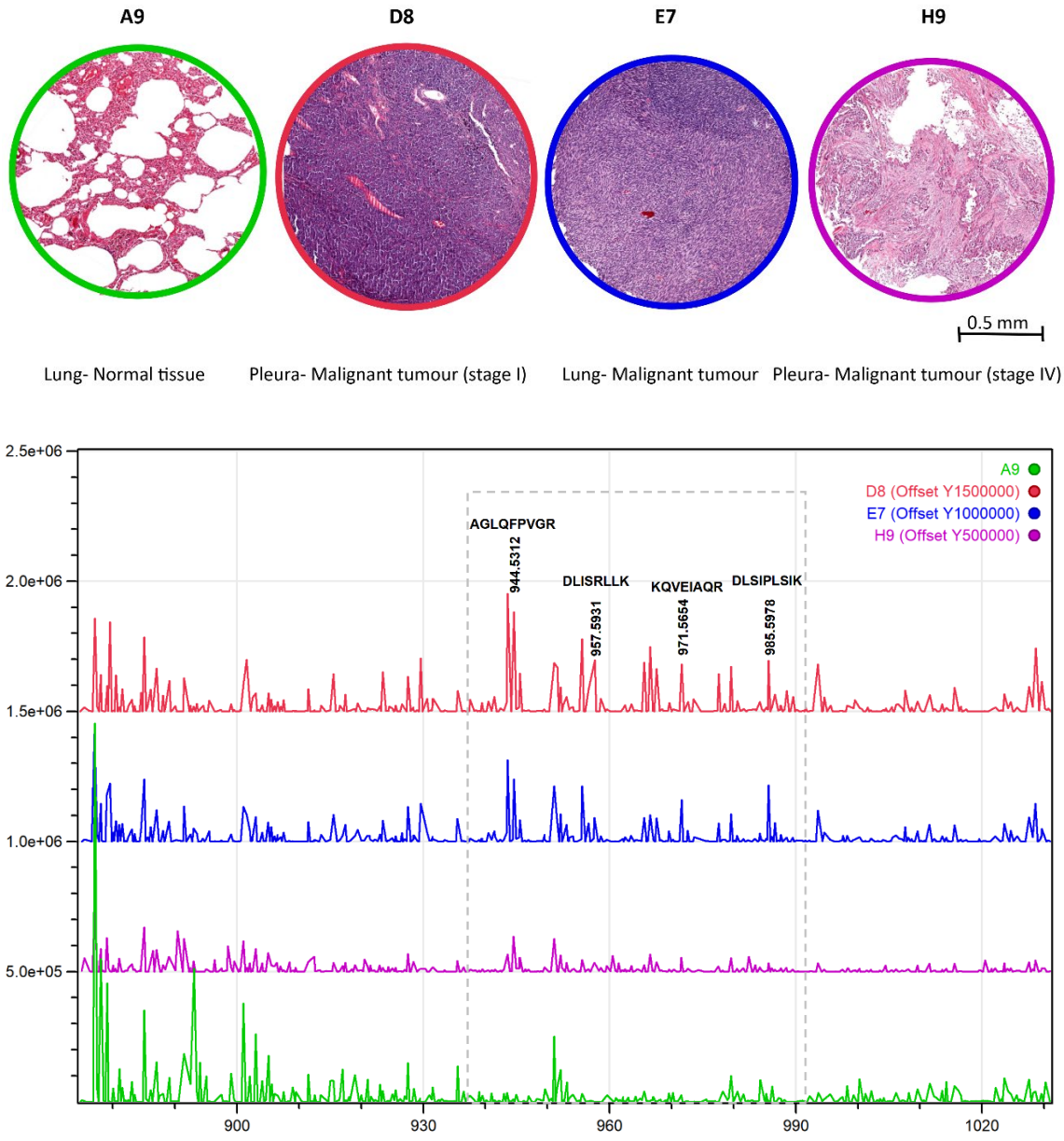

Figure 7.16 Top- Histological profile of selected cores (A9 Lung- Normal tissue, D8 Pleura-Malignant tumour stage I, E7 Lung- malignant tumour and H9 Pleura-Malignant tumour stage IV). Colours of the borders match the colour of each spectrum. Bottom- Offset spectra of the selected individual cores within the mass range m/z 870-1035. Peak picking was carried out in MMass and the settings were set at a S/N threshold of 5, and the picking height was 100%. Both the absolute intensity threshold and the relative intensity threshold was set to 0 with baseline correction and smoothing applied. Selected region presented in the dotted box includes peaks of interest and the corresponding putatively assigned peptide sequence. Individual spectrum presented in order of peak intensity.

The selected peptide signals detected within each core were identified through putative assignments by employing peptide resource tool (Uniprot.) and are presented in Table 7.2. Tandem MS for peptide identification was attempted on a serial section of the same TMA but failed to provide significant results and requires further optimisation. The theoretical masses for argininosuccinate synthase 1 (ASS1), BRCA1-associated protein 1 (BAP1), and histone 2A (H2A) were generally matched in the sample analysis with a small error (≤5 ppm). One mass (*m/z* 957.593), observed in all malignant cores, was associated with aurora-related kinase 1 (ARK-1), but with a relatively higher error. Peptide signals associated with HMGB1, mesothelin, and VISTA were also detected, but were excluded from the table due to the low signal intensity and high mass error (>20 ppm), reflecting the limited capabilities of the instrumentation.

Protein	Peptide theoretical m/z	Peptide observed m/z	Mass error (ppm)	Peptide sequence	Protein function
Argininosuccinate synthase 1 (ASS1)	971.563	971.565	2.2	KQVEIAQR	Argininosuccinate catalysis
Aurora-related kinase 1 (ARK-1)	957.609	957.593	-16.7	DLISRLLK	Onset and progression of mitosis
BRCA1-associated protein 1 (BAP1)	985.592	985.597	5.0	DLSIPLSIK	Tumour suppressor
Histone 2A (H2A)	944.531	944.530	-0.5	AGLQFPVGR	Nuclear structure

Table 7.2 Observed peptides after *in situ* digestion and MALDI-MS analysis. Observed m/z values in positive ion mode, the mass error (ppm), peptide sequence, and the protein function are included.

Representative images of each selected peak are presented in Figure 7.17. The results of this analysis identified distinct signals possibly linked to malignant transformation, tumour progression, and patient prognosis. Firstly, ASS1 expression in malignant tissues (D8, H9, E7) was significantly greater than in the normal tissue (A9), as seen in Figure 7.17 C. Despite some reports of mesothelioma being a ASS1 deprived tumour (Szlosarek *et al.*, 2016), ASS1 upregulation has been previously reported in mesothelioma TMAs and 3D cellular

spheroids and may play a key role in MPM chemotherapeutic resistance (Barbone *et al.*, 2016). This finding suggests that low ASS1 expression is linked with increased aggressiveness and late stage and monitoring the upregulation or downregulation of this protein might improve therapeutic strategies and lead to better OS.

Similarly, the most advanced tumour stage (H9 stage IV MPM) showed a slightly lower intensity of ARK1. ARK1, a member of the Aurora kinase family, plays an oncogenic role linked to its mitotic activity, and it is upregulated in cancerous tissue, when compared to normal tissue, as seen in Figure 7.17. Furthermore, high ARK1 signal in early stage MPM (D8) compared to normal lung tissue (A9) suggests that this protein could be a potential prognostic marker for MPM. However, a recent study suggested that overexpression of ARK1A is associated with poor prognosis (Guo *et al.*, 2021). Interestingly, BAP1 expression has also been shown to be linked to shorter OS (Arzt *et al.*, 2013), although contradictory reports have also been published (Baumann *et al.*, 2015). Due to limited patient information, the data herein can neither confirm or dispute these findings, but it can suggest a link between BAP-1 expression, increased ARK1 presence, and early stage MPM in younger patients, that has not been reported before. Interestingly, in terms of spatial localisation, overexpression of ARK1 and BAP-1 appeared to follow the same distribution pattern, particularly noticeable in D8 and E7 (Figure 7.17 B& D). Moreover, H2A, a known marker of aberrant post translational modifications in cancer (Zhao & Shilatifard, 2019), followed the same distribution (Figure 7.17 A). This finding highlights the importance of localisation studies for biomarker validation and the usefulness of imaging techniques such as MALDI-MSI.

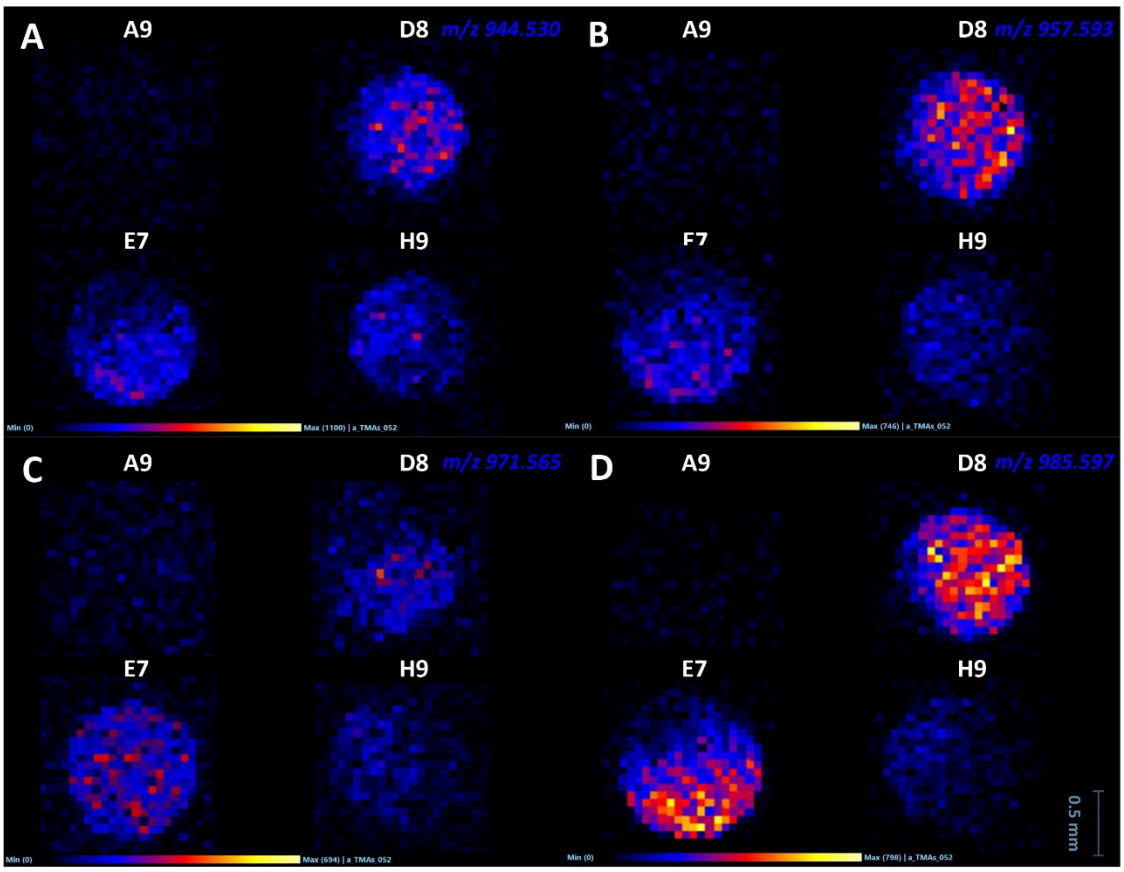

Figure 7.17 Representative MALDI-MS images A) *m/z* 944.530 B) *m/z* 957.593 C) *m/z* 971.565 D) *m/z* 985.597. The presence of selected peaks is associated with malignant events, with limited signal in the non-cancerous core (A9). Low intensities of the selected peaks are associated with more aggressive types of malignancy.

7.3 Conclusion and future perspectives

Despite several conflicting reports, the mesothelioma research community can agree on one thing- the urgent need for reliable MPM biomarkers. The work presented in this chapter aimed to characterise a small panel of emerging biomarkers, by employing a multi-modal analysis approach. Despite being an early attempt at biomarker characterisation and validation, the data adds to the knowledge surrounding MPM.

Firstly, flow cytometry was employed to analyse protein expression in several immortalised cell lines. Additionally, confocal microscopy was used to detect the markers within the cells and confirm the flow data. HeLa and U937 cells were]used as positive controls to confirm the suitability of the antibodies, as they are

known to express mesothelin and HMGB1 (Xia *et al.*, 2017; Ye *et al.*, 2019), and VISTA, respectively (Zhang *et al.*, 2021). Interestingly, several conflicting results were presented, notably the negative VISTA expression in NCI-H28 cells after flow analysis compared to positive staining following confocal microscopy, the latter being in line with literature (Muller *et al.*, 2020). Moreover, limited mesothelin expression was noted in Met-5A, MSTO-21H, and NCI-H28 cells, compared to the positive control, suggesting low sensitivity of antibody, but also the lack of specificity of this marker. One key finding was the distribution of mesothelin in protein aggregates within the membrane of MPM cell lines, suggesting that mesothelin presence or level of expression might not be MPM specific, but the pattern of distribution might play a more significant role in cancer development.

Next, human TMAs containing 80 tissue cores were subjected to untargeted MALDI-MSI within the range *m/z* 700-1800, a characteristic *m/z* range used for observation of small peptides. MALDI-MSI has been previously used as a tool to differentiate between healthy and diseased tissues (Mascini *et al.*, 2018), also demonstrating potential in this study as a biomarker characterisation technique. Despite the early stage, a few conclusive thoughts can be noted from the MALDI-MS data presented herein. Firstly, the technique highlighted the mesothelioma heterogeneity, by assessing *m/z* 985.5 signal intensity in two individual cores, from patients with similar diagnosis. The selected peak was identified as a key peptide of BAP1 protein through putative assignments and its preferential distribution consolidated the idea that asbestos-exposed individuals presenting with a family history of cancer should be considered for *BAP1* genetic testing for the purpose of early detection and intervention. Secondly, spectra of individual cores were compared, with the focus on four main peaks associated with ASS1, ARK1, BAP1, and H2A. These proteins have been emerging as MPM markers in recent literature (Cheung & Testa, 2017; Guo *et al.*, 2021; Szlosarek *et al.*, 2016; Yoshikawa *et al.*, 2020; Zhao & Shilatifard, 2019). By simultaneously analysing the presence and spatial distribution of the selected peaks in tissues of different histological profile, a correlation between marker expression can be noted, which has not been reported before. Notably, interlinked spatial distribution between

BAP1, H2A, and ARK1 has been observed. Further investigation is required to validate this finding, which emphasises the intricate process of cancer development.

There were several notable limitations in the biomarker characterisation side of work, including the small number of markers included in the panel and the use of immortalised cell lines, such as Met-5A whose reliability has been recently questioned (Pruett *et al.*, 2020). Further work using primary cells and human tissues is required to fully validate the selected markers. The addition to the panel of novel emerging biomarkers is also required. In terms of MALDI-MS analysis, the limitations revolved around the number of samples/ repeats, as well as limited instrument capabilities in relation to sensitivity, resolution, time of acquisition and reduced instrument ion mobility functionality. Moreover, only putative assignments were carried out to class the peaks of interest. Further liquid chromatography electrospray ionisation tandem mass spectrometry (LC-ESI-MS/MS) can allow precise identification and confirm the presence of selected markers. Additionally, this technique can be employed for biomarker discovery and validation in human tissues.

All in all, the final results chapter offers new avenues for mesothelioma research and adds to the knowledge surrounding mesothelioma diagnosis and progression. The early-stage data presented herein sets the base for future experiments and ultimately the development of a mesothelioma-specific panel of biomarkers that are inexpensive, reproducible, easy to obtain, and easily sampled with a minimally invasive technique.

Chapter 8 Conclusion

8.1 Overview

MPM is an incurable malignancy associated with high symptom burden and poor prognosis. Despite strict asbestos regulations being implemented in the Western World since the 1970s, MF continue to be a key factor in MPM onset (Kido *et al.*, 2017). Moreover, novel carbon nanotubes have the potential to trigger similar responses as asbestos fibres and have been linked to MM onset (Chernova *et al.*, 2017). Asbestos detection is essential in establishing a causal link between the fibres and this malignancy; however, current asbestos identification techniques fail to preserve the spatial information and to detect fibres smaller than 5 μm (Xue *et al.*, 2020). Additionally, the poor OS is a direct consequence of limited reliable blood and tissue MPM biomarkers. It has been established that early diagnosis significantly improves OS (Creaney & Robinson, 2017), prompting the mesothelioma scientific community to shift the focus on MPM biomarker discovery. Finally, there is little knowledge on the key functions that trace metals play in MPM onset, progression and chemoresistance, despite the previously reported link between metal homeostasis dysregulation and malignant pathogenesis (Serra *et al.*, 2020).

This chapter aims to offer a compendious conclusion of the study presented in detail in the previous chapters, by summarising the key research findings in relation to the research aims and objectives and discussing the value and contribution these results bring to the wider scientific community. Furthermore, the limitations of the study, as well as opportunities for future research are detailed below.

8.2 Asbestos and MF detection in cellular models using LA-ICP-MS imaging

MPM 2D cellular models of the cell-fibres interaction were developed to support the hypothesis that LA-ICP-MSI has the potential to be employed as an asbestos detection tool, centred around the elemental content of asbestiform and non-asbestiform fibres. Initial steps focused on investigating the hazardous effect of MF on human mesothelioma cells, normal mesothelial cells, and a NSCLC control cell line, in order to successfully develop suitable LA-ICP-MS cellular models.

Interestingly, the results indicated that chrysotile fibres have the potency to induce significant levels of cellular death, when compared to other established asbestos fibres previously reported to have higher toxicity (Hodgson & Darnton, 2000). Additionally, wollastonite, currently classed as a non-asbestiform fibre, also induced a decline in cell viability, albeit at a smaller rate. These results highlight the current classification as obsolete and support the growing evidence that an updated MF classification is needed (Yu *et al.*, 2019).

Another noteworthy finding was the possible synergistic role between asbestos-induced apoptosis and necrosis in MPM pathogenesis based on the real-time apoptosis/ necrosis *in vitro* data. Cellular necrosis induced by asbestos fibres has been previously reported to play an essential role in MPM pathogenesis (Yang, Haining *et al.*, 2010), but this was the first report of a possible synergistic role of apoptosis and necrosis in MPM. The data not only added to the knowledge surrounding MPM pathogenesis, but also opened an avenue to novel therapeutic targets.

Subsequently, LA-ICP-MS method optimisation for actinolite detection was carried out, helping set the basis of this proof-of-concept study. Following optimisation, actinolite and other MF were successfully detected in cellular models based on ^{24}Mg, ^{29}Si, and ^{57}Fe signal using a single-conduit, low ablation LA-ICP-MS. This was the first study that successfully identified MF based on elemental content using this prototype instrumentation (Voloaca *et al.*, 2020). To further add to the knowledge surrounding asbestos detection and LA-ICP-MSI applications, a prototype LA-ICP-TOFMS was employed for pseudo-spontaneous detection of the elements between mass 23 (Na) and mass 238 (U). The LA-ICP-TOFMS allowed for both identification of asbestos fibres, as well as correct asbestos classification in blind samples (Greenhalgh *et al.*, 2020). Current asbestos detection methods fail to maintain the spatial arrangement of the asbestos fibres by employing acid digestion in the sample preparation stages (Dement *et al.*, 2015). LA-ICP-MSI proved to be a powerful detection technique that can detect MF with high sensitivity, whilst offering information on the location of the MF within the samples.

These findings supported the potential of this tool and set the basis for the next key aim, the applicability of LA-ICP-MS as an asbestos and other MF detection tool in 3D models of MPM following sample preparation and consequent fibre fragmentation. There is a lack of 3D MPM model containing asbestos fibres, current models mostly focusing on tumour microenvironment and multicellular resistance (Barbone *et al.*, 2012; Jagirdar *et al.*, 2021; Mazzocchi *et al.*, 2018). A suitable 3D model that successfully recapitulated the MPM tumours was developed and subjected to sample preparation steps similar to those used to prepare human tissue blocks. This crucial step offered insight into the capabilities of LA-ICP-MS to detect small MF, fibre fragments, and MF positioned at different spatial orientations within the tumour. Furthermore, the results set the foundation for human tissue analysis.

8.3 Asbestos and MF detection in human tissues samples using LA-ICP-MSI

Detection of asbestos and other MF in human mesothelioma tissue samples was the ultimate goal of the current study. The results presented a novel way of detecting MF within human tissue samples but also highlighted the high performance of the LA-ICP-TOFMS instrument, particularly that of the laser. This was the first study to show the capabilities of the new Iradia laser ablation system to ablate soft biological matrices, as well as the acid resistant MF, with the same laser energy. Laser energy optimisation has been a challenging process in the LA-ICP-MS community, in order to avoid elemental fractionation (*i.e.,* enrichment of one element over the other) (Diwakar *et al.*, 2013). The thermal process resulting from the laser energy can result in preferential evaporation, melting, and ablation of certain elements from the sample, particularly in MPM samples with possible traces of asbestos and other MF. The results of this study address this gap in the knowledge and present to the wider community the possibility of applying LA-ICP-MSI with these types of challenging samples, with minimal sample fragmentation. Subsequently, other groups have attempted to image asbestos fibres using LA-ICP-MSI based on our published results (Šala *et al.*, 2021).

8.4 Characterisation of MPM metallome based on LA-ICP-MSI of human mesothelioma tissues

Dysregulation in metallome homeostasis has been previously linked to cancer onset and progression (Serra *et al.*, 2020). However, there is limited information on metallome disturbance and distribution in MPM samples. Most studies that explored metal distribution in MPM, focused on Fe distribution within the asbestos fibres or asbestos ferruginous bodies (Pascolo *et al.*, 2013). By employing state-of-the-art LA-ICP-TOFMS instrumentation, the current study addressed an important gap in the MPM knowledge- role of metallome dynamics in MPM presentation, prognosis, and therapeutic response. Additionally, the data questioned the benefits of an established procedure, talc pleurodesis, over the long-term damage induced to the tissues. Overall, the results highlighted the need for further investigations into the MPM metallomics and emphasise the applicability of LA-ICP-TOFMS both as a clinical and as a research tool.

8.5 Multi-modal characterisation of emerging biomarkers

The final part of the project focused on characterisation of selected emerging biomarkers. The panel of biomarkers was investigated using a combination of flow cytometry analysis and confocal microscopy, on MPM cells, normal mesothelial cells, and cells reported to express the investigated markers. The techniques employed in the study allowed for direct comparison in protein expression, but also offered information on expression levels and distribution of the selected biomarkers. One significant finding was the distribution of mesothelin in protein aggregates within the membrane of MPM cell lines, suggesting that mesothelin presence or level of expression might not be MPM specific, but the pattern of distribution might play a more significant role in cancer development. This is the first report of mesothelin aggregation within cell membranes, appearing to be characteristic to MPM cells. To better understand the implications of these results, future studies could investigate mesothelin aggregation in primary MPM cell lines, for example by using rotor molecule-dye that is essentially non-fluorescent until it binds to structural features associated with aggregated proteins (Direito *et al.*, 2021). Lastly, MALDI-MSI allowed for a rapid,

direct comparison of healthy and diseased human TMAs. The use of TMA allowed for the analysis of a large number of subjects (n=80) in the same run of analysis. The results focused on four emerging MPM biomarkers (ASS1, H2A, BAP1, and ARK1) which have not been analysed concomitantly in any previous studies. The MALDI-MS data suggested a relative connection between expression of these tentatively identified biomarkers and underlined their potential as differential, diagnostic, and prognosis markers.

8.6 Future directions

This project has generated several interesting findings in the field of MPM. Each of these findings has suggested areas of future research that may be of patient benefit/help to better understand the disease. Firstly, MPM onset appeared to be driven by a synergistic action of apoptosis and secondary necrosis induced by asbestos fibres. To better understand the implications of these results, future studies could address the link between the types of cell death induced by asbestos fibres in relevant MPM models.

Secondly, correct classification of asbestos fibres was attempted, but only as a proof-of-concept in a single sample, due to very limited access to the LA-ICP-TOFMS instrument. Future work will focus on both MF detection within a larger pool of human tissue samples and correct classification based on nominal structure, using state-of-the-art LA-ICP-TOFMS instrumentation. Based on the current results, future investigations should be carried out to determine the metallome role in the context of MPM onset, progression, and treatment outcome, with a focus on Fe, Zn, Mg, Na, and P normal and aberrant levels. The metallome surrounding asbestos fibres could also be determined at a cellular level, to help better understand the impact on elemental disturbances asbestos fibres induce in the tissues.

Overall, future work will focus on expanding the pool of subjects with the addition of benign and healthy tissue samples. Given the multiplexing capabilities of the LA–ICP–TOFMS instrumentation, which allows for the monitoring of the entire mass range in a single run, biomarker discovery and validation can be attempted

using monoclonal antibodies labelled with stable heavy-metal isotopes, an immunoassay that has gained increased popularity lately (Flint *et al.*, 2020; Neumann *et al.*, 2020). Coupled to LA-ICP-TOFMS, this technique allows for monitoring an extremely large number of targets, compared to current applied methodology, such as multicolour immunofluorescence assays, with high affinity and at superior resolution. Ultimately, LA-ICP-TOFMS imaging has the capability to simultaneously provide information on (a) MF location, (b) MF type and nominal content, (c) human tissue metallome, around the MF but also in different sections of the sample, and (d) biomarker localisation and quantification, all in one single run of analysis.

8.7 Concluding remarks

Being the first study of its kind, a substantial amount of time was dedicated to optimising sample preparation and analysis. Due to the multi-modal novel nature of this study, the data subsequently generated was successfully peer reviewed and published in the form of three journal articles (Greenhalgh *et al.*, 2020; Voloaca *et al.*, 2020; Voloaca *et al.*, 2022) but also opened avenues to several future research projects. It is worth noting that the study has several limitations. As a proof-of-concept study, the number of samples and repeats employed in LA-ICP-MS analysis, particularly in terms of tissue analysis, was limited, which needs to be addressed in future studies. Biomarker validation was limited by the use of a relatively small panel of targets, as well as the used of immortalised cell lines. Future work can explore the use of primary cultures and patient-derived organoids, coupled with established proteomics techniques such as LC-MS/MS, flow cytometry, western blot, as well as additional genomic analysis.

Several impediments encountered throughout the duration of the project are worth mentioning. Firstly, asbestos fibres are classed as extremely hazardous due to the carcinogenic nature and some difficulties were encountered in procuring the right research-grade asbestos, whilst adhering to the recommended H&S standards. Another major difficulty was instrument availability and performance, particularly the single-conduit LA-ICP-MS instrument employed in the initial analysis. A drawback in the workflow of the

study was obtaining human tissue samples due to delayed legal matters. Commercial human tissue samples were employed as a convenient alternative, but with limited pool size and increased costs. However, the challenges encountered throughout the study were carefully addressed and resolved. These challenges, but most importantly the research accomplishments, contributed to achieving the core aim of this work- adding to the knowledge surrounding mesothelioma and supporting the communal goal of increasing prognosis and life quality of MPM patients.

References

Ackerman, C. M., Lee, S., & Chang, C. J. (2017). Analytical methods for imaging metals in biology: From transition metal metabolism to transition metal signalling. *Analytical Chemistry, (Washington), 89*(1), 22-41. doi: 10.1021/acs.analchem.6b04631

Ai, J., & Stevenson, J. P. (2014). Current issues in malignant pleural mesothelioma evaluation and management. *The Oncologist, 19*(9), 975-984. doi:10.1634/theoncologist.2014-0122

Ali, J. M., Aresu, G., Peryt, A., & Coonar, A. S. (2018). Video-assisted thoracoscopic surgery in the management of mesothelioma. *Shanghai Chest, 2*, 46. doi:10.21037/shc.2018.05.05

Altomare, D. A., Vaslet, C. A., Skele, K. L., De Rienzo, A., Devarajan, K., Jhanwar, S. C., & Testa, J. R. (2005). A mouse model recapitulating molecular features of human mesothelioma. *Cancer Research, 65*(18), 8090-8095. doi:10.1158/0008-5472.CAN-05-2312

Andreozzi, G. B., Pacella, A., Corazzari, I., Tomatis, M., & Turci, F. (2017). Surface reactivity of amphibole asbestos: A comparison between crocidolite and tremolite. *Scientific Reports, 7*(1), 1. doi:10.1038/s41598-017-14480-z

Arem, H., & Loftfield, E. (2018). Cancer epidemiology: A survey of modifiable risk factors for prevention and survivorship. *American Journal of Lifestyle Medicine, 12*(3), 200-210. doi:10.1177/1559827617700600

Arsenic, metals, fibres, and dusts. (2012). *IARC Monographs on the Evaluation of Carcinogenic Risks to Humans, 100* (PtC), 11-465.

Arzt, L., Quehenberger, F., Halbwedl, I., Mairinger, T., & Popper, H. H. (2013). BAP1 protein is a progression factor in malignant pleural mesothelioma. *Pathology Oncology Research, 20*(1), 145-151. doi:10.1007/s12253-013-9677-2

ATCC. Retrieved from https://www.atcc.org/products/crl-2081

Attanoos, R. L., & Gibbs, A. R. (2004). The pathology associated with therapeutic procedures in malignant mesothelioma. *Histopathology, 45*(4), 393-397. doi:10.1111/j.1365-2559.2004.01928.x

Auerbach, O., Conston, A. S., Garfinkel, L., Parks, V. R., Kaslow, H. D., & Hammond, E. C. (1980). Presence of asbestos bodies in organs other than the lung. *Chest, 77*(2), 133-137. doi:10.1378/chest.77.2.133

Aust, A. E., Cook, P. M., & Dodson, R. F. (2011). Morphological and chemical mechanisms of elongated mineral particle toxicities. *Journal of Toxicology and Environmental Health. Part B, Critical Reviews, 14*(1-4), 40-75. doi:10.1080/10937404.2011.556046

Baas, P., Scherpereel, A., Nowak, A. K., Fujimoto, N., Peters, S., Tsao, A. S., & Zalcman, G. (2021). First-line nivolumab plus ipilimumab in unresectable malignant pleural mesothelioma (CheckMate 743): A multicentre, randomised, open-label, phase 3 trial. *The Lancet (British Edition), 397*(10272), 375-386. doi:10.1016/S0140-6736(20)32714-8

Bahnassy, A. A., Zekri, A. N., Abou-Bakr, A. A., El-Deftar, M. M., El-Bastawisy, A., Sakr, M. A., & Gaafar, R. M. (2012). Aberrant expression of cell cycle regulatory genes predicts overall and disease-free survival in malignant pleural mesothelioma patients. *Experimental and Molecular Pathology, 93*(1), 154-161. doi:10.1016/j.yexmp.2012.04.001

Barbone, D., Van Dam, L., Follo, C., Jithesh, P. V., Zhang, S., Richards, W. G., & Broaddus, V. C. (2016). Analysis of gene expression in 3D spheroids highlights a survival role for ASS1 in mesothelioma. *PloS One, 11*(3), e0150044. doi:10.1371/journal.pone.0150044

Barbosa, L. D., & Sussulini, A. (2020). Recent advances in LA-ICP-MS for biomedical applications. *Biomedical Spectroscopy and Imaging, 8*(3-4), 47-54. doi:10.3233/BSI-200193

Bardelli, F., Brun, F., Capella, S., Bellis, D., Cippitelli, C., Cedola, A., & Belluso, E. (2021). Asbestos bodies count and morphometry in bulk lung tissue samples by non-invasive X-ray micro-tomography. *Scientific Reports, 11*(1), 10608. doi:10.1038/s41598-021-90057-1

Baumann, F., Ambrosi, J., & Carbone, M. (2013). Asbestos is not just asbestos: An unrecognised health hazard. *The Lancet Oncology, 14*(7), 576-578. doi:10.1016/S1470-2045(13)70257-2

Baumann, F., Flores, E., Napolitano, A., Kanodia, S., Taioli, E., Pass, H., & Carbone, M. (2015). Mesothelioma patients with germline BAP1 mutations have 7-fold improved long-term survival. *Carcinogenesis (New York), 36*(1), 76-81. doi:10.1093/carcin/bgu227

Baur, X., & Frank, A. L. (2021). Ongoing downplaying of the carcinogenicity of chrysotile asbestos by vested interests. *Journal of Occupational Medicine and Toxicology (London, England), 16*(1), 6. doi:10.1186/s12995-021-00295-2

Becker, S. J., Matusch, A., Palm, C., Salber, D., & Morton, K. A. (2010). Bioimaging of metals in brain tissue by laser ablation inductively coupled plasma mass spectrometry (LA-ICP-MS) and metallomics. *Metallomics, 2*(2), 104-111. doi:10.1039/b916722f

Bellefroid, M. (2018). *Understanding mesothelioma chemoresistance and implication of ADAM in this process*

Below, J. E., Cox, N. J., Fukagawa, N. K., Hirvonen, A., & Testa, J. R. (2011). Factors that impact susceptibility to fiber-induced health effects. *Journal of Toxicology and Environmental Health, Part B: Critical Reviews, 14*(1-4), 246-266. doi:10.1080/10937404.2011.556052

Benton, D. M. (2013). Identification of asbestos using laser-induced breakdown spectroscopy: A viable alternative to the conventional approach? *ISRN Spectroscopy, 2013*, 1-6. doi:10.1155/2013/362694

Berardi, R., Caramanti, M., Fiordoliva, I., Morgese, F., Savini, A., Rinaldi, S., & Cascinu, S. (2015). Hyponatraemia is a predictor of clinical outcome for malignant pleural mesothelioma. *Supportive Care in Cancer, 23*(3), 621-626. doi:10.1007/s00520-014-2398-6

Berardi, R., Fiordoliva, I., De Lisa, M., Ballatore, Z., Caramanti, M., Morgese, F., & Cascinu, S. (2016). Clinical and pathologic predictors of clinical outcome of malignant pleural mesothelioma. *Tumori, 102*(2), 190-195. doi:10.5301/tj.5000418

Berardi, R., Torniai, M., Lenci, E., Pecci, F., Morgese, F., & Rinaldi, S. (2019). Electrolyte disorders in cancer patients: A systematic review. *Journal of Cancer Metastasis and Treatment, 2019*(12), 1-33. doi:10.20517/2394-4722.2019.008

Bernard, E., Lothenbach, B., Cau-Dit-Coumes, C., Pochard, I., & Rentsch, D. (2020). Aluminum incorporation into magnesium silicate hydrate (M-S-H). *Cement and Concrete Research, 128*, 105931. doi:10.1016/j.cemconres.2019.105931

Berzenji, L., Van Schil, P. E., & Carp, L. (2018). The eighth TNM classification for malignant pleural mesothelioma. *Translational Lung Cancer Research, 7*(5), 543-549. doi:10.21037/tlcr.2018.07.05

Beyer, H. L., Geschwindt, R. D., Sardesai, N. Y., Glover, C. L., Tran, L., Hellstorm, I., & Pass, H. I. (2007). MESOMARK™: A potential test for malignant pleural mesothelioma. *Clinical Chemistry (Baltimore, Md.), 53*(4), 666-672. doi:10.1373/clinchem.2006.079327

Bibby, A. C., Tsim, S., Kanellakis, N., Ball, H., Talbot, D. C., Blyth, K. G., & Psallidas, I. (2016). Malignant pleural mesothelioma: An update on investigation, diagnosis and treatment. *European Respiratory Review, 25*(142), 472-486. doi:10.1183/16000617.0063-2016

Bielefeldt-Ohmann, H., Fitzpatrick, D. R., Marzo, A. L., Jarnicki, A. G., Himbeck, R. P., Davis, M. R., & Robinson, B. W. S. (1994). Patho- and immunobiology of

malignant mesothelioma: Characterisation of tumour infiltrating leucocytes and cytokine production in a murine model. *Cancer Immunology and Immunotherapy, 39*(6), 347-359. doi:10.1007/BF01534421

Biomax.us. Retrieved from https://www.biomax.us/index.php?route=product/zoomify&park=59534

Blanquart, C., Jaurand, M., & Jean, D. (2020). The biology of malignant mesothelioma and the relevance of preclinical models. *Frontiers in Oncology, 10*, 388. doi:10.3389/fonc.2020.00388

Bloise, A., Ricchiuti, C., Punturo, R., & Pereira, D. (2020). Potentially toxic elements (PTEs) associated with asbestos chrysotile, tremolite and actinolite in the calabria region (italy). *Chemical Geology, 558*, 119896. doi:10.1016/j.chemgeo.2020.119896

Blum, Y., Meiller, C., Quetel, L., Elarouci, N., Ayadi, M., Tashtanbaeva, D., & Jean, D. (2019). Dissecting heterogeneity in malignant pleural mesothelioma through histo-molecular gradients for clinical applications. *Nature Communications, 10*(1), 1333. doi:10.1038/s41467-019-09307-6

Blyth, K. G., & Murphy, D. J. (2018). Progress and challenges in mesothelioma: From bench to bedside. *Respiratory Medicine, 134*, 31-41. doi:10.1016/j.rmed.2017.11.015

Bondanese, V. P., Lamboux, A., Simon, M., Lafont, J. E., Albalat, E., Pichat, S., & Albarède, F. (2016). Hypoxia induces copper stable isotope fractionation in hepatocellular carcinoma, in a HIF-independent manner. *Metallomics, 8*(11), 1177-1184. doi:10.1039/C6MT00102E

Bonde, A., Tischler, V., Kumar, S., Soltermann, A., & Schwendener, R. A. (2012). Intratumoral macrophages contribute to epithelial-mesenchymal transition in solid tumors. *BMC Cancer, 12*(1), 35. doi:10.1186/1471-2407-12-35

Bononi, A., Napolitano, A., Pass, H. I., Yang, H., & Carbone, M. (2015). Latest developments in our understanding of the pathogenesis of mesothelioma and the

design of targeted therapies. *Expert Review of Respiratory Medicine, 9*(5), 633-654. doi:10.1586/17476348.2015.1081066

Bonta, M., Lohninger, H., Laszlo, V., Hegedus, B., & Limbeck, A. (2014). Quantitative LA-ICP-MS imaging of platinum in chemotherapy treated human malignant pleural mesothelioma samples using printed patterns as standard. *Journal of Analytical Atomic Spectrometry, 29*(11), 2159-2167. doi:10.1039/c4ja00245h

Bonta, M., Török, S., Hegedus, B., Döme, B., & Limbeck, A. (2016). A comparison of sample preparation strategies for biological tissues and subsequent trace element analysis using LA-ICP-MS. *Analytical and Bioanalytical Chemistry, 409*(7), 1805-1814. doi:10.1007/s00216-016-0124-6

Both, K., Turner, D. R., & Henderson, D. W. (1995). Loss of heterozygosity in asbestos-induced mutations in a human mesothelioma cell line. *Environmental and Molecular Mutagenesis, 26*(1), 67-71. doi:10.1002/em.2850260110

Boulanger, G., Andujar, P., Pairon, J., Billon-Galland, M., Dion, C., Dumortier, P., & Jaurand, M. (2014). Quantification of short and long asbestos fibers to assess asbestos exposure: A review of fiber size toxicity. *Environmental Health, 13*(1), 59. doi:10.1186/1476-069X-13-59

Boylan, A. M., Sanan, D. A., Sheppard, D., & Broaddus, V. C. (1995). Vitronectin enhances internalization of crocidolite asbestos by rabbit pleural mesothelial cells via the integrin alpha v beta 5. *The Journal of Clinical Investigation, 96*(4), 1987-2001. doi:10.1172/JCI118246

Bradshaw, R., Bleay, S., Clench, M. R., & Francese, S. (2013). Direct detection of blood in fingermarks by MALDI MS profiling and imaging. *Science & Justice, 54*(2), 110-117. doi:10.1016/j.scijus.2013.12.004

Bradshaw, R., Denison, N., & Francese, S. (2017). Implementation of MALDI MS profiling and imaging methods for the analysis of real crime scene fingermarks. *Analyst (London), 142*(9), 1581-159. doi:10.1039/c7an00218a

Bradshaw, R., Rao, W., Wolstenholme, R., Clench, M. R., Bleay, S., & Francese, S. (2012). Separation of overlapping fingermarks by matrix assisted laser desorption ionisation mass spectrometry imaging. *Forensic Science International, 222*(1), 318-326. doi:10.1016/j.forsciint.2012.07.009

British lung foundation. Retrieved from https://statistics.blf.org.uk/mesothelioma

British Thoracic Society Standards of Care Committee. (2007). BTS statement on malignant mesothelioma in the UK, 2007. *Thorax, 62*(Suppl 2), ii1-ii19. doi:10.1136/thx.2007.087619

Broaddus, C. V., Follo, C., & Barbone, D. (2017). 3D models of mesothelioma in the study of mechanisms of cell survival. Asbestos and mesothelioma (pp. 237-257). *Cham: Springer International Publishing*. doi:10.1007/978-3-319-53560-9_11

Broaddus, V. C., Yang, L., Scavo, L. M., Ernst, J. D., & Boylan, A. M. (1996). Asbestos induces apoptosis of human and rabbit pleural mesothelial cells via reactive oxygen species. *The Journal of Clinical Investigation, 98*(9), 2050-2059. doi:10.1172/JCI119010

Brooks, A. S., Rozenwald, M. N., Geohring, L. D., Lion, L. W., & Steenhuis, T. S. (2000). Phosphorus removal by wollastonite: A constructed wetland substrate. *Ecological Engineering, 15*(1-2), 121-132. doi:10.1016/s0925-8574(99)00056-7

Brown, R. A. M., Richardson, K. L., Kabir, T. D., Trinder, D., Ganss, R., & Leedman, P. J. (2020). Altered iron metabolism and impact in cancer biology, metastasis, and immunology. *Frontiers in Oncology, 10*, 476. doi:10.3389/fonc.2020.00476

Burger, M., Gundlach-Graham, A., Allner, S., Schwarz, G., Wang, H. A. O., Gyr, L., & Günther, D. (2015). High-speed, high-resolution, multielemental LA-ICP-TOFMS imaging: Part II. Critical evaluation of quantitative three-dimensional imaging of major, minor, and trace elements in geological samples. *Analytical*

Chemistry (Washington), 87(16), 8259-8267. doi: 10.1021/acs.analchem.5b01977

Califf, R. M. (2018). Biomarker definitions and their applications. *Experimental Biology and Medicine (Maywood, N.J.), 243*(3), 213-221. doi:10.1177/1535370217750088

Callahan, D. L., Hare, D. J., Bishop, D. P., Doble, P. A., & Roessner, U. (2016). Elemental imaging of leaves from the metal hyperaccumulating plant noccaea caerulescens shows different spatial distribution of Ni, Zn and Cd. *RSC Advances, 6*(3), 2337-2344. doi:10.1039/C5RA23953B

Callejón-Leblic, B., Arias-Borrego, A., Pereira-Vega, A., Gómez-Ariza, J. L., & García-Barrera, T. (2019). The metallome of lung cancer and its potential use as biomarker. *International Journal of Molecular Sciences, 20*(3), 778. doi:10.3390/ijms20030778

Cancer research UK. Retrieved from https://www.cancerresearchuk.org/health-professional/cancer-statistics/statistics-by-cancer-type/mesothelioma/mortality

Cancer tomorrow. Retrieved from http://gco.iarc.fr/tomorrow/home

Capella, S., Bellis, D., & Belluso, E. (2016). *Diagnosis of asbestos-related diseases: The mineralogist and pathologist's role in medico-legal field* doi:10.1097/PAF.0000000000000206

Carbone, M., Adusumilli, P. S., Alexander, H. R., Baas, P., Bardelli, F., Bononi, A., & Pass, H. I. (2019). Mesothelioma: Scientific clues for prevention, diagnosis, and therapy. *CA: A Cancer Journal for Clinicians, 69*(5), 402-429. doi:10.3322/caac.21572

Carbone, M., & Yang, H. (2012). Molecular pathways: Targeting mechanisms of asbestos and erionite carcinogenesis in mesothelioma. *Clinical Cancer Research: An Official Journal of the American Association for Cancer Research, 18*(3), 598-604. doi:10.1158/1078-0432.CCR-11-2259

Cardile, V., Lombardo L., Belluso, E., Panico, A., Capella, S., & Balazy, M., (2007). Toxicity and carcinogenicity mechanisms of fibrous antigorite. *International Journal of Environmental Research and Public Health, 4*(1), 1-9. doi:10.3390/ijerph2007010001

Casalone, E., Allione, A., Viberti, C., Pardini, B., Guarrera, S., Betti, M., & Matullo, G. (2018). DNA methylation profiling of asbestos-treated MeT5A cell line reveals novel pathways implicated in asbestos response. *Archives of Toxicology, 92*(5), 1785-1795. doi:10.1007/s00204-018-2179-y

Casarsa, C., Bassani, N., Ambrogi, F., Zabucchi, G., Boracchi, P., Biganzoli, E., & Coradini, D. (2011). Epithelial-to-mesenchymal transition, cell polarity and stemness-associated features in malignant pleural mesothelioma. *Cancer Letters, 302*(2), 136-143. doi:10.1016/j.canlet.2011.01.009

Chen, L., Zeng, Y., & Zhou, S. (2018). Role of apoptosis in cancer resistance to chemotherapy *IntechOpen.*

Chen, Z., Gaudino, G., Pass, H. I., Carbone, M., & Yang, H. (2017). Diagnostic and prognostic biomarkers for malignant mesothelioma: An update. *Translational Lung Cancer Research, 6*(3), 259-269. doi:10.21037/tlcr.2017.05.06

Chernova, T., Murphy, F. A., Galavotti, S., Sun, X., Powley, I. R., Grosso, S., & MacFarlane, M. (2017). Long-fiber carbon nanotubes replicate asbestos-induced mesothelioma with disruption of the tumor suppressor gene Cdkn2a (Ink4a/arf). *Current Biology, 27*(21), 3302-3314.e6. doi:10.1016/j.cub.2017.09.007

Cheung, M., & Testa, J. R. (2017). BAP1, a tumor suppressor gene driving malignant mesothelioma. *Translational Lung Cancer Research, 6*(3), 270-278. doi:10.21037/tlcr.2017.05.03

Chou, A., Toon, C. W., Clarkson, A., Sheen, A., Sioson, L., & Gill, A. J. (2018). The epithelioid BAP1-negative and p16-positive phenotype predicts prolonged

survival in pleural mesothelioma. *Histopathology, 72*(3), 509-515. doi:10.1111/his.13392

Chu, G. J., van Zandwijk, N., & Rasko, J. E. J. (2019). The immune microenvironment in mesothelioma: Mechanisms of resistance to immunotherapy. *Frontiers in Oncology, 9*, 1366. doi:10.3389/fonc.2019.01366

Creativeproteomics.com retrieved from https://www.creative-proteomics.com/blog/wp-content/uploads/2017/11/Quadrupole.png

Cramer, G., Shin, M., Hagan, S., Katz, S. I., Simone, C. B., Busch, T. M., & Cengel, K. A. (2019). Modeling epidermal growth factor inhibitor-mediated enhancement of photodynamic therapy efficacy using 3D mesothelioma cell culture. *Photochemistry and Photobiology, 95*(1), 397-405. doi:10.1111/php.13067

Creaney, J., & Robinson, B. W. S. (2017). Malignant mesothelioma biomarkers: From discovery to use in clinical practice for diagnosis, monitoring, screening, and treatment. *Chest, 152*(1), 143-149. doi:10.1016/j.chest.2016.12.004

Creaney, J., Segal, A., Olsen, N., Dick, I. M., Musk, A. W., Skates, S. J., & Robinson, B. W. (2014). Pleural fluid mesothelin as an adjunct to the diagnosis of pleural malignant mesothelioma. *Disease Markers, 2014*, 413946-10. doi:10.1155/2014/413946

Cruz-Alonso, M., Fernandez, B., Navarro, A., Junceda, S., Astudillo, A., & Pereiro, R. (2019). Laser ablation ICP-MS for simultaneous quantitative imaging of iron and ferroportin in hippocampus of human brain tissues with alzheimer's disease. *Talanta (Oxford), 197*, 413-421. doi:10.1016/j.talanta.2019.01.056

Deer, W. A., Howie, R. A., & Zussman, J. (2013). An introduction to the rock-forming minerals (3. ed. ed.). *London: Minerological Society.*

Delsite, R., Reva, B., Shimizu, S., Wang, L., Creaney, J., Lake, R. A., & Zhou, Q. (2011). The nuclear deubiquitinase BAP1 is commonly inactivated by somatic

mutations and 3p21.1 losses in malignant pleural mesothelioma. *Nature Genetics, 43*(7), 668-672. doi:10.1038/ng.855

Dement, J. M., Kuempel, E. D., Zumwalde, R. D., Ristich, A. M., Fernback, J. E., & Smith, R. J. (2015). Airborne fiber size characterization in exposure estimation: Evaluation of a modified transmission electron microcopy protocol for asbestos and potential use for carbon nanotubes and nanofibers. *American Journal of Industrial Medicine, 58*(5), 494-508. doi:10.1002/ajim.22422

Dillon, B. J., Prieto, V. G., Curley, S. A., Ensor, C. M., Holtsberg, F. W., Bomalaski, J. S., & Clark, M. A. (2004). Incidence and distribution of argininosuccinate synthetase deficiency in human cancers. *Cancer, 100*(4), 826-833. doi:10.1002/cncr.20057

Direito, I., Monteiro, L., Melo, T., Figueira, D., Lobo, J., Enes, V., & Helguero, L. A. (2021). Protein aggregation patterns inform about breast cancer response to antiestrogens and reveal the RNA ligase RTCB as mediator of acquired tamoxifen resistance. *Cancers, 13*(13), 3195. doi:10.3390/cancers13133195

Diwakar, P. K., Gonzalez, J. J., Harilal, S. S., Russo, R. E., & Hassanein, A. (2014). Ultrafast laser ablation ICP-MS: Role of spot size, laser fluence, and repetition rate in signal intensity and elemental fractionation. *Journal of Analytical Atomic Spectrometry, 29*(2), 339-346. doi:10.1039/c3ja50315a

Doble, P. A., de Vega, R. G., Bishop, D. P., Hare, D. J., & Clases, D. (2021). Laser Ablation–Inductively coupled Plasma–Mass spectrometry imaging in biology. *Chemical Reviews,* doi:10.1021/acs.chemrev.0c01219

Donaldson, K., Murphy, F. A., Duffin, R., & Poland, C. A. (2010). Asbestos, carbon nanotubes and the pleural mesothelium: A review and the hypothesis regarding the role of long fibre retention in the parietal pleura, inflammation and mesothelioma. *Particle and Fibre Toxicology, 7*(1), 5. doi:10.1186/1743-8977-7-5

Dostert, C., Petrilli, V., Van Bruggen, R., Steele, C., Mossman, B. T., & Tschopp, J. (2008). Innate immune activation through Nalp3 inflammasome sensing of asbestos and silica. *Science, 320*(5876), 674-677. doi:10.1126/science.1156995

Douglas, D. N., Managh, A. J., Reid, H. J., & Sharp, B. L. (2015). High-speed, integrated ablation cell and dual concentric injector plasma torch for laser ablation-inductively coupled plasma mass spectrometry. *Analytical Chemistry, (Washington), 87*(22), 11285-11294. doi:10.1021/acs.analchem.5b02466

Egilman, D., Steffen, J. E., Tran, T., Clancy, R., Rigler, M., & Longo, M. (2019). Health effects of censored elongated mineral particles: A critical review, *Detection Limits in Air Quality and Environmental Measurements, Ed. M. Brisson (West Conshohocken, PA: ASTM International, 2019)*, 192-239.

Eichhorn, S. J., Textile Institute (Manchester, Jaffe, M., & Kikutani, T. (2009). Handbook of textile fibre structure: Natural, regenerated, inorganic and specialist fibres. *Cambridge: Elsevier Science & Technology.* Retrieved from https://ebookcentral.proquest.com/lib/[SITE_ID]/detail.action?docID=1639846

Eil, R., Vodnala, S. K., Clever, D., Klebanoff, C. A., Sukumar, M., Pan, J. H., & Restifo, N. P. (2016). Ionic immune suppression within the tumour microenvironment limits T cell effector function. *Nature (London), 537*(7621), 539-543. doi:10.1038/nature19364

Elmarimi, A., Kendall, A., Ellis, P., & Shee, C. D. (2004). Mesothelioma and a high potassium. *Journal of the Royal Society of Medicine, 97*(8), 390. doi:10.1258/jrsm.97.8.390

Elmore, S. (2007). *Apoptosis: A review of programmed cell death*. Thousand Oaks, CA: SAGE Publications. doi:10.1080/01926230701320337

Farrell, J., Kelly, C., Rauch, J., Kida, K., García-Muñoz, A., Monsefi, N., & Kriegsheim, A. V. (2016). *HGF induces epithelial-to-mesenchymal transition by modulating the mammalian hippo/MST2 and ISG15 pathways* Figshare.

Fazzini, A., D'Antongiovanni, V., Giusti, L., Da Valle, Y., Ciregia, F., Piano, I., & Mazzoni, M. R. (2014). Altered protease-activated receptor-1 expression and signaling in a malignant pleural mesothelioma cell line, NCI-H28, with homozygous deletion of the β-catenin gene. *PloS One, 9*(11), e111550. doi:10.1371/journal.pone.0111550

Feder, I. S., Tischoff, I., Theile, A., Schmitz, I., Merget, R., & Tannapfel, A. (2017). The asbestos fibre burden in human lungs: New insights into the chrysotile debate. *The European Respiratory Journal, 49*(6), 1602534. doi:10.1183/13993003.02534-2016

Feng, S. H., & Yang, S. (2019). The new 8th TNM staging system of lung cancer and its potential imaging interpretation pitfalls and limitations with CT image demonstrations. *Diagnostic and Interventional Radiology (Ankara, Turkey), 25*(4), 270-279. doi:10.5152/dir.2019.18458

Ferlay, J., Soerjomataram, I., Ervik, M., Dikshit, R., Eser, S., Mathers, C., & Bray, F. (2012). GLOBOCAN 2012: Estimated cancer incidence, mortality and prevalence worldwide in 2012 v1.0. Retrieved from https://publications.iarc.fr/Databases/Iarc-Cancerbases/GLOBOCAN-2012-Estimated-Cancer-Incidence-Mortality-And-Prevalence-Worldwide-In-2012-V1.0-2012

Fink, S. L., & Cookson, B. T. (2005). Apoptosis, pyroptosis, and necrosis: Mechanistic description of dead and dying eukaryotic cells. *Infection and Immunity, 73*(4), 1907-1916. doi:10.1128/IAI.73.4.1907-1916.2005

Fischer, A. H., Jacobson, K. A., Rose, J., & Zeller, R. (2008). Hematoxylin and eosin staining of tissue and cell sections. *Cold Spring Harbor Protocols, 2008*(6), pdb.prot4986. doi:10.1101/pdb.prot4986

Flint, L. E., Hamm, G., Ready, J. D., Ling, S., Duckett, C. J., Cross, N. A., & Clench, M. R. (2020). Characterization of an aggregated three-dimensional cell culture model by multimodal mass spectrometry imaging. *Analytical Chemistry (Washington), 92*(18), 12538-12547. doi:10.1021/acs.analchem.0c02389

Follo, C., Barbone, D., Richards, W. G., Bueno, R., & Broaddus, V. C. (2016). Autophagy initiation correlates with the autophagic flux in 3D models of mesothelioma and with patient outcome. *Autophagy, 12*(7), 1180-1194. doi:10.1080/15548627.2016.1173799

Frontini, F., Bononi, I., Torreggiani, E., Di Mauro, G., Mazzoni, E., Stendardo, M., & Tognon, M. (2021). Circulating microRNA-197-3p as a potential biomarker for asbestos exposure. *Scientific Reports, 11*(1), 23955. doi:10.1038/s41598-021-03189-9

Fujiwara, H., Kamimori, T., Morinaga, K., Takeda, Y., Kohyama, N., Miki, Y., & Yamamoto, S. (2005). An autopsy case of primary pericardial mesothelioma in arc cutter exposed to asbestos through talc pencils. *Industrial Health, 43*(2), 346-350. doi:10.2486/indhealth.43.346

Galateau-Salle, F., Churg, A., Roggli, V., & Travis, W. D. (2016). The 2015 world health organization classification of tumors of the pleura: Advances since the 2004 classification. *Journal of Thoracic Oncology, 11*(2), 142-154. doi:10.1016/j.jtho.2015.11.005

Gao, Y., Dai, Z., Yang, C., Wang, D., Guo, Z., Mao, W., & Chen, Z. (2022). Metabolomics of a cell line-derived xenograft model reveals circulating metabolic signatures for malignant mesothelioma. *PeerJ (San Francisco, CA), 10*, e12568. doi:10.7717/peerj.12568

Germine, M., & Puffer, J. H. (2020). Analytical transmission electron microscopy of amosite asbestos from South Africa. *Archives of Environmental & Occupational Health, 75*(1), 36-44. doi:10.1080/19338244.2018.1556201

Ghio, A., Churg, A., & Roggli, V. (2004). Ferruginous bodies: Implications in the mechanism of fiber and particle toxicity. *Toxicologic Pathology, 32*(6), 643-649. doi:10.1080/01926230490885733

Ginzberg, M. B., Kafri, R., & Kirschner, M. (2015). On being the right (cell) size. *Science, 348*(6236), 1245075. doi:10.1126/science.1245075

Gopal, N. O., Narasimhulu, K. V., & Rao, J. L. (2004). EPR, optical, infrared and raman spectral studies of actinolite mineral. *Spectrochimica Acta Part A: Molecular and Biomolecular Spectroscopy, 60*(11), 2441-2448. doi:10.1016/j.saa.2003.12.021

Goričar, K., Holcar, M., Mavec, N., Kovač, V., Lenassi, M., & Dolžan, V. (2021). Extracellular vesicle enriched miR-625-3p is associated with survival of malignant mesothelioma patients. *Journal of Personalized Medicine, 11*(10), 1014. doi:10.3390/jpm11101014

Goricar, K., Kovac, V., Dodic-Fikfak, M., Dolzan, V., & Franko, A. (2020). Evaluation of soluble mesothelin-related peptides and MSLN genetic variability in asbestos-related diseases. *Radiology and Oncology, 54*(1), 86-95. doi:10.2478/raon-2020-0011

Graham, T. A., & Sottoriva, A. (2017). Measuring cancer evolution from the genome. *The Journal of Pathology, 241*(2), 183-191. doi:10.1002/path.4821

Gray, A. L. (1985). Solid sample introduction by laser ablation for inductively coupled plasma source mass spectrometry. *Analyst, 11*(5), 551-556. doi:10.1039/AN9851000551

Greenhalgh, C. J., Karekla, E., Miles, G. J., Powley, I. R., Costa, C., de Jesus, J., & Managh, A. J. (2020). Exploration of matrix effects in laser ablation inductively coupled plasma mass spectrometry imaging of cisplatin-treated tumors. *Analytical Chemistry (Washington), 92*(14), 9847-9855. doi:10.1021/acs.analchem.0c01347

Greenhalgh, C. J., Voloaca, O. M., Shaw, P., Donard, A., Cole, L. M., Clench, M. R., & Haywood-Small, S. L. (2020). Needles in haystacks: Using fast-response LA chambers and ICP-TOF-MS to identify asbestos fibres in malignant mesothelioma models. *Journal of Analytical Atomic Spectrometry,* doi:10.1039/D0JA00268B

Grigoriu, B., Scheperrel, A., Devos, P., Chahine, B., Letourneux, M., Lebaily, P., & Lassale, P. (2007). Utility of osteopontin and serum mesothelin in malignant pleural mesothelioma diagnosis and prognosis assessment. *Clinical Cancer Research, 13*(10), 2928-2935. doi:10.1158/1078-0432.CCR-06-2144

Grillo, A., Salvi, L., Coruzzi, P., Salvi, P., & Parati, G. (2019). Sodium intake and hypertension. *Nutrients, 11*(9), 1970. doi:10.3390/nu11091970

Gualtieri, A. F., Bursi Gandolfi, N., Pollastri, S., Burghammer, M., Tibaldi, E., Belpoggi, F., & Dražić, G. (2017). New insights into the toxicity of mineral fibres: A combined in situ synchrotron μ-XRD and HR-TEM study of chrysotile, crocidolite, and erionite fibres found in the tissues of sprague-dawley rats. *Toxicology Letters, 274*, 20-30. doi:10.1016/j.toxlet.2017.04.004

Guo, Z., Shen, L., Li, N., Wu, X., Wang, C., Gu, Z., & Han, Y. (2021). Aurora kinase A as a diagnostic and prognostic marker of malignant mesothelioma. *Frontiers in Oncology, 11*, 789244. doi:10.3389/fonc.2021.789244

Gylseth, B., Churg, A., Davis, J. M., Johnson, N., Morgan, A., Mowe, & G., Roggli, V. (1985). Analysis of asbestos fibers and asbestos bodies in tissue samples from human lung an international interlaboratory trial. *Scandinavian Journal of Work, Environment & Health, 11*(2), 107-110. doi:10.5271/sjweh.2246

Hamada, T., Torikai, M., Kuwazuru, A., Tanaka, M., Horai, N., Fukuda, T., & Abeyama, K. (2008). Extracellular high mobility group box chromosomal protein 1 is a coupling factor for hypoxia and inflammation in arthritis. *Arthritis and Rheumatism, 58*(9), 2675-2685. doi:10.1002/art.23729

Hamid, R., Rotshteyn, Y., Rabadi, L., Parikh, R., & Bullock, P. (2004). Comparison of alamar blue and MTT assays for high through-put screening. *Toxicology in Vitro, 18*(5), 703-710. doi:10.1016/j.tiv.2004.03.012

Hanahan, D., & Weinberg, R. A. (2000). The hallmarks of cancer. *Cell, 100*(1), 57-70. doi:10.1016/s0092-8674(00)81683-9

Hanahan, D. (2022). Hallmarks of cancer: New dimensions. *Cancer Discovery, 12*(1), 31-46. doi:10.1158/2159-8290.CD-21-1059

Hanahan, D., & Weinberg, R. A. (2000). *The hallmarks of cancer* Elsevier Inc. doi:10.1016/S0092-8674(00)81683-9

Hanahan, D., & Weinberg, R. (2011). Hallmarks of cancer: The next generation. *Cell, 144*(5), 646-674. doi:10.1016/j.cell.2011.02.013

Hare, D. J., New, E. J., de Jonge, M. D., & McColl, G. (2015). Imaging metals in biology: Balancing sensitivity, selectivity and spatial resolution. *Chemical Society Reviews, 44*(17), 5941-5958. doi:10.1039/c5cs00055f

Hasegawa, S., Koshikawa, M., Takahashi, I., Hachiya, M., Furukawa, T., Akashi, M., & Saga, T. (2008). Alterations in manganese, copper, and zinc contents, and intracellular status of the metal-containing superoxide dismutase in human mesothelioma cells. *Journal of Trace Elements in Medicine and Biology, 22*(3), 248-255. doi:10.1016/j.jtemb.2008.05.001

Hassan, R., Morrow, B., Thomas, A., Walsh, T., Lee, M. K., Gulsuner, S., & Churpek, J. E. (2019). Inherited predisposition to malignant mesothelioma and overall survival following platinum chemotherapy. *Proceedings of the National Academy of Sciences - PNAS, 116*(18), 9008-9013. doi:10.1073/pnas.1821510116

He, J., Xu, S., Pan, H., Li, S., & He, J. (2020). Does size matter? —a population-based analysis of malignant pleural mesothelioma. *Translational Lung Cancer Research, 9*(4), 1041-1052. doi:10.21037/tlcr-19-488

Henderson, D., Rantanen, J., Barnhart, S., Dement, J., DeVuyst, P., Hillerdal, G., & Woitowitz, H. (1997). Asbestos, asbestosis, and cancer: The helsinki criteria for diagnosis and attribution. *Scandinavian Journal of Work, Environment & Health, 23*(4), 311-316.

Henson, K. E., Brock, R., Charnock, J., Wickramasinghe, B., Will, O., & Pitman, A. (2019). Risk of suicide after cancer diagnosis in england. *JAMA Psychiatry, 76*(1), 51-60. doi:10.1001/jamapsychiatry.2018.3181

Hessen, D. O., Elser, J. J., Sterner, R. W., & Urabe, J. (2013). Ecological stoichiometry. *Limnology and Oceanography, 58*(6), 2219-2236. doi:10.4319/lo.2013.58.6.2219

Hmeljak, J., Sanchez-Vega, F., Hoadley, K. A., Shih, J., Stewart, C., Heiman, D., & Ladanyi, M. (2018). Integrative molecular characterization of malignant pleural mesothelioma. *Cancer Discovery, 8*(12), 1548-1565. doi:10.1158/2159-8290.CD-18-0804

Hodgson, J. T., McElvenny, D. M., Darnton, A. J., Price, M. J., & Peto, J. (2005). The expected burden of mesothelioma mortality in great britain from 2002 to 2050. *British Journal of Cancer, 92*(3), 587-593. doi:10.1038/sj.bjc.6602307

Hodgson, J. T., & Darton, A. (2000). The quantitative risks of mesothelioma and lung cancer in relation to asbestos exposure. *The Annals of Occupational Hygiene, 44*(8), 565-601. doi:10.1016/S0003-4878(00)00045-4

Hopkins-Donaldson, S., Belyanskaya, A. L., Simões-Wüst, A. P., Sigrist, B., Kurtz, S., Zangemeister-Wittke, U., & Stahel, R. (2006). p53-induced apoptosis occurs in the absence of p14ARF in malignant pleural mesothelioma. *Neoplasia, 8*(7), 551-559. doi:10.1593/neo.06148

Huang, J., Hisanaga, N., Sakai, K., Iwata, M., Ono, Y., Shibata, E., & Takeuchi, Y. (1988). Asbestos fibers in human pulmonary and extrapulmonary tissues. *American Journal of Industrial Medicine, 14*(3), 331-339. doi:10.1002/ajim.4700140310

Huang, S. X. L., Jaurand, M., Kamp, D. W., Whysner, J., & Hei, T. K. (2011). Role of mutagenicity in asbestos fiber-induced carcinogenicity and other diseases. *Journal of Toxicology and Environmental Health. Part B, Critical Reviews, 14*(1-4), 179-245. doi:10.1080/10937404.2011.556051

Huang, X., Zhang, X., Li, E., Zhang, G., Wang, X., Tang, T., & Liang, T. (2020). VISTA: An immune regulatory protein checking tumor and immune cells in cancer immunotherapy. *Journal of Hematology and Oncology, 13*(1), 83. doi:10.1186/s13045-020-00917-y

Huuskonen, M. S., Tossavainen, A., Koskinen, H., Zitting, A., Korhonen, O., Nickels, J., & Vaaranen, V. (1983). Wollastonite exposure and lung fibrosis. *Environmental Research, 30*(2), 291-304. doi:10.1016/0013-9351(83)90215-3

Illei, P. B., Rusch, V. W., Zakowski, M. F., & Ladanyi, M. (2003). Homozygous deletion of CDKN2A and codeletion of the methylthioadenosine phosphorylase gene in the majority of pleural mesotheliomas. *Clinical Cancer Research, 9*(6), 2108-2113.

Ishida, T., Alexandrov, M., Nishimura, T., Minakawa, K., Hirota, R., Sekiguchi, K., & Kuroda, A. (2010). Selective detection of airborne asbestos fibers using protein-based fluorescent probes. *Environmental Science & Technology, 44*(2), 755-759. doi:10.1021/es902395h

Ishida, T., Fujihara, N., Nishimura, T., Funabashi, H., Hirota, R., Ikeda, T., & Kuroda, A. (2019). Live-cell imaging of macrophage phagocytosis of asbestos fibers under fluorescence microscopy. *Genes and Environment, 41*(1), 14. doi:10.1186/s41021-019-0129-4

Ivanov, S. V., Miller, J., Lucito, R., Tang, C., Ivanova, A. V., Pei, J., & Pass, H. I. (2009). Genomic events associated with progression of pleural malignant mesothelioma. *International Journal of Cancer, 124*(3), 589-599. doi:10.1002/ijc.23949

Jahnen-Dechent, W., & Ketteler, M. (2012). Magnesium basics. *Clinical Kidney Journal, 5*(Suppl 1), i3-i14. doi:10.1093/ndtplus/sfr163

Jasani, B., & Gibbs, A. (2012). Mesothelioma not associated with asbestos exposure. *Archives of Pathology & Laboratory Medicine, 136*(3), 262-267. doi:10.5858/arpa.2011-0039-RA

Jiang, Z., Shen, W., Ying, S., Gao, Z., He, X., Chen, R., & Lou, J. (2020). Overexpression of fibulin-3 in tumor tissue predicts poor survival of malignant mesothelioma patients from hand-spinning asbestos exposed area in eastern china. *Scientific Reports, 10*(1), 20373. doi:10.1038/s41598-020-77412-4

Jimenez, L. A., Zanella, C., Fung, H., Janssen, Y. M., Vacek, P., Charland, C., & Mossman, B. T. (1997). Role of extracellular signal-regulated protein kinases in apoptosis by asbestos and H2O2. *American Journal of Physiology - Lung Cellular and Molecular Physiology, 273*(5), 1029-1035. doi:10.1152/ajplung.1997.273.5.L1029

Jonkman, J. (2020). Rigor and reproducibility in confocal fluorescence microscopy. *Cytometry. Part A, 97*(2), 113-115. doi:10.1002/cyto.a.23924

Jube, S., Rivera, Z. S., Bianchi, M. E., Powers, A., Wang, E., Pagano, I., & Haining, Y. (2012). Cancer cell secretion of the DAMP protein HMGB1 supports progression in malignant mesothelioma. *Cancer Research (Chicago, Ill.), 72*(13), 3290-3301. doi:10.1158/0008-5472.CAN-11-3481

Kadariya, Y., Menges, C. W., Talarchek, J., Cai, K. Q., Klein-Szanto, A. J., Pietrofesa, R. A., & Testa, J. R. (2016). Inflammation-related IL1 /IL1R signaling promotes the development of asbestos-induced malignant mesothelioma. *Cancer Prevention Research, 9*(5), 406-414. doi:10.1158/1940-6207.CAPR-15-0347

Kaeding, A., Tarlock, K., Barwe, S., Gopalakrisnapillai, A., Alonzo, T. A., Gerbing, R. B., & Meshinchi, S. (2017). Mesothelin is a novel disease marker and potential therapeutic target in pediatric acute myeloid leukemia. *Blood, 130*, 2641. doi:10.1182/blood.V130.Suppl_1.2641.2641

Kamp, D. W. (2009). Asbestos-induced lung diseases: An update. *Translational Research, 153*(4), 143-152. doi:10.1016/j.trsl.2009.01.004

Kanellakis, N. I., Asciak, R., Hamid, M. A., Yao, X., McCole, M., McGowan, S., & Psallidas, I. (2020). Patient-derived malignant pleural mesothelioma cell cultures: A tool to advance biomarker-driven treatments. *Thorax, 75*(11), 1004-1008. doi:10.1136/thoraxjnl-2020-215027

Kang, R., Zhang, Q., Zeh, H. J., Lotze, M. T., & Tang, D. (2013). HMGB1 in cancer: Good, bad, or both? *Clinical Cancer Research, 19*(15), 4046-4057. doi:10.1158/1078-0432.CCR-13-0495

Karekla, E., Liao, W., Sharp, B., Pugh, J., Reid, H., Quesne, J. L., & Pringle, J. H. (2017). Ex vivo explant cultures of Non–Small cell lung carcinoma enable evaluation of primary tumor responses to anticancer therapy. *Cancer Research (Chicago, Ill.), 77*(8), 2029-2039. doi:10.1158/0008-5472.can-16-1121

Kehrer, J. P. (2000). The Haber–Weiss reaction and mechanisms of toxicity. *Toxicology (Amsterdam), 149*(1), 43-50. doi:10.1016/S0300-483X(00)00231-6

Kido, T., Morimoto, Y., Yatera, K., Ishimoto, H., Ogoshi, T., Oda, K., & Mukae, H. (2017). The utility of electron microscopy in detecting asbestos fibers and particles in BALF in diffuse lung diseases. *BMC Pulmonary Medicine, 17*(1), 71. doi:10.1186/s12890-017-0415-5

Kim, P., Weiskirchen, S., Uerlings, R., Kueppers, A., Stellmacher, F., Viveiros, A., & Weiskirchen, R. (2018). Quantification of liver iron overload disease with laser ablation inductively coupled plasma mass spectrometry. *BMC Medical Imaging, 18*(1), 51. doi:10.1186/s12880-018-0291-3

Klebe, S., Hocking, A. J., Soeberg, M., & Leigh, J. (2021). The significance of short latency in mesothelioma for attribution of causation: Report of a case with predisposing germline mutations and review of the literature. *International*

Journal of Environmental Research and Public Health, 18(24), 13310. doi:10.3390/ijerph182413310

Kojima, M., Kajino, K., Momose, S., Wali, N., Hlaing, M. T., Han, B., & Hino, O. (2020). Possible reversibility between epithelioid and sarcomatoid types of mesothelioma is independent of ERC/mesothelin expression. *Respiratory Research, 21*(1), 1-187. doi:10.1186/s12931-020-01449-2

Korchevskiy, A., Rasmuson, J. O., & Rasmuson, E. J. (2019). Empirical model of mesothelioma potency factors for different mineral fibers based on their chemical composition and dimensionality. *Inhalation Toxicology, 31*(5), 180-191. doi:10.1080/08958378.2019.1640320

Kupcho, K., Shultz, J., Hurst, R., Hartnett, J., Zhou, W., Machleidt, T., & Niles, A. (2018). A real-time, bioluminescent annexin V assay for the assessment of apoptosis. *Apoptosis (London), 24*(1-2), 184-197. doi:10.1007/s10495-018-1502-7

Kusiorowski, R., Zaremba, T., Gerle, A., Piotrowski, J., Simka, W., & Adamek, J. (2015). Study on the thermal decomposition of crocidolite asbestos. *Journal of Thermal Analysis and Calorimetry, 120*(3), 1585-1595. doi:10.1007/s10973-015-4421-7

Ladanyi, M. (2005). Implications of P16/CDKN2A deletion in pleural mesotheliomas. *Lung Cancer (Amsterdam, Netherlands), 49*, S95-S98. doi:10.1016/j.lungcan.2005.03.017

Larson, D., Powers, A., Ambrosi, J., Tanji, M., Napolitano, A., Flores, E. G., & Yang, H. (2016). Investigating palygorskite's role in the development of mesothelioma in southern nevada: Insights into fiber-induced carcinogenicity. *Journal of Toxicology and Environmental Health, Part B, 19*(5-6), 213. doi:10.1080/10937404.2016.1195321

Larsson, P., Engqvist, H., Biermann, J., Werner Rönnerman, E., Forssell-Aronsson, E., Kovács, A., Parris, T. Z. (2020). Optimization of cell viability assays

to improve replicability and reproducibility of cancer drug sensitivity screens. *Scientific Reports, 10*(1), 5798. doi:10.1038/s41598-020-62848-5

Lazzari, G., Couvreur, P., & Mura, S. (2017). Multicellular tumor spheroids: A relevant 3D model for the in vitro preclinical investigation of polymer nanomedicines. *Polymer Chemistry, 8*(34), 4947-4969. doi:10.1039/c7py00559h

Lei, H., Hofferberth, S. C., Liu, R., Colby, A., Tevis, K. M., Catalano, P., & Colson, Y. L. (2015). Paclitaxel-loaded expansile nanoparticles enhance chemotherapeutic drug delivery in mesothelioma 3-dimensional multicellular spheroids. *The Journal of Thoracic and Cardiovascular Surgery, 149*(5), 1417-1425.e1. doi:10.1016/j.jtcvs.2015.02.020

Leslie, T. K., James, A. D., Zaccagna, F., Grist, J. T., Deen, S., Kennerley, A., & Brackenbury, W. J. (2019). Sodium homeostasis in the tumour microenvironment. *Biochimica Et Biophysica Acta. Reviews on Cancer, 1872*(2), 188304. doi:10.1016/j.bbcan.2019.07.001

Levin, J. L., Rouk, A., Shepherd, S., Hurst, G. A., & McLarty, J. W. (2016). Tyler asbestos workers: A mortality update in a cohort exposed to amosite. *Journal of Toxicology and Environmental Health, Part B, 19*(5-6), 190. doi:10.1080/10937404.2016.1195319

Levresse, V., Renier, A., Fleury-Feith, J., Levy, F., Moritz, S., Vivo, C., & Jaurand, M. (1997). Analysis of cell cycle disruptions in cultures of rat pleural mesothelial cells exposed to asbestos fibers. *American Journal of Respiratory Cell and Molecular Biology, 17*(6), 660-671. doi:10.1165/ajrcmb.17.6.2854

Li, J., Cao, F., Yin, H., Huang, Z., Lin, Z., Mao, N., & Wang, G. (2020). Ferroptosis: Past, present and future. *Cell Death & Disease, 11*(2), 88. doi:10.1038/s41419-020-2298-2

Li, Y. C., Khashab, T., Terhune, J., Eckert, R. L., Hanna, N., Burke, A., & Richard Alexander, H. (2017). Preoperative thrombocytosis predicts shortened survival in patients with malignant peritoneal mesothelioma undergoing operative

cytoreduction and hyperthermic intraperitoneal chemotherapy. *Annals of Surgical Oncology, 24*(8), 2259-2265. doi:10.1245/s10434-017-5834-2

Liang, Y., Biao, H., Uematsu, K., Zhidong, X., Mazieres, J., Lee, A., & Jablons, D. M. (2004). Inhibition of wnt-1 signaling induces apoptosis in β-catenin-deficient mesothelioma cells. *Cancer Research (Chicago, Ill.), 64*(10), 3474-3478. doi:10.1158/0008-5472.CAN-04-0115

Liao, X., Hu, Z., Luo, T., Zhang, W., Liu, Y., Zong, K., & Zhang, J. (2019). Determination of major and trace elements in geological samples by laser ablation solution sampling-inductively coupled plasma mass spectrometry. *Journal of Analytical Atomic Spectrometry, 34*(6), 1126-1134. doi:10.1039/C9JA00027E

Limbeck, A., Galler, P., Bonta, M., Bauer, G., Nischkauer, W., & Vanhaecke, F. (2015). Recent advances in quantitative LA-ICP-MS analysis: Challenges and solutions in the life sciences and environmental chemistry. *Analytical and Bioanalytical Chemistry, 407*(22), 6593-6617. doi:10.1007/s00216-015-8858-0

Little, L. D., Carolan, V. A., Allen, K. E., Cole, L. M., & Haywood-Small, S. L. (2020). Headspace analysis of mesothelioma cell lines differentiates biphasic and epithelioid sub-types. *Journal of Breath Research, 14*(4), 046011. doi:10.1088/1752-7163/abaaff

Liu, B., Xu, N., Man, Y., Shen, H., Avital, I., Stojadinovic, A., & Liao, D. J. (2013). Apoptosis in living animals is assisted by scavenger cells and thus may not mainly go through the cytochrome C-caspase pathway. *Journal of Cancer, 4*(9), 716-723. doi:10.7150/jca.7577

Liu, X., Yang, W., Guan, Z., Yu, W., Fan, B., Xu, N., & Liao, D. J. (2018). There are only four basic modes of cell death, although there are many ad-hoc variants adapted to different situations. *Cell & Bioscience, 8*(1), 6. doi:10.1186/s13578-018-0206-6

Lobinski, R., Moulin, C., & Ortega, R. (2006). Imaging and speciation of trace elements in biological environment. *Biochimie, 88*(11), 1591-1604. doi:10.1016/j.biochi.2006.10.003

Luberto, F., Ferrante, D., Silvestri, S., Angelini, A., Cuccaro, F., Nannavecchia, A. M., & Magnani, C. (2019). Cumulative asbestos exposure and mortality from asbestos related diseases in a pooled analysis of 21 asbestos cement cohorts in italy. *Environmental Health, 18*(1), 71. doi:10.1186/s12940-019-0510-6

Luo, Y., Chihara, Y., Fujimoto, K., Sasahira, T., Kuwada, M., Fujiwara, R., & Kuniyasu, H. (2013). High mobility group box 1 released from necrotic cells enhances regrowth and metastasis of cancer cells that have survived chemotherapy. *European Journal of Cancer (1990), 49*(3), 741-751. doi:10.1016/j.ejca.2012.09.016

Ly, A., Longuespée, R., Casadonte, R., Wandernoth, P., Schwamborn, K., Bollwein, C., & Deininger, S. (2019). Site-to-Site reproducibility and spatial resolution in MALDI–MSI of peptides from Formalin-Fixed Paraffin-Embedded samples. *Proteomics. Clinical Applications, 13*(1), e1800029-n/a. doi:10.1002/prca.201800029

Stanton, M. F., & Wrench, C. (1972). Mechanisms of mesothelioma induction with asbestos and fibrous glass. *Journal of the National Cancer Institute, 48*(3), 797-821. doi:10.1093/jnci/48.3.797

MacDonald, R. S. (2000). The role of zinc in growth and cell proliferation. *Journal of Nutrition*, *130*(5) 1500S-1508S. doi:10.1093/jn/130.5.1500S

Maier, J. A., Castiglioni, S., Locatelli, L., Zocchi, M., & Mazur, A. (2021). Magnesium and inflammation: Advances and perspectives. *Seminars in Cell & Developmental Biology, 115*, 37-44. doi:10.1016/j.semcdb.2020.11.002

Managh, A. J., Douglas, D. N., Makella Cowen, K., Reid, H. J., & Sharp, B. L. (2016). Acquisition of fast transient signals in ICP-MS with enhanced time resolution.*31*(8), 1688-1692. doi:10.1039/c6ja00140h

Managh, A. J., & Reid, P. (2019). A new freeware tool for image processing and its application to high-speed LA-ICP-MS imaging. *Journal of Analytical Atomic Spectrometry, 34*(7), 1369-1373. doi:10.1039/c9ja00082h

Marshall, K., Jackson, S., Jones, J., Holme, J., Lyons, J., Barrett, E., & Evison, M. (2020). Homozygous deletion of CDKN2A in malignant mesothelioma: Diagnostic utility, patient characteristics and survival in a UK mesothelioma centre. *Lung Cancer (Amsterdam, Netherlands), 150*, 195-200. doi:10.1016/j.lungcan.2020.10.020

Mascini, N. E., Teunissen, J., Noorlag, R., Willems, S. M., & Heeren, R. M. A. (2018). Tumor classification with MALDI-MSI data of tissue microarrays: A case study. *Methods (San Diego, Calif.), 151*, 21-27. doi:10.1016/j.ymeth.2018.04.004

Matafora, V., Farris, F., Restuccia, U., Tamburri, S., Martano, G., Bernardelli, C., & Bachi, A. (2020). Amyloid aggregates accumulate in melanoma metastasis modulating YAP activity. *EMBO Reports, 21*(9), e50446-n/a. doi:10.15252/embr.202050446

Matsuzaki, H., Lee, S., Kumagai-Takei, N., Min, Y., Sada, N., Yoshitome, K., Otsuki, & Takemi, M. M. (2018). *Cytotoxicity caused by asbestos fibers and acquisition of resistance by continuous exposure in human T cells* IntechOpen.

Maxim, L. D., & McConnell, E. E. (2005). A review of the toxicology and epidemiology of wollastonite. *Inhalation Toxicology, 17*(9), 451-466. doi:10.1080/08958370591002030

Mazzocchi, A. R., Rajan, S. A. P., Votanopoulos, K. I., Hall, A. R., & Skardal, A. (2018). In vitro patient-derived 3D mesothelioma tumor organoids facilitate patient-centric therapeutic screening. *Scientific Reports, 8*(1), 2886-12. doi:10.1038/s41598-018-21200-8

McCambridge, A. J., Napolitano, A., Mansfield, A. S., Fennell, D. A., Sekido, Y., Nowak, A. K., & Peikert, T. (2018). Progress in the management of malignant Pleural Mesothelioma in 2017. *Journal of Thoracic Oncology: Official Publication*

of the International Association for the Study of Lung Cancer, 13(5), 606-623. doi:10.1016/j.jtho.2018.02.021

McConnell, E. E., Hall, L., & Adkins, B. (1991). Studies on the chronic toxicity (inhalation) of wollastonite in fischer 344 rats. *Inhalation Toxicology, 3*(3), 323-337. doi:10.3109/08958379109145292

McGregor, S., Dunning, R., Hyjek, E., Vigneswaran, W., Husain, A. N., & Krausz, T. (2015). BAP1 facilitates diagnostic objectivity, classification, and prognostication in malignant pleural mesothelioma. *Human Pathology, 46*(11), 1670-1678. doi:10.1016/j.humpath.2015.06.024

Meerang, M., Bérard, K., Friess, M., Bitanihirwe, B. K. Y., Soltermann, A., Vrugt, B., & Opitz, I. (2016). Low merlin expression and high survivin labeling index are indicators for poor prognosis in patients with malignant pleural mesothelioma. *Molecular Oncology, 10*(8), 1255-1265. doi:10.1016/j.molonc.2016.06.005

Melaiu, O., Stebbing, J., Lombardo, Y., Bracci, E., Uehara, N., Bonotti, A., & Landi, S. (2014). MSLN gene silencing has an anti-malignant effect on cell lines overexpressing mesothelin deriving from malignant pleural mesothelioma. *PloS One, 9*(1), e85935. doi:10.1371/journal.pone.0085935

Mesothelioma statistics. Retrieved from https://statistics.blf.org.uk/mesothelioma

Mesothelioma statistics for Great Britain, 2021. Retrieved from http://www.hse.gov.uk/statistics/tables/meso01.xlsx

Mezei, G., Chang, E. T., Mowat, F. S., & Moolgavkar, S. H. (2017). Epidemiology of mesothelioma of the pericardium and tunica vaginalis testis. *Annals of Epidemiology, 27*(5), 348-359.e11. doi:10.1016/j.annepidem.2017.04.001

Miliszkiewicz, N., Walas, S., Tobiasz, A., Kołodziej, M., & Szostek, K. (2017). Calibration for elemental dental tissue analysis by laser ablation inductively coupled plasma mass spectrometry. *Analytical Letters, 50*(8), 1345-1359. doi:10.1080/00032719.2016.1225305

Mirsadraee, M. (2014). Anthracosis of the lungs: Etiology, clinical manifestations and diagnosis: A review. *Tanaffus, 13*(4), 1-13.

Miserocchi, G., Sancini, G., Mantegazza, F., & Chiappino, G. (2008). Translocation pathways for inhaled asbestos fibers. *Environmental Health, 7*(1), 4. doi:10.1186/1476-069X-7-4

Mizuno, T., Murakami, H., Fujii, M., Ishiguro, F., Tanaka, I., Kondo, Y., & Sekido, Y. (2012). YAP induces malignant mesothelioma cell proliferation by upregulating transcription of cell cycle-promoting genes. *Oncogene, 31*(49), 5117-5122. doi:10.1038/onc.2012.5

Molinari, L. Mesothelioma stages. Retrieved from https://www.mesothelioma.com/mesothelioma/stages/

Monsó, E., Tura, J. M., Pujadas, J., Morell, F., Ruiz, J., & Morera, J. (1991). Lung dust content in idiopathic pulmonary fibrosis: A study with scanning electron microscopy and energy dispersive x ray analysis. *British Journal of Industrial Medicine, 48*(5), 327-331. doi:10.1136/oem.48.5.327

Moriyama, G., Tanigawa, M., Sakai, K., Hirata, Y., Kikuchi, S., Saito, Y., & Uematsu, K. (2018). Synergistic effect of targeting dishevelled-3 and the epidermal growth factor receptor-tyrosine kinase inhibitor on mesothelioma cells in vitro. *Oncology Letters, 15*(1), 833-838. doi:10.3892/ol.2017.7382

Muers, M. F., Stephens, R. J., Fisher, P., Darlison, L., Higgs, C. M., Lowry, E., & Parmar, M. K. (2008). Active symptom control with or without chemotherapy in the treatment of patients with malignant pleural mesothelioma (MS01): A multicentre randomised trial. *Lancet, The, 371*(9625), 1685-1694. doi:10.1016/S0140-6736(08)60727-8

Muller, S., Victoria Lai, W., Adusumilli, P. S., Desmeules, P., Frosina, D., Jungbluth, A., & Sauter, J. L. (2020). V-domain ig-containing suppressor of T-cell activation (VISTA), a potentially targetable immune checkpoint molecule, is highly

expressed in epithelioid malignant pleural mesothelioma. *Modern Pathology, 33*(2), 303-311. doi:10.1038/s41379-019-0364-z

Mutch, E., Blundy, J., Tattitch, B., Cooper, F., & Brooker, R. (2016). An experimental study of amphibole stability in low-pressure granitic magmas and a revised al-in-hornblende geobarometer. *Contributions to Mineralogy and Petrology, 171*(10), 1-27. doi:10.1007/s00410-016-1298-9

Mutsaers, S. E., Pixley, F. J., Prêle, C. M., & Hoyne, G. F. (2020). Mesothelial cells regulate immune responses in health and disease: Role for immunotherapy in malignant mesothelioma. *Current Opinion in Immunology, 64*, 88-109. doi:10.1016/j.coi.2020.04.005

Nagai, H., & Toyokuni, S. (2012). Differences and similarities between carbon nanotubes and asbestos fibers during mesothelial carcinogenesis: Shedding light on fiber entry mechanism. *Cancer Science, 103*(8), 1378-1390. doi:10.1111/j.1349-7006.2012.02326.x

Nagle, P. W., Plukker, J. T. M., Muijs, C. T., van Luijk, P., & Coppes, R. P. (2018). Patient-derived tumor organoids for prediction of cancer treatment response. *Seminars in Cancer Biology, 53*, 258-264. doi:10.1016/j.semcancer.2018.06.005

Nagy, I. Z., Lustyik, G., Nagy, V. Z., Zarándi, B., & Bertoni-Freddari, C. (1981). Intracellular Na+:K+ ratios in human cancer cells as revealed by energy dispersive x-ray microanalysis. *The Journal of Cell Biology, 90*(3), 769-777.

Nagy, J. D. (2007). Hypertumors in cancer can be caused by tumor phosphorus demand. *Proceedings in Applied Mathematics and Mechanics, 7*(1), 1121703-1121704. doi:10.1002/pamm.200700761

Napolitano, A., Antoine, D. J., Pellegrini, L., Baumann, F., Pagano, I., Pastorino, S., & Yang, H. (2016). HMGB1 and its hyperacetylated isoform are sensitive and specific serum biomarkers to detect asbestos exposure and to identify

mesothelioma patients. *Clinical Cancer Research, 22*(12), 3087-3096. doi:10.1158/1078-0432.CCR-15-1130

Nastase, A., Mandal, A., Lu, S. K., Anbunathan, H., Morris-Rosendahl, D., Zhang, Y. Z., Cookson, & William O. C. M. (2021). Integrated genomics point to immune vulnerabilities in pleural mesothelioma. *Scientific Reports, 11*(1), 19138. doi:10.1038/s41598-021-98414-w

Neumann, B., Hösl, S., Schwab, K., Theuring, F., & Jakubowski, N. (2020). Multiplex LA-ICP-MS bio-imaging of brain tissue of a parkinsonian mouse model stained with metal-coded affinity-tagged antibodies and coated with indium-spiked commercial inks as internal standards. *Journal of Neuroscience Methods, 334*, 108591. doi:10.1016/j.jneumeth.2020.108591

Nguyen, B. H., Montgomery, R., Fadia, M., Wang, J., & Ali, S. (2018). PD-L1 expression associated with worse survival outcome in malignant pleural mesothelioma. *Asia-Pacific Journal of Clinical Oncology, 14*(1), 69-73. doi:10.1111/ajco.12788

Norris, J. L., & Caprioli, R. M. (2013). Analysis of tissue specimens by matrix-assisted laser desorption/ionization imaging mass spectrometry in biological and clinical research. *Chemical Reviews, 113*(4), 2309-2342. doi:10.1021/cr3004295

Nuvoli, B., Camera, E., Mastrofrancesco, A., Briganti, S., & Galati, R. (2018). Modulation of reactive oxygen species via ERK and STAT3 dependent signalling are involved in the response of mesothelioma cells to exemestane. *Free Radical Biology & Medicine, 115*, 266-277. doi:10.1016/j.freeradbiomed.2017.12.008

Ohar, J. A., Cheung, M., Talarchek, J., Howard, S. E., Howard, T. D., Hesdorffer, M., Testa, J. R. (2016). Germline BAP1 mutational landscape of asbestos-exposed malignant mesothelioma patients with family history of cancer. *Cancer Research (Chicago, Ill.), 76*(2), 206-215. doi:10.1158/0008-5472.CAN-15-0295

Oikonomou, C. M., & Jensen, G. J. (2017). Cellular electron cryotomography: Toward structural biology in situ. *Annual Review of Biochemistry, 86*(1), 873-896. doi:10.1146/annurev-biochem-061516-044741

Okazaki, Y., Chew, S. H., Nagai, H., Yamashita, Y., Ohara, H., Jiang, L., & Toyokuni, S. (2020). Overexpression of miR-199/214 is a distinctive feature of iron-induced and asbestos-induced sarcomatoid mesothelioma in rats. *Cancer Science, 111*(6), 2016-2027. doi:10.1111/cas.14405

Orellana, F. A., Gálvez, C. G., Roldán, M. T., García-Ruiz, C., & García-Ruiz, C. (2013). Applications of laser-ablation-inductively-coupled plasma-mass spectrometry in chemical analysis of forensic evidence. *TrAC, Trends in Analytical Chemistry (Regular Ed.), 42*, 1-34. doi:10.1016/j.trac.2012.09.015

Osborn, M., Lowe, J., Attanoos, R., & Gibbs, A. (2017). Guidelines on autopsy practice industrial/occupational-related lung disease deaths including asbestos. *The Royal College of Pathologists*

Paleari, L., Rotolo, N., Imperatori, A., Puzone, R., Sessa, F., Franzi, F., & Paganuzzi, M. (2009). Osteopontin is not a specific marker in malignant pleural mesothelioma. *The International Journal of Biological Markers, 24*(2), 112-117. doi:10.5301/JBM.2009.5043

Pande, P., Mosleh, T. A., & Aust, A. E. (2006). Role of alphavbeta5 integrin receptor in endocytosis of crocidolite and its effect on intracellular glutathione levels in human lung epithelial (A549) cells. *Toxicology and Applied Pharmacology, 210*(1-2), 70-77.

Panou, V., Louw, A., Szejniuk, W. M., Meristoudis, C., Chai, S. M., Andersen, L. L., & Røe, O. D. (2020). BAP1 loss predicts longer survival for mesothelioma patients treated with pemetrexed-based chemotherapy. *European Respiratory Journal* 56: 4490; DOI: 10.1183/13993003.congress-2020.4490

Parvizi-Majidi, A., & Begum, S. (2015). *Whiskers and particulates* Elsevier Inc. doi:10.1016/B978-0-12-803581-8.03810-8

Pascolo, L., Gianoncelli, A., Kaulich, B., Rizzardi, C., Schneider, M., Bottin, C., & Melato, M. (2011). Synchrotron soft X-ray imaging and fluorescence microscopy reveal novel features of asbestos body morphology and composition in human lung tissues. *Particle and Fibre Toxicology, 8*(1), 7. doi:10.1186/1743-8977-8-7

Pascolo, L., Gianoncelli, A., Schneider, G., Salomé, M., Schneider, M., Calligaro, C., & Rizzardi, C. (2013). The interaction of asbestos and iron in lung tissue revealed by synchrotron-based scanning X-ray microscopy. *Scientific Reports, 3*(1), 1123. doi:10.1038/srep01123

Pass, H. I., Lott, D., Lonardo, F., Harbut, M., Liu, Z., Tang, N., & Wali, A. (2005). Asbestos exposure, pleural mesothelioma, and serum osteopontin levels. *The New England Journal of Medicine, 353*(15), 1564-1573. doi:10.1056/NEJMoa051185

Pedrosa D. A., Rodrigues K. A., de Carvalho L. C., Trópia de Abreu, A., & Garcia Praça L. M. (2019). Quantitative analysis of plant leaf elements using the LA-ICP-MS technique. *International Journal of Mass Spectrometry, 435*, 251-258. doi:10.1016/j.ijms.2018.10.037

Pellegrini, L., Xue, J., Larson, D., Pastorino, S., Jube, S., Forest, K. H., & Yang, H. (2017). HMGB1 targeting by ethyl pyruvate suppresses malignant phenotype of human mesothelioma. *Oncotarget, 8*(14), 22649-22661. doi:10.18632/oncotarget.15152

Penzo, M., Montanaro, L., Treré, D., & Derenzini, M. (2019). The ribosome Biogenesis—Cancer connection. *Cells (Basel, Switzerland), 8*(1), 55. doi:10.3390/cells8010055

Pfeifhofer-Obermair, C., Tymoszuk, P., Petzer, V., Weiss, G., & Nairz, M. (2018). Iron in the tumor microenvironment-connecting the dots. *Frontiers in Oncology, 8*, 549. doi:10.3389/fonc.2018.00549

Pierce, J. S., McKinley, M. A., Paustenbach, D. J., & Finley, B. L. (2008). An evaluation of reported no-effect chrysotile asbestos exposures for lung cancer

and mesothelioma. *CRC Critical Reviews in Toxicology, 38*(3), 191-214. doi:10.1080/10408440701845609

Pietrofesa, R. A., Velalopoulou, A., Albelda, S. M., & Christofidou-Solomidou, M. (2016). Asbestos induces oxidative stress and activation of Nrf2 signaling in murine macrophages: Chemopreventive role of the synthetic lignan secoisolariciresinol diglucoside (LGM2605). *International Journal of Molecular Sciences, 17*(3), 322. doi:10.3390/ijms17030322

Pirnay, J., Baudoux, E., Cornu, O., Delforge, A., Delloye, C., Guns, J., & Sterckx, S. (2015). Access to human tissues for research and product development: From EU regulation to alarming legal developments in belgium. *EMBO Reports, 16*(5), 557-562. doi:10.15252/embr.201540070

Pollastri, S., Perchiazzi, N., Gigli, L., Ferretti, P., Cavallo, A., Bursi Gandolfi, N., & Gualtieri, A. (2017). *The crystal structure of mineral fibres. 2. amosite and fibrous anthophyllite* Edizioni Nuova Cultura. doi:10.2451/2017PM693

Pollastri, S., Gualtieri, A. F., Vigliaturo, R., Ignatyev, K., Strafella, E., Pugnaloni, A., & Croce, A. (2016). Stability of mineral fibres in contact with human cell cultures. an in situ μXANES, μXRD and XRF iron mapping study. *Chemosphere (Oxford), 164*, 547-557. doi:10.1016/j.chemosphere.2016.08.139

Pornwilard, M., Weiskirchen, R., Gassler, N., Bosserhoff, A. K., & Becker, J. S. (2013). Novel bioimaging techniques of metals by laser ablation inductively coupled plasma mass spectrometry for diagnosis of fibrotic and cirrhotic liver disorders. *PloS One, 8*(3), e58702. doi:10.1371/journal.pone.0058702

Pott, F., Roller, M., Ziem, U., Reiffer, F. J., Bellmann, B., Rosenbruch, M., & Huth, F. (1989). Carcinogenicity studies on natural and man-made fibres with the intraperitoneal test in rats. *IARC Scientific Publications,* (90), 173.

Pruett, N., Singh, A., Shankar, A., Schrump, D. S., & Hoang, C. D. (2020). Normal mesothelial cell lines newly derived from human pleural biopsy

explants. *American Journal of Physiology. Lung Cellular and Molecular Physiology, 319*(4), L652-L660. doi:10.1152/ajplung.00141.2020

Pugnaloni, A., Giantomassi, F., Lucarini, G., Capella, S., Belmonte, M. M., Orciani, M., & Belluso, E. (2010). Effects of asbestiform antigorite on human alveolar epithelial A549 cells: A morphological and immunohistochemical study. *Acta Histochemica, 112*(2), 133-146. doi:10.1016/j.acthis.2008.10.002

Pulford, E., Huilgol, K., Moffat, D., Henderson, D. W., & Klebe, S. (2017). Malignant mesothelioma, BAP1 immunohistochemistry, and VEGFA: Does BAP1 have potential for early diagnosis and assessment of prognosis? *Disease Markers, 2017*, 1310478-10. doi:10.1155/2017/1310478

Puxeddu, E., Comandini, A., Cavalli, F., Pezzuto, G., D'Ambrosio, C., Senis, L., & Saltini, C. (2014). Iron laden macrophages in idiopathic pulmonary fibrosis: The telltale of occult alveolar hemorrhage? *Pulmonary Pharmacology & Therapeutics, 28*(1), 35-40. doi:10.1016/j.pupt.2013.12.002

Qi, F., Okimoto, G., Jube, S., Napolitano, A., Pass, H. I., Laczko, R., & Carbone, M. (2013). Continuous exposure to chrysotile asbestos can cause transformation of human mesothelial cells via HMGB1 and TNF-α signaling. *The American Journal of Pathology, 183*(5), 1654-1666. doi:10.1016/j.ajpath.2013.07.029

Qiu, W., Fu, Z., Xu, G. G., Grassucci, R. A., Zhang, Y., Frank, J., & Guo, Y. (2018). Structure and activity of lipid bilayer within a membrane-protein transporter. *Proceedings of the National Academy of Sciences - PNAS, 115*(51), 12985-12990. doi:10.1073/pnas.1812526115

Rake, C., Gilham, C., Hatch, J., Darnton, A., Hodgson, J., & Peto, J. (2009). Occupational, domestic and environmental mesothelioma risks in the british population: A case-control study. *British Journal of Cancer, 100*(7), 1175-1183. doi:10.1038/sj.bjc.6604879

Ramanaidou, E., Wells, M., Lau, I., & Laukamp, C. (2015). Characterization of iron ore by visible and infrared reflectance and, Raman spectroscopies. *Iron ore* (pp. 191-228) Elsevier Ltd. doi:10.1016/B978-1-78242-156-6.00006-X

Ramazzini, C. (2011). Asbestos is still with us: Repeat call for a universal ban. *American Journal of Industrial Medicine, 54*(2), 168-173. doi:10.1002/ajim.20892

Rampersad, S. N. (2012). Multiple applications of alamar blue as an indicator of metabolic function and cellular health in cell viability bioassays. *Sensors (Basel, Switzerland), 12*(9), 12347-12360. doi:10.3390/s120912347

Ramundo, V., Zanirato, G., & Aldieri, E. (2021). The epithelial-to-mesenchymal transition (EMT) in the development and metastasis of malignant pleural mesothelioma. *International Journal of Molecular Sciences, 22*(22), 12216. doi:10.3390/ijms222212216

Ravi, M., Paramesh, V., Kaviya, S. R., Anuradha, E., & Solomon, F. D. P. (2015). 3D cell culture systems: Advantages and applications. *Journal of Cellular Physiology, 230*(1), 16-26. doi:10.1002/jcp.24683

Rehrauer, H., Wu, L., Blum, W., Pecze, L., Henzi, T., Serre-Beinier, V., Felley-& Bosco, E. (2018). How asbestos drives the tissue towards tumors: YAP activation, macrophage and mesothelial precursor recruitment, RNA editing, and somatic mutations. *Oncogene, 37*(20), 2645-2659. doi:10.1038/s41388-018-0153-z

Revelli, M., Chiesa, F., Del Prato, A., Tagliafico, A., Rosenberg, I., Canessa, P. A., & Villa, A. (2016). Role of respiratory-triggered diffusion-weighted MRI in the assessment of pleural disease. *British Journal of Radiology, 89*(1064), 20160289. doi:10.1259/bjr.20160289

Riaz, S. P., Coupland, V. H., Lüchtenborg, M., Peake, M. D., & Møller, H. (2012). Mesothelioma incidence projections in Southeast England. *The European Respiratory Journal, 40*(4), 965-968. doi:10.1183/09031936.00168111

Ribatti, D., Tamma, R., & Annese, T. (2020). Epithelial-mesenchymal transition in cancer: A historical overview. *Translational Oncology, 13*(6), 100773. doi:10.1016/j.tranon.2020.100773

Ricchiuti, Pereira Dolores, Punturo Rosalda, Giorno Eugenia, Miriello Domenico, & Bloise Andrea. (2021). Hazardous elements in asbestos tremolite from the basilicata region, southern italy: A first step. *Fibers, 9*(47), 47. doi:10.3390/fib9080047

Riesop, D., Hirner, A. V., Rusch, P., & Bankfalvi, A. (2015). Zinc distribution within breast cancer tissue: A possible marker for histological grading? *Journal of Cancer Research and Clinical Oncology, 141*(7), 1321-1331. doi:10.1007/s00432-015-1932-3

Robinson, C., Walsh, A., Larma, I., O'Halloran, S., Nowak, A. K., & Lake, R. A. (2011). MexTAg mice exposed to asbestos develop cancer that faithfully replicates key features of the pathogenesis of human mesothelioma. *European Journal of Cancer (1990), 47*(1), 151-161. doi:10.1016/j.ejca.2010.08.015

Røe, O. D., & Stella, G. M. (2015). Malignant pleural mesothelioma: History, controversy and future of a manmade epidemic. *European Respiratory Review : An Official Journal of the European Respiratory Society, 24*(135), 115-131. doi:10.1183/09059180.00007014

Rooney, C., Nixon, C., Blyth, K., Sethi, T., Murphy, D., & McCaughan, F. (2019). S45 VISTA expression in malignant pleural mesothelioma. *Thorax, 74*(Suppl 2), A29. doi:10.1136/thorax-2019-BTSabstracts2019.51

Rosenthal, G. J., Germolec, D. R., Blazka, M. E., Corsini, E., Simeonova, P., Pollock, P., & Luster, M. I. (1994). Asbestos stimulates IL-8 production from human lung epithelial cells. *The Journal of Immunology (1950), 153*(7), 3237-3244.

Rusch, P., Hirner, A. V., Schmitz, O., Kimmig, R., Hoffmann, O., & Diel, M. (2021). Zinc distribution within breast cancer tissue of different intrinsic

subtypes. *Archives of Gynecology and Obstetrics, 303*(1), 195-205. doi:10.1007/s00404-020-05789-8

Rusch, V. W., Chansky, K., Kindler, H. L., Nowak, A. K., Pass, H. I., Rice, D. C., & Yoshimura, M. (2016). The IASLC mesothelioma staging project: Proposals for the M descriptors and for revision of the TNM stage groupings in the forthcoming (eighth) edition of the TNM classification for mesothelioma. *Journal of Thoracic Oncology, 11*(12), 2112-2119. doi:10.1016/j.jtho.2016.09.124

Russo, C., Brickelbank, N., Duckett, C., Mellor, S., Rumbelow, S., & Clench, M. R. (2018). Quantitative investigation of terbinafine hydrochloride absorption into a living skin equivalent model by MALDI-MSI. *Analytical Chemistry (Washington), 90*(16), 10031-10038. doi:10.1021/acs.analchem.8b02648

Saggar, J. K., Yu, M., Tan, Q., & Tannock, I. F. (2013). The tumor microenvironment and strategies to improve drug distribution. *Frontiers in Oncology, 3*, 154. doi:10.3389/fonc.2013.00154

Šala, M., Šelih, V. S., Stremtan, C. C., T ma, T., & van Elteren, J. T. (2021). Implications of laser shot dosage on image quality in LA-ICP-QMS imaging. *Journal of Analytical Atomic Spectrometry, 36*(1), 75-79. doi:10.1039/d0ja00381f

Saraya, T., Ohkuma, K., Fujiwara, M., & Ishii, H. (2022). Diagnostic method for malignant pleural effusion distinguishing malignant mesothelioma from lung cancer using pleural carcinoembryonic antigen and hyaluronic acid levels. *Medicine (Baltimore), 101*(1), e28517. doi:10.1097/MD.0000000000028517

Sato, T., & Sekido, Y. (2018). NF2/merlin inactivation and potential therapeutic targets in mesothelioma. *International Journal of Molecular Sciences, 19*(4), 988. doi:10.3390/ijms19040988

Sayan, M., & Mossman, B. T. (2015). The NLRP3 inflammasome in pathogenic particle and fibre-associated lung inflammation and diseases. *Particle and Fibre Toxicology, 13*(1) doi:10.1186/s12989-016-0162-4

Scaffidi, P., Misteli, T., & Bianchi, M. E. (2010). Release of chromatin protein HMGB1 by necrotic cells triggers inflammation. *Nature (London), 467*(7315), 622. doi:10.1038/nature09475

Schaper, F., Westra, J., & Bijl, M. (2014). Recent developments in the role of high-mobility group box 1 in systemic lupus erythematosus. *Molecular Medicine (Cambridge, Mass.), 20*(1), 72-79. doi:10.2119/molmed.2014.00019

Scheule, R. K., & Holian, A. (1990). Modification of asbestos bioactivity for the alveolar macrophage by selective protein adsorption. *American Journal of Respiratory Cell and Molecular Biology, 2*(5), 441-448. doi:10.1165/ajrcmb/2.5.441

Schiller, J. E., Payne, S. L., & Khalafalla, S. E. (1980). Surface charge heterogeneity in amphibole cleavage fragments and asbestos fibers. *Science, 209*(4464), 1530-1532. doi:10.1126/science.209.4464.1530

Schottenfeld, D., Beebe-Dimmer, J. L., Buffler, P. A., & Omenn, G. S. (2013). Current perspective on the global and united states cancer burden attributable to lifestyle and environmental risk factors. *Annual Review of Public Health, 34*(1), 97-117. doi:10.1146/annurev-publhealth-031912-114350

Sekido, Y. (2010). Genomic abnormalities and signal transduction dysregulation in malignant mesothelioma cells. *Cancer Science, 101*(1), 1-6. doi:10.1111/j.1349-7006.2009.01336.x

Sekido, Y., Pass, H. I., Bader, S., Mew, D. J. Y., Christman, M. F., Gazdar, A. F., & Minna, J. D. (1995). Neurofibromatosis type 2 (NF2) gene is somatically mutated in mesothelioma but not in lung cancer. *Cancer Research, 55*(6), 1227-1231.

Serra, M., Columbano, A., Ammarah, U., Mazzone, M., & Menga, A. (2020). Understanding metal dynamics between cancer cells and macrophages: Competition or synergism? *Frontiers in Oncology, 10*, 646. doi:10.3389/fonc.2020.00646

Shariatgorji, M., Nilsson, A., Bonta, M., Gan, J., Marklund, N., Clausen, F., & Andrén, P. E. (2016). Direct imaging of elemental distributions in tissue sections by laser ablation mass spectrometry. *Methods (San Diego, Calif.), 104*, 86-92. doi:10.1016/j.ymeth.2016.05.021

Sheard, M. A., & Vojtesek, B. (2002). Simian virus-40 infection inhibits DNA damage-induced enhancement of CD95 expression and function. *Oncogene, 21*(2), 190-197. doi:10.1038/sj.onc.1205043

Shen, J., Sun, X., & Zhou, J. (2020). Insights into the role of mesothelin as a diagnostic and therapeutic target in ovarian carcinoma. *Frontiers in Oncology, 10*, 1263. doi:10.3389/fonc.2020.01263

Shigemitsu, K., Sekido, Y., Usami, N., Mori, S., Sato, M., Horio, Y., & Shimokata, K. (2001). Genetic alteration of the [besa]-catenin gene in human lung cancer and malignant mesothelioma and identification of a new 3p21.3 homozygous deletion. *Oncogene, 20*(31), 4249. doi:10.1038/sj.onc.1204557

Shimadzu.com retrieved from https://www.shimadzu.com/an/service-support/technical-support/analysis-basics/fundamental/mass_analyzers.html

Shimizu, Y., Dobashi, K., Kusakbe, T., Nagamine, T., Oikawa, M., Satoh, T., & Mori, M. (2008). In-air micro-particle induced X-ray emission analysis of asbestos and metals in lung tissue. *International Journal of Immunopathology and Pharmacology, 21*(3), 567-576. doi:10.1177/039463200802100309

Shukla, A., Barrett, T. F., MacPherson, M. B., Hillegass, J. M., Fukagawa, N. K., Swain, W. A., & Mossman, B. T. (2011). An extracellular Signal–Regulated kinase 2 survival pathway mediates resistance of human mesothelioma cells to

asbestos-induced injury. *American Journal of Respiratory Cell and Molecular Biology, 45*(5), 906-914. doi:10.1165/rcmb.2010-0282OC

Spraggins, J. M., Rizzo, D. G., Moore, J. L., Noto, M. J., Skaar, E. P., & Caprioli, R. M. (2016). Next-generation technologies for spatial proteomics: Integrating ultra-high speed MALDI-TOF and high mass resolution MALDI FTICR imaging mass spectrometry for protein analysis. *Proteomics (Weinheim), 16*(11-12), 1678-1689. doi:10.1002/pmic.201600003

Steenstra, E. S., Berndt, J., Klemme, S., & Van Westrenen, W. (2019). LA-ICP-MS analyses of Fe-rich alloys: Quantification of matrix effects for 193 nm excimer laser systems. *Journal of Analytical Atomic Spectrometry, 34*(1), 222-231. doi:10.1039/C8JA00291F

Stewart, J. H., Tran, T., Levi, N., Tsai, W. S., Schrump, D. S., & Nguyen, D. M. (2007). The essential role of the mitochondria and reactive oxygen species in cisplatin-mediated enhancement of fas ligand-induced apoptosis in malignant pleural mesothelioma. *Journal of Surgical Research, 141*(1), 120-131. doi:10.1016/j.jss.2007.03.048

Stewart, T. J. (2019). Across the spectrum: Integrating multidimensional metal analytics for in situ metallomic imaging. *Metallomics, 11*(1), 29-49. doi:10.1039/c8mt00235e

Strohalm, M., Kavan, D., Novák, P., Volný, M., & Havlíček, V. (2010). mMass 3: A cross-platform software environment for precise analysis of mass spectrometric data. *Analytical Chemistry (Washington), 82*(11), 4648-4651. doi:10.1021/ac100818g

Sung, H., Ferlay, J., Siegel, R. L., Laversanne, M., Soerjomataram, I., Jemal, A., & Bray, F. (2021). Global cancer statistics 2020: GLOBOCAN estimates of incidence and mortality worldwide for 36 cancers in 185 countries. *CA: A Cancer Journal for Clinicians, 71*(3), 209-249. doi:10.3322/caac.21660

Surour, A. A. (2015). Cu–Mn–Fe alloys and mn-rich amphiboles in ancient copper slags from the jabal samran area, saudi arabia: With synopsis on chemistry of Fe–Mn(III) oxyhydroxides in alteration zones. *Journal of African Earth Sciences (1994), 101*, 70-83. doi:10.1016/j.jafrearsci.2014.09.005

Szlosarek, P. W., Phillips, M. M., Pavlyk, I., Steele, J., Shamash, J., Spicer, J., & Sheaff, M. (2020). Expansion phase 1 study of pegargiminase plus pemetrexed and cisplatin in patients with argininosuccinate synthetase 1–Deficient mesothelioma: Safety, efficacy, and resistance mechanisms. *JTO Clinical and Research Reports, 1*(4), 100093. doi:10.1016/j.jtocrr.2020.100093

Szlosarek, P. W., Steele, J. P., Nolan, L., Gilligan, D., Taylor, P., Spicer, J., & Hackshaw, A. (2016). Arginine deprivation with pegylated arginine deiminase in patients with argininosuccinate synthetase 1–Deficient malignant pleural mesothelioma: A randomized clinical trial. *JAMA Oncology, 3*(1), 58-66. doi:10.1001/jamaoncol.2016.3049

Tabata, C., Shibata, E., Tabata, R., Kanemura, S., Mikami, K., Nogi, Y., & Nakano, T. (2013). Serum HMGB1 as a prognostic marker for malignant pleural mesothelioma. *BMC Cancer, 13*(1), 205. doi:10.1186/1471-2407-13-205

Tannapfel, A. (2011). Malignant mesothelioma. *Springer.* Berlin, Heidelberg. doi:10.1007/978-3-642-10862-4

Technologynetworks.com retrieved from https://cdn.technologynetworks.com/tn/images/body/msseoarticleessentialimage21620135908336.png

Theiner, S., Schreiber-Brynzak, E., Jakupec, M. A., Galanski, M., Koellensperger, G., & Keppler, B. K. (2016). LA-ICP-MS imaging in multicellular tumor spheroids - a novel tool in the preclinical development of metal-based anticancer drugs. *Metallomics, 8*(4), 398-42. doi:10.1039/c5mt00276a

Theiner, S., Schweikert, A., Haberler, C., Peyrl, A., & Koellensperger, G. (2020). Laser ablation-ICP-TOFMS imaging of germ cell tumors of patients undergoing

platinum-based chemotherapy. *Metallomics, 12*(8), 1246-1252. doi:10.1039/D0MT00080A

Thompson, J. K., MacPherson, M. B., Beuschel, S. L., & Shukla, A. (2017). Asbestos-induced mesothelial to fibroblastic transition is modulated by the inflammasome. *The American Journal of Pathology, 187*(3), 665-678. doi:10.1016/j.ajpath.2016.11.008

Tomasetti, C., Li, L., & Vogelstein, B. (2017). Stem cell divisions, somatic mutations, cancer etiology, and cancer prevention. *Science (New York, N.Y.), 355*(6331), 1330-1334. doi:10.1126/science.aaf9011

Torre, L. A., Siegel, R. L., Ward, E. M., & Jemal, A. (2016). Global cancer incidence and mortality rates and trends--an update. *Cancer Epidemiology, Biomarkers & Prevention : A Publication of the American Association for Cancer Research, Cosponsored by the American Society of Preventive Oncology, 25*(1), 16-27. doi:10.1158/1055-9965.EPI-15-0578

Toyokuni, S. (2002). Iron and carcinogenesis: From fenton reaction to target genes. *Redox Report: Communications in Free Radical Research, 7*(4), 189-197. doi:10.1179/135100002125000596

Trevisan, E., Zabucchi, G., Pascolo, L., Pascotto, E., Casarsa, C., Lucattelli, M., & Borelli, V. (2016). Histopathological data of iron and calcium in the mouse lung after asbestos exposure. *Data in Brief, 6*, 769-775. doi:10.1016/j.dib.2016.01.026

Turini, S., Bergandi, L., Gazzano, E., Prato, M., & Aldieri, E. (2019). Epithelial to mesenchymal transition in human mesothelial cells exposed to asbestos fibers: Role of TGF-β as mediator of malignant mesothelioma development or metastasis via EMT event. *International Journal of Molecular Sciences, 20*(1), 150. doi:10.3390/ijms20010150

Ujiie, H., Kadota, K., Nitadori, J., Aerts, J. G., Woo, K. M., Sima, C. S., & Adusumilli, P. S. (2015). The tumoral and stromal immune microenvironment in malignant pleural mesothelioma: A comprehensive analysis reveals prognostic

immune markers. *Oncoimmunology, 4*(6), e1009285. doi:10.1080/2162402X.2015.1009285

Ulloa, L., Ochani, M., Yang, H., Tanovic, M., Halperin, D., Yang, R., & Tracey, K. J. (2002). Ethyl pyruvate prevents lethality in mice with established lethal sepsis and systemic inflammation. *Proceedings of the National Academy of Sciences - PNAS, 99*(19), 12351-12356. doi:10.1073/pnas.192222999

Uniprot. Retrieved from https://www.uniprot.org/blast/

Van Acker, T., Buckle, T., Van Malderen, S. J. M., van Willigen, D. M., van Unen, V., van Leeuwen, F. W. B., & Vanhaecke, F. (2019). High-resolution imaging and single-cell analysis via laser ablation-inductively coupled plasma-mass spectrometry for the determination of membranous receptor expression levels in breast cancer cell lines using receptor-specific hybrid tracers. *Analytica Chimica Acta, 1074*, 43-53. doi:10.1016/j.aca.2019.04.064

Van Acker, T., Van Malderen, Stijn J. M, Colina-Vegas, L., Ramachandran, R. K., & Vanhaecke, F. (2019). Selective ablation of biological tissue and single cells on a glass substrate by controlling the laser energy density of nanosecond 193 nm laser radiation. *Journal of Analytical Atomic Spectrometry, 34*(10), 1957-1964. doi:10.1039/C9JA00126C

Van Malderen, S. J. M., Van Acker, T., & Vanhaecke, F. (2020). Sub-micrometer nanosecond LA-ICP-MS imaging at pixel acquisition rates above 250 hz via a low-dispersion setup. *Analytical Chemistry (Washington), 92*(8), 5756-5764. doi:10.1021/acs.analchem.9b05056

Van Norman, G. A. (2019). Limitations of animal studies for predicting toxicity in clinical trials: Is it time to rethink our current approach? *JACC. Basic to Translational Science, 4*(7), 845-854. doi:10.1016/j.jacbts.2019.10.008

Van Oss, C. J., Naim, J. O., Costanzo, P. M., Giese, R. F., Wu, W., & Sorling, A. F. (1999). Impact of different asbestos species and other mineral particles on

pulmonary pathogenesis. *Clays and Clay Minerals, 47*(6), 697-707. doi:10.1346/CCMN.1999.0470603

Van Zandwijk, N., Clarke, C., Henderson, D., Musk, A. W., Fong, K., Nowak, A., & Penman, A. (2013). Guidelines for the diagnosis and treatment of malignant pleural mesothelioma. *Journal of Thoracic Disease, 5*(6), E254-E307. doi:10.3978/j.issn.2072-1439.2013.11.28

Vannucci, J., Bellezza, G., Matricardi, A., Moretti, G., Bufalari, A., Cagini, L., & Daddi, N. (2018). Observational analysis on inflammatory reaction to talc pleurodesis: Small and large animal model series review. *Experimental and Therapeutic Medicine, 15*(1), 733-738. doi:10.3892/etm.2017.5454

Villarroel-Espindola, F., Yu, X., Datar, I., Mani, N., Sanmamed, M., Velcheti, V., & Schalper, K. A. (2018). Spatially resolved and quantitative analysis of VISTA/PD-1H as a novel immunotherapy target in human non-small cell lung cancer. *Clinical Cancer Research, 24*(7), 1562-1573. doi:10.1158/1078-0432.CCR-17-2542

Virta, R. L. (2006). *Worldwide asbestos supply and consumption trends from 1900 through 2003*. Reston, Va: U.S. Geological Survey.

Visonà, S. D., Capella, S., Bodini, S., Borrelli, P., Villani, S., Crespi, E., & Belluso, E. (2021). Evaluation of deposition and clearance of asbestos (detected by SEM-EDS) in lungs of deceased subjects environmentally and/or occupationally exposed in broni (pavia, northern italy). *Frontiers in Public Health, 9*, 678040. doi:10.3389/fpubh.2021.678040

Vodnala, S. K., Eil, R., Kishton, R. J., Sukumar, M., Yamamoto, T. N., Ha, N., & Restifo, N. P. (2019). T cell stemness and dysfunction in tumors are triggered by a common mechanism. *Science (American Association for the Advancement of Science), 363*(6434), eaau0135. doi:10.1126/science.aau0135

Voloaca, O. M., Clench, M. R., Koellensperger, G., Cole, L. M., Haywood-Small, S. L., & Theiner, S. (2022). Elemental mapping of human malignant

mesothelioma tissue samples using high-speed LA-ICP-TOFMS imaging. *Analytical Chemistry (Washington),* doi:10.1021/acs.analchem.1c04857

Voloaca, O. M., Greenhalgh, C. J., Cole, L. M., Clench, M. R., Managh, A. J., & Haywood-Small, S. L. (2020). Laser ablation inductively coupled plasma mass spectrometry as a novel clinical imaging tool to detect asbestos fibres in malignant mesothelioma. *Rapid Communications in Mass Spectrometry, 34*(21), e8906-n/a. doi:10.1002/rcm.8906

Wagner, J. (2015). Analysis of serpentine polymorphs in investigations of natural occurrences of asbestos. *Environmental Science. Processes & Impacts, 17*(5), 985-996. doi:10.1039/c5em00089k

Walzl, A., Unger, C., Kramer, N., Unterleuthner, D., Scherzer, M., Hengstschläger, M., & Dolznig, H. (2014). The resazurin reduction assay can distinguish cytotoxic from cytostatic compounds in spheroid screening assays. *Journal of Biomolecular Screening, 19*(7), 1047-1059. doi:10.1177/1087057114532352

Webber, J., Yeung, V., & Clayton, A. (2015). Extracellular vesicles as modulators of the cancer microenvironment. *Seminars in Cell & Developmental Biology, 40*, 27-34. doi:10.1016/j.semcdb.2015.01.013

Wei, B., Yang, L., Yu, J., Ye, B., & Jia, X. (2013). Are metals accumulated in human hair affected by naturally occurring asbestos fiber contamination? A case study from a rural area of china. *Biological Trace Element Research, 156*(1), 12-21. doi:10.1007/s12011-013-9840-3

Weinstein, J. N., & Ludwig, J. A. (2005). Biomarkers in cancer staging, prognosis and treatment selection. *Nature Reviews. Cancer, 5*(11), 845-856. doi:10.1038/nrc1739

Wilck, N., Balogh, A., Markó, L., Bartolomaeus, H., & Müller, D. N. (2019). The role of sodium in modulating immune cell function. *Nature Reviews. Nephrology, 15*(9), 546-558. doi:10.1038/s41581-019-0167-y

Wolf, F. I., Cittadini, A. R. M., & Maier, J. A. M. (2009). Magnesium and tumors: Ally or foe? *Cancer Treatment Reviews, 35*(4), 378-382. doi:10.1016/j.ctrv.2009.01.003

Wong, K. (2021). Cancer survival in england for patients diagnosed between 2014 and 2018 and followed up until 2019. Retrieved from https://www.gov.uk/government/statistics/cancer-survival-in-england-for-patients-diagnosed-between-2014-and-2018-and-followed-up-until-2019/cancer-survival-in-england-for-patients-diagnosed-between-2014-and-2018-and-followed-up-to-2019

Woolhouse, I., Bishop, L., Darlison, L., De Fonseka, D., Edey, A., Edwards, J., & Maskell, N. A. (2018). British thoracic society guideline for the investigation and management of malignant pleural mesothelioma. *Thorax, 73*(Suppl 1), i1-i30. doi:10.1136/thoraxjnl-2017-211321

Wu, L., Amjad, S., Yun, H., Mani, S., & de Perrot, M. (2022). A panel of emerging EMT genes identified in malignant mesothelioma. *Scientific Reports, 12*(1), 1007. doi:10.1038/s41598-022-04973-x

Wu, S., Powers, S., Zhu, W., & Hannun, Y. A. (2016). Substantial contribution of extrinsic risk factors to cancer development. *Nature, 529*(7584), 43-47. doi:10.1038/nature16166

Wu, S., Zhu, W., Thompson, P., & Hannun, Y. A. (2018). Evaluating intrinsic and non-intrinsic cancer risk factors. *Nature Communications, 9*(1), 3490-12. doi:10.1038/s41467-018-05467-z

Wynn, T. (2008). Cellular and molecular mechanisms of fibrosis. *The Journal of Pathology, 214*(2), 199-210. doi:10.1002/path.2277

Xia, J., Yu, X., Song, X., Li, G., Mao, X., & Zhang, Y. (2017). Inhibiting the cytoplasmic location of HMGB1 reverses cisplatin resistance in human cervical cancer cells. *Molecular Medicine Reports, 15*(1), 488-494. doi:10.3892/mmr.2016.6003

Xie, D., Hu, J., Wu, T., Cao, K., & Luo, X. (2021). Four immune-related genes (FN1, UGCG, CHPF2 and THBS2) as potential diagnostic and prognostic biomarkers for carbon nanotube-induced mesothelioma. *International Journal of General Medicine, 14*, 4987-5003. doi:10.2147/IJGM.S324365

Xu, A., Smilenov, L. B., He, P., Masumura, K., Nohmi, T., Yu, Z., & Hei, T. K. (2007). New insight into intrachromosomal deletions induced by chrysotile in the gpt delta transgenic mutation assay. *Environmental Health Perspectives, 115*(1), 87-92. doi:10.1289/ehp.9425

Xu, J., Kadariya, Y., Cheung, M., Pei, J., Talarchek, J., Sementino, E., & Testa, J. R. (2014). Germline mutation of Bap1 accelerates development of asbestos-induced malignant mesothelioma. *Cancer Research, 74*(16), 4388-4397. doi:10.1158/0008-5472.CAN-14-1328

Xue, J., Patergnani, S., Giorgi, C., Suarez, J., Goto, K., Bononi, A., & Yang, H. (2020). Asbestos induces mesothelial cell transformation via HMGB1-driven autophagy. *Proceedings of the National Academy of Sciences - PNAS, 117*(41), 25543-25552. doi:10.1073/pnas.2007622117

Yamagishi, K., Onuma, K., Chiba, Y., Yagi, S., Aoki, S., Sato, T., & Yamanaka, T. (2012). Generation of gaseous sulfur-containing compounds in tumour tissue and suppression of gas diffusion as an antitumour treatment. *Gut, 61*(4), 554-561. doi:10.1136/gutjnl-2011-300721

Yamashita, K., Nagai, H., Kondo, Y., Misawa, N., & Toyokuni, S. (2013). Evaluation of two distinct methods to quantify the uptake of crocidolite fibers by mesothelial cells. *Journal of Clinical Biochemistry and Nutrition, 53*(1), 27-35. doi:10.3164/jcbn.12-104

Yang, H., Pellegrini, L., Napolitano, A., Giorgi, C., Jube, S., Preti, A., & Carbone, M. (2015). Aspirin delays mesothelioma growth by inhibiting HMGB1-mediated tumor progression. *Cell Death & Disease, 6*(6), e1786. doi:10.1038/cddis.2015.153

Yang, H., Rivera, Z., Jube, S., Nasu, M., Bertino, P., Goparaju, C., & Rowley, J. D. (2010). Programmed necrosis induced by asbestos in human mesothelial cells causes high-mobility group box 1 protein release and resultant inflammation. *Proceedings of the National Academy of Sciences of the United States of America,* 107(28), 12611-12616. doi:10.1073/pnas.1006542107

Yasuda, T., Ueda, T., Takeyama, Y., Shinzeki, M., Sawa, H., Nakajima, T., & Kuroda, Y. (2006). Significant increase of serum high-mobility group box chromosomal protein 1 levels in patients with severe acute pancreatitis. *Pancreas, 33*(4), 359-363. doi:10.1097/01.mpa.0000236741.15477.8b

Ye, L., Lou, Y., Lu, L., & Fan, X. (2019). Mesothelin-targeted second generation CAR-T cells inhibit growth of mesothelin-expressing tumors in vivo. *Experimental and Therapeutic Medicine, 17*(1), 739-747. doi:10.3892/etm.2018.7015

Yoshikawa, Y., Kuribayashi, K., Minami, T., Ohmuraya, M., & Kijima, T. (2020). Epigenetic alterations and biomarkers for immune checkpoint inhibitors-current standards and future perspectives in malignant pleural mesothelioma treatment. *Frontiers in Oncology, 10*, 554570. doi:10.3389/fonc.2020.554570

Yoshikawa, Y., Sato, A., Tsujimura, T., Emi, M., Morinaga, T., Fukuoka, K., & Hashimoto-Tamaoki, T. (2012). Frequent inactivation of the BAP1 gene in epithelioid-type malignant mesothelioma. *Cancer Science, 103*(5), 868-874. doi:10.1111/j.1349-7006.2012.02223.x

Yu, S., Choi, H., Kim, I. W., & Kim, T. (2019). Conditioned medium from asbestos-exposed fibroblasts affects proliferation and invasion of lung cancer cell lines. *PloS One, 14*(9), e0222160. doi:10.1371/journal.pone.0222160

Yu, S., Choi, H., Park, G., Kim, I. W., & Kim, T. (2019). Fibrogenic effects of crocidolite, amosite, and chrysotile asbestos fibers on lung fibroblasts. *Toxicological and Environmental Chemistry, 101*(1-2), 148-164. doi:10.1080/02772248.2019.1625358

Yu, Y., Tang, D., & Kang, R. (2015). Oxidative stress-mediated HMGB1 biology. *Frontiers in Physiology, 6*, 93. doi:10.3389/fphys.2015.00093

Zhang, W., Qiu, Y., Xie, X., Fu, Y., Wang, L., & Cai, Z. (2021). B7 family members in lymphoma: Promising novel targets for tumor immunotherapy? *Frontiers in Oncology, 11*, 647526. doi:10.3389/fonc.2021.647526

Zhang, W., Wu, X., Wu, L., Zhang, W., & Zhao, X. (2015). Advances in the diagnosis, treatment and prognosis of malignant pleural mesothelioma. *Annals of Translational Medicine, 3*(13), 182. doi:10.3978/j.issn.2305-5839.2015.07.03

Zhang, W., Dai, Y., Hsu, P., Wang, H., Cheng, L., Yang, Y., & You, L. (2017). Targeting YAP in malignant pleural mesothelioma. *Journal of Cellular and Molecular Medicine, 21*(11), 2663-2676. doi:10.1111/jcmm.13182

Zhang, X. D., Gillespie, S. K., & Hersey, P. (2004). Staurosporine induces apoptosis of melanoma by both caspase-dependent and -independent apoptotic pathways. *Molecular Cancer Therapeutics, 3*(2), 187-197.

Zhao, Z., & Shilatifard, A. (2019). Epigenetic modifications of histones in cancer. *Genome Biology, 20*(1), 245. doi:10.1186/s13059-019-1870-5

Zickert, A., Palmblad, K., Sundelin, B., Chavan, S., Tracey, K. J., Bruchfeld, A., & Gunnarsson, I. (2012). Renal expression and serum levels of high mobility group box 1 protein in lupus nephritis. *Arthritis Research & Therapy, 14*(1), R36. doi:10.1186/ar3747

Zupanc, C., Franko, A., Štrbac, D., Dodič Fikfak, M., Kovač, V., Dolžan, V., & Goričar, K. (2021). Serum calretinin as a biomarker in malignant mesothelioma. *Journal of Clinical Medicine, 10*(21), 4875. doi:10.3390/jcm10214875

Appendix

Scientific publications

Voloaca, O. M., Clench, M. R., Koellensperger, G., Cole, L. M., Haywood-Small, S. L., & Theiner, S. (2022). Elemental Mapping of Human Malignant Mesothelioma Tissue Samples Using High-Speed LA-ICP-TOFMS Imaging. *Analytical Chemistry (Washington),* 10.1021/acs.analchem.1c04857

Greenhalgh, C. J.*, Voloaca, O. M.*, Shaw, P., Donard, A., Cole, L. M., Clench, M. R., Managh, A. J., & Haywood-Small, S. L. (2020). Needles in haystacks: using fast-response LA chambers and ICP-TOF-MS to identify asbestos fibres in malignant mesothelioma models. *Journal of Analytical Atomic Spectrometry,* 10.1039/D0JA00268B

Voloaca, O. M., Greenhalgh, C. J., Cole, L. M., Clench, M. R., Managh, A. J., & Haywood-Small, S. L. (2020). Laser ablation inductively coupled plasma mass spectrometry as a novel clinical imaging tool to detect asbestos fibres in malignant mesothelioma. *Rapid Communications in Mass Spectrometry, 34*(21), e8906-n/a. 10.1002/rcm.8906

Russo, C., Heaton, C., Flint, L., Voloaca, O., Haywood-Small, S., Clench, M. R., Francese, S., & Cole, L. M. (2020). Emerging applications in mass spectrometry imaging; enablers and roadblocks. *Journal of Spectral Imaging,* 9(1), a13. 10.1255/jsi.2020.a13

*First authors; These authors contributed equally.

Conferences

15th Meeting of the International Mesothelioma Interest Group (iMig 2021), Virtual Event, May 2021

Virtual MSIS OurCon MS Imaging Seminars, October 2020

EACR 2020 Virtual Congress, June 2020

East Midlands Proteomics Workshop, Sheffield, UK, October 2019

IASLC World Conference on Lung Cancer, Barcelona, Spain September 2019

40th BMSS Annual Meeting, Manchester, UK, September 2019

67th ASMS Conference on Mass Spectrometry, Atlanta, GA, USA, June 2019

39th BMSS Annual Meeting, Cambridge, UK, September 2018

XXII International Mass Spectrometry Conference, Florence, Italy, August 2018

5th SIG BMSS Mass Spectrometry Imaging Symposium, Sheffield, UK, May 2017

Laboratory visits

Institut für Analytische Chemie, University of Vienna, Vienna, Austria, Oct 2021

Chemistry Department, Loughborough University, Loughborough, May 2018; Jan 2019: 2-week visit; Mar 2019: 2-week visit; Apr 2019: 1-week visit; May 2019: 2-week visit; Aug 2019: 2-week visit; Oct 2019: 2-week visit; Nov 2019: 1-week visit; Feb 2020: 2-week visit

Santia Asbestos Management Ltd, Mansfield, Feb 2018

Workshops and training courses

Translate MedTech- IP for MedTech, virtual event, Mar 2021

Translate MedTech – Patient and Public Involvement and Engagement, virtual event, Mar 2021

Doctoral Training Alliance (DTA) Biosciences Summer School, July 2020

BMSS Introduction to Mass Spectrometry Short Course, Cambridge, Sept 2018

Beckman Coulter Life Sciences Flow cytometry 2-day training course, Sept 2018

22nd International Mass Spectrometry Conference, Mass Spectrometry Imaging short course, University of Florence, Aug 2018

DTA Summer School, Huddersfield, July 2018

BACR Special Meeting - Building Capacity in 3D tissue modelling and applications in cancer research, Leeds, May 2018

DTA Elective, London, Mar 2018

Teaching Skills Course for Doctoral Students, Sheffield Hallam Doctoral School, 4-week course, Feb 2018

STEM Ambassador Training, Sheffield, Nov 2017

DTA Autumn School, Liverpool, Nov 2017

Outreach and events

Action Mesothelioma Day (AMD), June Hancock Mesothelioma Research Fund (JHMRF), virtual event, July 2020

Young Entrepreneurs Scheme (YES2018), University of Nottingham and GSK, Stevenage, Nov 2018

AMD, JHMRF - Meet the Experts, Leeds, July 2018

STEM Ambassador Science Week and Open Days, 2017-2020

Funding and awards

“MRN-iMig 2020 travel fellowship award” £2000, Feb 2020

“JHMRF 2020 Travel Grant”, £500, Jan 2020

“Researcher-led Activities Fund” £150 towards organising “Wellbeing Week” for PGR Students, June 2019

“John Beynon Travel and Conference Fund” £350, awarded by BMSS, Apr 2019

Analytical Chemistry Trust Fund, £650 awarded by RSC, Mar 2019

ASMS Student Stipend 200$, awarded by ASMS, Feb 2019

“Nico Nibbering Travel Award” £200, awarded by the IMSF, Aug 2018

“John Beynon Travel and Conference Fund” £300, awarded by BMSS, July 2018

“Researcher-led Activities Fund” £500 towards organising “Wellbeing Week” for PGRS, Nov 2017